Science books for inquisitive kids p. 1108

The perils of mining sand from beaches p. 1116

Stellar evidence of super-heavy elements p. 1177

Science

$15
8 DECEMBER 2023
science.org

AAAS

CURIOUS MINDS

The cognitive powers of farm animals p. 1103

EDITORIAL

New hope for methane reduction

The Paris Agreement is not on track to meet its goals. But there's a sliver of hope. Something can be done about methane, the second-most important anthropogenic greenhouse gas. With a lifetime of around a decade, cutting methane will have rapid impact. Much of the hope rests on China's new Methane Emissions Control Action Plan, accompanying the joint commitment for methane action announced with Chinese Premier Xi's and US President Biden's November meeting.

The UN climate summit now underway (COP28) intends a "global stocktake" of Paris Agreement progress. The unexpected complication is methane's accelerating growth, now around 15 parts per billion per year. Although methane's growth may include climate feedbacks in the natural biosphere, the remedy is urgent deep cuts in human emissions. Toward this, COP26 in 2021 launched the Global Methane Pledge: 150 countries have promised 30% reductions in anthropogenic emissions by 2030. If these pledges are fully implemented, the Paris Agreement still has a chance.

> "If these pledges are fully implemented, the Paris Agreement still has a chance."

But for many signatory nations, there is a widening gap between promises and concrete actions—a gap that urgently needs to be tracked by improved independent scientific measurement. Critically, China, the world's biggest source of anthropogenic methane, has not joined the Pledge, nor have major emitters India, Russia, Iran, Venezuela, or South Africa. Satellite observation suggests that Chinese emissions in 2019 were about 65 million tonnes (Mt), or 15 to 20% of global anthropogenic emission, comparable with China's proportion of Earth's population. Thus, China's new plan has major importance, although it lacks timetabled targets.

To join the Pledge, China must cut emissions by around 20 Mt/year by 2030. Is this achievable? There is precedent. In a similar period, 2002 to 2009, Britain cut methane emissions by more than 30%, with per capita emissions now lower than China's and approaching India's. Some mitigation costs are low or even negative. Satellite observation, although with very wide uncertainty, suggests that China annually emits roughly 19 Mt from the energy sector, 18 Mt from livestock, 16 Mt from waste and other sources, and 12 Mt from rice agriculture. Between 1997 and 2004, the UK nearly halved methane leaks from energy sources. Although reducing coal emissions is not easy, by 2030 China may achieve up to 8 Mt in cuts. From waste and other sources, China may cut another 8 Mt. Some livestock emissions (such as manure) and rice emissions are tractable: China might cut 4 Mt. With determination, China could meet the Pledge by 2030.

Europe and the United States are doing much to reduce emissions, tightening regulatory frameworks. If China too fulfills the Global Methane Pledge, the benefits will be profound, to China and to the world. India, another great methane emitter and possible critical point of failure for the Paris Agreement, might address its waste heaps, coal vents, and biomass fires, also cutting air pollution. Big nonsignatory emitters Russia, Iran, Venezuela, Algeria, and South Africa similarly have multiple reduction options.

Coal, a huge methane source, troubles many nonsignatory nations. Coal provides mass employment and energy security. Abandoning coal takes decades and brings social distress, unless balanced by investment in alternatives. Europe made many mistakes reducing its coal industry. The political costs still reverberate. But it can be done.

COP28 will hear clamor for loss and damage climate reparations. In the Rio Declaration and March 1994 Framework Convention on Climate Change, humanity first recognized global warming's danger. There is thus a "polluter pays" argument that anthropogenic greenhouse gas emissions since 1994 are culpable, incurring reparation obligations. A good way to begin lessening reparation risk is to fulfill the Global Methane Pledge.

China and India, the most populous nations, will suffer greatly from climate warming impacts. So will the United States, Australia, and Canada, with much higher per capita methane emissions. Nations must prioritize between energy security and food security. If gas and coal come first, and anthropogenic methane emissions continue to drive global warming, the climate threat to food crops grows. Energy has many sources, but food has few. To eat securely means minimizing climate risk. All nations need urgent, determined action to cut methane emissions, giving the Paris Agreement a chance.

US President Lincoln once offered this choice to Congress: "We shall nobly save or meanly lose the last best hope of Earth." To avert ruinous climate impacts, Earth's last best hope is the Paris Agreement. We should not abandon that hope. It has a chance; we should nobly save it.

– Euan G. Nisbet*

PHOTO: COURTESY OF EUAN G. NISBET

Euan G. Nisbet is emeritus professor at Royal Holloway, University of London, Egham, UK, and honorary fellow of Darwin College, University of Cambridge, Cambridge, UK. He is a member, without remuneration, of the Scientific Oversight Committee of the United Nations Environment Programme's (UNEP) International Methane Emissions Observatory (IMEO), part of the Global Methane Pledge. e.nisbet@rhul.ac.uk

*The views expressed are those of the author and neither reflect nor represent the views of the IMEO and UNEP.

10.1126/science.adn0134

NEWS

> "I respect the science in everything I do."
>
> **Oil company executive Sultan Al Jaber,** who is the COP28 climate summit's president and an engineer and economist, in *The New York Times*, saying that news media misquoted his recorded comment that no science indicates phasing out fossil fuels would accomplish climate targets.

IN BRIEF

Edited by
Jeffrey Brainard

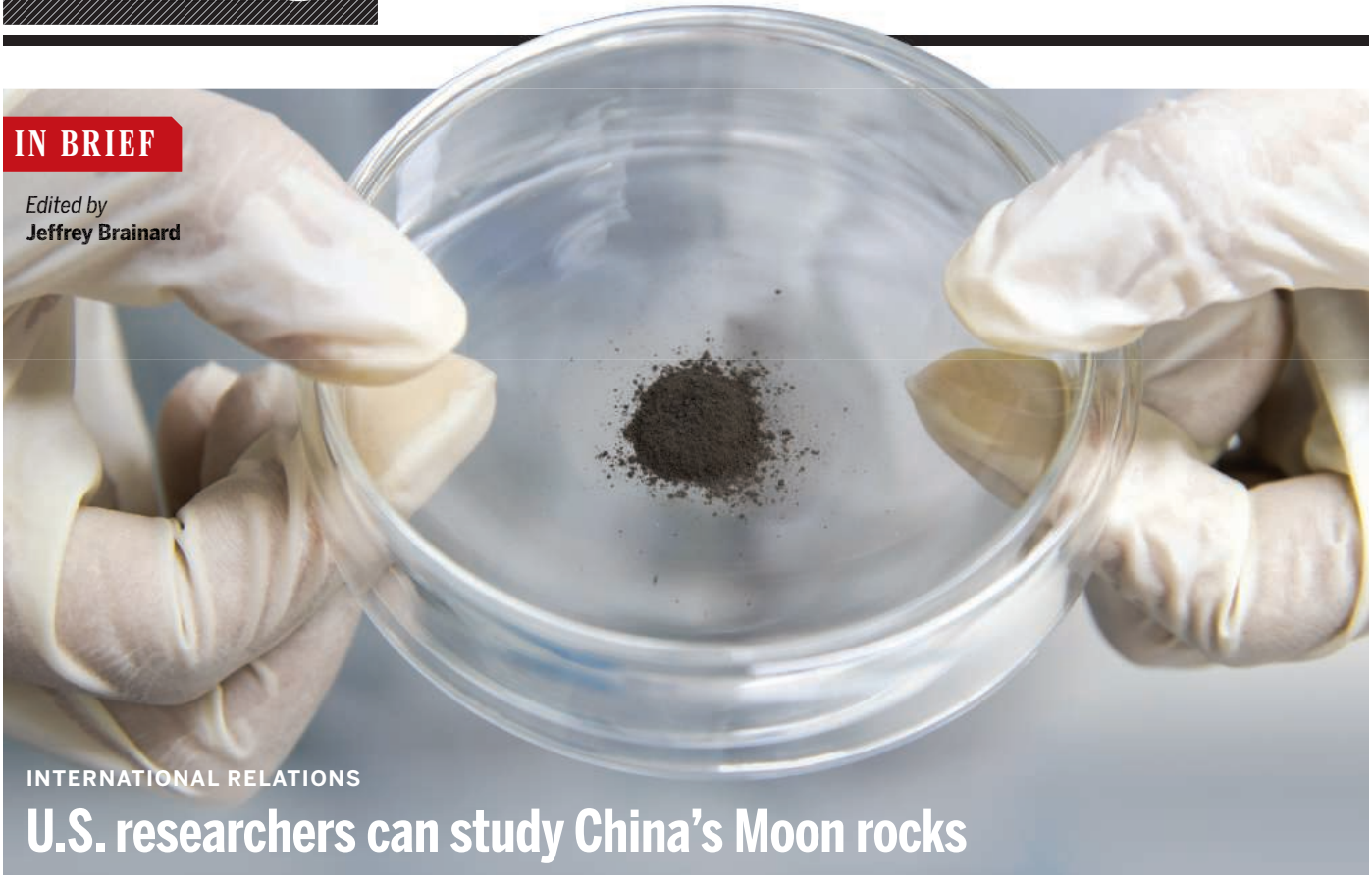

INTERNATIONAL RELATIONS

U.S. researchers can study China's Moon rocks

In a rare case of U.S.-Chinese cooperation in space, NASA is urging researchers it funds to apply to China's space agency for access to lunar soil and rock samples it collected. Such collaborations are barred by U.S. law unless NASA informs Congress in advance. The China National Space Administration (CNSA) holds 1.7 kilograms of Moon material returned to Earth in 2020 by its Chang'e 5 mission. The samples could hold clues to volcanic activity, and last week NASA told researchers in an email that their scientific value justifies what the agency described as a one-time exception to the prohibition. Some U.S. researchers have already sidestepped the restriction by forgoing NASA funding while co-authoring studies of the samples with Chinese colleagues. Multiple countries are expected to apply for samples, which until now CNSA reserved only for Chinese researchers.

Lunar samples are handled at the Chinese Academy of Sciences in Beijing.

NIH pauses stroke trial over safety

BIOMEDICINE | The U.S. National Institutes of Health (NIH) has paused the start of a major human trial of an experimental drug aimed at protecting the brain after stroke. At the same time, the agency launched an investigation into recently aired concerns about the drug's safety and whether lab studies supporting its promise contain manipulated images and data. The agency's mid-November move, confirmed by the company developing the drug and NIH's stroke consortium, came days after a *Science* investigation (17 November, p. 754) into studies of the candidate drug, called 3K3A-APC. Whistleblowers argued that data from an earlier phase 2 trial, sponsored by a company called ZZ Biotech, hinted that 3K3A-APC might increase deaths or disabilities in stroke patients. They further identified potential scientific misconduct in dozens of papers, some on 3K3A-APC or related topics, by University of Southern California neuroscientist Berislav Zlokovic and colleagues. Zlokovic, a co-founder of ZZ Biotech, did not respond to a request for comment on NIH's actions.

FDA probes CAR-T link to cancer

BIOMEDICINE | The U.S. Food and Drug Administration (FDA) says it is investigating the "serious risk" that a type of blood cancer is caused, in rare cases, by a breakthrough cancer treatment. Chimeric antigen T cell (CAR-T) therapy uses viruses to engineer a patient's immune cells to destroy their malignant cells. Six such treatments are

approved for blood cancers and more than 30,000 people have received them. Last week, news media reported that FDA has received 19 reports of malignancies that start in T cells in patients who received CAR-T therapy, surprising physicians in the field because this side effect has been largely undocumented until now. Some viruses used to deliver genes to treat other conditions have been linked occasionally to cancer because they may activate a cancer gene or give the engineered cells a growth advantage. But CAR-T researchers note that patients face a higher risk of cancers from other treatments, including the chemotherapy used to wipe out existing immune cells before CAR-T therapy. For now, FDA says, the treatment's benefits outweigh its risks.

Strike kills Gaza physicist, leader

WAR | Physicist and mathematician Sufyan Tayeh, rector of the Islamic University of Gaza (IUG), was killed in an Israeli airstrike on the northern Gaza Strip on 2 December, according to the Palestinian Ministry of Higher Education and Scientific Research. After earning a doctorate at Ain Shams University in 2007, Tayeh, a Palestinian, led IUG's physics department from 2008 to 2011 and held the university's UNESCO Chair for Physical, Astrophysical and Space Sciences in Palestine. Palestinian officials say Tayeh, who was 52, is among the more than 15,000 Gazans killed in the current conflict, which began after Hamas terrorists killed more than 1200 Israeli citizens and foreign nationals, and took nearly 250 hostages, in a 7 October surprise attack.

Harvard gift blamed in dismissal

ACADEMIC FREEDOM | A former Harvard University researcher who studies misinformation in social media has accused the university of shutting down her work this year to please the internet company Meta. In a civil rights complaint last week to the U.S. Department of Education, Joan Donovan said Harvard became critical of her work after receiving a pledge in 2021 of $500 million for research on artificial intelligence from the Chan Zuckerberg Initiative, a foundation co-founded by Meta CEO Mark Zuckerberg. At a meeting at Harvard earlier that year, Donovan had presented leaked documents showing that staff at Meta's Facebook knew of the harms of misinformation on its platform; she said a former Facebook executive at the meeting asserted she misinterpreted the documents. In a statement to *The Washington Post*, Harvard denied Donovan's allegations, saying it eliminated her staff position only after failing to find a faculty member to oversee her research, as university policy requires.

Ukraine war damages heritage

ARCHAEOLOGY | Russia's invasion of Ukraine, nearly 2 years old, threatens to destroy ancient heritage sites not yet excavated and documented, researchers reported last week in *Antiquity*. Bombs have already smashed centuries-old churches, and trenches and craters have cut through their graveyards. The damage may also include Paleolithic hunter-gatherer mammoth bone sites, Neolithic settlements, and Bronze Age burial mounds; Ukraine is the homeland of the Yamnaya, the Bronze Age herders who swept into Europe 5000 years ago. Researchers cannot inspect the extent of this destruction because of war restrictions on drone photography, the need to clear mines in government-controlled areas, and continuing fighting in others. An interview with the study's co-authors is at https://scim.ag/UkraineArcheo.

'Anthrobots' help tissues heal

BIOTECHNOLOGY | In a step toward engineering molecular "physicians" to diagnose and treat illness from within the body, researchers last week unveiled tiny, self-propelling spheres of human cells that promoted repair of damaged nerve tissue in a lab dish. These "anthrobots," no bigger than poppy seeds, consist of human tracheal cells cultured in a 3D scaffolding to form spheres. Researchers coaxed them to grow so that the cells' hairlike cilia faced outward for movement. They hope the work, published in *Advanced Science*, could lead to new ways to treat spinal cord damage.

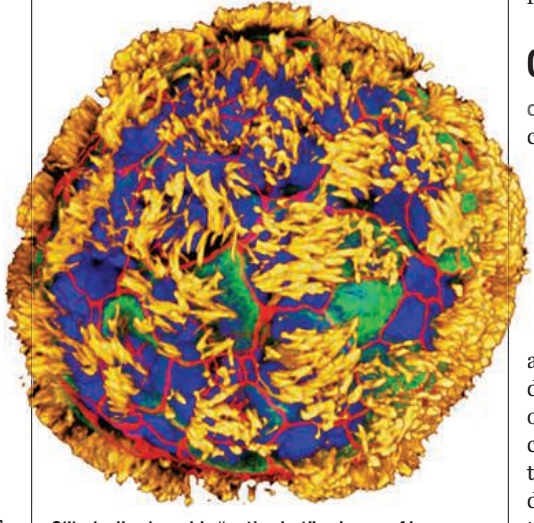

Cilia (yellow) enable "anthrobot" spheres of human cells to move. Red marks cell boundaries; blue, nuclei.

IMAGE: GIZEM GUMUSKAYA *ET AL.*, 2023 *ADVANCED SCIENCE*

NEJM reckons with its past

SOCIAL JUSTICE | *The New England Journal of Medicine* (*NEJM*) this week published the first-ever self-examination of its complicity in U.S. slavery and racism. The perspective, co-authored by historians of medicine, is part of a planned series that will examine how the journal perpetuated biases and injustices since its founding in 1812. In this first paper, the authors outline, for instance, how a Philadelphia physician suggested in *NEJM*'s pages in 1904 that "plantation life" had protected enslaved people against tuberculosis. Authors continued to mention slavery without condemning it or acknowledging that the practice and its continuing legacy contributed to U.S. health disparities, according to the analysis. In an accompanying editorial, *NEJM* editors say the series' aim is to start a conversation, and that in learning from past mistakes, they can prevent new ones.

Vote bans funerary images

RESEARCH ETHICS | The Southeastern Archaeological Conference (SEAC) has voted to maintain a new policy that prohibits its flagship journal from publishing photographs of objects, such as jewelry and ceramics, buried with Indigenous ancestors. Many tribes with ties to the U.S. Southeast say seeing images of such objects is a profound spiritual violation and that publishing them is exploitative. Critics of SEAC's new policy, who called the vote, worry it will infringe on academic freedom and shut down important research. Researchers on both sides expect similar image restrictions to spread to other journals, conferences, and classrooms in the United States and Canada.

Climate damage fund launched

CLIMATE POLICY | At the U.N. climate conference in Dubai, United Arab Emirates, last week, nations agreed to a draft resolution for a "loss and damage" fund to compensate developing countries for harms caused by climate change when adapting to them is not possible. Many of those countries face risks from increased storms, drought, and other effects of global warming, despite not being responsible for the bulk of historic fossil fuel emissions. Wealthy countries have already promised more than $700 million for the fund. But many details of its operation, including the body that will ultimately administer it, remain to be settled.

IN DEPTH

CLIMATE CHANGE

Al Gore's climate watchdog spots emission gaps

At U.N. meeting, Climate Trace reveals missing greenhouse gases in nations' inventories

By **Paul Voosen**

The carbon dioxide and methane that have such palpable effects on climate are frustratingly elusive. Even advanced satellites struggle to pinpoint plumes of the gases, which are the dominant drivers of global warming. Instead, countries assess their emissions by piecing together direct measurements, statistics on agriculture and fossil fuel use, and modeling. This week, at the United Nations's annual climate change conference in the United Arab Emirates (UAE), countries are presenting those emissions inventories to show whether they have made progress on promised cuts.

Yet the figures are often misleading, according to Climate Trace, an independent watchdog that is tracking emissions based on new kinds of satellite data, together with artificial intelligence (AI). Its latest assessment, released today, shows that in 2021 Russia left out greenhouse gases equivalent to 1.5 billion tons of carbon dioxide and the United States missed 400 million tons, much of it driven by carbon dioxide and methane emissions from oil and gas operations. Overall that year, among wealthy nations required to report to the U.N., Climate Trace estimates 3 billion tons of carbon dioxide equivalent gases went unreported—some 5% of total global emissions.

Other large polluters are not yet required to submit inventories. China last reported one in 2014, but Climate Trace estimates the country's emissions have grown by 17% since then. The UAE, meanwhile, last estimated emissions of 225 million tons in 2019, but Climate Trace found at least 354 million tons for that year. "Why the difference?" asks Gavin McCormick, Climate Trace's cofounder. "Unclear."

Backed by former U.S. Vice President Al Gore, Climate Trace is a coalition of nonprofits and academics that made headlines 2 years ago with its first analysis of 72,000 of the world's largest greenhouse gas sources. Its newest assessment looks at 352 million greenhouse gas sources. "It is really incredibly powerful," Gore says. "This serves a purpose that is at the top of humanity's priority list."

Long term, Gore hopes Climate Trace will be integrated into the U.N. process. And in the meantime, it is helping less developed regions keep track of their emissions. "Especially in the industrial sector, there was much data we did not have access to," says Samanta Della Bella, general manager for climate change in the state of Penambuco in Brazil.

For Gore, Climate Trace fulfills a dream he laid out in a 1998 speech at the California Science Center, when he called for a "digital Earth." To monitor how humans are changing the planet, he called for the "automatic interpretation of imagery, the fusion of data from multiple sources, and intelligent agents that could find and link information." That goal seemed out of reach until 2020, when he first encountered McCormick's work.

An economist by training, McCormick founded WattTime, a nonprofit dedicated to identifying the daily timing of renewable energy surpluses and wiring thermostats and electric car chargers to take advantage of it. Many countries do not track the ebbs and flows of energy, so his team wondered whether satellite data—imagery of steam pouring out of smokestacks or cooling-water releases into rivers, or detections of air pollutants—could identify when dirty power plants were operating, and through that activity, their emissions. Now part of Climate Trace, those estimates grew this year to some 30,000 plants, covering 90% of global capacity. "We're focusing on easy to spot things from space that make huge differences on emissions," McCormick says.

Climate Trace has also assimilated similar models for other emissions sources, creating one central estimate of emissions across all human activity. One key addition was the Oil Climate Index Plus Gas, a model developed by Deborah Gordon, a researcher at the Rocky Mountain Institute, and her colleagues that is fed by granular statistics for drilling sites, such as oil composition and weight, which help indicate the energy, and carbon dioxide emissions, needed to extract and move the fuel. The model also estimates methane leakages based on detections of gas flaring

Climate Trace has found systematic underreporting of greenhouse gas emissions from oil and gas operations, including those from refineries in Saudi Arabia.

by U.S. weather satellites and readings from instruments mounted on planes and the International Space Station. The results make it clear that reported national inventories are missing a lot of methane, which is 80 times more potent at warming the planet than carbon dioxide in the short term. "Methane is the wild west," Gordon says.

For other sectors, Climate Trace enlists AI. In agriculture the three biggest emission sources are cattle and rice paddies, which give off methane; and fertilizer use, a source of nitrous oxide, another potent greenhouse gas. By training an AI to recognize cattle farms and rice paddies in satellite images, and then factoring in the number of cattle or inundated acreage, they could quickly chart their global extent and emissions. For fertilizer, meanwhile, the team is experimenting with using satellite imagery to detect crop yields, photosynthesis, and the capacity of the soil to take up nutrients, all of which can then be used to infer how much fertilizer is applied.

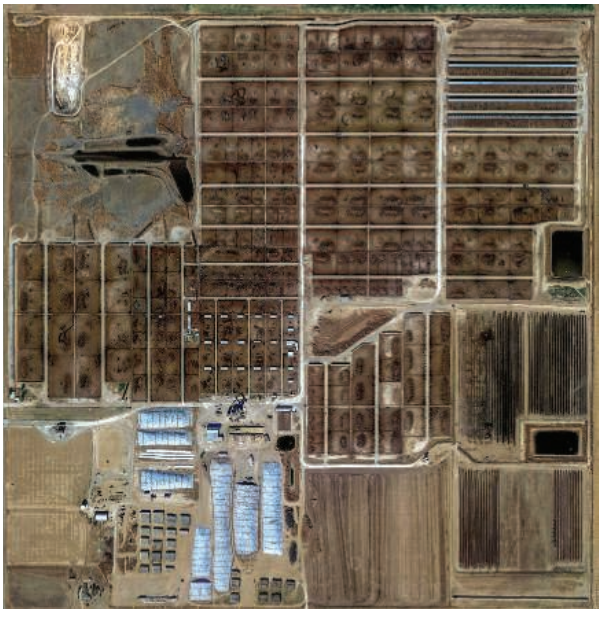

A dairy farm in Texas. Emissions inventories for cattle operations were built by training an artificial intelligence on satellite pictures.

IMAGE: GOOGLE EARTH

To estimate emissions from transportation, Climate Trace draws on an AI developed at the Johns Hopkins University Applied Physics Laboratory (APL) that analyzes infrastructure seen in satellite images. By combining imagery from Europe's Sentinel-2 satellite with roadways identified by OpenStreetMap, the researchers found that an AI could—somehow—sense the number of cars on a road, even though the satellite could not see them individually. "We don't know what it is picking out from those images to produce results," says Marisa Hughes, who leads the APL team. By adding measured emissions from cars and adjusting for the car mix of individual countries, the new version is estimating emissions for hundreds of thousands of road segments.

Funded at first by personal donations from Gore and his partners at Generation Investment Management, Climate Trace does not accept corporate or government sponsorship, and runs on a budget of $12 million. It also submits its methods to peer review, although not always in advance of putting them into operation. For now, it aims to provide a simple reality check on global emissions. But in the next few years, developing countries will be required to submit their own inventories, and Climate Trace is in discussions with the U.N. to provide those estimates for free, Gore says. "Many of these countries don't have the ability to do it, nor should they be expected to."

But some governments may be reluctant to factor in emissions identified by Climate Trace, given they have already made pledges based on flawed data, especially when it comes to methane, Gordon cautions. "There's a lot of hesitancy to reflect reality, even if they know they're wrong."

A new generation of satellites that directly sense greenhouse gases could challenge Climate Trace. Using NASA's Orbiting Carbon Observatory-3, for example, researchers have traced carbon dioxide emissions in megacities like Los Angeles to different sectors, such as highways, industry, and shipping. But ultimately, "These techniques are complementary," says Riley Duren, a remote-sensing scientist at the University of Arizona and CEO of Carbon Mapper, which next year will launch a pair of satellites designed to spot small plumes of methane and carbon dioxide.

One thing is for certain: As Climate Trace grows more comprehensive, and its claims more definitive, it will draw more scrutiny, and opposition. But opposing countries and industries are welcome to make their case. "Our numbers are public," McCormick says. "And anyone who has different numbers will need to have a reason they're different." ■

EUROPE

Far-right election win worries Dutch academics

A government led by Geert Wilders could restrict international students and scrap key climate policies

By **Jop de Vrieze**

The day after voters in the Netherlands recently delivered a surprise victory to far-right parties that have vowed to restrict immigration, Vinod Subramaniam, a nanoscientist and president of the board at the University of Twente, sent a letter to students and employees. "We are concerned about the effects of these results on higher education in general, and about the feelings within our community," Subramaniam wrote. "As a university, we stand for an open, diverse and inclusive community, looking outwards."

Subramaniam was reacting to the unexpected victory of the Party for Freedom (PVV) led by anti-Islamist Geert Wilders. The PVV won roughly 23% of the vote in the 22 November election, making it the largest party in the Dutch parliament and first in line to attempt to form a coalition government. Those potentially lengthy negotiations began last week, and political analysts say they could ultimately produce a government dominated by Wilders's right-wing allies—a prospect that worries many Dutch researchers, who see their nationalist and anti-immigrant agenda as a threat to the scientific community.

One concern is that a Wilders-led government would place major restrictions on international students, who make up 15% of students at Dutch universities. The country has recently been debating how to cope with the pressure placed on university staff and facilities by the "internationalization" of higher education. The outgoing science minister, theoretical physicist Robbert Dijkgraaf, has proposed reducing international student numbers by mandating that two-thirds of bachelor's courses be taught in Dutch and not, for example, in English.

A government led by Wilders is expected to push a lot harder on this issue. In its election manifesto, the PVV writes that universities' primary responsibility should be to Dutch students; the party wants student migration to be "rigorously limited" and plans to eliminate all English-language undergraduate courses. Several other potential coalition partners, including the center-right New Social Contract, have expressed similar desires.

A large reduction in international students would create financial challenges for most Dutch universities, Subramaniam warns. And he asserts that an exodus of English-speaking staff and foreign students would lower the quality of education. "Our Dutch students learn a lot from their international peers," he says.

Subramaniam notes that another European nation, Denmark, took steps in 2021 to reduce its cohort of international students. But it is now partly reversing course because these students are needed to fill jobs in many sectors. Subramaniam hopes that scenario can be prevented in the Netherlands. "Once talent leaves, it takes a lot of time to get them back," he says.

Geert Wilders's Party for Freedom began coalition negotiations last week, after a surprise win.

Wilders also wants the Netherlands to leave the European Union, stating that the country pays in more than it receives. But in the science funding arena, the opposite is true, says Marcel Levi, chair of the Dutch Research Council, the national science funder, because Dutch scientists are so successful at applying for funds from the EU's Horizon Europe funding scheme. A so-called Nexit would also restrict the ability of Dutch scientists to study and work elsewhere in Europe. "Knowledge doesn't stop at the border," says Marileen Dogterom, president of the Royal Netherlands Academy of Arts and Sciences. "It harms Dutch students and academics if they cannot go abroad."

The PVV also intends to scrap climate policies aimed at reducing carbon dioxide emissions and focus only on adaptation measures, such as raising dikes to prevent flooding. It wants to get rid of measures to reduce nitrogen emissions—such as limiting livestock numbers and closing farms—which have led to conflicts with the nation's farmers. Eliminating the nitrogen rules is also a key goal of the Farmers and Citizens Party, a potential coalition partner that emerged in protest to these measures in 2019.

The PVV's manifesto is light on detail about other science-related policies. Although Wilders wants to abolish government subsidies for arts and culture, party platforms don't mention investments in science and technology. But the PVV's potential coalition partners seem relatively positive about the value of research. "That offers some hope," Levi says. "We will continue to emphasize our message that investing in science is an investment that pays for itself." On the other hand, Wilders has a reputation for refuting facts and data that contradict his opinions and framing experts as part of the elite he is opposing.

A Wilders-led government is not yet a sure thing. He has appointed Ronald Plasterk, a former molecular biologist and science minister who has criticized the Dutch government's climate policy and reliance on renewable energy, to explore possible coalition options. In the meantime, Subramaniam is trying to send a clear, reassuring message to the international members of his community and the academic community as a whole: "You belong here. You are welcome."

Jop de Vrieze is a journalist in Amsterdam.

INFECTIOUS DISEASES

Rare studies expose bats to SARS-CoV-2

Infecting captive species could help gauge pandemic risk of coronaviruses that have yet to infect humans

By **Jon Cohen**

It's not easy to work with captive horseshoe bats, as Linfa Wang discovered. In 2005, the molecular virologist wanted to infect the animals with the virus that had caused the outbreak of severe acute respiratory syndrome (SARS) a few years earlier to find out whether it would evolve to grow well in the bats. Working in a maximum-biosecurity lab, he and his team at the Australian Animal Health Laboratory struggled to feed the small insectivores while wearing full-body protective gear. "We had to fly small worms in front of them while wearing these spacesuits," recalls Wang, who is now at the Duke-NUS Medical School. In the end, he says, his technicians balked before they had publishable results.

But the potential payoff of such experiments was alluring, because of mounting evidence that bats serve as reservoirs for emerging viruses that could kill humans. Infecting captive bats could show how bat coronaviruses—related to the human viruses responsible for SARS and now COVID-19—spill over into other animals and potentially people. Captive bat studies could also help clarify the risk of what's called reverse zoonosis, in which humans or other animals infect bats with pathogens they could spread far and wide. And understanding how bats can carry heavy burdens of virus without getting sick might even uncover clues to new treatments.

In the pandemic era the potential payoffs are even more compelling. Even though bats are sometimes difficult to feed and breed and few reagents exist to assess immune responses and other biological processes, researchers are now following in Wang's footsteps—this time, with SARS-CoV-2.

Horseshoe bats (genus *Rhinolophus*) are a particularly appealing study subject because they are known to harbor ancestral relatives of SARS-CoV-2. No lab has yet

managed to keep them in captivity to study their response to the virus, but one just won a grant from the National Institute of Allergy and Infectious Diseases (NIAID) to try. A handful of labs are studying bats from other genera, and initial findings suggest they have varying abilities to excrete and transmit the pandemic virus.

Critics, including the animal rights group White Coat Waste Project, have assailed the work because of unproven concerns that the COVID-19 pandemic traces back to experiments with bat coronaviruses. Work by Vincent Munster, a virologist who studies bats at NIAID's Rocky Mountain Laboratories (RML), led to an unsuccessful bid in Congress last month to cut his annual salary to $1. Two senators also questioned the director of the National Institutes of Health (NIH) on 8 November about plans by RML to house bats at a new $125 million vivarium it's building.

Munster and others insist their experiments carry little risk. "This work is so relevant and so frequently ignored," says Raina Plowright of Cornell University, a disease ecologist who heads an international research consortium called Bat One Health. She says concerns about the experiments have been "really overblown" as all have been done in high-level biosecurity facilities under strict biosafety precautions. "If we don't do this in-depth work on understanding how these viruses operate within their reservoir hosts," she says, "we're just blind to one of humanity's biggest impending risks."

As with studies of other animal hosts, test tube experiments and work with live bats have yielded conflicting results. For example, Wang initially wanted to test whether fruit-eating cave nectar bats (*Eonycteris spelaea*) from his captive colony could contract SARS-CoV-2, but was discouraged from trying when he found their cells did not become infected. But virologist Martin Beer at Germany's Friedrich Loeffler Institute (FLI) decided to skip the cell experiments and try to infect Egyptian fruit bats (*Rousettus aegyptiacus*) from a colony FLI's Anne Balkema-Buschmann established in 2013. The researchers inoculated nine animals with SARS-CoV-2 and housed them with three others.

As they reported in July 2020, all of the inoculated bats became infected, and the virus spread to one of the three cage mates, but none became ill. "They probably control the virus pretty easily," Beer says. "They may be a little bit better prepared [than humans] to deal with these types of viruses." He adds that the fruit bats' ability to contract and spread SARS-CoV-2 without getting sick suggests that if they picked up the virus from humans or other animals, they could become reservoirs, potentially infecting still more species.

SARS-CoV-2 infected but didn't sicken Egyptian fruit bats from a colony at the Friedrich Loeffler Institute.

PHOTO: ANNE BALKEMA-BUSCHMANN

Others are focused on the risks to the bats themselves. Despite the findings in Egyptian fruit bats, some researchers worry that other species may be sickened after contracting SARS-CoV-2 from contact with humans. Virologist Jeffrey Hall of the U.S. Geological Survey's National Wildlife Health Center led a team that tried to infect big brown bats (*Eptesicus fuscus*)—which often roost in human houses—with SARS-CoV-2. None of the eight inoculated bats excreted or transmitted the virus to cage mates, they reported in January 2021, suggesting this species, at least, is resistant to infection.

Another prime candidate for reverse zoonosis is the Brazilian (or Mexican) free-tailed bat (*Tadarida brasiliensis*), a migratory insectivore that roosts in large colonies in urban areas of North America, where people gather to watch the bats fly out each night from bridges and caves. Hall's group found that five of 10 intentionally infected bats excreted the virus, but none transmitted it to cage mates. Another team, led by veterinarian Angela Bosco-Lauth at Colorado State University (CSU), inoculated 18 Mexican free-tailed bats with two different strains of SARS-CoV-2 and reported that none even shed the virus. The two experiments have the same bottom line, Bosco-Lauth says: "These bats are certainly not shedding the same kind of volumes that a person or a domestic cat might shed," she says, which suggests they're unlikely to become a reservoir.

CSU immunologist Tony Schountz and his team also found low replication and no transmission of SARS-CoV-2 in 18 Jamaican fruit bats (*Artibeus jamaicensis*) from a colony they have maintained since 2006. So they decided to "come up with creative ways of forcing the infection a little bit," he says. SARS-CoV-2 enters cells via a receptor called angiotensin-converting enzyme 2 (ACE2), which bats have in their lungs, but only at low levels. So Schountz and his team adapted a strategy used to make lab mice susceptible to SARS-CoV-2: They introduced a human *ACE2* gene into another 18 bats and then infected them.

Unlike mice, the bats did not get sick, though the infection did cause moderate damage to their lungs, Schountz's team reported on 19 October in *PLOS Pathogens*. Those findings are "hugely interesting," Munster says, in part because they suggest something other than ACE2 receptor levels curbs the virus in bats.

Schountz's team hopes the animals might help reveal innate immune responses that give bats a first line of defense against SARS-related coronaviruses. "If there's some innate pathway that really controls coronaviruses in bats, then can we develop a drug that mimics some molecule in that pathway?" he asks. "We just have to figure out what the bats already have learned through evolutionary pressure."

New studies are on the horizon. Schountz received a $1.7 million NIH grant in September and plans to spend some of it to create a colony of *Rhinolophus* bats. CSU, with $6.7 million from NIH, is also building a new facility to house bat colonies, which the school expects will begin to operate in 2025.

Until the new vivarium at RML opens, Munster is using a colony of Jamaican fruit bats maintained at CSU to conduct his own studies of innate immune responses to SARS-CoV-2. He soon plans to post a preprint of his group's findings about key immune messengers called interferons. "We think something in the interferon signaling is quenching this particular virus, and so even though it gets in, it's actually not doing that much," he says. "Understanding that gives us a broader sense of what makes viruses successful—and, in this case, pandemic." ■

This Congolese child likely got mpox from an anim
but the same strain is passing among adults sexual

INFECTIOUS DISEASES

Deadliest mpox outbreak ever sparks a new worry

Congo cases suggest viral strain there is spreading sexually, like less lethal one that triggered last year's global outbreak

By **Jon Cohen**

Last month, the World Health Organization (WHO) revealed that the Democratic Republic of the Congo (DRC) was experiencing its largest, most deadly outbreak of mpox ever, with more than 12,000 suspected cases so far this year. The nearly 600 deaths far surpass those from the global outbreak of the same viral disease over the past 2 years. The WHO report and a study out last week also explore a worrisome possibility: that the strain of virus in the DRC, far deadlier than the one that drove the global outbreak, is in some cases spreading between sexual partners.

Originally known as monkeypox, the disease is caused by a virus (MPXV) that long has sporadically infected people in rural areas of the DRC, mostly though contact with infected squirrels and other rodents. Researchers have documented occasional spread among household contacts, but the MPXV strain in the DRC, designated clade I, has never been linked to sexual transmission, a major mode of transmission for the clade IIb strain in the global outbreak. Researchers are now rushing to analyze the latest DRC cases to see whether the virus has changed genetically, and some scientists suggest the country should consider at least targeted use of the mpox vaccines that are now widely available in wealthy countries outside of Africa.

It's "shocking" that vaccination is not yet accessible in DRC," says Yale University epidemiologist Gregg Gonsalves. "As a question of equity, it's hard to stomach." Gonsalves went to the DRC in the spring to help model how much vaccine the country would need to combat mpox, but the recent revelation that MPXV might be spreading sexually there "scrambles things a bit," he says.

MPXV can produce skin blisters and lesions and cause particularly severe disease in immunocompromised people. The first human case of mpox was detected in 1970 in the DRC, and until recently it was only endemic in sub-Saharan African countries. (WHO renamed the disease because of concerns that monkeypox was "racist and stigmatizing" language.) But last year, more than 85,000 cases occurred outside of Africa, primarily among men who have sex with men (MSM), leading WHO to ring its loudest alarm, a Public Health Emergency of International Concern.

Now, the same pattern of transmission may have emerged with the more deadly virus. WHO's 23 November Disease Outbreak News and a study posted last week in *Emerging Infectious Diseases* (*EID*) conclude that clade I MPXV is being passed sexually among MSM and sex workers in the DRC. The studies describe two clusters, one in MSM and one in 20 sex workers. "Is this something new or something that we've been missing?" asks University of Manitoba virologist Jason Kindrachuk, who co-leads the International Mpox Research Consortium and is the corresponding author of the *EID* paper.

Eddy Kinganda-Lusamaki, a clinician based at the DRC's National Institute of Biomedical Research (INRB) who co-authored the *EID* report, says improved surveillance could account for some of the unprecedented surge in the DRC cases and deaths, which WHO puts at 581 this year. "Monkeypox surveillance was at some point neglected in our country because of lack of resources to investigate," says Kinganda-Lusamaki, who is working on a Ph.D. in virology at the University of Montpellier. But he doesn't think surveillance is the whole story. "Cases have been detected in areas that did not report cases in the past," he notes, including Kinshasa, a city of 17 million people that has far more accessible health care than the rural communities traditionally hit hardest by mpox.

Epidemiologist Anne Rimoin of the University of California, Los Angeles, another *EID* co-author, has studied mpox in the DRC for 2 decades and says it's unclear whether sexual transmission made a significant contribution to the apparent explosion in cases—or whether it's truly even a new phenomenon in the country. "If you're not looking for it, you're unlikely to find it," Rimoin says. She adds that people with genital lesions may not seek care, especially if they are MSM or sex workers. "There's stigma associated with transmission in this manner, so it's going to be very hard to document," she says.

Rimoin also notes that the vast majority of cases have not been confirmed by polymerase chain reaction (PCR) tests that detect genetic signatures of the viruses. "That's going to be really important to parse out," she says. Virologist Martine Peeters, Kinganda-Lusamaki's Ph.D. adviser, says her lab has a new test that can confirm infections that PCR misses by looking for antibodies to MPXV, which last longer in the blood than the virus. "Maybe there are more asymptomatic or postsymptomatic cases, which means [the DRC tally] may even be underreported," she says.

The *EID* and WHO reports offer different and somewhat conflicting details about the MSM cluster. WHO says the first sexually transmitted case traces back to a resident of

Belgium who arrived in Kinshasa on 15 March with "anal itching and discomfort," but the next day traveled to a town 260 kilometers away. He sought medical care there a week later, and tests sent to INRB confirmed he had mpox and that it was clade I virus. An epidemiological investigation found that the man had sex with four men and one woman who later tested positive themselves.

The *EID* report describes the same cluster differently, saying the first mpox diagnosis was a Congolese man who reported having sex in Europe with a man who frequently visited the DRC and had mpox symptoms. The report describes the virus from the original DRC man and four of his contacts who became infected. "We need to better investigate and better characterize what's going on and what has circulated," says Kinganda-Lusamaki, who is not convinced the cluster started with a man infected in Europe. "It's more likely that the patient got infected in the country [DRC]," he says. "We are still at the level of hypothesis."

For the clade IIb virus that spread globally, genetic analyses showed that several mutations likely explain how it began to transmit more readily through sex. But there's no evidence yet that the viruses isolated from the DRC cases have undergone the same changes. "The analysis is not that easy," Peeters says.

When clade IIb surfaced in MSM last year, there was an immediate demand for a smallpox vaccine made by Bavarian Nordic that the U.S. Food and Drug Administration had approved for mpox. The company's CEO, Paul Chaplin, says the DRC has never requested the vaccine. "Bavarian Nordic has not been approached by any African country" for doses, he notes. WHO has a multistep process that gives a stamp of approval to vaccines for use worldwide, and Chaplin says the company has filed the initial paperwork with the agency. The company, he says, "is willing to support the current situation in the DRC."

Rimoin says the DRC's reluctance to vaccinate stemmed in part from the difficulty of determining who should receive the shots when the disease appeared to mainly spread sporadically from animals in rural areas. Targeting groups at high-risk of sexual transmission of the virus, she says, simplifies the task. "It's a much easier thing to tackle than widespread vaccination in very remote, logistically complex areas," Rimoin says.

Kinganda-Lusamaki is uncertain what the demand for the vaccine would be in the DRC. "But the country may need it," he says.

Kindrachuck says he hopes the DRC can benefit from recent advances in mpox surveillance, diagnostics, treatments, and vaccines among non-African countries. "Let's try and ensure that we use what we learned to help with the ongoing situation," he says. ■

PHOTO: WELLCOME IMAGES/SCIENCE SOURCE

CANCER

Tumor-killing viruses score rare success in late-stage trial

Bladder cancer results suggest that after decades of failure, the viruses could finally reach their potential

By **Mitch Leslie**

Once touted as the next big thing in cancer therapy, tumor-attacking viruses have been a letdown, failing in multiple clinical trials as far back as 1949. But preliminary results from a small phase 3 study presented at a conference last week suggest these unconventional cancer treatments, known as oncolytic viruses, might work after all. The data showed that an oncolytic virus developed by Irvine, California–based CG Oncology eliminated tumors in 64% of 66 patients with bladder cancer that didn't respond to mainline treatment.

The follow-up period was only 6 months, and much more research is necessary. But even a positive phase 3 result is enough to "shake the world of oncolytic viruses," says surgical oncologist Omeed Moaven of the Louisiana State University Medical Center. And if the promise shown in these early data holds up, the oncolytic virus could become only the second in the United States to receive regulatory approval, a milestone that would bode well for the dozens of other trials now underway. Success would also vindicate a strategy of designing the viruses to draw an immune attack on the tumor rather than only hitting malignant cells directly.

"In the early days, we thought things would progress rapidly," says virologist Grant McFadden of Arizona State University. The viruses—usually benign varieties such as the herpes simplex viruses and adenoviruses that are often modified to make them safer and more potent—can reproduce in tumor cells but not in healthy cells. Cancer cells are congenial for the viruses because they frequently shut down the first line of defense—known as the interferon response—against viral infections.

Doses of the viruses worked beautifully in animal studies, sometimes achieving 100% cure rates. But after more than 70 years of clinical trials around the world, only T-VEC, a modified herpes simplex virus type 1 (HSV1) that targets advanced melanoma, has performed well enough to receive the Food and Drug Administration's go-ahead. (And other melanoma therapies work better for most patients.) Three other oncolytic viruses were OK'd outside the U.S., most recently a treatment for glioma brain tumors approved in Japan in 2021.

Virologist Mary Hitt of the University of Alberta cites one reason for the clinical trial failures. At first, "everyone was afraid they wouldn't be safe." As a result, she says, many trials used weakened viruses that were too feeble to do much good. Another problem was that researchers didn't understand how oncolytic viruses worked.

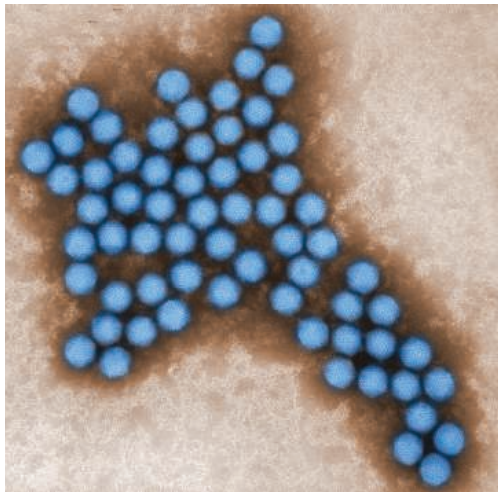

Genetically modified adenoviruses similar to these shrank bladder tumors in a clinical trial.

Scientists once thought that "these viruses were magic bullets" that killed tumor cells directly, says immunologist Greg Delgoffe of the University of Pittsburgh. But through animal studies and analyses of tumor samples from patients treated in clinical trials, researchers realized that the viruses themselves take out relatively few tumor cells. Instead, oncolytic viruses rile the immune system, triggering inflammation and attracting anticancer warriors such as T cells, and they help break down the defenses that shield tumors. That picture helps explain the early failures. Participants typically had already undergone several rounds of therapies that could

inhibit their immune systems, McFadden says. Because the patients couldn't muster an immune response, the trials "were doomed," he says.

A slew of companies is now trying to apply these lessons and turn oncolytic viruses into therapies, and more than 90 clinical trials are testing them or are about to start. CG Oncology's virus—a harmless adenovirus—is one contender. The company outfitted it with a gene that spurs infected cancer cells to produce an immune-stimulating molecule, promoting attacks by T cells.

The phase 3 trial tested the virus in patients with a form of bladder cancer that hadn't penetrated the muscular wall of the organ. If tumors like these grow unchecked, patients often need to have their bladders removed, but the virus may delay or prevent that outcome. Doctors assessed the participants every 3 months after the treatment began. In 76% of the patients, tumors were undetectable at one or more of these checkups. And in 74% of that group, the tumors did not return for at least 6 months.

"It's an interim analysis, but what we've seen is a good start," says urologic oncologist Mark Tyson of the Mayo Clinic, who has several patients enrolled in the trial and unveiled the findings at the Society of Urologic Oncology conference. Researchers will track the patients for a total of 3 years to determine whether the benefits persist, says Tyson, who has no connection to CG Oncology.

> **"When you do everything well, you can get good clinical outcomes."**
> **Grant McFadden**, Arizona State University

The study shows that "when you do everything well, you can get good clinical outcomes," McFadden says. The company chose a type of cancer that is easy to target. The modified virus powerfully stimulated the immune system. And the enrolled patients had not undergone previous chemotherapy that would prevent their immune systems from responding to their treatment.

Other candidate oncolytic viruses may soon get their chance. For example, neurosurgeon E. Antonio Chiocca of Brigham and Women's Hospital and his colleagues are testing an engineered HSV1 against glioblastoma, a type of glioma that usually kills patients in less than 2 years. In previous efforts to pit this virus against glioblastoma, scientists removed a gene essential for viral reproduction, hoping to prevent brain inflammation, a possible side effect of the treatment. But the modification also left the virus "attenuated," Chiocca says.

Instead, he and his team used a version of the virus with the gene restored, but it was engineered to switch on only in glioblastoma cells. This version was safe, the researchers found in a phase 1 trial with 41 patients whose tumors had returned after surgery or other treatments. The virus also allowed T cells to invade the tumors. The more T cells entered, the longer the patients survived, the scientists reported in October in *Nature*.

Other efforts to improve the viruses aim to counter cancer cells' ability to blunt an immune response. Immunologist Jianhua Yu of City of Hope and his colleagues have created two viruses that shrank tumors in animals and could soon be in phase 1 trials. One delivers a molecule that attracts immune cells to a tumor's vicinity, and the other provides an antibody that attaches to tumor cells and allows immune cells known as macrophages to eat them.

Still another avenue to improve oncolytic viruses is pairing them with other immune therapies or with chemotherapy and radiation. Checkpoint inhibitors are obvious partners because they stymie tumors' mechanisms for shutting down T cells. In a phase 1 trial reported in June, medical oncologist Ann Silk of the Dana-Farber Cancer Institute and her team dosed patients who had melanoma with the checkpoint inhibitor pembrolizumab and a coxsackievirus, which usually causes mild respiratory symptoms in children. Tumors shrank in about 47% of the patients, compared with 42% of patients in a separate trial of pembrolizumab alone. The company Oncolytics Biotech has performed two successful phase 2 trials of a tumor-attacking reovirus, combined with various types of chemotherapy and checkpoint inhibitors, in patients with breast cancer or pancreatic cancer. The company hopes to begin phase 3 trials of the virus for both cancer types as soon as 2024.

CG Oncology's virus also performs well with pembrolizumab, a phase 2 study showed in 2022. A year after the treatment, tumors still hadn't returned in 68% of bladder cancer patients. Pembrolizumab alone in this group usually eliminates tumors only in about 20% of patients, says urologic oncologist Roger Li of the Moffitt Cancer Center, who headed the trial and took part in the other CG Oncology study.

The many clinical trial failures frustrated researchers, but also paid off by convincing scientists and regulators that oncolytic viruses are safe, Yu says. Now, he and others are eager to show that they are potent as well. "They can have major impact," McFadden says. ■

PUBLISHING

'Hijacked' journals mar top database

Scopus listed hundreds of papers published on stolen sites

By **Jeffrey Brainard**

Scopus, a widely used database of scientific papers operated by publishing giant Elsevier, plays an important role as an arbiter of scholarly legitimacy. But users beware, a new study warns. As of September, the database listed hundreds of papers from 67 "hijacked" journals: legitimate publications taken over by unscrupulous operators to make an illicit profit by charging authors fees of up to $1000.

These ersatz publications represent a tiny fraction of the more than 26,000 active, peer-reviewed journals indexed in Scopus. Still, says Anna Abalkina, who authored the study, published on 27 November in the *Journal of the Association for Information Science and Technology*, any number above zero is troubling because it means the scholarly record is being corrupted. Some of the work published in hijacked journals may be legitimate, says Abalkina, a social scientist at the Free University of Berlin. But previous analyses have found that many papers in hijacked journals were plagiarized, fabricated, or not peer reviewed. Thieves can commandeer a journal by paying to renew an expiring internet address before the true owners do, or by getting Scopus to list a URL other than the real journal's that links to the hijackers' website.

"Nine of these [67] journals are medical journals," notes Salim Moussa, a marketing professor at the University of Gafsa who has studied hijacked journals. "They and their contents pose a health risk to society." Of the 67 journals, found by checking Scopus for 321 hijacked journals identified by others, 41 were still operating as of September, and Abalkina says her list is probably not complete.

In response to Abalkina's study, Elsevier has "started a thorough investigation," says global media relations director Dan DiPietro-James. When *Science* went to press, Elsevier had removed 13 journal homepage links from Scopus, he says. "Maintaining the integrity and high-quality, curated content indexed on Scopus is of paramount importance to us." ■

WHAT ARE FARM ANIMALS THINKING?

New research is revealing surprising complexity in the minds of goats, pigs, and other livestock

By **David Grimm**, *in Dummerstorf, Germany*

PHOTO: RICHARD BAILEY/GETTY IMAGES

You'd never mistake a goat for a dog, but on an unseasonably warm afternoon in early September, I almost do. I'm in a red-brick barn in northern Germany, trying to keep my sanity amid some of the most unholy noises I've ever heard. Sixty Nigerian dwarf goats are taking turns crashing their horns against wooden stalls while unleashing a cacophony of bleats, groans, and retching wails that make it nearly impossible to hold a conversation. Then, amid the chaos, something remarkable happens. One of the animals raises her head over her enclosure and gazes pensively at me, her widely spaced eyes and odd, rectangular pupils seeking to make contact—and perhaps even connection.

It's a look we see in other humans, in our pets, and in our primate relatives. But not in animals raised for food. Or maybe we just haven't been looking hard enough.

That's the core idea here at the Research Institute for Farm Animal Biology (FBN), one of the world's leading centers for investigating the minds of goats, pigs, and other livestock. On a campus that looks like a cross between a farm and a small research institute—with low-rise buildings nestled among pastures, stables, and the occasional dung pile—scientists are probing the mental and emotional lives of animals we've lived with for thousands of years, yet, from a cognitive perspective, know almost nothing about.

The work is part of a small, but growing field that's beginning to overturn the idea that livestock are dumb and unworthy of scientific attention. Over the past decade, researchers at FBN and elsewhere have shown that pigs show signs of empathy, goats rival dogs in some tests of social intelligence, and, in one of the field's, um, splashiest recent finds, cows can be potty trained, suggesting a self-awareness behind the blank stares and cud chewing that has shocked even some experts.

"There's a lot to be learned by studying the mental lives of these creatures," says Christopher Krupenye, a Johns Hopkins University psychologist who explores cognition in humans and more traditional animal models such as chimpanzees and dogs. Ignoring livestock, he says, has been a "missed opportunity" by the scientific community.

The field faces challenges, however, and not just because of rambunctious goats. Farm animals can be huge, many are hard to train, and traditional funders and high-profile journals have generally spurned such studies. But as scientists push past these obstacles, they are gaining insights not only into the minds of livestock, but into the evolution of our own cognition as well. What they learn could even change the way we house and treat these creatures.

"If we don't understand how these animals think, then we won't understand what they need," says Jan Langbein, an applied ethologist at FBN. "And if we don't understand what they need, we can't design better environments for them."

IN AN ENCLOSED L-shaped barn at FBN that houses more than 700 pigs, I'm in for a bit of hazing. Or at least that's what it feels like at first. Before entering the main part of the building, my guides tell me to strip down to my underwear and don a baggy pair of blue overalls. "Now we'll see who's gone to the gym this week," jokes Birger Puppe, director of FBN's Institute of Behavioural Physiology. In truth, the researchers don't want visitors bringing in deadly diseases like African swine fever. But the disrobing has other benefits: A thick, sour miasma of pig excrement engulfs me as I make my way inside, and I'm glad I've left my clothes behind.

In a small room, researchers are herding hulking hogs—just 6 months old but already 120 kilograms—one by one into a run with a treadmill. Instead of a conventional treadmill's control panel, there's a grapefruit-size glowing blue button at snout height that the animals can press to run the machine for a few seconds. Today, however, no one seems very interested in working out.

Like a person having second thoughts about their gym membership, most of the pigs step briefly onto the treadmill, then walk off, emitting squeals and deep, belch-like grunts as they exit through a door on the other side of the run.

"We have sports pigs, but also couch potato pigs," Puppe laughs. Katharina Metzger and Annika Krause, the postdoc and technician, respectively, running the study, tell me I may be making the animals nervous. Last week, they say, one pushed the button seven

Goats are an integral part of research at FBN, where scientists entice them to participate in cognition tests with crunchy pieces of dried pasta.

times and kept coming back for more.

The goal is to train the pigs for an experiment that will test whether they'll exercise just because it makes them feel good, a window into their emotions. "The idea comes from human sports physiology," Puppe says. "That exercise can improve mood."

A couple of decades ago, work like this would have been laughed out of the barn. There are an estimated 78 billion farm animals on Earth—a number that dwarfs monkeys, rodents, and humans combined—and we have lived with them longer than any other creature save dogs. Yet in an era where researchers are modeling rat brains on computers and showing that our canine pals may be able to intuit our thoughts, livestock remain a black box.

That's because, until recently, scientists didn't take their cognition seriously. "When I went to my first research conferences, people didn't understand why I was studying the minds of farm animals," says Christian Nawroth, a behavioral biologist at FBN. *Why waste your time if it's not going to improve milk or meat production*, he recalls them asking. "They didn't see the point."

Nawroth did. Though he began his career researching decision-making in great apes, he switched to livestock in 2010. He was looking for a Ph.D. position when an intriguing opportunity popped up at a German zoo. He came to run some pilot tests on minipigs, exploring whether the animals were capable of "object permanence"—understanding that something still exists when it "disappears" behind a barrier, an important milestone in the cognitive development of children. Nawroth was hooked. "Almost nothing had been done on farm animals," he says. "You had a feeling of being one of the first explorers."

In an open arena, pigs learn that one side always contains a box with a treat, whereas the other features a "punishment." If they decide to explore a box in between, scientists interpret that as a sign of optimism.

IN A DIFFERENT ROOM in the pig barn, Nawroth's colleagues are investigating whether pigs are sensitive to one another's feelings. Ten 6-week-old piglets cower together in the corner of a gated pen spread with straw. Like the treadmill hogs, they don't seem to be fans of strangers. The question is, are they fans of each other?

Ethologist Liza Moscovice is hoping to find out. At an opening in the pen, she has placed a large box with a mesh window and a door. After a few minutes, the pigs begin to explore the new installation, congregating around a handle on the door. None has been trained to open a box like this, but they are soon sniffing and biting the lever until a couple realize that they can snout it up to open the door. Several then rush inside and begin to nose around.

In recent experiments, the box becomes a trap. Once a piglet enters, the door closes. Will the others come to its rescue? The study is a test of empathy inspired by a 2020 incident on a wildlife preserve near Prague. Several boars—the ancestors of modern pigs—gathered around a cage containing two younglings, until one figured out how to open it. At FBN, Moscovice and her colleagues have observed something similar in piglets. In a study published this summer, the team showed that, 85% of the time, the animals freed a trapped companion within 20 minutes.

The liberators were more likely to open the box when a pig was trapped inside than when it was empty, ruling out mere curiosity. Those that spent more time staring at their trapped companion were also more likely to help, especially if that companion squealed in distress, suggesting the helpers were sensitive to the "emotional state" of the boxed pigs.

"We think the helping behavior is based on some understanding of the other's needs," Moscovice says. "That's a critical component of empathy that's really exciting to see."

Critics have argued that animals might help others simply to alleviate their own stress at seeing or hearing a trapped companion. But saliva samples Moscovice collected did not show elevated levels of the stress hormone cortisol in the helper pigs, consistent with a more selfless reason for the assistance.

PHOTOS: THOMAS HÄNTZSCHEL/NORDLICHT

Elsewhere in the barn, behavioral biologist Sandra Düpjan has been replicating the famous "marshmallow test" with pigs. As with humans, the goal is to see whether the animals can delay gratification, forgoing a smaller reward now in hopes of a larger one later. For pigs, the prize isn't marshmallows but applesauce, an especially favored treat. "They will sell their mother for it," Düpjan jokes.

Studies in the early 1970s suggested children who pass the test tend to be more successful later in life (though those findings have been disputed). Pigs aren't going to college, but the experiment may help probe why some animals seek out more productive feeding grounds instead of settling for closer, poorer foraging.

Düpjan is also exploring what some consider signs of optimism and pessimism in pigs. In an open arena, the animals learn that one side always contains a box with a treat (again, the applesauce), whereas the other always features a "punishment." (The applesauce is inaccessible, and the researchers wave a plastic bag over the pigs, which they apparently hate.) The scientists then place a box in the middle of the arena. If the pigs explore it, it's a sign of optimism—they're willing to make the effort, hoping they'll get applesauce again; if they don't, it's a sign of pessimism—they're expecting the bag.

Cows, too, show signs of optimism and pessimism, other researchers have shown. And like pigs, they may be capable of much more.

A SQUAT YELLOW building about 1 kilometer north of the pig facility doesn't look like much, but it's home to one of the most headline-grabbing findings in farm animal research. Two years ago, scientists potty trained cows here, teaching the animals to hold their bladder as they navigated a metal-gated hallway to a patch of artificial turf. That may not seem like a big deal to us, but it was startling in creatures that seem to have no control over their excretions. Not only did the cattle learn to "hold it" faster than many children do, their very ability to sense that they had to go countered the conventional wisdom that they lack "interoceptive awareness"—the capacity to think about what's going on in their own bodies, which in humans has been linked to happiness, love, and even life satisfaction.

"These are not dumb creatures," says Langbein, a co-author on the potty training study. "They have a rich emotional life and personality."

Langbein's new work could cement this idea. Next door, he shows me around a (blessedly) open-air stable, where four groups of dairy cows munch hay in separate quarters. Data cables run to blue troughs, recording how much and how often each animal eats. Collars around their necks send wireless signals to metal boxes in the ceiling, which, along with mounted cameras, track the precise location of each cow in real time, documenting which companion they associate with, and for how long. It all seems pretty complicated, but the goal here is simple.

"We're trying to figure out if cows have friends," says Annkatrin Pahl, the Ph.D. student leading the project. On a real farm, she explains, farmers move dairy cows around multiple times a year, disrupting their social groups. Are they also breaking up besties?

After identifying each cow's ostensible best friend and worst enemy, Pahl brings the pairs into an open arena. In a recent trial, "enemy" cows began head butting. But when one was placed with her friend, the two began grooming each other and following each other around. As part of the study, which is still in its early stages, Pahl is also collecting heart rate and hormone level data to see how being separated from the group affects a cow's stress levels, and whether pairing it with a preferred companion can help.

> **"These are not dumb creatures. They have a rich emotional life and personality."**
> **Jan Langbein**, FBN

"If a farmer knows which of his cows like each other, it might be better to keep them together when moving the herd around," Langbein says. He's not just speaking academically. Langbein trained as a cattle breeder 40 years ago, and he's especially sensitive to the housing conditions on modern dairy farms, where animals are often tied up for long stretches or confined to tight pens.

But convincing farmers to change their ways is going to take more than a few scientific publications, Langbein says. "That's why we publish in farm journals, too, so they understand what we're discovering in the language of normal people." Already, he's starting to see changes. "When I worked as a cattle breeder, nobody talked about how these animals think or feel. Now, we have heated waterbeds for piglets and automatic brushes for cattle to groom themselves," he says. "I think farmers are more willing to accept that these animals are not just production units."

NAWROTH LIKES to describe himself as the man who stares at goats. He's referencing the 2009 George Clooney movie based on a Jon Ronson book about the U.S. Army's attempts to harness psychic energy to kill the animals by glaring intently at them. (The efforts, shockingly, weren't successful.)

Nawroth's own studies are more grounded. After abandoning his early work with pigs because he found the animals too hard to train, he switched to goats, which seemed just as interested in him as he was in them. "They pay a lot of visual attention to what you're doing," he says. "It may not seem like there's a lot going on in their head, but they are processing information all the time, even if they're just standing there looking at you."

It's the sense of connection I experienced myself, and it has driven much of Nawroth's research. In early work, he explored how goats measure up to dogs in a battery of cognitive tests. In an experiment known as the "impossible task," dogs confronted with a food bowl they can't access turn to humans for help, a behavior that's been chalked up to their intensive coevolution with us. But Nawroth showed that goats did the same, the first time the experiment had been tried with a food animal. (Speaking of which, yes FBN has a slaughterhouse, and yes Nawroth has partaken in its spoils. This may be the only field of research where scientists eat their subjects when the study is over.) "Some of them started hoofing the experimenter, as if they were begging for help," he says. "You thought it was a dog in goat's clothing."

Further experiments showed that goats, like dogs, could distinguish between pictures of happy and angry people, suggesting they are tuned into our emotional states; that they could locate food behind an obstacle more quickly if they watched humans move the food there first, a rare example of cross-species learning; and, in Nawroth's most significant finding, that goats seem to understand what we mean when we point at something, a complex reading of our social cues that eludes even chimpanzees.

"Christian's work has exposed a lot of commonalities that people would be surprised to find," says Krupenye, the Hopkins psychologist. That's the advantage of studying livestock, he says. Because farm animals encompass so many different species that are so far apart on the tree of life, they allow scientists to test just how widespread certain cognitive abilities are. And because humans may have domesticated themselves when they began living in close-knit groups, such studies could even provide insight into the evolution of our own minds. The studies on livestock, Krupenye says, are providing "a really important insight."

Now, Nawroth is pushing his goat research even further.

IN A YARD BEHIND FBN's goat barn, Nawroth shows me a "fake apple tree." A tall metal pole juts out of the grass with another one balanced across the top. The resulting seesaw holds a brick on one end and a birdfeeder-like container on the other. Dangling from the center of the contraption is a square platform covered in artificial turf. The whole thing wouldn't be out of place at a modern art museum.

The device took Nawroth and his colleagues 3 years to perfect. The idea is to explore in a far more controlled environment a phenomenon that's been observed in the wild: goats pulling down the branches of an apple tree so that a companion can reach the fruit. The behavior might sound like altruism, and that's what Nawroth hopes to test.

When a goat jumps on the platform, the birdfeeder (filled with dried penne pasta, which the animals munch like potato chips) lowers into a fenced-off area of the yard. The goat on the platform can't reach it, but a nearby goat can. And in some cases, the platform goat lowers the food without any attempt to get it herself; she seemingly wants to help her companion reach it.

Nawroth, says it's too soon to say whether the animals are exhibiting altruism. But Krupenye says any insight into the behavior will help scientists understand whether altruism truly exists in the animal kingdom—a subject of debate—and, if so, how it works. "It's going to be really important for nailing down the mechanism."

Meanwhile, inside the barn, a goat is playing with an oversize iPad. Or at least that's what it looks like. The animal is poking her head through an aperture in her enclosure, nosing a thin computer monitor that's displaying a livestock version of the "which one doesn't belong?" game. Four pictures of goat faces flash on the screen, one slightly different from the rest. When she nuzzles the correct one, which she always seems to do, a tube squirts water into her bowl. (The game is harder than it sounds. The images are nearly identical, and when I try it myself, I'm quite relieved when I get a squirt.)

The setup can test memory, too. In other experiments, the animals have learned the order of 28 symbols, and correctly recalled it weeks later—a performance comparable to that of primates and dolphins.

Nawroth finds it easy to work with goats—"They don't throw poo at you like great apes," he says—and most are game to participate in his experiments. But farm animals can still be challenging to study. The sheer weight of cows and pigs makes them dangerous, and most livestock are used to living in herds; they can become uncooperative when separated from their group. Elodie Briefer, an ethologist at the University of Copenhagen, says it can take up to a month for sheep to participate in her studies of emotion. "Even then, very often you don't get results."

When the results do come, big journals often don't take notice. They go to the dogs—literally. "It seems like there's a dog paper every day," says Alan McElligott, a zoologist at the City University of Hong Kong who has studied the minds of goats and other farm animals. "It's almost impossible to keep up with it." What's worse, others say, most money for livestock research still goes to studies aimed at improving milk or meat yields, not to figuring out how these creatures think.

All of this may be keeping young scientists away, says Rebecca Nordquist, a biological psychologist at Utrecht University who explores cognition in pigs and chickens. There are only about a half-dozen labs researching livestock cognition worldwide, and no conferences dedicated exclusively to the topic. She also worries that many people may not want to know if the animals they think of as dinner turn out to have rich inner lives. "Some would prefer to keep them dumb."

Still, Nawroth is optimistic. He's spearheading a major initiative called ManyGoats that will connect dozens of researchers across the globe to share data, increasing sample sizes and bringing more rigor to livestock studies. "I hope it will be an example for other labs," he says.

Jean-Loup Rault, head of the Institute of Animal Welfare Science at the University of Veterinary Medicine Vienna, is starting to see interest from researchers who used to scoff at farm animal studies. When he presented some of his early livestock cognition findings in 2010 at the Society for Neuroscience conference—which typically attracts tens of thousands of attendees—he was the only one with a pig poster. "Now, there's more of us," says Rault, a collaborator on FBN's pig empathy and fake apple tree studies, "and people are becoming more interested in our work."

Krupenye says the growing pains in the farm animal field remind him of dog cognition research, which had to fight for its own respect a couple of decades ago when it was still in its infancy. "Dogs have really helped people see that there's a lot of value to studying species beyond primates and rodents," he says. "I think the livestock folks are riding a similar wave."

At the very least, Nawroth hopes the work will give people new respect for animals that have been overlooked for so long. Getting inside their minds will expand our own, he says. "Different species play by different rules. We have to see the world not just how we see it, but how they do." ■

Christian Nawroth focuses on the cognitive abilities of goats. This test gauges whether the animals can understand the human pointing gesture—a sign of advanced social cognition.

PHOTO: THOMAS HÄNTZSCHEL/NORDLICHT

Mining is removing sand from coastal sites, such as this one in Colombia, faster than natural processes can replenish it.

PERSPECTIVES

CONSERVATION

The unsustainable harvest of coastal sands

Sustainable management approaches are needed to protect coastal environments

By **Nelson Rangel-Buitrago**[1] *and* **William Neal**[2]

Although coasts form a crucial part of the natural wealth of the planet, their conservation is increasingly jeopardized owing to the growing human footprint. With 50% of the world's population living within 150 km of a coastline, increasing urbanization and population pressures are threatening these fragile ecosystems (*1*). Activities such as extreme urbanization, litter generation, and sand mining have imposed substantial stress on these environments. Among these pressures, coastal sand mining—estimated to remove 40 to 50 billion metric tons of sand each year (*2*)—stands as a pervasive, damaging, and rapidly expanding activity (*3*, *4*).

Sand, with its diverse properties, has garnered substantial commercial attention. Mineral sands are rich in heavy minerals, such as ilmenite and zircon, and are primarily extracted for use in metal production and other industrial applications (*3*). By contrast, aggregate sands, which are angular and contain a mix of granules of various sizes, are primarily used in construction (*4*). Recent studies indicate that mineral sands make up ~5% of the total sand volume used globally, whereas aggre-

gate sands account for ~40% of the total sand used (*2*, *4*). Although desert sands are plentiful, their smooth texture, a result of aeolian abrasion, renders them ineffective for construction aggregate. Conversely, coastal sands, which are less prevalent, have jagged and angular granules, which makes them the preferred choice for concrete aggregate (*3*). Another notable type is manufactured sand, which is derived from crushing hard rocks like granite or basalt. Given its consistent quality and adaptability, manufactured sand is a potential sustainable alternative to natural sands. The current rate of coastal sand extraction outstrips the natural replenishment rate of quality sand suitable for standard uses, which makes it unsustainable (*2*).

Sand plays a pivotal role in three major economic sectors: construction, mineral mining, and beach nourishment (*5*). Construction is the predominant consumer, accounting for an estimated 85% of all sand mined globally (*4*, *5*). Swift urbanization, particularly in coastal regions, has catalyzed an escalating demand for sand. Mineral mining, which consumes ~10% of the global sand volume extracted, targets coastal sands for minerals (*3*). Extracting minerals from coastal sands often presents a more cost-effective alternative compared with inland or deep-sea mining. However, this method results in a substantial volume of waste sands, posing environmental challenges irrespective of geographical location. Beach nourishment (the addition of large quantities of sand to a beach), which uses ~5% of the sand mined globally, offers a temporary solution to coastal erosion (*6*). Although it provides a short-term remedy, beach nourishment disrupts natural ecosystems and yields less-resilient, artificial beaches that necessitate costly, recurrent replenishments. Another demand for sand is for use as fill for coastal land expansion (for example, in China, Dubai, and Singapore); however, the volumes used are not publicized.

The "sand cycle" provides a comprehensive understanding of the processes involved in sand formation, use, and ultimate end (*5*). The cycle starts with weathering and erosion at Earth's surface that break rocks into smaller fragments, with sand-sized sediments being deposited in distinct environments, such as beaches, dunes, riverbeds, deltas, and deserts. The extraction phase follows, where concentrated and well-sorted sand deposits are mined, often causing notable environmental degradation. The transportation of mined sand is driven by local or regional sand market dynamics and has an environmental footprint resulting from carbon emissions and habitat disturbances. The processing stage of the sand cycle involves desalination of marine sands and size-based screening. The sand cycle ends with usage. Recent data indicate that only 20% of sand from construction waste is recycled, with the majority being discarded or ending up in landfills (*4*).

Coastal sand mining results in numerous physical impacts, including the disruption of beach development and dune growth, changes in beach topography, and accelerated beach scouring (erosion of the beach's surface layer of sand, revealing a rougher, often coarser substrate). Collectively, these effects contribute to heightened coastal erosion (*7*). Additional ramifications include shifts in groundwater levels, the potential for saline water to infiltrate freshwater sources, alterations in local climate, and degradation of soil quality.

"Despite the extensive consequences of sand extraction, global political attention... is unexpectedly minimal."

Sand mining also poses substantial threats to local biotic communities (*7*, *8*), which comprise a diverse array of organisms such as aquatic plants, crustaceans, mollusks, and various fish species. The extraction process often results in the direct elimination of these communities, damaging their natural habitats and, consequently, affecting intricate food chains. The subsequent ecological changes can weaken the surviving species, resulting in shifts in species composition around mining sites. These disruptions can further interrupt natural plant-community successions and have cascading negative effects on the entire food web. Mining activities also necessitate land use alterations—for example, establishment of stockpile areas and haulage access routes—which have resulted in the destruction of up to 40% of local ecosystems in heavily mined regions (*8*).

From a human health perspective, the implications of coastal sand mining are multifaceted. They encompass deterioration in water and air quality, the spread of contaminants, and an elevated risk of conditions such as silicosis among mining workers. For example, workers involved in sand mining face a risk of respiratory diseases that is up to three times as high as those in other professions. Additionally, communities in proximity to sand mining sites have reported a 15% increase in infectious diseases. This rise is likely attributable to environmental alterations and pollutants resulting from sand mining activities (*5*). Noise pollution, a by-product of mining operations, is another concern. Not only does it disrupt natural soundscapes, but in some regions with sand mining activities, 20% increases in noise-related stress and sleep disturbances have been reported among local inhabitants (*2*, *9*).

Sand mining also has socioeconomic repercussions (*10*). Economies that are heavily dependent on beach environments face direct impacts, with some regions reporting up to a 25% decline in revenue after the initiation of sand mining operations (*10*). Indirectly, there is a loss of tourism potential, with certain destinations experiencing a 30% drop in tourist visits because of the aesthetic degradation of coastal areas caused by mining activity (*2*, *10*).

A less frequently discussed yet deeply concerning issue is the exploitation of people, particularly children and women, in some sand mining–intensive regions, for example, in Mexico, Kenya, South Africa, and India (*3*). Thousands are being forced into labor, and a substantial proportion are underaged. This exploitation often leads to a surge in violence and criminal activities. One such criminal manifestation is the emergence of "sand mafias" (*3*). These are organized crime groups that illegally mine and trade sand, often resorting to violence, bribery, and intimidation to maintain control over sand territories and supply routes. Their operations are vast, with some groups generating illicit revenues exceeding $200 million US dollars annually (*3*, *5*).

Despite the extensive consequences of sand extraction, global political attention toward regulating the practice is unexpectedly minimal. Current legislation primarily falls under national jurisdiction, with some regional conventions indirectly addressing the issue (*11*, *12*). The evident lack of a robust global framework to inform national policies highlights an important gap in standards for coastal sand mining. Addressing this omission requires decisive global action, which could encompass the establishment of a Global Sand Mining Council to oversee worldwide activities and ensure environmentally sustainable practices. International treaties could standardize regulations and promote best practices, and a global monitoring system could track extraction rates and ecological

[1]Programa de Física, Facultad de Ciencias Básicas, Universidad del Atlántico, Barranquilla, Atlántico, Colombia. [2]Department of Geology, Grand Valley State University, Allendale, MI, USA.
Email: nelsonrangel@mail.uniatlantico.edu.co

impacts. Financial measures, both incentives and penalties, could drive compliance with international standards and sustainable practices.

The United Nations Environment Programme (UNEP) advocates 10 recommendations that highlight the need to treat coastal and riverine sands as strategic assets that are vital for ecological stability and human sustenance (*2*). UNEP's emphasis on terms of best practices underscores methods that prioritize environmental conservation, sustainable extraction, and the welfare of communities linked to the mining sector. To ensure that these practices are upheld, clear national standards are proposed, which would be tailored to each country's specific context but which also share a universal goal of responsible sand extraction. Furthermore, the notion of "sand rights" demands renewed attention. This principle protects the rights of downstream ecosystems reliant on consistent sand flow in both rivers and beaches. It mandates comprehensive impact assessments before mining approvals, promoting sustainability in the extraction process.

To manage coastal sand mining effectively, approaches should center on fulfilling current requirements without jeopardizing the ability of future generations to meet their needs (*13*). These strategies ought to be grounded in scientific understanding; tailored to local concerns; and designed to bolster the economic, environmental, and social health of local communities. Specific interventions could include establishing buffer zones around sensitive habitats, using satellite imagery to monitor illegal mining activities, and investing in technologies that reduce sand consumption in construction.

Several innovative approaches and technologies have already been developed to mitigate sand mining impacts, including reducing sand consumption (i.e., using alternative material and recycling used sand); using manufactured sand; implementing taxation and royalty policies for sand extraction; and developing laws, regulations, and standards relating to coastal sand mining (*5*). Technological innovations include dry mining, which involves extracting material (without the use of water) from nickeliferous sulfides, nontitaniferous magnetite, diamond, chromite, and corundum as well as from various types of ore deposits. Concrete recycling, using construction and demolition waste for beach nourishment, and the use of different materials, such as microplastics, in concrete production (*14*) could also help reduce the need for coastal sand mining. The implementation of postmining projects in regions including Indonesia and Colombia (*6*) has achieved partial ecological recovery. However, there is also evidence that certain interventions, such as relocating mining activities without addressing consumption patterns, only shift the problem elsewhere (*3*, *5*, *11*).

Unfortunately, much coastal sand mining is conducted illegally (although it is difficult to determine the exact amount) and is linked to poverty and adverse social conditions (*15*). Factors such as financial gains, rising local and regional demand, lack of effective control systems (monitoring mechanisms, permit and licensing systems, reporting platforms, feedback and grievance mechanisms, and comprehensive regulatory frameworks), and the role of sand mafias exacerbate the problem. Illegal sand mining could be curtailed through stringent regulations and penalties, improved surveillance, incentives for industries to minimize sand use, and better enforcement of restricted areas. However, implementing such regulations is challenging, particularly in developing nations grappling with other pressing issues or where resources are scarce and corruption is rampant. There is an urgent need to reevaluate the use of sand because the current trajectory foreshadows severe consequences if left unchecked. ■

REFERENCES AND NOTES

1. UN-Habitat, *UN-Habitat Annual Report 2009* (United Nations, 2020).
2. UNEP, *UNEP Yearbook: Emerging Issues in Our Global Environment* (UNEP, 2002).
3. O. H. Pilkey *et al.*, *Vanishing Sands: Losing Beaches to Mining* (Duke Univ. Press, 2022).
4. UNEP, "The Search for Sustainable Sand Extraction is Beginning" (2022); https://www.unenvironment.org/news-and-stories/story/search-sustainable-sand-extraction-beginning.
5. N. Rangel-Buitrago *et al.*, *Ocean Coast. Manage.* **235**, 106492 (2023).
6. N. Rangel-Buitrago, W. J. Neal, in *Encyclopedia of Coastal Science*, C. W. Finkl, C. Makowski, Eds. (Springer, 2019).
7. M. A. Maun, *The Biology of Coastal Sand Dunes* (Oxford Univ. Press, 2009).
8. J. P. Doody, *Coastal Conservation and Management: An Ecological Perspective* (Springer, 2013).
9. D. O. B. Jones *et al.*, *Elements* **14**, 325 (2018).
10. N. Rangel-Buitrago, Ed., *Coastal Scenery: Evaluation and Management* (Springer, 2019).
11. R. Radzevičius *et al.*, *J. Coast. Res.* **51**, 15 (2010).
12. A. Williams, A. Micallef, Eds., *Beach Management: Principles and Practice* (Routledge, 2009).
13. European Commission, "Commission welcomes Parliament's adoption of Maritime Spatial Planning legislation" (Publications Office of the European Union, 2014).
14. B. Arhoun *et al.*, *Resour. Conserv. Recycling* **179**, 106044 (2022).
15. UNEP, *Sand and Sustainability: Finding New Solutions for Environmental Governance of Global Sand Resources* (UNEP, 2019).

ACKNOWLEDGMENTS

This work is a contribution from "Geología, Geofísica y Procesos Marino-Costeros," Universidad del Atlántico; the Department of Geology, Grand Valley State University (USA); and the Santa Aguila Foundation.

10.1126/science.adj9593

PHYSICS

Entanglement with tweezed molecules

Controlled molecular connection will advance quantum technologies

By **Augusto Smerzi**[1,2]

The application of quantum science to information processing requires the controlled generation and manipulation of quantum entanglement (*1*), a state in which multiple particles cannot be expressed as a simple combination of the individual states of each particle. This situation reflects an inherent interparticle connection that transcends classical notions of particle separability. Although entanglement has been achieved in various atomic (*2*), photonic (*3*), and superconducting (*4*) platforms, the controlled creation of entanglement with molecules has been a long-standing challenge. On pages 1138 and 1143 of this issue, Bao *et al.* (*5*) and Holland *et al.* (*6*), respectively, report a method for tailoring the quantum states of individually addressable molecules to achieve quantum entanglement on demand. This strategy presents a promising new platform for the realization of different quantum technologies, such as computation and sensing, among other applications.

The main obstacle to controlling the entanglement of molecules is the level of complexity that arises from numerous internal rotational and vibrational energy states. The thermal population of these states conflicts with the necessity to control the internal states of the molecules at the single quantum level and thereby steer them to the desired quantum states. Achieving this requires cooling molecules to low-enough temperatures. Recent years have seen remarkable breakthroughs in cooling molecules through techniques such as direct laser cooling (*7*).

Bao *et al.* and Holland *et al.* leveraged the long-range electric dipolar interaction between pairs of calcium monofluoride (CaF) molecules trapped in a reconfigurable optical tweezer array. Both groups successfully demonstrate the creation of an important class of entangled quantum states—the so-called "Bell states" (*8*). These are characterized by the strongest possible connection (correla-

Cold, confined, controlled, and coherent

Tailoring the quantum states of individually addressable molecules achieves quantum entanglement on demand.

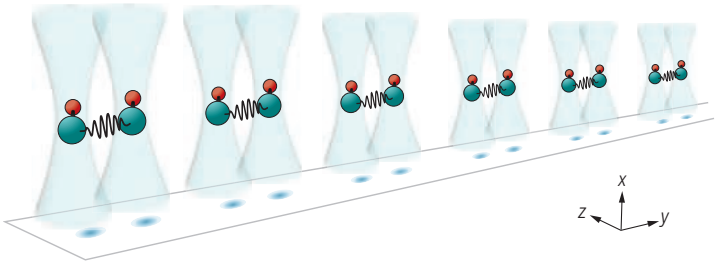

Individual ultracold calcium monofluoride (CaF) molecules are trapped within a one-dimensional array of optical tweezer pairs. Internal energy states of the molecules are uniformly set through the application of microwaves and optical pumping.

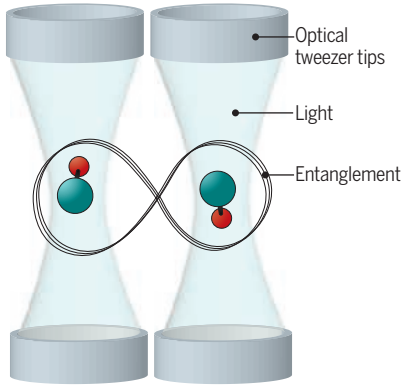

CaF molecules within each distinct pair of tweezers interact through long-range electric dipolar force (**Left**). This leads to dipolar spin exchange of rotational energy states, which steers the two molecules into an entangled quantum state (**right**).

tion) between two rotational energy levels of a CaF molecule with the two rotational energy levels of a different, nearby molecule. The two energy levels constitute a "qubit," the fundamental unit of quantum information that generalizes the classical notion of a bit.

Bell states play a pivotal role in quantum information and communication protocols. These include quantum teleportation, in which an unknown state of one particle is transmitted to another distant particle through entanglement and classical communication. It is also relevant to quantum key distribution, a technique to create a shared secret key between two parties, which is subsequently used for encryption purposes (*1*). Furthermore, Bell states play a special role in the field of quantum foundations, which is the study of the conceptual framework that underlies the theory of quantum mechanics, because the states maximally violate the so-called Bell inequalities (*8*), a set of mathematical expressions designed to test the predictions of classical theories against those of quantum mechanics. The experimentally observed violations of these inequalities have demonstrated the fundamental nonlocal character of nature. Nonlocality is a purely quantum phenomenon in which distinct particles correlate their behaviors instantaneously, even when separated by great distances. This has been observed with photons, atoms, and superconducting circuits (*8*). There is an ongoing discussion regarding whether nonlocality persists when transitioning from the atomic to the macroscopic realm. Large molecules are ideal systems to use for the exploration of nonlocality in highly complex systems. Such studies will provide fundamental tests of quantum theory alongside experimental observations, such as the quantum superposition of molecules containing up to 2000 atoms (*9*).

The achievements presented by Bao *et al.* and Holland *et al.* are built upon the precise control of individual molecules. Single CaF molecules are trapped in a reconfigurable one-dimensional array of approximately 20 optical tweezers spaced by a few microns (see the figure). After rearranging the array to eliminate unoccupied sites, the internal states of the molecules are set into a single state using microwave transfer and optical pumping. Despite energy losses due to movement of the tweezer traps and other factors, this experimental protocol provides a highly controlled molecular array that is ready for quantum operations. Bao *et al.* and Holland *et al.* used this setup to create an ensemble of maximally entangled molecule pairs. Two CaF molecules located in neighboring optical tweezers were placed close enough to sense their respective long-range electric dipolar interaction. This led to a rotational dipolar spin-exchange interaction between tweezer pairs across the array, which dynamically created a Bell state out of the two previously uncorrelated molecules. The controlled dynamics effectively implemented an iSWAP two-qubit quantum gate (*1*) that would be, in principle, sufficient to create a universal set of quantum gates for quantum computation.

The demonstrated manipulation and characterization of entanglement of individually tailored molecules by Bao *et al.* and Holland *et al.* paves the way for developing new versatile platforms for quantum technologies (*10*). The distinctive features of their methods include large molecular electric dipole moments, which can greatly exceed typical values in atoms (*11*), and the rich structure of long-lived coherent states. This will allow, for instance, the study of previously uncharacterized topological phases of matter and the development of sensors with entanglement-enhanced sensitivities (*2*) for detecting ultraweak electric fields. Applications span from electroencephalography to measure electrical activity in the brain to monitoring changes in electric fields in the Earth's crust for earthquake predictions. Additionally, because molecules are presently used as individual-photon emitters and nonlinear components (*12*), entanglement among molecules can serve as a means to control the quantum properties of emitted photons. On another front, molecular spectroscopy schemes can be implemented for metrology applications (*13*), aiming at fundamental physics tests beyond those applied to the Standard Model of particle physics (*14*). Ultimately, it is anticipated that hybrid architectures that integrate diverse molecular, atomic, optical, and superconducting platforms will be a central theme in near-future quantum technologies.

Molecules are complex objects. Their richness can provide versatility for quantum simulations (*15*) and offer the possibility to process qudits, a multilevel extension of two-level qubits. However, they can readily couple with their surrounding environment, making entanglement vulnerable to decoherence. Achieving long coherence times requires advancements in techniques for cooling molecules to ultralow temperatures. The eventual success of this endeavor will allow exploration of uncharted paths in fundamental science and quantum technologies. ■

[1]QSTAR, INO-CNR, Largo Enrico Fermi 6, Firenze, Italy.
[2]LENS, Largo Enrico Fermi 6, Firenze, Italy.
Email: augusto.smerzi@ino.cnr.it

GRAPHIC: N. CARY/*SCIENCE*

REFERENCES AND NOTES

1. M. A. Nielsen, I. L. Chuang, *Quantum Computation and Quantum Information* (Cambridge, Univ. Press, 2010).
2. L. Pezzè *et al.*, *Rev. Mod. Phys.* **90**, 0355005 (2018).
3. T. Giordani *et al.*, *Riv. Nuovo Cim. Soc. Ital. Fis.* **46**, 71 (2023).
4. M. Kjaergaard *et al.*, *Annu. Rev. Condens. Matter Phys.* **11**, 369 (2020).
5. Y. Bao *et al.*, *Science* **382**, 1138 (2023).
6. C. M. Holland *et al.*, *Science* **382**, 1143 (2023).
7. T. Langen *et al.*, arXiv:2305.13445 (2023).
8. N. Brunner *et al.*, *Rev. Mod. Phys.* **86**, 419 (2014).
9. Y. Y. Fein *et al.*, *Nat. Phys.* **15**, 1242 (2019).
10. A. Gaita-Ariño *et al.*, *Nat. Chem.* **11**, 301 (2019).
11. J. J. Hudson *et al.*, *Phys. Rev. Lett.* **89**, 023003 (2002).
12. C. Toninelli *et al.*, *Nat. Mater.* **20**, 1615 (2021).
13. R. Aiello *et al.*, *Nat. Commun.* **13**, 7016 (2022).
14. M. S. Safronova *et al.*, *Rev. Mod. Phys.* **90**, 025008 (2018).
15. A. Micheli *et al.*, *Nat. Phys.* **2**, 341 (2006).

ACKNOWLEDGMENTS

Discussions with C. Toninelli, G. Santambrogio, and P. De Natale are acknowledged. A.S. is supported by the European Commission through the Horizon 2020 program QuantERA ERA-NET Cofund in Quantum Technologies project "MENTA."

10.1126/science.adl4179

MEDICINE

Delivering drugs with microrobots

Biomedical microrobots could overcome current challenges in targeted therapies

By **Bradley J. Nelson** and **Salvador Pané**

More than 90% of drug candidates fail during clinical trials. There are many reasons for failure—lack of efficacy, poor material properties, and a lack of commercial need. Notably, ~30% of drug candidates fail clinical testing owing to unmanageable toxicity, which is usually caused by the systemic delivery methods that most drugs require (*1*). What if this unmanageable toxicity could be improved, for at least some of these drugs, by ensuring that they are delivered precisely to the location of the disease and not throughout the entire body? This is the promise of microrobots—physically targeted therapeutic delivery by cargo-carrying micromachines. The potential applications of microrobots could allow the reconsideration of drugs that have been abandoned because of toxicity and encourage drug developers to pursue new chemistries.

A primary motivation to create microrobots, small devices ranging from several nanometers to submillimeter sizes that propel through body fluids and tissue to specified locations, is to overcome the limitations of how drugs diffuse throughout the body. Slow diffusion rates represent the same evolutionary pressure that microorganisms respond to in developing their locomotion strategies. The power stroke that the cilia of paramecia exhibit, the traveling wave of eukaryotic flagella such as spermatozoa tails, and the fascinating rotary motors that flagellated bacteria such as *Escherichia coli* evolved, all help these microorganisms move toward locations in their environment that are more favorable to survival (*2*). These locomotion strategies solve profound engineering challenges that exist owing to the vastly different physics that predominates at small scales. Therefore, many of the microrobots created thus far have been inspired by motile microorganisms such as *Trypanosoma brucei*, which changes its morphology when it needs to swim, and *E. coli* (*3*). Rather than moving toward locations to prolong survival and help ensure reproduction, microrobots are designed to move to the source of disease, such as blood flow–blocking thrombi or malignant tumors, where they can then release drugs that will have a highly toxic yet localized therapeutic effect.

Progress in shape-changing soft materials during the past two decades has led microroboticists to engineer and fabricate motile devices that use complex mechanisms for propulsion. Examples of these include spring-mass systems that can glide across surfaces to harvest biomaterials, nanofilament-based motors with flexible joints that replicate the undulatory propulsion of flagella on spermatozoa, and light-induced motion that mimics the peristaltic movements of worms (*4*). More advanced vehicles, such as microcars, microboats, and five-legged spiders, all composed of interlocked polymer-metal microarchitectures, have also been developed (*5*). Methods for transporting cargo and delivering therapies have been devised, with an increasing number of in vivo studies, including the application of magnetotactic bacteria as microrobotic platforms to transport drug-loaded liposomes to tumors in mice (*6*). Additionally, magnetic reso-

Multi-Scale Robotics Lab, Department of Mechanical and Process Engineering, ETH Zürich, 8092, Zürich, Switzerland. Email: bnelson@ethz.ch

A potential medical procedure with microrobots

A catheter or endoscope delivers microrobots to the body region being treated, for example, to a tumor or blood clot. Microrobot assemblies are deployed into the vasculature, and they navigate to the target. The microrobots disassemble, releasing therapeutic agents. Then, the microrobots are degraded and are either absorbed or cleared from the body.

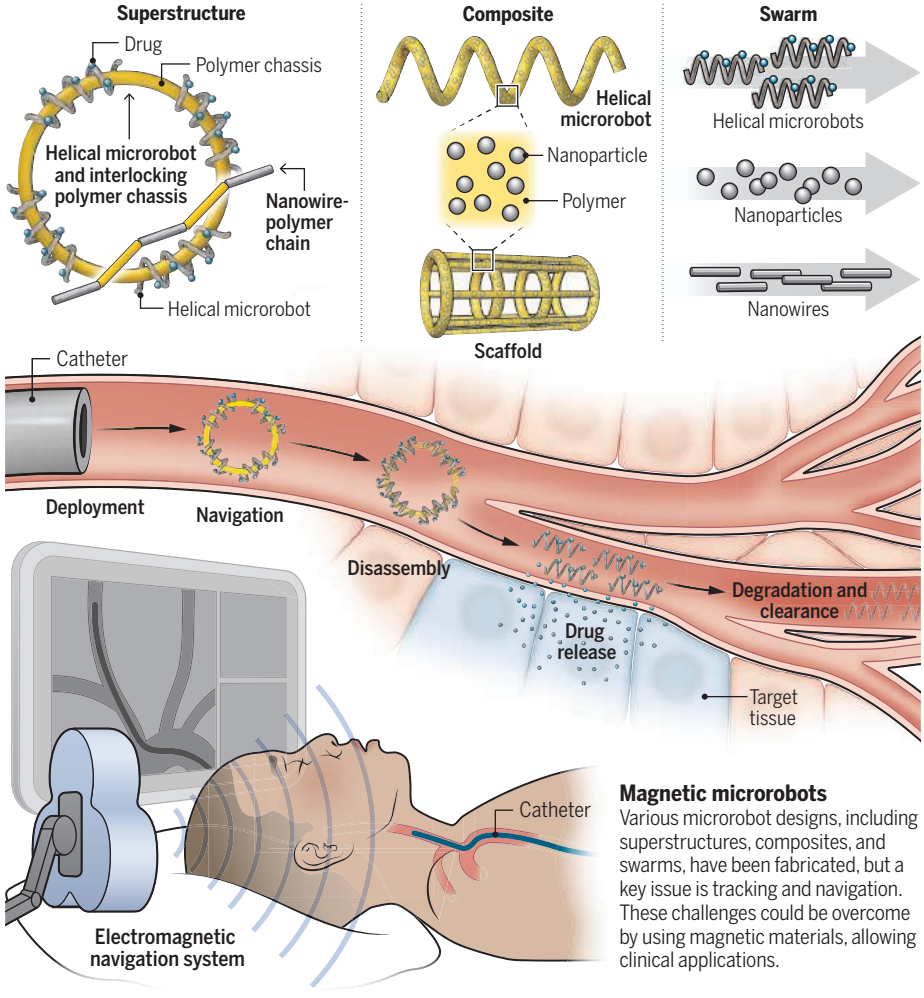

Magnetic microrobots
Various microrobot designs, including superstructures, composites, and swarms, have been fabricated, but a key issue is tracking and navigation. These challenges could be overcome by using magnetic materials, allowing clinical applications.

nance imaging (MRI)–trackable multifunctional microrobots have been developed for treating liver cancer and tested in rats (*7*), and microrobots capable of stem cell delivery within the peritoneal cavity have been tested in a mouse model (*8*). These preclinical studies demonstrate that microrobots can navigate in vivo and deliver a localized therapy; first-in-human trials are only a matter of time.

Propelling microrobots in body fluids and tissue is a key challenge. A large body of research has been dedicated to chemical propulsion, which relies on chemical gradients arising from reactions on the device surface. The use of these systems in vivo is challenging because of limitations in controlling trajectory and the need for an appropriate fuel at the proper concentration. For therapies in which motion control is less relevant, devices have demonstrated potential for in vivo applications, such as enzymatically propelled nanomotors within the rodent bladder (*9*). Another possibility for propulsion is to use external sources of energy to provide motion to small-scale structures (*10*). Light can propel small-scale devices by imparting momentum or by inducing photocatalytic reactions. However, light penetration into tissues is often limited. A more practical strategy for microdevice actuation in vivo entails the use of ultrasound, because this method displays biocompatibility over a broad window of frequencies. Recently, ultrasound was used to trap and navigate microstructures within mouse capillaries (*11*). However, this approach also faces challenges such as limited navigation capabilities and the absorption of ultrasound by body tissues.

Externally generated magnetic fields are likely to be the most viable option for the navigation and actuation of small-scale structures within the human body, at least in the near term. Magnetic fields offer a diverse range of locomotion strategies for microrobots (*11*). Different approaches are based on structural design and the type of magnetic fields used, such as field gradients and oscillating or rotating fields. Magnetic fields can also be combined with other propulsion approaches to improve navigability and control, as well as trigger other functionalities of the microrobot such as shape-morphing, heating, and magnetoelectricity. Shape transformation, for example, can be used for optimizing navigation or tissue interaction. Magnetic fields can induce hyperthermia in magnetic microrobots, which can serve as an effective approach for tumor ablation. The incorporation of magnetoelectric materials into microrobots generates localized electric fields by external magnetic field stimulation. These electric fields activate calcium channels that can stimulate and repair damaged tissues in the nervous system, cartilage, or bone (*12*).

An important challenge is the core magnetic material needed for device propulsion. Many magnetic microrobots reported so far comprise materials with poor biocompatibility characteristics, such as nickel-, cobalt-, and neodymium-based metals and alloys. The most promising candidate is iron (*6*), the only magnetic element that simultaneously displays excellent saturation magnetization, which is the maximum magnetic response that a material can exhibit when subjected to increasing magnetic fields, and a relatively low cytotoxicity. A possible concern with iron is its poor resistance to corrosion, a feature that is appealing for biodegradable microrobots but that poses substantial fabrication challenges at small scales. Thus, remaining options for biocompatible magnetic materials include iron-based alloys and iron-based oxides. Iron-based alloys, such as iron-platinum (FePt) nanomagnets, have shown promise in transfecting DNA plasmids in cancer cells (*13*). However, to preserve the hard-magnetic properties of FePt, it must be processed into a specific stoichiometry in sizes suitable for body clearance (less than 10 nm in diameter). Iron oxide–based nanoparticles seem to be a good option for biomedical microrobots because they can be processed in clearable sizes, and their saturation magnetization and coercivity (responsiveness to magnetic fields) can be widely tailored.

"...innovations must align with clinical needs and real-world health care practice."

Tracking microrobots after implantation is also important. Among medical imaging techniques, x-ray computed tomography (CT) and MRI display the highest spatial resolution of 1000 and 500 μm, respectively. This means that in vivo imaging of a single microrobot is difficult. However, it is unlikely that a single microrobot would accomplish a therapeutic task; swarms, superstructure assemblies, or polymeric composites of microrobots that deliver therapeutic payloads to tissues are envisioned. The most realistic procedure is to inject these agents in groups that are sufficiently numerous to be tracked by conventional medical imaging techniques. It is preferable for the devices to degrade harmlessly in the body, rather than require removal. Recently, microrobots composed of polymeric composite bodies that can degrade through mechanisms such as pH or enzymatic digestion have been designed. Additionally, their chemical structure can be programmed to slowly dissolve and be cleared by the body (*14*). With recent advances in additive micromanufacturing, such as two-photon polymerization, sophisticated designs can be created. Many of these microrobots use photosensitive chemicals that cause inflammation or cytotoxicity. Ongoing work aims to create high-resolution bio-inert inks (*15*), which are synthetic or animal-based, for microrobot production.

Two important questions remain. How many microrobots are necessary to deliver a therapeutic dose of a drug to a target tissue? And how will a medical procedure be performed with these devices? Motion performance of magnetic microrobots in vivo is being increasingly investigated, especially in the blood vasculature, and the requirements for magnetic field properties are becoming clearer. However, with speeds of a few body lengths per second (i.e., ~100 μm/s), a microrobot could take up to 3 hours to travel from the arm (point of injection) to the brain (~1 m). This time scale is too long for many applications, such as stroke treatment. Thus, catheters or endoscopes could be used. These devices have high levels of dexterity and flexibility and can move through the vasculature rapidly, so they could deliver microrobots near the target. The deployed microrobots could move with or against the blood flow, or the flow could be briefly interrupted to enable them to swim unimpeded to locations deeper within the vasculature (see the figure). For example, by precisely delivering thrombolytics to hard-to-reach vessels in the brain, the systemic risks of hemorrhage and side effects associated with these agents could be overcome by using microrobots in the treatment of stroke.

Magnetic navigation systems that generate the necessary magnetic fields and field gradients to direct microrobots in the body are a key component for realizing medical procedures. These systems will be positioned near the patient, so they must be compatible with clinical settings and easily integrate with health care facilities in terms of building infrastructure and medical imaging techniques. They should also pose no risk both to the patient and clinician. Many systems under consideration are based on mobile permanent magnets. These magnets cannot be switched off, and consequently can become hazardous, because they can exert forces on magnetic medical tools.

Permanent magnet-based systems are also limited in terms of versatility and limited dynamic response. By contrast, electromagnetic navigation systems can produce rapidly varying, complex fields and field gradients to steer robots. For example, the Navion consists of a relatively compact electromagnetic system, making it easily transportable throughout clinics, integrable into standard operating rooms, and adaptable to commercial fluoroscopy and CT systems. In vivo trials of diagnostic cerebral angiography with magnetic robotic catheters are currently being conducted in large animal models, demonstrating that human-scale navigation is possible.

Obtaining regulatory approval is a major barrier for integrating microrobotic technologies into the clinic. Regulatory hurdles, which include extensive biocompatibility and pharmacodynamic studies, must be considered from device conception to thoroughly understand possible side effects. Partnering with clinicians is also key in understanding treatment procedures (i.e., surgical workflow, medical devices needed, sterilization procedures) and the complexities of health care facilities (i.e., operating theater space, imaging, available trained personnel). In other words, innovations must align with clinical needs and real-world health care practice. Imagining procedures from only an engineering perspective can lead to rejection by practitioners owing to unnecessary complexity. It is important to focus on simplicity, at least for the first attempts when translating microrobots from the lab to clinics. ■

REFERENCES AND NOTES

1. D. Sun, W. Gao, H. Hu, S. Zhou, *Acta Pharm. Sin. B* **12**, 3049 (2022).
2. H. C. Berg, *Phys. Today* **53**, 24 (2000).
3. H. W. Huang, M. S. Sakar, A. J. Petruska, S. Pané, B. J. Nelson, *Nat. Commun.* **7**, 12263 (2016).
4. C. Hu, S. Pané, B. J. Nelson, *Annu. Rev. Control. Robot. Auton. Syst.* **1**, 53 (2018).
5. C. C. J. Alcântara *et al.*, *Nat. Commun.* **11**, 5957 (2020).
6. O. Felfoul *et al.*, *Nat. Nanotechnol.* **11**, 941 (2016).
7. G. Go *et al.*, *Sci. Adv.* **8**, eabq8545 (2022).
8. S. Jeon *et al.*, *Sci. Robot.* **4**, eaav4317 (2019).
9. A. C. Hortelao *et al.*, *Sci. Robot.* **6**, eabd2823 (2021).
10. J. Li, B. Esteban-Fernández de Ávila, W. Gao, L. Zhang, J. Wang, *Sci. Robot.* **2**, eaam6431 (2017).
11. W. C. Lo, C.-H. Fan, Y.-J. Ho, C.-W. Lin, C.-K. Yeh, *Proc. Natl. Acad. Sci. U.S.A.* **118**, e2023188118 (2021).
12. M. Dong *et al.*, *Adv. Funct. Mater.* **30**, 1910323 (2020).
13. V. M. Kadiri *et al.*, *Adv. Mater.* **32**, 2001114 (2020).
14. J. Llacer-Wintle *et al.*, *Adv. Mater.* **33**, 2102049 (2021).
15. M. Falandt *et al.*, *Adv. Mater. Technol.* **8**, 2300026 (2023).

ACKNOWLEDGMENTS

B.J.N. is a co-founder of Nanoflex Robotics AG and MagnetbotiX AG. B.J.N. and S.P. are inventors on patents related to microrobots. B.J.N. is an inventor on patents related to magnetic navigation systems.

10.1126/science.adh3073

CHEMISTRY

Controlling precision on the ring

Desired borylation of fluoroaromatic compounds is achieved with cobalt catalysts

By **Guillaume Berionni**

The synthesis of aromatic and heteroaromatic molecules is foundational to the design of many desirable agrochemicals and pharmaceuticals (*1*). Their chemical diversity can be achieved by converting a carbon-hydrogen bond (C–H) to a C–X bond (where X is usually oxygen, nitrogen, or carbon) in a selective manner (*2*). Such C–H functionalization with boron (B) is particularly useful because C–B bonds can readily be converted into a variety of substituents, creating the building blocks for compounds of interest (*3*). However, it is challenging to functionalize a specific position on an aromatic ring by C–H borylation. On page 1165 of this issue, Roque *et al.* (*4*) report a sustainable and cost-effective cobalt-catalyzed C–H borylation method that generates important borylated fluoroaromatics and heteroaromatics that are medicinally relevant compounds.

"...it is challenging to functionalize a specific position on an aromatic ring by C–H borylation."

One of the most versatile C–H borylation methods uses catalysts containing iridium—an expensive, extremely rare transition metal (*5*). Complete control over the position on an aromatic ring that gets selectively borylated is usually achieved by exploiting the aromatic substrate's steric properties and with the assistance of functional groups and chelating agents that bond with the metal center of the catalyst (*5*). However, it is challenging to selectively functionalize a desired position of an aromatic substrate by undirected C–H borylation (*6*)—that is, having the modification occur specifically at a C–H bond without first coordinating and orienting the metal in proximity to the target site on the ring. It is also difficult to replace iridium with a more abundant metal (a metal in the first row of the periodic table) because of their lower reactivity.

Roque *et al.* achieved undirected *meta*-borylation of fluoroaromatics and heteroaromatics by highly selective, catalyst-controlled functionalization of the distal *meta* C–H bond to fluorine. The undirected C–H borylation of fluorinated compounds is a long-standing challenge in chemistry owing to the weak coordinating ability of fluoro substituents and their similar size to hydrogen (*4*). Key to this achievement was the use of a pincer cobalt complex as a catalyst. Cobalt complexes supported by electron-rich pincer ligands participate in C–H activation reactions with arenes (*7*) and offer complementary regioselectivity to iridium (*8*, *9*).

Part of the catalyst design strategy of Roque *et al.* was to use an *N*-alkyl-imidazole–substituted pyridine dicarbene (ACNC) electron-rich pincer ligand to stabilize the reactive methyl-cobalt fragment. Pincer ligands are typically based on a planar scaffold and consist of a central aromatic or heteroaromatic core tethered to two usually bulky electron-donor moieties (such as amines, phosphines, and *N*-heterocyclic carbenes) (*10*). Although the pincer-type ligand platform is one of the most highly versatile and widely used for modifying and controlling the reactivities of transition metals, such as iridium and rhodium, first-row transition metals and nonprecious metals have become the focus of extensive research efforts for performing C–H activations in recent years.

The well-defined methyl-cobalt complexes reported by Roque *et al.* were characterized by x-ray diffraction crystallography, providing a detailed steric cartography (*11*) of the cobalt atom coordination sphere. Key to efficient C–H activation was the steric disposition of the wingtip groups of the *N*-heterocyclic carbenes, which control accessibility of the cobalt center without excessively shielding it. The so-called sterically attenuated ACNC cobalt complex was crucial because the *N*-heterocyclic carbenes bearing large aryl groups shut down the process. This fine-tuning of the steric and electronic properties of the cobalt center provided an optimal balance between conformational rigidity and steric accessibility of the target fluorinated aromatic substrates.

Department of Chemistry and Namur Institute of Structured Matter, Université de Namur, 5000 Namur, Belgium.
Email: guillaume.berionni@unamur.be

A large variety of substrates ranging from mono- to tetra-substituted arenes underwent selective *meta* C–H borylation with high yields (>80%) and selectivities [>9:1 *meta*-to-*ortho* (m:o)] to produce valuable and previously difficult to access functionalized borylated fluoroaromatics. The systematic screening performed by Roque *et al.* on three generations of pincer cobalt complexes indicated that catalyst-controlled *meta*-selectivity was much greater than that with previous first and second generations.

Roque *et al.* observed that C–H activation *para*-to-boron and *meta*-to-fluorine occurred independently of the substrate, indicating insensitivity of the pincer cobalt catalyst to substrate modifications and providing a general synthetically useful route to diborylarenes and borylated fluoroarenes. Pyridines, the second most encountered heterocyclic compound in clinically approved pharmaceuticals, also displayed *meta*-selective C–H borylation as well as a range of nonfluorinated aromatics.

Future developments will surely be directed to making further use of sterically attenuated cobalt complexes in the borylation of fluorinated compounds. Breakthroughs in the late-stage C–H borylation (*12*) of complex molecules and drugs are therefore anticipated. The combination of pincer ligands with nonprecious metals and with main-group elements (*13*–*15*) will provide future opportunities for new types of reactivity. ■

REFERENCES AND NOTES

1. A. Nilova *et al.*, *J. Med. Chem.* **63**, 13389 (2020).
2. J. Yamaguchi, A. D. Yamaguchi, K. Itami, *Angew. Chem. Int. Ed.* **51**, 8960 (2012).
3. J. W. B. Fyfe, A. J. B. Watson, *Chem* **3**, 31 (2017).
4. J. B. Roque *et al.*, *Science* **382**, 1165 (2023).
5. I. F. Yu, J. W. Wilson, J. F. Hartwig, *Chem. Rev.* **123**, 11619 (2023).
6. B. Ramadoss *et al.*, *Science* **375**, 658 (2022).
7. J. V. Obligacion, S. P. Semproni, P. J. Chirik, *J. Am. Chem. Soc.* **136**, 4133 (2014).
8. T. P. Pabst, P. J. Chirik, *J. Am. Chem. Soc.* **144**, 6465 (2022).
9. T. P. Pabst, L. Quach, K. T. MacMillan, P. J. Chirik, *Chem* **7**, 237 (2021).
10. J. I. van der Vlugt, J. N. H. Reek, *Angew. Chem. Int. Ed.* **48**, 8832 (2009).
11. H. Clavier, S. P. Nolan, *Chem. Commun.* **46**, 841 (2010).
12. L. Zhang, T. Ritter, *J. Am. Chem. Soc.* **144**, 2399 (2022).
13. G. Berionni, *Angew. Chem. Int. Ed.* **61**, e202210284 (2022).
14. S. A. Iqbal, J. Pahl, K. Yuan, M. J. Ingleson, *Chem. Soc. Rev.* **49**, 4564 (2020).
15. N. R. Judge, A. Logallo, E. Hevia, *Chem. Sci.* **14**, 11617 (2023).

ACKNOWLEDGMENTS

The Fonds de la Recherche Scientifique (FRS-FNRS) and the European Research Council (ERC) (grant agreement no. 101044649) are acknowledged for financial support.

10.1126/science.adl4860

GRAPHIC: K. HOLOSKI/*SCIENCE*

GEOLOGY

Sediment austerity is the new coastal norm

Insufficient river-derived sediment for tidal marshes requires creative, local management

By **Laurel G. Larsen**[1,2] *and* **Brett Milligan**[3]

Tidal marshes provide habitat for juvenile fish, birds, and other wildlife; defend coastlines against storms; and are a major global carbon sink. However, relative sea-level rise (RSLR) threatens them with drowning. Marshes continually build elevation by accreting sediment, but whether riverine sediment supplies are adequate to support accretion that keeps pace with RSLR has remained uncertain. On page 1191 of this issue, Ensign *et al.* (*1*) show that even in a best-case scenario, when all riverine sediment is deposited on marshes in the receiving estuaries across the United States, existing supplies are generally insufficient for accretion to keep pace with RSLR. This finding underscores the need for creative coastal planning in a time of sediment austerity that recognizes that change is inevitable and capitalizes on natural sediment redistribution processes that will prolong marsh persistence.

Coastal marshes build elevation naturally by trapping sediment delivered by tides and floods and producing organic matter. In many of these marshes, suspended sediment delivery is the key factor driving elevation change (*2*, *3*). Diminishing the delivery of sediment to the coast by trapping it behind dams is thought to threaten coastal marsh resilience. Furthermore, satellite data suggest that suspended sediment at river outlets has declined by nearly half in the northern hemisphere since 1984 (*4*).

Ensign *et al.* studied 4972 US rivers and used observational data to determine volumes of sediment available for estuarine tidal marshes. The results suggest that an order-of-magnitude more sediment would be needed for marshes to keep up with RSLR. In most locations, dam removal

Managing sediment to protect tidal marshes

Sediment supply from rivers is not sufficient to enable tidal marshes to keep pace with sea-level rise. This necessitates active, human-led redistribution of sediment (sediment choreography). These activities can include facilitating the delivery of riverine sediment to the coast. Sediment can also be excavated inland and strategically placed in areas where natural processes (e.g., resuspension, longshore currents) will distribute it to desired locations. Sediment can also be directly sprayed onto priority areas, for example, marshes that are near tipping points or whose loss would threaten important human assets. In some places, accepting retreat of marshland may be inevitable. In others, marshes may be able to expand inland, although new marshes will also require sediment deliveries.

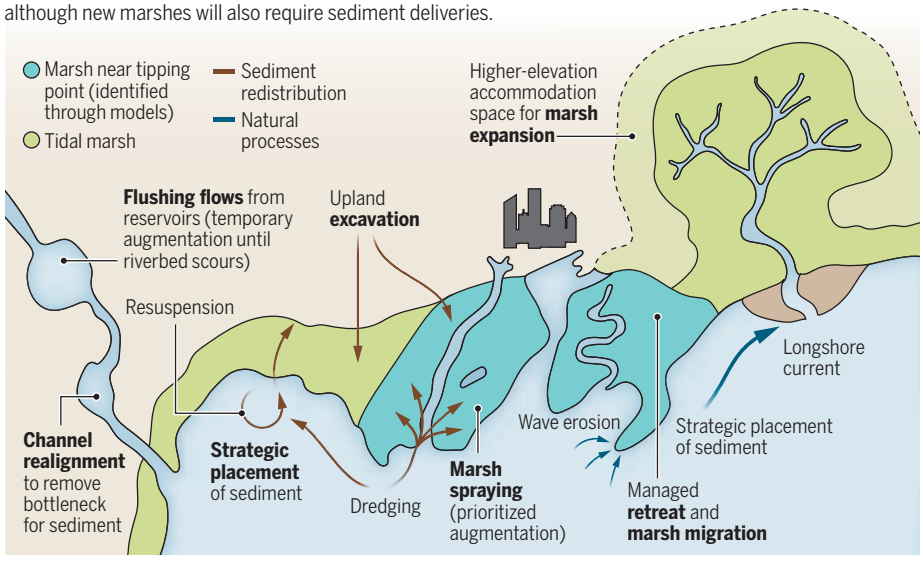

would not supply the needed sediment. Yet in more than half of the 93 sites with accretion data, marshes are building elevation faster than would be expected from the supply of sediment from rivers. Why?

Organic sediment accretion resulting from incomplete decomposition of vegetation can increase with RSLR, depending on the species and the preexisting marsh elevation. However, recent findings suggest that in at least some salt marshes, most of the carbon that accumulates long term is old carbon originating from elsewhere rather than produced in place (*5*). Ensign *et al*. additionally found that accounting for an average rate of organic accretion does not substantially change the fraction of marshes that are gaining elevation.

Recent work underscores the role of sediments from eroding coastlines or resuspended from the offshore seabed in helping marshes build elevation. For example, despite rapid RSLR and a 70% decline in riverine sediment, marshes in the Yangtze River delta in China are accreting rapidly, fed by resuspended material eroded from the delta front (*6*, *7*). Worldwide, measured sediment accumulation rates in offshore deposits accelerated in the 20th century and are attributed to enhanced coastal and near-coastal erosion (*8*). Furthermore, RSLR may make this material more available to marshes. For the Plum Island Estuary in Massachusetts, USA, 0.5 m of RSLR has been estimated to produce 35% more resuspension of mud and 6.6% more sediment deposited on marshes (*9*).

Notably, the unexpected resilience of marshes reported by Ensign *et al*. is likely to be temporary under rapid RSLR. Tidal wetlands that build elevation mostly through organic accretion are widely regarded as less resilient than others because of susceptibility to waterlogging, sulfide toxicity, or species shifts (*10*, *11*). Furthermore, RSLR promotes tidal channel deepening and ebb dominance (by which flows are faster and sediment loads higher on ebb tides than flood tides), leading to net export of sediment from the estuary (*9*). Ultimately, this process can lead to steepening of the continental shelf and more lateral marsh erosion by waves (*6*). Models project that resuspension of coastal sediment may have prolonged the persistence of marshes in the Yellow River delta in China by about a century and will likely prolong the existence of marshes in the Yangtze River delta by about 150 years (*6*). This process can explain why marshes seem to survive higher threshold rates of RSLR today compared with that in the stratigraphic record (for which temporal resolution is too poor to detect temporary resilience) (*12*). However, these collective findings suggest that without sufficient riverine sediment supply from inland, eventual losses are inevitable.

Coastal communities must proactively manage, or "choreograph," sediment (*13*), exploiting relatively untapped sources, such as excavated sediment, construction waste, and dredged materials. However, these solutions are unlikely to match the magnitude of demand, requiring clear priorities and community objectives for coastal management. Site-specific models and planning that account for offshore hydrodynamics, changing seabed elevations, multiscale sediment feedbacks, and diverse sediment sources are needed to help identify where marshes would most benefit from augmentation and where sediments might be most strategically placed so that natural processes aid delivery to desired locations (see the figure). Pilot projects and experimentation are also needed to better understand how sediment augmentation practices might be refined and scaled up. End users of this science must also grapple with the inevitability of surprise. For decades, the observed changes to tidal marshes have differed from conceptualizations and model predictions. Large uncertainties remain regarding lateral sediment redistribution processes; dynamic bathymetry (seabed elevations); changes to sediment supply from watersheds as they adjust to more intense precipitation, changing vegetation cover, and increased fire frequency; and how marsh vegetation—sediment trappers—will respond to a range of stressors that include more frequent climate extremes and changing nutrient inputs. ■

[1]Department of Geography, University of California, Berkeley, CA, USA. [2]Department of Civil and Environmental Engineering, University of California, Berkeley, CA, USA. [3]Department of Human Ecology, University of California, Davis, CA, USA. Email: laurel@berkeley.edu; bmilligan@ucdavis.edu

REFERENCES AND NOTES

1. S. H. Ensign *et al*., *Science* **382**, 1191 (2023).
2. Z. Liu *et al*., *Commun. Earth Environ.* **2**, 1 (2021).
3. O. Gourgue *et al*., *Earth Surf. Dyn.* **10**, 531 (2022).
4. E. N. Dethier, C. E. Renshaw, F. J. Magilligan, *Science* **376**, 1447 (2022).
5. M. Van de Broek *et al*., *Glob. Change Biol.* **24**, 2498 (2018).
6. S. L. Yang *et al*., *Limnol. Oceanogr.* **65**, 1990 (2020).
7. H. F. Yang *et al*., *Geomorphology* **381**, 107646 (2021).
8. A. B. Rodriguez, B. A. McKee, C. B. Miller, M. C. Bost, A. N. Atencio, *Nat. Commun.* **11**, 3249 (2020).
9. X. Zhang *et al*., *Geophys. Res. Lett.* **47**, e2020GL087862 (2020).
10. M. L. Kirwan, J. P. Megonigal, G. L. Noyce, A. J. Smith, *Nat. Rev. Earth Environ.* **4**, 393 (2023).
11. C. Zhu, J. A. Langley, L. H. Ziska, D. R. Cahoon, J. P. Megonigal, *Sci. Adv.* **8**, eabn0054 (2022).
12. T. E. Törnqvist *et al*., *AGU Adv.* **2**, e2020AV000334 (2021).
13. B. Milligan, R. Holmes, *Shore Beach* **85**, 2 (2017).

10.1126/science.adl4251

ECOLOGY

Human–wild bird cooperation

Honeyguides learn distinct signals made by honey hunters from different cultures

By **William A. Searcy**[1] *and* **Stephen Nowicki**[2]

Mutualisms in which humans cooperate with wild animals are exceedingly rare (*1*). One such system involves the greater honeyguide (*Indicator indicator*), a small African bird that leads humans to sources of honey, principally the nests of African honey bees (*Apis mellifera)*. Once a nest is found, the human honey hunters break into it to obtain honey and bee larvae, and the birds benefit from consuming beeswax in the now-exposed honeycomb. Both the birds and the humans use specialized sounds to communicate their availability to participate in this cooperative interaction (*2*). On page 1155 of this issue, Spottiswoode and Wood (*3*) reveal a new layer of complexity in this remarkable mutualism, demonstrating that humans in two geographic areas use different sounds to communicate to the honeyguides, and that the birds respond preferentially to the signals used in their own local area. The coordination between signal and response suggests that cultural coevolution has occurred.

The two areas studied by Spottiswoode and Wood are northern Mozambique, where the honey hunters are from the Yao cultural group, and northern Tanzania, where the honey hunters are from the Hadza culture. The Yao communicate with honeyguides using a trill followed by a grunt ("brrrr-hm"), whereas the Hadza use a melodic whistle. The authors show through field playback experiments that honeyguides in the Yao area are almost three times as likely to initiate guiding in response to the Yao's brrrr-hm as to the Hadza's whistle, whereas honeyguides in the Hadza area are more than three times as likely to respond to the Hadza's whistle as to the Yao's brrrr-hm. Thus, signal and response both vary geographically, with each species' behavior

meshing with that of its local counterparts of the other species.

Which human signal is used where might be explained by environmental transmission, with hunters using a signal that transmits particularly well in the habitats in which they forage. Measurements of signal attenuation, however, do not support this idea, as the Hadza whistle attenuates less rapidly with distance than the Yao brrrr-hm in both geographic areas. Spottiswoode and Wood instead favor an economic explanation for the choice of signal. Hadza men, who typically hunt small game while foraging for honey, claim their whistles sound like birds, and therefore presumably are unlikely to scare away prey. The Yao do not hunt animals while foraging for honey, so scaring game is not an issue for them. The word-like signal they use in attracting honeyguides may instead identify them as humans and thereby help ward off dangerous animals such as buffalo and lions.

The greater honeyguide (*Indicator indicator*) leads humans to African honey bee (*Apis mellifera*) nests and consumes beeswax that is exposed when humans remove the honey.

PHOTO: NIGEL J. DENNIS

Spottiswoode and Wood propose that the geographic variation they have identified in this mutualism is the product of cultural coevolution. To qualify as cultural, the cooperative behaviors would have to be acquired through social learning from individuals of the same species. That proposition is noncontroversial on the human side, and indeed, Yao honey hunters report learning their honeyguide signal from their fathers (*2*). Social learning, however, is less of a given on the honeyguide side. The taxonomic order of birds to which honeyguides belong (*Piciformes*) is thought not to exhibit vocal production learning (*4*), meaning that birds in this order do not acquire the form of their vocal signals through experience with the signals of others. Learning geographic signal variants is not required of the honeyguides, however, as they use the same chatter vocalization to communicate to humans throughout their range (*5, 6*). Instead, what is required of honeyguides is another form of vocal learning—comprehension learning—in which the meaning of a signal is learned (*7*). Comprehension learning is common in birds (*8*) and is the simplest explanation for how honeyguides in different areas come to respond to different signals. Whether social learning is involved, however, is not so obvious.

Honeyguides might learn to respond to the local honeyguide-directed signal by watching and copying the behavior of older honeyguides, but other explanations are possible. One possibility is that young honeyguides form an association between the human signal and the reward directly, through encountering honey hunters giving the signal and then consuming beeswax made available by the hunters' activities. For behavioral traditions in general, observations of geographic variation, even when coupled with detailed evidence of the behavior's development, are usually considered insufficient to demonstrate that social learning has occurred (*9*). Experiments will be necessary to establish conclusively whether the match of honeyguide response to human signal is maintained by social learning, for example, experiments that determine whether young honeyguides acquire different response patterns depending on which pattern is modeled for them by older birds.

The human–honeyguide interaction superficially gives the impression of idyllic benevolence: Honeyguides put in considerable effort helping their human partners find food and are faithfully rewarded by being given food in return. As is common for biological mutualisms (*10*), the details of the interaction turn out to be messier than this. In some human cultures, honey hunters purposefully leave out honeycomb to reward honeyeaters, but in others the hunters actively seek to deny the birds any reward, by collecting, burying, or burning any honeycomb exposed when they depredate a nest (*5*, *6*). The rationale given for these acts is that keeping the birds hungry causes them to continue guiding. In cultures in which honey hunters purposefully leave honeycomb for the guiding birds, that resource may be exploited by a variety of other animals, including mammals such as honey badgers and birds such as other, nonguiding species of honeyeaters (*11*). Exploiters also often include greater honeyguide individuals who themselves have not guided but are nevertheless able to scrounge beeswax exposed through the guiding efforts of others (*12*). A promising question for future research is whether geographic differences in human cultural preferences for rewarding or not rewarding honeyguides affect the preferences of individual birds for guiding versus exploiting the guiding of others. ■

[1]Department of Biology, University of Miami, Miami, FL, USA.
[2]Department of Biology, Duke University, Durham, NC, USA.
Email: wsearcy@miami.edu

REFERENCES AND NOTES

1. D. L. Cram *et al.*, *People Nat.* **4**, 841 (2022).
2. C. N. Spottiswoode, K. S. Begg, C. M. Begg, *Science* **353**, 387 (2016).
3. C. N. Spottiswoode, B. M. Wood, *Science* **382**, 1155 (2023).
4. E. D. Jarvis *et al.*, *Science* **346**, 1320 (2014).
5. B. M. Wood, H. Pontzer, D. A. Raichlen, F. W. Marlowe, *Evol. Hum. Behav.* **35**, 540 (2014).
6. J. E. M. van der Wal, I. I. Gedi, C. N. Spottiswoode, *Front. Conserv. Sci.* **2**, 727479 (2022).
7. V. M. Janik, P. J. B. Slater, *Anim. Behav.* **60**, 1 (2000).
8. W. A. Searcy, S. Nowicki, *Anim. Behav.* **151**, 217 (2019).
9. B. G. Galef, *Learn. Behav.* **32**, 53 (2004).
10. J. L. Bronstein, *Ecol. Lett.* **4**, 277 (2001).
11. D. J. Lloyd-Jones *et al.*, *Proc. R. Soc. B* **289**, 20221443 (2022).
12. D. L. Cram *et al.*, *Proc. R. Soc. B* **290**, 20232024 (2023).

10.1126/science.adl5923

MATERIALS SCIENCE

Using ultrasound to 3D-print materials

Ultrasound allows additive manufacturing to go deeper—potentially inside the body

By **Yuxing Yao**[1,2] and **Mikhail G. Shapiro**[1,2,3]

Additive manufacturing is an emerging technology that involves the progressive assembly of spatially patterned material, and it is reshaping materials fabrication. This process is becoming widely adopted for products ranging from architectural prototypes to consumer footwear (*1*). However, most existing methods to produce three-dimensional (3D) shapes require a raster-scanning printer (*2*–*4*) or use patterned light (*5*, *6*) to induce material formation, which limits manufacturing to physically or optically accessible conditions. In principle, ultrasound could be used to print within centimeter-scale volumes of optically opaque media at a spatial resolution of ~100 μm. This strategy could even work inside the body. On page 1148 of this issue, Kuang *et al.* (*7*) present an ultrasound-based volumetric printing method, showcasing fast and precise printing capabilities, and demonstrate its use for noninvasive biomaterial printing inside living tissue ex vivo.

"...noninvasive biomaterial printing inside living tissue ex vivo."

Ultrasound is commonly used in diagnostic imaging and therapy because of its deep penetration into a variety of materials. But using ultrasound for 3D printing has two major challenges: To induce material polymerization, ultrasound energy must be converted into chemical reactions, which does not happen directly (unlike photochemistry). Additionally, as it travels through a liquid, ultrasound can cause streaming flows that disturb the medium and can blur the resolution and resulting structural features, which would impede accurate 3D printing. Kuang *et al.* overcame these challenges by developing a new "sono-ink." This concoction of polymers, particles, and chemical initiators absorbs sound waves to form a gel to prevent streaming flow and simultaneously initiate heat-triggered acrylate polymerization, leading to localized material fabrication.

Previous work on ultrasonic 3D printing used acoustic bubble cavitation, which involves the rapid growth and collapse of gas bubbles, to generate reactive oxygen species, leading to local material synthesis (*8*). However, this uses a relatively low-viscosity fluid that results in streaming and requires a 2D platform on which to deposit the printed materials. The key to the sono-ink is that it eschews cavitation and harnesses the effects of ultrasound-generated heat to control fluid flow and drive reactions. In response to a small initial temperature increase at the ultrasound focus, a heat-responsive polymer in the ink rapidly undergoes a phase transition to form a gel, which reduces streaming and keeps the heat-driven chemistry voxel sharp. The gel efficiently absorbs ultrasound and converts it to more heat, enhancing confinement and accelerating polymerization. As a result, it is possible to print voxels of ~1 mm, only two to three times the wavelength of the ultrasound used, at a depth of several centimeters to form complex geometries.

An interesting application of sono-ink is the noninvasive fabrication of biomaterials. Kuang *et al.* provide proofs of concept for how this could be used to address bone defects through the in situ fabrication of artificial bone or to treat a form of atrial fibrillation by occluding a left atrial appendage of the heart. Both of these demonstrations were performed in ex vivo tissues infused with sono-ink. If optimized and demonstrated in live animal models, these approaches could be a promising way to convert open surgeries to less-invasive ultrasound-based treatments.

Some concerns must be addressed for this technology to be applied in patients. Volumetric printing inside the body requires the infusion of sono-ink at high concentrations, which may cause toxicity (*9*). Additionally, the transient high ultrasound pressure at the focus (35 to 55 MPa) and the accompanying temperature increase (which exceeds 70°C locally) can cause tissue damage if it is not adequately targeted and confined in space and time. These considerations will likely guide the development of biocompatible sono-inks and accompanying ultrasound techniques. This further work would also benefit from a deeper understanding of the mechanisms that allow sono-inks to favor thermal effects over cavitation effects, even at relatively high pressure. In principle, the penetration depth of ultrasound gives this approach an advantage over competing methods that fabricate biomaterials in vivo using infrared light (*10*).

On a more fundamental level, the sono-ink concept presents interesting problems for ultrasound engineering, chemistry, and materials. For example, in this inherently nonlinear process, the increased sound absorption of a printing focus can change the ultrasound pattern downstream of that focus, casting a type of "shadow." This will make it less straightforward to combine this technique with advanced ultrasound methods such as acoustic holography (*11*), which could otherwise allow a whole object to be printed at once.

Further development of acoustic 3D printing could construct body-machine interfaces. 3D-printed soft materials could offer a diverse range of functionalities, such as electric conductivity, drug elution, and mechanical robustness. For example, coupled with conductive polymers (*12*), acoustic printing could noninvasively pattern flexible electronics for interfacing with organs such as the heart, enabling long-term monitoring and actuation of a patient's cardiac function. Additionally, as shown by Kuang *et al.*, materials formed with sono-ink could elute drugs, facilitating localized chemotherapy to prevent tumor recurrence after resection. Furthermore, in situ biomaterial fabrication with intricate shapes and mechanical properties can stimulate cell or tissue interactions, potentially guiding cell differentiation and controlling organ regeneration (*13*, *14*). Beyond biomedical applications, fast printing speed and the ability to operate in optically opaque materials also have applications in consumer product fabrication. It is conceivable that the running shoes of the future could be printed with the same acoustic method that repairs bones. ■

[1]Division of Chemistry and Chemical Engineering, California Institute of Technology, Pasadena, CA, USA. [2]Division of Engineering and Applied Science, California Institute of Technology, Pasadena, CA, USA. [3]Howard Hughes Medical Institute, California Institute of Technology, Pasadena, CA, USA. Email: mikhail@caltech.edu

REFERENCES AND NOTES

1. J. R. Tumbleston *et al.*, *Science* **347**, 1349 (2015).
2. Y. S. Zhang *et al.*, *Nat. Rev. Methods Primers* **1**, 75 (2021).
3. N. M. Larson *et al.*, *Nature* **613**, 682 (2023).
4. M. A. Skylar-Scott *et al.*, *Nature* **575**, 330 (2019).
5. B. E. Kelly *et al.*, *Science* **363**, 1075 (2019).
6. F. Han *et al.*, *Science* **378**, 1325 (2022).
7. X. Kuang *et al.*, *Science* **382**, 1148 (2023).
8. M. Habibi *et al.*, *Nat. Commun.* **13**, 1800 (2022).
9. L. S. Andrews, J. J. Clary, *J. Toxicol. Environ. Health* **19**, 149 (1986).
10. Y. Chen *et al.*, *Sci. Adv.* **6**, eaba7406 (2020).
11. K. Melde *et al.*, *Sci. Adv.* **9**, eadf6182 (2023).
12. Y. Wang *et al.*, *Sci. Adv.* **3**, e1602076 (2017).
13. N. Gjorevski *et al.*, *Science* **375**, eaaw9021 (2022).
14. W. Sun *et al.*, *Biofabrication* **12**, 022002 (2020).

10.1126/science.adl5887

RETROSPECTIVE

Philip N. Benfey (1953–2023)

A "ring" master of plant development and cellular genomics

By **Gloria M. Coruzzi** *and* **Kenneth D. Birnbaum**

Philip N. Benfey, scientist and entrepreneur, died on 26 September at the age of 70. He was a luminary in the field of developmental genetics and genomics whose work led to a better understanding of how plants pattern their organs and whose innovations pioneered plant cellular genomics with real-world applications.

Born on 31 January 1953 in Bryn Mawr, Pennsylvania, Philip, a self-described "accidental scientist," never studied biology in high school or college. He dropped out of college to gain the life experience necessary to write the Great American Novel. During more than 6 years of world travels, he worked as a logger in Oregon, a bricklayer in Melbourne, and a gardener in Japan, and he organized a train strike to fight for safety measures in Western Australia. After a trip on the Trans-Siberian Railroad, he worked as a carpenter in Paris. It was there that he found his two true and lasting loves: his wife, Elisabeth, and biology, a field she encouraged him to pursue as a "day job" to supplement his writing.

In pursuit of a career in biology, Philip received an undergraduate degree from the University of Paris VI. In 1986, he earned a PhD from Harvard Medical School under the mentorship of Philip Leder in the field of immunology. Recognizing the power of new techniques in transgenics, and with the notion that basic discoveries could be translated into transgenic plants more readily than in animals, he did postdoctoral work (1987–1990) at the Rockefeller University with Nam-Hai Chua, whose lab pioneered the cloning and use of genes in transgenic plants. In 1991, Philip started a lab in the Department of Biology at New York University (NYU), where he rose through the ranks from assistant professor to full professor. He moved to Duke University in 2002, where he was named the Paul Kramer Distinguished Professor of Biology and served as chair of the biology department for 5 years and director of the Center for Systems Biology for 6 years.

With the goal of applying basic discoveries in plant development to practical outcomes, Philip founded Grassroots Biotechnology in 2007, a computational biology company (eventually acquired by Monsanto) seeking to improve plant traits. In 2014, he cofounded Hi Fidelity Genetics with Spencer Maughan, a company that uses novel sensors and data science to inform crop decisions. And just this year, Philip cofounded Raleigh Biosciences with Ross Sozzani, which focuses on single-cell gene expression and machine learning to advance plant biology research.

Philip's primary contribution was unraveling the ways in which plant roots attain and adapt their exquisite rings of cells during development, starting from stem cells. Signaling between cells is often envisioned as a chain of envoys on a diplomatic mission—a master regulator known as a transcription factor instigates protein production, and a signal is sent across cells, where it is received by a special class of protein receptors that ultimately convey the message to the seat of power in the nucleus. Defying this paradigm, Philip's pioneering work at NYU showed that plants could take a completely different path. A transcription factor that he named SHORTROOT (SHR) can deliver the message personally, traveling through plant-specific conduits known as plasmodesmata to direct gene expression in the neighboring ring of cells in the plant root. In another classic paper, Philip and Yrjö Helariutta at the University of Helsinki showed that signaling goes both ways, with SHR's destination cell layer, the endodermis, talking back to SHR's home layer, the central cylinder (or stele).

PHOTO: LES TODD

The SHR signaling circuit established an elegant principle of a plant's self-organizing rings, with a central layer generating a division to create an outer layer that subsequently communicates back to pattern the inner layer. SHR also firmly established the concept of the mobile transcription factor in plants—subsequently shown to be a recurring mechanism in plant development. Many labs have since shown that SHR is reused in evolution as a "ring-maker," from corn to rice to the symbiosis-hosting structures in legumes.

Philip pursued another big idea in the late 1990s. What if one could identify the active genes in any given specialized ring of cells? Plants can be broken apart into constituent cells using techniques dating back to 1902. However, once broken apart, the different specialized cells mix together, making them impossible to disentangle. The Benfey lab's new twist on this method was to generate a panel of cell-specific fluorescent markers that keep track of each cell type after the root cells are broken apart. With David Galbraith at the University of Arizona, Philip showed that the glowing cells could be captured by an instrument more common to medical centers: the fluorescence-activated cell sorter. The idea met with polite skepticism and, at first, failed to obtain funding. But Philip knew when to trust his instincts and persist. Ultimately, the risky idea worked and went on to produce the gold-standard resource of cell type–specific data for the plant community.

More recently at Duke, the Benfey lab discovered oscillating gene expression circuits in plants, drawing parallels between plant lateral root initiation and somite formation in animals. The lab also showed how developmental regulators were mechanistically linked to cell cycle genes that could switch the orientation of cell division and form new layers of cell types—another addendum to ring formation. This body of work made Philip a key figure in bridging the rigor of developmental genetics with the quantitative power of genomics.

Philip was inducted into the US National Academy of Sciences in 2010, included in the Howard Hughes Medical Institute's first cohort of plant investigators in 2011, and honored as an American Society of Plant Biologists "Pioneer" in 2022 with tributes from colleagues—including G.M.C.—and mentees in his academic family tree—including K.D.B. In all his academic and entrepreneurial ventures, Philip was larger than life, and not just because of his six-foot-plus height. He commanded a room with his razor-sharp observations and visions for the future, but his demeanor melted into affection when Elisabeth walked into the room. He was also a dedicated father to his two sons, Sam and Julian. Those of us who knew Philip well grieve the loss of a friend, mentor, and colleague whose legacy will shape our field for many decades to come. ■

Department of Biology, New York University, New York, NY, USA. Email: gloria.coruzzi@nyu.edu; ken.birnbaum@nyu.edu

10.1126/science.adl4710

POLICY FORUM

INNOVATION POLICY

Improving equity in patent inventorship

Expanding who gets credit for invention may boost participation in innovation

By **Colleen V. Chien**[1] *and*
Lisa Larrimore Ouellette[2]

Inequality among patent inventors is a policy concern. For example, in the United States, if women, racial minorities, and people from low-income backgrounds invented at the same rate as that of high-income white men, the overall invention rate would quadruple (*1*). Disparities in patenting are far larger than disparities in other measures of innovation, such as scientific paper authorship or STEM (science, technology, engineering, and mathematics) workforce participation (*2*). One driver of this "innovator-inventor" gap may be the nature of attribution practices: Bias in who receives credit and differing standards for patent inventorship and scientific paper authorship suggest that marginalized scientists are more likely to be excluded as inventors, limiting their future inventive opportunities. Recent legislation requires the US Patent and Trademark Office (USPTO) to address this problem of patenting disparities, and many firms and nonprofits have committed to improving inventor equity. Here, we identify opportunities to better understand what policy interventions would be most effective at closing these attribution gaps.

THE VALUE OF ATTRIBUTION

Although the social value of strengthening or weakening patent rights remains contested, patents are widely used as a measure of innovation and bring substantial private value to the innovators named on patents (*3*). But these benefits are not equally distributed. Gaps in patenting by attributes such as gender would be substantially smaller if the pool of inventors more closely mirrored the STEM workforce or the authors of scientific papers. Women hold 29% of US science and engineering jobs but make up less than 13% of US-based patent inventors (*4*). In 2017, only 1% of female scientists and engineers received a patent; the share of male patentees among scientists and engineers was three times higher (*4*). One study of scientific research teams finds that compared with men, women are 13% less likely to be named as authors on articles and a staggering 58% less likely to be named on patents, even controlling for seniority and field (*5*). The implication is that if women were recognized on patents to the degree they are on papers, it would substantially narrow the gender patent gap.

These disparities likely have multiple causes, including inequalities in opportunity (*1*), but one factor may be attribution practices. It seems likely that scientists in less senior positions—disproportionately including women and racial minorities—are more likely to be excluded as patent inventors. One study of patent-paper pairs found junior and female scientists named as authors on a paper to be less likely than their counterparts to be named as inventors on the corresponding patent (*6*, *7*). Similarly, survey data from life scientists who contributed to a patent-paper pair suggest that hierarchical status in research groups strongly affects one's likelihood of being named a patent inventor (*8*).

Equitable inventor attribution matters not only for fairness but also because being named as a patent inventor leads to professional and economic benefits that accumulate over a career. Patents increase the earnings of inventors (*1*, *9*) and make them more invested in and less likely to leave their employers (*10*). Systemic inequity in attribution reinforces those disparities, decreasing lifetime earnings and making it harder to rise to more highly compensated positions. In the long term, this inequity affects not only who is recognized as an inventor but also what type of innovations are created. For example, all-female inventor teams are more likely to focus on women's health (*11*).

WORSE FOR PATENTS THAN PAPERS

A research team that has created a new invention may not simply list whomever they like as an inventor on their patent application. In the United States, the courts have held that each listed inventor must have contributed to the initial idea or "conception" of one of the claims in the patent, or else the patent can be invalidated. Thus, a researcher who did not contribute to the conception of an invention may not be listed on the resulting patent, even if the researcher performed the often challenging work of figuring out whether the idea actually works and how to implement it in practice—work that often qualifies for authorship of scholarly papers. In one prominent example, scientists with the US National Institutes of Health were held not to be inventors after they used their cell lines to determine that a new compound was effective against HIV/AIDS, despite being named lead authors on the corresponding scientific papers (*12*).

Despite the importance of this rule, it has no standard justification. The USPTO does not verify inventorship during the examination process, but third parties can ask the USPTO or the courts to correct inventorship or to invalidate patents with improper inventorship. Patent lawyers regularly warn clients against naming incorrect inventors because of these potential legal consequences. Jurisdictions outside the United States also generally have more restrictive criteria for inventorship than authorship.

One potential explanation for the innovator-inventor gap is bias in attribution. Because the conception standard created by US courts is not entirely clear, it is ripe for unconscious bias, and there is evidence that women scientists receive less credit than men do for similar contributions (*5*). These biases may be more pronounced for patents than for papers because attribution carries financial as well as reputational implications. Researchers who recognize that they were improperly omitted can sue to have inventorship corrected, but such lawsuits are rare, likely because of the financial and reputational costs of litigating against one's employer.

But a second potential explanation has received less attention: The legal standard for patent inventorship differs from typical norms for paper authorship in ways that are less friendly to scientists with lower status within research teams. For example, if women are less likely to play "conceptualizer" roles (such as setting a research team's direction) than implementation roles that are also crucial for bringing innovation to fruition, then they are also less likely to be permitted to add their names to resulting patents, even if they made substantial technical contributions sufficient to warrant authorship on a paper.

Empirically investigating this second explanation is challenging because the contributions of each member of a research team to

patented inventions are not routinely coded. But the specific contributions of researchers to scientific publications have been coded by using the recently introduced Contributor Roles Taxonomy (CRediT) taxonomy of 14 research roles, allowing us to quantify whether women are disproportionately less likely to play a conceptualizer role in this context.

We used data from an earlier study (*13*) of authors in PLOS journals that include details about the CRediT roles played by each author (see supplementary materials). We used the World Gender-Name Dictionary and the UCI Archive Gender-by-Name Dictionary to assign binary gender according to an author's first name to about 90% of authors in the CRediT dataset. Across all papers, women were only 38% of authors credited with "conceptualization," which is the closest role to the patent conception required of inventorship. By contrast, women were 45% of authors credited with "investigation," or actually performing the experiments and collecting data (see the figure). If a similar disparity holds for research teams working on patentable inventions, limiting inventorship to those who contributed to conception may be exacerbating the patent gender gap. In that case, expanding recognition beyond only those responsible for conception to also include those who perform experiments could boost female recognition by as much as 75% and could close the patent gender gap by 10% (see the supplementary materials).

POLICY PILOTS

To reduce disparities in patenting, stakeholders in the patent system can develop more rigorous evidence on which factors cause attribution gaps and which interventions are most effective at addressing these problems. For example, when a female paper author is left off the corresponding patent, is the problem that she should have been on the patent and was omitted because of bias, or that she could not legally have been on the patent because she did not contribute to conception?

If bias in attribution is a problem, then employers of innovators who seek numerous patents—including universities and large firms—could experiment with how they solicit information about who should be listed as an inventor. The USPTO could use policy pilots (*3*, *14*) to experiment with proactively requesting more information about who was involved in the inventive process, such as through a formal rubric. Policy-makers could also consider shoring up incentives to prevent the exclusion of inventors from the start.

[1]Berkeley Law and Berkeley Center for Law and Technology, University of California at Berkeley, Berkeley, CA, USA. [2]Stanford Law School, Stanford University, Stanford, CA, USA. Email: cchien@berkeley.edu; ouellette@law.stanford.edu

Female authorship contributions

Contributor Roles Taxonomy (CRediT) roles among PLOS publications from 2017–2018 were reported in (*13*). There were 80,643 observations of authors of identifiable binary gender with a "conceptualization" role and 86,156 with an "investigation" role (see supplementary materials).

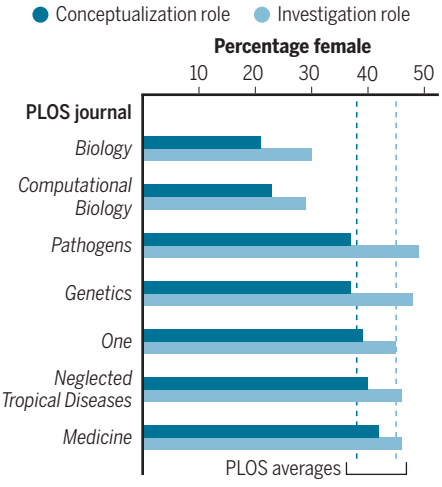

GRAPHIC: M. HERSHER/*SCIENCE*

To the extent that the problem instead stems from the constrained legal standard for inventorship, then US courts or Congress could consider whether this standard should be revised. But stakeholders could also take more modest steps to recognize contributors to patents—such as those who ran the experiments to determine whether and how an invention works—even if they are not recognized as legal inventors. For example, employers could formally credit employees as "contributors" to specific inventions. The USPTO could list this new category of invention contributors on the face of the patent alongside the names of inventors, boosting recognition of underrepresented innovators. This recognition might provide contributors with some of the same financial and other benefits that inventors enjoy while also opening up future inventive opportunities.

In this sense, the patent system could draw inspiration from the spread of approaches such as CRediT that allow for greater recognition of the contributions of individuals to scientific research. Formalizing inventorship roles could help remind senior inventors of team members who might otherwise have been omitted through unconscious bias and could provide a clearer framework for recognizing and valuing all substantial contributors to an invention. First-time and underrepresented innovators would likely obtain even more of a career boost from this kind of recognition, and this engagement with the patent system may inspire them to contribute more substantially to future inventions. Policy pilots could be used to evaluate whether these benefits would outweigh the administrative costs of implementation.

The time is ripe for intervention because there is interest across the political spectrum in developing more rigorous evidence on inventor diversity. The US Study of Underrepresented Classes Chasing Engineering and Science Success (SUCCESS) Act of 2018 and the Unleashing American Innovators Act of 2022 tasked the USPTO with studying and tackling the problem of increasing patenting by women, minorities, rural populations, and other innovators underrepresented in patent filings. The USPTO's current Learning Agenda, developed under the Evidence Act of 2018, commits the agency to assessing participation in the patent system by underserved populations. In support of these goals, the USPTO recently completed a randomized controlled trial showing that a new program to help patent applicants who began the patenting process without legal representation led to a substantial increase in inventors' willingness to continue engaging in the patent process to the point of receiving a patent (*15*). This completely closed the gender gap in application success rate in the areas in which women were doing the worst and among first-time US applicants. Hopefully this level of interest from the USPTO will inspire the use of many more rigorous experiments to test other diversity interventions, both within the agency and in the private sector. To that end, we have created the Diversity Pilots Initiative (https://diversitypilots.org) to help organizations rigorously test and evaluate diversity interventions. ■

REFERENCES AND NOTES

1. A. Bell, R. Chetty, X. Jaravel, N. Petkova, J. Van Reenen, *Q. J. Econ.* **134**, 647 (2019).
2. C. V. Chien, *UCLA Law Rev.* 10.2139/ssrn.4213799 (2023).
3. L. L. Ouellette, *Va. Law Rev.* **101**, 65 (2015).
4. A. Toole *et al.*, "Progress and potential: 2020 update on U.S. women inventor-patentees" (USPTO, 2020); www.uspto.gov/sites/default/files/documents/OCE-DH-Progress-Potential-2020.pdf.
5. M. B. Ross *et al.*, *Nature* **608**, 135 (2022).
6. F. Lissoni, F. Montobbio, L. Zirulia, *Ind. Corp. Change* **29**, 1471 (2020).
7. A. Manjunath *et al.*, *Nat. Biotechnol.* **41**, 610 (2023).
8. C. Haeussler, H. Sauermann, *Res. Policy* **42**, 688 (2013).
9. P. Kline, N. Petkova, H. Williams, O. Zidar, *Q. J. Econ.* **134**, 1343 (2019).
10. E. Melero, N. Palomeras, D. Wehrheim, *Manage. Sci.* **66**, 5485 (2020).
11. R. Koning, S. Samila, J.-P. Ferguson, *Science* **372**, 1345 (2021).
12. *Burroughs Wellcome Co.* v. *Barr Laboratories, Inc.*, 40 F.3d 1223 (Fed. Cir. 1994).
13. V. Larivière, D. Pontille, C. R. Sugimoto, *Quant. Sci. Stud.* **2**, 111 (2021).
14. C. V. Chien, *Iowa Law Rev.* **104**, 2313 (2019).
15. N. A. Pairolero *et al.*, "Closing the gender gap in patenting: evidence from a randomized control trial at the USPTO" (USPTO, 2022); https://ssrn.com/abstract=4265093.

ACKNOWLEDGMENTS

The authors thank A. Kundadka and C. Garg for their assistance with the calculation of female authorship percentages.

SUPPLEMENTARY MATERIALS

science.org/doi/10.1126/science.adj2911

10.1126/science.adj2911

INSIGHTS

BOOKS *et al.*

REVIEW ROUNDUP

Tomes and tales for fledgling scientists

Dead whales, rotten apples, and parasites that consume their hosts from the inside out may seem like strange fodder for children, but in the capable hands of the authors of the books reviewed here, each of these unusual themes serves as an accessible entry point into an exciting area of scientific inquiry. Human anatomy, wearable tech, and Solar System science also feature among the timely topics covered in the finalists for the 2024 AAAS/Subaru SB&F Prizes for Excellence in Science Books, a collection of awards sponsored by Subaru of America, Inc., in partnership with the American Association for the Advancement of Science (AAAS, the publisher of *Science*). Read on for reviews of each of the books long-listed for the awards, winners of which will be announced in February 2024. **—Valerie Thompson**

CHILDREN'S SCIENCE PICTURE BOOK

We Go Way Back

Reviewed by **Madeleine Seale**[1]

This beautifully illustrated book addresses one of the most fundamental scientific questions—how did life begin? This is a challenging question even for researchers in this area and is particularly difficult to explain to a young audience. Colorful full-spread illustrations dominate the visuals, with small sections of text woven around the swirling images.

The book starts with an exploration of diversity among humans, the characteristics of existing living organisms, and ideas around genealogy. The authors make an admirable attempt at an overview of historical theories about the nature of life before delving back in time to try to explain the current consensus on how life began. At this point, the book becomes more abstract, trying to explain the gradual organization of elements and molecules into cells, which it calls "bubbles." It then jumps forward again to a world of multicellular creatures before presenting a final foldout page illustrating the diversity of living organisms today.

We Go Way Back seeks to provide children with a sense of awe and wonder at the beauty and diversity of life, primarily through its visual appeal, while giving some explanation of how such diversity came about. I struggled to identify its target readership though. On one hand, the focus on pictures and the limited textual explanation suggest an audience of quite

young children. However, it is hard to imagine a 5- or 6-year-old being able to understand terms such as "self-reproduction," "proteic structures," and "autocatalytic." On the other hand, an older child might have benefited from a bit more depth. Perhaps it could be read and then revisited as a child becomes more curious about the world, serving as a starting point for talking about the origins of life and evolution.

We Go Way Back: A Book About Life on Earth and How It All Began, *Idan Ben-Barak, Illustrated by Philip Bunting*, Roaring Brook Press, 2023, 40 pp.

Whale Fall

Reviewed by **Caroline Ash**[2]

The subject of *Whale Fall*—a dead whale that falls to the ocean floor—is not an obvious one for a young audience, for whom such animals are iconic and beloved. Yet the book is not dismaying—it shows how the natural world has the capacity for a long succession of recycling by revealing how the demise of one beautiful animal allows a huge diversity of other lives to flourish.

Artist Rob Dunlavey shows readers the long afterlives of whales in illustrations that are blue and delicate and place the action deep underwater. Yet despite the loveliness of the images, some of those other lives are superficially unappealing. What's to like about animals called rattails, eelpouts, hagfish, sleeper sharks, and zombie worms? Author Melissa Stewart explains how these species are vital components of marine ecosystems because they form part of the cleanup squad. Much like vultures and hyenas on land, these deep-sea scavengers prevent the environment from being littered with corpses.

After the blubber and flesh of the fallen whale are eaten by various fishes and crustaceans, the zombie boneworms (also known by the more euphonious moniker *Osedax*) penetrate the skeleton and dissolve what is left, themselves succumbing to predation by a variety of invertebrates. Finally, diverse microorganisms consume the last scraps of oil, themselves providing fuel for microecosystems to establish.

The illustrations may be ethereal in the narrative first section of the book, but the words tell readers concretely about ecological succession and interdependence among organisms. The second part of the book provides more precise illustrations, facts, and resources for learning about the creatures mentioned in the story. Although some of the vocabulary is advanced, this book should appeal to readers under 10 years old and will perhaps offer some consolation that there can be life after death.

Whale Fall: Exploring an Ocean-Floor Ecosystem, *Melissa Stewart, Illustrated by Rob Dunlavey*, Random House Studio, 2023, 40 pp.

Before Colors

Reviewed by **Yevgeniya Nusinovich**[3] *and* **Isaac Nusinovich Ucko**[4]

Before Colors is a gorgeously illustrated and, of course, colorful book that introduces readers to the origins of different pigments and dyes used throughout history and in the present day. This may seem like a difficult topic to organize into a single narrative, but author Annette Bay Pimentel cleverly ties the stories of each color together. The book's discussion of the color brown, for example, eventually reveals how brown roots can make yellow dye. Each subsequent color is connected to the next in a similar manner, echoing the children's

classic *Brown Bear, Brown Bear, What Do You See?*

Pimentel's introductions to each color are very straightforward and accessible, even for young children. They feature detailed illustrations and a brief summary of how a pigment or dye of that color might be made using minimal technology. Readers learn, for example, that brown pigment can be made by mixing burnt rock with water. Subsequent pages present scientific explanations of color perception as well as historical vignettes, the latter of which are mainly focused on individuals who made important contributions to dyeing or color preservation techniques. Iwan Tirta, for example, was an Indonesian fashion designer who preserved the traditional methods of fabric art called batik, while also modernizing the techniques for use with different fabric types and patterns. Each color section concludes with a collection of plants, animals, and minerals from which the pigments or dyes of that color might be made in different eras and geographic locations.

This book lends itself nicely to families with members of varying ages: The image-heavy introductions will appeal to younger kids, while the more dense, science-heavy sections will satisfy older readers. Regardless of readers' ages, all are likely to learn something new about colors, pigments, and dyes.

Before Colors: Where Pigments and Dyes Come From, *Annette Bay Pimentel, Illustrated by Madison Safer*, Abrams Books for Young Readers, 2023, 88 pp.

Ada Twist, Scientist: The Science of Baking

Reviewed by **Seth Thomas Scanlon**[5]

Kneading dough, mixing batter, decorating cookies and cakes, and sampling the final product are fun (and often messy) endeavors that simultaneously help children work on their interpersonal communication and fine motor skills. Baking also entails precise measurements and miraculous, but tangible, transformations that are certain to awaken the budding scientists within them all.

In *The Science of Baking*, authors Andrea Beaty and Theanne Griffith offer a helpful introduction to some of the biological, chemical, and physical phenomena that can be found in the kitchen. The book is narrated by Ada Twist, a fictional young scientist who made her first appearance in Beaty's 2016 picture book *Ada Twist, Scientist* and who now stars in an eponymous Netflix animated series. With Ada as our guide, *The Science of Baking* touches on sundry topics such as the anatomy of eggs, the role that yeast and baking soda play in making baked goods fluffy, and how flour and sugar contribute to the mouthfeel and structure of kids' favorite treats.

Credit goes to designer Charice Silverman and illustrator Steph Stilwell for capturing the exuberant spirit of a young scientist's lab notebook, with text, doodles, and cartoons accompanied by stock photos "taped" onto a gridded background along with some stills taken from the animated series. Indeed, *The Science of Baking*'s accessible and breezy style are suitable for very young readers, with pages devoted to the history of baking (with a focus on the contribution of women and minorities) and a short profile of baker Lasheeda Perry offering welcome variety.

The dearth of in-depth scientific content, however, may be frustrating to children who really want to understand the "why" behind baking or are hoping for a hands-on experience. *The Science of Baking* only includes a few experiments and covers most topics superficially. The book closes by posing some fascinating questions, such as "why do some burned cookies taste bad?," "why are some cookies crunchy, but some are chewy?," and "could an astronaut make a cake in space?" Unfortunately, these questions remain unanswered, leaving space for other books to offer more fully baked treatments.

Ada Twist, Scientist: The Science of Baking, *Andrea Beaty and Theanne Griffith, Illustrated by Steph Stilwell*, Amulet Books, 2022, 80 pp.

MIDDLE GRADES SCIENCE BOOK

The Planets Are Very, Very, Very Far Away

Reviewed by **Keith T. Smith**[6]

Most diagrams of the Solar System show the orbits of the planets as evenly separated circles, all packed closely together, with the planets themselves often arranged in a straight line. Although that representation

is compact, it is misleading and not remotely to scale. The sheer size of the Solar System—and the amount of empty space within it—is difficult to convey on a single page. "Just about every model or map has to lie about one thing: size," writes author Mike Vago. "[Y]ou can't have a book the size of the solar system. How would it fit in your room?" This short book uses multiple large pullout sections, six landscape pages wide, to illustrate the Solar System using a series of scale diagrams.

Each section of the Solar System is introduced in turn, starting from the center and working outward, with successive diagrams increasing the scale by a factor of 10. Those are balanced with pages that give brief facts about each of the objects, illustrated with large color images. Readers learn about the Sun, inner rocky planets, outer gas giants, distant dwarf planets, and even the closest stars. The text is refreshingly honest about the simplifications being made, which are necessary to represent the Solar System on flat paper while ensuring that all the objects are visible. The graphic design is excellent, with colorful pictures and diagrams presented against the blackness of space, while the writing is lighthearted and engaging.

The frequently changing scales are necessary but difficult to keep track of, so while the main message that the planets are very far away comes across well, the relative sizes and distances might not. There are occasional jokes, but I found them distracting and misleading; some are not clearly distinguished from the facts, and others rely on pop culture references that children are unlikely to be familiar with. Nevertheless, the book is a great way to show how vast and empty the Solar System is.

The Planets Are Very, Very, Very Far Away: A Journey Through the Amazing Scale of the Solar System, *Mike Vago*, The Experiment, 2022, 54 pp.

Good Food, Bad Waste

Reviewed by **Mattia Maroso**[7]

In recent years, the Western world has seen a proliferation of food-based entertainment in the form of social media content, TV shows, books, podcasts, magazines, and more. However, very few resources are invested in educating people on the consequences of food waste. In *Good Food, Bad Waste*, author Erin Silver takes young readers on an emotional journey through the overaccumulation of food and the production of exceptional amounts of food waste in the industrialized world. The book describes how the problem of food waste emerged and how we reached the critical situation in which we now find ourselves. It analyzes the consequences of food waste at individual and planetary levels and provides a very welcome large section on what we, as individuals and citizens, can do to minimize it.

Along the way, readers meet incredible "food-waste heroes"—everyday people who, through their day-to-day efforts, promote a more sustainable and healthier future

for the planet and its inhabitants. "Food for Thought" and "Bits + Bites" sections feed the reader's cravings for data and provide valuable points of discussion for family dinner table conversation. In the second part of the book, Silver introduces small- and large-scale strategies to reduce food waste and raise awareness about its consequences.

Suharu Ogawa's beautiful illustrations are a critical contribution, and the book's colorful graphs, photographs of everyday life, and expressively rendered cartoon characters will appeal to young readers. I witnessed this myself—my 11-year-old niece couldn't put it down! By now, my sister and my brother-in-law have likely learned so much from her that I wouldn't be surprised if they had started their own compost project. Do the next generations a favor: Give this book a chance. Your kids—and the planet—will thank you.

Good Food, Bad Waste: Let's Eat for the Planet, *Erin Silver, Illustrated by Suharu Ogawa*, Orca Book Publishers, 2023, 96 pp.

Superpower?: The Wearable-Tech Revolution

Reviewed by **Marc S. Lavine**[8]

In *Superpower? The Wearable-Tech Revolution*, Elaine Kachala describes the development of wearable devices and technology that can enhance human abilities, discusses the ethics associated with the use and potential misuse of this technology, and introduces readers to wearable-tech inventors, many of whom started designing and creating when they were not much older than the target readership.

Prosthetics, wearable devices, and implants have existed for centuries, but the technology used to manufacture them and the technology that can be directly embedded in them have changed drastically in the past several decades. Modern prosthetics can include robotic elements, can be controlled using a brain-computer interface, and can be rapidly manufactured and customized using 3D printing. As Kachala reveals, this means going beyond simply restoring functionality and extending to the inclusion of personalized artistic elements. She discusses how artist Sophie de Oliveira Barata creates custom limbs with elaborate and futuristic embellishments for athletes, musicians, models, and others. Prosthetics can also push beyond human abilities. Here, for example, Kachala describes a prosthetic arm that shoots glitter. This raises the specter of creating "superhumans"—an exciting prospect for many, but one with the potential to dehumanize us all.

The ability to collect, transmit, and process large amounts of data enables wearable devices to be reprogrammed from user experiences and allows subsequent iterations of a device to be revised on the basis of data gained from collective experiences. However, it raises the questions of who owns device-generated data, who should be allowed to access it, and for what purposes—questions that also exist in the broader technological sphere. Kachala rightfully points to ethical concerns that emerged from the "move fast and break things" approach to tech design and deployment.

Overall, *Superpower?* aims to inspire a new generation of wearable-tech creators, while reminding aspiring designers to consider the potential pitfalls and misuses of their work as an essential part of the development process.

Superpower?: The Wearable-Tech Revolution, *Elaine Kachala, Illustrated by Belle Wuthrich*, Orca Book Publishers, 2022, 112 pp.

ILLUSTRATION: SUHARU OGAWA/ORCA BOOK PUBLISHERS

How Do Meerkats Order Pizza?

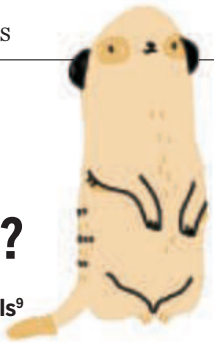

Reviewed by **Jennifer Sills**[9]

Most books that provide amazing animal trivia isolate the fun facts from the efforts behind them. Not so in *How Do Meerkats Order Pizza?*, which not only describes how the yeti crab eats bacteria that grows on its furry arms, for example, but also tells the rest of the story. Readers learn that when she discovered the yeti crab, biologist Cindy Lee Van Dover was thousands of feet under the sea in a submersible named *Alvin*. The three scientists in the tiny vehicle, only one of whom could look out the window, wore socks but not shoes. The dive lasted 9 hours, and *Alvin* had no restroom.

Through quirky, fourth wall–breaking humor and a drawing style resembling comic art, Brooke Barker conveys her obvious love for both animals and the process of learning about them. Fast-paced chapters, packed with personality, each highlight a different researcher and animal. Together, they provide a taste of the curiosity and persistence that drive scientists to pursue questions about the natural world, as well as the thrill of discovery that serves as the reward for hard work. In one chapter, biologist Natalia de Souza Albuquerque, who as a child wanted to understand the inner lives of animals, studies how dogs interpret human emotions. In another, ornithologist Corina Newsome wears waders and sunglasses to collect data about sparrow nests during the 4 hours that the tide is out. Later, readers meet entomologist Nicholas Teets. When he was young, his favorite animal was the cheetah; now he travels over rough waters to Antarctica to study tiny insects called midges—he brings a plastic bag, a spoon, and a backup spoon to collect them.

In answering its titular question—meerkats don't actually order pizza, but they do build group consensus while hunting for food using a strategy akin to voting—and many others readers might never have thought to ask, *How Do Meerkats Order Pizza?* expands the idea of fact-finding fun from the animal world to the pursuit of science.

How Do Meerkats Order Pizza?: Wild Facts About Animals and the Scientists Who Study Them, *Brooke Barker, Illustrated by Brooke Barker*, Simon & Schuster Books for Young Readers, 2022, 200 pp.

YOUNG ADULT SCIENCE BOOK

Wilder

Reviewed by **Sacha Vignieri**[10]

In *Wilder*, conservation journalist Millie Kerr tells many interesting "rewilding" stories, describing efforts underway to restore ecosystems altered by humanity in regions of Africa, Argentina, Texas, and more. Each story has a similar arc, describing how a particular region was damaged, the individuals leading recovery efforts, and how the process of rewilding is being conducted.

Readers learn about the reintroduction of the scimitar-horned oryx to its native North African habitat following massive declines due to hunting and war. In another story, Kerr relates how Doug and Kris Tompkins—former executives at outdoor retailers The North Face and Patagonia—helped to restore hundreds of thousands of acres in Argentina. The book's most compelling stories, to me, were those to which Kerr is personally connected. These include her retelling of the restoration of the San Antonio River and a meditation on the grief she experienced when her family sold their Texas ranch in 2015.

In each story, there is at least one charismatic protagonist who has led the rewilding charge, often through the investment of financial resources. I appreciated the insight into these leaders, but I also would have welcomed a few stories about what happens when nature is left to rewild itself, as is happening in many "abandoned" regions.

Wilder is a book about the destruction people create and the good we can do with the right heart and resources. It is important to remember, however, that nature is not ours to destroy or repair, but a complex set of organisms and processes that govern life on the planet. The kinds of inspiring projects Kerr describes are essential in today's human-dominated world, but if we want to move forward into a more stable future, we must also provide space and autonomy for "the wild" to return and exist without our interference.

Wilder: How Rewilding Is Transforming Conservation and Changing the World, *Millie Kerr*, Bloomsbury Sigma, 2022, 368 pp.

Wildscape

Reviewed by **Michael A. Funk**[11]

In *Wildscape*, Nancy Lawson guides readers through a sensory wonderland that transcends the usual human inclinations and concerns. Instead, one learns about the curious preferences of cuckoos for spiky, stinging caterpillars; the fetid allure stinkhorn mushroom spores have for passing flies; and the fog of sensory confusion wrought by chemicals in automobile exhaust and lawn treatments. For anyone who relishes a walk in the woods, this book offers fascinating new rabbit holes to hop down.

The book is organized around the five main human senses, but the stories inevitably burst out of these categories. For example, a good portion of the chapter on touch is dedicated to how animals build homes that comfort and protect. Sight becomes a vehicle to discuss how human preferences for tidy landscapes distort or even extinguish the messy cycles of growth and consumption that sustain ecosystems. Not all stories about the senses are pretty. Parasites and parasitoids, such as wasps whose larvae consume their hosts from the inside out, star in several chapters, as they have developed many ingenious tricks to find and exploit their hosts' senses.

Lawson includes quotes and comments from professional scientists, naturalists, and writers that add additional perspectives and highlight how current research is addressing questions close to home. She walks readers through her own homegrown investigation into the mysterious behavior of butterflies that gather alkaloids from the damaged leaves of certain plants, possibly as protection against infection. Her story highlights the importance of sharing observations and keeping an open and curious mind, a theme that resonates throughout each chapter. Although the concepts and writing style are

PHOTO: TONI GENBERG

appropriate for middle and high school–age students, even experienced naturalists will find new and exciting facts to ponder, and the excellent photographs (most captured by the author) are a delight to take in as well.

Wildscape: Trilling Chipmunks, Beckoning Blooms, Salty Butterflies, and Other Sensory Wonders of Nature, *Nancy Lawson*, Chronicle Books, 2023, 304 pp.

The Sounds of Life

Reviewed by **Benjamin Gottesman**[12]

In *The Sounds of Life*, Karen Bakker describes how it is possible to sense sound with no ears, reveals the noise that makes elephants cower in terror, and explains why coral reefs are as lively as city centers, all by introducing readers to the emerging field of digital bioacoustics. Each of the book's 10 chapters focuses on a different organism—from singing whales to dancing honey bees to growling turtles—and the scientists working to understand the meaning behind the sounds they make. These vignettes demonstrate how animal sounds, long relied on for tracking and hunting, have become key to understanding and conserving species and ecosystems.

The sounds emitted by bats, for example, are far more socially complex than we once thought. Beyond echolocation calls, some bat species babble like human babies in their early days, learn courtship songs from their fathers as juveniles, and have hundreds of call types for different contexts as adults. Meanwhile, real-time listening stations are drastically reducing the number of ship strikes of the North Atlantic right whale, one of North America's most endangered marine mammals. And in Southeast Asia, scientists-turned-DJs are broadcasting the spirited sounds of healthy coral reefs to attract larval fish and coral to artificial reefs.

Bakker leaves space to consider what is to come. She imagines a future where artificial intelligence–enabled robots intermingle in animal worlds, where battery-less audio recording networks monitor biodiversity in real time across unprecedented spatial scales, and where animal languages are decoded into translatable dictionaries. Although the road may be bumpier than Bakker acknowledges, her contemplation of where we are going is thoughtful and rigorous.

There have been a handful of other books that delve into bioacoustics, but Bakker's meticulously researched and colorfully presented offering is the first to integrate so many dimensions of the field in a way that is accessible to nonexperts. It is a wonderful mix of animal ecology, narratives of science-doing, futurism, and accounts of Indigenous knowledge that is as interdisciplinary as the field itself.

For a longer review of *The Sounds of Life*, see "Babbling bats and raucous reefs," *Science* **378**, 254 (2022).

The Sounds of Life: How Digital Technology Is Bringing Us Closer to the Worlds of Animals and Plants, *Karen Bakker*, Princeton University Press, 2022, 368 pp.

The Milky Way

Reviewed by **Adrian Cho**[13]

For millennia, humanity knew next to nothing about the Milky Way Galaxy. To the Greeks, it was milk spilled across the night sky. To the Armenians, it was a path of stolen straw. To some Northern Europeans, it was a trail of godly tears. For less than a century, scientists have known that our Milky Way is one of billions of galaxies in the observable Universe. Only in recent decades have they deduced how the vast pinwheel of trillions of stars evolved. Now, in an insouciant and imaginative book, the Milky Way steps up to tell its own story.

Our Galaxy is 13.5 billion years old, but astrophysicist Moiya McTier portrays it as a young person—snappy, irreverent, and brash. "There are, of course, other galaxies besides me out in the universe, all of them

less spectacular than me, with one remarkable exception," it proclaims. Perhaps McTier's Milky Way is a bit like herself? Just as the brightest star forms from a mere cloud of gas, she rose from humble origins, growing up in a cabin with no running water in a tiny town in rural Pennsylvania and going on to attend Harvard and earn a PhD from Columbia University.

The Milky Way explains its own vague origins in the merger of protogalaxies, recounts the evolution of the cosmos from the Big Bang, and reveals glimpses of its curvy anatomy. It pines for Andromeda, the neighboring galaxy with whom it will someday merge; mourns the stars it has lost; and resents the massive black hole that lurks in its heart like so much anger. It is vaguely obsessed with death. That darkness under the spangles makes McTier's Milky Way a bit less Taylor Swift, a bit more Billie Eilish. And that makes it easier to relate to and even more fun to read about.

The Milky Way: An Autobiography of Our Galaxy, *Moiya McTier, Illustrated by AnnaMarie Salai*, Grand Central Publishing, 2022, 256 pp.

HANDS-ON SCIENCE BOOK

The Kitchen Pantry Scientist: Ecology for Kids

Reviewed by **Katie Langin**[14]

"I am cooking hard-boiled eggs as I write so that we can do a quick experiment before dinner," Liz Lee Heinecke wrote in a 2009 blog post on her website, *The Kitchen Pantry Scientist*. A molecular biologist by training, Heinecke started the website to chronicle her journey helping her three children learn about science. Since then, she has published a series of books with kid-friendly science activities, including *Biology for Kids*, *Sheet Pan Science* (also reviewed here), *Outdoor Science Lab for Kids*, and *Chemistry for Kids*.

In her latest installment, *Ecology for Kids*, Heinecke describes activities readers can complete in their kitchen, their backyard, or nearby parks or natural areas. She explains how to grow beans in soil with different pH levels, how to construct a Secchi disk to measure water quality, and how to build pitfall traps to catch insects. Each of the 25 activities is paired with a description of a scientist; for instance, alongside an activity that asks kids to clean up a mock oil spill, Heinecke tells readers about the career of oceanographer Sylvia Earle. Some activities also come with safety warnings: "Avoid fast-moving rivers or streams," one says. "Never eat wild mushrooms unless an expert identifies them as edible," warns another.

The activities and the scientific concepts attached to them appear to target different age ranges, but the book does not specify what those age ranges are. "This one seems meant for really little kids," a 14-year-old neighbor who has an interest in ecology said of an activity that asks kids to fish plastic sea animals out of a container of water, adding that "some experiments seem more like craft projects than actual experiments." She was, however, able to find some activities that were of interest, including one that teaches echolocation.

So if you know a youngster with an interest in science, it is likely that *Ecology for Kids* has something to offer.

The Kitchen Pantry Scientist: Ecology for Kids, *Liz Lee Heinecke, Illustrated by Kelly Anne Dalton*, Quarry Books, 2023, 128 pp.

Sheet Pan Science

Reviewed by **Melisa Yashinski**[15]

"Most kids enjoy making a mess, and science can be wonderfully messy," writes Liz Lee Heinecke in her book *Sheet Pan Science*, which features 25 exploratory science projects that can be carried out inside a sheet pan, or rimmed baking sheet, to conveniently contain all the drips and spills without sacrificing any of the fun.

The book's 25 activities are divided into five chapters: fizzy science, fluid science, edible science, material science, and natural science. Each chapter opens with an easy-to-understand explanation of the phenomenon under investigation. For example, in the description of fluid science, the concept of surface tension is explained as "the way water molecules on the surface of a liquid stick together to form a sort of 'skin' on the top."

Within each chapter are five "labs." Each lab includes a "mess factor" and "complexity" ranking from low to high, a list of materials, and some safety tips and hints. Most of the materials are common household items such as dish soap and milk, but some, such as the aluminum sulfate used in the "Marbled Paper" lab, may require an extra trip to the store. Many of the labs are simple enough for older elementary school–age children to follow themselves, but some will require adult supervision, such as when gelatin is dissolved in boiling water for the "Shrinking Window Gels" lab.

The protocol for each lab is written out in a list of easy-to-follow steps. Most of the steps have accompanying figures that include photographs of real kids performing each task. Each lab description ends with a section titled "The Science Behind the Fun" that explains the phenomena observed in an activity and leaves young scientists with a new understanding of the world around them.

Sheet Pan Science: 25 Fun, Simple Science Experiments for the Kitchen Table, *Liz Lee Heinecke*, Quarry Books, 2022, 128 pp.

Human Body Learning Lab

Reviewed by **Valerie Thompson**[16]

In *Human Body Learning Lab*, pediatrician Betty Choi helpfully pulls back the curtain on a topic that is of great interest and great mystery to many elementary school–age children: human anatomy and physiology. Describing each of the body's systems in friendly prose, the book seeks to encourage children's curiosity and bodily autonomy through a combination of colorful diagrams, simple activities, and fun facts about everything from the skin to the endocrine system.

As it is in nearly every children's book dedicated to this topic, the perennial favorite question of the under-12 set—why do we burp and fart?—is answered here. However, two features make the book a notable standout in the genre. The first is its timely, repeated reference to the potential health consequences of screen use. "Limit screen time, and keep screens out of your bedroom," Choi advises in a section dedicated to protecting one's growing brain. "Looking at screens for a long time can cause dry eyes, blurry vision, and headaches," she writes later in the vision section. "Protect your eyes by taking breaks to look out the window." The second is its refreshing affirmation and normalization of difference. In the book's section on hearing, for example, Choi observes that some people who are deaf use devices such as hearing aids or cochlear implants but also that "many people who are deaf prefer not to use hearing devices and live full lives without hearing." Later, while discussing the reproductive system, the book notes that there are many ways people form families, that children are not always raised by biological parents, and that many people choose not to have children at all.

"Teaching children about the human body is one of the best ways we can empower them to be safe and healthy," writes Choi in the book's opening pages. *Human Body Learning Lab* is a great place to begin.

Human Body Learning Lab: Take an Inside Tour of How Your Anatomy Works, *Betty Choi*, Storey, 2022, 144 pp.

Wild Child

Reviewed by **Lauren Kmec**[17]

In the opening pages of *Wild Child*, teenage naturalist Dara McAnulty's enchanting and approachable introduction to the natural word, readers are invited on a journey of discovery, a "wild wandering." The book's five ensuing chapters offer a glimpse of nature from a different vantage point—the window, the garden, the woods, the open country, and the river. Every section opens with a whimsical poem before venturing into fun facts about the habitat's animals and plants. Readers will discover, for example, that wrens embellish their nests with spider egg sacs, earthworms "see" without eyes, and a single oak tree can produce 10 million acorns. Each chapter then dives slightly deeper into one topic (e.g., animal migration, tree propagation) and concludes with a simple activity or experiment. Tasks such as terrarium building can be done in the home, but others (e.g., exploring life-forms in a body of water) require a trip outdoors.

Certain aspects of this book have particular charm. The illustrations, for example, are a distinctive blend of realistic and ethereal. A delightful two-page spread lists collective nouns for bird species (a banditry of chickadees, a quarrel of sparrows, a confusion of chiffchaffs!). Throughout the book, McAnulty speaks directly to the reader and emphasizes the importance of treating nature with respect. Still, a few parts—some descriptions of predatory behavior in birds, an unsettling myth about fairies and bluebell flowers—could be upsetting for some children. In addition, the book occasionally mixes folklore with facts, which may confuse less-advanced readers. Overall, though, *Wild Child* is a joyful exploration of various natural habitats and would be a welcome addition to the curious young reader's bookshelf. ■

Wild Child: Nature Adventures for Young Explorers—with Amazing Things to Make, Find, and Do, *Dara McAnulty, Illustrated by Barry Falls*, The Experiment, 2023, 64 pp.

10.1126/science.adm8436

ILLUSTRATION: BARRY FALLS/THE EXPERIMENT

[1]The reviewer is an associate editor at *Science*. Email: mseale@science-int.co.uk [2]The reviewer is a senior editor at *Science*. Email: cash@science-int.co.uk [3]The reviewer is a senior editor at *Science*. Email: ynusinov@aaas.org [4]The reviewer is a kindergarten student at College Gardens Elementary School, Rockville, MD 20850, USA. [5]The reviewer is the editor of *Science Immunology*. Email: sscanlon@science-int.co.uk [6]The reviewer is a senior editor at *Science*. Email: ksmith@science-int.co.uk [7]The reviewer is a senior editor at *Science*. Email: mmaroso@aaas.org [8]The reviewer is a senior editor at *Science*. Email: mlavine@aaas.org [9]The reviewer is the senior Letters editor at *Science*. Email: jsills@aaas.org [10]The reviewer is a deputy editor at *Science*. Email: svignier@aaas.org [11]The reviewer is a senior editor at *Science*. Email: mfunk@aaas.org [12]The reviewer is at the K. Lisa Yang Center for Conservation Bioacoustics, Cornell Lab of Ornithology, Cornell University, Ithaca, NY 14850, USA. Email: ben.gottesman@cornell.edu [13]The reviewer is a news writer at *Science*. Email: acho@aaas.org [14]The reviewer is an associate news editor at *Science*. Email: klangin@aaas.org [15]The reviewer is an associate editor at *Science Robotics*. Email: myashinski@aaas.org [16]The reviewer is a senior editor at *Science*. Email: vthompso@aaas.org [17]The reviewer is the managing editor of the *Science* family of journals. Email: lkmec@aaas.org

The Central Hall of China's Longmen Temple was built during the Northern Song Dynasty (960 to 1127 CE).

Edited by **Jennifer Sills**

Document meaning behind China's cultural relics

Ancient sites, tombs, buildings, and carvings have historical and artistic value, and modern sites and buildings related to historical events and figures are important to historical education (*1*). Such cultural relics provide insights into human values and achievements throughout history. After the Chinese Revolution in 1949, China faced the challenge of rebuilding from ruins, necessitating extensive construction while also considering the importance of cultural heritage protection. China's State Council conducted a nationwide survey of cultural relics in 1956, 1981, and 2007 (*2*). In November, China launched its fourth national survey on cultural relics (*3*), which aims to provide better understanding, protection, and management of immovable cultural relics across the country. It also offers an opportunity to document their cultural significance.

The fourth national survey will catalog the name of each cultural relic, its location, the level of protection it receives, its age, who or what entity claims ownership of it, how it is used (e.g., for tourism or education), and the strategies in place to preserve it (e.g., restoration efforts and climate control). The survey will also categorize the relics by their location, including those found aboveground, underground, and underwater (*3*).

Although the survey will capture important data, it assesses the superficial condition of the relics rather than their cultural value. Cultural relics embody Chinese architectural and artistic achievement (*4*) and play an indispensable role in understanding the history of Chinese civilization (*5*, *6*). Thus, in the spirit of the UN Educational, Scientific and Cultural Organization (UNESCO) Convention (*7*), the survey should focus more on cultural connotations.

To better protect cultural relics, develop their cultural value, and promote the dissemination of Chinese culture, the fourth national survey should record the cultural connotation of each cultural relic, especially those that are immovable (*8*). For example, the Longmen Temple, a collection of Buddhist temples initially built during the Northern Qi Dynasty (550 CE), were used for hundreds of years, and the existing structures span the Song, Jin, Yuan, Ming, and Qing Dynasties (*9*). The State Council should document the historical, cultural, religious, and artistic function of such sites and their significance and value in a contemporary context. The survey should also supplement its findings with cutting-edge technologies such as three-dimensional scanning, virtual and augmented reality devices, artificial intelligence, and multimodal large-scale models. These tools can achieve detailed digitization and reconstruction of cultural relics. Furthermore, the government should promote the creation of a nationally managed virtual public platform for ancient cultural relics, allowing the general public to enhance their historical and cultural awareness by accessing and interacting with cultural relics online.

Biao Li[1], Gang Kou[1,2]*, Hemin Li[1], Kun Guo[3,4,5], Yong Shi[3,4,5]

[1]School of Business Administration, Faculty of Business Administration, Southwestern University of Finance and Economics, Chengdu 611130, China. [2]Xiangjiang Laboratory, Changsha 410205, China. [3]School of Economics and Management, University of Chinese Academy of Sciences, Beijing 100190, China. [4]Key Laboratory of Big Data Mining and Knowledge Management, Chinese Academy of Sciences, Beijing 100190, China. [5]Research Center on Fictitious Economy & Data Science, Chinese Academy of Sciences, Beijing 100190, China.
*Corresponding author.
Email: kougang@swufe.edu.cn

REFERENCES AND NOTES

1. State Administration of Cultural Heritage, "Guidelines for the identification of immovable cultural relics (trial version)" (2018); https://www.gov.cn/zhengce/zhengceku/2018-12/31/content_5433133.htm [in Chinese].
2. State Administration of Cultural Heritage, "A responsible official from the State Administration of Cultural Heritage answers reporters' questions regarding the fourth national survey of cultural relics" (2023); https://www.gov.cn/zhengce/202310/content_6912886.htm [in Chinese].
3. The State Council, China, "Notice of the State Council on conducting the Fourth National Survey of Cultural Relics" (2023); https://www.gov.cn/zhengce/content/202310/content_6912287.htm [in Chinese].
4. Y. S. Ruan, *J. Tongji Univ. Soc. Sci.* **13**, 1 (2002) [in Chinese].
5. Y. J. Tang, *Southeast Culture* **4**, 16 (1995).
6. M. Balter, *Science* **323**, 5915 (2009).
7. UNESCO, "Convention on the protection and promotion of the diversity of cultural expressions" (2005); https://www.unesco.org/en/legal-affairs/convention-protection-and-promotion-diversity-cultural-expressions.
8. H. Pu, X. Wang, *Sci. Culture* **9**, 2 (2023).
9. *National Key Cultural Relics Protection Units: The First to Fifth Batches* (Cultural Relics Press, 2004) [in Chinese].

10.1126/science.adl5907

Surge in nocturnal ozone pollution

Exposure to ozone (O_3) can inhibit plant growth and biomass, decrease microbial diversity, cause oxidative stress, and contribute to pathological conditions and increased mortalities in humans and other animals (*1*–*3*). Present and predicted future O_3 exposures, which already vastly exceed the maximum safe levels for human health and vegetation (*1*–*3*), underestimate the full extent of exposure. Urban population exposure to O_3 increased by about 0.8% per year from 2000 to 2019 (*1*), but O_3 exposure metrics and critical levels include only daytime O_3 levels, overlooking rising nighttime concentrations (*3*). The revision of regulatory standards is urgently needed.

Nocturnal O_3 exposures have historically been considered low and unthreatening. As a result, analyses exclude hours with global radiation of less than 50 W m^{-2} (when the sun is low or has set). However, O_3 uptake into mature conifer trees at night can reach up to 25% of daytime maximum levels (*4*). The safety of nocturnal fauna such as birds, insects, and microorganisms that are adversely affected by O_3 pollution (*2*, *5*) is also overlooked by daytime-focused metrics.

Increases in nocturnal O_3 exposures have been reported in the United States, the European Union, and Asia (*6*–*10*). In China, the average annual frequency of nocturnal O_3-enhancement events (NOEEs)—substantial increases in short amounts of time—is 46% higher than in the United States and Europe (*8*). NOEEs are more pronounced in industrialized cities in China (*8*, *9*), in some cases reaching levels that exceed daytime concentrations in different parts of the world. NOEEs are about 10% higher in the warm season than in the cold season (*8*).

Emitted primary pollutants, mainly nitrogen oxides (NO_x) and volatile organic compounds (VOCs), react under sunlight to produce O_3 (*3*, *6*). Meanwhile, O_3 titration by NO_x leads to O_3 destruction. For example, NO reacts with O_3 to produce NO_2 and O_2, and NO_2 reacts with O_3 to produce NO_3 and O_2. Air pollutant mitigation policies have successfully decreased NO_x concentrations in the United States, European Union, and more recently China, but they have not decreased VOCs to the same degree (*1*, *6*, *7*). Reduced NO_x emissions weaken the NO_x titration effect and, without similar reductions in VOCs, may be responsible for rising nocturnal O_3 levels (*6*, *7*).

A high proportion of VOCs relative to NO_x increases O_3 concentrations (*1*). To reduce nighttime and daytime O_3 exposure, emissions of pollutants such as NO_x and O_3 should be monitored and evaluated (*7*). Given the considerable variation of nighttime O_3 levels, city- or region-specific risk assessments are needed to identify local O_3 risks. In cases where NO_x is effectively reduced, additional efforts should be implemented to keep O_3 levels low by minimizing VOCs as well (*1*). Because the majority of VOCs are biogenic (predominantly emitted by vegetation), reducing urban O_3 levels will require the selection of appropriate low VOC-emitting plant species in urban areas, such as lindens, parasol trees, jacarandas, maples, ashes, elms, *Melia* trees, and whitebeams (*11*). Conversely, high VOC-emitting species, such as eucalypts, casuarinas, locusts, poplars, oaks, willows, and Chinese lantern trees, should be avoided (*11*).

Evgenios Agathokleous[1], Zhaozhong Feng[1], Pierre Sicard[2,3]
[1]Collaborative Innovation Center on Forecast and Evaluation of Meteorological Disasters, Nanjing University of Information Science and Technology, Nanjing 210044, Jiangsu, China. [2]ARGANS, Sophia Antipolis, France. [3]Institutul Național de Cercetare-Dezvoltare în Silvicultură "Marin Drăcea," Voluntari, Romania.
*Corresponding author.
Email: evgenios@nuist.edu.cn

REFERENCES AND NOTES

1. P. Sicard *et al.*, *Sci. Total Environ.* **858**, 160064 (2023).
2. E. Agathokleous *et al.*, *Sci. Adv.* **6**, eabc1176 (2020).
3. A. S. Lefohn *et al.*, *Elem. Sci. Anth.* **6**, 28 (2018)
4. R. Matyssek *et al.*, *Atmos. Environ.* **38**, 2271 (2004).
5. J. Reif *et al.*, *Sci. Total Environ.* **876**, 162711 (2023).
6. H. Wang *et al.*, *Nat. Geosci.* **16**, 217 (2023).
7. J. Wang *et al.*, *Atmos. Pollut. Res.* **13**, 101387 (2022).
8. C. He *et al.*, *Atmos. Chem. Phys.* **22**, 15243 (2022).
9. L. Zhang *et al.*, *Atmos. Res.* **294**, 106978 (2023).
10. X. Li *et al.*, *Geophys. Res. Lett.* **50**, e2023GL103242 (2023).
11. P. Sicard *et al.*, *Science* **377**, 585 (2022).

10.1126/science.adm7628

ONLINE BUZZ

Complexities of plastic cleanup

In the News story "Cleaning up ocean 'garbage patches' could destroy delicate ecosystems" (17 May, https://scim.ag/3vU), A. B. Vigil explained that an abundance of biodiversity has grown reliant on floating pollution and could be put at risk by cleanup efforts. In the Letter "Begin ocean garbage cleanup immediately" (11 August, p. 612), Z. Long responded that the relevant species are widespread and that cleanup efforts, which will take years to complete, could be adjusted as more data becomes available. Readers added that solutions must account for the complexities of plastic production and terrestrial plastic pollution. Excerpts of their comments are below. To read all the eLetters, and post your own, go to https://www.science.org/doi/10.1126/science.adj0102#elettersSection.

A selection of your thoughts:

...[Long] overlooks the potential long-term loss of ecosystem function and biodiversity from nonselective plastic removal technologies (PRTs), such as bycatch mortality....A single Ocean Cleanup net could affect 675 tons of zooplankton annually....Long grossly underestimates the difficulty of making PRTs efficient and scalable....200 Ocean Cleanup devices, operating for 130 years, would capture only 5% of the world's floating plastics....It is the exponential growth in plastic production, not delayed removal, that drives increasing marine plastic pollution....

Hans Peter H. Arp *et al.*

...[T]he stock of floating marine debris (0.3 Mt, million metric tons) is merely the tip of the global plastics iceberg. Estimates of subsurface ocean and marine sediment plastic stocks amount to approximately 200 Mt, most of it supplied by a steady inflow of 1 to 13 Mt plastics per year in river runoff....[C]leaning up floating marine plastics... amount[s] to mopping the floor with the bathtub overflowing and the tap running.... [T]oday, 70% of the 8000 Mt of plastic waste that has accumulated since 1950 still resides on land in dumps, landfills, and...terrestrial ecosystems. This legacy plastic waste, together with new mismanaged waste, will be continuously and increasingly mobilized by river runoff to marine waters in the coming decades....[E]ven if we succeed in limiting plastics production and usage, the large amount of legacy plastics in the terrestrial environment will continue to disperse by river runoff to the marine environment....Closing the tap on plastics [requires] remediation efforts of legacy plastics on land in addition to curbing plastics production....

Jeroen E. Sonke and Théo Segur

10.1126/science.adn2157

RESEARCH

IN *SCIENCE* JOURNALS

Edited by **Michael Funk**

Hotter droughts will transform forests, including those in California's Sierra Nevada.

FOREST ECOLOGY

Wetter isn't better for drought effects

The increase in drought conditions caused by climate change threatens tree growth and survival. Heilmayr *et al*. investigated whether trees are most stressed by drought in relatively wet or dry regions. In drier areas, trees increasingly experience more severe conditions but may also be better adapted to withstand drought. Using tree ring measurement records from more than 100 tree species, the authors found that trees growing in the wetter parts of their range are more drought sensitive, and hot, wet regions are predicted to have the greatest declines in growth under future climate change. Therefore, land management and policy focused solely on drought effects in drier regions will underestimate climate change vulnerability in forests. —BEL

Science, adi1071, this issue p. 1171

NUCLEOSYNTHESIS

Fission contributes to elements in stars

The rapid neutron capture process (r-process) occurs in neutron-rich environments such as neutron star mergers or certain types of supernovae. This process is thought to produce many of the chemical elements heavier than iron, but the details are poorly understood and cannot be studied in the laboratory. Roederer *et al*. analyzed r-process element abundances previously observed in stars. They identified correlated excess abundances of certain elements in some stars, which is consistent with these elements being fission products of even heavier elements. These results indicate that some r-process events make elements heavier than uranium, which then decay into the elements observed in stars. —KTS

Science, adf1341, this issue p. 1177

CROP SCIENCE

Maize biofortification

Fortifying crops with micronutrients could be a good way to improve population health. Maize is a staple for many in sub-Saharan Africa, but the edible portions are typically low in iron. By investigating a population of natural genetic maize variants, Yan *et al*. identified a transcription factor that regulates iron content in the kernels. The authors found that some maize lines exhibited different sequences in the NAC78 promoter, and the presence of these promoter variants was correlated with the expression of NAC78 in the endosperm transfer cells. In these cells, iron transporters are up-regulated, suggesting that more iron is transferred into the kernel. This work opens a route to enhancing maize iron content, which may help to address iron deficiency where it is prevalent. —MRS

Science, adf3256, this issue p. 1159

FISHERIES

Grand dames

The decline of the size of individuals within a species, from trees to fishes, is a human impact that we often overlook. However, the loss of large individuals can have population- and ecosystem-level impacts. Olsen *et al*. looked at historically large female Atlantic cod, some of which still remain

in the waters off Norway, and found that they make longer, more complex, movements than smaller females. Such movements not only benefit the breeding females, but also connect populations and habitats in a way that a population with only smaller females would be unable to do. —SNV

Science, adi1826, this issue p. 1181

CELL BIOLOGY

Getting chromosome attachment right

Kinetochores are large molecular machines that attach chromosomes to the mitotic spindle. A kinetochore-mediated error correction mechanism ensures that chromosomes are correctly oriented so that DNA is equally segregated into two daughter cells. Muir *et al*. present the cryo–electron microscopy structure of the budding yeast outer kinetochore bound to microtubules. The error correction machinery resets incorrect attachments by breaking contacts between outer kinetochore components, including dismantling a protein ring that encircles the microtubule. This study helps to explain how kinetochores harness the energy of microtubule depolymerization to move chromosomes to opposite poles of the cell. —SMH

Science, adj8736, this issue p. 1184

ORGANIC CHEMISTRY

Selective delivery of boron by cobalt

Modification of specific sites on aryl rings is an essential step in the synthesis of numerous pharmaceuticals, agrochemicals, and functional materials. Precious metal–catalyzed borylation is a particularly selective method for this purpose, although the catalyst cost is a drawback. Roque *et al*. report that an optimized ligand confers high site selectivity for borylation catalyzed by the Earth-abundant cobalt (see the Perspective by Berionni). The catalyst substitutes boron two carbons away from a fluoride substituent, an especially challenging target site. Moreover, use of a different boron reagent can switch the regioselectivity to the adjacent ortho site. —JSY

Science, adj6527, this issue p. 1165; see also adl4860, p. 1122

NEUROSCIENCE

Learning with lipid modifications

Palmitoylation regulates the stability and localization of proteins that are important for neuronal function. Liu *et al*. found that palmitoylation of the synaptic protein Sept8-204 promoted morphological changes in hippocampal neurons associated with learning and memory. Palmitoylation of three cysteine residues promoted the interaction of Sept8-204 with the actin cytoskeleton, enabling dendritic outgrowth and branching and promoting cognition in mice. Mice lacking Sept8-204 or the enzyme that mediates its palmitoylation had learning and memory deficits and showed anxiety-like behaviors. —LKF

Sci. Signal. (2023) 10.1126/scisignal.adi8645

VAGINAL CANDIDIASIS

A zinc gel for recurrent yeast infections

Vaginal yeast infections resulting from *Candida albicans* pathogenic overgrowth can be difficult to treat, especially when recurrent. Roselletti *et al*. have shown that *PRA1*, a gene in the pathogen, is up-regulated in response to local zinc limitation during vaginal yeast infection in mice. *PRA1* expression was associated with vaginal tissue pathology and local immune response, both of which were blocked in the models by *PRA1* down-regulation or topical zinc. In a pilot study, a commercially available zinc gel alleviated symptoms and prevented reinfection in women with recurrent vaginal yeast infections, suggesting a potentially simple solution for treating this chronic disease. —CAC

Sci. Transl. Med. (2023) 10.1126/scitranslmed.adi3363

IN OTHER JOURNALS

Edited by **Caroline Ash** *and* **Jesse Smith**

Desymmetrization is the key to the chemical synthesis of incargranine A, a molecule made by the Chinese trumpet creeper.

ORGANIC SYNTHESIS

Trumpeting a natural product configuration

The Chinese trumpet creeper produces beautifully vivid orange flowers. In addition, in much tinier quantities, it produces a fascinating molecule with an ornate core of saturated rings called incargranine A. Miller *et al.* report a nine-step chemical synthesis of just one of two possible mirror image variants of the compound. Key to their success was an innovative desymmetrization reaction (a conjugate addition to a dienone) catalyzed by a metal-free iminophosphorane. Characterization of the synthetic product suggested that the plant produces both mirror images, in keeping with a previous biosynthetic hypothesis. —JSY

Angew. Chem. Int. Ed. (2023) 10.1002/anie.202314308

ANCIENT DNA

Eroding barriers to gene flow in cats

One of many threats to conserved species is admixture with domesticated species, which often leads to reduced genetic diversity in already stressed populations. For many species, it can also be difficult to quantify how much gene flow occurred historically between wild and domesticated species, which potentially obscures the scope of the impact. Jamieson *et al.* assessed 14 ancient nuclear genomes, 75 ancient mitochondrial genomes, and 31 modern genomes from European and Near Eastern wildcats. Their analyses revealed that despite the proximity of these populations for several millennia, there

PHOTO: CLARANILA/ISTOCK PHOTO

ALSO IN *SCIENCE* JOURNALS

Edited by **Michael Funk**

CONSERVATION

The dangers of coastal sand mining

Sand is used across the globe for a wide range of purposes, including metal extraction and construction. However, mining of sand from coastal regions, which is estimated to produce 40 to 50 billion tons of sand each year, has far-reaching ecological, public health, and socioeconomic implications. The current rate of coastal sand extraction also outstrips natural replenishment, making the approach unsustainable. In a Perspective, Rangel-Buitrago and Neal discuss these issues and potential solutions and highlight the need for a global framework to help make the sand-mining industry sustainable. —SAL

Science, adj9593, this issue p. 1116

MEDICINE

Microrobots for localized drug delivery

To avoid systemic toxicities during drug administration, microrobots could provide a method to deliver highly toxic drugs to the target site. In a Perspective, Nelson and Pané discuss the therapeutic opportunities provided by microrobots, for example, in stroke and cancer treatment. A key issue is how to accurately direct microrobots through body fluids and tissues to release their payload. Magnetic devices are proposed to be the most likely to be amenable to clinical application, but challenges remain to ensure that the microrobots are safe and can be easily cleared from the body afterward. Addressing how microrobots might be used effectively in medical procedures and integrated with health care facilities is an important goal in their development. —GKA

Science, adh3073, this issue p. 1120

METABOLISM

Ribosome changes cause bigger problems

Under conditions of food scarcity, metabolic flexibility was historically important for humans to optimize storage and access to energy when food was not readily available. By contrast, the constant access to high-calorie foods in modern societies has become a liability, contributing to the rise in obesity and metabolic diseases. Reactive oxygen species are thought to contribute to the metabolic dysregulation associated with obesity and aging, but the underlying process was not well understood. Snieckute *et al*. have now identified a mechanism linking reactive oxygen species, a protein called ZAKα, and resulting changes in ribosome function, which then contribute to the observed metabolic changes across multiple model animal species. —YN

Science, adf3208, this issue p. 1135

ATMOSPHERE

Carbon dioxide over the Cenozoic

The concentration of atmospheric carbon dioxide is a fundamental driver of climate, but its value is difficult to determine for times older than the roughly 800,000 years for which ice core records are available. The Cenozoic Carbon Dioxide Proxy Integration Project ($CenCO_2PIP$) Consortium assessed a comprehensive collection of proxy determinations to define the atmospheric carbon dioxide record for the past 66 million years. This synthesis provides the most complete record yet available and will help to better establish the role of carbon dioxide in climate, biological, and cryosphere evolution. —HJS

Science, adi5177, this issue p. 1136

IMMUNOLOGY

Putting BCR and TCR sequences on the map

Although current spatial transcriptomics technologies can locate gene expression within tissues, they are unable to map full-length B cell receptor (BCR) and T cell receptor (TCR) sequences in this context. Engblom *et al*. developed a method called spatial transcriptomics for variable, diversity, and joining sequences (Spatial VDJ), which spatially annotates full-length immunoglobulin and T cell antigen receptor transcripts in frozen human tissue sections. This approach, which also resolves whole transcriptomes and tissue morphology, results in high-fidelity mapping and spatial lineage tracing of B and T cell clones in both human lymphoid and tumor tissues. This technology has the potential to advance our understanding of lymphocyte spatial dynamics in various clinically relevant phenomena such as infection, vaccination, and cancer. —STS

Science, adf8486, this issue p. 1137

QUANTUM INFORMATION

Entangled molecules

Ultracold atoms have long been candidates to be the building blocks of quantum information. Even more appealing are cold molecules, which have a richer energy-level structure and offer possibilities that atoms do not. However, achieving entanglement, one of the essential ingredients of a quantum information platform, has been difficult in a molecular system. Now, two groups, Holland *et al*. and Bao *et al*., have reached this goal using the dipolar interactions between calcium fluoride molecules placed in optical tweezers (see the Perspective by Smerzi). —JS

Science, adf4272, adf8999, this issue pp. 1143, 1138; see also adl4179, p. 1118

3D PRINTING

A sound way to print deep

Most methods for three-dimensional (3D) printing of polymers use focused light to control the formation of volume units (voxels). Kuang *et al*. developed a technique that they call deep-penetrating acoustic volumetric printing (DAVP), which uses a viscoelastic ink and high-intensity focused ultrasound (see the Perspective by Yao and Shapiro). A key feature of the technique is the sono-ink they used, which prevents curing beyond the focal point, thus preventing solidification beyond the intended voxel. A key advantage of using ultrasound is that it can penetrate multiple centimeters deep into opaque media. —MSL

Science, adi1563, this issue p.1148; see also adl5887, p. 1126

CULTURAL COEVOLUTION

A sweet interspecies collaboration

Honeyguides, a species of African bird, are well known to guide other species to beehives. They have even been known to work with honey badgers, but their closest and most successful collaborators are humans. Several indigenous African groups work with these birds across their range. Looking at these interactions in Tanzania and Mozambique, Spottiswoode and Wood have shown that honeyguides respond more readily to the specific calls of their local honey-hunting partners than they do to the calls of honey hunters from other regions (see the Perspective by Searcy and Nowicki). Thus, honeyguides appear to learn the calls of their local partners, and honey hunters maintain these successful calls over generations. — SNV

Science, adh4129, this issue p. 1155; see also adl5923, p. 1124

SEDIMENT LOADING

Insufficient accretion

Sea-level rise threatens to overtake coastal wetlands, but elevation-building processes, including deposition of sediments from upstream, can help keep wetlands above water. Ensign *et al*. investigated whether watershed sediment loads are enough to keep up with sea-level rise at US coasts (see the Perspective by Larsen and Milligan). Their model conservatively estimated that incoming sediment loads may be sufficient in the western Gulf of Mexico and Pacific coasts but insufficient in other regions where most watersheds are smaller. Local accretion is often higher than predicted from the model, suggesting an important role for biological processes to raise marsh elevation in the face of sea-level rise. —BEL

Science, adj0513, this issue p. 1191; see also adl4251, p. 1123

ADAPTIVE IMMUNITY

Catch of the day

Adaptive immunity evolved in ectothermic jawed vertebrates, yet how and where these immune responses are mounted in the apparent absence of germinal centers is not clear. To determine whether teleost fish have organized lymphoid structures, Shibasaki *et al.* searched the spleens of parasite-infected trout for proliferating lymphocytes. They identified regions of B and T cell proliferation in close proximity to melanomacrophage centers (MMCs), which they termed MMC-associated lymphoid aggregates (M-LAs). M-LAs contained immunoglobulin M^+ antigen-specific B cells, which expressed aicda and had undergone somatic hypermutation. M-LA B cells were polyclonal, and a significant portion were apoptotic, indicative of clonal expansion. These findings demonstrate that induction of adaptive immune responses in teleost fish occurs in organized secondary lymphoid structures that are functionally analogous to germinal centers. —HMI

Sci. Immunol. (2023) 10.1126/sciimmunol.adf1627

MATERNAL HEALTH

Cellular tress in the placental barrier

Hypertensive disorders of pregnancy such as pre-eclampsia (PE) affect a growing number of expectant mothers. Without a mechanistic understanding of these disorders, treatment remains elusive. Oxidative stress has been implicated, particularly in the syncytiotrophoblast layer called the multinucleated placental barrier. Opichka *et al.* demonstrated enhanced $G\alpha_q$ signaling in conjunction with mitochondrial reactive oxygen species in human placenta samples. They successfully generated PE phenotypes in mice by selective induction of $G\alpha_q$ signaling. Syncytiotrophoblast stress is a common end point of multiple divergent disease phenotypes, including in early- versus late-onset PE. This $G\alpha_q$ pathway represents a single potential treatment target regardless of the complexities of the syndromic PE condition. —MLO

Sci. Adv. (2023) 10.1126/sciadv.adg8118

Diversity of belowground invertebrates in upland UK soils, such as in the Yorkshire Dales, is sustained by grazing animals.

SOIL ECOLOGY

Supported by sheep

Livestock grazing has been present in some landscapes for centuries, keeping the vegetation in an open state that often supports unique biodiversity. However, the use of mountainous areas for pasture is declining. Schrama *et al.* used sheep exclusion experiments to determine how the loss of grazing affects the diversity of soil communities across 12 montane grasslands in the UK. They found lower diversity of microbes, nematodes, and plants in ungrazed versus grazed plots, with lower abundances of rare species, including rare springtails. These taxa were also more homogeneous across ungrazed plots, but loss of grazing increased spatial variability in soil invertebrates. Abandoning historical grazing will likely affect biodiversity and ecosystem functions provided by soil communities. —BEL *Proc. R. Soc. London Ser. B* (2023) 10.1098/rspb.2023.1345

appeared to be little historical admixture until about 70 years ago, which was likely caused by anthropogenic pressures on wildcat habitats and populations. —CNS

Curr. Biol. (2023)
10.1016/j.cub.2023.08.031

PANDEMIC PREPAREDNESS

Scenario modeling

Mathematical modeling underpinned much of our decision-making in response to the emergence of the severe acute respiratory syndrome coronavirus 2 (SARS-CoV-2) pandemic. Howerton *et al.* gathered the results from multiple modeling teams (13 in all) to estimate how reliable projections can be for weekly cases, hospitalizations, and deaths. Model scenarios stayed close to reality for an average of 22 weeks until a new variant evolved with different transmission properties that overturned key model assumptions. The team concluded that despite variation between models, maintaining an ensemble of models was more reliable than any single model for planning, resource allocation, and comparison of potential control strategies. —CA

Nat. Commun. (2023)
10.1038/s41467-023-42680-x

NEUROSCIENCE

Dysregulated neurogenesis in autism

The *synaptic Ras GTPase-activating protein 1* gene (*SYNGAP1*) is a top autism spectrum disorder (ASD) risk gene. *SYNGAP1* and many other ASD risk genes are involved in synaptic function, but it is not clear how they contribute to the dysregulated formation of neurons in the developing cortex that is thought to play a role in ASD. Birtele *et al*. studied the development of human cortical organoids derived from an individual with a mutation in *SYNGAP1* and found that the protein was important for the proper organization and maturation of neurons in the developing cortex. These findings indicate that SYNGAP1-related brain disorders can arise through mechanisms other than synaptic dysfunction. —SAL

Nat. Neurosci. (2023)
10.1038/s41593-023-01477-3

IMPACT CRATERS

How old are Saturn's large icy moons?

The ages of airless moons can be determined from the density of impact craters on their surfaces after correcting for their sizes, with more craters indicating older bodies. For the inner Solar System, crater counts are calibrated using radiometric dating of lunar samples. The population of impacting bodies differs in the outer Solar System, so it must be estimated from simulations. Wong *et al.* simulated the impacter rates in the Saturn system and then applied them to crater counts for five of its moons. They found that the moons Thethys, Dione, and Rhea formed about 4.3 billion years ago, and Mimas and Enceladus are about 200 million years younger. —KTS

Icarus (2023)
10.1016/j.icarus.2023.115763

HYDROGELS

Multifunctional antibacterial hydrogels

Gelatin has been used in the manufacture of contact lenses and for tissue engineering scaffolds and drug delivery. However, gelatin-based hydrogels are dependent on the gelatin source and can suffer from a lack of overall stability. Ruan *et al.* studied a family of gelatin-based hydrogels synthesized using a combination of dopamine, which is known for its adhesion properties; the zwitterionic monomer SBMA, which can repel bacteria and prevent ice formation; and zinc sulfate, which also shows antibacterial properties and improves the gel's conductivity. In addition to the basic properties expected from the constituent components, the gels showed self-healing, fatigue resistance, and mechanical stability across a wide temperature range, thus making these gels potentially suitable for antibacterial coatings and wearable sensors. —MSL

ACS Appl. Mater. Interfaces (2023)
10.1021/acsami.3c10477

RESEARCH ARTICLE SUMMARY

METABOLISM

ROS-induced ribosome impairment underlies ZAKα-mediated metabolic decline in obesity and aging

Goda Snieckute†, Laura Ryder†, Anna Constance Vind†, Zhenzhen Wu, Frederic Schrøder Arendrup, Mark Stoneley, Sébastien Chamois, Ana Martinez-Val, Marion Leleu, René Dreos, Alexander Russell, David Michael Gay, Aitana Victoria Genzor, Beatrice So-Yun Choi, Astrid Linde Basse, Frederike Sass, Morten Dall, Lucile Chantal Marie Dollet, Melanie Blasius, Anne E. Willis, Anders H. Lund, Jonas T. Treebak, Jesper Velgaard Olsen, Steen Seier Poulsen, Mary Elizabeth Pownall, Benjamin Anderschou Holbech Jensen, Christoffer Clemmensen, Zach Gerhart-Hines, David Gatfield, Simon Bekker-Jensen*

INTRODUCTION: When ribosomes stall and/or collide during mRNA translation, ribosomal surveillance mechanisms are activated. These pathways signal the presence of ribotoxic stress and coordinate the resolution of nonproductive ribosomes. The ribosome-binding and stress-sensing MAP3 kinase ZAKα is at the nexus of the ribotoxic stress response (RSR) that culminates in the activation of and signaling through the stress-associated MAP kinases p38 and JNK. The RSR pathway is nonessential, and little is known about the in vivo conditions in which translational problems occur and the contexts in which the RSR is physiologically important.

RATIONALE: Reactive oxygen species (ROS) activate p38 and JNK and impair ribosomal translation. We rationalized that these responses may be coupled, and that ROS, which is associated with a range of physiological and pathological biological transitions, is a source of RSR activation in vivo. ZAK knockout (KO) mice display a mild metabolic phenotype with leanness and decreased adiposity, suggesting that the RSR is involved in metabolic regulation. Further, p38 and JNK are involved in metabolic transitions such as the emergence of insulin resistance and liver steatosis in obesity. In the context of obesity and metabolic regulation, activation of these kinases is driven by elusive metabolic stress signals that could be mediated by any of the 21 known p38- and JNK-directed MAP3 kinases. We thus sought to investigate the potential links among ROS, RSR signaling, and metabolic regulation using cellular, zebrafish, and mouse models.

RESULTS: We confirmed that ROS activates the RSR in cellular models, associated with both stalling and collision of ribosomes. In vitro translation reactions highlighted that these effects are primarily mediated by effects on soluble translation factors, including transfer RNAs. When exposed to a pathological burst of ROS, developing zebrafish larvae deficient for the *zakα* gene were strongly protected against early lethality, likely due to prevention of RSR-induced programmed cell death. ZAK KO mice fed a high-fat high-sugar (HFHS) diet, which is associated with rapid weight gain and ROS-driven pathology in rodents, were protected against early manifestations of metabolic maladaptation, including blood glucose intolerance and liver steatosis. These phenotypes were accompanied by deregulated RSR signaling in ZAK KO mouse livers. In HFHS-fed mice, highly translated liver mRNAs displayed increased stalling and queuing of ribosomes, indicating the presence of known ZAKα-activating structures. Finally, aging in male mice is also associated with increased ROS production and metabolic deterioration manifested as impaired blood glucose intolerance, stochastic liver steatosis, and whitening of brown adipose tissue. ZAK KO mice were protected against all of these hallmarks of metabolic aging.

CONCLUSION: Our study uncovers ROS as a physiologically relevant source of translational aberrations and RSR activation. Furthermore, impaired ribosomes constitute at least a portion of the metabolic stress signals that drive unwanted metabolic maladaptation in obesity and aging. The strong protection against these reactions offered by *Zak* gene deletion in mice warrants investigation of the ZAKα kinase as a potential drug target for metabolic conditions such as nonalcoholic steatohepatitis, hypertension, and dyslipidemia. Additional work will be needed to unravel the tissue-specific contributions of RSR signaling to the above phenotypes and to identify other physiologically relevant sources of ribotoxic stress. ■

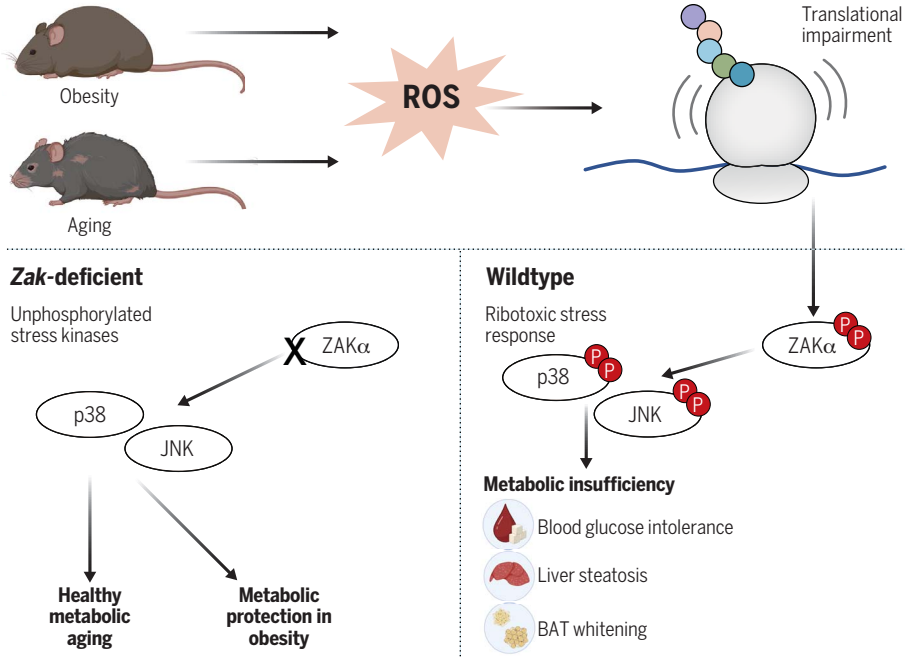

The ribotoxic stress response drives metabolic maladaptation in obesity and aging. ROS are a physiologically relevant source of translational impairment and activation of the stress kinases ZAKα, p38, and JNK. In obese and aging mice, this RSR drives metabolic maladaptation manifested by blood glucose intolerance, liver steatosis, and whitening of brown adipose tissue (BAT). [Figure created with BioRender.]

The list of author affiliations is available in the full article online.
***Corresponding author. Email: sbj@sund.ku.dk**
†These authors contributed equally to this work.
Cite this article as G. Snieckute *et al.*, *Science* 382, eadf3208 (2023). DOI: 10.1126/science.adf3208

READ THE FULL ARTICLE AT
https://doi.org/10.1126/science.adf3208

RESEARCH ARTICLE

METABOLISM

ROS-induced ribosome impairment underlies ZAKα-mediated metabolic decline in obesity and aging

Goda Snieckute[1,2]†, Laura Ryder[1,2]†, Anna Constance Vind[1,2]†, Zhenzhen Wu[1,2], Frederic Schrøder Arendrup[3], Mark Stoneley[4], Sébastien Chamois[5], Ana Martinez-Val[6], Marion Leleu[7], René Dreos[5], Alexander Russell[8], David Michael Gay[3], Aitana Victoria Genzor[1,2], Beatrice So-Yun Choi[9], Astrid Linde Basse[10], Frederike Sass[10], Morten Dall[10], Lucile Chantal Marie Dollet[10], Melanie Blasius[1,2], Anne E. Willis[4], Anders H. Lund[3], Jonas T. Treebak[10], Jesper Velgaard Olsen[6], Steen Seier Poulsen[9], Mary Elizabeth Pownall[8], Benjamin Anderschou Holbech Jensen[9], Christoffer Clemmensen[10], Zach Gerhart-Hines[10], David Gatfield[5], Simon Bekker-Jensen[1,2]*

The ribotoxic stress response (RSR) is a signaling pathway in which the p38- and c-Jun N-terminal kinase (JNK)–activating mitogen-activated protein kinase kinase kinase (MAP3K) ZAKα senses stalling and/or collision of ribosomes. Here, we show that reactive oxygen species (ROS)–generating agents trigger ribosomal impairment and ZAKα activation. Conversely, zebrafish larvae deficient for ZAKα are protected from ROS-induced pathology. Livers of mice fed a ROS-generating diet exhibit ZAKα-activating changes in ribosomal elongation dynamics. Highlighting a role for the RSR in metabolic regulation, ZAK-knockout mice are protected from developing high-fat high-sugar (HFHS) diet-induced blood glucose intolerance and liver steatosis. Finally, ZAK ablation slows animals from developing the hallmarks of metabolic aging. Our work highlights ROS-induced ribosomal impairment as a physiological activation signal for ZAKα that underlies metabolic adaptation in obesity and aging.

A high degree of metabolic flexibility allows for optimal release and utilization of energy when resources are scarce and efficient storage of energy when resources are abundant (*1*, *2*). In contemporary societies, continuous access to calorie-rich foods has caused a global obesity epidemic (*3*). In this setting, otherwise beneficious mechanisms for dynamic metabolic regulation negatively affect homeostasis. A deeper understanding of the underlying signaling pathways is needed to direct the development of new treatment principles for obesity and associated metabolic maladies (*4*). These include type 2 diabetes, nonalcoholic steatohepatitis (NASH), hypertension, and dyslipidemia. Hallmarks of early obesity-associated metabolic dysfunction include insulin resistance, pancreatic β-cell insufficiency, hepatic accumulation of lipids (steatosis), and adipose tissue hypertrophy (*5*, *6*). Similar changes occur during the process of aging (*7*), suggesting that the underlying mechanisms of metabolic alteration are related. One potential driver of metabolic dysregulation is reactive oxygen species (ROS), the production of which is increased in both obesity and aging (*8*, *9*). Elevated ROS has the potential to disturb the redox balance of cells and damage macromolecules such as proteins, DNA, and RNA. At the same time, ROS within a physiological range are prerequisite signaling molecules for homeostasis with beneficial functions (*10*, *11*). It is not clear how elevated ROS perturb metabolic functions on an organismal scale, and the underlying mechanism(s) may include indiscriminate oxidative damage to macromolecules and regulation of metabolic signaling pathways.

The stress-activated mitogen-activated protein kinases p38 and c-Jun N-terminal kinase (JNK) are activated by multiple cell stress agents such as ROS, ultraviolet (UV) light, heat stress, and mechanical perturbation. Signaling from these kinases determines diverse cellular outcomes, including cell cycle arrest, cell death, cell differentiation, stress adaptation, and inflammation (*12*). Less appreciated are the powerful roles of p38 and JNK in metabolic regulation, which have been demonstrated in a wide range of conditional knockout (KO) mouse models (*13*, *14*). These studies implicate JNK kinases in the regulation of tissue-specific and systemic insulin sensitivity, hepatic lipid deposition, and production of adipokines, among others (*14*). Among its many roles in metabolic regulation, p38 regulates β cell survival (*15*) and key processes in adipose tissues such as thermogenesis and lipolysis (*16*). Activation of p38 and JNK is associated with obesity and metabolic syndrome, and targeting of these kinases or nonessential components of their signaling pathways has been proposed as a therapeutic approach for the treatment or prevention of these metabolic diseases (*13*, *17*). In particular, the protection of JNK-deleted mice against high-fat diet–induced insulin resistance and hepatic steatosis (*14*, *18*, *19*) points to MAP kinase signaling pathways as key regulators of metabolic flexibility and drivers of metabolic decline.

MAP kinases are activated through signal transduction cascades involving upstream MAP kinase kinases (MAP2Ks) and MAP kinase kinase kinases (MAP3Ks) (*12*). The most upstream of these components, the MAP3Ks, are a group of 21 human kinases, of which we only know the activation mechanisms and signals for a few. One MAP3K that has recently attracted interest is ZAKα, which interacts with the ribosome and is a sensor of translational impairment (*20*). ZAKα binds to ribosomes by virtue of two C-terminal ribosome-binding domains (*21*) and is activated by perturbations such as stalling and/or collision of ribosomes (*22*, *23*). This pathway for monitoring ribosomal function and converting ribosomal aberrations into p38 and JNK activation is known as the ribotoxic stress response (RSR) (*24*). Our knowledge about the function of the RSR has been gleaned in mammalian cell lines with treatments such as ribotoxin enzymes (including ricin, Shiga toxin, and α-sarcin, all of which have pathological relevance as human toxins), antibiotics (including anisomycin and cycloheximide), or UV irradiation (*25*, *26*), which damage or chemically inhibit the ribosome or damage mRNA templates, respectively. Except for UVB irradiation of keratinocytes in the skin (*27*), these treatments neither offer much insight into the physiological sources of ribosome stalling, ribosome collision, and RSR activation nor provide any clues as to the physiological roles of this signaling pathway in the context of a whole organism. Here, we show that ROS is a powerful activator of ZAKα and downstream RSR signaling, and that a ROS-generating obesogenic diet is associated with altered ribosomal elongation dynamics in the mouse liver. In the context of obesity and aging, the RSR pathway mediates well-known but unwanted metabolic transitions such as deregulated glucose tolerance and liver steatosis. Our work offers mechanistic insights into metabolic regulation by MAP kinase signaling and

[1]Center for Healthy Aging, Department of Cellular and Molecular Medicine, University of Copenhagen, DK-2200 Copenhagen, Denmark. [2]Center for Gene Expression, Department of Cellular and Molecular Medicine, University of Copenhagen, DK-2200 Copenhagen, Denmark. [3]Biotech Research and Innovation Center, University of Copenhagen, DK-2200 Copenhagen, Denmark. [4]MRC Toxicology Unit, University of Cambridge, Cambridge CB2 1QR, UK. [5]Center for Integrative Genomics, University of Lausanne, 1015 Lausanne, Switzerland. [6]Mass Spectrometry for Quantitative Proteomics, Proteomics Program, The Novo Nordisk Foundation Center for Protein Research, Faculty of Health and Medical Sciences, University of Copenhagen, DK-2200 Copenhagen N, Denmark. [7]Bioinformatics Competence Center, Ecole Polytechnique Fédérale de Lausanne and University of Lausanne, CH-1015 Lausanne, Switzerland. [8]Department of Biology, University of York, York YO10 5DD, UK. [9]Department of Biomedical Sciences, University of Copenhagen, DK-2200 Copenhagen, Denmark. [10]Novo Nordisk Foundation Center for Basic Metabolic Research, Faculty of Health and Medical Sciences, University of Copenhagen, DK-2200 Copenhagen, Denmark.
*Corresponding author. Email: sbj@sund.ku.dk
†These authors contributed equally to this work.

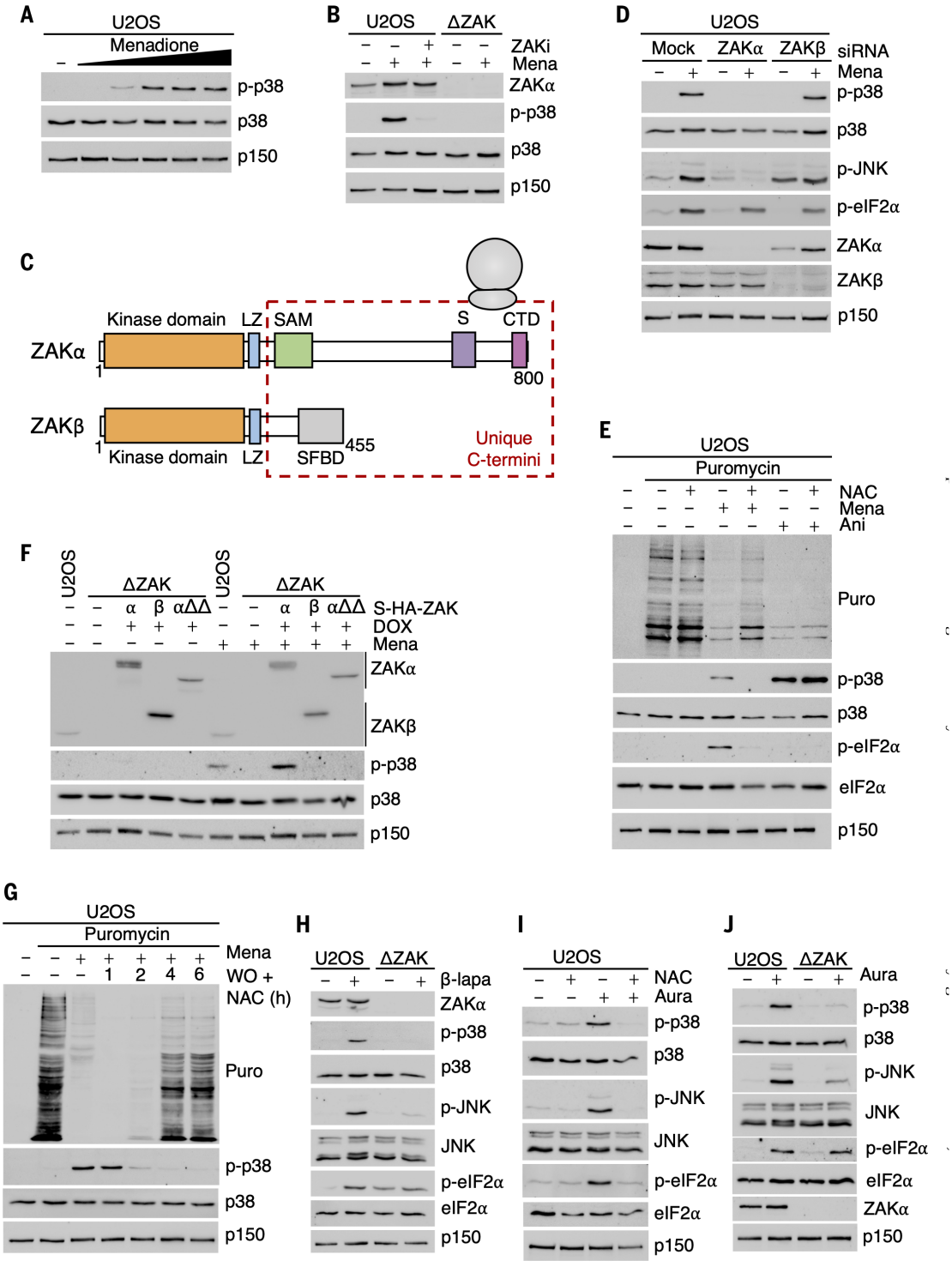

Fig. 1. ROS inhibit translation and activate the RSR. (**A**) U2OS cells were treated with increasing concentrations of menadione (25, 50, 150, 250, and 500 μM for 1 hour). Lysates were analyzed by immunoblotting with the indicated antibodies. (**B**) WT U2OS cells or U2OS cells deleted for ZAK (ΔZAK) were treated with a ZAK inhibitor (ZAKi, 2 μM) and menadione (Mena, 250 μM for 1 hour). Lysates were analyzed as in (A). (**C**) Schematic of ZAK protein isoforms. LZ, leucine zipper; SAM, sterile alpha-motif; S, sensor domain; CTD, C-terminal domain; SFBD, stress fiber binding domain. (**D**) U2OS cells were transfected with control (mock) small interfering RNA (siRNA) or siRNAs targeting the α or β isoforms of ZAK. Cells were treated with menadione (250 μM for 1 hour), and lysates were analyzed as in (A). (**E**) U2OS cells were pretreated with NAC (10 mM for 1 hour) followed by addition of menadione (250 μM for 1 hour) or anisomycin (Ani, 1 μg/ml for 1 hour) as indicated. Puromycin (10 μg/ml) was added to the culture 10 min before harvest, and lysates were analyzed by immunoblotting with the indicated antibodies. (**F**) U2OS cells, ΔZAK cells, and ΔZAK cells rescued with WT and mutated forms of ZAKα and WT ZAKβ were treated as in (D) [αΔΔ is a deletion of the "S" and "CTD" domain in (C)]. Lysates were analyzed as in (A). (**G**) U2OS cells were treated with menadione (250 μM for 1 hour) followed by washout (WO) in the presence of NAC (10 mM) for the indicated times. Cells were pulse treated with puromycin (10 μg/ml, 10 min) before harvest as in (E). Lysates were analyzed as in (A). (**H**) Cells from (B) were treated with ROS-generating β-lapachone (β-lapa, 20 μM for 1 hour) and lysates were analyzed as in (A). (**I**) U2OS cells were pretreated with NAC (10 mM for 1 hour), followed by addition of auranofin (Aura, 5 μM for 1 hour) as indicated. Lysates were analyzed as in (A). (**J**) Cells from (B) were treated with auranofin (5 μM for 1 hour), and lysates were analyzed as in (A).

points to the ribosome as a hitherto unappreciated sensor of metabolic stress.

Results

ROS inhibit protein synthesis and activate the RSR

Oxidative stress and ROS are both inhibitory to translation (*28*) and lead to activation of p38 and JNK (*29*). In search of a potential link between these effects, we treated U2OS cells with a p38-activating dose of menadione, which causes intracellular superoxide radical generation through a futile reduction-oxidation cycle (Fig. 1A). p38 activation was completely abrogated both by an inhibitor of ZAK kinase activity and by CRISPR-mediated inactivation of the *Zak* gene (Fig. 1B). Menadione appeared to activate the RSR, becausae p38 activation required the ribosome-binding α-isoform, but not the unrelated β-isoform, of ZAK (Fig. 1, C and D). In further support of this notion, we found that menadione strongly inhibited bulk

translation in a puromycin-incorporation assay (Fig. 1E) and required functional ribosome-binding domains in ZAKα for p38 activation (Fig. 1F). These effects were reversible, because cells both resumed translation and silenced p38 activity, albeit with some delay, when menadione was washed out in the presence of the ROS scavenger N-acetylcysteine (NAC) (Fig. 1G). Menadione also activated the integrated stress response (ISR), as evidenced by eIF2α phosphorylation, and all of the above effects could be circumvented by preincubation of cells with NAC (Fig. 1E and fig. S1A). These effects of ROS were not restricted to menadione, because we found that the redox cycling agent β-lapachone and the thioredoxin reductase inhibitor auranofin similarly reduced ribosomal output and activated both p38 and JNK in a ZAK-dependent and NAC-reversible manner (Fig. 1, H to J, and fig. S1, B to D). On the basis of these results, we conclude that ROS exposure acutely triggers RSR signaling in cells.

ROS induce ribosome stalling in vivo and impair translation in vitro

ZAKα responds to both stalling and collision of ribosomes (*22*, *23*). To understand the mechanistic basis of ROS-induced RSR activation, we analyzed ribosome collisions in cells by digesting polysomes with micrococcal nuclease (MNase) and resolving the collided ribosomes on a sucrose gradient (*30*). Upon treatment of cells with menadione for 30 min or 1 hour, this approach did not reveal an increase in MNase-resistant polysome peaks, which are indicative of stacked ribosomes (Fig. 2A and fig. S1E, left). However, treatment of U2OS cells with β-lapachone for 30 min produced a small increase in collided ribosomes (fig. S1F, left). These results were in clear contrast to anisomycin treatment, which gave rise to substantial amounts of ribosome collisions (fig. S1G), as previously reported (*22*, *30*). We and others have previously reported that amino acid deprivation results in stalling of elongating ribosomes, but these stalled ribosomes are only converted to collisions upon inhibition of the ISR (*30*, *31*). Because ROS also activate the ISR (Fig. 1), we wondered if this response also limits ribosome collisions in response to menadione and β-lapachone. Treatment of cells with the pan-ISR inhibitor ISRIB did stimulate low levels of ribosome collision at 30 min after both menadione and β-lapachone addition (Fig. 2A and fig. S1F, right, and H), but these effects were transient and largely undetectable at the 1- and 2-hour time points (fig. S1E). These data suggest that cells react acutely to ROS-generating agents with both stalling and collision of ribosomes, and that high levels of ROS themselves interfere with translation initiation at later time points. Indeed, both menadione and β-lapachone treatments were accompanied by a time-dependent loss of polysomes that could not be reversed by ISRIB (fig. S1, I and J). Targeting of initiating 80*S* ribosomes with harringtonine resulted in the fast runoff of elongating ribosomes (Fig. 2B, left), as previously shown (*32*). This runoff was impeded for the remaining translating ribosomes in menadione-treated cells (Fig. 2B, right), further supporting that ROS slow down and/or stall elongating ribosomes. Consistent with the above, and in contrast to anisomycin treatment, ribosome-enriched pellets from menadione-treated cells were negative for all biochemical markers of collided elongating [EDF1 (*33*, *34*), ubiquitylated RPS10 and ZNF598 (*35*, *36*)] and initiating [ubiquitylated RPS2 (*37*, *38*)] ribosomes (fig. S2, A and B). In addition, the endoplasmic reticulum (ER) stress–responsive kinase PERK, and not ribosome-associated GCN2, appeared to be the more relevant eIF2α kinase upon treatment of cells with menadione and auranofin (Fig. 2C and fig. S2C). These and previous (*23*) data indicate that activation of ZAKα upon acute ROS exposure can occur independently of widespread ribosome collision and may thus largely depend on stalling and slowing of individual ribosomes (fig. S2D). Our results also highlight that the triggers of ER stress and ribotoxic stress are overlapping. Indeed, the ER stress–inducing agent thapsigargin strongly repressed bulk ribosomal translation and induced ZAKα activation (fig. S2, E to G).

ROS have the potential to damage nucleotides in DNA as well as RNA, and oxidative modification of both ribosomal RNA (rRNA) and mRNA bases has previously been associated with translational impairment (*39*). To understand which components of the translation process are sensitive to ROS, we developed a tripartite in vitro translation system from lysates of HeLa cells (Fig. 2D). This cell line also displayed menadione-induced and NAC-reversible translational inhibition and p38 activation (fig. S2, H and I). Our approach consisted of isolating ribosomes from one culture of HeLa cells and a ribosome-free cytoplasmic fraction containing transfer RNAs (tRNAs) and initiation and elongation factors from another, which only upon combination supported translation of an in vitro–transcribed luciferase-encoding mRNA (Fig. 2D and fig. S2J). To introduce oxidative damage to the in vitro translation system, we treated only one of the three components at a time with hydrogen peroxide for 10 min. To prevent carryover effects, we subsequently neutralized the hydrogen peroxide with catalase before combining the fractions and determining the extent of luciferase protein production. To our surprise, the ability of ribosomes or luciferase mRNA to support translation was not impaired by hydrogen peroxide treatment, rather, it was the cytoplasmic fraction that was exquisitely sensitive to oxidative damage (Fig. 2E). This result was in stark contrast to collision-causing UVB irradiation, which negatively affected exclusively the mRNA component (Fig. 2F), as previously described (*22*). We also prepared the ribosomal and cytoplasmic fractions directly from menadione- and NAC-treated HeLa cells (Fig. 2G). In these experiments as well, our results indicated that the cytoplasmic fraction, but not the ribosomal fraction, contained one or more soluble ROS-sensitive components (Fig. 2, H and I). Using a biotin switch assay (*40*), we did not find biochemical evidence for cysteine oxidation in a number of relevant translation initiation and elongation factors after menadione treatment (fig. S3A). Global inspection of tRNA integrity also did not indicate large-scale degradation of the tRNA pool in the cytoplasmic fraction (Fig. 2J). However, Northern blotting for the tRNA Arg-TCT revealed marked cleavage and fragmentation, which was induced by menadione and reversed by NAC (Fig. 2K). Similar but much weaker effects were observed for the tRNAs Leu-CAA, Gly-GCC, and iMet-CAT (fig. S3, B to D), without an apparent effect on tRNA charging (fig. S3E). Angiogenin is a tRNA-cleaving RNase that is activated upon a multitude of cellular stress insults to produce translation-inhibiting tRNA fragments (*41*, *42*). Activation of angiogenin by menadione and ensuing tRNA cleavage was recently demonstrated (*43*). Although these effects may not be the only relevant ones, we conclude that ROS-inducing agents interfere with translation in vivo and in vitro and activate ZAKα and the RSR.

Additive contributions from ZAKα and ASK1 underlie ROS-induced p38 and JNK activation

When challenged with menadione, p38 activation occurred in two distinct waves, one starting at 5 min after exposure and peaking at 10 to 15 min, and another starting at 45 min and peaking at 1 to 2 hours (Fig. 3A). Only the second of these peaks coincided with ISR activation, translation shutdown, and appearance of oxidized proteins (Fig. 3A and fig. S3F). When analyzing U2OS cells deleted for the *ZAK* and *ASK1* genes either individually or in combination, the ROS-activated MAP3K ASK1 (*44*) appeared to be involved only in the first of these responses, whereas ZAKα was exclusively required for the second wave (Fig. 3B). These data imply that ASK1 is a faster responder to oxidative stress, and that damage to macromolecules and ribosomal impairment precedes activation of the RSR. We also challenged our U2OS cells with hydrogen peroxide and observed a partial dependency for both ZAK and ASK1 kinase activity for stress-associated MAPK activation (fig. S3G). Our results add to the existing knowledge about ASK1 as a ROS-activated MAP3K and highlight ZAKα as a nexus in a parallel pathway that relays ROS-induced translational impairment toward MAPK signaling (Fig. 3C).

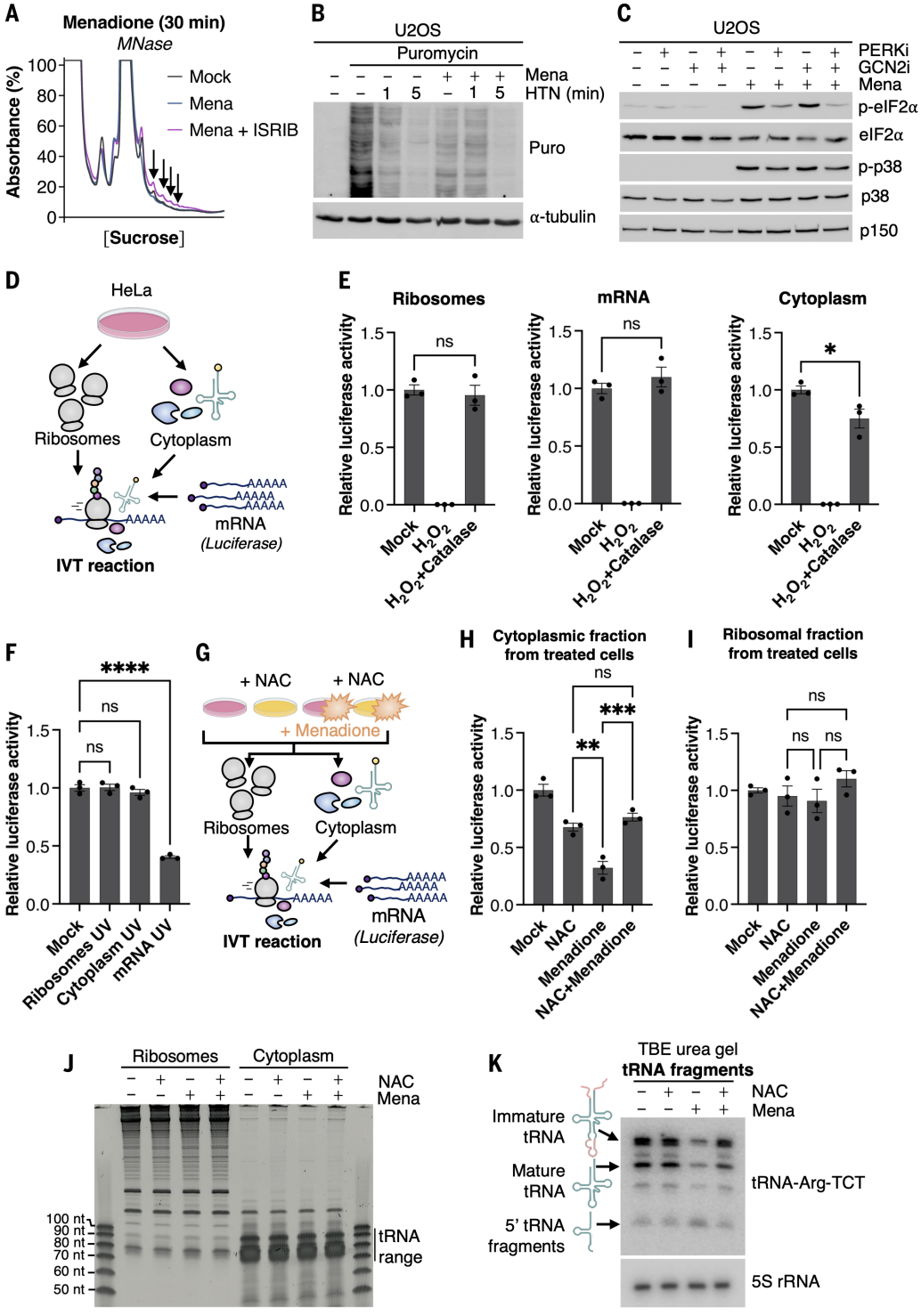

Fig. 2. ROS-induced ZAKα activation is associated with ribosome stalling and collision. (**A**) U2OS cells were treated with menadione (Mena, 250 μM for 30 min) and ISRIB (200 nM). Lysates were digested with MNase and separated on a linear sucrose gradient. Arrows highlight UV peaks that are indicative of increased ribosome collision. (**B**) U2OS cells were pretreated with menadione (250 μM for 1 hour) as indicated and harringtonine (HTN, 2 μg/ml) for the indicated times to induce ribosome run-off. Puromycin (10 μg/ml) was added to the culture for 5 min before harvest (but after HTN incubation time) and lysates were analyzed by immunoblotting with the indicated antibodies. (**C**) U2OS cells were treated with menadione (250 μM for 1 hour) and inhibitors (i, 1 μM) against PERK and GCN2 as indicated. Lysates were analyzed as in (B). (**D**) Schematic of tripartite in vitro translation (IVT) approach. Ribosomes, ribosome-free cytoplasm, and mRNA can be individually treated before combination. (**E**) The three fractions from (D) were individually treated with hydrogen peroxide (10 min) and neutralized by the addition of catalase as indicated. Translation efficiency in the combined reaction was determined by luciferase assay. (**F**) As in (E), except that the fractions were individually irradiated with UVB (500 J/m^2) before in vitro translation. (**G**) Schematic of modified tripartite IVT assay. In contrast to (D), HeLa cells were pretreated with NAC (10 mM for 1 hour), followed by addition of menadione (250 μM for 1 hour) before purification of fractions. (**H**) Combined IVT reactions with treated with ribosome-free cytoplasm from (G). (**I**) As in (H), except that treated ribosomes from (G) were used. All values indicate luciferase activity normalized to the control. For (E), (F), (H), and (I), data are plotted as means, and all error bars represent the SEM (n = 3 biological replicates). ns, nonsignificant; *$P \le 0.05$; **$P \le 0.01$; ***$P \le 0.001$; ****$P \le 0.0001$ by Student's t test for two groups and one-way ANOVA with Tukey's post hoc test for more than two groups. (**J**) Whole-cell RNA isolated from HeLa cell fractions from (G) was separated on urea agarose gel and stained for RNA. nt, nucleotides. (**K**) Northern blot for tRNA-Arg-TCT on RNA samples from (J). Schematic of tRNA intermediates corresponding to distinct bands are shown on the left side of the blot.

ZAKα mediates ROS-induced death in zebrafish larvae

To probe the organismal consequences of ROS-induced RSR signaling, we turned to zebrafish as a model organism. Zebrafish is amenable to CRISPR-mediated genetic manipulation and is an attractive organism for developmental studies because of its fast extrauterine development (*45*). Whereas mammals contain a single *Zak* gene that encodes two distinct splice variants (Fig. 1C), zebrafish express clear orthologs of ZAKα and ZAKβ from two independent genes (fig. S3H). We thus proceeded to interrupt these two genes in zebrafish (Fig. 3D) and generated single- and double-KO animals (Fig. 3E). The genetically introduced deletions to interrupt the open reading frames of the two paralogs also reduced their mRNA

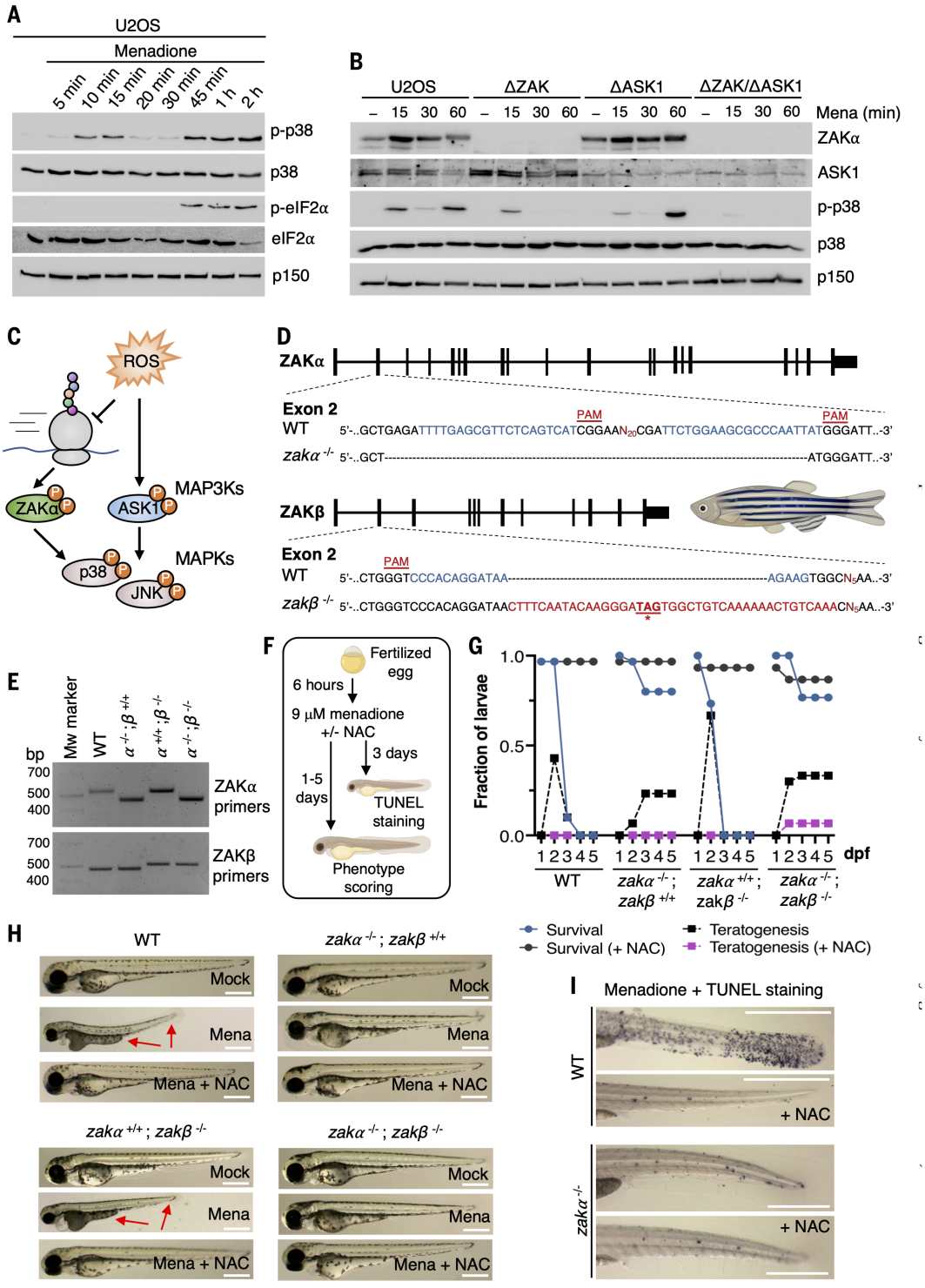

Fig. 3. ZAKα mediates menadione-induced apoptosis and death in zebrafish. (**A**) U2OS cells were treated with menadione (250 μM) for the indicated times. Lysates were analyzed by immunoblotting with the indicated antibodies. (**B**) U2OS cells individually deleted for ZAK (ΔZAK), ASK1 (ΔASK1), and both (ΔZAK/ΔASK1) were treated with menadione (250 μM) for the indicated times. Lysates were analyzed as in (A). (**C**) Model of ROS-induced activation of p38 and JNK kinases by parallel sensing mechanisms. ZAKα responds to ROS-induced impairment of ribosomal translation (left), whereas ASK1 activity is directly controlled by intracellular ROS levels (right). (**D**) Genomic location of guide RNA sequences (blue) and derived knockout alleles in exon 2 of zebrafish *zakα* (top) and *zakβ* (bottom) genes. A 33-bp insertion in mutated *zakβ* is highlighted in red, with the position of an in-frame STOP codon underlined and in bold. PAM, protospacer adjacent motif. (**E**) Genotyping of WT and CRISPR-modified alleles of *zakα* and *zakβ* genes from (D). A single zebrafish larva per genotype was lysed and submitted to genomic PCR with the indicated primer pairs. Amplified bands were resolved by agarose gel electrophoresis. (**F**) Schematic of experiments with menadione treatment of zebrafish larvae. Zebrafish eggs were incubated in the presence of menadione (9 μM) and/or NAC (60 μM) from 6 hours postfertilization and up to 5 days. Larvae were scored as dead or alive once per day, and the number of fish with developmental phenotypes was determined. For detection of apoptosis, larvae treated for 3 days were fixed and subjected to TUNEL staining. (**G**) Thirty zebrafish larvae with each of the indicated genotypes were treated and scored as in (F). Only larvae with cardiac arrest were scored as dead. The data shown are from one representative experiment out of the three performed. dpf, days post fertilization. (**H**) Representative images of larvae from (G) at day 3. WT fish treated with menadione (Mena) presented with darkened yolk sac, cardiac edema, and short kinked tails (red arrows). The addition of NAC or deletion of *zakα* largely obliviated these pathologies. (**I**) WT and *zakα*$^{-/-}$ larvae were treated as in (F) for 3 days, fixed, and subjected to TUNEL staining. Photographs show representative images of the tail part of the larvae. All scale bars, 500 μm.

abundances, with *zakβ* knockout additionally affecting *zakα* expression (50% reduction) (fig. S3I).

Exposure of fertilized wild-type (WT) zebrafish eggs to menadione resulted in death (scored as cardiac arrest) of most of the larvae after 3 to 4 days (Fig. 3, F and G). This was preceded by the appearance of a range of developmental phenotypes such as edema of the yolk sac and heart, curved spine or tail, and decreased length (Fig. 3H). All of these marked effects could be attributed to pathological ROS generation because they were prevented by the coadministration of NAC in the culture water (Fig. 3, G and H). Although *zakβ*$^{-/-}$ fish were

similarly sensitive to the effects of menadione, *zakα*$^{-/-}$ and double-KO larvae were largely resistant to death and to the appearance of pathological phenotypes (Fig. 3, G and H). Menadione-induced pathology was associated with apoptotic cell death, as visualized by TUNEL-positive cells in the tails of WT larvae, and this effect could also be prevented by co-administration of NAC or *zakα* deletion (Fig. 3I). We conclude that ZAKα, but not ZAKβ, responds to ROS in an organismal setting and that *zakα*$^{-/-}$ zebrafish larvae are quite protected, at least in the short term, against the harmful effects of a pathological burst of ROS.

ZAK$^{-/-}$ *mice are protected against metabolic dysfunction when fed a calorie-rich diet*

Examining the relative expression levels of *ZAKα* and *ASK1* transcripts across human tissues, we observed that the liver contained relatively little *ASK1* mRNA while at the same time being one of the very few tissues in which the expression of *ZAKα* exceeds that of *ZAKβ* (fig. S3J; data from the GTExPortal: https://gtexportal.org/). Reanalysis of a recent tissue-resolved draft of the mouse proteome (*46*) also indicated that the ZAKα protein is expressed at higher levels than ASK1 in several metabolic organs, including the liver (fig. S3K). We proceeded by subjecting male WT and ZAK$^{-/-}$ mice to a diet rich in lipids and sugar (high-fat, high-sugar: HFHS) for 25 weeks, only interrupted by intraperitoneal glucose tolerance tests (ipGTT) and magnetic resonance (MR) scans to determine body composition (Fig. 4A). This diet is known to result in increased adiposity, insulin resistance, and liver steatosis (*47*), with increased ROS generation serving, at least in part, as an underlying pathological driver (*48*). As we previously reported (*49*), the starting weights of the male ZAK$^{-/-}$ mice were slightly lower than those of their WT littermates (fig. S4A). Initial weight gain was also somewhat delayed in ZAK$^{-/-}$ mice when shifted from chow to HFHS diet, but mice then proceeded to gain weight in a largely genotype-independent manner (Fig. 4B) and ingested similar amounts of food throughout the experiment (fig. S4B). MR scanning revealed that fat mass increased as expected in WT mice (fig. S4C), but with some retardation in ZAK$^{-/-}$ mice (fig. S4C), in both cases with a relatively constant lean mass (fig. S4D). In WT mice, HFHS feeding also resulted in the expected loss of blood glucose control as determined by ipGTT, being evident at 8 weeks and exacerbated at 19 weeks (Fig. 4C). Conversely, HFHS-fed ZAK$^{-/-}$ mice were well protected against such functional metabolic decline and performed similarly to chow-fed mice in ipGTT at the 8-week time point (Fig. 4C, top versus middle). At the 19-week time point, ZAK$^{-/-}$ mice appeared to have developed a certain degree of glucose intolerance, albeit this was less pronounced than in the WT (Fig. 4C, bottom). Consistent with this, ZAK$^{-/-}$ mice exhibited less insulin resistance at the 19-week time point, as evidenced by 50% reduced HOMA-IR (Homeostatic Model Assessment for Insulin Resistance) values (Fig. 4D and fig. S4, E and F). In contrast to glucose intolerance, frank insulin resistance, assessed by HOMA-IR or an insulin challenge test developed over a longer time span (*50*). Consistent with this and in a distinct mouse cohort, WT mice appeared insulin sensitive and thus not significantly different from ZAK$^{-/-}$ mice after 8 weeks of HFHS feeding (Fig. 4E), thus not fully recapitulating the reported phenotype of JNK-deficient mice (*51*). Liver weights measured after euthanasia were similar between WT and ZAK$^{-/-}$ mice (fig. S4G), yet the hepatic triglyceride content was ~50% lower in HFHS-fed ZAK$^{-/-}$ mice despite indistinguishable serum triglyceride levels (Fig. 4F and fig. S4H). This difference also manifested as lower steatosis grades in ZAK$^{-/-}$ livers (Fig. 4, G and H).

The observed early protection against diet-induced glucose intolerance and the long-term protection against hepatic steatosis in ZAK$^{-/-}$ over WT mice despite a similar whole-body insulin sensitivity at 8 weeks of feeding prompted us to search for alternative explanations for the metabolic protection offered by *Zak* deletion. First, we subjected WT and ZAK$^{-/-}$ mice on an HFHS diet for 10 weeks to a glucose-tracing experiment using tritiated 2-deoxy-D-glucose (2DG). Mice were euthanized 1 hour after injection, and uptake of radioactive glucose was determined in several central and peripheral tissues (fig. S4I). Consistent with our glucose challenge experiments (Fig. 4C), radioactivity was cleared faster from the bloodstream of ZAK$^{-/-}$ mice (fig. S4J, top left), although uptake of 2DG and its conversion to 2DG-6-phosphate (2DG6P) at the end point was similar between genotypes (fig. S4J, remaining panels). These results indicate an equal total capacity for glucose uptake in WT and ZAK$^{-/-}$ tissues after 60 min, with potential kinetic effects at earlier time points. Second, we placed mice of both genotypes that had been fed chow or HFHS for 6 weeks in metabolic chambers for 1 week and monitored their movement, consumption of O_2, and production of CO_2 (fig. S5A). Locomotor activity and energy expenditure were largely independent of genotype (for within-genotype variance = 0.0022 kcal/h^2, see fig. S5, B to D; for between-genotype variance = 0.00027 kcal/h^2, see fig. S5C). However, we observed a substantial increase in the respiratory exchange ratio in ZAK$^{-/-}$ mice over WT when they were fed the regular chow diet (fig. S5, E to G). This result indicates a preferred utilization of carbohydrates over lipids as energy sources in ZAK$^{-/-}$ mice, likely as a consequence of the reduced adiposity of these animals (*23*). This readout was only observable in chow-fed mice, and the pronounced HFHS-induced suppression of respiratory exchange ratio exceeded that of the two genotypes, thus impeding further interrogation of obese mice.

To evaluate the contribution of ROS to metabolic phenotypes associated with ZAK KO, we combined HFHS feeding with 10 g per liter NAC supplementation in the drinking water. IpGTT assays were performed at 5 and 10 weeks, and mice were euthanized after 12 weeks of treatment (fig. S6A). In this experiment, weight gain was also initially delayed in ZAK$^{-/-}$ mice and was further reduced by the high dose of NAC (fig. S6B). IpGTT assays confirmed the progressive development of glucose intolerance and HOMA-IR elevation in WT mice, whereas ZAK$^{-/-}$ mice were fully protected against such metabolic decline after both 5 and 10 weeks of HFHS feeding (fig. S6, C to G). NAC supplementation completely nullified these differences between genotypes in terms of ipGTT (fig. S6, C and D), fasting insulin levels (fig. S6F), and HOMA-IR (fig. S6G). Conversely, NAC supplementation only partly improved the liver steatosis grade in WT mice and did not appear to offer the same protection as ZAK KO against this outcome (fig. S6, H and I). Our results indicate that RSR signaling activated by ROS and other sources of ribosomal impairment mediates at least some aspects of metabolic adaptation to an obesogenic diet.

Phospho-proteomic analysis reveals deregulation of MAPK signaling in livers of ZAK$^{-/-}$ *HFHS-fed mice*

We used phosphoproteomics to investigate signaling toward p38 and JNK kinases in livers of mice fed HFHS for 5 weeks and euthanized during the dark phase, when hepatic ROS levels are maximal (*52*) (Fig. 5A). We identified ~5500 unique proteins and ~12,500 unique phosphorylation sites (tables S1 and S2). Principal component analysis (PCA) revealed little separation of samples at the protein level (fig. S7A) but a clear separation and clustering according to both genotype and diet at the level of phosphorylation sites (Fig. 5B). We used this dataset to investigate phosphorylation changes annotated as regulatory on all recorded MAPK, MAP2K, and MAP3K components (fig. S7B). This analysis revealed HFHS- and *Zak*-dependent regulation of activation-associated phosphorylation sites on several components of p38 and JNK signaling cascades. A finer analysis of the relevant phosphopeptides across all conditions revealed a decrease in activation-associated phosphorylation of JNK2 (MAPK9-Y185) upon HFHS feeding of ZAK$^{-/-}$ but not WT mice (Fig. 5C, fig. S7C, and table S2). However, Western blot analysis on the same liver samples did not indicate decreased HFHS-induced JNK phosphorylation in ZAK$^{-/-}$ mice (Fig. 5D). A portion of the HFHS-induced RSR

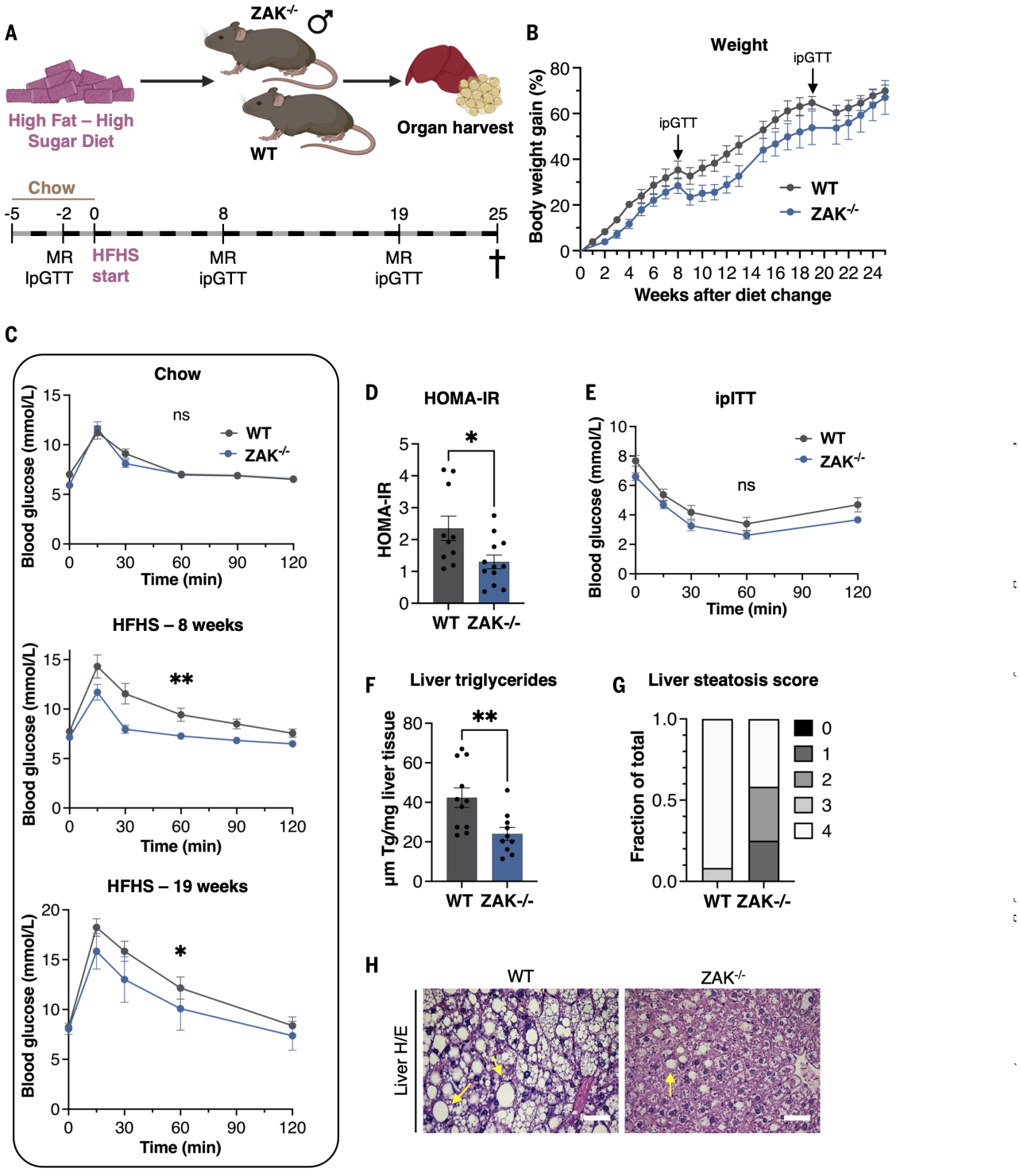

Fig. 4. ZAK$^{-/-}$ mice are protected against obesity-associated metabolic dysfunction. (**A**) Schematic of mouse feeding experiment. Ten- to 12-week-old male WT (n = 13) and ZAK$^{-/-}$ (n = 12) mice were maintained on chow and subjected to MR scanning and ipGTT 2 weeks before shifting to a HFHS diet. Mice were subjected to MR scanning and ipGTT after a further 8 and 19 weeks of HFHS feeding. Mice were euthanized and tissues were collected 25 weeks after the diet shift. (**B**) Percent body weight gain of mice from (A). Arrows mark the time of IpGTT assay and resulting transient weight loss. (**C**) Blood glucose concentrations of mice from (A) subjected to ipGTT assay. (**D**) HOMA-IR of mice from (A). (**E**) Blood glucose concentration of mice from fig. S4I subjected to the IpITT at the 8-week time point (WT, n = 12; ZAK$^{-/-}$, n = 7). (**F**) Liver triglyceride content of mice in (A). (**G**) Scoring of liver steatosis grade (scale, 0 to 4) of mice from (A). (**H**) Images of representative hematoxylin & eosin (H&E)–stained WT and ZAK$^{-/-}$ liver sections from mice in (A). Arrows indicate areas of steatosis. For (B) to (F), all data are plotted as mean and all error bars represent the SEM. For (C) and (E), statistical analysis is based on the area under the curve (AUC) for each experimental group. *$P \leq 0.05$; **$P \leq 0.01$ by Welch's t test in (D) and (F) and Mann-Whitney U test in (C) and (E). All scale bars, 50 µm.

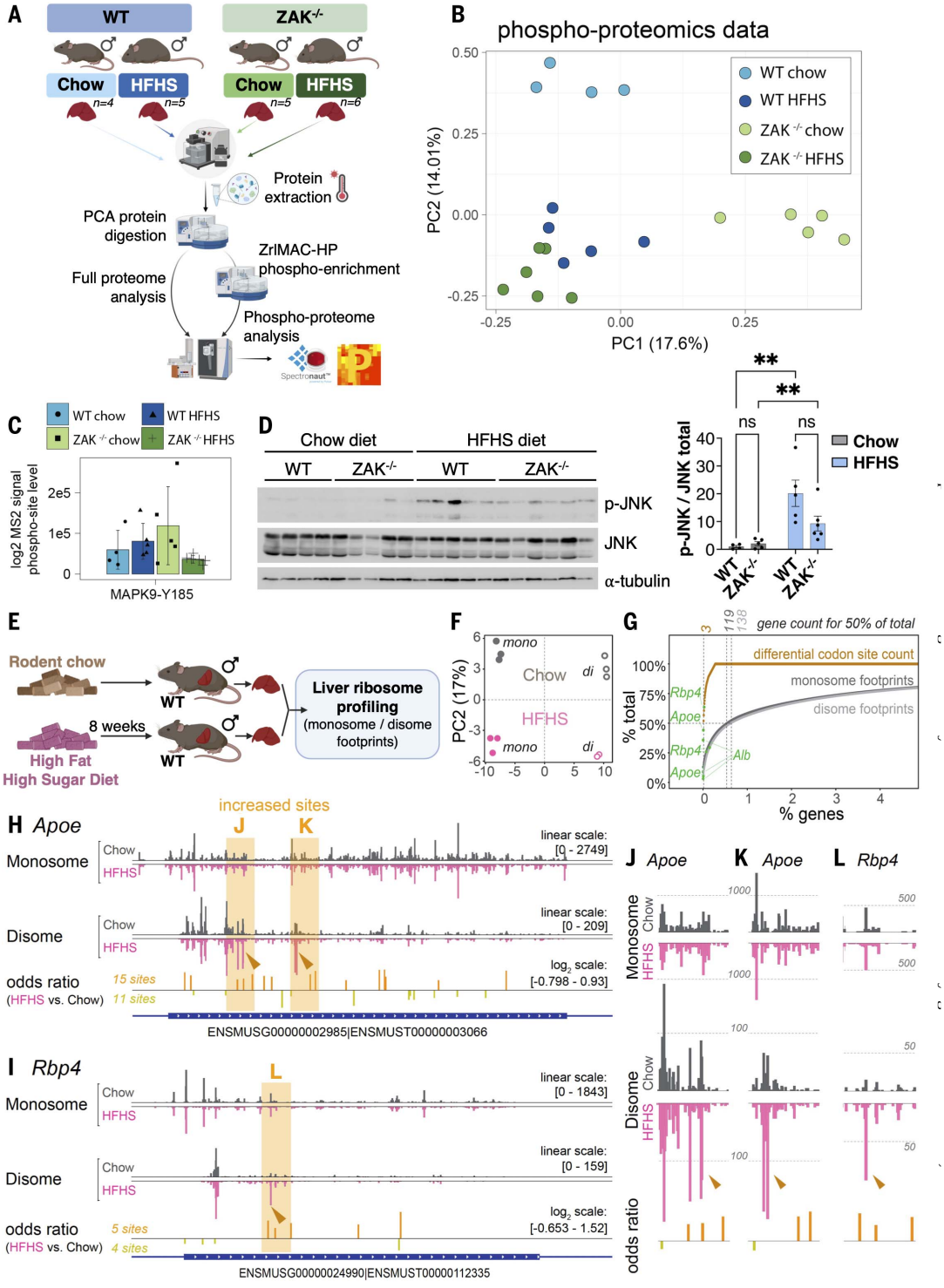

Fig. 5. Ribosome profiling of monosome and disome footprints reveals discreet changes to the translation landscape upon HFHS feeding. (**A**) Experimental design and workflow for proteomic and phosphoproteomic profiling of mouse livers. Ten- to 12-week-old mice of the indicated genotypes were fed chow or HFHS for 5 weeks (n = 4 to 6). (**B**) PCA of the phosphoproteomic profiles of mouse livers from (A). (**C**) Barplots of intensities derived from MS2 data for activation-associated phosphorylation sites on MAPK9 (JNK2). Height of the bars represents the average of the measurements and error bars the SE. Missing values in the MS data are plotted as zero values. (**D**) Lysates of livers from (A) were analyzed by immunoblotting with the indicated antibodies (left) and p-JNK divided by total JNK signals was quantified (right). Data are plotted as mean, and all error bars represent the SEM. *$P \leq 0.05$; **$P \leq 0.01$ by two-way ANOVA with Tukey's post hoc test. (**E**) Schematic of in vivo monosome and disome profiling experiment. Twelve-week-old male WT mice were fed normal chow or a HFHS diet for 8 weeks (n = 3). (**F**) PCA on monosome (closed circles) and disome (open circles) footprint data from individual mice, using the top 500 expressed genes. (**G**) Contribution of the most prominent genes to cumulative total signal for monosome footprints (dark gray), disome footprints (light gray), and differential codon sites from fig. S8C (orange). The locations of *Alb*, *Apoe*, and *Rbp4* in the cumulative datasets are highlighted. (**H**) Position-specific A-site signal for monosome and disome footprints across the *Apoe* mRNA for chow-fed (gray) and HFHS-fed (pink) conditions. Below monosome and disome tracks, positions of differential codon sites are depicted, with height corresponding to odds ratio values, and the same color coding is used as in fig. S8C. (**I**) As in (H) but for *Rbp4*. (**J**) Magnification of the left highlighted region of *Apoe* from (H) with high disome signal specifically in HFHS, and neighboring differential codon sites, consistent with increased collisions in this area. (**K**) As in (J) but for the right highlighted region. (**L**) As in (J) and (K) but for the high-disome site from the *Rbp4* transcript in (I).

signaling in WT mice likely occurs in steatotic hepatocytes, in which we managed to detect weak p-JNK positivity by immunohistochemistry (IHC) (fig. S7D). We also conducted a mouse experiment in which we fed WT and ZAK$^{-/-}$ mice either chow or HFHS for 16 weeks. These mice were starved overnight before euthanasia (*53*) and their livers analyzed for p-JNK by Western blotting (fig. S7E). This approach also failed to highlight deregulation of HFHS-associated JNK activity, which may be explained by our small sample size (fig. S7F).

Liver ribosome profiling reveals effects on global translation and distinct stalling and collision sites on highly expressed transcripts upon HFHS treatment

Using ribosome profiling (ribo-seq), we next investigated to what extent the HFHS diet–induced

phenotype was accompanied by translational alterations in liver (Fig. 5E). We prepared riboseq libraries from two footprint species: standard ~30 nt monosome-protected footprints and ~60 nt disome footprints, which are indicative of ribosomal stacking and collisions (*54*–*56*). Abundant disome footprints can be observed in mouse liver and at specific positions even under physiological conditions (*54*), likely diagnostic of sites of temporary translation slowdown that will not elicit a collision response such as the RSR. In our analyses, we aimed at identifying exacerbated disome coverage or new sites dependent on HFHS. First, PCA on footprint signal from the top 500 expressed genes indicated separation by library type (monosome or disome) followed by diet (chow or HFHS) (Fig. 5F). Monosome footprint analyses suggested that HFHS diet was not associated with strong systematic, transcriptome-wide effects on elongation kinetics, as indicated by footprint alignment to the 5′ and 3′ ends of coding sequences (fig. S8A) and an analysis of codon dwell times (*57*) (fig. S8B). Next, we extended our analyses to specific sites on the translatome. We calculated position-specific ribosome occupancies transcriptome-wide using a recently reported pause score metric (*58*, *59*), yielding 150 sites with increased and 160 sites with decreased relative ribosome occupancy in HFHS- versus chow-fed animals (fig. S8C, left panel). Many of these sites corresponded to positions on the translatome with high ribosomal occupancy (fig. S8C, right panel), so we explored the possibility that translational alterations affecting a relatively small number of sites on transcripts with very high translational volume could be associated with HFHS treatment. Thus, we quantified how individual high-expression genes contributed to overall translational activity in liver, which revealed a strong bias toward a few dominating transcripts, in particular mRNAs that encode bloodstream-secreted proteins such as albumin (*Alb*, 8.9% of all hepatic translation), apolipoprotein E (*Apoe*, 4.2%), and other mRNAs (Fig. 5G, dark gray curve; 119 genes make up 50% of all hepatic translation). A globally similar distribution was found for disome footprints (Fig. 5G, light gray curve). The group of differential codon sites showed an even stronger bias toward highly dominant transcripts, with three mRNAs, *Alb*, *Apoe*, and *Tfr*, accounting for half of the detected sites (Fig. 5G, orange curve, and table S3). To follow up on this observation, we inspected monosome and disome coverage and differential codon sites across the top-ranked transcripts. These analyses established that overall footprint distributions were highly similar and reproducible between HFHS- and chow-fed animals, as exemplified by the monosome and disome coverage patterns on *Alb* mRNA (fig. S8D). However, for some highly abundant mRNAs, such as *Apoe* (Fig. 5H) and retinol-binding protein 4 *(Rbp4*; Fig. 5I), we identified strongly enriched disome sites specifically in HFHS livers (Fig. 5, H and I, orange shading and arrows). Closer inspection of these transcript regions (Fig. 5, J to L) revealed that these disome positions were just upstream, in close proximity to increased differential sites from the monosome footprint odds ratio analysis, a constellation compatible with increased collisions at these sites.

ZAK$^{-/-}$ *mice are protected against metabolic decline in aging*

Male mice develop insulin resistance during aging (*60*), which at a very old age can be compensated for by pancreatic islet hypertrophy (*61*). Given the marked protection of ZAK$^{-/-}$ mice against metabolic dysfunction in obesity, we allowed chow-fed mice of both sexes to reach between 14 and 16 months of age before subjecting them to ipGTT (Fig. 6A). At this age, and similar to young mice, WT males were slightly heavier than their *Zak*-deleted counterparts (fig. S8E), whereas the weight of female mice was independent of genotype (fig. S8F). Aged male WT mice presented with a strongly impaired blood glucose control in ipGTT assay, as expected (Fig. 6B, top), whereas the performance of aged ZAK$^{-/-}$ male mice was undistinguishable from young male mice in this assay (Fig. 4C, top, and Fig. 6B, top). As previously reported (*60*), female mice did not present with pronounced aging-induced metabolic decline (Fig. 6B, bottom). The protection against aging-associated decline in glycemic control in ZAK$^{-/-}$ male mice was further underscored by reduced fasting blood glucose and insulin as well as lower HOMA-IR values (Fig. 6, C to E). Similar to early (8 weeks) HFHS-induced obesity (Fig. 4, C to E), these changes in males occurred in the absence of a measurable difference in whole-body insulin sensitivity assessed by an insulin tolerance test (fig. S8G). Inspection of the livers from these mice revealed different degrees of hepatic steatosis in three of seven WT mice, whereas only one of six ZAK$^{-/-}$ mice displayed the mildest degree of this hallmark of metabolic disease (Fig. 6, F and G), thus mirroring the genotype-specific characteristics of diet-induced obesity reported in Fig. 4.

These results suggest an overlap in the underlying metabolic stress signals in obesity and aging, albeit with a different magnitude and duration. To compare the extent of the oxidative burden of livers in the two conditions, we performed IHC to evaluate the content of 4-HNE in livers from young versus old and chow-fed versus HFHS-fed WT mice. 4-HNE is a commonly used marker of lipid peroxidation that has prognostic value in the diagnosis of NASH and other diseases associated with oxidative stress (*62*). Although IHC analysis of 4-HNE in young, chow-fed livers resulted only in homogeneous background staining (fig. S9A), the same analysis of HFHS-fed mice from Fig. 4A revealed a markedly increased overall staining, as well as the typical enrichment in steatotic areas around portal veins (*63*) (fig. S9B). These patterns were not observed in livers from aged mice (fig. S9C). This analysis indicates that oxidative stress load is increased in aged mouse livers but to a lesser extent than in HFHS-fed mice.

Deterioration of brown adipose tissue structure and function is attenuated in ZAK$^{-/-}$ *mice*

Adipose tissues undergo aging-induced deterioration in male mice as well as humans (*64*), including "whitening" of brown adipose tissue (BAT) (*65*). Compared with BAT sections from aged WT mice, the staining intensity of aged ZAK$^{-/-}$ mice more closely resembled that of BAT from young mice (fig. S10A, top and middle panels, and fig. S11A). These differences were also evident at the microscopic level, where the transition of multilocular BAT to a more unilocular WAT-like tissue was much more evident in old versus young WT samples compared with those from ZAK$^{-/-}$ mice (Fig. 6, H and I). Although the effects were in general smaller, we observed a similar protection against BAT whitening when reexamining our 25-week HFHS cohort (Fig. 4A; fig. S10, bottom panel; and fig. S11, A and B). These structural differences prompted us to evaluate functional BAT thermogenesis by infrared imaging of interscapular BAT on shaved mice. Although HFHS feeding was associated with the expected reduction of BAT temperature and thus thermogenesis in WT mice, ZAK$^{-/-}$ mice maintained a high temperature in this tissue (fig. S11, C and D).

Discussion

Here, we show that ROS potently interfere with ribosomal function in vitro, in human cell lines, and in mice. These aberrations activate the RSR pathway, culminating in oxidative stress-induced activation of the p38 and JNK kinases. This response has clear relevance for both pathological organismal responses to oxidative stress (zebrafish experiments) and physiological adaptations to increased ROS production. In mice, ROS-induced RSR signaling underlies at least some of the metabolic adaptations to high-fat diet–induced obesity and aging, such as the loss of glycemic control and development of hepatic steatosis. This is underscored by the protection of ZAK$^{-/-}$ mice against metabolic dysfunction when fed an HFHS diet, as well as the healthy metabolic aging observed in aged ZAK$^{-/-}$ male mice (Fig. 6J). The above insights highlight ribosomal impairment as an important metabolic stress signal used for the regulation of metabolism at an organismal level. Ribosomes are perfectly placed to perform the role of scaffolds

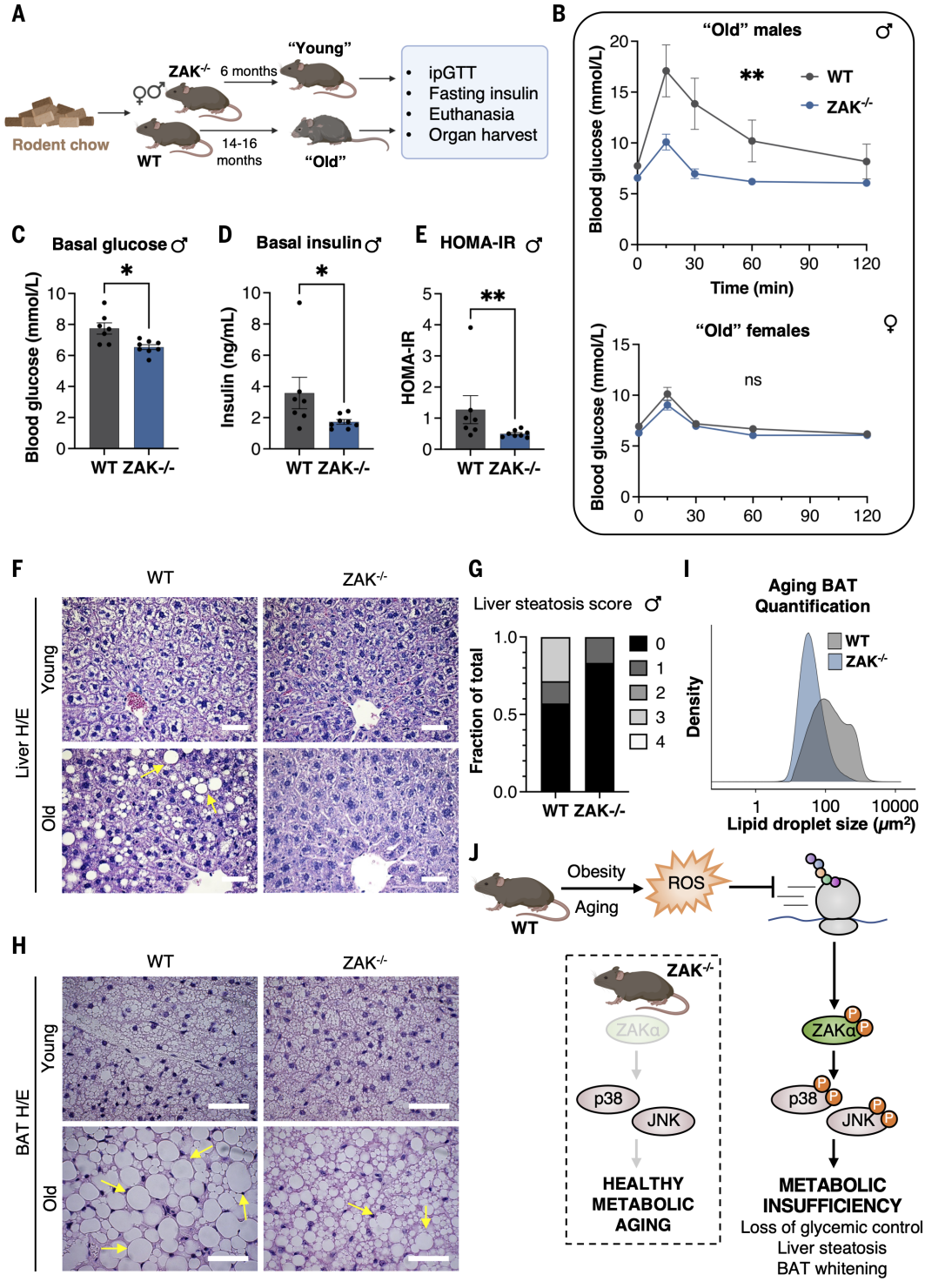

Fig. 6. Healthy metabolic aging in male ZAK$^{-/-}$ mice. (**A**) Schematic of mouse aging experiment. WT (male, n = 7; female, n = 16) and ZAK$^{-/-}$ (male, n = 7; female, n = 12) mice were maintained on a normal chow diet until 14 to 16 months of age ("old group"). Mice were subjected to ipGTT and euthanized 2 weeks later for collection of tissues. Tissues from 6-month-old WT and ZAK$^{-/-}$ male mice ("young group") were used for comparison. (**B**) Blood glucose concentrations of "old" male (top) and female (bottom) mice from (A) subjected to ipGTT assay. Statistical analysis is based on the AUC for each experimental group. (**C** to **E**) Basal glucose levels (C), basal insulin levels (D), and HOMA-IR (E) of fasted "old" male mice from (A). (**F**) Images of representative H&E-stained liver section from male mice in (A). Arrows indicate areas of steatosis. (**G**) Scoring of liver steatosis grade (scale, 0 to 4) of male mice from (A). (**H**) Images of representative H&E-stained sections of BAT from male mice in (A). Arrows indicate areas of notable lipid droplet condensation and BAT whitening. (**I**) Whole-mount BAT scans from (fig. S10A) were segmented according to lipid droplets. Individual droplet sizes for all aged WT and ZAK$^{-/-}$ samples were computed and represented in the form of histograms (n = 6). (**J**) Model of metabolic regulation by the RSR in obesity and aging in male mice. ROS produced as a result of HFHS feeding or during the course of aging impair ribosomal translation and activate the RSR sensor ZAKα. Downstream MAP kinase (p38 and JNK) signaling mediates features of metabolic decline such as glucose intolerance, liver steatosis, and BAT whitening. For (B) to (E), all data are plotted as mean and all error bars represent the SEM. *$P \leq 0.05$; **$P \leq 0.01$ by Welch's t test in (C) and by Mann-Whitney U test in (B), (D), and (E). All scale bars, 50 μm.

for mild stress signals in a broad context. Because they are present in high amounts in every cell and are constantly performing their function, compromised processivity of just a few ribosomes can provide for a highly sensitive and rapid readout of cellular perturbations (*39*). Previous work has highlighted oxidative damage to mRNA as a source of translational impairment (*39*), but our in vitro translation experiments highlight soluble cytoplasmic factors as the more sensitive components. These may include tRNAs and initiation and elongation factors. Although we did not obtain evidence of oxidative damage to the latter, we corroborated recently published evidence of ROS-induced tRNA cleavage and fragmentation (*43*). In addition to representing a depletion of key translation components, these fragments, likely generated by the RNase angiogenin, are generally considered to be inhibitory to ribosomal function (*41*, *42*).

JNK signaling promotes both insulin resistance and liver steatosis in obese mice (*14*). Specifically, mice conditionally deleted for JNK1 and JNK2 in the liver are protected against these outcomes when fed a high-fat diet (*19*). Among the relevant JNK targets is RXRα, the phosphorylation of which inhibits the PPARα complex and transcriptional activation of the *Fgf21* gene (*51*). FGF21 is a metabolic stress-induced hormone that has beneficial effects on both insulin sensitivity and liver adiposity (*66*), and these effects are exacerbated in *jnk*-deleted mice (*51*). Conversely, mice defective for p38 activation in the myeloid compartment are defective for hepatic FGF21 production and sensitized to metabolic dysfunction when fed a high-fat diet (*67*). A picture is emerging in which p38 and JNK signaling may compete for opposing outcomes depending on the tissue, cell type, and metabolic context. These intricacies likely allow for a fine-tuned mode of metabolic regulation that collectively manifests in an extremely well-buffered system. Unexpectedly, $ZAK^{-/-}$ mice, were protected against key aspects of metabolic dysfunction in the apparent absence of increased insulin sensitivity at intermediate time points (8 to 10 weeks). Alternative explanations may include stimulation of insulin-independent glucose uptake mechanisms and/or altered utilization of energy sources.

MAP3K ASK1 is a major ROS-induced activator of p38 and JNK in cell lines and mouse models (*44*) and has also been linked to metabolic regulation (*68*–*70*). Other ROS-activated MAP3Ks that have been implicated in metabolic control are MLK2/3 and MAP3K4 (*71*, *72*). In this work, we describe a clear protection of ZAK KO mice against HFHS-induced glucose intolerance and liver steatosis, and at least some of these phenotypes were related to ROS-mediated activation of ZAKα and the RSR. In one plausible model for the interplay of ZAKα and ASK1 in ROS-induced activation of p38 and JNK, ASK1 is the more relevant kinase upon sudden bursts of pathological levels of ROS, whereas ZAKα, through its ability to sense translational impairment, is more sensitive to the effects of slight elevations in intracellular ROS. Furthermore, the division of labor between these two kinases (as well as MLK2/3, MAP3K4, and potentially others) is likely tissue specific, because ZAKα levels in particular are highly variable among organs. It should be noted that the experimental systems used here differ widely in the source, duration, and magnitude of ROS exposure. In aggregate, we found that the role of ZAKα as the primary inducer of p38 and JNK activation and organismal protection was most evident in our experiments featuring excessive ROS levels in cell lines and zebrafish. In settings of prolonged exposure to lower levels of ROS (mouse obesity and aging), alternative mechanisms, as alluded to above, may play equally important roles. Additional work will be required to map the full inventory of ROS-activated MAP3 kinases and their relevance for ROS-driven physiological and pathological responses.

Next to glucose intolerance and stochastic liver steatosis, $ZAK^{-/-}$ male mice are also, at least partially, protected against BAT whitening and disruption of BAT integrity upon obesity and aging. These findings suggest that metabolic control exerted by the RSR pathway is not restricted to the liver, and that several tissues may contribute to the overall metabolic phenotypes of $ZAK^{-/-}$ mice. Indeed, a recent report described an independent role for the *Zak* gene in promoting stem cell plasticity in the small intestine of leucine-restricted mice (*73*). Further adding to the complexity of our current mouse model, the ZAKβ isoform is activated by volumetric cell compression and protects against muscle pathology in mice and humans (*49*, *74*), and this splice variant is also interrupted in the whole-body ZAK KO animals. For the present study, generation of mouse models for conditional KO of the *Zakα* isoform was not achieved. Future efforts in this direction will be crucial for uncovering the tissue-specific contributions of the RSR to the metabolic phenotypes that we describe. We also did not manage to detect *Zak*-dependent activation of p38 and JNK kinase isoforms in liver, adipose tissues, and other metabolically relevant organs. We suspect that the underlying technical explanation is a prolonged but weak overactivation of these stress kinases during HFHS feeding, which is difficult to detect with conventional methods because of high mouse-to-mouse variation. Although p38 and JNK are well-established effectors in the RSR, the lack of a direct signaling link from ZAKα to these kinases in vivo limits our conclusions regarding the mechanisms underlying metabolic protection of ZAK KO mice. Finally, we do not know to what extent our findings in mice can be extrapolated to humans. Patients with nonsense mutations in the common kinase domain of ZAKα and ZAKβ present with severe early-onset myopathy but with no reports of phenotypes of a metabolic nature (*74*). However, the feeding paradigm for mice used in this study is generally considered a good model of human obesity and associated metabolic complications. In humans, *Zakα* mRNA is robustly identified in all major metabolic tissues (see https://gtexportal.org/), so we consider it likely that the RSR also mediates metabolic adaptation in our own species.

In summary, our work uncovers a role of the ribosome as a signaling platform for metabolic regulation and highlights the RSR pathway as an important inducer of metabolic changes associated with obesity and aging. These findings may present opportunities for the development of therapeutic strategies to combat metabolic diseases.

Materials and methods summary

Polysome profiling

After cells were exposed to various treatments, cytosolic lysates were prepared using 20 mM HEPES, pH 7.5, 100 mM NaCl, 5 mM $MgCl_2$, 100 μg/ml digitonin, 100 μg/ml cycloheximide, 1× protease inhibitor cocktail (Sigma, catalog #P8340), and 200 U NxGen RNase inhibitor (Lucigen, catalog #30281). Extracts were incubated on ice for 5 min before centrifugation at 17,000*g* for 5 min at 4°C. After adding calcium chloride to a final concentration of 1 mM, lysates were optionally digested with 500 U MNase (New England Biolabs, catalog #M0247) for 30 min at 22°C. Digestion was terminated by adding 2 mM EGTA. Equivalent amounts of lysate (250 mg of undigested RNA or 350 to 400 mg of MNase-digested RNA) were resolved on 15 to 50% sucrose gradients. Gradients were centrifuged at 38,000 rpm in a Sorvall TH64.1 rotor for 2 hours at 4°C. The gradients were passed through an ISCO density gradient fractionation system with continuous monitoring of the absorbance at 254 nm.

Reconstituted in vitro translation

Translation reactions were reconstituted by mixing one part isolated ribosomes, five parts cytoplasmic lysates, one part in vitro transcribed luciferase mRNA (final concentration 1 to 10 ng/μl), and three parts translation buffer [final concentrations of 1.6 mM HEPES, 10 mM creatine phosphate (Sigma Aldrich, catalog #27920), 50 ng/μl creatine kinase (Sigma Aldrich, catalog #10127566001), 10 μM spermidine (Sigma Aldrich, catalog # S0266), 10 μM amino acids (Promega, catalog # L4461), 65 mM KAc, 0.75 mM $MgAc_2$, and murine RNase inhibitor]. Luciferase mRNA with an EMCV IRES was transcribed from a plasmid using HiScribe T7 ARCA mRNA Kit with tailing (New England Biolabs, catalog #E2060) according to manufacturer's specifications. Translation reactions were incubated at 37°C for 30 min, and translational output was measured as luciferase activity detected with Dual-Glo Luciferase Assay System (Promega, catalog #E2940) according to the manufacturer's specifications. For H_2O_2 treatment, fractions were treated with 5 mM H_2O_2 (Sigma-Aldrich, catalog #H1009) for 10 min at 25°C, followed by treatment with either 1 μg/μl catalase (Sigma-Aldrich, C1345-1G) or vehicle (1 mM potassium phosphate). For UV irradiation, fractions were irradiated with 500 J/m^2 UVB and immediately added to the in vitro translation reaction.

Menadione treatment of zebrafish larvae

Freshly collected zebrafish eggs were incubated in E3 medium (5 mM NaCl, 0.17 mM KCl, 0.33 mM $CaCl_2$, 0.33 mM $MgSO_4$, and 0.00001%

methylene blue). Unfertilized and dead eggs were removed, and embryos around the early gastrula stage, ~6 hours postfertilization, were randomly distributed into 12-well plates with 10 embryos per well. Menadione powder was dissolved as a 25 mM stock solution in E3 medium and diluted to a working concentration of 9 μM in E3 with or without 60 μM NAC. This medium was refreshed daily, and dead eggs were removed. To enforce full hatching of all genotypes, 1 day postfertilization (dpf) eggs were incubated overnight with 6 μg/ml Pronase (Sigma-Aldrich, catalog #10165921001). Embryos were scored as dead in the absence of a beating heart. Darkened yolk, cardiac edema, or shortened tails were scored as teratogenic (developmental) effects. All larvae were euthanized at maximally 5 dpf.

Mouse experiments

ZAK KO mice were on a mixed C57BL/6NJ background. Experimental cohorts of WT and ZAK KO mice were obtained by in-house breeding of heterozygotes. For feeding experiments, young male littermate mice with an age span of 10 to 15 weeks of age were used. Body weight and food intake were measured weekly. Fresh HFHS food pellets were provided to the mice once per week. For NAC supplementation, the compound was added directly to the drinking water at 10 g per liter, and the solution was refreshed three times per week. Body composition was determined by quantitative MR using the 4in1 Body Composition Analyzer (EchoMRI). In the aging cohort, male and female mice were group caged according to their sex with ad libitum access to chow diet and water, subjected to ipGTT analysis at 13 to 15 months of age, and euthanized and dissected 1 month later.

Ribosome profiling (monosome and disome) of mouse livers

Livers were harvested and flash-frozen in liquid nitrogen. Starting with 200-mg liver pieces from individual animals, lysates and ribosome footprints were generated by RNase I digestion and purified. Briefly, 5 μg of RNase I-digested RNA was separated on 15% urea-polyacrylamide gels to excise monosome (~30 nt) and disome (~60 nt) footprints. From the gel slices, RNA was extracted overnight at 4°C on a rotating wheel before precipitation in isopropanol for 3 hours at −20°C. RNA 3′-end repair was performed with 2 U/μl of T4 PNK (Lucigen) before a 2 hours of adapter ligation at 25°C using T4 RNA Ligase 1 (NEB) and T4 RNA Ligase 2 Deletion Mutant (Lucigen) and 1 μl of a 20 μM 5′-adenylated DNA adapter. Adapter removal was performed by treating individual libraries with 5′deadenylase (NEB) and RecJf exonuclease (NEB) for 1 hour at 30°C and 1 hour at 37°C. Using Zymo Clean & Concentrator columns, samples were purified and pooled. Ribosomal RNA was depleted according to siTools Biotech rRNA depletion kit specifications with a custom-made riboPOOL. The clean-up step was performed using Zymo Clean & Concentrator columns. Further library preparation steps were performed as described. The amplification of libraries was performed using i5 and i7 [NexteraD502 or NexteraD503 (monosomes) and NexteraD504 or NexteraD505 (disomes)] primers. Libraries were sequenced on a NovaSeq6000 (Illumina).

REFERENCES AND NOTES

1. B. H. Goodpaster, L. M. Sparks, Metabolic flexibility in health and disease. *Cell Metab.* **25**, 1027–1036 (2017). doi: 10.1016/j.cmet.2017.04.015; pmid: 28467922
2. R. L. Smith, M. R. Soeters, R. C. I. Wüst, R. H. Houtkooper, Metabolic flexibility as an adaptation to energy resources and requirements in health and disease. *Endocr. Rev.* **39**, 489–517 (2018). doi: 10.1210/er.2017-00211; pmid: 29697773
3. B. A. Swinburn *et al.*, The global obesity pandemic: Shaped by global drivers and local environments. *Lancet* **378**, 804–814 (2011). doi: 10.1016/S0140-6736(11)60813-1; pmid: 21872749
4. T. D. Müller, M. Blüher, M. H. Tschöp, R. D. DiMarchi, Anti-obesity drug discovery: Advances and challenges. *Nat. Rev. Drug Discov.* **21**, 201–223 (2022). doi: 10.1038/s41573-021-00337-8; pmid: 34815532
5. M. Blüher, Obesity: Global epidemiology and pathogenesis. *Nat. Rev. Endocrinol.* **15**, 288–298 (2019). doi: 10.1038/s41574-019-0176-8; pmid: 30814686
6. M. W. Schwartz *et al.*, Obesity pathogenesis: An Endocrine Society scientific statement. *Endocr. Rev.* **38**, 267–296 (2017). doi: 10.1210/er.2017-00111; pmid: 28898979
7. A. K. Palmer, M. D. Jensen, Metabolic changes in aging humans: Current evidence and therapeutic strategies. *J. Clin. Invest.* **132**, e158451 (2022). doi: 10.1172/JCI158451; pmid: 35968789
8. T. Finkel, The metabolic regulation of aging. *Nat. Med.* **21**, 1416–1423 (2015). doi: 10.1038/nm.3998; pmid: 26646498
9. S. Furukawa *et al.*, Increased oxidative stress in obesity and its impact on metabolic syndrome. *J. Clin. Invest.* **114**, 1752–1761 (2004). doi: 10.1172/JCI21625; pmid: 15599400
10. H. J. Shields, A. Traa, J. M. Van Raamsdonk, Beneficial and detrimental effects of reactive oxygen species on lifespan: A comprehensive review of comparative and experimental studies. *Front. Cell Dev. Biol.* **9**, 628157 (2021). doi: 10.3389/fcell.2021.628157; pmid: 33644065
11. M. Schieber, N. S. Chandel, ROS function in redox signaling and oxidative stress. *Curr. Biol.* **24**, R453–R462 (2014). doi: 10.1016/j.cub.2014.03.034; pmid: 24845678
12. E. F. Wagner, A. R. Nebreda, Signal integration by JNK and p38 MAPK pathways in cancer development. *Nat. Rev. Cancer* **9**, 537–549 (2009). doi: 10.1038/nrc2694; pmid: 19629069
13. B. Canovas, A. R. Nebreda, Diversity and versatility of p38 kinase signalling in health and disease. *Nat. Rev. Mol. Cell Biol.* **22**, 346–366 (2021). doi: 10.1038/s41580-020-00322-w; pmid: 33504982
14. I. Nikolic, M. Leiva, G. Sabio, The role of stress kinases in metabolic disease. *Nat. Rev. Endocrinol.* **16**, 697–716 (2020). doi: 10.1038/s41574-020-00418-5; pmid: 33067545
15. G. Sumara *et al.*, Regulation of PKD by the MAPK p38delta in insulin secretion and glucose homeostasis. *Cell* **136**, 235–248 (2009). doi: 10.1016/j.cell.2008.11.018; pmid: 19135240
16. M. Leiva, N. Matesanz, M. Pulgarín-Alfaro, I. Nikolic, G. Sabio, Uncovering the Role of p38 Family Members in Adipose Tissue Physiology. *Front. Endocrinol. (Lausanne)* **11**, 572089 (2020). doi: 10.3389/fendo.2020.572089; pmid: 33424765
17. B. Cicuéndez, I. Ruiz-Garrido, A. Mora, G. Sabio, Stress kinases in the development of liver steatosis and hepatocellular carcinoma. *Mol. Metab.* **50**, 101190 (2021). doi: 10.1016/j.molmet.2021.101190; pmid: 33588102
18. G. Sabio *et al.*, A stress signaling pathway in adipose tissue regulates hepatic insulin resistance. *Science* **322**, 1539–1543 (2008). doi: 10.1126/science.1160794; pmid: 19056984
19. G. Tuncman *et al.*, Functional in vivo interactions between JNK1 and JNK2 isoforms in obesity and insulin resistance. *Proc. Natl. Acad. Sci. U.S.A.* **103**, 10741–10746 (2006). doi: 10.1073/pnas.0603509103; pmid: 16818881
20. A. C. Vind, A. V. Genzor, S. Bekker-Jensen, Ribosomal stress-surveillance: Three pathways is a magic number. *Nucleic Acids Res.* **48**, 10648–10661 (2020). doi: 10.1093/nar/gkaa757; pmid: 32941609
21. A. C. Vind *et al.*, ZAKα Recognizes Stalled Ribosomes through Partially Redundant Sensor Domains. *Mol. Cell* **78**, 700–713.e7 (2020). doi: 10.1016/j.molcel.2020.03.021; pmid: 32289254
22. C. C. Wu, A. Peterson, B. Zinshteyn, S. Regot, R. Green, Ribosome Collisions Trigger General Stress Responses to Regulate Cell Fate. *Cell* **182**, 404–416.e14 (2020). doi: 10.1016/j.cell.2020.06.006; pmid: 32610081
23. G. Snieckute *et al.*, Ribosome stalling is a signal for metabolic regulation by the ribotoxic stress response. *Cell Metab.* **34**, 2036–2046.e8 (2022). doi: 10.1016/j.cmet.2022.10.011; pmid: 36384144
24. M. S. Iordanov *et al.*, Ribotoxic stress response: Activation of the stress-activated protein kinase JNK1 by inhibitors of the peptidyl transferase reaction and by sequence-specific RNA damage to the alpha-sarcin/ricin loop in the 28S rRNA. *Mol. Cell. Biol.* **17**, 3373–3381 (1997). doi: 10.1128/MCB.17.6.3373; pmid: 9154836
25. D. Y. Ouyang, Y. Y. Wang, Y. T. Zheng, Activation of c-Jun N-terminal kinases by ribotoxic stresses. *Cell. Mol. Immunol.* **2**, 419–425 (2005). pmid: 16426491
26. X. Wang *et al.*, Complete inhibition of anisomycin and UV radiation but not cytokine induced JNK and p38 activation by an aryl-substituted dihydropyrrolopyrazole quinoline and mixed lineage kinase 7 small interfering RNA. *J. Biol. Chem.* **280**, 19298–19305 (2005). doi: 10.1074/jbc.M413059200; pmid: 15737997
27. K. S. Robinson *et al.*, ZAKα-driven ribotoxic stress response activates the human NLRP1 inflammasome. *Science* **377**, 328–335 (2022). doi: 10.1126/science.abl6324; pmid: 35857590
28. D. Shenton *et al.*, Global translational responses to oxidative stress impact upon multiple levels of protein synthesis. *J. Biol. Chem.* **281**, 29011–29021 (2006). doi: 10.1074/jbc.M601545200; pmid: 16849329
29. J. A. McCubrey, M. M. Lahair, R. A. Franklin, Reactive oxygen species-induced activation of the MAP kinase signaling pathways. *Antioxid. Redox Signal.* **8**, 1775–1789 (2006). doi: 10.1089/ars.2006.8.1775; pmid: 16987031
30. M. Stoneley *et al.*, Unresolved stalled ribosome complexes restrict cell-cycle progression after genotoxic stress. *Mol. Cell* **82**, 1557–1572.e7 (2022). doi: 10.1016/j.molcel.2022.01.019; pmid: 35180429
31. A. M. Darnell, A. R. Subramaniam, E. K. O'Shea, Translational control through differential ribosome pausing during amino acid limitation in mammalian cells. *Mol. Cell* **71**, 229–243.e11 (2018). doi: 10.1016/j.molcel.2018.06.041; pmid: 30029003
32. N. T. Ingolia, L. F. Lareau, J. S. Weissman, Ribosome profiling of mouse embryonic stem cells reveals the complexity and dynamics of mammalian proteomes. *Cell* **147**, 789–802 (2011). doi: 10.1016/j.cell.2011.10.002; pmid: 22056041
33. S. Juszkiewicz *et al.*, Ribosome collisions trigger cis-acting feedback inhibition of translation initiation. *eLife* **9**, e60038 (2020). doi: 10.7554/eLife.60038; pmid: 32657267
34. N. K. Sinha *et al.*, EDF1 coordinates cellular responses to ribosome collisions. *eLife* **9**, e58828 (2020). doi: 10.7554/eLife.58828; pmid: 32744497
35. S. Juszkiewicz, R. S. Hegde, Initiation of quality control during poly(A) translation requires site-specific ribosome ubiquitination. *Mol. Cell* **65**, 743–750.e4 (2017). doi: 10.1016/j.molcel.2016.11.039; pmid: 28065601
36. E. Sundaramoorthy *et al.*, ZNF598 and RACK1 regulate mammalian ribosome-associated quality control function by mediating regulatory 40S ribosomal ubiquitylation. *Mol. Cell* **65**, 751–760.e4 (2017). doi: 10.1016/j.molcel.2016.12.026; pmid: 28132843
37. A. Garzia, C. Meyer, T. Tuschl, The E3 ubiquitin ligase RNF10 modifies 40S ribosomal subunits of ribosomes compromised in translation. *Cell Rep.* **36**, 109468 (2021). doi: 10.1016/j.celrep.2021.109468; pmid: 34348161
38. D. M. Garshott *et al.*, iRQC, a surveillance pathway for 40S ribosomal quality control during mRNA translation initiation. *Cell Rep.* **36**, 109642 (2021). doi: 10.1016/j.celrep.2021.109642; pmid: 34469731
39. K. Q. Kim, H. S. Zaher, Canary in a coal mine: Collided ribosomes as sensors of cellular conditions. *Trends Biochem. Sci.* **47**, 82–97 (2022). doi: 10.1016/j.tibs.2021.09.001; pmid: 34607755
40. J. R. Burgoyne, P. Eaton, Contemporary techniques for detecting and identifying proteins susceptible to reversible thiol oxidation. *Biochem. Soc. Trans.* **39**, 1260–1267 (2011). doi: 10.1042/BST0391260; pmid: 21936799
41. S. Yamasaki, P. Ivanov, G. F. Hu, P. Anderson, Angiogenin cleaves tRNA and promotes stress-induced translational repression. *J. Cell Biol.* **185**, 35–42 (2009). doi: 10.1083/jcb.200811106; pmid: 19332886

42. H. Fu *et al*., Stress induces tRNA cleavage by angiogenin in mammalian cells. *FEBS Lett.* **583**, 437–442 (2009). doi: 10.1016/j.febslet.2008.12.043; pmid: 19114040
43. Y. Akiyama *et al*., RTCB complex regulates stress-induced tRNA cleavage. *Int. J. Mol. Sci.* **23**, 13100 (2022). doi: 10.3390/ijms232113100; pmid: 36361884
44. S. Shiizaki, I. Naguro, H. Ichijo, Activation mechanisms of ASK1 in response to various stresses and its significance in intracellular signaling. *Adv. Biol. Regul.* **53**, 135–144 (2013). doi: 10.1016/j.jbior.2012.09.006; pmid: 23031789
45. E. E. Patton, L. I. Zon, D. M. Langenau, Zebrafish disease models in drug discovery: From preclinical modelling to clinical trials. *Nat. Rev. Drug Discov.* **20**, 611–628 (2021). doi: 10.1038/s41573-021-00210-8; pmid: 34117457
46. P. Giansanti *et al*., Mass spectrometry-based draft of the mouse proteome. *Nat. Methods* **19**, 803–811 (2022). doi: 10.1038/s41592-022-01526-y; pmid: 35710609
47. P. Ranea-Robles, J. Lund, C. Clemmensen, The physiology of experimental overfeeding in animals. *Mol. Metab.* **64**, 101573 (2022). doi: 10.1016/j.molmet.2022.101573; pmid: 35970448
48. N. Matsuzawa-Nagata *et al*., Increased oxidative stress precedes the onset of high-fat diet-induced insulin resistance and obesity. *Metabolism* **57**, 1071–1077 (2008). doi: 10.1016/j.metabol.2008.03.010; pmid: 18640384
49. C. Nordgaard *et al*., ZAKβ is activated by cellular compression and mediates contraction-induced MAP kinase signaling in skeletal muscle. *EMBO J.* **41**, e111650 (2022). doi: 10.15252/embj.2022111650; pmid: 35899396
50. M. T. F. Damgaard *et al*., Age-dependent alterations of glucose clearance and homeostasis are temporally separated and modulated by dietary fat. *J. Nutr. Biochem.* **54**, 66–76 (2018). doi: 10.1016/j.jnutbio.2017.09.026; pmid: 29268121
51. S. Vernia *et al*., Phosphorylation of RXRα mediates the effect of JNK to suppress hepatic FGF21 expression and promote metabolic syndrome. *Proc. Natl. Acad. Sci. U.S.A.* **119**, e2210434119 (2022). doi: 10.1073/pnas.2210434119; pmid: 36282921
52. J. F. Pei *et al*., Diurnal oscillations of endogenous H_2O_2 sustained by $p66^{Shc}$ regulate circadian clocks. *Nat. Cell Biol.* **21**, 1553–1564 (2019). doi: 10.1038/s41556-019-0420-4; pmid: 31768048
53. S. Vernia *et al*., The PPARα-FGF21 hormone axis contributes to metabolic regulation by the hepatic JNK signaling pathway. *Cell Metab.* **20**, 512–525 (2014). doi: 10.1016/j.cmet.2014.06.010; pmid: 25043817
54. A. B. Arpat *et al*., Transcriptome-wide sites of collided ribosomes reveal principles of translational pausing. *Genome Res.* **30**, 985–999 (2020). doi: 10.1101/gr.257741.119; pmid: 32703885
55. S. Meydan, N. R. Guydosh, Disome and Trisome Profiling Reveal Genome-wide Targets of Ribosome Quality Control. *Mol. Cell* **79**, 588–602.e6 (2020). doi: 10.1016/j.molcel.2020.06.010; pmid: 32615089
56. T. Zhao *et al*., Disome-seq reveals widespread ribosome collisions that promote cotranslational protein folding. *Genome Biol.* **22**, 16 (2021). doi: 10.1186/s13059-020-02256-0; pmid: 33402206
57. C. Gobet, F. Naef, Ribo-DT: An automated pipeline for inferring codon dwell times from ribosome profiling data. *Methods* **203**, 10–16 (2022). doi: 10.1016/j.ymeth.2021.10.004; pmid: 34673173
58. K. C. Stein, A. Kriel, J. Frydman, Nascent polypeptide domain topology and elongation rate direct the cotranslational hierarchy of Hsp70 and TRiC/CCT. *Mol. Cell* **75**, 1117–1130.e5 (2019). doi: 10.1016/j.molcel.2019.06.036; pmid: 31400849
59. K. C. Stein, F. Morales-Polanco, J. van der Lienden, T. K. Rainbolt, J. Frydman, Ageing exacerbates ribosome pausing to disrupt cotranslational proteostasis. *Nature* **601**, 637–642 (2022). doi: 10.1038/s41586-021-04295-4; pmid: 35046576
60. T. H. Reynolds *et al*., The impact of age and sex on body composition and glucose sensitivity in C57BL/6J mice. *Physiol. Rep.* **7**, e13995 (2019). doi: 10.14814/phy2.13995; pmid: 30706674
61. E. Tudurí *et al*., The effects of aging on male mouse pancreatic beta-cell function involve multiple events in the regulation of secretion: Influence of insulin sensitivity. *J. Gerontol. A Biol. Sci. Med. Sci.* **77**, 405–415 (2022). doi: 10.1093/gerona/glab276; pmid: 34562079
62. S. Dalleau, M. Baradat, F. Guéraud, L. Huc, Cell death and diseases related to oxidative stress: 4-hydroxynonenal (HNE) in the balance. *Cell Death Differ.* **20**, 1615–1630 (2013). doi: 10.1038/cdd.2013.138; pmid: 24096871
63. M. J. Ronis *et al*., Increased 4-hydroxynonenal protein adducts in male GSTA4-4/PPAR-α double knockout mice enhance injury during early stages of alcoholic liver disease. *Am. J. Physiol. Gastrointest. Liver Physiol.* **308**, G403–G415 (2015). doi: 10.1152/ajpgi.00154.2014; pmid: 25501545
64. M. Schosserer, J. Grillari, C. Wolfrum, M. Scheideler, Age-induced changes in white, brite, and brown adipose depots: A mini-review. *Gerontology* **64**, 229–236 (2018). doi: 10.1159/000485183; pmid: 29212073
65. L. F. Gonçalves *et al*., Ageing is associated with brown adipose tissue remodelling and loss of white fat browning in female C57BL/6 mice. *Int. J. Exp. Pathol.* **98**, 100–108 (2017). doi: 10.1111/iep.12228; pmid: 28543963
66. J. Silva *et al*., Ribosome impairment regulates intestinal stem cell identity via ZAKa activation. *Nat. Commun.* **13**, 4492 (2022). doi: 10.1038/s41467-022-32220-4; pmid: 35918345
67. N. Vasli *et al*., Recessive mutations in the kinase ZAK cause a congenital myopathy with fibre type disproportion. *Brain* **140**, 37–48 (2017). doi: 10.1093/brain/aww257; pmid: 27816943
68. S. Keipert, M. Ost, Stress-induced FGF21 and GDF15 in obesity and obesity resistance. *Trends Endocrinol. Metab.* **32**, 904–915 (2021). doi: 10.1016/j.tem.2021.08.008; pmid: 34526227
69. M. Crespo *et al*., Myeloid p38 activation maintains macrophage-liver crosstalk and BAT thermogenesis through IL-12-FGF21 axis. *Hepatology* **77**, 874–887 (2023). doi: 10.1002/hep.32581; pmid: 35592906
70. T. D. Challa *et al*., Liver ASK1 protects from non-alcoholic fatty liver disease and fibrosis. *EMBO Mol. Med.* **11**, e10124 (2019). doi: 10.15252/emmm.201810124; pmid: 31595673
71. F. C. Lucchini *et al*., ASK1 inhibits browning of white adipose tissue in obesity. *Nat. Commun.* **11**, 1642 (2020). doi: 10.1038/s41467-020-15483-7; pmid: 32242025
72. E. Yamamoto *et al*., Olmesartan prevents cardiovascular injury and hepatic steatosis in obesity and diabetes, accompanied by apoptosis signal regulating kinase-1 inhibition. *Hypertension* **52**, 573–580 (2008). doi: 10.1161/HYPERTENSIONAHA.108.112292; pmid: 18678790
73. S. M. Craige, M. M. Reif, S. Kant, Mixed - Lineage Protein kinases (MLKs) in inflammation, metabolism, and other disease states. *Biochim. Biophys. Acta* **1862**, 1581–1586 (2016). doi: 10.1016/j.bbadis.2016.05.022; pmid: 27259981
74. Z. He *et al*., Identification of MAP3K4 as a novel regulation factor of hepatic lipid metabolism in non-alcoholic fatty liver disease. *J. Transl. Med.* **20**, 529 (2022). doi: 10.1186/s12967-022-03734-8; pmid: 36376950
75. Y. Perez-Riverol *et al*., The PRIDE database resources in 2022: A hub for mass spectrometry-based proteomics evidences. *Nucleic Acids Res.* **50** (D1), D543–D552 (2022). doi: 10.1093/nar/gkab1038; pmid: 34723319
76. M. Leleu, R. Dreos, Monosome and disome profiling of livers from HFHS-fed mice, Zenodo (2023); https://doi.org/10.5281/zenodo.8309532.

ACKNOWLEDGMENTS

We thank P. Rengtved Lundegaard (University of Copenhagen, Denmark) for help with zebrafish work, X. Lu (Jinan University, China) for the kind gift of ZAK inhibitors, V. Li (Crick Institute, United Kingdom) for providing access to the ZAK KO mouse strain, and the Department of Experimental Medicine (University of Copenhagen, Denmark) for help with housing of mice and zebrafish. **Funding:** Work in S.B.-J.'s laboratory was supported by grants from the Novo Nordisk Foundation (grant NNF21OC0071475), the Nordea Foundation, and the European Research Council (ERC) under the European Union's Horizon 2020 research and innovation program (grant 863911, PHYRIST). Center for Gene Expression (CGEN) is a Center of Excellence funded by The National Danish Research Foundation (grant DNRF166). A.C.V. is supported by the BRIDGE – Translational Excellence Program funded by the Novo Nordisk Foundation (grant NNF20SA0064340). The Novo Nordisk Foundation Center for Basic Metabolic Research is an independent Research Center based at the University of Copenhagen, Denmark, and is partially funded by an unconditional donation from the Novo Nordisk Foundation (www.cbmr.ku.dk) (grant NNF18CC0034900). D.M.S. is supported by the Swiss National Science Foundation through the National Center of Competence in Research RNA & Disease (grant 141735 and individual grant 179190). A.E.W. and M.S. are supported by the Medical Research Council, UK through MRC program core funding (grant 5TR00). Work in B.A.H.J.'s laboratory was funded by the Novo Nordisk Foundation (grant NNF21OC0066931). Work in J.V.O.'s laboratory at The Novo Nordisk Foundation Center for Protein Research (CPR) is funded in part by a generous donation from the Novo Nordisk Foundation (grant NNF14CC0001). **Author contributions:** S.B.-J., G.S., L.R., and A.C.V. conceived the study. G.S., L.R., A.C.V., Z.W., F.S.A., M.S., S.C., A.M.V., M.L., R.D., A.R., D.M.G., A.V.G., B.S.-Y.C., A.L.B., F.S., M.D., L.C.M.D., M.B., and S.S.P. performed experiments and analyzed data. A.E.W., A.H.L., J.T.T., J.V.O., M.E.P., B.A.H.J., C.C., Z.G.-H., D.G., and S.B.-J. supervised experiments and provided data interpretation. S.B.-J. wrote the manuscript with input from D.G. **Competing interests:** The authors declare no competing interests. **Data and materials availability:** The mass spectrometry proteomics data have been deposited to the ProteomeXchange Consortium through the PRIDE (75) partner repository with the dataset identifier PXD043071. Sequencing data files have been deposited in NCBI Gene Expression Omnibus (GEO) with the accession code GSE235700. The scripts for data analysis have been deposited on Zenodo (76). All other data are available in the main text or the supplementary materials. Plasmids and cell lines generated in this study are available upon request and without the need for a material transfer agreement.

License information: Copyright © 2023 the authors, some rights reserved; exclusive licensee American Association for the Advancement of Science. No claim to original US government works. https://www.science.org/about/science-licenses-journal-article-reuse

SUPPLEMENTARY MATERIALS

science.org/doi/10.1126/science.adf3208
Materials and Methods
Figs. S1 to S11
References (*77*–*89*)
MDAR Reproducibility Checklist
Tables S1 to S3

Submitted 13 October 2022; resubmitted 4 July 2023
Accepted 3 November 2023
10.1126/science.adf3208

RESEARCH ARTICLE SUMMARY

IMMUNOLOGY

Spatial transcriptomics of B cell and T cell receptors reveals lymphocyte clonal dynamics

Camilla Engblom†, Kim Thrane†, Qirong Lin†, Alma Andersson, Hosein Toosi, Xinsong Chen, Embla Steiner, Chang Lu, Giulia Mantovani, Michael Hagemann-Jensen, Sami Saarenpää, Mattias Jangard, Julio Saez-Rodriguez, Jakob Michaëlsson, Johan Hartman, Jens Lagergren, Jeff E. Mold*‡, Joakim Lundeberg‡, Jonas Frisén‡

INTRODUCTION: B cells and T cells respond to infections and inflammation, regulate tissue homeostasis, and maintain immunological memory. The targeted reactivity of B and T cells is determined by their clonally heritable antigen receptors, encoded by immunoglobulin (IG) and T cell (TR) antigen receptor genes. Spatial analysis of lymphocyte clonality may link specific antigen receptors to their regulatory niche or antigen (tumor-associated, self, or foreign). This, in turn, may help identify and harness antigen-specific clones for therapy.

RATIONALE: Single-cell technologies permit the study of antigen receptors at a cellular level but lack spatial resolution. Current spatial transcriptomics methods locate gene expression in tissues, but do not retain full-length antigen receptor sequences. Thus, methodologies that comprehensively map B and T cell receptor sequences within tissues are needed. We therefore developed spatial transcriptomics for variable, diversity, and joining (VDJ) sequences (Spatial VDJ), which spatially resolves full-length IG and TR transcripts, tissue morphology, and the whole transcriptome simultaneously in human tissue.

RESULTS: We developed two versions of Spatial VDJ that are compatible with whole-transcriptome 3′ arrays for frozen human tissue sections: (i) long-read (LR) Spatial VDJ for full-length IG and TR antigen receptor transcripts and (ii) short-read (SR) Spatial VDJ for TR only. For both approaches, we enriched for antigen receptor transcripts using hybridization capture targeting the IG and TR constant regions.

Spatial VDJ captured thousands of B and T cell receptor sequences in human tonsil tissue sections. The antigen receptor distribution matched canonical B and T cell locations and spatial gene expression patterns. Amplified clonal sequences were also confirmed by orthogonal methods, and the LR and SR Spatial VDJ versions to capture TR clones yielded comparable results. We found spatial congruency between paired receptor chains and developed a computational framework that identified IG heavy and light chain receptor pairs validated by single-cell VDJ analysis in human breast cancer. Distinct IG receptors spatially segregated across different tumor-associated areas within the same tumor, opening up the possibility of using Spatial VDJ as a first screen for tumor-associated antibodies.

Spatial VDJ also uncovered B cell clonal family diversity measures within and between distinct B cell follicles (containing germinal centers), which are key sites for B cell clonal expansion and maturation. Spatial phylogenetic analysis of B cell clones identified simultaneous lineage tree branching and geographical spreading to distinct germinal centers.

CONCLUSION: This study describes a method that allows for full-length antigen receptor mapping within human tissue. Spatial VDJ reveals B and T cell clonal dynamics in both lymphoid and cancer tissue. This includes linking clones to tumor-associated gene expression programs and spatially reconstructing B cell clonal diversity and lineage trajectories across their anatomical niches. Ultimately, Spatial VDJ may be useful to discriminate B and T cell clonal dynamics in the context of infections, vaccination, and anticancer immune responses, with the goal of harnessing antigen-specific clones for engineered cell- and antibody-based therapeutics. ■

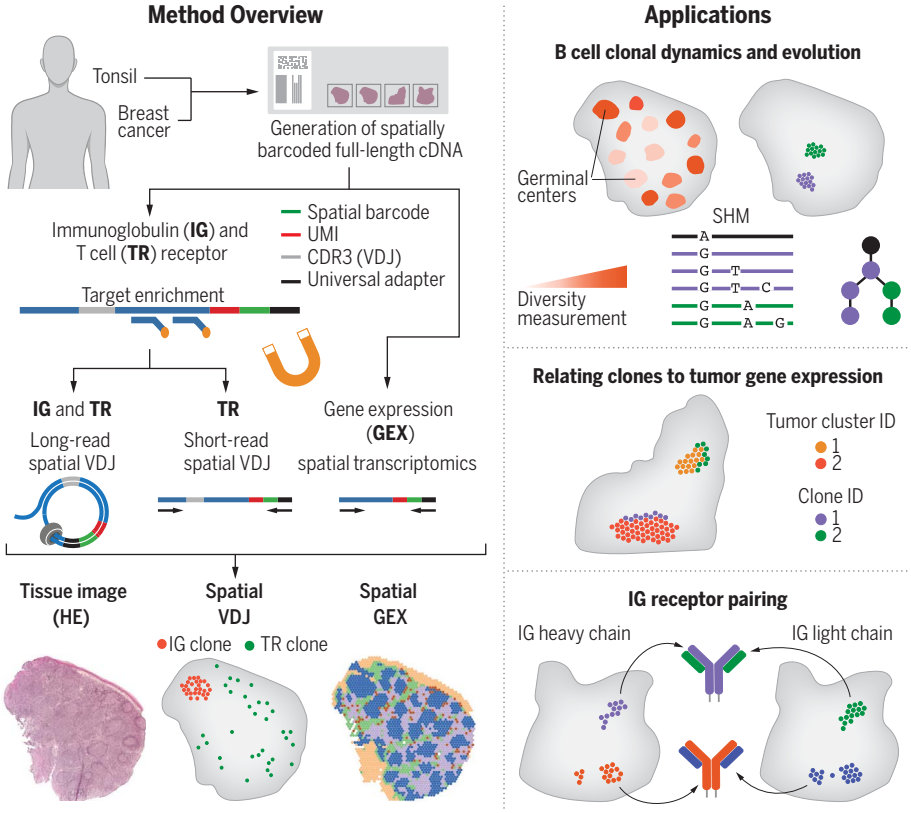

Spatial transcriptomics–based method to map B cell and T cell receptors. Targeted capture of antigen receptor sequences from spatial transcriptomics gene expression libraries resolves full-length receptor distribution alongside tissue anatomy and whole transcriptome in human tissue sections. Spatial VDJ uncovers B and T cell clonal dynamics, including linking clones to tumor-associated gene expression, pairing receptor chains, and reconstructing spatial B cell lineage trajectories.

The list of author affiliations is available in the full article online.
*Corresponding author. Email: jeff.mold@ki.se
†These authors contributed equally to this work.
‡These authors contributed equally to this work.
Cite this article as C. Engblom *et al.*, *Science* **382**, eadf8486 (2023). DOI: 10.1126/science.adf8486

READ THE FULL ARTICLE AT
https://doi.org/10.1126/science.adf8486

RESEARCH ARTICLE

IMMUNOLOGY

Spatial transcriptomics of B cell and T cell receptors reveals lymphocyte clonal dynamics

Camilla Engblom[1]†, Kim Thrane[2]†, Qirong Lin[1]†, Alma Andersson[2], Hosein Toosi[3], Xinsong Chen[4], Embla Steiner[1], Chang Lu[5], Giulia Mantovani[1], Michael Hagemann-Jensen[1], Sami Saarenpää[2], Mattias Jangard[6], Julio Saez-Rodriguez[5], Jakob Michaëlsson[7], Johan Hartman[4,8], Jens Lagergren[3], Jeff E. Mold[1]*‡, Joakim Lundeberg[2]‡, Jonas Frisén[1]‡

The spatial distribution of lymphocyte clones within tissues is critical to their development, selection, and expansion. We have developed spatial transcriptomics of variable, diversity, and joining (VDJ) sequences (Spatial VDJ), a method that maps B cell and T cell receptor sequences in human tissue sections. Spatial VDJ captures lymphocyte clones that match canonical B and T cell distributions and amplifies clonal sequences confirmed by orthogonal methods. We found spatial congruency between paired receptor chains, developed a computational framework to predict receptor pairs, and linked the expansion of distinct B cell clones to different tumor-associated gene expression programs. Spatial VDJ delineates B cell clonal diversity and lineage trajectories within their anatomical niche. Thus, Spatial VDJ captures lymphocyte spatial clonal architecture across tissues, providing a platform to harness clonal sequences for therapy.

B cells and T cells respond to infections and inflammation, regulate tissue homeostasis, and maintain immunological memory. The targeted reactivity of B and T cells is determined by their clonally heritable antigen receptors. Single-cell technologies permit the study of antigen receptors at a cellular level but lack spatial resolution. Current spatial transcriptomics (ST) methods do not retain full-length antigen receptor transcripts because library preparation steps fragment away the complementarity determining region 3 (CDR3) needed to define lymphocyte clonality (fig. S1A). Spatial analysis of lymphocyte clonality may link specific antigen receptors to tumor-associated, self, or foreign antigens, which may help identify and harness antigen-specific clones for therapy. Several techniques have been developed to spatially resolve antigen receptor sequences within human tissues. These include polymerase chain reaction (PCR)–based amplification of T cell receptors (TCRs) from either ST (*1*) or Slide-seq libraries (*2*), laser-guided microdissection coupled with sequencing (*3*, *4*), and capture through deep sequencing of rare longer immunoglobulin (IG) transcripts containing the CDR3 region sequence that remained post-fragmentation in ST libraries (*5*). However, methodologies that comprehensively map full-length B cell receptor (BCR) and TCR sequences and their lineage relationships within tissues in a high-throughput, user-friendly manner are lacking.

In this work, we developed spatial transcriptomics for variable, diversity, and joining (VDJ) sequences (Spatial VDJ), which maps full-length BCR and TCR transcripts in human tissue (Fig. 1A). Spatial VDJ is an extension of Visium Spatial Gene Expression (Spatial GEX) for fresh frozen tissue, which relies on 3′-targeted barcoding of polyadenylated RNAs in a tissue section (fig. S1A) (*6*). Spatial GEX libraries from human tonsil tissue showed ample BCR and TCR constant gene expression (fig. S1, B to E). Still, they constituted a small fraction of the total library. Prior to the fragmentation steps, the CDR3 region sequence could be PCR amplified from spatially barcoded full-length Visium cDNA (fig. S1F). Thus, sequencing the CDR3 region and the spatial barcode from Spatial GEX cDNA libraries should be a feasible approach to determine both clonality and the location of antigen receptor transcripts.

We developed two Spatial VDJ versions (Fig. 1A): (i) long-read (LR) Spatial VDJ, which generates spatially barcoded libraries of full-length IG and T cell (TR) antigen receptor transcripts, and (ii) short-read (SR) Spatial VDJ for TR sequences only, which uses a two-step seminested PCR-based approach with CDR3-adjacent V primers (data S1). For both approaches, we used hybridization capture probes directed at the TR and IG constant regions to enrich for antigen receptor transcripts while preserving the spatial barcode, unique molecular identifier (UMI), and full-length receptor sequences (*7*, *8*). Hybridization capture significantly increased the TR and IG UMI and spatial barcode counts compared with the non-enriched Spatial GEX library and preserved the IG and TR transcript distribution (fig. S2).

Spatial VDJ permits high-fidelity B and T cell clonal mapping

We applied LR and SR Spatial VDJ to the human tonsil owing to its abundance and spatial compartmentalization of B and T cell lineages (Fig. 1, A to E, and fig. S3). We identified 62,533 unique IG (*IGH*, *IGK*, and *IGL*) and TR (*TRB* and *TRA*) clonal sequences (fig. S4A), hereafter referred to as "clonotypes" or "clones." We detected fewer TRA than TRB clones, likely because of *TRA*'s lower transcriptional abundance (fig. S1D) (*7*). The TR clone counts were slightly lower in SR than LR Spatial VDJ libraries (Fig. 1B), but the SR method recapitulated more than half of the clonal sequences, with increased sharing for expanded clones (fig. S4). Additionally, clonal abundance correlated well between LR and SR Spatial VDJ datasets (fig. S4E), and clones shared between both datasets showed greater expansion (fig. S4, E to G). We visualized the overall antigen receptor distribution (Fig. 1, C to E) and individual expanded clones (figs. S5 and S6). Notably, the same TR clonal sequence retrieved by either LR or SR Spatial VDJ exhibited overlapping spatial distribution, demonstrating that these approaches yield comparable results.

The antigen receptor distribution differed across the tonsil gene expression landscape (Fig. 1F and fig. S7). The unique IG clone count was the highest within tissue regions annotated as "isotype-switched cells," "squamous epithelium," and "B cell follicles/germinal centers (GCs)" (Fig. 1G). Isotype here refers to the IGH constant chain (IGHA, IGHD, IGHE, IGHG, and IGHM) that can be exchanged to confer diverse antibody effector functions while retaining antigen specificity (*9*). The IGH isotype fraction was consistent across sections (fig. S8A) and corresponded well to the Spatial GEX cluster groups (fig. S8B). The unique TR clone count was the highest in T cell zone–associated areas (Fig. 1G). Antigen receptor chain expression was also concordant between the Spatial VDJ and GEX datasets (fig. S8 and data S2). We next inferred the cell-type distribution by deconvoluting the Spatial GEX data using the *stereoscope* software package (*10*, *11*) (Fig. 1H and fig. S9, A to C), which matched well-established B cell, plasma cell, and T cell–associated marker-gene expression

[1]Department of Cell and Molecular Biology, Karolinska Institutet, Stockholm, Sweden. [2]SciLifeLab, Department of Gene Technology, KTH Royal Institute of Technology, Stockholm, Sweden. [3]SciLifeLab, Computational Science and Technology department, KTH Royal Institute of Technology, Stockholm, Sweden. [4]Department of Oncology-Pathology, Karolinska Institutet, Stockholm, Sweden. [5]Heidelberg University, Faculty of Medicine and Heidelberg University Hospital, Institute for Computational Biomedicine, Heidelberg, Germany. [6]ENT Unit, Sophiahemmet University Research Laboratory and Sophiahemmet Hospital, Stockholm, Sweden. [7]Center for Infectious Medicine, Department of Medicine Huddinge, Karolinska Institutet, Stockholm, Sweden. [8]Department of Clinical Pathology and Cancer Diagnostics, Karolinska University Hospital, Stockholm, Sweden.
***Corresponding author. Email: jeff.mold@ki.se**
†These authors contributed equally to this work.
‡These authors contributed equally to this work.

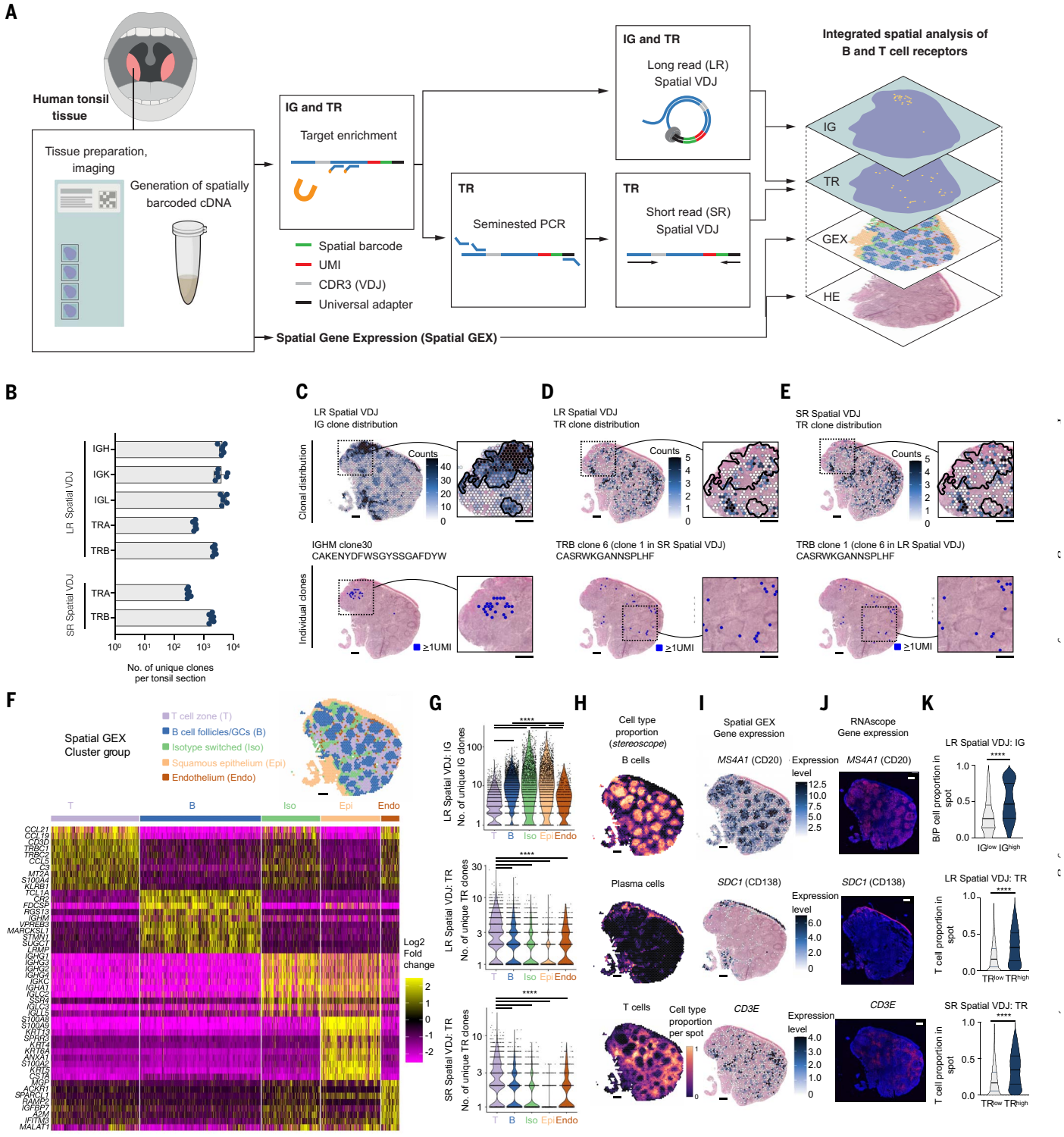

Fig. 1. Spatial VDJ maps antigen receptors in human tonsil–matching canonical B and T cell distributions. (**A**) Overview of long-read (LR) and short-read (SR) Spatial VDJ method in human tonsil tissue. (**B**) Unique *IGH*, *IGK*, *IGL*, *TRA*, and *TRB* clonotype sequences for each tonsil section (n = 6). (**C** to **E**) Unique IG (C) and TR (D) clonal receptor sequence distribution for LR Spatial VDJ and TR (E) clonal distribution for SR Spatial VDJ with a maximum cut-off above the 95th percentile. The black outline indicates regions with high IG clonal diversity. (**F**) Spatial GEX cluster group spatial distribution on tonsil tissue (top) and enriched genes (bottom). (**G**) Number of unique IG or TR clonotypes across Spatial GEX cluster groups (Kruskal–Wallis test, Dunn's multiple comparison test; ****P < 0.0001). (**H**) Visualization of major cell type distribution within the tonsil defined by single-cell deconvolution. (**I**) Spatial GEX of canonical B (top), plasma (middle), and T (bottom) cell markers (*MS4A1*, *SDC1*, and *CD3E*, respectively). Legends show UMI counts. (**J**) In situ hybridization of genes shown in (I) on proximal tissue sections to those analyzed by Spatial GEX or VDJ. (**K**) Cell type proportion for spots containing high or low clonotype counts (IG or TR) (Mann–Whitney U test; ****P < 0.0001). Scale bars, 500 μm. [(A) to (K)] Spatial VDJ was performed in two batches (two experiments). [(F), (G), and (K)] Data are pooled from six individual sections. [(C) to (E), (H), and (I)] Data are from one representative section (Tonsil section number 17). GC, germinal center.

(*MS4A1*, *SDC1*, and *CD3E*, respectively) shown by Spatial GEX (Fig. 1I) and in situ hybridization (Fig. 1J and fig. S9D). For spots that contained IG high (IG^{high}) versus low (IG^{low}) clonal content, the proportion of B cells and plasma cells was significantly higher, whereas TR^{high} versus TR^{low} spots had elevated T cell proportions (Fig. 1K and fig. S9E). The antigen-receptor distribution also matched known lymphoid tissue–associated chemokine gradients (fig. S10) (*12*). Thus, Spatial VDJ delineates diverse spatial distributions for B and T cell clones consistent with canonical secondary lymphoid tissue architecture and cell distribution.

The spatial segregation of individual clonotypes was highly reproducible and the most abundant clones were detected across sequential tonsil sections (Fig. 2, A to C, and figs. S5A, S6A, and S11A). However, TRA clones were rarely found across all six sections, likely because of lower *TRA* capture. Most clones appeared in one section, but expanded clones were detected across multiple or all sections, corresponding to higher UMI counts per clone (fig. S11, B and C). These results were expected, as many lymphocytes in secondary lymphoid organs are naïve or nonexpanded clones (*11*) and unlikely to be in multiple array spots or sections. To validate Spatial VDJ–defined clonal sequences, we analyzed nearby or adjacent sections from the same sample by a VDJ-targeted Smart-seq3 (SS3) protocol for bulk RNA (figs. S3A and S12). Bulk SS3 and Spatial VDJ showed comparable IGH isotype fractions (fig. S12, B and C). Of the IG clonotypes identified by LR Spatial VDJ, almost half were found by bulk SS3 VDJ (Fig. 2D and fig. S12, G and H). Bulk SS3 VDJ reproduced approximately a third of the TR clones captured by Spatial VDJ. The clones detected by multiple methods had higher UMI counts on average, and more expanded clones were more likely to be detected across methods (Fig. 2E and fig. S12, I to L). Additionally, the clone fraction of shared clonal sequences correlated well between datasets (Fig. 2F), in line with Slide-TCR-seq (*2*). Bulk SS3 VDJ captured substantially more TR clones, most of which were found in a single tissue section. Our combined analysis suggested that this was due to multiple factors, including better capture of rare mRNA transcripts by Bulk SS3 VDJ. Nonetheless, Spatial VDJ reproducibly detects expanded B and T cell clonal sequences.

Spatial VDJ captures B and T cell clones in human tumors

We next extended Spatial VDJ to human breast tumor tissue. Tumor infiltration by lymphocytes correlates with positive disease outcomes and treatment response across solid cancers, including breast cancer (*13*, *14*). Mapping B and T cell clones within tumors may help identify and therapeutically harness individual or groups of clones to boost tumor-associated immunity. We generated Spatial GEX and VDJ libraries from two untreated HER2-positive breast tumors (P1 and P2) (Fig. 3, figs. S13 to S19, and data S3). To better capture intrapatient heterogeneity, biopsies were divided into multiple regions, denoted as Region A (RegA) to RegE, each containing tumor, a tumor border, and adjacent nontumor tissue. We identified thousands of unique IG clonal sequences and hundreds of unique clonal TR sequences per patient (fig. S16) and section (Fig. 3C), with the highest number of distinct clones found outside the tumor area (Fig. 3D and fig. S17). The highest IG clonotype counts were in array spots enriched for plasmablasts and *APOE*-expressing macrophages (Fig. 3D and figs. S17C and S19), suggesting an association between tumor-infiltrating macrophages and plasma cells, as we observed previously (*10*). The spots with the highest TR receptor count were enriched for both myeloid and T cell–associated genes (fig. S17D) and cell subsets (fig. S19), which in P2 resembled mature tertiary lymphoid structures (TLS), but not in P1 (*15*). Some IGH clones were shared between the TLS-like and plasmablast-rich areas (fig. S17E), suggesting that at least some of the tumor-associated plasmablasts may derive from TLS-activated B cells.

Approximately half of the Spatial VDJ–defined TR receptor chains were confirmed by matched single-cell RNA sequencing (RNA-seq) VDJ (scVDJ) analysis of the same tumors (figs. S20 and S21A), similar to a spatial PCR–based TRB amplification protocol (*1*). For IG clones, we confirmed only 3.0 and 2.9% of the LR Spatial VDJ dataset by scVDJ. We detected approximately 10-fold more TR than IG clones by scVDJ, with the opposite ratio in Spatial VDJ (Fig. 3C and fig. S21B). Our analysis suggests that Spatial VDJ (compared with scVDJ) more easily captures plasma cell clones, likely owing to the abundant IG transcript expression per plasma cell (fig. S21C) (*16*) and sensitivity of plasma cells to single-cell dissociation protocols. Conversely, the reduced detection of TR clones by Spatial VDJ likely resulted from inefficient capture of rare transcript on the array (owing to low TR expression per cell and/or low cell number per clone) (fig. S21, C and D). These limitations may have also applied to rare B cell clones, because B cells express IG transcripts at lower levels compared with plasma cells. Supporting the notion that Spatial VDJ captures more expanded clones, the scVDJ TR clones that were shared with Spatial VDJ had more cells per clone (fig. S21E), and scVDJ clones detected in multiple tumor regions were more frequently captured by Spatial VDJ (fig. S20, F to I).

Expanded tumor-infiltrating B and T cell clones may indicate local antigen-specific interactions with tumor-regulatory potential (*14*, *17*). Tumors contain phenotypically diverse lymphocytes, but identifying which B or T cell clones and subsets interact directly with tumors is challenging. Spatial VDJ coupled with scVDJ on matched tumor biopsies revealed that expanded T cell clones were enriched in the tumor border relative to nontumor regions or within the tumor (Fig. 3E). These clones exhibited phenotypes ranging from CD4 or CD8 effectors to regulatory T cells (fig. S22). Thus, Spatial VDJ provides a platform to define putative tumor-reactive clonotypes according to spatial distribution and cell state, which is not possible when analyzing dissociated tissues. We found this particularly relevant for expanded B cell clones. In P2, we identified four distinct tumor clusters (figs. S15B and S18B). Different IG clones were distinctively enriched in the border to individual tumor clusters (Fig. 3F and fig. S23), two of which (IGLclone6 and IGLclone39) matched to class-switched B cells (IGHA1 and IGHG1, respectively). Most clones were enriched in limited parts of the tumor border, indicating localized antigen-binding responses (e.g., IG clonal colocalization with distinct tumor subclones expressing different antigens). All tumor clusters were enriched for cancer cells (figs. S18B and S19B) but exhibited differently enriched genes (fig. S23E). This intratumoral heterogeneity may result in differential tumor outgrowth and treatment responses within the same tumor [e.g., by distinct IG clones driving antibody-dependent tumor-cell killing in different tumor locations (*14*)]. Thus, the combination of unsupervised methodology with Spatial VDJ can identify potential tumor-reactive antigen receptors enriched in specific tumor regions.

Paired BCR or TCR sequences determine antigen binding. Spatial VDJ captures individual antigen receptor transcripts and cannot therefore define receptor pairs by itself. However, paired receptor chains should colocalize in the tissue. Using the matched single-cell VDJ dataset to verify paired receptor usage, we observed a high spatial correlation for most IG pairs across biopsied regions (Fig. 3, G and H, and fig. S24A). We lacked sufficient data points for TR pairs to evaluate their spatial distribution in a statistically robust manner. To predict antigen receptor pairing based on the Spatial VDJ data alone, we developed a computational framework called "repair." We tested our model on data from P1 at different cut-offs of receptor chain abundance (minimal spot count per clone) and the pairing score (fig. S24, B and C, and data S4), which approximated the confidence of the pairing. We achieved the maximum accuracy (95.8%) and number of correct pairs (n = 23) when the IGH clonal chain had to be present in at least 10 spots and the pairing score was at least 0.35. At these settings, we obtained 157 de novo identified receptor pairs (i.e., receptor chains that were not both present in our scVDJ

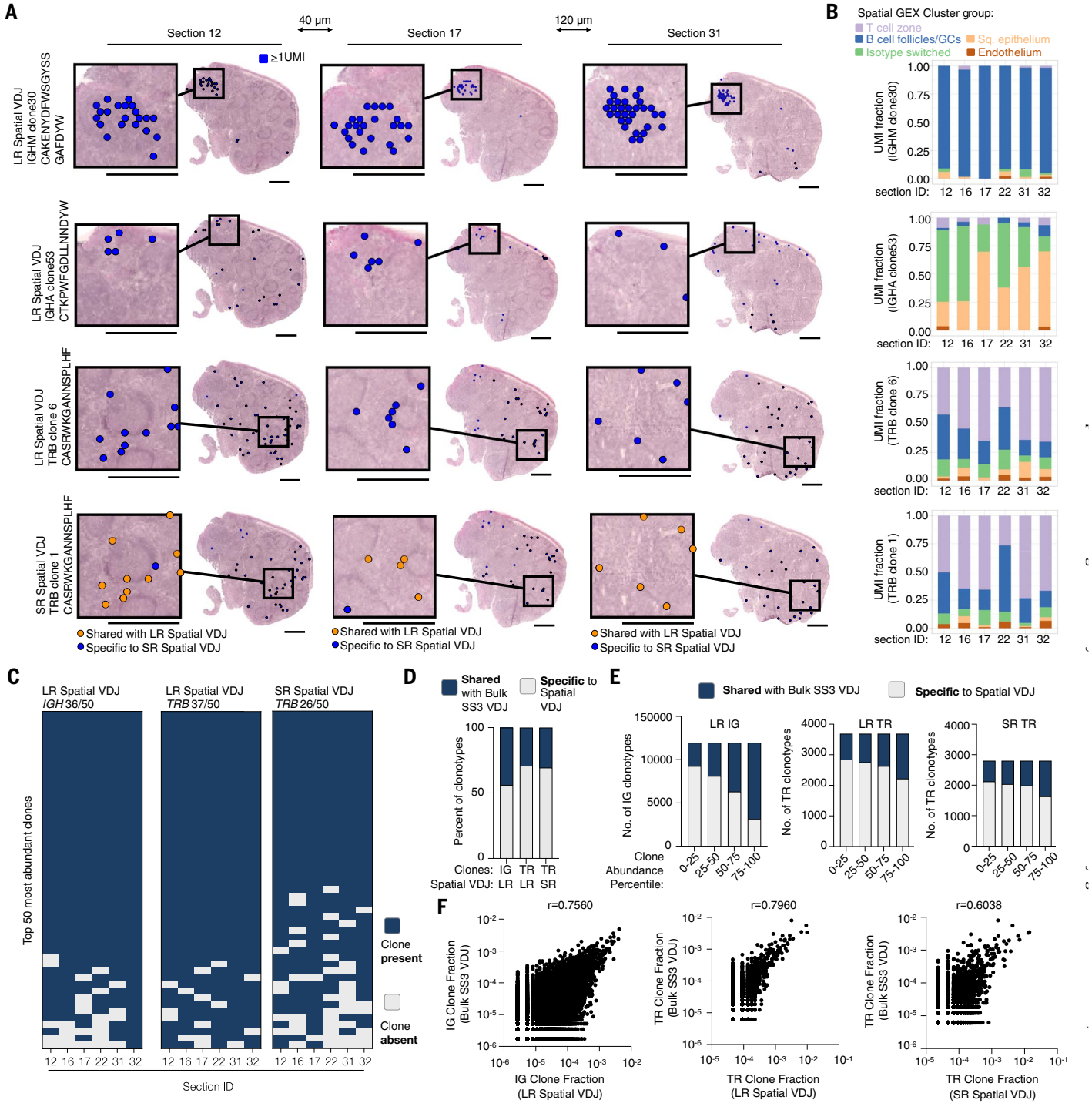

Fig. 2. Spatial VDJ reproducibly delineates B and T cell clones across tissue sections and amplifies validated clonal sequences. (**A**) Spatial distribution of individual clones across representative tonsil sections from the same tonsil sample. Distance between sections (orthogonal to the tissue plane) above the arrows. All sections (n = 6) are shown in figs. S5 (IG) and S6 (TR). Matched *TRB* clonotype sequence (identical ntCDR3; see materials and methods) captured by LR and SR Spatial VDJ is shown, and concordant spots are indicated in orange (bottom row). Clone ID numbering occurs independently within LR and SR Spatial VDJ datasets. Scale bars, 1 mm. (**B**) UMI distribution for each clone in (A) across Spatial GEX cluster groups and sections. (**C**) Presence or absence of the top 50 *IGH*, *IGK*, or *TRB* clonotypes (based on UMI count and sorted on number of sections) across tonsil sections. (**D**) Percent shared and not shared clonotype sequences between Spatial VDJ and Bulk SS3 VDJ validation (see fig. S3A). (**E**) The number of shared versus not shared clonotype sequences with Bulk SS3 VDJ across increased clonal abundance in LR (left, middle) or SR (right) Spatial VDJ datasets. (**F**) Clone fraction of each shared IG (left) or TR (middle, right) clonotypes between the datasets listed. Pearson correlation coefficient (r) is denoted. [(A) to (F)] Spatial VDJ was performed in two batches (two experiments). Bulk SS3 VDJ was performed in a single experiment, with four technical replicate reactions per tissue section. [(D) to (F)] Data are pooled from six individual sections.

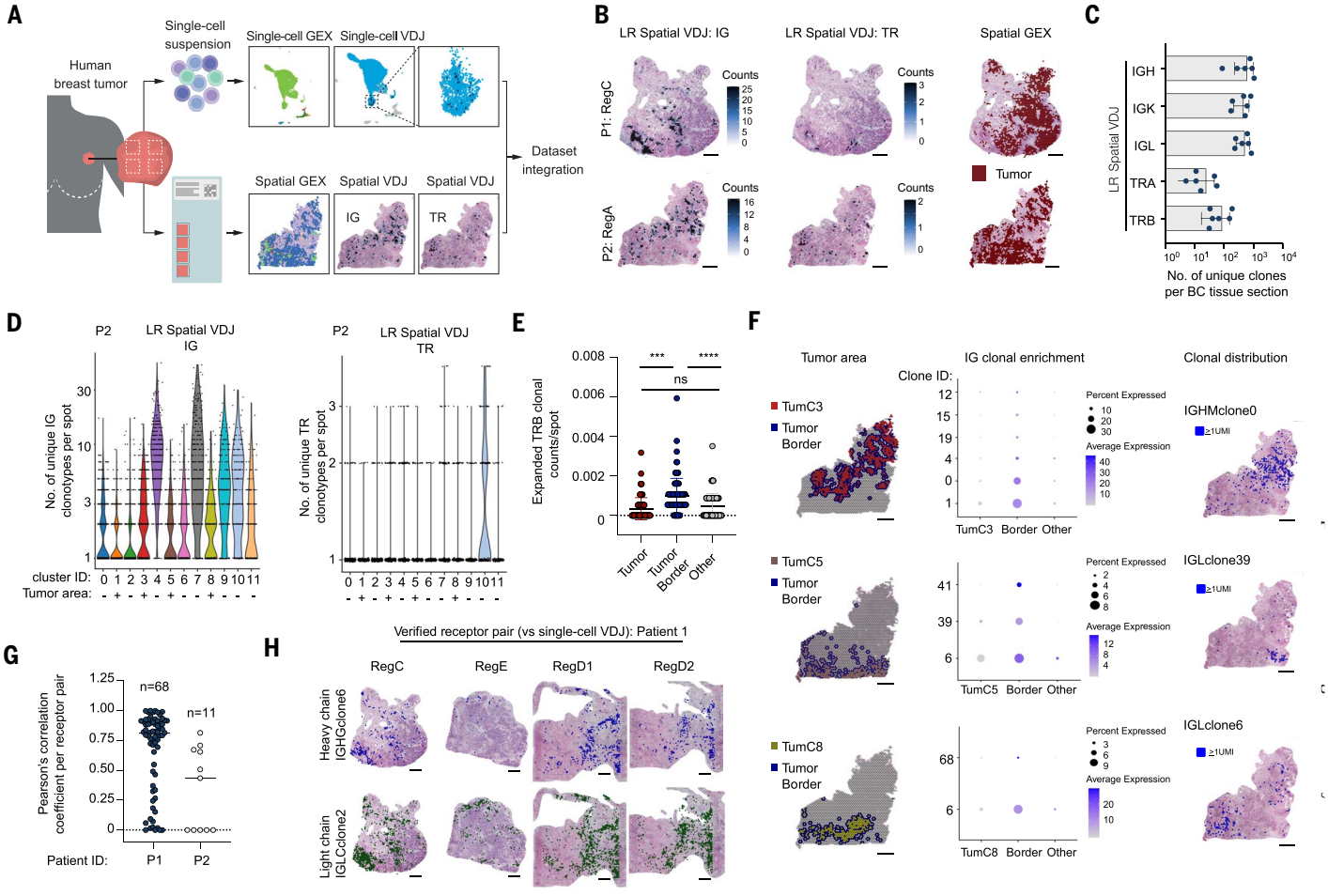

Fig. 3. Distinct B cell lineage clones spatially segregate along different breast tumor areas. (**A**) Outline of the breast cancer patient experiments. (**B**) Unique clonal distribution for LR Spatial VDJ (IG, left; TR, middle) and tumor area (right) for two biopsy regions from patients 1 (P1) and 2 (P2) with a maximum cut-off above the 95th percentile. (**C**) Unique clonotype count from LR Spatial VDJ libraries from breast cancer sections: P1 (n = 3 sampled regions, with one section for regions C and E, and two replicate sections for region D) and P2 (n = 2 sampled regions, one section prepared per region). (**D**) Number of unique IG (left) and TR (right) clonotypes per spot in different Spatial GEX clusters (+ denotes tumor cluster). (**E**) UMI count per spot for expanded TRB clones across spots belonging to the tumor, tumor border, and other areas. Statistical significance was calculated using the Friedman's test, then Dunn's multiple comparison's test (***P < 0.001, ****P < 0.0001). (**F**) (Left) Tumor 3, 5, and 8 clusters (TumC3, TumC5, and TumC8) and their surrounding borders visualized on P2 Region A. (Middle) Dot plots showing expression of significantly enriched IG clones per corresponding area. (Right) Spatial distribution of representative IG clonotypes. See fig. S23. (**G**) Pearson correlation coefficient (r) between the light versus heavy chain UMI count per spot for each IG receptor pair verified by scVDJ. Data are pooled from all tumor regions on a per patient basis. See fig. S24. (**H**) Spatial distribution of two IG light and heavy chain receptor pairs, verified by single-cell analysis. Scale bars, 1 mm. [(A) to (H)] Spatial VDJ was performed in two batches (two experiments). Single-cell processing was performed for each patient separately. [(D) to (F)] Data are from both P2 tumor regions. BC, breast cancer; Reg, region; Tum, tumor.

dataset) (fig. S24D and data S4). When "repair" was applied to P2, we found 25 predicted pairs with one out of two pairs present in the scVDJ dataset verified at these settings. Thus, "repair" with Spatial VDJ may potentially be used to predict de novo paired IG receptors in human tissues for further antibody studies.

Spatial VDJ uncovers B cell spatial evolution

B cells undergo affinity-dependent selection and clonal expansion in GCs. Multiple clones can simultaneously cycle through a single or several GCs, generating a dynamic clonal interplay (*18*). In the human tonsil, we annotated individual B cell follicles (Fig. 4A and fig. S7) that contained GCs with compartments resembling the dark and light zone (fig. S25), which are enriched for somatic hypermutation and clonal expansion versus clonal selection, respectively (*18*). The highest IGH clonal family density (i.e., clone count per spot) was in the light zone (fig. S25, E and F), possibly reflecting ongoing clonal selection. IGH clonal family diversity measures, including species richness (*Chao1*), D50, largest clone fraction, the inverse Simpson index, and Shannon entropy, varied across follicles (Fig. 4B and fig. S26), indicating diverse interfollicular B cell clonal responses. The total IGH clonal family number per follicle positively correlated with follicle size (fig. S26C). Most clonal families were present in a single follicle, but some appeared in multiple follicles, with 150 clonal families coincident in four or more follicles (Fig. 4C). Expanded follicular IGH clonal families both appeared primarily in one follicle ("restricted") or spread more evenly across multiple follicles ("nonrestricted") (Fig. 4, D and E). Thus, IGH clonal families may expand and presumably undergo affinity hypermutation in multiple GCs simultaneously. This is in line with laser microdissection studies in humans (*3*, *4*) and photoactivation studies in mice (*19*). Nonrestricted IGH clonal families may be more mature as they had an increased fraction of downstream isotypes and a higher fraction

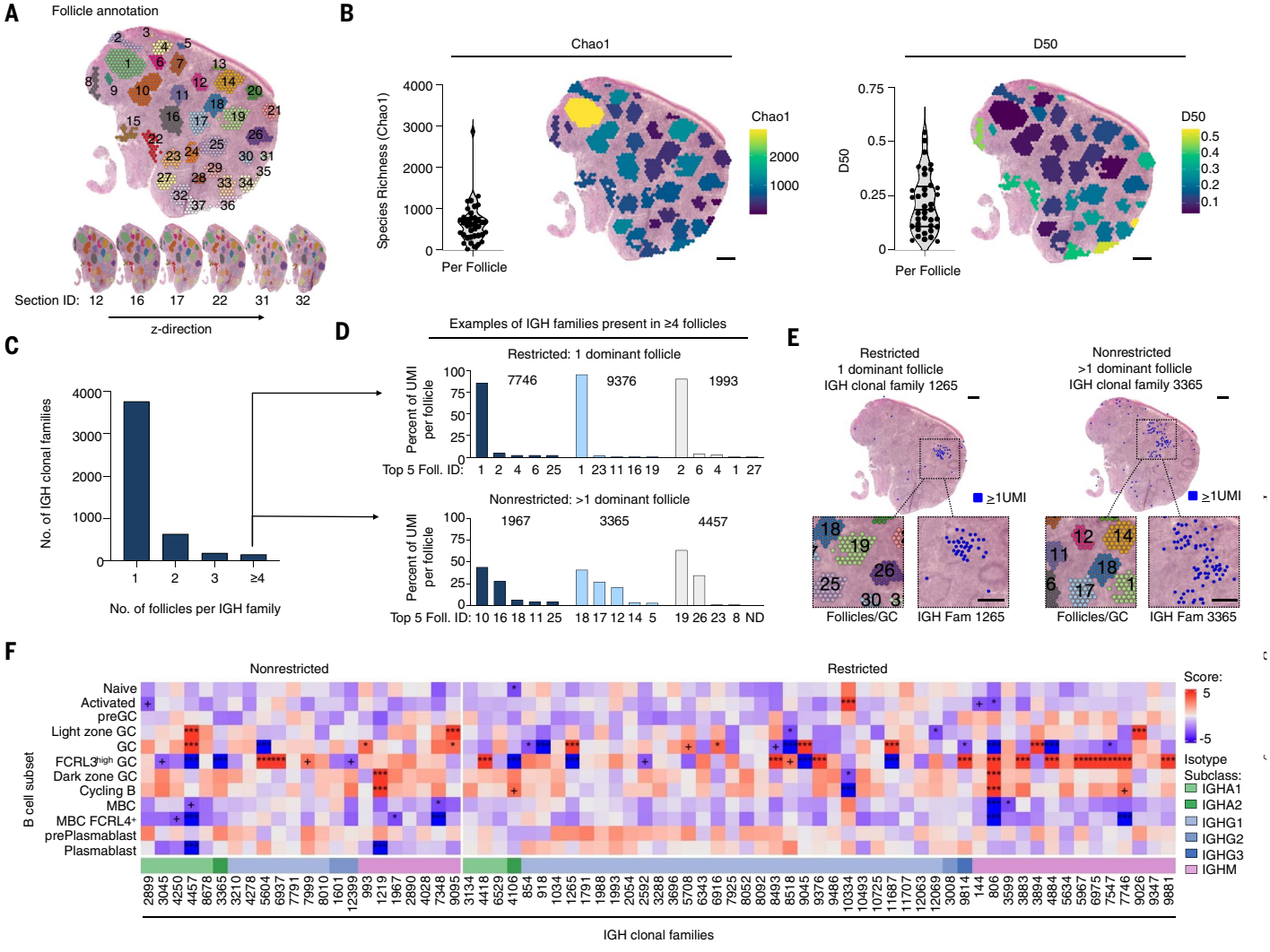

Fig. 4. Spatial VDJ delineates IG clonal diversity in B cell follicles. (**A**) B cell follicle annotation across human tonsil replicate sections. 36 of 37 follicles contained GC-like areas. (**B**) The IGH clonal family species richness Chao1 (left) and D50 (right) for each follicle and visualized on tonsil tissue. For one follicle, the D50 value was higher than 0.5 because 7 of 13 clones with UMI of 1 were needed to reach 50% of total UMIs. (**C**) Individual follicular IGH clonal family distribution across follicles. (**D**) The percentage UMI distribution across the top five follicles for six representative IGH clonal families present in ≥4 follicles. ND, not detected. (**E**) Spatial distribution for a clonal family with (left) one or (right) multiple dominant follicles. (**F**) Association analysis between IGH clonal families and the B cell single-cell deconvolution data. *P* values were corrected with the Benjamini-Hochberg procedure and denoted by + ($P_{adj} < 0.1$; *$P_{adj} < 0.05$; **$P_{adj} < 0.01$; ***$P_{adj} < 0.001$, with statistical significance considered at *$P_{adj} < 0.05$.) Scale bars, 500 μm. [(A) to (F)] Spatial VDJ was performed in two batches (two experiments) and data from six replicate sections of the same tonsil sample are pooled. [(B) and €] Pooled data are visualized on one representative section (tonsil section number 17).

of multiple isotypes within a single clonal family (fig. S27). Both restricted and nonrestricted clonal families were broadly associated with GC-related cell subset phenotypes (Fig. 4F). Restricted families were more often significantly associated with an Fc receptor-like 3 ($FCRL3^{high}$) GC cell phenotype than nonrestricted families (*11*) (12 of 49 and 24.4% versus 2 of 22 and 9.1%, respectively), possibly reflecting different transcriptional states or colocalization with such cells. These multifollicular clonal families may derive from recently activated B cells that migrated from one follicle to another or from reactivated clonally related memory B cell clones that entered separate follicles. Thus, high B cell clonal diversity exists across GCs with both restricted and multifollicular clonal expansion.

Antibodies further diversify their functions by class switch recombination (CSR), which is an intrachromosal deletion recombination event that replaces the heavy chain constant region to confer diverse effector functions. In contrast to earlier work, recent studies have shown that B cells mainly undergo CSR prior to GC entry (*18*). However, where CSR occurs in human lymphoid tissues remains understudied. A recent putative CSR (pCSR) event may appear in our dataset as two (or more) colocalized transcripts from the same IGH clonal family with different isotypes but identical variable (V) gene sequences. We detected 810 IGH clonal families containing multiple isotypes. Of these, 137 had identical V gene sequence alignments matched with multiple isotypes, and 17 occurred in the same spatial barcode (Fig. 5A and fig. S28). These 17 pCSR events all occurred extrafollicularly and were mainly switches from IGHG1 to IGHG2 (Fig. 5B); some of these pCSR events (e.g., clonal family 12298) occurred in an array spot with concurrent expression of genes encoding critical enzymes that mediate CSR (Fig. 5C). In sum, Spatial VDJ detected pCSR in human tissue that occurred extrafollicularly.

To better understand how IGH clonal families undergoing somatic hypermutation spatially segregate, we generated phylogenetic trees for a subset of expanded IGH clonal families. First, we

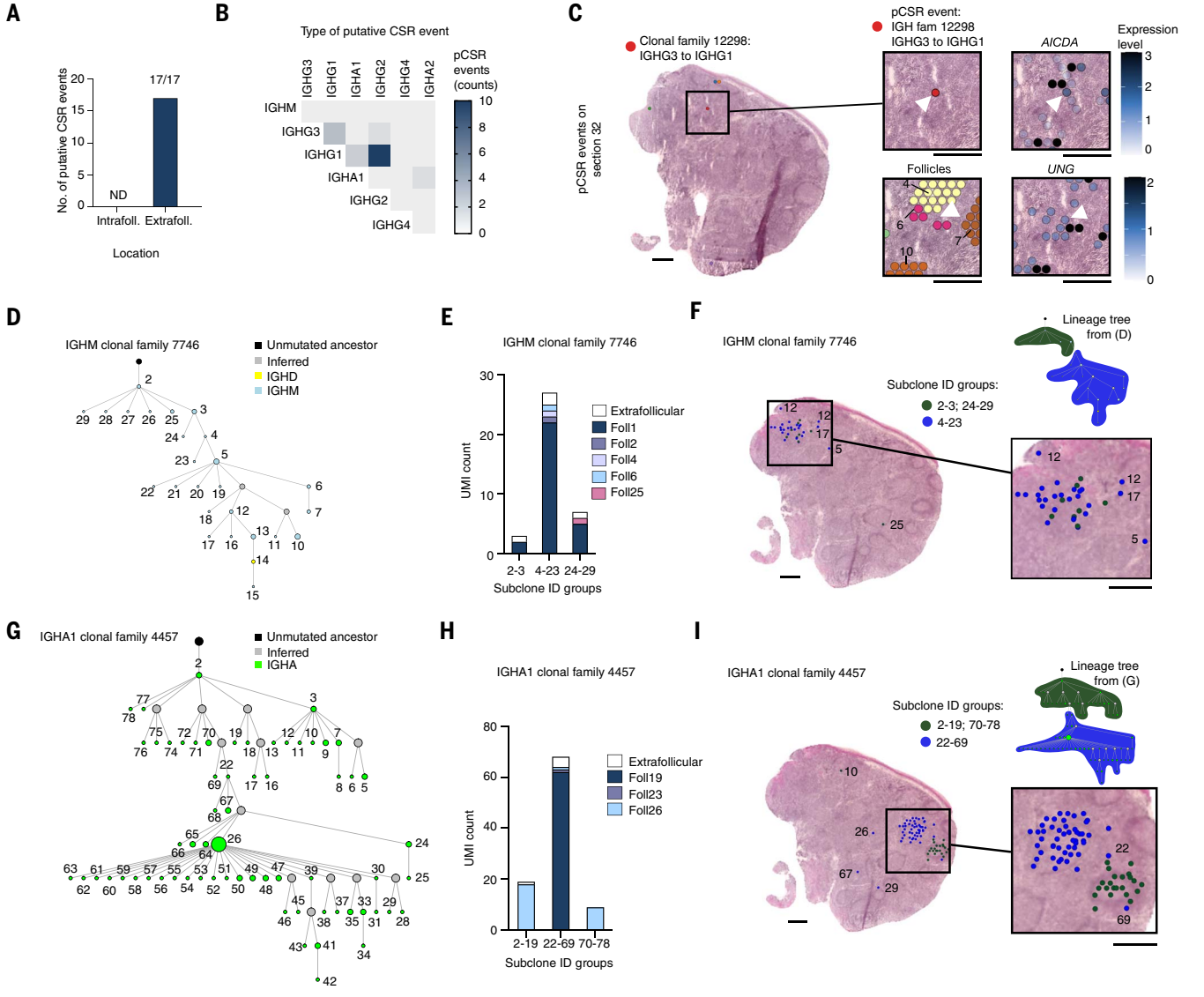

Fig. 5. Spatial VDJ uncovers IG spatial clonal evolution in human lymphoid tissue. (**A**) The number of pCSRs (n = 17) occurring within (+) or outside (−) follicle areas. (**B**) Types of pCSR events. (**C**) An individual pCSR event is visualized on section 32 (top left zoom-in), and its position is indicated relative to the follicles (bottom left) and the expression of CSR-associated enzymes *AICDA* (top right) and *UNG* (bottom right) with a maximum cut-off above the 95th percentile. The white arrows indicate the pCSR event in IGH clonal family 12298. (**D**) Lineage tree of IGHM clonal family 7746. Each node of the tree ("subclone") represents a unique V sequence, and the size of the node is proportional to the number of distinct reads in that node. All subclones are of the IGHM isotype (blue). Inferred clones (not present in the data) are gray and lack a subclone ID. (**E**) Intra- and extrafollicular UMI distribution for IGHM clonal family 7746 subclones. (**F**) Distribution of IGHM clonal family 7746 on tonsil tissue. (**G**) Lineage tree of IGHA1 clonal family 4457, as in (D). (**H**) Intra- and extrafollicular UMI distribution for IGHA1 clonal family 4457 subclones. (**I**) Spatial distribution of IGHA1 clonal family 4457. [(A) to (I)] Spatial VDJ was performed in two batches (two experiments). [(A), (B), and (D) to (I)] Data from six replicate sections are pooled. (C) Data are from section 32. [(F) and (I)] Pooled data are overlayed on section number 17 H&E image. Scale bars, 500 μm.

mapped mutational events occurring primarily in one follicle [e.g., clonal family 7746 (Fig. 5, D to F) and the most prominent clonal family, 806 (fig. S28, D to F)]. Given their considerable clonal size, exclusive and concurrent *IGHM* and *IGHD* expression, minor spreading of subclones across follicles, and almost exclusive follicular location, these clones were likely recently activated naïve B cells undergoing somatic hypermutation. By contrast, clonal family 4457 was an expanded, seemingly actively mutating family spread primarily across two follicles (Fig. 5, G to I). A branch of subclones (IDs 22 to 69) was almost exclusively found in follicle 19, whereas the remaining subclones (IDs 2 to 19 and 70 to 78) were only found in follicle 26. These findings suggest that a subclone 22 (or a closely related, undetected subclone), likely a GC B cell, migrated from follicle 19 to seed follicle 26. Thus, Spatial VDJ enables high-resolution demarcation of clonal composition and evolution across human GCs.

Discussion

Spatial VDJ maps full-length B and T cell receptor sequences in human tissue. The performance of Spatial VDJ depends on several factors, including the quality of the starting material, lymphocyte abundance, tissue compatibility with the Visium Spatial GEX fresh frozen protocol, antigen receptor expression level, clonal cell count, and clonal tissue distribution. For example, Spatial VDJ optimally captures expanded clones and plasma cell clones owing to high cell count per clone and high receptor expression per cell, respectively. By contrast, Spatial VDJ's ability to capture non-expanded clones or clones for which the antigen receptor is expressed at low levels is more limited owing

to transcript dropout and partial coverage of the tissue by array spots. Nevertheless, our TCR results were comparable to other spatial retrieval methods (*1*, *2*). Spatial VDJ cannot (yet) fully resolve a clone's cell state(s) or receptor chain pairing as the capture array lacks single-cell resolution. Computational modeling developed in this study permitted receptor pairing for IG but not TR chains because of data sparseness for the latter. Improved analytical tools, increased resolution of the capture array, inclusion of γδ T cell receptor gene probes, and protein co-capture could further extend Spatial VDJ's performance.

Several key elements distinguish Spatial VDJ from other spatial antigen receptor methods (*1*, *2*). First, LR Spatial VDJ simultaneously maps TR and IG clones. Second, LR Spatial VDJ captures full receptor sequences, which for B cells permits spatial lineage tracing (including somatic hypermutation and class switching). Deep sequencing of Visium libraries permits some IG light chain clonal recovery, but not full transcript recovery, owing to fragmentation steps (*5*). Laser-guided microdissection coupled with BCR genomic repertoire sequencing (*4*) avoids IG expression bias but is more arduous, lower throughput, and at lower resolution. Third, Spatial VDJ is an extension of Visium for fresh frozen tissue, which is commercially available, frequently used, requires no specialized equipment, and allows data projection onto matched histologically stained (or fluorescent) images. Thus, Spatial VDJ should be straightforward to implement. Compared with Slide-seq, Visium has a larger capture area but lower spatial resolution (*2*). Lastly, Spatial VDJ offers a long-read and short-read version for spatial TCR analysis. Both methods reproducibly map the most abundant clones, but LR Spatial VDJ captured slightly higher clonal numbers and required fewer PCR cycles, potentially reducing PCR artefacts. However, SR Spatial VDJ may be more accessible, as short-read sequencing services are more broadly available and higher throughput.

We predict that Spatial VDJ will be useful across research fields to study urgent clinically relevant phenomena, particularly to discriminate B cell clonal dynamics during infections and vaccination. For example, robust and persistent GC responses have been linked to productive memory B cells and antibodies after severe acute respiratory syndrome coronavirus 2 (SARS-CoV-2) vaccination, whereas a failure to generate such responses may relate to severe SARS-CoV-2 infections (*20*). The use of Spatial VDJ to resolve spatial dynamics of GC B cell clonal evolution across many individuals may help clarify what triggers protective versus insufficient B cell responses [e.g., by linking IG and TR sequence distributions to antigen receptor reactivities and affinities, IG and TR germline variations (*21*), protein expression, and clinical outcomes]. Likewise, extending Spatial VDJ to model organisms and/or settings in which the antigen is known and can be tracked may be highly useful to study such questions. These analyses are highly applicable to cancer (*2*, *5*, *22*) given the critical contribution of lymphocytes [and tertiary lymphoid structures (*15*, *23*)] to antitumor immunity and the simultaneous challenge to identify functionally relevant B and T cell clones (*14*, *24*). Spatial VDJ may offer a distinct vantage point to enrich for tumor-regulatory clones. Ultimately, we envision that Spatial VDJ may serve to link B and T cell clones to their spatial niches to identify candidate antigen-specific clones for engineered cell- or antibody-based therapeutics.

Materials and Methods

Tonsil samples

The tonsil samples were obtained from anonymous adult patients undergoing tonsillectomy due to obstructive sleep apnea syndrome. Permission to collect these unidentified tissues was obtained from the Ethical Review Authority in Stockholm, Sweden (2006/646-31/4, amendments 2015/1083-2, and 2017/1659-32). All patients gave informed consent prior to collecting tissue. From each tonsil a smaller piece (≈0.5 cm^3) was cut out, immediately embedded in OCT, placed on dry ice, and stored at −80°C.

Breast tumor samples

Breast cancer samples were obtained by Dr. J. Hartman from the Department of Clinical Pathology and Cancer Diagnostics at Karolinska University Hospital, Stockholm, Sweden. Experimental procedures and protocols of the study were previously approved by the regional ethics review board (Etikprövningsnämnden) in Stockholm (2016/957-31, amendment 2017/742-32, 2021-00795, and 2022-05245-02). Breast tumor samples were collected from two patients with untreated invasive ductal carcinomas during surgery (fig. S13A). Histological evaluations of patient tumors were performed by pathologists for diagnostic purposes: tumor characteristics, including hormone receptor, HER2, and Ki67 expression (data S3). Both tumors were HER2 positive. For each tumor biopsy, different regions (n = 4 to 5) were selected by the pathologists depending on the size of the tumor (fig. S13A). From each region, tissue was isolated for immediate embedding in OCT and for gene expression analysis with spatial transcriptomics and Spatial VDJ analysis. We prepared Spatial GEX and VDJ libraries for three regions for Patient 1 (P1) (figs. S13 and 14), and two regions for Patient 2 (P2) (figs. S13 and S15). The remaining material for each tumor region was used for single-cell RNA and VDJ sequencing analysis. Samples for spatial transcriptomics were immediately frozen and stored at −80°C until further analysis. The tissues obtained for single-cell analysis were processed directly.

Preparation and sequencing of Spatial GEX

Sections of fresh-frozen breast tumor and tonsil tissue were cut at 10-μm thickness and mounted onto slides from the Visium Spatial Gene Expression Slide & Reagent kit (10x Genomics). For Tonsil #2, six sections were analyzed, covering 200 μm in the z-axis (orthogonal to the tissue plane) of the sample (fig. S3A). Sequencing libraries were prepared following the manufacturer's protocol (Document number CG000239 Rev A, 10x Genomics). Prior to imaging, coverslips were mounted on the slides according to the protocol's optional step "Coverslip Application & Removal." Tissue images were taken at 20X magnification using the Metafer Slide Scanning platform (Microscope stand: AxioImager.Z2 with ScopeLED Illumination, Zeiss; Camera: CoolCube 4m, MetaSystems; Objective: Plan-Apochromat 20X/0.80 M27, a = 0.55 mm, Zeiss, Software: Metafer5 version 3.14.192). Raw images were stitched with VSlide software (version 1.1.128; MetaSystems). Adaptations of the protocol were made in that the Hematoxylin staining time was reduced to 4 min and tissue permeabilization was performed for 12 min. Final libraries were sequenced on NextSeq2000 (Illumina) or NovaSeq6000 (Illumina).

Target enrichment of spatial cDNA with hybridization capture (LR and SR Spatial VDJ)

For target enrichment we used IDT xGen Hybridization and Wash Kit (#1080584) with one Discovery pool (IDT) each for BCR and TCR transcripts (IG and TCR pool) (data S1). The BCR consists of two heavy chains (encoded by the *IGH* gene loci) and two light chains (*IGK* or *IGL*) (*25*). The TCR is either composed of an α (*TRA*) and β chain (*TRB*) or a γ (*TRG*) and δ (*TRD*) chain (*26*), with T cells expressing TCRs encoded by *TRA* and *TRB* (αβ T cells) being more abundant. We focused our spatial analysis in this study on αβ T cells; (i.e., probes targeting *TRD* and *TRG* were not included). Custom blocking oligos (IDT) (data S1) were designed to hybridize to universal adaptor sequences of the cDNA library, to prevent off-target fragments from binding to BCR or TCR transcripts and contaminating the enriched library. To ensure sufficient product for the hybridization capture protocol, we cocaptured the TR and IG transcripts in the same reaction. Regardless of whether the user selects LR (both IG and TR analysis) versus SR Spatial VDJ (TR only), we would recommend always including both IG and TR capture probes for the hybridization capture step, since the low TR transcript count in the cDNA libraries is likely a limiting step to a successful target enrichment reaction. We did not pursue a short-read option for IG receptor sequences since we wanted to capture the full-length transcripts to map somatic hypermutation

and class switching events. Additionally, owing to its very long constant region, a similar semi-nested approach for IG receptor sequences would still likely result in an inability for the IG heavy chain transcripts to cluster on the sequencer instrument.

The input cDNA libraries were amplified prior to target enrichment to ensure sufficient material. We took 10 μl of Visium cDNA per library (since this is typically considered representative of the entire spatial GEX library) and split into subsamples of 10 ng per PCR reaction (number of subsamples varied depending on the cDNA concentration in each library). PCR reactions were performed using 25 μl of KAPA HiFi HotStart ReadyMix (2X) (KK2602, Roche), 7.5 μl of cDNA primers (10x Genomics), and 17.5 μl of sample in Milli-Q water. The following settings were used for the PCRs:

1. 98°C: 3 min
2. 98°C: 15 s
3. 63°C: 30 s
4. 72°C: 2 min
5. Repeat steps 2 to 5 six times for a total of five cycles
6. 72°C: 1 min

The subsamples were pooled again before bead wash with 0.6X SPRIselect (Beckman-Coulter) and eluted in 40 μl Elution buffer (#19086, Qiagen) each.

We followed the protocol "xGen hybridization capture of DNA libraries," version 4 (Integrated DNA Technologies), with the optional Appendix A "AMPure XP Bead DNA concentration protocol" followed by "Plate protocol" from step 13 (in tube strips), with the hybridization reaction carried out overnight (16 hours). The IG and TCR discovery pools were mixed at a final ratio of 1:3 or 1:12 (IG:TR) in the hybridization reaction which yielded comparable results. We opted to use 1:3 for subsequent experiments. The 1:3 ratio was achieved by triplicating the TR probe sequences versus the IG in the IDT order and adding equivalent volumes of the produced pools in the hybridization reaction (i.e., two separate pools were ordered, with each TR bait probe sequence listed three times and each IG listed once). For one (out of two) Spatial VDJ experiment, the enriched and purified libraries were amplified twice with an AMPure bead wash after each PCR, using 25 μl of KAPA HiFi HotStart ReadyMix (2X) (KK2602, Roche), 7.5 μl of cDNA primers (10x Genomics), and 17.5 μl of the sample in Milli-Q water. The following settings were used for the PCRs:

7. 98°C: 3 min
8. 98°C: 15 s
9. 63°C: 30 s
10. 72°C: 2 min
11. Repeat steps 2 to 5 six times for a total of seven cycles (PCR 1) and four times for a total of five cycles (PCR 2)
12. 72°C: 1 min

For the second Spatial VDJ experiment, the enriched libraries were amplified in one PCR reaction as described above, but with 14 cycles.

Long-read library preparation and sequencing (LR Spatial VDJ for IG and TR)

The product from the hybridization capture was used as input into the SMRTbell library preparation (PacBio). We concentrated the DNA by AMPure Bead Purification (0.8X), eluting in 6 μl of EB buffer, using 1 μl for Qubit measurements. We used at least 1 μg of input for each library and multiplexed eight samples in one sequencing run. PacBio Barcoded Overhand Adapters were used for multiplexing and followed the manufacturer's instructions for the library preparations. This protocol indexed the enriched libraries by ligation to avoid unnecessary PCR cycles, which can introduce errors and chimeric reads that are particularly problematic for long-read sequencing. The pooled library had more than the minimum amount required for sequencing. A SMRT Enzyme clean-up kit was used to remove linear and single-stranded DNA. The final libraries were sequenced on a Sequel II at the National Genomics Infrastructure (NGI)/Uppsala Genome Center.

Short-read library preparation and sequencing (SR Spatial VDJ for TR only)

After hybridization capture and post-capture PCR amplification (14 cycles), further *TRA* and *TRB* enrichment was performed by semi-nested PCR reactions with the following primers: V primers targeting either the *TRAV* or *TRBV* genes, 5′ of the CDR3 region (i.e., "Outer" *TRAV* or *TRBV* primers) and a primer ("partRead1") targeting the universal partial read 1 sequence present on all poly-dT captured transcripts in Visium Gene Expression cDNA libraries (see data S1 for primer sequences). PartRead1 is also compatible with TruSeq indexes to allow sample multiplexing for sequencing. The Outer V primer PCR input was 2.5-5 ng of hybridization captured cDNA from tonsil Visium Gene Expression libraries and the reaction was run with KAPA HiFi HotStart ReadyMix (2X) (KK2602, Roche). Four replicate reactions were prepared per sample and pooled at the final indexing step. All primers were diluted 40X for a final concentration of 2.5 μM from 100 μM stocks (Integrated DNA Technologies). The PCR was run for 12 cycles for *TRB* and 14 cycles for *TRA*, under the following conditions:

1. 98°C: 5 min
2. 98°C: 20 s
3. 65°C: 30 s
4. 72°C: 1 min 30 s
5. Repeat steps 2-5 11 or 13 times for a total of 12 or 14 cycles
6. 72°C: 7 min

Quantitative real-time PCR was performed to determine the appropriate number of cycles (to limit exponential amplification). The Outer V primer PCR product was purified using a magnetic bead clean-up with AMPure beads (0.6X), followed by two 80% EtOH washes. The Outer V primer PCR product was eluted in EB buffer after incubation at 15 min at 37°C. The cleaned PCR product was quantified using Qubit and Bioanalyzer (Agilent). Five ng of each PCR product was used as input to the subsequent Inner V primer PCR.

The Inner V primer PCR was performed with the following primers: V primers targeting either the *TRAV* or *TRBV* genes, close/adjacent to the CDR3 region (i.e., "Inner" V primers) and the same universal partRead1 primer as described for the Outer V primer PCR (see data S1 for primer sequences). These Inner V primers have a handle compatible with TruSeq indexing (data S1). The primer concentrations and reagents were as described for the Outer V primer PCR. Quantitative real-time PCR was performed again to determine the appropriate number of cycles (to avoid exponential amplification). The following conditions were used for the PCR reaction:

1. 98°C: 5 min
2. 98°C: 20 s
3. 72°C: 30 s
4. 72°C: 1 min 30 s
5. Repeat steps 2-5 seven times for a total of eight cycles
6. 72°C: 7 min

The PCR product was cleaned using AMPure magnetic bead-clean up and ethanol washes as described above. The final eluted PCR products were quantified using Qubit and Bioanalyzer (Agilent). For the indexing step, 10 ng of input material was used from each replicate. All replicates for each individual sample were pooled at this stage and received the same index. The samples were PCR indexed using TruSeq Indexes, according to the conditions listed below and as described previously (*6*):

1. 98°C: 3 min
2. 98°C: 20 s
3. 60°C: 30 s
4. 72°C: 1 min 30 s
5. Repeat steps 2-5 seven times for a total of eight cycles
6. 72°C: 5 min

The PCR product was cleaned using AMPure magnetic bead-clean up and ethanol washes as described above. The final eluted PCR products were quantified using Qubit and Bioanalyzer (Agilent) and pooled for sequencing. The samples were sequenced on a Novaseq6000 SP flowcell using a short read 1 and a longer read 2 to capture the entire CDR3 region and part of the constant region from the 5′ end (read 1, 35 nt; index read, 6 nt; read 2, 259 nt).

RNAscope

Fresh frozen tissue sections were fixed for 1 hour in pre-chilled 4% PFA. The procedure was then performed according to the RNAscope® Multiplex

Fluorescent Reagent Kit v2 Assay User Manual (Document Number 323100-USM). For tonsil section #25 (fig. S3A), probes targeting *SDC1* (Cat#: 416961-C2; lot#: 22076C) and *MS4A1* (Cat#: 426771-C3; lot#: 22076C) were used. For tonsil section #26 (fig. S3A), probes targeting *CD3E* (Cat#: 553971-C2; lot# 22076D) and *MS4A1* were used. Control tonsil sections were incubated with either the RNAscope® 3-plex Positive Control Probe_Hs (320861; lot# 21258A) or the RNAscope® 3-plex Negative Control Probe_Hs (320871; lot# 21285A).

The TSA Vivid Fluorophore kit 570 (7526/1 KIT; batch 1A) was assigned to channel 2 with a dilution of 1:1500 for tonsil section #25 and a dilution of 1:750 for tonsil section #26. The TSA Vivid Fluorophore kit 650 (7527/1 KIT; batch 1A) was assigned to channel 3 with a dilution of 1:750 for both tonsil sections. For the control tonsil sections the TSA Vivid Fluorophores were assigned to the channels according to the RNAscope® Multiplex Fluorescent Reagent Kit v2 Assay User Manual. The following reagents were also used:

RNAscope® multiplex fluorescent detection reagents v2 (Cat#: 323110; lot# 2014906)

RNAscope® hydrogen peroxide (Cat#322335; lot#2015184)

RNAscope® protease IV (Cat#322336; lot#: 2015288)

Images were acquired with Zeiss LSM700 confocal microscope and the Zen2012 software with 10X (Plan-Apochromat 10x/0.45) objective. The Diode555, Diode405-5 Diode488 and Diode639 excitation lasers were directed through a photomultiplier tube (LSM, Carl Zeiss). Tile scan stitching was performed with Zen 2012 software and image processing was performed with Image J/Fiji software (version 1.53 for Mac; Java 1.8.0_172). Images were processed by using Fiji functions of splitting channels, contrast enhancement, merging channels, rotating images, and adding scale bar.

Bulk SS3-based VDJ library preparation (Bulk SS3 VDJ)

We modified the recently described Smart-seq3 (SS3) method (*27*) to accommodate the use of low concentrations (10 to 100 ng) of purified RNA as the input (as opposed to single cells) and the use of many replicates to reduce amplification biases. This method will amplify UMI-barcoded IG and TR cDNA using primers directed to constant regions and a universal sequence 5′ of the UMI region, similar to the 10x Genomics VDJ 5′ protocol. We first lysed each selected fresh-frozen tonsil tissue sections and isolated total RNA. We then performed reverse transcription and amplification following the Smart-seq3 protocol to generate cDNA libraries for each section. After bead purification, those libraries were split to amplify IG or TR amplicons by target-specific primers (forward: universal sequence introduced by a template-switching step; reverse: constant region-specific primers for TR or IG), followed up by bead purification. A second PCR (with constant primers binding closer to the CDR3) with subsequent bead purification was then performed for both IG and TR amplicons to shorten the 3′ end of each amplicon for Illumina sequencing of the internal VDJ recombinant sequence (CDR3). Individual samples were indexed and pooled for sequencing by the National Genomics Infrastructure, SciLifeLab (Solna). Detailed descriptions for this method can be found in the section labeled "Bulk SS3-based VDJ library preparation (Bulk SS3 VDJ)" in the Supplementary Materials file.

Cell processing for single-cell RNA sequencing

Single-cell suspensions from separate breast tumor regions (P1, $n = 5$; P2, $n = 4$) were prepared by enzymatic tissue dissociation using the human Tumor Dissociation Kit (Miltenyi Biotec, 130-095-929) and gentleMACS dissociator (Miltenyi Biotec). Cell suspensions were stained with the Zombie Aqua Fixable viability dye (Biolegend, 423101) at room temperature for 20 min, then washed with phosphate buffered saline (PBS). The cells were incubated with Human TruStain Fc block (Biolegend, 422302) for 10 min to limit nonspecific antibody binding, then stained for 20 min with anti-CD45 (1:40, Biolegend, 304021), anti-EPCAM (1:40, Biolegend, 324206) and cell hashing TotalSeq-C antibodies (Biolegend; 394661, 394663, 394665, 394667, 394669) in fluorescence-activated cell sorting (FACS) buffer (PBS + 0.5% bovine serum albumin). Each tumor region was labeled with a unique TotalSeq-C antibody to enable pooling all tumor regions into one sample for single-cell gene expression and VDJ analysis. The cells were subsequently washed and resuspended in FACS buffer. FACS was performed using an influx flow cytometer (BD Biosciences) to sort live $EPCAM^{-}CD45^{+}$ single cells for 10x Genomics Chromium Single Cell gene expression analysis. At least 2.5×10^4 to 3×10^4 cells were sorted per tumor region and all tumor regions for each patient were sorted into the same tube. Single-stain controls (cells and beads) and fluorescence minus one (FMO) controls—containing all the fluorochromes in the panel except the one being measured—were used to set voltages and to define the proper gating strategy.

10x Genomics Chromium Single-Cell library preparation and sequencing

Single-cell gene expression (GEX), VDJ clonotype, and feature barcoding libraries were generated from $EPCAM^{-}CD45^{+}$ cells using the 10x Genomics Chromium Single Cell 5′ assay, following the manufacturer's instructions. Libraries were profiled and quantified using a Bioanalyzer High Sensitivity DNA kit (Agilent Technologies) and Qubit High sensitivity kit (ThermoFischer Scientific). Final single-cell gene expression libraries were sequenced (30,000 reads per cell for GEX; 4000 to 6000 reads per cell for VDJ clonotype, and 4000 to 5000 reads per cell for feature barcode libraries) on a NovaSeq 6000 SP flowcell (Illumina, 150-8-8-150 read setup) by the National Genomics Infrastructure, SciLifeLab (Solna).

Data processing of Spatial GEX libraries

Following demultiplexing of bcl files, read 2 fastq files were trimmed using Cutadapt (*28*) to remove full-length or truncated template switch oligo (TSO) sequences from the 5′ end (beginning of read 2) and polyA homopolymers from the 3′ end (end of read 2). The TSO sequence (AAGCAGTGGTATCAACGCAGAGTACATGGG) was used as a non-internal 5′ adapter with a minimum overlap of 5, meaning that partial matches (up to five base pairs) or intact TSO sequences were removed from the 5′ end. The error tolerance was set to 0.1 for the TSO trimming to allow for a maximum of 3 errors. For the 3′ end homopolymer trimming, a sequence of 10 As was used as a regular 3′ adapter to remove potential polyA tail products regardless of its position in the read, also with a minimum overlap of five base pairs. The trimmed data were processed with the Space Ranger pipeline (10x Genomics), version 1.2.1 (tonsil) and version 1.0.0 (BC) and mapped to the GRCh38 v93 genome assembly.

Long-read sequencing analysis (LR Spatial VDJ)

The input to the analysis was demultiplexed consensus reads from the long-read Pacbio sequencing. The analysis was performed using Python programming language, see the Zenodo repository (*29*): scripts/functions/long-read-processing-STAR-paper-main.zip. Scripts are also available on GitHub (*30*). First, the fastq files were parsed into a dataframe with readID, sequence, and quality columns. Second, we searched for the Truseq adapter and the TSO sequence to anchor the ends of each read and discarded the reads that lacked these sequences. Third, we searched for the pattern "CGACGCTCTTCCGATCT" which is part of the Truseq adapter starting in the first seven bases of either the read or its reverse complement. If any of the positions matched the sequence with hamming distance of one or less, we marked it. We did the same for the TSO sequence ("TCTGCGTTGATACCACT"). We reverse-complemented the reads as needed so that all the reads have the Truseq adapter at the beginning and the TSO at the end. We identified the spatial barcode and the UMI by obtaining the first 16 bases following the Truseq adapter for the spatial barcode and the 12 bases following that as the UMI. We made sure that the following four bases were all T's and filtered out the reads that had any other bases in that interval. The most common UMI was a polydT, which was considered an artifact. Those reads were consequently

removed. We also defined the end of polyT region as the first matching position for the pattern "[^T]T{0,2}[^T]T{0,2}[^T]" after 28 bases after the end of the Truseq adapter location.

LR Spatial VDJ clonotype analysis

To run MiXCR (version 3.0.3), we trimmed the polyT and TSO and wrote the reads to a new fastq file. We used MiXCR (*31*) with this command:

mixcr analyze shotgun -s hsa–align -OsaveOriginalReads=true–starting-material rna <TrimmedFastq> <SampleName>

We then ran another MiXCR command to report alignments for each read:

mixcr exportAlignments -f -cloneIdWithMappingType -cloneId -readIds -descrsR1 <SampleName>.clna <ReportFile>

We then used the resulting tabular file to assign the reads to the clonotypes in MiXCR output. To use UMIs, we filtered out reads that did not map to any clone (cloneId == −1), then grouped the reads table by the Visium barcode and UMI and counted how many reads they have and how many clones were associated with each UMI. We filtered out UMIs that had been assigned to more than one clonotype, as they were likely due to PCR or sequencing errors. A count matrix (clone ID × spatial barcode) was generated and merged to the clone list exported by MiXCR. After removing spots outside the tissue section (as is standard for the Space Ranger pipeline), we imported the gene expression cluster and follicle annotations in R (version 4.2.0), then calculated UMI, spatial barcode, and overlaps among different clusters, follicles, and sections. Script for clone analysis can be found in the Zenodo repository (*29*): tonsil: scripts/tonsil/1_LR-SpatialVDJ/tonsil LR clonotype analysis.Rmd; breast cancer: scripts/breast_cancer/1_LR-SpatialVDJ/BC LR clonotype analysis.Rmd.

SR Spatial VDJ clonotype analysis

To preprocess short-read sequences, we modified the example workflow of "UMI Barcoded Illumina MiSeq 325+275 paired-end 5′ RACE BCR mRNA" from pRESTO (version 0.6.2, Immcantation group) (*32*). Reads with less than 20 Phred quality scores were regarded as low-quality sequences and were removed. Then, we removed reads that lacked a valid spatial barcode by comparing the reads to the Visium barcode list. We only kept the reads that included the "inner V" primer sequences used in the second step of the *TRA* and *TRB* seminested PCR enrichment steps. Input fastq files that included more than 13 million were downsampled to 13 million reads by SplitSeq.py samplepair, owing to the platform limitation (downsample rate: 0.76-0.94). To have a more accurate UMI collapsing result, we regarded both the UMI and spatial barcode sequence as the "UMI" region in the pipeline. We selected UMIs with at least three reads per group in tonsil for repertoire analysis.

We merged all reads from different tonsil sections and used MiXCR (version 3.0.13) with the following commands:

mixcr analyze amplicon–library repseqio.v1.5–species hsa–starting-material rna–5-end no-v-primers–3-end c-primers–adapters adapters-present–align "-OsaveOriginalReads=true"–assemble "–write-alignments" <R1Fastq> <R2Fastq> <SampleName>

To report the alignments for each read, we further ran the MiXCR command:

mixcr exportAlignments -cloneId -descrsR2 -targetSequences -nFeature CDR3 -jGene <SampleName.clns> <SampleName.tsv>

We then used customized R scripts to create the clonal UMI count matrix for each tonsil section (R version 4.2.0). The exported UMI collapsed reads that lacked a valid CDR3 call from MiXCR output, did not map to any clone (cloneId == −1), or had fewer read counts than three reads per UMI were removed. We observed some cases of index hopping (i.e., where individual UMI collapsed reads from different samples contained identical nucleotide CDR3 sequence, J gene, spatial barcode, and UMI sequence). The clone that contained the most read count in its UMI group was considered the true UMI collapsed reads and the rest discarded. At these settings, we still observed a small number (1 to 4 per section) of TR clones with an unexpectedly high spatial barcode number per clone (that was not reproduced in the LR-Spatial VDJ data), suggestive of PCR overamplification and artifacts in spatial barcode region. We therefore removed those clones from further analysis. Section overlap was calculated the same way as we did for LR reads. Scripts can be found in the Zenodo repository (*29*): scripts/tonsil/2_SR-SpatialVDJ/tonsil SR-Spatial VDJ analysis.Rmd and scripts/tonsil/2_SR-SpatialVDJ/tonsil seminested TR on-off analysis.Rmd.

Visualization and analysis of spatial data

Gene expression data of tonsil #1

Two sets of tissue images, spatial coordinates, and count matrices generated through the Space Ranger (10x Genomics) pipeline were imported into R (version 4.0.5, R Core Team, 2017) using the InputFromTable() function of the STUtility package (*33*). For fig. S1C, when applicable, features were collapsed based on antigen receptor chain identity and visualized using the FeatureOverlay() function. Tonsil #1 Space Ranger output data can be found in the Zenodo repository (*29*): data/tonsil/5_spatial_GEX/spaceranger_output/. R script for reproducing figures in fig. S1: scripts/tonsil/5_spatial_GEX/tonsil1_GEX_v2.Rmd.

Spatial GEX and LR and SR Spatial VDJ tonsil and tumor data

Space Ranger output data were imported into R (version 4.0.5) as described in previous paragraphs. One Seurat object (*34*) per sample type or patient (tonsil, P1, and P2) was created using the STUtility package. For each dataset, genes were filtered for a minimum of 100 counts across the entire dataset and a minimum of five spots. Spots were also filtered based on the number of counts. Spots with at least 300 counts (P1) or 500 (tonsil and P2) were kept. To add clonotype data to the Seurat objects described above, the clonotype count matrices were modified to contain the same barcodes (bcs) as the gene expression count matrices. Accordingly, bcs absent in the gene expression count matrix (after filtering described above) were removed and only bcs present in the gene expression count matrix were added to the clonotype count matrix and filled with zeros for each clone. Finally, clonotype names were edited to include the first four letters from the "C hit" column of the MiXCR output, followed by "clone" and the number assigned by MiXCR. Each modified clonotype count matrix was then loaded as a new assay into its respective Seurat object (tonsil, P1, and P2), whereafter genes and clonotypes were visualized on the tissue images using built-in functions of the STUtility package. Scripts for generating all figure panels are listed as in the Zenodo repository (*29*): paths in data S5, and Seurat objects with descriptions can be found in:

Tonsil #2: data/tonsil/0_integrated/tonsil_-se_PartIV.rds

Breast Cancer Patient 1: data/breast_cancer/0_integrated/P2/BC_P1_PartIII.rds

Breast Cancer Patient 2: data/breast_cancer/0_integrated/P2/BC_P2_PartIII.rds

Normalization and clustering of GEX data

The gene expression data of tonsil, P1, and P2, respectively, were normalized across spots with Seurat SCTransform() function in R (version 4.0.5). Dimensionality reduction was performed with nonnegative matrix factorization by using STUtility RunNMF() function with 24 factors. These factors were subsequently used for clustering using Seurat FindNeighbors() function followed by Seurat FindClusters() at resolution 0.8.

For Tonsil #2, this strategy rendered 13 clusters, which were annotated and grouped based on shared gene expression and single cell deconvolution results from *stereoscope* (method described below). The cluster groups were consistent with known anatomical structures observed in H&E stains of each section. For follicle annotation on tonsil sections, each follicle or GC had to contain at least two spots belonging to at least one of the four clusters annotated as B cell follicle or GC cluster group (c1, 4, 5, or 7) and be found in at least two independent sections.

For P1 and P2 breast tumor samples, the strategy described above generated 18 and 12 clusters, respectively. Tumor areas were annotated based on gene expression cluster and single-cell deconvolution results per Spatial GEX cluster

from *stereoscope* (method described below) (*35*). All tumor clusters had enriched tumor-associated gene expression and cancer epithelial cell signatures. Cluster 13 (P1) exhibited a heterogeneous epithelial signal, with cancer and normal epithelial cell enrichment varying across sample regions. Due to the presence of cancer epithelial signature in at least one sampled region, it was denoted as "Tumor," but likely contained normal breast epithelial tissue as well. For P2, we identified four distinct tumor clusters, three of which were detected primarily within Region A (Tumor C3, C5, and C8). Tumor C3, C5, and C8 were all enriched for cancer cells, but exhibited differently enriched genes. Tumor C3 spots had elevated expression of genes involved in hormone-receptor signaling, including *TFF1* and *TFF3* (*36*), and expressed by breast glandular cells (e.g., *SCGB1D2* and *SCGB2A2*) (*37*–*39*). Conversely, Tumor C5 and C8 shared many enriched genes, including tumor-associated *S100A7-9*, *CD44*, and *PABPC1*, which are involved in cell migration, proliferation, and cell-to-cell interactions (*40*–*43*), as well as genes expressed by macrophages [e.g., *LYZ* and *APOE* (*44*)], including those infiltrating tumors. Based on the breast cancer spatial cluster annotation and border detection with STUtility RegionNeighbors() function, we adapted Seurat FindMarkers() function for calculating differentially expressed LR Spatial VDJ IG clones across regions. Specifically, we used the Poisson test, with a minimum of 0.2-fold difference and 0.01 as the minimum percentage of spots in an area expressing a clonotype. The latter parameter is drastically reduced from the default of 0.1, which is optimized for scRNA-seq analysis. We reasoned that spatial VDJ data should require a lower value to reveal clonotypes that are region-specific but only expressed in a minority of spots in that region. This workflow is provided as an R markdown file in the Zenodo repository (*29*): scripts/breast_cancer/0_integrated/IG_enrichment_BC_v1.Rmd. For script paths to all figure panels, see data S5.

We applied a previously developed script to analyze enrichment or depletion of the single-cell deconvolution analysis across Spatial GEX clusters (version used in this paper is in the Zenodo repository (*29*): scripts/functions/enriched-region-add-legend.py. Scripts are also available in the GitHub repository (*45*). In general, we calculated the average proportion of each cell type within the region as "true average". Then, we randomly shuffled the spatial barcodes of deconvolution results to assign a different region and calculated the "permuted average" of them. This shuffling and calculation were conducted 10000 times, and the mean value of difference divided by standard deviation was visualized as enrichment/depletion score. Script for generating input datasheet can be found in the Zenodo repository (*29*): scripts/tonsil/7_enrichment/tonsil enrichment analysis.Rmd; scripts/breast_cancer/8_enrichment/BC enrichment analysis.Rmd; scripts/breast_cancer/8_enrichment/bc enrichment depletion per clone.Rmd.

Single-cell deconvolution (*stereoscope*) analysis

We used the software *stereoscope* (v.0.3) to decompose the Spatial GEX profiles into contributions from specific cell types, also known as single-cell mapping (*35*). Stereoscope uses a probabilistic framework that models both single-cell and spatial transcriptomics data with a negative binomial distribution. In short, *stereoscope* first learns cell type and gene specific parameters from the single-cell data (where no mixing of cells occurs), to then use these parameters in a guided decomposition of the mixed gene expression profiles in the spatial transcriptomics data.

The input to *stereoscope* is the raw (unnormalized) single-cell UMI count data, cell type annotations, and raw (unnormalized) spatial transcriptomics UMI count data. The output from *stereoscope* is a [spot] × [cell type] matrix, where each element gives the proportion of cells at a given spot that belongs to a specific cell type. For more details we refer to the original *stereoscope* publication. In the supplementary materials, we outline the two analyses in more detail.

Single-cell gene expression and VDJ data processing

Sequencing outputs were processed by Cell Ranger (version 5.0, 10x Genomics) (*46*). Gene-barcode count matrices were analyzed with the Seurat package (version 4.0, Satija Lab) in R (version 4.0.1). Two steps of filtering were introduced here. First, raw gene expression matrices were subset by the barcode list in VDJ output, including B and T cell subsets. Based on the UMI count, gene count, and mitochondrial percentage of raw gene expression matrices and their subsets, each threshold was selected to keep the maximum count of high-quality cells and avoid losing B and T cells which have VDJ sequencing outputs. Second, feature barcodes are used for doublet detection and removal by the "Demultiplexing with hashtag oligos (HTOs)" workflow from Seurat. Specifically, doublets in each sample were detected by HTODemux() function and removed for the downstream analysis. Cutoffs for UMI and gene count, mitochondrial percentage and HTO threshold (positive.quantile) can be found in data folder deposited in the Zenodo repository (*29*): data/breast_cancer/3_single-cell_GEX/preprocessing_output. All samples were integrated and scaled into one count matrix by Seurat. Dimension reduction, UMAP generation, and clustering, were performed on the merged dataset by Seurat. The merged dataset was clustered by a gradient of the resolution, from 0.2 to 2. We chose 0.8 as the final resolution by comparing the top-listed differentially expressed genes in each cluster. Cell types were annotated by differentially expressed genes and their marker genes expression level. Our scRNAseq dataset also lacked neutrophils and eosinophils, which is a common occurrence in single cell RNAseq analysis and may be due to cell loss during tissue digestion (of note, neutrophils typically have a lower per cell UMI count, but we did not observe neutrophils even when lowering the UMI threshold during analysis). To further account for doublets after the first round of annotation, we removed T/NK cells that had BCRs, B cells that had TCRs, and cells from nonlymphocyte clusters that had either TCRs or BCRs in the single-cell dataset. We also removed potential doublets from B and T cell VDJ output by excluding cells with more than two pairs of chain. After quality filtering, only cells that met either one of these criteria were kept: only one *TRB* chain, one *TRA* and one *TRB* chain, or one *TRB* chain and two *TRA* chains. Then, we reanalyzed the single-cell dataset and created new UMAP coordinates, differential gene expression list, and cluster/subcluster annotation. We used the following parameters for generating breast cancer single-cell UMAP and cluster: runUMAP: dims = 1:15, n.neighbors = 25,min.dist = 0.2; findNeighbors: dims = 1:30; FindClusters: resolution = 0.8. For T cell subclustering, we used following parameters: runUMAP: dims = 1:10, n.neighbors = 30, min.dist = 0.2; FindNeighbors: dims = 1:10; FindClusters: resolution = 0.3. Scripts can be found in the Zenodo repository (*29*): scripts/breast_cancer/4_single-cell_GEX/BC single-cell new cluster.Rmd; scripts/breast_cancer/4_single-cell_GEX/single-cell clustering without integration.Rmd; scripts/breast_cancer/4_single-cell_GEX/single-cell GEX versus VDJ coverage.Rmd.

For additional VDJ clonotype quality filtering and to calculate the clonal overlap with the Spatial VDJ output (defined by MiXCR), cells that belonged to different clones from Cell Ranger VDJ output but with identical nucleotide CDR3 sequence and J gene in both receptors (i.e., *TRA*/*TRB* in T cells, IG light chain/IG heavy chain in B cells, etc.) would be merged and assigned with a renamed clone ID by a customized R script, all cells within the new clone were assigned the minimum clone ID within the group. The T cells that had a single *TRB* sequence, which Cell Ranger had identified as separate clones, were merged to other clones expressing the matched *TRB* nucleotide CDR3 and J gene. We kept unmatched single chain *TRB* clones in the clonal list. In addition, we removed one potential doublet with cell barcode "TGCTACCGTTCAGGCC-4" by comparing its receptor chains to other cells in the same clone. All the dimension reduction and annotation results, along with the VDJ output files were imported into Loupe Browser (version 5.0, 10x Genomics) and Loupe VDJ Browser (version

4.0, 10x Genomics) for interactive analysis. Detailed code for VDJ clonotype quality filtering can be found in the Zenodo repository (*29*): scripts/breast_cancer/5_single-cell_VDJ/T_B cell VDJ analysis.Rmd.

Clonotype overlap analysis

To compare clonal lists from the MiXCR analysis result, including LR Spatial, SR Spatial, and Bulk SS3 VDJ, we used customized R script (R version 4.2.0) (Zenodo repository (*29*): scripts/tonsil/4_VDJ_overlap/tonsil overlap analysis.Rmd; scripts/tonsil/4_VDJ_overlap/tonsil LR-SR-bulk clonal overlap analysis.Rmd) and marked clones with identical nucleotide CDR3 sequence and J gene as the overlapped clones, which was consistent with the default components that MiXCR used for collapsing reads into clone. If multiple clones had identical nucleotide CDR3 sequence and J gene, we grouped them together as one overlapped case. To compare clonal lists from Cell Ranger VDJ (single-cell) and MiXCR (LR- and SR-Spatial VDJ) outputs, we analyzed the single-cell clone list with MiXCR output by matched nucleotide CDR3 sequence and J gene. We then calculated the percentage of LR Spatial VDJ clones that overlapped with other analysis methods. Clone fraction was calculated based on dividing each clonotype's UMI count with the total TR (*TRA* and *TRB*) or IG (*IGH*, *IGK*, and *IGL*) UMI count from either LR Spatial VDJ, SR Spatial VDJ, or bulk datasets. Detailed script can be found in the Zenodo repository (*29*): scripts/breast_cancer/6_VDJ_overlap/breast cancer LR single-cell VDJ overlap.Rmd;scripts/breast_cancer/6_VDJ_overlap/breast cancer single-cell VDJ clone overlap.Rmd.

Clonal evolution analysis

Preprocessing steps

For this analysis, we collapsed reads within the same UMI group to generate a consensus read by customized script in R (version 4.2.0). Individual reads from the same sample with identical UMI and spatial barcode were grouped by their full-length sequence. One or more read groups with the most abundant read count were selected. Then, we calculated the average sequencing quality score for each read group. First, we kept the read groups with the highest quality score. Second, if multiple groups were present, we selected the group with the longest sequence. Third, for the remaining read groups with identical length, average quality score, and read count, we masked the different bases between the groups as N and generated the final sequence for that UMI group. We then extracted the section information from the R1 header (descrsR1 column) from the reads alignment output, grouped reads by sections or replicates, and converted them to a count matrix (clone ID = row name; section number = column ID). Postfiltered LR Spatial VDJ reads were split into different segments including V, D, J, etc., by using anchor points ("refpoints" column) per sequence from the MiXCR alignment output. We referred to the anchor point definition and the script named "mixcr2imgt.py" from the Immcantation group to split LR-Spatial VDJ reads (*32*, *47*). Then, we loaded the read list into R and converted the column name to the Adaptive Immune Receptor Repertoire (AIRR) compatible format (*48*). We restricted our analyses to the heavy chain (*IGH*), as it should provide the richest clonal structure (*49*). IGH clones defined by MIXCR have unique CDR3 sequences, which separates closely related IGH clones that have undergone somatic hypermutation. To group the MIXCR-defined clones together to define "IGH clonal families", we adapted the instruction named "Clustering sequences into clonal groups" from the Immcantation group. We calculated the nearest neighbor distances (minimum normalized hamming distance) between the nucleotide junction sequence and selected 0.1 as the threshold according to their distribution for tonsil LR IGH clonal families. The CDR3 sequence contains the conserved cysteine and tryptophan/phenylalanine residues on its 5′ and 3′ side according to the AIRR standards documentation. However, the MiXCR results already included those two residues in the CDR3 sequence. Therefore, we simply renamed the nucleotide MiXCR CDR3 sequence to "junction". Finally, we grouped the IGH clones into IGH clonal families by "DefineClones.py" script from SHazaM (version 1.1.1, Immcantation group) (*47*). We extracted the IGH reads, removed the ones without a valid C region annotation, and excluded one read that had an IGLC alignment. The final read list was used for class-switching and lineage analysis. Script for this analysis can be found in the Zenodo repository (*29*): scripts/tonsil/1_LR-SpatialVDJ/tonsil LR clonal family analysis.Rmd and script for previously described steps can be found in scripts/tonsil/1_LR-SpatialVDJ/ tonsil LR read preprocessing.Rmd.

For the breast cancer samples, we defined the IGH clonal families only as the input data for receptor pairing (see section below on 'repair'). Here, we performed the same analysis as for the tonsil (described above) with the following thresholds (Patient 1: 0.1; Patient 2: 0.08).

IGH clonal family analysis

We imported the tonsil LR Spatial VDJ IGH clonal family read list and the STUtility object into the R (version 4.2.0), extracted gene expression cluster and follicle annotation and merged them into the read list. For follicle analysis (detailed script can be found in the Zenodo repository (*29*): scripts/tonsil/1_LR-SpatialVDJ/tonsil LR clonal family analysis.Rmd), we determined the follicle count per clonal family by counting distinct follicle ID per clone. Then, we converted all follicles as "in" to define intrafollicular IGH clonal families. We grouped reads by follicle to calculate follicle stats including UMI count, spatial barcode count, clonal family count and their ratio. To describe the expansion level within each follicle, we ranked the follicles for each clonal family based on the max UMI percentage and extracted the value per follicle. We used vdjtools to calculate IGH clonal family diversity measures (*50*, *51*), including Chao1 estimate (*52*), Inverse Simpson index, and Shannon Entropy (script for this process can be found in in the Zenodo repository (*29*): scripts/tonsil/1_LR-SpatialVDJ/vdjtools_stats.sh). The D50 diversity index (defined as the minimum number of UMI needed to reach 50% of the total clone sequences) was calculated manually (*53*, *54*). To compare IGH clonal families with different spatial distributions, we divided IGH clonal families into "restricted" versus "nonrestricted" using the following thresholds:

- Restricted IGH clonal families: more than 75% of its UMI count belonged to a single follicle.
- Nonrestricted IGH clonal families: less than or equal to 75% of its UMI count belonged to a single follicle and at least 25% of its total UMI belonging to its second largest follicle.

We only considered expanded IGH clonal families for this analysis (defined as having at least 20 UMI in total and being present in at least 10 spatial barcodes across all replicate tonsil sections).

To determine the IGH clonal family isotype fraction, we selected the dominant isotype (with the highest UMI) per clone family, since some of them had multiple isotypes per family. The number of IGH clonal families with or without multiple isotypes were also calculated. Script for this analysis can be found in the Zenodo repository (*29*): scripts/tonsil/1_LR-SpatialVDJ/tonsil follicle distribution.Rmd.

Class-switch recombination analysis

To analyze class-switching events, we used R (version 4.2.0) and removed *IGHGP* and *IGHD* reads from the tonsil LR Spatial VDJ IGH clonal family read list because *IGHGP* is a pseudogene and *IGHD* is regarded as an alternative splicing result from *IGHM*. B cells that exclusively express *IGHD* as a result of a "true" class-switching event are most often rare, but can occur in mucosal tissues, including the tonsil (*11*, *55*, *56*). However, we detected very few clones with IGHD as the dominant isotype. Therefore, we concluded that this individual had few, if any, true IGHD class-switched clones, and these were not investigated further for the purpose of class-switching. We also removed IGH clonal families with less than two reads since they would not contain class-switching events. We grouped reads within each clonal family by follicle, cluster, or spatial barcode, and extracted class-switched reads within the samples. Putative class switch recombination events (pCSR) were defined as two sequences with identical V

gene sequences with two different IGH constant chains/isotypes colocalizing in the same spatial barcode. For reads with identical V sequences within an IGH clonal family, we allowed one hamming distance in the nucleotide CDR3 sequence within an IGH clonal family (1 of 17 pCSR events). The script for this analysis can be found in the Zenodo repository (*29*): scripts/tonsil/8_IGH_clonal_evolution/tonsil LR IGH class-switching analysis.Rmd.

Lineage relationship analysis

To create lineage trees with SHazaM (Immcantation group) (*47*) in R (version 4.2.0), we imported the tonsil LR Spatial VDJ IGH clonal family read list and removed the reads that lacked a valid CDR3 sequence or contained indel(s) in the V sequence compared with the reference. We recovered the reference sequence based on the mutation patterns from the "bestVAlignment" column and inserted IMGT gaps. Then, we removed the reads that did not have a valid junction length (not divisible by 3, which potentially represented a frame-shift mutation). To create the lineage tree and assign unique subclone IDs to each node, we followed the vignettes of "Lineage reconstruction" in Alakazam (version 1.2.0, Immcantation group) (*47*) with phylip (version 3.697, J. Felsenstein) for creating lineage trees (*57*). Each node of the tree (hereafter referred to as "subclone") represented a distinct V sequence versus the others and the size of the node is proportional to the number of UMIs belonging to that node. We traversed the lineage tree through depth-first search to assign adjacent ID to closely related subclones. We then plotted lineage trees and exported count matrices for visualizing nodes within the tissue section. We also matched the spatial barcodes to their follicle and cluster identity. Finally, we generated all possible trees and created the clone family subclones versus spatial barcode count matrix for statistical analysis and spatially visualization. The script for this analysis can be found in the Zenodo repository (*29*): scripts/tonsil/8_IGH_clonal_evolutiontonsil LR IGH lineage analysis.Rmd.

Visualizations of IGH clonal families and subclones on tissue

Count matrices of IGH clonal families and subclones were imported into R (version 4.0.5) and added to the tonsil object as new assays. To generate aligned x and y coordinates of all six tonsil sections, and enable plotting of all data jointly, we used the functions MaskImages() and AlignImages() of the STUtiliy package. Next, all nonzero observations of an IGH clonal family or subclone were plotted and colored by tissue section on a transparent background. The same IGH clonal family or subclone was then visualized on one of the sections using the STUtility FeatureOverlay() function. The joint data image was superimposed on the tissue image and aligned by matching shared spots in the two image types using Adobe Illustrator. Details on how these plots were generated are provided in the Zenodo repository (*29*): /scripts/tonsil/0_integrated/IGHfam_subclones_v2.Rmd. For script paths to all figure panels, see data S5

Association between single-cell deconvolution data and IGH clonal families in tonsil tissues

Given that $A \in R^{N*c}$ is the cell type proportion matrix, and $B \in R^{N*d}$ is the IGH clonal family matrix, where N is the total number of spots, c is the number of cell types and d is the number of selected IGH families. In this study, we removed the spots that were expressed as 0 on all selected IGH families. Thus, N = 2047, d = 71, and c = 30. The associations between cell subsets and 30 IGH families in tonsil tissue was defined as follows

$$Score = B^T A$$

The final normalized score was defined as the z-score of the quartiles of the association score on the null model (generated by 5000-times sample-wise permutation). P values were corrected using the Benjamini-Hochberg procedure. The script for this analysis was generated in R (version 4.2.2) and can be found in the Zenodo repository (*29*): scripts/tonsil/1_LR-SpatialVDJ/IGHfam_Celltype_Association.Rmd.

Pairing IG receptor chains with repair

Repair analysis workflow

For pairing receptor chains, we filtered the LR Spatial VDJ count matrix to include all IGL and IGK clonotypes, but to simplify the pairing, only one IGH clonotype per IGH clonal family (the one with highest counts), since multiple IGH chains could pair with a single light chain due to somatic hypermutation. The resulting count matrix was used as input in repair (see below for details, deposited in the Zenodo repository (*29*): scripts/functions/star-repair-master.zip. Scripts are also deposited on GitHub (*58*), which is a method that we developed for pairing of receptor chains. Different values of spot and pairing score cut-offs were used to find the threshold that would generate the highest number of correct pairs and minimum number of incorrect pairs. A predicted pair was assigned as correct only if the two chains were a verified pair in the ground truth scVDJ dataset (which contained only pairs where both chains overlapped in both the spatial and single cell VDJ datasets), and incorrect if any of the chains were paired with another chain in the ground truth dataset.

The following command was used to run repair:

repair analyze -i [path_to_input] -o [path_to_output] -ap "^(IGH)" -bp "^(IGL)|^(IGK)" -mxo [cut_off_value] -x 1 -b 100 -nb 1

For each sample (P1 and P2), repair was executed with different values (1, 5, 10, 15, and 20) for -mxo (minimum number of spots). Further details as well as input files and results are provided in the Zenodo repository (*29*): data/breast_cancer/10_repair/repair_run.

The repair method

As discussed above, repair was developed for unsupervised pairing of the receptor chains. In this method, we consider the task of pairing the different chains as an optimization problem. Below we elaborate on the details of this problem:

If $A \in R^{NxC_a}$ is the normalized expression matrix for the chains of type a, and $B \in R^{NxC_b}$ is the equivalent matrix for chains of type b, then we want to find a matrix $M \in R_+^{C_a x C_b}$ and scalar $g \in R_+$ such that $A = gBM^T$. Here, N represents the number of observations, and the number of a type chains and b type chains are given by C_a and C_b respectively. M can be considered as a "mapping matrix" between chains of type b to chains of type a. In layman's terms, element (i,j) in M tells us how much of chain b_j contributes to chain a_i's expression, once we've accounted for the difference in abundance between the different chain types (taken care of by g). The scaling factor is taken as a scalar, shared across all chains, an assumption that equates to assuming that the difference in abundance between chains of type a and b is not influenced by the chains' identities.

During optimization we do not immediately learn the parameters M and g but rather the matrix Q and scalar p which relates to the former accordingly

$$M_{ij} = \frac{pow(c, Q_{ij})}{\sum_k pow(c, Q_{ik})} \text{ and } g = exp(p)$$

Where $pow(c,x) = c^x$. Hence, M is the row-wise generalized softmax (if $c = e$, then this equals the standard softmax) of Q, meaning that $M_{ij} \in (0,1)$. There are two benefits to using the (generalized) softmax function: (i) it allows us to interpret the element M_{ij} as the probability that chain b_j is paired with chain a_i, and (ii) the larger the value of the base c, the more focused the probability mass will be on a single value. The second feature is considered as a benefit since it favors sparse mapping from chains of type b to chains of type a, i.e., one b chain dominates the explanation of one a chain's expression; notably, the same b chain can map to multiple a chains.

Thus, the final optimization problem becomes: $\min_{g,M} ||A - gBM^T||^2$, with g and M defined as above. To solve this, we use stochastic optimization (Adams optimizer), implemented using the *jax* python package (v.0.3.1).

Once an optimal solution to M is found, as a pruning step, we formulate an unbalanced linear assignment problem (LAP) where we

negate this M and use the result as our cost matrix. This generates a bijective (one-to-one) pairing between a subset of all chain types of a and b (if $C_a > C_b$ each b chain will be paired to an a chain, but not every a chain will be paired with a b chain, and vice versa for $C_a < C_b$. If $C_a = C_b$, then each a chain and b chain will be assigned a partner). See the Zenodo repository (*29*): scripts/functions/star-repair-master.zip. Scripts are also available on GitHub (*58*).

Statistical analysis and figure presentation

Data was processed using R, Python, and Microsoft Excel for Microsoft 365 (version 16.76). For R and Python versions, see details under the correct subheading for each analysis. Statistical analyses were performed and figures were prepared using R, GraphPad Prism (version 9.4.01), and Keynote (version 11.2). The experimental outlines in Fig. 1A, Fig. 3A, and fig. S3A were prepared by graphic designer M. Karlén. Other illustrations were prepared in Keynote or Adobe Illustrator by the authors.

REFERENCES AND NOTES

1. W. H. Hudson, L. J. Sudmeier, Localization of T cell clonotypes using the Visium spatial transcriptomics platform. *STAR Protoc.* **3**, 101391 (2022). doi: 10.1016/j.xpro.2022.101391; pmid: 35707680
2. S. Liu *et al*., Spatial maps of T cell receptors and transcriptomes reveal distinct immune niches and interactions in the adaptive immune response. *Immunity* **55**, 1940–1952.e5 (2022). doi: 10.1016/j.immuni.2022.09.002; pmid: 36223726
3. R. J. Bende *et al*., Germinal centers in human lymph nodes contain reactivated memory B cells. *J. Exp. Med.* **204**, 2655–2665 (2007). doi: 10.1084/jem.20071006; pmid: 17938234
4. A. Pelissier *et al*., Convergent Evolution and B-Cell Recirculation in Germinal Centers in a Human Lymph Node. bioRxiv 2022.11.09.463832 [Preprint] (2022); https://doi.org/10.1101/2022.11.09.463832.
5. M. Meylan *et al*., Tertiary lymphoid structures generate and propagate anti-tumor antibody-producing plasma cells in renal cell cancer. *Immunity* **55**, 527–541.e5 (2022). doi: 10.1016/j.immuni.2022.02.001; pmid: 35231421
6. P. L. Ståhl *et al*., Visualization and analysis of gene expression in tissue sections by spatial transcriptomics. *Science* **353**, 78–82 (2016). doi: 10.1126/science.aaf2403; pmid: 27365449
7. A. A. Tu *et al*., TCR sequencing paired with massively parallel 3′ RNA-seq reveals clonotypic T cell signatures. *Nat. Immunol.* **20**, 1692–1699 (2019). doi: 10.1038/s41590-019-0544-5; pmid: 31745340
8. M. Singh *et al*., High-throughput targeted long-read single cell sequencing reveals the clonal and transcriptional landscape of lymphocytes. *Nat. Commun.* **10**, 3120 (2019). doi: 10.1038/s41467-019-11049-4; pmid: 31311926
9. J. Stavnezer, J. E. J. Guikema, C. E. Schrader, Mechanism and regulation of class switch recombination. *Annu. Rev. Immunol.* **26**, 261–292 (2008). doi: 10.1146/annurev.immunol.26.021607.090248; pmid: 18370922
10. A. Andersson *et al*., Spatial deconvolution of HER2-positive breast cancer delineates tumor-associated cell type interactions. *Nat. Commun.* **12**, 6012 (2021). doi: 10.1038/s41467-021-26271-2; pmid: 34650042
11. H. W. King *et al*., Single-cell analysis of human B cell maturation predicts how antibody class switching shapes selection dynamics. *Sci. Immunol.* **6**, eabe6291 (2021). doi: 10.1126/sciimmunol.abe6291; pmid: 33579751
12. J. G. Cyster, Chemokines, sphingosine-1-phosphate, and cell migration in secondary lymphoid organs. *Annu. Rev. Immunol.* **23**, 127–159 (2005). doi: 10.1146/annurev.immunol.23.021704.115628; pmid: 15771568
13. W. H. Fridman, F. Pagès, C. Sautès-Fridman, J. Galon, The immune contexture in human tumours: Impact on clinical outcome. *Nat. Rev. Cancer* **12**, 298–306 (2012). doi: 10.1038/nrc3245; pmid: 22419253
14. C. M. Laumont, A. C. Banville, M. Gilardi, D. P. Hollern, B. H. Nelson, Tumour-infiltrating B cells: Immunological mechanisms, clinical impact and therapeutic opportunities. *Nat. Rev. Cancer* **22**, 414–430 (2022). doi: 10.1038/s41568-022-00466-1; pmid: 35393541
15. C. Sautès-Fridman, F. Petitprez, J. Calderaro, W. H. Fridman, Tertiary lymphoid structures in the era of cancer immunotherapy. *Nat. Rev. Cancer* **19**, 307–325 (2019). doi: 10.1038/s41568-019-0144-6; pmid: 31092904
16. G. E. Phad *et al*., Clonal structure, stability and dynamics of human memory B cells and circulating plasmablasts. *Nat. Immunol.* **23**, 1076–1085 (2022). doi: 10.1038/s41590-022-01230-1; pmid: 35761085
17. T. N. Schumacher, R. D. Schreiber, Neoantigens in cancer immunotherapy. *Science* **348**, 69–74 (2015). doi: 10.1126/science.aaa4971; pmid: 25838375
18. G. D. Victora, M. C. Nussenzweig, Germinal Centers. *Annu. Rev. Immunol.* **40**, 413–442 (2022). doi: 10.1146/annurev-immunol-120419-022408; pmid: 35113731
19. L. Mesin *et al*., Restricted Clonality and Limited Germinal Center Reentry Characterize Memory B Cell Reactivation by Boosting. *Cell* **180**, 92–106.e11 (2020). doi: 10.1016/j.cell.2019.11.032; pmid: 31866068
20. B. J. Laidlaw, A. H. Ellebedy, The germinal centre B cell response to SARS-CoV-2. *Nat. Rev. Immunol.* **22**, 7–18 (2022). doi: 10.1038/s41577-021-00657-1; pmid: 34873279
21. K. Peng *et al*., Diversity in immunogenomics: The value and the challenge. *Nat. Methods* **18**, 588–591 (2021). doi: 10.1038/s41592-021-01169-5; pmid: 34002093
22. L. J. Sudmeier *et al*., Distinct phenotypic states and spatial distribution of $CD8^+$ T cell clonotypes in human brain metastases. *Cell Rep. Med.* **3**, 100620 (2022). doi: 10.1016/j.xcrm.2022.100620; pmid: 35584630
23. T. N. Schumacher, D. S. Thommen, Tertiary lymphoid structures in cancer. *Science* **375**, eabf9419 (2022). doi: 10.1126/science.abf9419; pmid: 34990248
24. V. Leko, S. A. Rosenberg, Identifying and Targeting Human Tumor Antigens for T Cell-Based Immunotherapy of Solid Tumors. *Cancer Cell* **38**, 454–472 (2020). doi: 10.1016/j.ccell.2020.07.013; pmid: 32822573
25. D. G. Schatz, Y. Ji, Recombination centres and the orchestration of V(D)J recombination. *Nat. Rev. Immunol.* **11**, 251–263 (2011). doi: 10.1038/nri2941; pmid: 21394103
26. M. M. Davis, P. J. Bjorkman, T-cell antigen receptor genes and T-cell recognition. *Nature* **334**, 395–402 (1988). doi: 10.1038/334395a0; pmid: 3043226
27. M. Hagemann-Jensen *et al*., Single-cell RNA counting at allele and isoform resolution using Smart-seq3. *Nat. Biotechnol.* **38**, 708–714 (2020). doi: 10.1038/s41587-020-0497-0; pmid: 32518404
28. M. Martin, Cutadapt removes adapter sequences from high-throughput sequencing reads. *EMBnet. J.* **17**, 10–12 (2011). doi: 10.14806/ej.17.1.200
29. C. Engblom *et al*., Spatial transcriptomics of B and T cell receptors uncovers lymphocyte clonal dynamics, version 2.0, Zenodo (2022); https://zenodo.org/record/7961605.
30. H. Toosi, *long-read-processing-STAR-paper*, Github (2022); https://github.com/HoseinT/long-read-processing-STAR-paper.
31. D. A. Bolotin *et al*., MiXCR: Software for comprehensive adaptive immunity profiling. *Nat. Methods* **12**, 380–381 (2015). doi: 10.1038/nmeth.3364; pmid: 25924071
32. J. A. Vander Heiden *et al*., pRESTO: A toolkit for processing high-throughput sequencing raw reads of lymphocyte receptor repertoires. *Bioinformatics* **30**, 1930–1932 (2014). doi: 10.1093/bioinformatics/btu138; pmid: 24618469
33. J. Bergenstråhle, L. Larsson, J. Lundeberg, Seamless integration of image and molecular analysis for spatial transcriptomics workflows. *BMC Genomics* **21**, 482 (2020). doi: 10.1186/s12864-020-06832-3; pmid: 32664861
34. T. Stuart *et al*., Comprehensive Integration of Single-Cell Data. *Cell* **177**, 1888–1902.e21 (2019). doi: 10.1016/j.cell.2019.05.031; pmid: 31178118
35. A. Andersson *et al*., Single-cell and spatial transcriptomics enables probabilistic inference of cell type topography. *Commun. Biol.* **3**, 565 (2020). doi: 10.1038/s42003-020-01247-y; pmid: 33037292
36. J. K. Perry, N. Kannan, P. M. Grandison, M. D. Mitchell, P. E. Lobie, Are trefoil factors oncogenic? *Trends Endocrinol. Metab.* **19**, 74–81 (2008). doi: 10.1016/j.tem.2007.10.003; pmid: 18054496
37. M. Karlsson *et al*., A single-cell type transcriptomics map of human tissues. *Sci. Adv.* **7**, eabh2169 (2021). doi: 10.1126/sciadv.abh2169; pmid: 34321199
38. Single cell type - SCGB1D2, The Human Protein Atlas; https://www.proteinatlas.org/ENSG00000124935-SCGB1D2/single+cell+type.
39. Single cell type - SCGB2A2, The Human Protein Atlas; https://www.proteinatlas.org/ENSG00000110484-SCGB2A2/single+cell+type.
40. M. Uhlén *et al*., Proteomics. Tissue-based map of the human proteome. *Science* **347**, 1260419 (2015). doi: 10.1126/science.1260419; pmid: 25613900
41. S100A8 protein expression summary, The Human Protein Atlas; https://www.proteinatlas.org/ENSG00000143546-S100A8.
42. CD44 protein expression summary, The Human Protein Atlas; https://www.proteinatlas.org/ENSG00000026508-CD44.
43. PABPC1 protein expression summary, The Human Protein Atlas; https://www.proteinatlas.org/ENSG00000070756-PABPC1.
44. R.-Y. Ma, A. Black, B.-Z. Qian, Macrophage diversity in cancer revisited in the era of single-cell omics. *Trends Immunol.* **43**, 546–563 (2022). doi: 10.1016/j.it.2022.04.008; pmid: 35690521
45. A. Andersson, *Cell type enrichment within spatial regions*, Github (2021); https://github.com/almaan/her2st/blob/master/scripts/enriched-region.py.
46. G. X. Y. Zheng *et al*., Massively parallel digital transcriptional profiling of single cells. *Nat. Commun.* **8**, 14049 (2017). doi: 10.1038/ncomms14049; pmid: 28091601
47. N. T. Gupta *et al*., Change-O: A toolkit for analyzing large-scale B cell immunoglobulin repertoire sequencing data. *Bioinformatics* **31**, 3356–3358 (2015). doi: 10.1093/bioinformatics/btv359; pmid: 26069265
48. J. A. Vander Heiden *et al*., AIRR Community Standardized Representations for Annotated Immune Repertoires. *Front. Immunol.* **9**, 2206 (2018). doi: 10.3389/fimmu.2018.02206; pmid: 30323809
49. J. Q. Zhou, S. H. Kleinstein, Cutting Edge: Ig H Chains Are Sufficient to Determine Most B Cell Clonal Relationships. *J. Immunol.* **203**, 1687–1692 (2019). doi: 10.4049/jimmunol.1900666; pmid: 31484734
50. M. Shugay *et al*., VDJtools: Unifying Post-analysis of T Cell Receptor Repertoires. *PLOS Comput. Biol.* **11**, e1004503 (2015). doi: 10.1371/journal.pcbi.1004503; pmid: 26606115
51. M. O. Hill, Diversity and evenness: A unifying notation and its consequences. *Ecology* **54**, 427–432 (1973). doi: 10.2307/1934352
52. A. Chao, C.-H. Chiu, Species richness: Estimation and comparison in *Wiley StatsRef: Statistics Reference Online* (Wiley, 2016), pp. 1–26; https://doi.org/10.1002/9781118445112.stat03432.pub2.
53. J. Han, Immunodiversity assessment method and its use, *World Patent* (2012); https://patentimages.storage.googleapis.com/15/3d/a3/fc66068d388212/WO2012097374A1.pdf.
54. Y. Yang *et al*., Distinct mechanisms define murine B cell lineage immunoglobulin heavy chain (IgH) repertoires. *eLife* **4**, e09083 (2015). doi: 10.7554/eLife.09083; pmid: 26422511
55. C. Gutzeit, K. Chen, A. Cerutti, The enigmatic function of IgD: Some answers at last. *Eur. J. Immunol.* **48**, 1101–1113 (2018). doi: 10.1002/eji.201646547; pmid: 29733429
56. B. S. Steiniger, L. Raimer, A. Ecke, B. A. Stuck, Y. Cetin, Plasma cells, plasmablasts, and $AID^+/CD30^+$ B lymphoblasts inside and outside germinal centres: Details of the basal light zone and the outer zone in human palatine tonsils. *Histochem. Cell Biol.* **154**, 55–75 (2020). doi: 10.1007/s00418-020-01861-1; pmid: 32172287
57. J. Felsenstein, PHYLIP - Phylogeny Inference Package (Version 3.2). *Cladistics* **5**, 164–166 (1989).
58. A. Andersson, *star-repair*, Github (2022); https://github.com/almaan/star-repair.

ACKNOWLEDGMENTS

We acknowledge M. Stoeckius, C. Gallant, and K. Pfeiffer at 10x Genomics, Inc., for resources and technical support; M. Karlén's graphical design; H. Lönnqvist, A. Mollbrink, S. Giatrellis, L. Larsson, J. Tanevski, L. Franzén, and L. Bergenstråhle for expert assistance; and Frisén, Lundeberg, and Sandberg lab members and G. Al-Eryani for critical feedback. **Funding:** This work was supported by the Swedish Research Council (201806217_VR) (J.La., J.F., and J.H.), the Swedish Cancer Society (J.F. and J.Lu.), the European Union's Horizon 2020 research and innovation program under the Marie Skłodowska-Curie Actions grant agreement no. 844712 (C.E.), and German state funds approved by the State Parliament of Baden-Württemberg for the Innovation Campus Health + Life Science Alliance Heidelberg Mannheim (C.L.). The authors acknowledge support from the National Genomics Infrastructure in Stockholm and Uppsala funded by Science for Life Laboratory, the Knut and Alice Wallenberg Foundation, the Swedish Research Council, and SNIC/Uppsala Multidisciplinary Center for

Advanced Computational Science for assistance with massively parallel sequencing and access to the UPPMAX computational infrastructure. **Author contributions:** Conceptualization: J.Mo., C.E., K.T., and J.F.; Methodology: C.E., K.T., Q.L., J.Mo., A.A., H.T., M.H.J., J.Lu., and J.F.; Data curation: K.T., Q.L., and C.E.; Formal analysis: C.E., K.T., Q.L., A.A., H.T., C.L., and S.S.; Funding acquisition: J.Mo., C.E., J.La., J.H., J.Lu., and J.F.; Investigation: C.E., K.T., Q.L., J.Mo, X.C., E.S., C.L., G.M., and M.H.J.; Project administration: C.E., K.T., and J.Mo.; Resources: M.J., J.Mi., J.H., J.La., J.Mo., J.Lu., and J.F.; Software: K.T., Q.L., A.A., C.L., and H.T.; Supervision: J.Mo., J.H., J.S.R, J.La., J.Lu., and J.F.; Validation: C.E., K.T., Q.L., and J.Mo.; Visualization: K.T., Q.L., and C.E.; Writing – original draft: C.E., K.T., Q.L., and J.Mo.; Writing – review and editing: all authors. **Competing interests:** C.E., K.T., J.Mo., J.F., J.Lu., and Q.L. are inventors on patent (US Patent no. US11692218B2) encompassing this work. C.E., K.T., Q.L., A.A., H.T., S.S., J.Mo., J.Lu., and J.F. are scientific consultants for 10x Genomics Inc, which holds IP rights to this spatial technology. J.F. and J.L. have stock options in 10x Genomics, Inc, and J.Mo. has stock in Pacific Biosciences. J.S.R. reports funding from GSK, Pfizer, and Sanofi and fees from Travere and Astex Therapeutics. The remaining authors declare no competing interests. **Data and materials availability:** All data, code, and images needed to reproduce the figures in the manuscript are deposited on Zenodo (*29*). References to data and code per figure panel are annotated in table S5. The sequencing data have been deposited at the European Genome-phenome Archive (EGA), which is hosted by the EBI and the CRG, under accession numbers EGAD00001011061 (breast cancer) and EGAD00001011062 (tonsil). **License information:** Copyright © 2023 the authors, some rights reserved; exclusive licensee American Association for the Advancement of Science. No claim to original US government works. https://www.science.org/about/science-licenses-journal-article-reuse. This research was funded in whole or in part by Swedish Research Council (201806217_VR) and the European Union's Horizon 2020 research and innovation program (844712). The author will make the Author Accepted Manuscript (AAM) version available under a CC BY public copyright license.

SUPPLEMENTARY MATERIALS

science.org/doi/10.1126/science.adf8486
Materials and Methods
Figs. S1 to S28
References (*59*–*66*)
MDAR Reproducibility Checklist
Data S1 to S5

Submitted 22 November 2022; accepted 23 October 2023
10.1126/science.adf8486

RESEARCH ARTICLE SUMMARY

ATMOSPHERE

Toward a Cenozoic history of atmospheric CO_2

The Cenozoic CO_2 Proxy Integration Project ($CenCO_2PIP$) Consortium

INTRODUCTION: Anthropogenic carbon dioxide (CO_2) emissions have driven an increase in the global atmospheric CO_2 concentration from 280 parts per million (ppm) before industrialization to an annual average of 419 ppm in 2022, corresponding to an increase in global mean surface temperature (GMST) of 1.1°C over the same period. If global CO_2 emissions continue to rise, atmospheric CO_2 could exceed 800 ppm by the year 2100. This begs the question of where our climate is headed. The geologic record is replete with both brief and extended intervals of CO_2 concentration higher than today and thus provides opportunities to project the response of the future climate system to increasing CO_2. For example, it has been estimated that global surface temperature 50 million years ago (Ma) was ~12°C higher than today, in tandem with atmospheric CO_2 concentrations some 500 ppm higher (i.e., more than doubled) than present-day values. Consistent with these estimates, Antarctica and Greenland were free of ice at that time. However, reconstructing these values prior to direct instrumental measurements requires the use of paleoproxies—measurable properties of geological archives that are closely, but only indirectly, related to the parameter in question (e.g., temperature, CO_2). To date, at least eight different proxies from both terrestrial and marine archives have been developed and applied to reconstruct paleo-CO_2, but their underlying assumptions have been revised over time, and published reconstructions are not always consistent. This uncertainty complicates quantification of the climate responses to the ongoing rise of atmospheric CO_2 concentrations.

RATIONALE: Although earlier studies have compiled published paleo-CO_2 estimates, those studies typically applied only limited proxy vetting, included estimates that were made before the proxies were sufficiently validated, and/or focused on only a subset of available proxy data. The international consortium of the Cenozoic CO_2 Proxy Integration Project ($CenCO_2PIP$) has undertaken a 7-year effort to document, evaluate, and synthesize published paleo-CO_2 records from all available archives, spanning the past 66 million years. The most reliable CO_2 estimates were identified, some records were recalculated to conform with the latest proxy understanding, age models were updated where necessary and possible, and data were categorized according to the community's level of confidence in each estimate. The highest-rated data were eventually combined into a reconstruction of the Cenozoic history o mospheric CO_2.

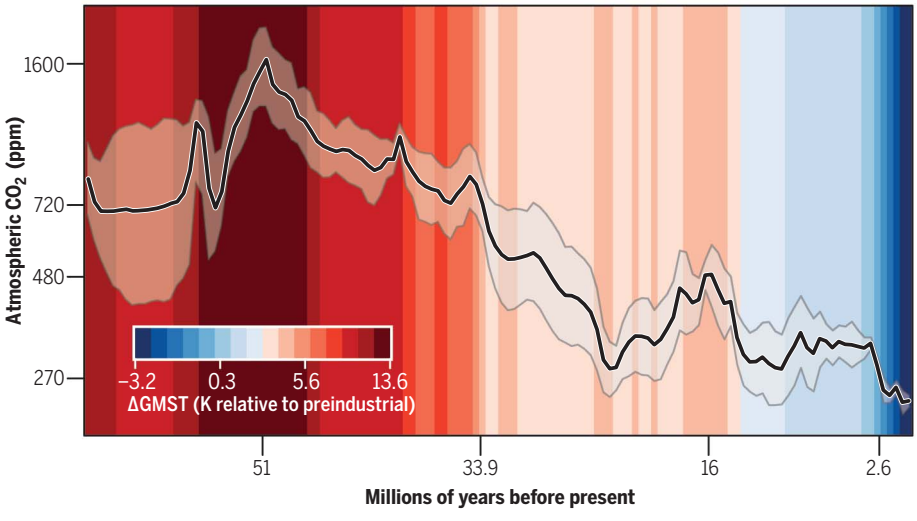

Community-vetted quantitative CO_2 record. Paleo-CO_2 (including 95% credible intervals) is superimposed on the GMST trend over the past 66 million years. Age and CO_2 labels highlight notable climate extrema and transitions as described in the text.

RESULTS: The resulting reconstruction illustrates a more quantitatively robust relationship between CO_2 and global surface temperature, yielding greater clarity and confidence than previous syntheses. The new record suggests that early Cenozoic "hothouse" CO_2 concentrations peaked around 1600 ppm at ~51 Ma. Near 33.9 Ma, the onset of continent-wide Antarctic glaciation coincided with an atmospheric CO_2 concentration of 720 ppm. By ~32 Ma, atmospheric CO_2 had dropped to 550 ppm, and this value coincided with the onset of radiation in plants with carbon-concentrating mechanisms that populate grasslands and deserts today. CO_2 remained below this threshold for the remainder of the Cenozoic and continued its long-term decrease toward the present. Along this trajectory, the middle Miocene (~16 Ma) marks the last time that CO_2 concentrations were consistently higher than at present; Greenland was not yet glaciated at that time, and independent estimates suggest that sea level was some 50 m higher than today. Values eventually dropped below 270 ppm at the Plio-Pleistocene boundary (2.6 Ma), when Earth approached our current "icehouse" state of bipolar glaciation. This and other climatic implications of the revised CO_2 curve, including the evolution of the cryosphere, flora, and fauna, along with the cross-disciplinary data assessment process, are detailed in the full online article.

CONCLUSION: This community-vetted CO_2 synthesis represents the most reliable data available to date and a means to improve our understanding of past changes in global climate and carbon cycling as well as organismal evolution. However, this effort is still incomplete. Data remain sparse during the earlier part of the record and in some instances are dominated by estimates from a single proxy system. Generating a paleo-CO_2 record with even greater confidence will require further research using multiple proxies to fill in data gaps and increase overall data resolution, resolve discrepancies between estimates from contemporaneous proxy analyses, reduce uncertainty of established methods, and develop new proxies. ■

The $CenCO_2PIP$ Consortium authors and affiliations are listed in the full article online.
Corresponding authors: Bärbel Hönisch (hoenisch@ldeo.columbia.edu); Dana L. Royer (droyer@wesleyan.edu); Daniel O. Breecker (breecker@jsg.utexas.edu); Gabriel J. Bowen (gabe.bowen@utah.edu); Pratigya J. Polissar (polissar@ucsc.edu); Andy Ridgwell (andy@seao2.org)
Cite this article as The $CenCO_2PIP$ Consortium, *Science* **382**, eadi5177 (2023). DOI: 10.1126/science.adi5177

READ THE FULL ARTICLE AT
https://doi.org/10.1126/science.adi5177

RESEARCH ARTICLE

ATMOSPHERE

Toward a Cenozoic history of atmospheric CO_2

The Cenozoic CO_2 Proxy Integration Project ($CenCO_2PIP$) Consortium*†

The geological record encodes the relationship between climate and atmospheric carbon dioxide (CO_2) over long and short timescales, as well as potential drivers of evolutionary transitions. However, reconstructing CO_2 beyond direct measurements requires the use of paleoproxies and herein lies the challenge, as proxies differ in their assumptions, degree of understanding, and even reconstructed values. In this study, we critically evaluated, categorized, and integrated available proxies to create a high-fidelity and transparently constructed atmospheric CO_2 record spanning the past 66 million years. This newly constructed record provides clearer evidence for higher Earth system sensitivity in the past and for the role of CO_2 thresholds in biological and cryosphere evolution.

The contribution of atmospheric CO_2 to Earth's greenhouse effect and the potential for variations in the global carbon cycle to cause climate change have been known for more than a century (*1*), but it was only in 1958 that direct measurements of the concentration of CO_2 in the atmosphere (or molar mixing ratio—the mole fraction of a gas in one mole of air) were systematically collected. Alongside reconstructions of the historical rise in Earth's surface temperature (*2*), this record has become one of the most influential and scientifically valuable environmental time series, documenting the continuous rise in annual mean CO_2 from 315 parts per million (ppm) in 1958 to 419 ppm in 2022 (*3*). Projecting beyond these records to estimate how Earth's climate will respond to further increases in CO_2 requires global climate models (*4*). However, despite successfully explaining observed historical climate change (*2*), models leave doubt as to whether global mean temperature will rise linearly as a function of future doubling of CO_2 (an invariant "climate sensitivity") or whether climate feedbacks will lead to an increasing (or "state-dependent") sensitivity of climate to CO_2 in the future (*5*, *6*).

We can turn to the geological record to help constrain models and improve our understanding of nonlinearities in the climate system (*7*), as it documents a variety of global climate changes and, critically, climate states warmer than today. Leveraging this record, however, requires the paired quantification of both past atmospheric CO_2 and temperature. In parallel with recent efforts to compile and vet paleotemperature estimates (*8*), here we focus on paleo-CO_2 estimates. Samples of ancient air can be extracted and analyzed from bubbles preserved in ancient polar ice (*9*, *10*), but continuous ice core records currently only extend our knowledge of CO_2 back about 800 thousand years (kyr) [for a compilation, see (*11*)], with isolated time slices extending to ~2 Ma (million years ago) (*12*, *13*). Importantly, at no point during the Pleistocene (2.58 Ma to 11,700 years ago) did CO_2 come close to present-day values (419 ppm in the year 2022), with 300 ppm being the highest value measured to date (*14*). In contrast, depending on the extent of future human emissions, atmospheric CO_2 could reach between 600 and 1000 ppm by the year 2100 (*2*). Feedbacks between changing climate and the carbon cycle may also amplify or diminish emissions from surficial carbon reservoirs (e.g., thawing permafrost, adjustments in size and composition of the terrestrial biosphere and marine carbon pool), creating additional uncertainty in future CO_2 projections (*15*, *16*). Past changes in CO_2 inherently include the role of these feedbacks, and their study could help reduce uncertainty in Earth system models (*17*).

A solid understanding of atmospheric CO_2 variation through geological time is also essential to deciphering and learning from other features of Earth's history. Changes in atmospheric CO_2 and climate are suspected to have caused mass extinctions (*18*, *19*) but also evolutionary innovations (*20*, *21*). During the Cenozoic, long-term declines in CO_2 and associated climate cooling have been proposed as the drivers of changing plant physiology (e.g., carbon-concentrating mechanisms), species competition and dominance, and, relatedly, mammalian evolution. A more refined understanding of past trends in CO_2 is therefore central to understanding how modern species and ecosystems arose and may fare in the future.

Extending the CO_2 record beyond the temporally restricted availability of polar ice requires the use of "proxies." In essence, a CO_2 proxy could be any biological and/or geochemical property of a fossil or mineral that responds to the concentration of ambient CO_2 when it is formed. Unfortunately, unlike in the case of bubbles of ancient air trapped in polar ice, this response is invariably indirect. The connection between a proxy signal and atmospheric CO_2 is often strongly mediated by biological "vital effects" (e.g., concentration of or discrimination against certain molecules, elements, or isotopes as a result of physiological processes such as biomineralization, photosynthesis, respiration), may be indirectly connected to the atmosphere through dissolution of carbon in seawater or lakes, may involve isotopic or other chemical fractionation steps, or a combination of these. When preserved in terrestrial or marine sediments, proxy substrates can also be affected by postdepositional (i.e., diagenetic) processes that must be accounted for. Relationships between proxies and CO_2 are typically calibrated using observations or laboratory experiments; in biological systems, these calibrations are often limited to modern systems (e.g., modern organisms or soils), and applications to the distant past focus on physiologically or physically similar systems preserved in the sediment and rock record (e.g., similar fossil organisms or fossil soils). Most CO_2 proxies also require estimation of one or more additional environmental parameters and hence depend on additional proxy records. The complexity of proxy-enabled paleoclimate reconstructions thus presents a major challenge for creating a self-consistent estimate of atmospheric CO_2 through geological time and requires careful validation.

One of the first paleo-CO_2 proxies to be devised is based on the observation that vascular plants typically optimize the density, size, and opening and closing behavior of stomatal pores on their leaf surfaces to ensure sufficient CO_2 uptake while minimizing water loss (*22*). A count of stomatal frequencies then provides a simple proxy for the CO_2 concentration experienced by the plant (*23*). Changes in ambient CO_2 can also drive a cascade of interrelated effects on photosynthesis, the flux of CO_2 into the leaf (largely determined by stomatal size and density), and the carbon isotopic fractionation during photosynthesis ($\Delta^{13}C$) (*22*–*24*). Despite lacking functional stomata, nonvascular plants such as liverworts also exhibit isotopic fractionation during photosynthesis, and their $\delta^{13}C$ values are thus similarly controlled by ambient CO_2. The list of terrestrial paleo-CO_2 proxies also includes inorganic carbonate nodules precipitated in ancient soils (i.e., paleosols) and sodium carbonate minerals precipitated in continental lacustrine evaporites. Whereas the paleosol proxy uses the carbon isotope composition of carbonate nodules and deconvolves the mixture of atmospheric and soil-respired CO_2 in soil porewaters using models of soil CO_2 (*25*, *26*), the nahcolite

*Corresponding authors: Bärbel Hönisch (hoenisch@ldeo.columbia.edu); Dana L. Royer (droyer@wesleyan.edu); Daniel O. Breecker (breecker@jsg.utexas.edu); Gabriel J. Bowen (gabe.bowen@utah.edu); Pratigya J. Polissar (polissar@ucsc.edu); Andy Ridgwell (andy@seao2.org)
†The $CenCO_2PIP$ Consortium authors and affiliations are listed at the end of this paper.

proxy is based on the CO_2 dependence of sodium carbonate mineral equilibria (*27*, *28*). Analogously to nonvascular plants on land, phytoplankton fractionate carbon isotopes during photosynthesis in response to the concentration of dissolved CO_2 in seawater, creating an isotopic signal stored in organic biomolecules that can be retrieved from ocean sediments (*29*). Boron proxies recorded in fossil shells of marine calcifying organisms are related to seawater pH, which in turn can be related back to atmospheric CO_2 (*30*, *31*). An in-depth discussion of the analytical details, entrained assumptions, and inherent uncertainties of currently available CO_2 proxies, plus summaries of recent advances and opportunities for further validation, is presented in the supplementary materials and in table S1.

Although each of these proxies has been validated extensively, comparing reconstructions from different proxies often reveals discrepancies. Compilations of paleo-CO_2 and explorations of the CO_2-climate linkage already exist (*32*–*34*); however, those studies apply limited proxy vetting, include CO_2 estimates that predate major innovations in some methods, and use rather basic data interpolation to assess broad CO_2 trends. Earlier CO_2 reconstructions are also often insufficiently constrained by ancillary data (e.g., concomitant temperature, isotopic composition of seawater or atmosphere) to be consistent with modern proxy theory, have incomplete or missing uncertainty estimates for CO_2 and/or sample age, and may exhibit fundamental disagreement with other proxies, leaving our current understanding of past CO_2 concentrations incomplete.

Here we present the results of a 7-year endeavor by an international consortium of researchers whose collective expertise spans the reconstruction of paleo-CO_2 from all available terrestrial and marine archives. We have jointly created a detailed, open-source database of published paleo-CO_2 estimates including all raw and ancillary data together with associated analytical and computational methods. Each record was vetted and categorized in view of the most recent proxy understanding, with calculations adopting a common methodology including full propagation of uncertainties. We focused our efforts on the Cenozoic, when the spatial distribution of continents and ocean basins, as well as the structure of marine and terrestrial ecosystems, was similar to modern times, yet profound changes in CO_2 and climate occurred. Identifying the most-reliable Cenozoic CO_2 estimates published to date allows us to quantify important physical (e.g., temperature, ice volume) and biological (i.e., physiological, ecosystem) thresholds and tipping points.

We structure this investigation as follows: First we summarize the methodology by which we assessed the CO_2 proxies and associated estimates. We then apply these methods to derive a series of paleo-CO_2 compilations composed of data with different levels of quality or confidence, and we statistically integrate the "top-tier" data to create a realization of the Cenozoic variability in atmospheric CO_2. This is followed by a discussion of the climatic implications (including climate sensitivity) of the paleo-CO_2 curve and a presentation of an evolutionary perspective. We finish with a road map for further advances in understanding past changes in atmospheric CO_2.

Critical assessment of atmospheric CO_2 proxies

The basis of our synthesis is a set of comprehensive data templates documenting all types of proxy data and their corresponding CO_2 estimates (a total of 6247 data points). The completed data sheets for each study can be accessed as the paleo-CO_2 "Archive" (https://www1.ncdc.noaa.gov/pub/data/paleo/climate_forcing/trace_gases/Paleo-pCO2/) in the National Oceanic and Atmospheric Administration's National Centers for Environmental Information (NOAA NCEI). These "Archive" sheets report all underlying data at face value from the original publications, but their unprecedented level of detail is designed to facilitate critical evaluation and recalculation of each CO_2 estimate.

From the "Archive," published CO_2 estimates were evaluated by teams of experts—often including the original authors of the respective data—who are active in validating and applying these proxies. No new proxy data were collected as part of this effort, but estimates were recalculated where needed and possible, and age models were revised where new evidence was readily accessible. Additionally, CO_2 and age uncertainties were updated, as necessary, to consistently reflect propagated 95% confidence intervals (CIs). The vetting criteria are summarized in table S1 and detailed in paleo-CO_2 "Product" sheets (https://www.ncei.noaa.gov/pub/data/paleo/climate_forcing/trace_gases/Paleo-pCO2/product_files/). These CO_2 estimates are categorized as follows: "Category 1" estimates (Fig. 1A; 1673 data points or ~27% of the original total) are based on data whose uncertainty is fully documented and quantifiable in view of current proxy understanding. "Category 2" estimates (Fig. 1B; 1813 data points) contain sources of uncertainty that are not yet fully constrained. These uncertainties vary between proxies and datasets and include, for example, insufficient replication, poorly constrained proxy sensitivity to parameters other than CO_2, or extrapolation of calibration curves. "Category 3" estimates (the residual 2761 data points, or ~44% of the Cenozoic paleo-CO_2 estimates published to date) are either superseded by newer, independently published evaluations from the same raw data or are considered unreliable owing to factors such as incomplete supporting datasets, which prevent full quantification of uncertainties, or outdated sample preparation methods.

Although objective criteria are applied throughout, the vetting process was particularly challenging for the paleosol- and phytoplankton-based proxies because multiple approaches are currently in use for interpreting these proxy data (*35*–*41*). Given the lack of a universally agreed-upon method, we compared multiple approaches for treating the data of these two proxies whenever possible. For the paleosol proxy, the greatest source of uncertainty is in the estimation of paleo-soil CO_2 concentration derived from respiration. Two different approaches are commonly used to estimate paleo-soil CO_2 concentration. The first method is based on proxy-estimated mean annual rainfall, whereas the second is based on soil order (i.e., the most general hierarchical level in soil taxonomy, comparable to kingdom in the classification of biological organisms). However, few records in the database allow for a direct comparison between the two approaches. An opportunity for comparison exists with two Eocene records (*37*, *42*), where recalculation using each of the two different methods leads to CO_2 estimates that do not overlap within 95% CIs for most stratigraphic levels (fig. S6). This implies that the uncertainty in estimating paleo-soil CO_2 concentration derived from respiration cannot be fully quantified with either of these approaches. Thus, most paleosol-based CO_2 estimates were designated as Category 2. For the phytoplankton proxy, routinely applied methods differ in how algal cell size and growth rate are accounted for, as well as the assumed sensitivity of algal $\delta^{13}C$ values to aqueous CO_2 concentration (see supplementary materials for details). Where data were available, we compared both newer and traditional methods, finding that although there are deviations between the resulting CO_2 estimates, they do agree within 95% CIs. We hence assign many phytoplankton CO_2 estimates to Category 1 and present mean CO_2 and uncertainty values that reflect the range of results from the different methods.

Toward a Cenozoic history of atmospheric CO_2

Our composite Category 1 and 2 realizations of Cenozoic CO_2 (Fig. 1, A and B) display much better agreement among proxies than does the raw, uncurated collection ("Archive," Fig. 1C). Encouragingly, objective criteria applied to the original data products automatically placed the earlier-reported estimates of "negative" CO_2, as well as some unusually high values, into Category 3, and without subjective intervention to otherwise filter them. We note that the Category 1 composite is now largely dominated by marine proxy estimates, with some intervals (e.g., the middle Paleocene, ~63 to

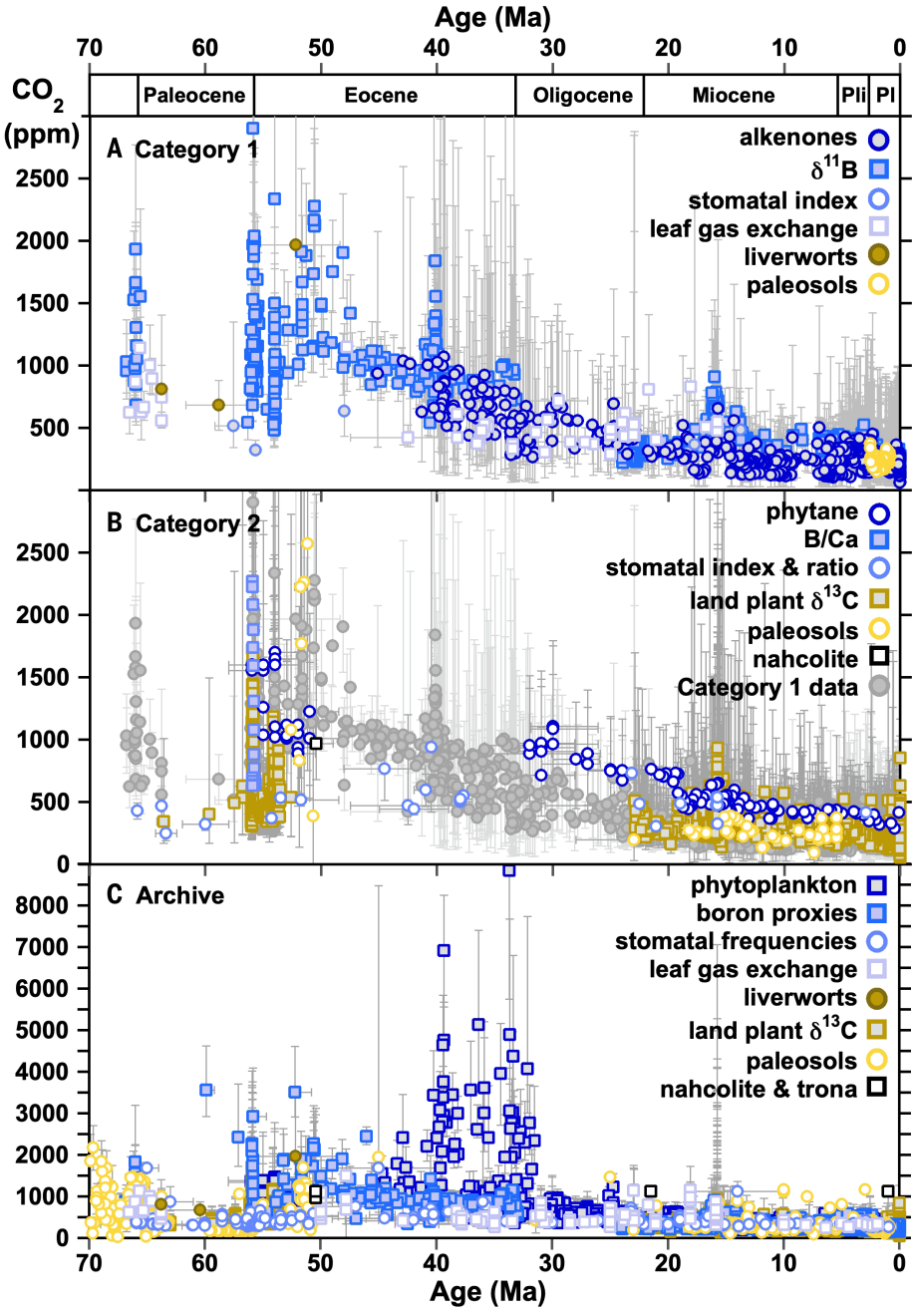

Fig. 1. Documentation and assessment of all Cenozoic paleo-CO_2 estimates published to date. Individual proxy estimates, as defined by the colored symbols in the legends. (**A**) Vetted Category 1 estimates with their fully developed uncertainty estimates (95% CIs); age uncertainties have been updated or established to the best of current understanding. (**B**) Vetted Category 2 estimates whose uncertainty is not yet fully constrained. Category 1 data are shown in gray for reference. (**C**) Archive compilation of all CO_2 estimates in their originally published quantification. To toggle view of individual proxy records in (A) and (C), please go to https://paleo-co2.org/. Pli, Pliocene; Pl, Pleistocene.

57 Ma) very sparsely sampled. Furthermore, some intervals (e.g., Oligocene, Miocene) still exhibit notable differences between proxies; for instance, marine-based CO_2 estimates start high and decline during the Oligocene (~34 to 23 Ma), whereas plant-based estimates suggest overall lower and constant CO_2 (Fig. 1A). Estimates of global temperature (Fig. 2B) during this time interval are largely invariant, which leaves us with the question of whether CO_2 and climate were decoupled during this interval, or whether there is a systematic bias in the marine or plant-based CO_2 proxies and/or in the temperature proxies. All proxy-based estimates become more uncertain further back in time as our knowledge of vital effects in biological proxy carriers, secular changes in the elemental and isotopic composition of ocean and atmosphere, and proxy sensitivity to environmental parameters that change along with CO_2 (e.g., temperature, rainfall; see supplementary materials for details) becomes less certain. In some cases, ancillary constraints and uncertainties are shared across multiple proxies (e.g., assumed atmospheric $\delta^{13}C$ is common to proxies based on land plant $\delta^{13}C$, leaf gas exchange, and paleosols), creating interdependence of estimates from seemingly independent proxies. More robust paleo-CO_2 reconstruction thus requires not only continued application of all proxies but also replication from different locations.

Although some uncertainties and proxy disagreements remain, the much-improved agreement within the vetted paleo-CO_2 compilation gives us confidence that a quantitative reconstruction of Cenozoic CO_2 based on the combined Category 1 data is possible. To do so, we statistically model mean CO_2 values at 500-kyr intervals, together with uncertainties in age and proxy CO_2 estimates (Fig. 2A; see supplementary materials for details). Our choice of a 500-kyr resolution interval reflects a compromise driven by the proxy data compilation. Although parts of the Cenozoic, particularly the Plio-Pleistocene, are sampled at higher temporal resolution, the density of records remains relatively sparse throughout much of the Paleogene (1 datum per 190 kyr on average). As a result, the data (and in some cases the underlying age models) are not suited to interpreting higher-frequency (e.g., Milankovitch-scale) variations in atmospheric composition, and we focus here on low-frequency (e.g., multimillion year) trends and transitions. Proxy sampling within some intervals may be biased toward conditions that deviate from the 500-kyr mean [most notably here, the Paleocene-Eocene Thermal Maximum (PETM)]. We do not attempt to remove this bias but instead recommend caution in interpreting any features expressed at submillion-year timescales.

This curve (Fig. 2A) allows us to constrain Cenozoic paleo-CO_2 and its uncertainty with greater confidence than earlier efforts. The highest CO_2 values of the past 66 Myr appear during the Early Eocene Climatic Optimum (EECO; ~53 to 51 Ma), whereas the lowest values occur during the Pleistocene. In contrast to earlier compilations, which suggested early Cenozoic CO_2 concentrations of <400 ppm (*33*), rigorous data vetting and newly published records place early Paleocene mean CO_2 in our reconstruction between 650 and 850 ppm. However, the Paleocene remains data-poor, and uncertainty in the curve remains large. Although the Paleocene record is predominantly based on the boron isotope proxy (Fig. 1A), inclusion of other (nonmarine) proxy data does

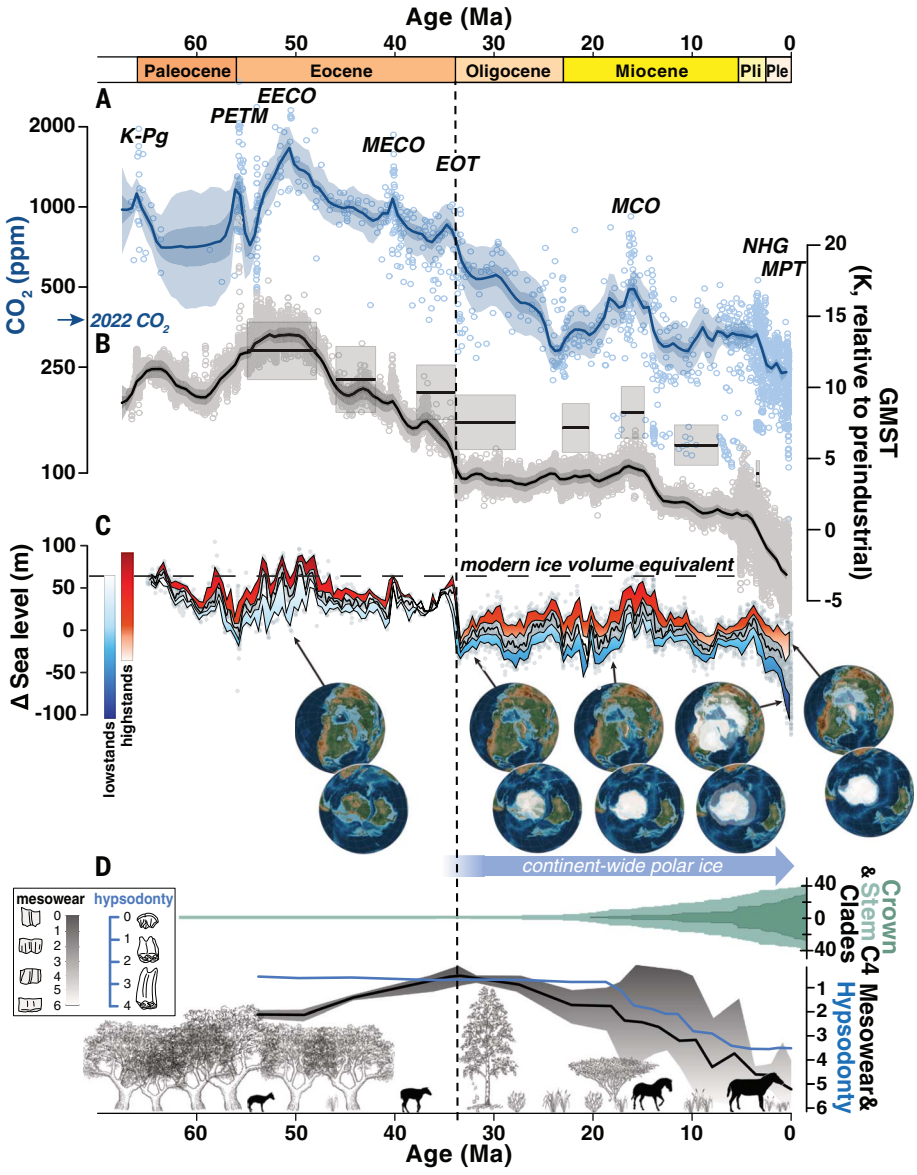

Fig. 2. Category 1 paleo-CO_2 record compared to global climate signals. The vertical dashed line indicates the onset of continent-wide glaciation in Antarctica. (**A**) Atmospheric CO_2 estimates (symbols) and 500-kyr mean statistical reconstructions (median and 50 and 95% credible intervals: dark and light-blue shading, respectively). Major climate events are highlighted: K-PG, Cretaceous/Paleogene boundary; PETM, Paleocene Eocene Thermal Maximum; EECO, Early Eocene Climatic Optimum; MECO, Middle Eocene Climatic Optimum; EOT, Eocene/Oligocene Transition; MCO, Miocene Climatic Optimum; NHG, onset of Northern Hemisphere Glaciation; and MPT, Mid-Pleistocene Transition. The 2022 annual average atmospheric CO_2 of 419 ppm is indicated for reference. (**B**) Global mean surface temperatures estimated from benthic $\delta^{18}O$ data following Westerhold *et al*. (*43*) (solid line, individual proxy estimates as symbols, and statistically reconstructed 500-kyr mean values shown as the continuous curve, with 50 and 95% credible intervals) and from surface temperature proxies (gray boxes) (*45*). (**C**) Sea level after (*66*) with gray dots displaying raw data; the solid black line reflects median sea level in a 1-Myr running window. High- and lowstands are defined within a running 400-kyr window, with lower and upper bounds of highstands defined by the 75th and 95th percentiles, and lower and upper bounds of lowstands defined by the 5th and 25th percentiles in each window. Globes depict select paleogeographic reconstructions and the growing presence of ice sheets in polar latitudes from (*116*). (**D**) Crown ages show that C_4 clades, with CCMs adapted to low CO_2, initially diversified in the early Miocene, and then rapidly radiated in the late Miocene (*117*). Flora transition from dominantly forested and woodland to open grassland habitats based on fossil phytolith abundance data (*96*). North American equids typify hoofed animal adaptations to new diet and environment (*103*), including increasing tooth mesowear (black line; note the inverted scale), hypsodonty (blue line), and body size.

influence and refine the reconstruction through this epoch, supporting the value of the multi-proxy approach (fig. S10). After the rapid CO_2 rise and fall associated with the PETM at 56 Ma, mean CO_2 steadily rose to peak values of ~1600 ppm around 51 Ma during the EECO. The middle and late Eocene recorded slightly lower values (800 to 1100 ppm). Mean CO_2 dropped to <600 ppm across the Eocene-Oligocene transition (EOT; 33.9 Ma) and reached values that generally fall between ~400 and 200 ppm during the Miocene through Pleistocene, except for a notable increase during the Middle Miocene (~17 to 15 Ma) to a mean of ~500 ppm. Uncertainty in the mean CO_2 values drops substantially in the Plio-Pleistocene (fig. S11), as expected given a drastic increase in data density. Our analysis suggests that ~14.5 to 14 Ma was the last time the 500-kyr–mean CO_2 value was as high as it is at present (fig. S11) and that all Plio-Pleistocene peak interglacial CO_2 concentrations were exceptionally likely to be less than those of the modern atmosphere (fig. S12). In contrast, before the Miocene, there is very little support (<2.5% probability) for Cenozoic 500-kyr–mean CO_2 values reaching or falling below preindustrial levels.

Climatic implications of the revised CO_2 curve

Relationship with global temperature change and climate sensitivity

Our reconstructed Cenozoic CO_2 trends are broadly coherent with those for global temperature as inferred, for instance, from the oxygen isotopic composition ($\delta^{18}O$) of fossil benthic foraminifera shells (*43*, *44*) and compilations of global surface temperature (*45*) (Fig. 2B). The Paleocene and Eocene epochs display overall higher temperatures and atmospheric CO_2 concentrations as compared with the later Oligocene, Miocene, and Pliocene—consistent with a predominantly greenhouse gas–regulated global energy budget. More specifically, the slow rise and subsequent fall of CO_2 over the course of the Paleocene and Eocene are mirrored by global temperatures, just as a transient Miocene CO_2 rise coincides with a period of warming at the Miocene Climatic Optimum (MCO). The EOT is identifiable in both the CO_2 and temperature records, despite the smoothing introduced by the curve fitting and 500-kyr binning interval.

Despite this overall agreement, rates and timing of CO_2 are not always synchronized with temperature changes in the two records (Fig. 2, A and B). For example, CO_2 appears broadly static or even rising during the late Eocene (37 to 34 Ma) and late Miocene (11 to 5 Ma) despite global cooling at these times (*46*). Conversely, decreasing CO_2 during the early Oligocene corresponds with relatively stable global temperatures [Fig. 2B, but see also (*47*, *48*)] and ice volume (Fig. 2C) at that time.

We note that the reconstructed Oligocene CO_2 decrease is driven by the contribution of marine proxies to the composite curve, whereas estimates from leaf gas exchange proxies are low and broadly static (Fig. 1C), a discrepancy that cannot be resolved without further experimentation and data collection. We caution that, even at the 500-kyr resolution of our study, the relative timing of CO_2 and temperature change might be unresolved in poorly sampled intervals (i.e., middle Paleocene) but should be well resolved during more-recent, well-sampled intervals (i.e., late Miocene through present; fig. S8). Is the occasional divergence of temperature and CO_2 change evidence for occasional disconnects between CO_2 forcing and climate response? Although one might posit bias in the CO_2 reconstruction, the strength of our multiproxy approach is the reduced likelihood that multiple proxies exhibit common bias during particular periods of the Cenozoic. We suggest that some cases of divergence between temperature and CO_2 could reflect non-CO_2 effects on climate [e.g., changes in paleogeography affecting ocean circulation, albedo, and heat transport (*49*)], or the temperature reconstructions used herein could be biased by nonthermal influences [e.g., uncertain elemental and isotopic composition of paleoseawater, physiological or pH effects on proxies (*48*, *50*)].

Our updated CO_2 curve, in conjunction with existing global temperature reconstructions, gives us the opportunity to reassess how climate sensitivity might have evolved through the Cenozoic. The most commonly reported form of climate sensitivity is equilibrium climate sensitivity (ECS), which focuses on fast feedback processes (e.g., clouds, lapse rate, snow, sea ice) and is therefore best suited for predicting present-day warming [~3°C for a doubling of CO_2 above the preindustrial condition (*2*)]. Because the average temporal resolution of our CO_2 database is coarser than 1000 years, we cannot estimate ECS directly. Instead, our data are most appropriate for interpreting an Earth system sensitivity [$ESS_{[CO2]}$, following the taxonomy of (*51*)]—the combination of short-term climate responses to doubling CO_2 plus the effects of slower, geological feedback loops such as the growth and decay of continental ice sheets. We compare our reconstructed 500-kyr–mean CO_2 values with two different estimates of global surface temperature. We apply the same Bayesian inversion model used in the CO_2 reconstruction to derive 500-kyr–mean surface temperatures from the benthic foraminiferal $\delta^{18}O$ compilation of (*43*), which we convert to temperatures using the methodology of (*44*) (Fig. 2B). In addition, we pair a set of multiproxy global surface temperature estimates for eight Cenozoic time intervals (Fig. 2B) (*45*) with posterior CO_2 estimates from time bins corresponding to each interval. The two temperature reconstructions are broadly similar, although the benthic record suggests relatively higher temperatures during the hothouse climate of the Paleocene and Eocene, whereas the multiproxy reconstruction is elevated relative to the benthic record during the Oligocene and Neogene.

The coevolution of atmospheric CO_2 and global mean surface temperature (GMST) over the Cenozoic is shown in Fig. 3. Because CO_2 is on a log scale, the slopes of lines connecting two adjacent points in time reflect the average intervening $ESS_{[CO2]}$. Benthic $\delta^{18}O$–derived temperatures suggest that early Paleocene warming occurs with a very high $ESS_{[CO2]}$ (>8°C per CO_2 doubling), although CO_2 uncertainties are large during this time interval. $ESS_{[CO2]}$ steadily declines toward the peak of Cenozoic warmth at ~50 Ma, then steepens again to ~8°C per CO_2 doubling for much of the cooling through to the EOT at ~34 Ma. In contrast, the multiproxy global temperature record suggests a lower $ESS_{[CO2]}$ of ~5°C between the early Eocene and earliest Oligocene. During the Oligocene and early part of the Miocene, both temperature records imply a near-zero $ESS_{[CO2]}$,

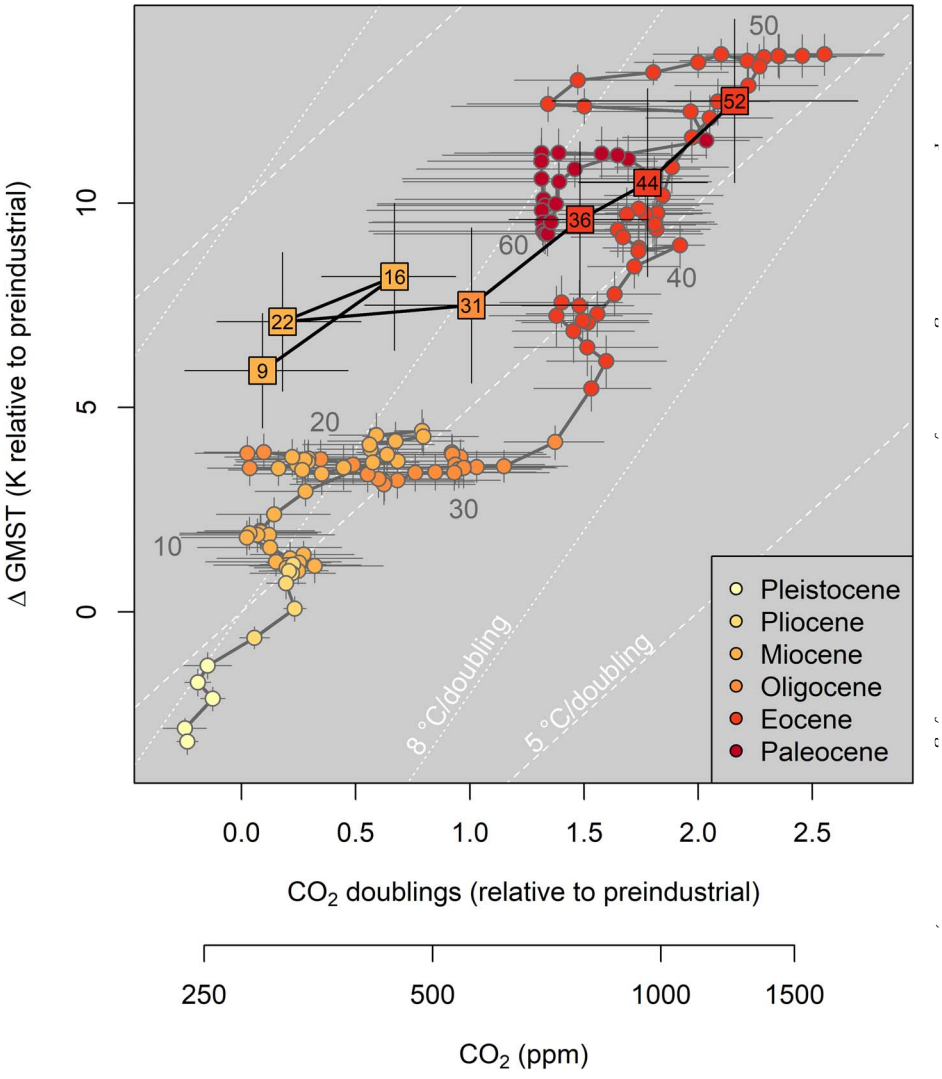

Fig. 3. Application of the Category 1 CO_2 record to determine $ESS_{[CO2]}$. GMST deviation (kelvin) from preindustrial global average surface temperature of 14.15°C is displayed versus paleo-CO_2 doublings relative to the preindustrial baseline of 280 ppm (upper *x* axis) and paleo-CO_2 estimates on a log scale (lower *x* axis). The slopes between two points in time reflect the average $ESS_{[CO2]}$. Circles reflect 500-kyr binned Category 1 CO_2 estimates paired with corresponding GMST means from (*43*); squares pair CO_2 and GMST means from compilations of sea surface temperature (*45*) in seven coarsely resolved time intervals. Note that this figure omits the Pliocene temperature estimate of (*45*) because it samples too short a time interval (compare with Fig. 2) to be comparable with mean CO_2. Data from Cenozoic epochs are color coded and shift from red (Paleocene) to yellow (Pleistocene); labels indicate specific age bins (Ma). Dashed lines indicate reference $ESS_{[CO2]}$ lines of 8° and 5°C warming per doubling of CO_2.

meaning that CO_2 values appear to decline with no appreciable global cooling. $ESS_{[CO2]}$ implied by both temperature reconstructions steepens again from the middle Miocene (~16 Ma) to present, averaging 8°C per CO_2 doubling over the past 10 Myr.

An alternative perspective on early Cenozoic climate forcing was introduced by (*44*), who hypothesized that all pre-Oligocene climate change was the response of direct and indirect CO_2 radiative forcing plus long-term change in solar output (i.e., constant albedo). Consequently, they converted Paleocene and Eocene benthic $\delta^{18}O$–derived GMST to estimates of CO_2 change required to explain the temperature record. Our reconstruction offers a direct test of this hypothesis, and although it compares well with the $\delta^{18}O$ approach of (*44*) throughout much of the early Cenozoic, our curve suggests that the late Eocene decline in CO_2 was less severe than expected under the constant albedo assumption (fig. S13). This result is consistent with a growing contribution of glacier and sea ice albedo effects (*52*, *53*) and the opening of Southern Ocean gateways (*54*) to climate cooling preceding the Eocene-Oligocene boundary.

In summary, the Cenozoic compilation confirms a strong link between CO_2 and GMST across timescales from 500 kyr to tens of millions of years, with $ESS_{[CO2]}$ generally within the range of 5° to 8°C—patterns consistent with most prior work (*32*–*34*, *45*, *51*, *55*–*60*) and considerably higher than the present-day ECS of ~3°C. Both temperature reconstructions imply relatively high $ESS_{[CO2]}$ values during the last 10 Myr of the Cenozoic, when global ice volumes were highest. This agrees with expectations of an amplified $ESS_{[CO2]}$ due to the ice-albedo feedback (*61*). However, even during times with little to no ice (Paleocene to early Eocene), we find elevated values of $ESS_{[CO2]}$ (approaching or exceeding 5°C per CO_2 doubling). This implies that fast, non-ice feedbacks, such as clouds or non-CO_2 greenhouse gases (*60*, *62*–*65*), were probably stronger in the early Paleogene than they are in the present-day climate system (*5*). The Oligocene to early Miocene is the most enigmatic interval, with an apparent decrease in CO_2 despite relatively stable temperature, implying near-zero $ESS_{[CO2]}$. It should be noted that this is one interval where different CO_2 proxies disagree on CO_2 change (Fig. 1A), with relatively stable values from plants but a decline in values from alkenones. More work is needed to confirm these CO_2 and temperature findings, but if these estimates are correct, this could partly reflect transition from a climate state too cold to support the strong, fast feedbacks (e.g., clouds) of the early Eocene (*5*) but not cold enough to generate strong ice-albedo feedback. Tectonic changes in the arrangement of continents and the opening of critical ocean gateways may also be confounding derivation of $ESS_{[CO2]}$ at that time (*49*, *54*).

Relationship with the evolution of the cryosphere

Our composite CO_2 record also enables reexamination of the evolution of Earth's cryosphere (Fig. 2C) in relation to CO_2 radiative forcing. We use the sea level estimation of (*66*) for this comparison because it covers the entire Cenozoic and is somewhat independent of the benthic $\delta^{18}O$ stack (*43*) used for the GMST derivation in Fig. 2B and also of the more recent sea level reconstruction of (*67*). Although there are substantial differences between the two sea level estimates, the main features discussed herein are broadly consistent between them. The establishment of a permanent, continent-wide Antarctic ice shield at the EOT (~34 Ma) comes at the end of a ~10-Myr period of generally slowly decreasing CO_2. There is evidence for isolated, unstable Antarctic glaciers at various points during the 10-Myr interval preceding the EOT (*50*, *53*, *66*, *68*), which is consistent with the increasing paleogeographic isolation of Antarctica and Southern Ocean cooling (*54*), and CO_2 may have been sufficiently low to enable the repeated crossing of a glaciation threshold by periodic orbital forcing. Tectonic cooling of Antarctica would have progressively raised the CO_2 glaciation threshold, which has been modeled to be between 560 and 920 ppm (*69*, *70*). Our composite CO_2 record allows us to further assess this glaciation threshold but requires determining the point during glacial inception when strong positive feedbacks (e.g., ice-albedo and ice sheet elevation) commenced and ice sheet growth accelerated (*71*). Using the sea level curve of (*66*), we determine this point to be 33.75 ±0.25 Ma, where our composite CO_2 record suggests 719^{+180}_{-152} ppm (95% CIs). Once established, the land-based Antarctic ice sheet likely persisted for the remainder of the Cenozoic, although substantial retreat of land-based ice has been modeled (30 to 36 m sea level equivalent) (*72*) and estimated from proxies (Fig. 2C) for the MCO. During the MCO, 500-kyr–mean CO_2 values increased to ~500 ppm (Fig. 2A and fig. S10), and benthic foraminiferal $\delta^{18}O$ (Fig. 2B) (*43*) and clumped isotopes (*50*) indicate warming. Although the stability of the land-based Antarctic ice sheet depends on many factors in addition to CO_2-induced global warming [e.g., hysteresis (*73*) and bed topography (*74*)], our composite record indicates that considerable retreat of land-based ice did not occur below 441 to 480 ppm (2.5th to 50th percentiles), and some land-based ice may have persisted up to 563 ppm (97.5th percentile) during the MCO. Excepting the MCO, atmospheric CO_2 has remained below our current value of 419 ppm since the late Oligocene (Fig. 2A and fig. S10), with relatively small sea level variations [up to ~20 m; Fig. 2C and (*67*)] being driven by orbitally forced melting of the marine-based ice sheet (*72*, *75*). Finally, at ~2.7 Ma, the transition to intensified Northern Hemisphere glaciation and orbitally driven glacial cycles coincided with CO_2 values that began decreasing after a relative high during the Pliocene (Fig. 2A).

Evolutionary implications of the revised CO_2 curve

Whereas geologic trends in terrestrial floral and faunal habitat ranges (*76*, *77*) and diversity (*78*–*80*) are largely thought to be controlled by temperature and associated climate patterns, atmospheric CO_2 has been hypothesized to drive the evolution of biological carbon-concentrating mechanisms (CCMs) and their subsequent diversification in terrestrial plants (Fig. 2D) (*81*, *82*). Our realization of how atmospheric CO_2 has varied through the Cenozoic allows us to reexamine this hypothesis. The two primary CCMs in terrestrial plants are the crassulacean acid metabolism (CAM) and C_4 photosynthetic syndromes. CCMs in terrestrial C_4 and CAM plants confer competitive advantages over the ancestral C_3 pathway under higher growing season temperatures, low rainfall, and lower atmospheric CO_2. As a result, C_4 photosynthesis contributes about 23% of today's global terrestrial gross primary production (*83*).

Plant clades with the C_4 pathway first emerged in the early Oligocene (*84*, *85*), yet they did not expand to ecological significance until the late Miocene [i.e., they contributed <5% of gross primary production before ~10 Ma; Fig. 2D and (*86*–*88*)]. CAM plants (e.g., cacti, ice plants, agaves, and some orchids) underwent substantial diversification events around the late Oligocene and late Miocene (*89*–*91*). Taken together, two general biological thresholds emerge from our CO_2 record: (i) All known origins of C_4 plants occurred when atmospheric CO_2 was lower than ~550 ppm [i.e., after 32 Ma; Fig. 2, A and D, and (*84*)], which is in agreement with theoretical predictions (*92*, *93*). (ii) All major Cenozoic CAM diversification events coincided with intervals when CO_2 was lower than ~430 ppm (i.e., after 27 Ma) (*89*, *90*). Our record is thus consistent with decreasing atmospheric CO_2 (<550 ppm) being a critical threshold for the Cenozoic origin, diversification, and expansion of C_4 and CAM plants within grasslands, arid habitats (such as deserts), and habits (such as epiphytes), and provides strong data support for previous hypotheses (*20*, *84*, *86*, *88*, *89*, *92*, *94*, *95*). Notably, after their origin in the early Oligocene, C_4 plants did not immediately proliferate. By ~24 to ~18 Ma, open habitat grasslands are evident on most continents (*96*), yet widespread dispersal of C_4 plants was delayed until the late Miocene and without any apparent decline in CO_2 (Fig. 2D). Therefore, the rise of C_4 plants to their dominance in many tropical and subtropical ecosystems was likely driven (and is maintained today) by other factors,

such as fire, seasonality of rainfall, and herbivory (i.e., grazing that keeps landscapes open) (*97*, *98*). The temporal evolution of these factors warrants further study as we move toward a future where CO_2 may rise above the 550-ppm threshold that was key to the origin, taxonomic diversification, and spread of C_4 plants.

Terrestrial mammals evolved and adapted to the changing and more-open floral ecosystems of the late Cenozoic (*99*–*101*) and are thus indirectly linked to the 550-ppm atmospheric CO_2 threshold discovered herein. In particular, dental wear patterns (such as the shape of the chewing surface of a tooth, i.e., mesowear) and tooth morphology, such as crown height, reflect an increasingly abrasive and tough diet (*102*, *103*) and can be traced across many herbivore lineages during this period. For instance, mesowear in North American Equidae (horses and their ancestors) (Fig. 2D) began to increase in the late Eocene and steadily continued to increase into the Quaternary. Similarly, equids evolved high-crowned (hypsodont) teeth in the Miocene (*103*–*105*), and their body size increased to accommodate higher intake of more-abrasive, grassy vegetation (Fig. 2D).

Evolutionary trends are a little less clear in the ocean, because marine algal CCMs are ubiquitous and diverse in form (*106*) and are believed to have an ancient origin. Moreover, the large spatial and seasonal variance of dissolved CO_2 in the surface ocean (as compared with the relatively uniform seasonal and spatial concentration of CO_2 in the air) may somewhat decouple their evolution from geologic trends in atmospheric CO_2. Evidence exists that marine algae, and in particular the coccolithophores (i.e., the source of the alkenone biomarkers), express CCMs to a greater extent when CO_2 is lower (*107*–*109*), with estimates of cellular carbon fluxes suggesting that enhanced CCM activity in coccolithophores began between ~7 and 5 Ma (*110*). However, our revised CO_2 curve displays mean atmospheric CO_2 broadly constant at 300 to 350 ppm since at least ~14 Ma (Fig. 2A and fig. S10), suggesting that increased CCM activity may reflect other proximal triggers, perhaps involving changes in ocean circulation and nutrient supply.

Perspectives and opportunities for further advances

Our community-assessed composite CO_2 record and statistically modeled time-averaged CO_2 curve exhibit greater clarity in the Cenozoic evolution of CO_2 and its relationship with climate than was possible in previous compilations and furthermore highlight the value of cross-disciplinary collaboration and community building. Generating a paleo-CO_2 record with even greater confidence requires targeted efforts using multiple proxies to fill in data gaps, higher resolution and replication from multiple locations, and novel approaches to resolve remaining differences between CO_2 proxy estimates. Specifically, although the number and diversity of paleo-CO_2 proxy records continue to grow, data remain relatively sparse during several key parts of the Cenozoic record (e.g., middle Paleocene, Oligocene). Moreover, records from the Paleocene and Eocene are dominated by estimates from the boron isotope proxy, increasing the potential for bias. Targeted efforts are hence needed to expand the number and diversity of data through these intervals and to refine multiproxy reconstructions. Additionally, despite substantial progress, there remains a lack of consensus regarding the identity and/or quantification of some of the factors underlying each of the proxy systems analyzed here. New experimental and calibration studies, particularly those that isolate and quantify specific mechanistic responses and/or their interactions, need to be undertaken to reduce potential biases and uncertainty for each method. For instance, the emerging fields of genomics, evolutionary and developmental biology, and proteomics provide exciting opportunities for improving and understanding paleoproxy systematics. Furthermore, and associated with improved experimental quantification, refining our theoretical and mechanistic understanding of how proxies are encoded will allow us to create explicit and self-consistent representations of the processes involved. The development of proxy system forward models provides a promising leap in this direction (*111*). Bayesian statistical methods can then enable the full suite of models and data to be integrated and constrain the range of environmental conditions, including atmospheric CO_2 and other variables that are consistent with the multiproxy data (*112*, *113*). Finally, development of new proxies is also a realistic and desirable aim. For instance, while this study focuses on more established proxies, new proxies such as coccolith calcite stable isotopes (*114*) and mammalian bone and teeth oxygen-17 anomalies (*115*) show promising results for reconstructing paleo-CO_2 but perhaps require further validation before they can be assessed with confidence.

Proxies and proxy-based reconstructions of how atmospheric CO_2 has varied through deep time have improved immeasurably over the past few decades. Although they will never allow us to reconstruct past CO_2 with the same fidelity as direct air measurement, our study shows how community-based consensus assessment, together with a critical reanalysis of proxy models and assumptions, can progressively move us toward a quantitative history of atmospheric CO_2 for geological time.

REFERENCES AND NOTES

1. S. Arrhenius, XXXI. On the influence of carbonic acid in the air upon the temperature of the ground. *Lond. Edinb. Dublin Philos. Mag. J. Sci.* **41**, 237–276 (1896). doi: 10.1080/14786449608620846
2. IPCC, *Climate Change 2021: The Physical Science Basis. Contribution of Working Group I to the Sixth Assessment Report of the Intergovernmental Panel on Climate Change*, V. Masson-Delmotte *et al.*, Eds. (Cambridge Univ. Press, 2021).
3. P. Tans, R. Keeling, "Carbon cycle greenhouse gases: Trends in atmospheric carbon dioxide" (National Oceanic and Atmospheric Administration, Earth System Research Laboratories, Global Monitoring Laboratory, 2023); www.esrl.noaa.gov/gmd/ccgg/trends/.
4. K. E. Taylor, R. J. Stouffer, G. A. Meehl, An overview of CMIP5 and the experiment design. *Bull. Am. Meteorol. Soc.* **93**, 485–498 (2011). doi: 10.1175/BAMS-D-11-00094.1
5. R. Caballero, M. Huber, State-dependent climate sensitivity in past warm climates and its implications for future climate projections. *Proc. Natl. Acad. Sci. U.S.A.* **110**, 14162–14167 (2013). doi: 10.1073/pnas.1303365110; pmid: 23918397
6. J. Zhu, C. J. Poulsen, On the increase of climate sensitivity and cloud feedback with warming in the community atmosphere models. *Geophys. Res. Lett.* **47**, e2020GL089143 (2020). doi: 10.1029/2020GL089143
7. J. Zhu, C. J. Poulsen, B. L. Otto-Bliesner, High climate sensitivity in CMIP6 model not supported by paleoclimate. *Nat. Clim. Chang.* **10**, 378–379 (2020). doi: 10.1038/s41558-020-0764-6
8. E. J. Judd *et al.*, The PhanSST global database of Phanerozoic sea surface temperature proxy data. *Sci. Data* **9**, 753 (2022). doi: 10.1038/s41597-022-01826-0; pmid: 36473868
9. R. J. Delmas, J.-M. Ascencio, M. Legrand, Polar ice evidence that atmospheric CO_2 20,000 yr BP was 50% of present. *Nature* **284**, 155–157 (1980). doi: 10.1038/284155a0
10. A. Neftel, H. Oeschger, J. Schwander, B. Stauffer, R. Zumbrunn, Ice core sample measurements give atmospheric CO_2 content during the past 40,000 yr. *Nature* **295**, 220–223 (1982). doi: 10.1038/295220a0
11. B. Bereiter *et al.*, Revision of the EPICA Dome C CO_2 record from 800 to 600 kyr before present. *Geophys. Res. Lett.* **42**, 542–549 (2015). doi: 10.1002/2014GL061957
12. Y. Yan *et al.*, Two-million-year-old snapshots of atmospheric gases from Antarctic ice. *Nature* **574**, 663–666 (2019). doi: 10.1038/s41586-019-1692-3; pmid: 31666720
13. J. A. Higgins *et al.*, Atmospheric composition 1 million years ago from blue ice in the Allan Hills, Antarctica. *Proc. Natl. Acad. Sci. U.S.A.* **112**, 6887–6891 (2015). doi: 10.1073/pnas.1420232112; pmid: 25964367
14. C. Nehrbass-Ahles *et al.*, Abrupt CO_2 release to the atmosphere under glacial and early interglacial climate conditions. *Science* **369**, 1000–1005 (2020). doi: 10.1126/science.aay8178; pmid: 32820127
15. C. Le Quéré *et al.*, Trends in the sources and sinks of carbon dioxide. *Nat. Geosci.* **2**, 831–836 (2009). doi: 10.1038/ngeo689
16. P. Friedlingstein *et al.*, Global carbon budget 2022. *Earth Syst. Sci. Data* **14**, 4811–4900 (2022). doi: 10.5194/essd-14-4811-2022
17. P. Valdes, Built for stability. *Nat. Geosci.* **4**, 414–416 (2011). doi: 10.1038/ngeo1200
18. W. Kiessling, M. Aberhan, L. Villier, Phanerozoic trends in skeletal mineralogy driven by mass extinctions. *Nat. Geosci.* **1**, 527–530 (2008). doi: 10.1038/ngeo251
19. J. L. Payne, A. M. Bush, N. A. Heim, M. L. Knope, D. J. McCauley, Ecological selectivity of the emerging mass extinction in the oceans. *Science* **353**, 1284–1286 (2016). doi: 10.1126/science.aaf2416; pmid: 27629258
20. E. J. Edwards *et al.*, The origins of C_4 grasslands: Integrating evolutionary and ecosystem science. *Science* **328**, 587–591 (2010). doi: 10.1126/science.1177216; pmid: 20431008
21. F. A. McInerney, S. L. Wing, The Paleocene-Eocene Thermal Maximum: A perturbation of carbon cycle, climate, and biosphere with implications for the future. *Annu. Rev. Earth Planet. Sci.* **39**, 489–516 (2011). doi: 10.1146/annurev-earth-040610-133431
22. W. Konrad, D. L. Royer, P. J. Franks, A. Roth-Nebelsick, Quantitative critique of leaf-based paleo-CO_2 proxies: Consequences for their reliability and applicability. *Geol. J.* **56**, 886–902 (2020). doi: 10.1002/gj.3807
23. J. C. McElwain, M. Steinthorsdottir, Paleoecology, ploidy, paleoatmospheric composition, and developmental biology: A review of the multiple uses of fossil stomata. *Plant Physiol.* **174**, 650–664 (2017). doi: 10.1104/pp.17.00204; pmid: 28495890
24. B. A. Schubert, A. H. Jahren, The effect of atmospheric CO_2 concentration on carbon isotope fractionation in C_3 land plants. *Geochim. Cosmochim. Acta* **96**, 29–43 (2012). doi: 10.1016/j.gca.2012.08.003

25. T. E. Cerling, Carbon dioxide in the atmosphere; evidence from Cenozoic and Mesozoic Paleosols. *Am. J. Sci.* **291**, 377–400 (1991). doi: 10.2475/ajs.291.4.377
26. D. O. Breecker, Quantifying and understanding the uncertainty of atmospheric CO_2 concentrations determined from calcic paleosols. *Geochem. Geophys. Geosyst.* **14**, 3210–3220 (2013). doi: 10.1002/ggge.20189
27. E. A. Jagniecki, T. K. Lowenstein, D. M. Jenkins, R. V. Demicco, Eocene atmospheric CO_2 from the nahcolite proxy. *Geology* **43**, 1075–1078 (2015).
28. T. K. Lowenstein, R. V. Demicco, Elevated Eocene atmospheric CO_2 and its subsequent decline. *Science* **313**, 1928 (2006). doi: 10.1126/science.1129555; pmid: 17008525
29. M. Pagani, "12.13 - Biomarker-based inferences of past climate: The alkenone pCO_2 proxy" in *Treatise on Geochemistry*, vol. 12, H. D. Holland, K. K. Turekian, Eds. (Elsevier, ed. 2, 2014), pp. 361–378. doi: 10.1016/B978-0-08-095975-7.01027-5
30. B. Hönisch *et al*., *Boron Proxies in Paleoceanography and Paleoclimatology*, Analytical Methods in Earth and Environmental Science Series (John Wiley & Sons, Ltd., 2019).
31. J. W. B. Rae, "Boron isotopes in foraminifera: Systematics, biomineralisation, and CO_2 reconstruction" in *Boron Isotopes: The Fifth Element*, H. Marschall, G. Foster, Eds. (Springer International Publishing, 2018), pp. 107–143. doi: 10.1007/978-3-319-64666-4_5
32. D. J. Beerling, D. L. Royer, Convergent Cenozoic CO_2 history. *Nat. Geosci.* **4**, 418–420 (2011). doi: 10.1038/ngeo1186
33. G. L. Foster, D. L. Royer, D. J. Lunt, Future climate forcing potentially without precedent in the last 420 million years. *Nat. Commun.* **8**, 14845 (2017). doi: 10.1038/ncomms14845; pmid: 28375201
34. J. W. B. Rae *et al*., Atmospheric CO_2 over the past 66 million years from marine archives. *Annu. Rev. Earth Planet. Sci.* **49**, 609–641 (2021). doi: 10.1146/annurev-earth-082420-063026
35. S. Ji *et al*., A symmetrical CO_2 peak and asymmetrical climate change during the middle Miocene. *Earth Planet. Sci. Lett.* **499**, 134–144 (2018). doi: 10.1016/j.epsl.2018.07.011
36. J. Da, Y. G. Zhang, G. Li, X. Meng, J. Ji, Low CO_2 levels of the entire Pleistocene epoch. *Nat. Commun.* **10**, 4342 (2019). doi: 10.1038/s41467-019-12357-5; pmid: 31554805
37. E. Hyland, N. D. Sheldon, M. Fan, Terrestrial paleoenvironmental reconstructions indicate transient peak warming during the early Eocene climatic optimum. *Geol. Soc. Am. Bull.* **125**, 1338–1348 (2013). doi: 10.1130/B30761.1
38. J. Henderiks, M. Pagani, Refining ancient carbon dioxide estimates: Significance of coccolithophore cell size for alkenone-based pCO_2 records. *Paleoceanography* **22**, PA3202 (2007). doi: 10.1029/2006PA001399
39. S. R. Phelps *et al*., Carbon isotope fractionation in Noelaerhabdaceae algae in culture and a critical evaluation of the alkenone paleobarometer. *Geochem. Geophys. Geosyst.* **22**, e2021GC009657 (2021). doi: 10.1029/2021GC009657
40. H. M. Stoll *et al*., Upregulation of phytoplankton carbon concentrating mechanisms during low CO_2 glacial periods and implications for the phytoplankton pCO_2 proxy. *Quat. Sci. Rev.* **208**, 1–20 (2019). doi: 10.1016/j.quascirev.2019.01.012
41. Y. G. Zhang, J. Henderiks, X. Liu, Refining the alkenone-pCO2 method II: Towards resolving the physiological parameter 'b'. *Geochim. Cosmochim. Acta* **281**, 118–134 (2020). doi: 10.1016/j.gca.2020.05.002
42. E. G. Hyland, N. D. Sheldon, Coupled CO_2-climate response during the Early Eocene Climatic Optimum. *Palaeogeogr. Palaeoclimatol. Palaeoecol.* **369**, 125–135 (2013). doi: 10.1016/j.palaeo.2012.10.011
43. T. Westerhold *et al*., An astronomically dated record of Earth's climate and its predictability over the last 66 million years. *Science* **369**, 1383–1387 (2020). doi: 10.1126/science.aba6853; pmid: 32913105
44. J. Hansen, M. Sato, G. Russell, P. Kharecha, Climate sensitivity, sea level and atmospheric carbon dioxide. *Philos. Trans. A Math. Phys. Eng. Sci.* **371**, 20120294 (2013). doi: 10.1098/rsta.2012.0294; pmid: 24043864
45. S. J. Ring, S. G. Mutz, T. A. Ehlers, Cenozoic proxy constraints on earth system sensitivity to greenhouse gases. *Paleoceanogr. Paleoclimatol.* **37**, e2021PA004364 (2022). doi: 10.1029/2021PA004364
46. T. D. Herbert *et al*., Late Miocene global cooling and the rise of modern ecosystems. *Nat. Geosci.* **9**, 843–847 (2016). doi: 10.1038/ngeo2813
47. D. E. Gaskell *et al*., The latitudinal temperature gradient and its climate dependence as inferred from foraminiferal $\delta^{18}O$ over the past 95 million years. *Proc. Natl. Acad. Sci. U.S.A.* **119**, e2111332119 (2022). doi: 10.1073/pnas.2111332119; pmid: 35254906
48. C. L. O'Brien *et al*., The enigma of Oligocene climate and global surface temperature evolution. *Proc. Natl. Acad. Sci. U.S.A.* **117**, 25302–25309 (2020). doi: 10.1073/pnas.2003914117; pmid: 32989142
49. D. J. Lunt *et al*., Palaeogeographic controls on climate and proxy interpretation. *Clim. Past* **12**, 1181–1198 (2016). doi: 10.5194/cp-12-1181-2016
50. A. N. Meckler *et al*., Cenozoic evolution of deep ocean temperature from clumped isotope thermometry. *Science* **377**, 86–90 (2022). doi: 10.1126/science.abk0604; pmid: 35771913
51. PALAEOSENS Project Members, Making sense of palaeoclimate sensitivity. *Nature* **491**, 683–691 (2012). doi: 10.1038/nature11574; pmid: 23192145
52. A. Tripati, D. Darby, Evidence for ephemeral middle Eocene to early Oligocene Greenland glacial ice and pan-Arctic sea ice. *Nat. Commun.* **9**, 1038 (2018). doi: 10.1038/s41467-018-03180-5; pmid: 29531221
53. H. D. Scher, S. M. Bohaty, B. W. Smith, G. H. Munn, Isotopic interrogation of a suspected late Eocene glaciation. *Paleoceanography* **29**, 628–644 (2014). doi: 10.1002/2014PA002648
54. I. Sauermilch *et al*., Gateway-driven weakening of ocean gyres leads to Southern Ocean cooling. *Nat. Commun.* **12**, 6465 (2021). doi: 10.1038/s41467-021-26658-1; pmid: 34753912
55. D. L. Royer, Climate sensitivity in the geologic past. *Annu. Rev. Earth Planet. Sci.* **44**, 277–293 (2016). doi: 10.1146/annurev-earth-100815-024150
56. R. M. Brown, T. B. Chalk, A. J. Crocker, P. A. Wilson, G. L. Foster, Late Miocene cooling coupled to carbon dioxide with Pleistocene-like climate sensitivity. *Nat. Geosci.* **15**, 664–670 (2022). doi: 10.1038/s41561-022-00982-7
57. T. E. Wong, Y. Cui, D. L. Royer, K. Keller, A tighter constraint on Earth-system sensitivity from long-term temperature and carbon-cycle observations. *Nat. Commun.* **12**, 3173 (2021). doi: 10.1038/s41467-021-23543-9; pmid: 34039993
58. D. L. Royer, M. Pagani, D. J. Beerling, Geobiological constraints on Earth system sensitivity to CO_2 during the Cretaceous and Cenozoic. *Geobiology* **10**, 298–310 (2012). doi: 10.1111/j.1472-4669.2012.00320.x; pmid: 22353368
59. J. E. Tierney *et al*., Spatial patterns of climate change across the Paleocene-Eocene Thermal Maximum. *Proc. Natl. Acad. Sci. U.S.A.* **119**, e2205326119 (2022). doi: 10.1073/pnas.2205326119; pmid: 36215472
60. E. Anagnostou *et al*., Proxy evidence for state-dependence of climate sensitivity in the Eocene greenhouse. *Nat. Commun.* **11**, 4436 (2020). doi: 10.1038/s41467-020-17887-x; pmid: 32895377
61. J. Hansen *et al*., Target atmospheric CO: Where should humanity aim? *Open Atmos. Sci. J.* **2**, 217–231 (2008). doi: 10.2174/1874282300802010217
62. J. T. Kiehl, C. A. Shields, Sensitivity of the Palaeocene-Eocene Thermal Maximum climate to cloud properties. *Philos. Trans. A Math. Phys. Eng. Sci.* **371**, 20130093 (2013). doi: 10.1098/rsta.2013.0093; pmid: 24043867
63. J. Zhu, C. J. Poulsen, J. E. Tierney, Simulation of Eocene extreme warmth and high climate sensitivity through cloud feedbacks. *Sci. Adv.* **5**, eaax1874 (2019). doi: 10.1126/sciadv.aax1874; pmid: 31555736
64. D. J. Beerling, A. Fox, D. S. Stevenson, P. J. Valdes, Enhanced chemistry-climate feedbacks in past greenhouse worlds. *Proc. Natl. Acad. Sci. U.S.A.* **108**, 9770–9775 (2011). doi: 10.1073/pnas.1102409108; pmid: 21628580
65. T. Schneider, C. M. Kaul, K. G. Pressel, Possible climate transitions from breakup of stratocumulus decks under greenhouse warming. *Nat. Geosci.* **12**, 163–167 (2019). doi: 10.1038/s41561-019-0310-1
66. K. G. Miller *et al*., Cenozoic sea-level and cryospheric evolution from deep-sea geochemical and continental margin records. *Sci. Adv.* **6**, eaaz1346 (2020). doi: 10.1126/sciadv.aaz1346; pmid: 32440543
67. E. J. Rohling *et al*., Sea level and deep-sea temperature reconstructions suggest quasi-stable states and critical transitions over the past 40 million years. *Sci. Adv.* **7**, eabf5326 (2021). doi: 10.1126/sciadv.abf5326; pmid: 34172440
68. M. J. Henehan *et al*., Revisiting the Middle Eocene Climatic Optimum "carbon cycle conundrum" with new estimates of atmospheric pCO_2 from boron isotopes. *Paleoceanogr. Paleoclimatol.* **35**, e2019PA003713 (2020). doi: 10.1029/2019PA003713
69. E. Gasson *et al*., Uncertainties in the modelled CO_2 threshold for Antarctic glaciation. *Clim. Past* **10**, 451–466 (2014). doi: 10.5194/cp-10-451-2014
70. R. M. Deconto *et al*., Thresholds for Cenozoic bipolar glaciation. *Nature* **455**, 652–656 (2008). doi: 10.1038/nature07337; pmid: 18833277
71. R. M. DeConto, D. Pollard, Rapid Cenozoic glaciation of Antarctica induced by declining atmospheric CO_2. *Nature* **421**, 245–249 (2003). doi: 10.1038/nature01290; pmid: 12529638
72. E. Gasson, R. M. DeConto, D. Pollard, R. H. Levy, Dynamic Antarctic ice sheet during the early to mid-Miocene. *Proc. Natl. Acad. Sci. U.S.A.* **113**, 3459–3464 (2016). doi: 10.1073/pnas.1516130113; pmid: 26903645
73. D. Pollard, R. M. DeConto, Hysteresis in Cenozoic Antarctic ice-sheet variations. *Global Planet. Change* **45**, 9–21 (2005). doi: 10.1016/j.gloplacha.2004.09.011
74. G. J. G. Paxman, E. G. W. Gasson, S. S. R. Jamieson, M. J. Bentley, F. Ferraccioli, Long-term increase in Antarctic Ice Sheet vulnerability driven by bed topography evolution. *Geophys. Res. Lett.* **47**, e2020GL090003 (2020). doi: 10.1029/2020GL090003
75. J. J. Fürst *et al*., The safety band of Antarctic ice shelves. *Nat. Clim. Chang.* **6**, 479–482 (2016). doi: 10.1038/nclimate2912
76. J. C. McElwain, Paleobotany and global change: Important lessons for species to biomes from vegetation responses to past global change. *Annu. Rev. Plant Biol.* **69**, 761–787 (2018). doi: 10.1146/annurev-arplant-042817-040405; pmid: 29719166
77. S.-M. Popescu *et al*., Mangrove distribution and diversity during three Cenozoic thermal maxima in the Northern Hemisphere (pollen records from the Arctic–North Atlantic–Mediterranean regions). *J. Biogeogr.* **48**, 2771–2784 (2021). doi: 10.1111/jbi.14238
78. C. Jaramillo, M. J. Rueda, G. Mora, Cenozoic plant diversity in the neotropics. *Science* **311**, 1893–1896 (2006). doi: 10.1126/science.1121380; pmid: 16574860
79. J. Y. Lim *et al*., The Cenozoic history of palms: Global diversification, biogeography and the decline of megathermal forests. *Glob. Ecol. Biogeogr.* **31**, 425–439 (2022). doi: 10.1111/geb.13436
80. A. Graham, The age and diversification of terrestrial New World ecosystems through Cretaceous and Cenozoic time. *Am. J. Bot.* **98**, 336–351 (2011). doi: 10.3732/ajb.1000353; pmid: 21613130
81. J. R. Ehleringer, R. K. Monson, Evolutionary and ecological aspects of photosynthetic pathway variation. *Annu. Rev. Ecol. Syst.* **24**, 411–439 (1993). doi: 10.1146/annurev.es.24.110193.002211
82. H. Griffiths, "Carbon dioxide concentrating mechanisms and the evolution of CAM in vascular epiphytes" in *Vascular Plants as Epiphytes: Evolution and Ecophysiology*, U. Lüttge, Ed. (Springer, 1989), pp. 42–86. doi: 10.1007/978-3-642-74465-5_3
83. C. J. Still, J. A. Berry, G. J. Collatz, R. S. DeFries, Global distribution of C_3 and C_4 vegetation: Carbon cycle implications. *Global Biogeochem. Cycles* **17**, 1006 (2003). doi: 10.1029/2001GB001807
84. P.-A. Christin *et al*., Oligocene CO_2 decline promoted C_4 photosynthesis in grasses. *Curr. Biol.* **18**, 37–43 (2008). doi: 10.1016/j.cub.2007.11.058; pmid: 18160293
85. A. Vicentini, J. C. Barber, S. S. Aliscioni, L. M. Giussani, E. A. Kellogg, The age of the grasses and clusters of origins of C_4 photosynthesis. *Glob. Change Biol.* **14**, 2963–2977 (2008). doi: 10.1111/j.1365-2486.2008.01688.x
86. P. J. Polissar, C. Rose, K. T. Uno, S. R. Phelps, P. deMenocal, Synchronous rise of African C_4 ecosystems 10 million years ago in the absence of aridification. *Nat. Geosci.* **12**, 657–660 (2019). doi: 10.1038/s41561-019-0399-2
87. L. Tauxe, S. J. Feakins, A reassessment of the chronostratigraphy of late Miocene C_3–C_4 transitions. *Paleoceanogr. Paleoclimatol.* **35**, e2020PA003857 (2020). doi: 10.1029/2020PA003857
88. T. E. Cerling *et al*., Global vegetation change through the Miocene/Pliocene boundary. *Nature* **389**, 153–158 (1997). doi: 10.1038/38229
89. M. Arakaki *et al*., Contemporaneous and recent radiations of the world's major succulent plant lineages. *Proc. Natl. Acad.*

Sci. U.S.A. **108**, 8379–8384 (2011). doi: 10.1073/pnas.1100628108; pmid: 21536881
90. T. J. Givnish *et al*., Orchid phylogenomics and multiple drivers of their extraordinary diversification. *Proc. Biol. Sci.* **282**, 20151553 (2015). doi: 10.1098/rspb.2015.1553; pmid: 26311671
91. E. J. Edwards, Evolutionary trajectories, accessibility and other metaphors: The case of C_4 and CAM photosynthesis. *New Phytol.* **223**, 1742–1755 (2019). doi: 10.1111/nph.15851; pmid: 30993711
92. J. R. Ehleringer, T. E. Cerling, B. R. Helliker, C_4 photosynthesis, atmospheric CO_2, and climate. *Oecologia* **112**, 285–299 (1997). doi: 10.1007/s004420050311; pmid: 28307475
93. H. Zhou, B. R. Helliker, M. Huber, A. Dicks, E. Akçay, C_4 photosynthesis and climate through the lens of optimality. *Proc. Natl. Acad. Sci. U.S.A.* **115**, 12057–12062 (2018). doi: 10.1073/pnas.1718988115; pmid: 30401739
94. C. E. R. Lehmann, S. A. Archibald, W. A. Hoffmann, W. J. Bond, Deciphering the distribution of the savanna biome. *New Phytol.* **191**, 197–209 (2011). doi: 10.1111/j.1469-8137.2011.03689.x; pmid: 21463328
95. W. M. Kürschner, Z. Kvacek, D. L. Dilcher, The impact of Miocene atmospheric carbon dioxide fluctuations on climate and the evolution of terrestrial ecosystems. *Proc. Natl. Acad. Sci. U.S.A.* **105**, 449–453 (2008). doi: 10.1073/pnas.0708588105; pmid: 18174330
96. C. A. E. Strömberg, Evolution of grasses and grassland ecosystems. *Annu. Rev. Earth Planet. Sci.* **39**, 517–544 (2011). doi: 10.1146/annurev-earth-040809-152402
97. A. T. Karp, K. T. Uno, P. J. Polissar, K. H. Freeman, Late Miocene C_4 grassland fire feedbacks on the Indian subcontinent. *Paleoceanogr. Paleoclimatol.* **36**, e2020PA004106 (2021). doi: 10.1029/2020PA004106
98. T. Kukla *et al*., Drier winters drove Cenozoic open habitat expansion in North America. *AGU Adv.* **3**, e2021AV000566 (2022). doi: 10.1029/2021AV000566
99. M. Fortelius *et al*., Evolution of Neogene mammals in Eurasia: Environmental forcing and biotic interactions. *Annu. Rev. Earth Planet. Sci.* **42**, 579–604 (2014). doi: 10.1146/annurev-earth-050212-124030
100. F. Kaya *et al*., The rise and fall of the Old World savannah fauna and the origins of the African savannah biome. *Nat. Ecol. Evol.* **2**, 241–246 (2018). doi: 10.1038/s41559-017-0414-1; pmid: 29292396
101. C. M. Janis, J. Damuth, J. M. Theodor, Miocene ungulates and terrestrial primary productivity: Where have all the browsers gone? *Proc. Natl. Acad. Sci. U.S.A.* **97**, 7899–7904 (2000). doi: 10.1073/pnas.97.14.7899; pmid: 10884422
102. M. Fortelius, N. Solounias, Functional characterization of ungulate molars using the abrasion-attrition wear gradient: A new method for reconstructing paleodiets. *Am. Mus. Novit.* **3301**, 1–36 (2000). doi: 10.1206/0003-0082(2000)301<0001:FCOUMU>2.0.CO;2
103. M. C. Mihlbachler, F. Rivals, N. Solounias, G. M. Semprebon, Dietary change and evolution of horses in North America. *Science* **331**, 1178–1181 (2011). doi: 10.1126/science.1196166; pmid: 21385712
104. C. A. E. Strömberg, Evolution of hypsodonty in equids: Testing a hypothesis of adaptation. *Paleobiology* **32**, 236–258 (2006). doi: 10.1666/0094-8373(2006)32[236:EOHIET]2.0.CO;2
105. C. M. Janis, M. Fortelius, On the means whereby mammals achieve increased functional durability of their dentitions, with special reference to limiting factors. *Biol. Rev. Camb. Philos. Soc.* **63**, 197–230 (1988). doi: 10.1111/j.1469-185X.1988.tb00630.x; pmid: 3042033
106. M. R. Badger, D. Hanson, G. D. Price, Evolution and diversity of CO_2 concentrating mechanisms in cyanobacteria. *Funct. Plant Biol.* **29**, 161–173 (2002). doi: 10.1071/PP01213; pmid: 32689463
107. M. P. S. Badger, Alkenone isotopes show evidence of active carbon concentrating mechanisms in coccolithophores as aqueous carbon dioxide concentrations fall below 7 μmol L^{-1}. *Biogeosciences* **18**, 1149–1160 (2021). doi: 10.5194/bg-18-1149-2021
108. Y. G. Zhang, M. Pagani, Z. Liu, S. M. Bohaty, R. Deconto, A 40-million-year history of atmospheric CO_2. *Philos. Trans. A Math. Phys. Eng. Sci.* **371**, 20130096 (2013). doi: 10.1098/rsta.2013.0096; pmid: 24043869
109. P. D. Tortell, Evolutionary and ecological perspectives on carbon acquisition in phytoplankton. *Limnol. Oceanogr.* **45**, 744–750 (2000). doi: 10.4319/lo.2000.45.3.0744
110. C. T. Bolton, H. M. Stoll, Late Miocene threshold response of marine algae to carbon dioxide limitation. *Nature* **500**, 558–562 (2013). doi: 10.1038/nature12448; pmid: 23985873
111. M. N. Evans, S. E. Tolwinski-Ward, D. M. Thompson, K. J. Anchukaitis, Applications of proxy system modeling in high resolution paleoclimatology. *Quat. Sci. Rev.* **76**, 16–28 (2013). doi: 10.1016/j.quascirev.2013.05.024
112. G. J. Bowen, B. Fischer-Femal, G. J. Reichart, A. Sluijs, C. H. Lear, Joint inversion of proxy system models to reconstruct paleoenvironmental time series from heterogeneous data. *Clim. Past* **16**, 65–78 (2020). doi: 10.5194/cp-16-65-2020
113. M. B. Osman *et al*., Globally resolved surface temperatures since the Last Glacial Maximum. *Nature* **599**, 239–244 (2021). doi: 10.1038/s41586-021-03984-4; pmid: 34759364
114. C. Godbillot, F. Minoletti, F. Bassinot, M. Hermoso, Parallel between the isotopic composition of coccolith calcite and carbon levels across Termination II: developing a new paleo-CO_2 probe. *Clim. Past* **18**, 449–464 (2022). doi: 10.5194/cp-18-449-2022
115. A. Pack, A. Gehler, A. Süssenberger, Exploring the usability of isotopically anomalous oxygen in bones and teeth as paleo-CO_2-barometer. *Geochim. Cosmochim. Acta* **102**, 306–317 (2013). doi: 10.1016/j.gca.2012.10.017
116. C. R. Scotese, An atlas of Phanerozoic paleogeographic maps: the seas come in and the seas go out. *Annu. Rev. Earth Planet. Sci.* **49**, 679–728 (2021). doi: 10.1146/annurev-earth-081320-064052
117. P. A. Christin, C. P. Osborne, R. F. Sage, M. Arakaki, E. J. Edwards, C_4 eudicots are not younger than C_4 monocots. *J. Exp. Bot.* **62**, 3171–3181 (2011). doi: 10.1093/jxb/err041; pmid: 21393383

ACKNOWLEDGMENTS

We thank C. Major at NSF and the many researchers who contributed advice and enthusiasm for this project over the years. We are grateful to the staff at the National Centers for Environmental Information (NCEI) for facilitating curation of the paleo-CO_2 database, and to LDEO, the UCLA Lake Arrowhead Lodge, and the Lady Bird Johnson Wildflower Center for hosting the three workshops that framed this work. Two anonymous reviewers provided valuable comments that improved this manuscript. This study is dedicated to Wally Broecker and Taro Takahashi, who pioneered the study of CO_2 dynamics in a changing climate. **Funding:** This work was supported by National Science Foundation grant OCE 16-36005 (B.H. and P.J.P.), Heising-Simons Foundation grant 2018-0996 (B.H. and V.F.), National Science Foundation grant EAR 21-21649 (B.H., V.F., J.J.M., and C.F.G.), National Science Foundation grant EAR 21-21170 (G.J.B.), National Science Foundation grant EAR 20-02370 (Y.C.), National Science Foundation grant 18-43285 (A.P.), Columbia University's Center for Climate and Life (K.T.U.), the G. Unger Vetlesen Foundation (K.T.U.), National Science Foundation grant 21-00537 (A.P. and P.J.P.), National Science Foundation grant 21-00509 (P.J.P.), National Science Foundation grant EAR 21-21165 (A.R.), National Science Foundation grant EAR 18-06015 (Y.G.Z.), National Science Foundation grant DGE 16-44869 (S.R.P.), National Science Foundation grant 18-13703 (E.G.H.), National Science Foundation grant OCE 16-58023 (J.C.Z.), National Science Foundation grant 16-02905 (M.H.), Swedish Research Council grant NT7-2016 04905 (M.S.), European Research Council grant 101020824 (J.C.M.), SFI/RC/2092 (J.C.M.), UK Research and Innovation grant 101045371 (M.J.H.), Natural Environment Research Council grant NE/X000567/1 (M.P.S.B.), Royal Society grant DHF\R1\221014 (C.R.W.), Australian Research Council grant DP150104007 (P.J.F.), Deutsche Forschungsgemeinschaft grant RA 2068/4-1 (M.R.), European Research Council grant 805246 (J.W.B.R.), an ETH Fellowship (J.K.C.R.), National Science Foundation of China grant 42030503 (J.D.), the Sandal Society Museum (G.J.R.), a Royal Society Tata Fellowship (B.D.A.N.), and Natural Environment Research Council grant NE/P019048/1 (G.L.F.). **Author contributions:** Conceptualization: B.H., G.J.B., D.O.B., M.J.H., M.J.K., A.P., P.J.P., S.R.P., A.R., D.L.R., M.S., R.S.B., P.J.F., M.H., M.F.S., J.K.C.R., N.D.S., and Y.G.Z. Data curation: B.H., G.J.B., D.O.B., Y.C., M.J.H., M.J.K., J.C.M., P.J.P., D.L.R., M.S., S.R.P., E.A., M.P.S.B., R.S.B., T.B.C., E.d.I.V., K.A.D., C.F.G., M.Gut., D.T.H., L.L.H., T.K.L., M.Gui., J.N.M., R.W., A.R.-N., M.F.S., N.D.S., S.S., C.R.W., Y.G.Z., J.M.C., J.D., D.D.E., G.L.F., E.G.H., B.D.A.N., J.W.B.R., M.R., G.J.R., O.S., and L.Z. Formal analysis: B.H., G.J.B., D.O.B., Y.C., M.J.H., P.J.P., D.L.R., A.M., and C.E.L. Investigation: B.H., D.L.R., D.O.B., P.J.P., S.R.P., G.J.B., M.J.H., Y.C., M.S., J.C.M., M.J.K., A.P., E.A., M.P.S.B., R.S.B., P.J.F., W.K., T.K.L., M.F.S., and Y.G.Z. Software: G.J.B., V.F., J.J.M., and R.W. Visualization: B.H., G.J.B., M.J.H., M.S., J.C.M., K.T.U., P.J.P., D.O.B., J.A., B.A.K., C.R.S., J.J.M., and R.W. Funding acquisition: B.H., P.J.P, D.L.R., D.O.B., G.J.B., M.J.K., A.P., R.M.D., M.H., K.E.S., and V.F. Project administration: B.H., D.L.R., D.O.B., P.J.P., and G.J.B. Writing – original draft: B.H., D.L.R., D.O.B., P.J.P., G.J.B., M.J.H., Y.C., M.S., J.C.M., M.J.K., A.P., K.T.U., A.R., and S.R.P. Writing – review & editing: All authors. **Competing interests:** The authors have no competing interests to declare. **Data and materials availability:** The completed data sheets for each study can be accessed as the paleo-CO_2 "Archive" at NOAA's NCEI (https://www1.ncdc.noaa.gov/pub/data/paleo/climate_forcing/trace_gases/Paleo-pCO2/). The specific choice of category, as well as the updated CO_2 and age estimates, are documented in "Product" sheets for each dataset and proxy. In contrast to the "Archive," which will grow with new publications but will otherwise remain passive, the paleo-CO_2 "Product" is a living database that will be updated when newly published data or ancillary data constraints become available and/or when methodological improvements are developed that enable modernization of previously underconstrained datasets. The "Product" sheets created for this study can be accessed at NCEI (https://www.ncei.noaa.gov/pub/data/paleo/climate_forcing/trace_gases/Paleo-pCO2/product_files/), and this is also the place where future data updates will be made available in consecutive versions of the data "Product." **License information:** Copyright © 2023 the authors, some rights reserved; exclusive licensee American Association for the Advancement of Science. No claim to original US government works. https://www.science.org/about/science-licenses-journal-article-reuse

The CenCO$_2$PIP Consortium

Bärbel Hönisch[1,2], Dana L. Royer[3], Daniel O. Breecker[4], Pratigya J. Polissar[5], Gabriel J. Bowen[6], Michael J. Henehan[7], Ying Cui[8], Margret Steinthorsdottir[9], Jennifer C. McElwain[10], Matthew J. Kohn[11], Ann Pearson[12], Samuel R. Phelps[13], Kevin T. Uno[2], Andy Ridgwell[14], Eleni Anagnostou[15], Jacqueline Austermann[1,2], Marcus P. S. Badger[16], Richard S. Barclay[17], Peter K. Bijl[18], Thomas B. Chalk[19], Christopher R. Scotese[20], Elwyn de la Vega[21], Robert M. DeConto[22], Kelsey A. Dyez[23], Vicki Ferrini[2], Peter J. Franks[24], Claudia F. Giulivi[2], Marcus Gutjahr[15], Dustin T. Harper[6], Laura L. Haynes[25], Matthew Huber[26], Kathryn E. Snell[27], Benjamin A. Keisling[28], Wilfried Konrad[29], Tim K. Lowenstein[30], Alberto Malinverno[2], Maxence Guillermic[31], Luz María Mejía[32], Joseph N. Milligan[17], John J. Morton[2], Lee Nordt[33], Ross Whiteford[34], Anita Roth-Nebelsick[35], Jeremy K. C. Rugenstein[36], Morgan F. Schaller[37], Nathan D. Sheldon[23], Sindia Sosdian[38], Elise B. Wilkes[39], Caitlyn R. Witkowski[7], Yi Ge Zhang[40], Lloyd Anderson[1,2], David J. Beerling[41], Clara Bolton[19], Thure E. Cerling[6], Jennifer M. Cotton[42], Jiawei Da[4], Douglas D. Ekart[43], Gavin L. Foster[44], David R. Greenwood[45], Ethan G. Hyland[46], Elliot A. Jagniecki[47], John P. Jasper[48], Jennifer B. Kowalczyk[49], Lutz Kunzmann[50], Wolfram M. Kürschner[51], Charles E. Lawrence[52], Caroline H. Lear[38], Miguel A. Martínez-Botí[44,53], Daniel P. Maxbauer[54], Paolo Montagna[55], B. David A. Naafs[56], James W. B. Rae[34], Markus Raitzsch[57], Gregory J. Retallack[58], Simon J. Ring[59], Osamu Seki[60], Julio Sepúlveda[61], Ashish Sinha[62], Tekie F. Tesfamichael[63], Aradhna Tripati[31], Johan van der Burgh[64], Jimin Yu[65], James C. Zachos[66], Laiming Zhang[67]

[1]Department of Earth and Environmental Sciences of Columbia University, New York, NY, USA. [2]Lamont-Doherty Earth Observatory of Columbia University, Palisades, NY, USA. [3]Department of Earth and Environmental Sciences, Wesleyan University, Middletown, CT, USA. [4]Department of Earth and Planetary Sciences, Jackson School of Geosciences, University of Texas at Austin, Austin, TX, USA. [5]Department of Ocean Sciences, University of California, Santa Cruz, Santa Cruz, CA, USA. [6]Department of Geology and Geophysics, University of Utah, Salt Lake City, UT, USA. [7]School of Earth Sciences, University of Bristol, Bristol, UK. [8]Department of Earth and Environmental Studies, Montclair State University, Montclair, NJ, USA. [9]Swedish Museum of Natural History, Stockholm, Sweden. [10]Department of Botany, Trinity College Dublin, Dublin, Ireland. [11]Department of Geosciences, Boise State University, Boise, ID, USA. [12]Department of Earth and Planetary Sciences, Harvard University, Cambridge, MA, USA. [13]CIM Group, New York, NY, USA. [14]Earth and Planetary Sciences Department, University of California, Riverside, Riverside, CA, USA. [15]GEOMAR Helmholtz Centre for Ocean Research Kiel, Kiel, Germany. [16]School of Environment, Earth and Ecosystem Sciences, The Open University, Milton Keynes, UK. [17]Department of Paleobiology, Smithsonian Institution, Washington, DC, USA. [18]Department of Earth Sciences, Utrecht University, Utrecht, Netherlands. [19]Aix Marseille University, CNRS, IRD, INRAE, CEREGE, Aix-en-Provence, France. [20]Department of Earth and Planetary Sciences, Northwestern University, Evanston, IL, USA. [21]School of Geography, Archaeology and Irish Studies, University of Galway, Ollscoil na Gaillimhe, Galway, Ireland. [22]Department of

Earth, Geographic, and Climate Sciences, University of Massachusetts, Amherst, MA, USA. [23]Department of Earth and Environmental Sciences, University of Michigan, Ann Arbor, MI, USA. [24]School of Life and Environmental Sciences, The University of Sydney, Sydney, Australia. [25]Department of Earth Science and Geography, Vassar College, Poughkeepsie, NY, USA. [26]Department of Earth, Atmospheric, and Planetary Sciences, Purdue University, West Lafayette, IN, USA. [27]Department of Geological Sciences, University of Colorado Boulder, Boulder, CO, USA. [28]University of Texas Institute for Geophysics, Austin, TX, USA. [29]Department of Geosciences, University of Tübingen, Tübingen, Germany. [30]Department of Earth Sciences, Binghamton University, Binghamton, NY, USA. [31]Department of Earth, Planetary and Space Sciences, University of California, Los Angeles, Los Angeles, CA, USA. [32]MARUM, University of Bremen, Bremen, Germany. [33]Department of Geosciences, Baylor University, Waco, TX, USA. [34]School of Earth and Environmental Sciences, University of St Andrews, St Andrews, UK. [35]State Museum of Natural History, Stuttgart, Germany. [36]Department of Geosciences, Colorado State University, Fort Collins, CO, USA. [37]Department of Earth and Environmental Sciences, Rensselaer Polytechnic Institute, Troy, NY, USA. [38]School of Earth and Environmental Sciences, Cardiff University, Cardiff, UK. [39]Ginkgo Bioworks, Boston, MA, USA. [40]Department of Oceanography, Texas A&M University, College Station, TX, USA. [41]School of Biosciences, University of Sheffield, Sheffield, UK. [42]Department of Geological Science, California State University, Northridge, Northridge, CA, USA. [43]Department of Earth Science, Utah Valley University, Orem, UT, USA. [44]School of Ocean and Earth Science, National Oceanography Centre, University of Southampton, Southampton, UK. [45]Department of Biology, Brandon University, Brandon, Manitoba, Canada. [46]Department of Marine, Earth, and Atmospheric Sciences, North Carolina State University, Raleigh, NC, USA. [47]Utah Geological Survey, Salt Lake City, UT, USA. [48]Nature's Fingerprint Authentication, Molecular Isotope Technologies, LLC, Niantic, CT, USA. [49]Department of Earth, Environmental and Planetary Sciences, Brown University, Providence, RI, USA. [50]Senckenberg Natural History Collections, Dresden, Germany. [51]Department of Geosciences, University of Oslo, Oslo, Norway. [52]Department of Applied Mathematics, Brown University, Providence, RI, USA. [53]EIT Urban Mobility, Barcelona, Spain. [54]Department of Geology, Carleton College, Northfield, MN, USA. [55]Institute of Polar Sciences–National Research Council, Bologna, Italy. [56]School of Chemistry, University of Bristol, Bristol, UK. [57]Dettmer Group KG, Bremen, Germany. [58]Department of Earth Sciences, University of Oregon, Eugene, OR, USA. [59]Deutsches GeoForschungsZentrum GFZ, Potsdam, Germany. [60]Institute of Low Temperature Science, Hokkaido University, Sapporo, Japan. [61]Department of Geological Sciences and Institute of Arctic and Alpine Research, University of Colorado Boulder, Boulder, CO, USA. [62]Department of Earth Science, California State University, Dominguez Hills, Carson, CA, USA. [63]School of Earth Sciences, Addis Ababa University, Addis Ababa, Ethiopia. [64]Independent researcher, Rossum, Netherlands. [65]Laoshan Laboratory, Qingdao, China. [66]Department of Earth and Planetary Sciences, University of California, Santa Cruz, Santa Cruz, CA, USA. [67]Frontiers Science Center for Deep-time Digital Earth, School of Earth Sciences and Resources, China University of Geosciences (Beijing), Beijing, China.

SUPPLEMENTARY MATERIALS

science.org/doi/10.1126/science.adi5177
Supplementary Text
Figs. S1 to S13
Tables S1 to S3
References (*118*–*439*)

Submitted 2 May 2023; accepted 30 October 2023
10.1126/science.adi5177

RESEARCH ARTICLE

QUANTUM INFORMATION

Dipolar spin-exchange and entanglement between molecules in an optical tweezer array

Yicheng Bao[1,2]*, Scarlett S. Yu[1,2], Loïc Anderegg[1,2], Eunmi Chae[3], Wolfgang Ketterle[2,4], Kang-Kuen Ni[1,2,5], John M. Doyle[1,2]

Ultracold polar molecules are promising candidate qubits for quantum computing and quantum simulations. Their long-lived molecular rotational states form robust qubits, and the long-range dipolar interaction between molecules provides quantum entanglement. In this work, we demonstrate dipolar spin-exchange interactions between single calcium monofluoride (CaF) molecules trapped in an optical tweezer array. We realized the spin-$\frac{1}{2}$ quantum XY model by encoding an effective spin-$\frac{1}{2}$ system into the rotational states of the molecules and used it to generate a Bell state through an iSWAP operation. Conditioned on the verified existence of molecules in both tweezers at the end of the measurement, we obtained a Bell state fidelity of 0.89(6). Using interleaved tweezer arrays, we demonstrate single-site molecular addressability.

Quantum entanglement is one of the key ingredients that fundamentally distinguishes quantum mechanics from classical mechanics (*1*). It is considered an essential resource for quantum information processing but remains generally challenging to create experimentally. One mechanism of realizing quantum entanglement between particles is using the electric dipole-dipole interaction, as demonstrated in systems such as Rydberg atoms (*2*) and silicon quantum dots (*3*). Polar molecules possess permanent, long-range, and spatially anisotropic electric dipoles whose interaction could be harnessed for high-fidelity entanglement generation. Therefore, they have been proposed as a powerful platform for realizing quantum simulations of strongly interacting many-body dynamics (*4*–*7*) and for scalable quantum computing (*8*–*12*). Ultracold molecules can be produced through either direct laser cooling (*13*–*17*), assembly of individual ultracold atoms (*18*–*24*), or optoelectrical Sisyphus cooling (*25*, *26*). Current experimental progress has established the capability of preparing and manipulating ultracold molecules with high fidelity (*27*–*33*). In particular, rearrangeable tweezer arrays offer an attractive quantum platform owing to their scalability and potential for single-site addressability (*24*, *34*–*38*). Toward this aim, molecules have been demonstrated to have long qubit (rotational and hyperfine state) coherence times, which are substantially longer than the predicted molecule-molecule dipolar gate times (*28*, *31*, *39*, *40*). In this work, we report the entanglement of pairs of molecules—the critical ingredient in quantum computing and simulation based on molecules—by leveraging long molecular coherence and intrinsic dipolar interactions with individual particle addressability.

A key step toward using ultracold polar molecules for quantum simulations and multiparticle quantum gates is the generation of coherent dipole-dipole couplings between molecules (*12*, *41*), which has been shown in sparsely filled three-dimensional (3D) lattices (*27*) and 2D layers (*42*) and in a molecular quantum gas microscope (*33*). Here, we used resonant electric dipole-dipole coupling for coherent exchange of rotational angular momentum between pairs of laser-cooled CaF molecules individually trapped in optical tweezers. With the ability to tune the angle of the molecular quantization axis in the lab frame, our system realizes both ferromagnetic and antiferromagnetic couplings in a quantum XY spin-exchange model by effectively encoding a spin-$\frac{1}{2}$ system into molecular rotational states. Using this spin-exchange Hamiltonian, we performed iSWAP two-qubit gate operations. An iSWAP gate, when sequentially combined with single-qubit operations, can generate bipartite entanglement deterministically and form a universal set of quantum gates, which is the essential resource for all quantum information applications (*12*, *43*). We found that the fidelity of generated Bell states is presently limited by the thermal motion of molecules within the tweezer traps. Finally, we demonstrate the use of an interleaved dual tweezer-array system, which allows for robust single-site addressability and fast gate operations between molecules. This, combined with expected improved molecular cooling (*44*), has the potential to greatly increase the fidelity of two-qubit operations in this system. This work is parallel and concurrent with that of another study (*45*).

Initial-state preparation of CaF molecules in a 1D optical tweezer array

We began the experiment by loading CaF molecules from a cryogenic buffer gas beam source (*46*) into a radio-frequency magneto-optical trap (*14*). Next, we loaded the molecules into a 1D optical lattice using Λ-enhanced gray molasses

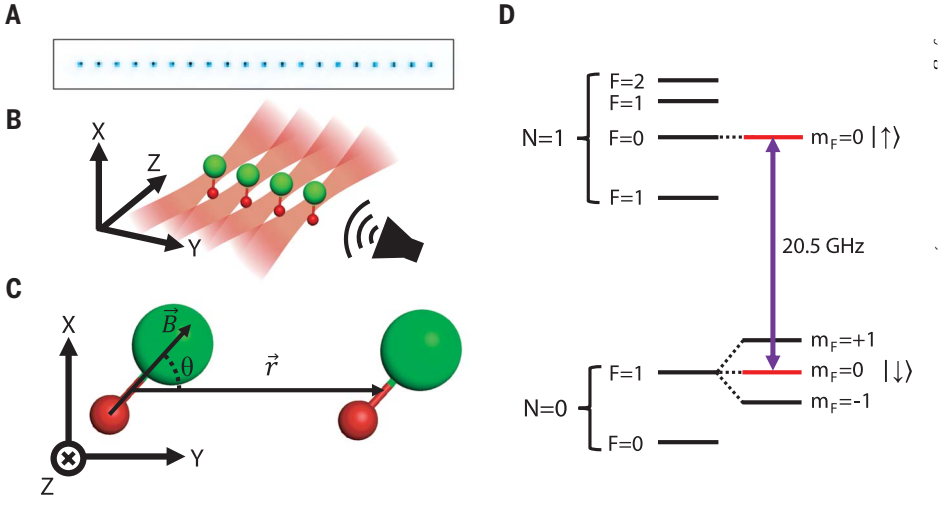

Fig. 1. Experimental setup and relevant energy levels. (**A**) The image of averaged fluorescence from a 20-site optical tweezer array of CaF molecules. (**B**) An illustration of the optical tweezers and the coordinate system used in this work. For visual clarity, only four sites of the realized 20-site array are depicted. (**C**) An illustration showing the relative angle between the applied bias magnetic field $\vec{B}$ (in the *XY* plane) and the intermolecular vector $\vec{r}$. The tweezer light propagates along *Z*. (**D**) Relevant rotational (*N*) and hyperfine (*F*) states in the ground electronic state of CaF.

[1]Department of Physics, Harvard University, Cambridge, MA 02138, USA. [2]Harvard-MIT Center for Ultracold Atoms, Cambridge, MA 02138, USA. [3]Department of Physics, Korea University, Seongbuk-gu, Seoul 02841, South Korea. [4]Department of Physics, Massachusetts Institute of Technology, Cambridge, MA 02139, USA. [5]Department of Chemistry and Chemical Biology, Harvard University, Cambridge, MA 02138, USA.
*Corresponding author. Email: bao@g.harvard.edu

cooling on the electronic $X^2\Sigma^+$–$A^2\Pi_{1/2}$ transition (*47*, *48*) and optically transported them into a glass cell using a focus-tunable moving lattice, as characterized previously (*49*).

We used a microscope objective with 0.6 numerical aperture to project a 1D optical tweezer array in the glass cell, as well as collect fluorescence from the molecules during Λ-imaging (*47*). The array is formed by passing single-frequency 776-nm laser light through a shear-mode acousto-optic deflector (AOD) driven with a multitone waveform (*37*), which is generated by a high-speed arbitrary waveform generator (AWG). This allows for control of the position of individual optical tweezer sites as well as trap depth. We started with a 20-site array formed by a single AOD (Fig. 1A).

We loaded the molecules into the tweezers by overlapping the array with a transported molecular cloud that is held in an optical dipole trap in the presence of the Λ-cooling light. We observed an average probability of 35% for loading a single site with a single molecule. After loading the array, we applied a Λ-imaging pulse and collected fluorescence onto a camera to identify the tweezer sites that are loaded with single molecules in the ground electronic and vibrational state (or empty) with a detection fidelity of 98(1)% and nondestructive detection fidelity of 94(1)% (*37*, *47*). Because the Λ-cooling technique relies on closed photon cycling between the $X, N = 1$ and $A, J = 1/2$ manifolds (N is the rotational angular momentum, and J is the total angular momentum, excluding nuclear spin), only molecules in the $X, N = 1$ rotational manifold can be loaded into the tweezers and detected in this phase of the experiment.

Imaging distributes the population of molecules over all 12 hyperfine states. To prepare the molecules in a single quantum state, we used a combination of optical pumping and microwave transfer. Using short X–A laser pulses resonant with all hyperfine levels in the X, $v = 0$, $N = 1$ manifold except the $|X, N = 1, F = 0, m_F = 0\rangle$ state (v is the vibrational quantum number; F is the total angular momentum, including nuclear spin; and m_F is the magnetic quantum number of F), we pumped most of the molecular population into the latter state. We then linearly ramped down the trap depth of the tweezers in 5 ms and applied a bias magnetic field of ≈3.2 G. A subsequent microwave π-pulse transfers the population from $|X, N = 1, F = 0, m_F = 0\rangle$ to the $|X, N = 0, F = 1, m_F = 0\rangle$ state (Fig. 1B). Finally, we applied an X–A laser pulse that contains frequencies to drive all the hyperfine components in order to remove any molecular population left over in the $X, N = 1$ manifold. In the end, all the remaining molecules in the array were in the $|X, N = 0, F = 1, m_F = 0\rangle$ state, initializing the qubits and effectively encoding a spin-$\frac{1}{2}$ model in the subspace spanned by the $|X, N = 0, F = 1, m_F = 0\rangle \equiv |\uparrow\rangle$ and $|X, N = 0, F = 1, m_F = 0\rangle \equiv |\downarrow\rangle$ states (Fig. 1B). The total state preparation and detection efficiency is 60(2)%, which is limited by the residual population in other hyperfine states within $X, N = 1$ and imperfect imaging fidelity. This state preparation efficiency can be improved by an optimized optical pumping scheme (*45*).

Single-molecule rotational coherence time

To observe high-fidelity dipolar spin-exchange interactions, a long rotational coherence time comparable to the timescale of the dipolar interaction is required. With a sample of molecules at finite temperature in optical tweezers, it is important to control the differential ac Stark shift broadening caused by the molecule's thermal motion in the tweezer trap (*28*, *50*–*52*). To suppress this broadening, the tweezer laser is linearly polarized at a "magic" angle relative to the quantization axis that is defined by the applied bias magnetic field, as detailed previously (*31*) (Fig. 1A). To maximize the single-qubit

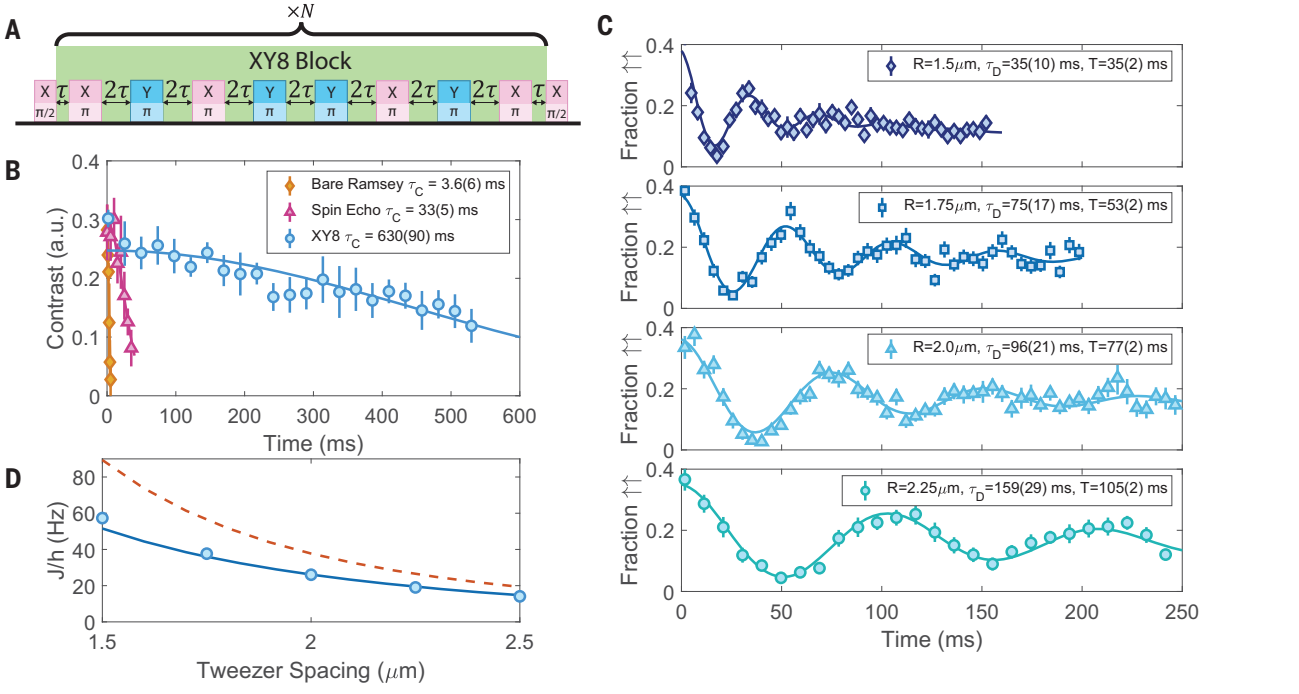

Fig. 2. Rotational coherence and dependence of dipolar interactions on tweezer spacing. (**A**) The Ramsey sequence with XY8 dynamical decoupling used in this work. $X_{\pi/2}$ represents a $\frac{\pi}{2}$-pulse, which rotates the quantum state around the x axis of the Bloch sphere by 90°. Similarly, X_π (Y_π) represents a 180° rotation around the x axis (y axis) on the Bloch sphere. At the top, "×N" means that the block of XY8 pulses is repeated multiple times during the evolution time. (**B**) Measured single-molecule rotational coherence time between $|\uparrow\rangle$ ($N = 1$) and $|\downarrow\rangle$ ($N = 0$) using Ramsey, single–π-pulse spin echo, and the XY8 dynamical decoupling sequences. The coherence time is fitted as a Gaussian $1/e$ decay time constant. (**C**) Dipolar spin-exchange oscillation at various tweezer spacings, with fitted decay-time constant and oscillation period shown in the legends. (**D**) Dipolar spin-exchange interaction strength J versus the tweezer spacing $|\vec{R}|$. The dashed orange line is the theoretical prediction of J at zero temperature. The solid blue line is the simulated result of J with the thermal motion of the molecules taken into account (*59*). In (B) and (C), error bars represent one standard deviation of uncertainty.

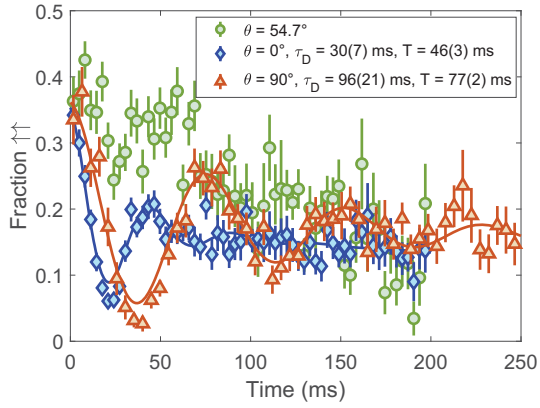

Fig. 3. Dipolar spin-exchange interaction at different angles. Shown are the data for θ = 0°, 54.7°, and 90°. The θ = 0° and θ = 90° data are fitted to an exponentially decaying sinusoidal model, with decay-time constant τ_D and oscillation cycle time T shown in solid lines. Error bars represent one standard deviation of uncertainty.

coherence time, it is beneficial to adiabatically lower the trap depth as much as possible without unduly spilling molecules from the trap. However, this is not optimal for maximizing the number of observed dipolar spin-exchange oscillation cycles. At finite temperature, the instantaneous dipolar interaction strength fluctuates owing to thermal motion, which becomes more prominent in a shallow trap. This is the main mechanism of dephasing. To mitigate this issue, we confined the molecules more tightly by operating the tweezer at a higher trap light intensity for which the magic angle is close to 90°. The work described in this manuscript was performed under these conditions.

We measured the rotational qubit coherence time under conditions of three different microwave pulse sequences used to drive transitions between $|\uparrow\rangle$ and $|\downarrow\rangle$ and observed the population in $|\uparrow\rangle$. With a Ramsey sequence, we observed a single-qubit coherence time of τ_c = 3.6(6) ms. By adding a single π spin-echo pulse, τ_c is extended to 33(5) ms. We used active magnetic field cancellation to remove long-term drift on the order of 10 mG, but the system we used does not remove magnetic field fluctuation within a power line cycle time of less than 1/(60 Hz). This limits the effective interval between spin-echo pulses to an integer multiple of 60 Hz, making it difficult to measure fast dipolar oscillations with only a single π-pulse. Instead, we used dynamical decoupling schemes to preserve the qubit coherence. This technique is used in a variety of quantum information systems (*53*, *54*), including molecular systems (*27*, *30*, *45*). We chose the XY8 dynamical decoupling sequence (Fig. 2A) with a cycle length of 1.6 ms (*55*), which is much shorter than 1/(60 Hz), and achieved a coherence time of τ_c = 630(90) ms. This dynamical decoupling was used for all of our measurements except where noted. Figure 2B shows the measured contrast versus time for single-particle oscillations between $|\uparrow\rangle$ and $|\downarrow\rangle$, from which τ_c is determined.

Coherent dipolar spin-exchange interaction

The dipolar spin-exchange interaction Hamiltonian (*41*) is

$$H_{\text{dip}} = \frac{J}{2}\left(\hat{S}_1^+\hat{S}_2^- + \hat{S}_1^-\hat{S}_2^+\right) = J\left(\hat{S}_1^x\hat{S}_2^x + \hat{S}_1^y\hat{S}_2^y\right) \quad (1)$$

where, respectively, $\hat{S}_i^+(\hat{S}_i^-, \hat{S}_i^x, \hat{S}_i^y)$ is the spin-$\frac{1}{2}$ raising (lowering, Pauli-X, Pauli-Y) operator for molecule number i in a tweezer pair. J is the dipolar interaction strength that can be further expressed as

$$J = \frac{d^2}{4\pi\epsilon_0 r^3}\left(1 - 3\cos^2\theta\right) \quad (2)$$

where d is the transition dipole moment between the $|\uparrow\rangle$ and $|\downarrow\rangle$ state ($d \approx 1$ Debye), ϵ_0 is the vacuum permittivity, r is the intermolecular spacing, and θ is the angle between the quantization axis and the intermolecular axis direction. Apart from molecular systems (*27*, *30*, *33*), this XY spin Hamiltonian was previously studied with Rydberg atoms in optical tweezers (*56*) and atoms in optical lattices (*57*, *58*).

We set the bias magnetic field perpendicular to both the k-vector of the tweezer light and the direction of the 1D tweezer array. The polarization of the linearly polarized tweezer light is rotated to the tweezer array direction (i.e., a magic angle close to 90°). This configuration provides the largest "magic trap depth" (the tightest confinement) at a given magnetic field.

We first prepared pairs of tweezers spaced at $|\vec{R}|$~5 μm, with each site loaded with a single molecule prepared in the $|\downarrow\rangle$ state (or empty), yielding the $|\downarrow\downarrow\rangle$ state. At this separation, the dipolar interaction strength J is negligible (J/h < 3 Hz, where h is Planck's constant). In a time period of ~1 ms, we then moved the even numbered sites toward the odd numbered sites by sweeping the AOD frequency tones of the even sites, which reduces the separation and has the effect of increasing the dipolar interaction strength. We then applied a $\frac{\pi}{2}$-pulse to prepare both molecules in the superposition state $(|\uparrow\rangle + |\downarrow\rangle)/\sqrt{2}$. Then, we applied XY8 dynamical decoupling sequence of microwave pulses. Under the time evolution of dipolar spin-exchange Hamiltonian (H_{dip}), a relative phase accumulated between $(|\downarrow\uparrow\rangle + |\uparrow\downarrow\rangle)/\sqrt{2}$ and $(|\uparrow\uparrow\rangle + |\downarrow\downarrow\rangle)/\sqrt{2}$. (Because the XY8 sequence only contains π-pulses, it will not affect the phase accumulation during the evolution under H_{dip}.) After a wait time, we applied another $\frac{\pi}{2}$-pulse and then moved the molecules apart. To read out the final qubit state, we used a second Λ-imaging pulse to project the system to $|\uparrow\uparrow\rangle$. We selected the data where both sites in a tweezer pair are initially loaded with single molecules. Our measurement yielded the probability $P_{\uparrow\uparrow}$ of detecting both molecules in the $|\uparrow\rangle$ state. To summarize, starting from the initial state $|\downarrow\downarrow\rangle$, a microwave pulse sequence creates a final state that evolves in time as $\psi(t) = \frac{1}{2}\left[\left(1 - e^{-i\frac{J}{2\hbar}}\right)|\downarrow\downarrow\rangle - \left(1 + e^{-i\frac{J}{2\hbar}}\right)|\uparrow\uparrow\rangle\right]$, resulting in the probability $P_{\uparrow\uparrow} = \cos^2\frac{Jt}{4\hbar} = \frac{1}{2}(1 + \cos\frac{Jt}{2\hbar})$, which oscillates at an angular frequency of $\omega_J = \frac{J}{2\hbar}$, where $\hbar$ is reduced Planck's constant.

At smaller tweezer spacings, we observed increased ω_J because of the stronger dipolar interaction between the two molecules (Fig. 2C). By fitting the data to an exponentially decaying sinusoidal model, we extracted the dipolar oscillation cycle period T and contrast decay time constant τ_D. The dipolar spin-exchange strength J at different tweezer spacings can then be calculated from T (Fig. 2D). We found that the measured J is slightly smaller than the theoretical prediction and deviates more as the spacing decreases. This can be explained by the finite temperature of the molecules causing the effective intermolecular spacing $|\vec{r}|$ to be larger than the tweezer spacing $|\vec{R}|$. We used Monte Carlo simulations to describe the behavior of the molecules in the tweezer, including the thermal motion of the molecules, and show in Fig. 2D that the simulated results agree with the experimental data. Additionally, the simulation captures that the thermal motion reduces the observed number of coherent dipolar oscillations as tweezer spacing is decreased (*59*).

Anisotropy of the dipolar interaction

The general dipole-dipole Hamiltonian described in Eqs. 1 and 2 is inherently anisotropic owing to the θ-dependent term. We studied the effect of the anisotropy of spin exchange experimentally by varying the angle θ and measuring the corresponding dipolar interaction strength. The angle θ is varied by rotating the quantization axis relative to the line between the centers of the tweezers. The quantization axis is set by

the applied bias magnetic field and can be changed by tuning the current through two pairs of magnetic field coils while simultaneously rotating the tweezer light polarization to maintain the same magic angle.

In Fig. 3, we show $P_{\uparrow\uparrow}$ at three characteristic angles θ = 0°, 54.7°, and 90°, all taken with a $|\vec{R}| = 2$ μm tweezer spacing. We observed dipolar spin-exchange oscillations in both the θ = 0° and θ = 90° configurations, with the oscillation at θ = 0° being at twice the frequency as that at θ = 90°. No clear oscillation is observed for the θ = 54.7° configuration, which was as expected because the dipolar interaction averages to zero at this angle. These results agree with the absolute value of the magnitude of the anisotropic term in each configuration. We also observed a larger number of oscillation cycles at θ = 90° than at θ = 0°. Our Monte Carlo simulation indicated that thermal motion dephasing is the dominant cause. At θ = 0°, the larger motional wave function spread in the more-weakly trapped axial direction of the optical tweezers results in a large fluctuation of the instantaneous value of θ. The θ = 90° configuration is less affected because of the tight confinement of the optical tweezers in the radial direction.

Fidelity of created Bell states

Dipolar spin-exchange can be used in a two-qubit iSWAP gate to generate entanglement between molecules in neighboring tweezers (*12*). At a dipolar spin-exchange interaction time of $t = T/4 = 19.2$ ms, where T is the oscillation period of the spin-exchange oscillation, the system has evolved into a maximally entangled state known as a Bell state. To test the fidelity of the Bell state that was generated in our system, we applied a third $\frac{\pi}{2}$-pulse (see Fig. 4 legend) around a variable rotation axis on the Bloch sphere (angled ϕ relative to the x axis on the equatorial plane) (Fig. 4A). By varying ϕ and measuring the survival probability of all four possible final-state outcomes, one can construct the parity quantity Π (*43*, *60*):

$$\Pi = \langle \hat{\Pi} \rangle = \left\langle \hat{S}_1^z \hat{S}_2^z \right\rangle = P_{\uparrow\uparrow} + P_{\downarrow\downarrow} - P_{\uparrow\downarrow} - P_{\downarrow\uparrow} \quad (3)$$

Here, $\langle\rangle$ denotes averaging over all occurrences where both sites in a tweezer pair are initially loaded with single molecules, and $\hat{S}_i^z$ represents the Pauli-Z operator on the number i molecule in a pair.

Starting from a Bell state, this sequence will result in a 4π oscillation in Π as ϕ is varied from 0 to 2π (*61*). In Fig. 4B, Π is displayed for both the θ = 0° and θ = 90° configurations. Extracting the contrast of the oscillation for the θ = 90° case, we measured a Bell state fidelity of $\mathcal{F} = 0.32(2)$ and a state preparation and measurement (SPAM)–corrected fidelity of $\mathcal{F}_{\mathrm{SPAM}} = 0.89(7)$. The phase of the parity oscillation reveals the sign of the anisotropic term $(1 - 3\cos^2\theta)$, also seen previously (*45*). Our data show that the θ = 0° configuration leads to a negative J, which corresponds to a ferromagnetic interaction, and the θ = 90° configuration leads to a positive J, which corresponds to an antiferromagnetic interaction.

$\mathcal{F}_{\mathrm{SPAM}}$ is measured to be significantly higher than $\mathcal{F}$, with imperfect state preparation and detection being the surmised cause. In detail, during initial-state preparation, molecules that fail to be prepared in the desired $|N = 0, F = 1, m_F = 0\rangle(|\downarrow\rangle)$ state are intentionally removed by a resonant laser pulse, resulting in an empty trap or traps. During the final readout, if the molecule is in the $|\downarrow\rangle$ state or the trap is simply empty, both would appear dark. We used a π-pulse and additional imaging pulse (Fig. 4C) to distinguish between these two cases. If the molecule is in the $|\downarrow\rangle$ state, it will be transferred to the $|\uparrow\rangle$ state and detected, whereas an empty trap will remain dark. This information is used to exclude the cases of empty traps during the final readout, which improves the contrast of the parity oscillation (Fig. 4D). The resulting Bell state fidelity corrected for measurement error is determined to be $\mathcal{F}_{\mathrm{ex}} = 0.89(6)$, which is higher than the threshold of $\mathcal{F}_{\mathrm{th}} = 0.5$ (*60*), showing, under these conditions, the conditional preparation of entanglement of two molecules in a tweezer pair. The evolution of the system to create a Bell state is an iSWAP operation, and, although we have not fully characterized the system as an iSWAP gate, the Bell state fidelity indicates how it would perform.

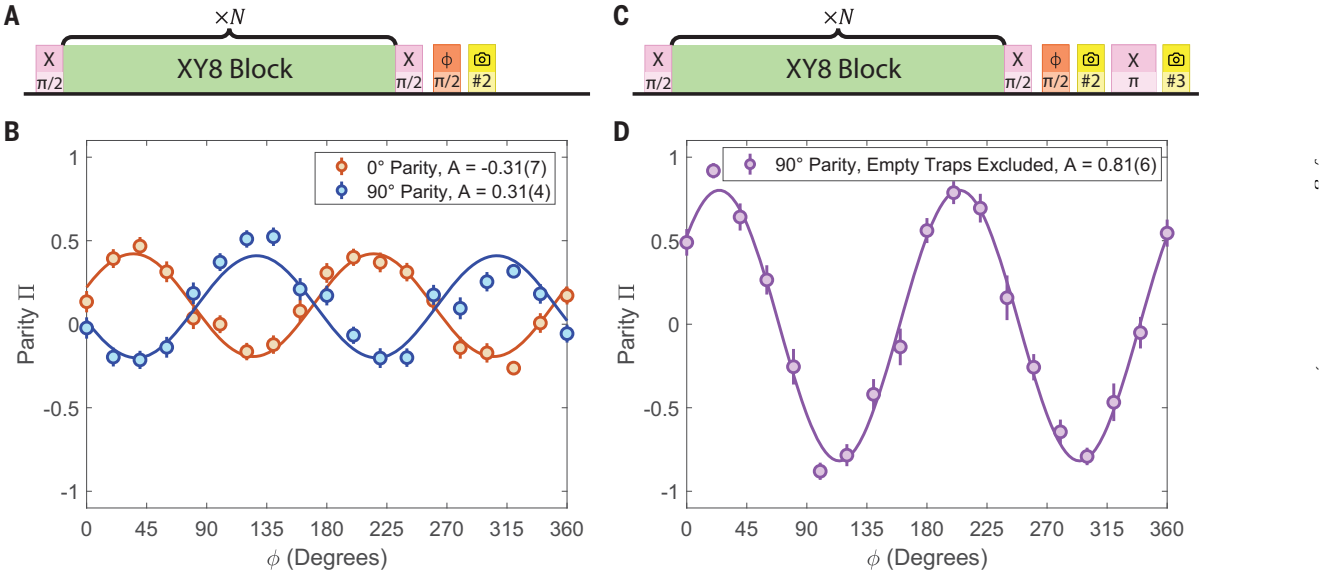

Fig. 4. Parity measurements showing the creation of Bell state pairs. (**A**) The microwave pulse and detection sequence used in the parity oscillation measurement. The XY8 block is the same as that in Fig. 2A. $\phi_{\pi/2}$ denotes a $\frac{\pi}{2}$-pulse with a microwave phase shifted by ϕ relative to the first $X_{\pi/2}$ pulse in the sequence, effectively rotating the quantum state around an axis that is angled ϕ relative to the x axis on the Bloch sphere. The pulse in yellow with a camera symbol represents imaging of the molecules. Note that the first imaging pulse for tweezer-loading identification, as well as the microwave pulses for initial-state preparation, are applied before this sequence and not shown in this figure. (**B**) Parity oscillation at θ = 0° and θ = 90°. A is the fitted parity oscillation amplitude. (**C**) With the addition of a π-pulse and a third imaging step to the sequence shown in (A), molecules are verified to be present throughout the entanglement and readout process. (**D**) Parity oscillation for θ = 90°, with empty traps excluded and corrected for measurement error, using the sequence depicted in (C). In (B) and (D), error bars represent one standard deviation of uncertainty.

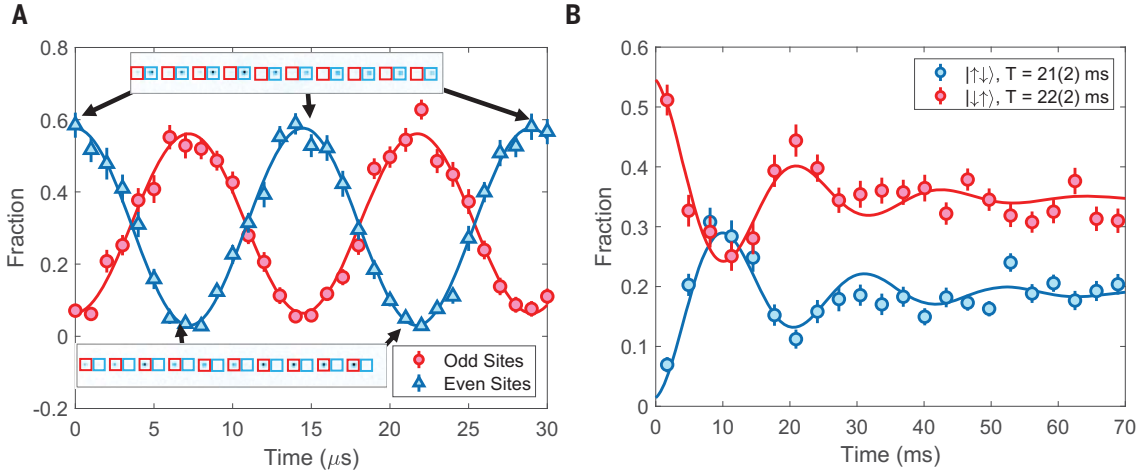

Fig. 5. Single-site–resolved state preparation. (**A**) Rabi oscillation after preparation of the molecular pair in $|\downarrow\uparrow\rangle$. (**B**) Dipolar spin-exchange oscillation with an initial $|\uparrow\downarrow\rangle$ state at θ = 90°. Shown here is the outcome of $|\downarrow\uparrow\rangle$ and $|\uparrow\downarrow\rangle$. In (A) and (B), error bars represent one standard deviation of uncertainty.

Toward arbitrary initial-state preparation

Motivated by the desire to perform robust single-site addressing, instead of using a single AOD to generate all sites in the array, we switched to using one AOD to generate the odd numbered sites and another AOD to generate the even numbered sites. This allowed for convenient independent trap-depth control over each molecule in a pair and uniformity across the array. Additionally, by offsetting the frequency of the tweezer light of the even and odd sites, molecules can be moved in close proximity without experiencing the heating that can arise in a single AOD system (*34*, *38*). For a given trap depth, the differential ac Stark shift results in molecules in even numbered sites being away from the resonance of the $|\uparrow\rangle \rightarrow |\downarrow\rangle$ microwave transition, therefore allowing separate microwave addressing of the odd sites. By applying a microwave π-pulse when odd sites are detuned away, we could prepare an antiferromagnetic initial state $|\uparrow\downarrow\rangle$. Under H_{dip}, an initial state $|\uparrow\downarrow\rangle$ evolves as $\psi(t) = \cos\frac{Jt}{2\hbar}|\uparrow\downarrow\rangle - i\sin\frac{Jt}{2\hbar}|\downarrow\uparrow\rangle$, and $P_{\downarrow\uparrow} = \cos^2\frac{Jt}{2\hbar} = \frac{1}{2}\left(1+\cos\frac{Jt}{\hbar}\right)$ will thus oscillate at an angular frequency of $\frac{J}{\hbar}$.

To demonstrate individual addressing, we first prepared the molecules (both in the even and odd sites) in initial state $|\downarrow\downarrow\rangle$. We then adiabatically ramped the trap depth of the odd sites to seven times that of the even sites, so as to detune the transition of the molecules in the odd sites out of resonance. The microwave π-pulse then only transfers the molecules in the even sites from $|\downarrow\rangle$ to $|\uparrow\rangle$. This creates an antiferromagnetic state $|\downarrow\uparrow\rangle$. By then applying a microwave pulse with variable length of time and detecting molecules in the $|\uparrow\rangle$ state, we observed Rabi oscillations in both even and odd sites with opposite phase (Fig. 5A). To observe dipolar spin exchange, we moved the tweezers to a smaller spacing ($|\vec{R}| = 2$ μm). As with the single AOD system, we applied the XY8 dynamical decoupling pulses and then separated the pairs for detection. The resultant outcome probabilities are shown in Fig. 5B, with a clear display of spin exchange.

Conclusions and outlook

We observed dipolar spin-exchange interactions and created Bell-state entangled pairs with single CaF molecules trapped in optical tweezers. We studied the dipolar interaction and entanglement by tuning the spacing of the optical tweezers and the angle of the electric dipole quantization axis. By applying detection at the end of the entanglement sequence to include only cases where two molecules are present, we determined a Bell state fidelity of $\mathcal{F}_{\mathrm{ex}} = 0.89(6)$ through a parity oscillation measurement. Parity measurements confirm that the interaction in this system can be tuned between ferromagnetic and antiferromagnetic.

The coherence time of dipolar interactions and the single-molecule rotational coherence time are both limited by the finite temperature of the molecules. Implementation of further cooling using other techniques, for example, Raman sideband cooling (*44*), would substantially reduce motional dephasing, extend the single-qubit rotational coherence time (*31*), and thus increase the two-qubit gate fidelity (*12*). The approach presented in this work can be extended to ultracold polyatomic molecules, which have robust parity doublet states that give rise to an advantageous Stark level structure (*62*, *63*).

REFERENCES AND NOTES

1. J. Preskill, *Cal. Inst. Technol.* **16**, 1–8 (1998).
2. D. Barredo *et al.*, *Phys. Rev. Lett.* **114**, 113002 (2015).
3. D. M. Zajac *et al.*, *Science* **359**, 439–442 (2018).
4. A. Micheli, G. Brennen, P. Zoller, *Nat. Phys.* **2**, 341–347 (2006).
5. B. Gadway, B. Yan, *J. Phys. At. Mol. Opt. Phys.* **49**, 152002 (2016).
6. M. A. Baranov, *Phys. Rep.* **464**, 71–111 (2008).
7. M. Wall, K. Hazzard, A. M. Rey, *From Atomic to Mesoscale: The Role of Quantum Coherence in Systems of Various Complexities* (World Scientific, 2015), pp. 3–37.
8. D. DeMille, *Phys. Rev. Lett.* **88**, 067901 (2002).
9. S. Yelin, K. Kirby, R. Côté, *Phys. Rev. A* **74**, 050301 (2006).
10. M. Karra, K. Sharma, B. Friedrich, S. Kais, D. Herschbach, *J. Chem. Phys.* **144**, 094301 (2016).
11. R. Sawant *et al.*, *New J. Phys.* **22**, 013027 (2020).
12. K.-K. Ni, T. Rosenband, D. D. Grimes, *Chem. Sci.* **9**, 6830–6838 (2018).
13. J. F. Barry, D. J. McCarron, E. B. Norrgard, M. H. Steinecker, D. DeMille, *Nature* **512**, 286–289 (2014).
14. L. Anderegg *et al.*, *Phys. Rev. Lett.* **119**, 103201 (2017).
15. S. Truppe *et al.*, *Nat. Phys.* **13**, 1173–1176 (2017).
16. A. L. Collopy *et al.*, *Phys. Rev. Lett.* **121**, 213201 (2018).
17. N. B. Vilas *et al.*, *Nature* **606**, 70–74 (2022).
18. K.-K. Ni *et al.*, *Science* **322**, 231–235 (2008).
19. P. K. Molony *et al.*, *Phys. Rev. Lett.* **113**, 255301 (2014).
20. T. Takekoshi *et al.*, *Phys. Rev. Lett.* **113**, 205301 (2014).
21. J. W. Park, S. A. Will, M. W. Zwierlein, *Phys. Rev. Lett.* **114**, 205302 (2015).
22. M. Guo *et al.*, *Phys. Rev. Lett.* **116**, 205303 (2016).
23. T. M. Rvachov *et al.*, *Phys. Rev. Lett.* **119**, 143001 (2017).
24. L. R. Liu *et al.*, *Science* **360**, 900–903 (2018).
25. M. Zeppenfeld *et al.*, *Nature* **491**, 570–573 (2012).
26. A. Prehn, M. Ibrügger, R. Glöckner, G. Rempe, M. Zeppenfeld, *Phys. Rev. Lett.* **116**, 063005 (2016).
27. B. Yan *et al.*, *Nature* **501**, 521–525 (2013).
28. F. Seeßelberg *et al.*, *Phys. Rev. Lett.* **121**, 253401 (2018).
29. H. J. Williams *et al.*, *Phys. Rev. Lett.* **120**, 163201 (2018).
30. J.-R. Li *et al.*, *Nature* **614**, 70–74 (2023).
31. S. Burchesky *et al.*, *Phys. Rev. Lett.* **127**, 123202 (2021).
32. W. B. Cairncross *et al.*, *Phys. Rev. Lett.* **126**, 123402 (2021).
33. L. Christakis *et al.*, *Nature* **614**, 64–69 (2023).
34. M. Endres *et al.*, *Science* **354**, 1024–1027 (2016).
35. D. Barredo, S. de Léséleuc, V. Lienhard, T. Lahaye, A. Browaeys, *Science* **354**, 1021–1023 (2016).
36. H. Bernien *et al.*, *Nature* **551**, 579–584 (2017).
37. L. Anderegg *et al.*, *Science* **365**, 1156–1158 (2019).
38. J. T. Zhang *et al.*, *Quantum Sci. Technol.* **7**, 035006 (2022).
39. J. W. Park, Z. Z. Yan, H. Loh, S. A. Will, M. W. Zwierlein, *Science* **357**, 372–375 (2017).
40. P. D. Gregory, J. A. Blackmore, S. L. Bromley, J. M. Hutson, S. L. Cornish, *Nat. Phys.* **17**, 1149–1153 (2021).
41. A. V. Gorshkov *et al.*, *Phys. Rev. Lett.* **107**, 115301 (2011).
42. W. G. Tobias *et al.*, *Science* **375**, 1299–1303 (2022).
43. Q. Turchette *et al.*, *Phys. Rev. Lett.* **81**, 3631–3634 (1998).
44. L. Caldwell, M. Tarbutt, *Phys. Rev. Res.* **2**, 013251 (2020).
45. C. M. Holland, Y. Lu, L. W. Cheuk, arXiv:2210.06309 [cond-mat.quant-gas] (2022).
46. N. R. Hutzler, H.-I. Lu, J. M. Doyle, *Chem. Rev.* **112**, 4803–4827 (2012).
47. L. W. Cheuk *et al.*, *Phys. Rev. Lett.* **121**, 083201 (2018).
48. L. Anderegg *et al.*, *Nat. Phys.* **14**, 890–893 (2018).
49. Y. Bao *et al.*, *New J. Phys.* **24**, 093028 (2022).
50. B. Neyenhuis *et al.*, *Phys. Rev. Lett.* **109**, 230403 (2012).
51. E. Chae, *Phys. Chem. Chem. Phys.* **23**, 1215–1220 (2021).
52. J. Lin, J. He, X. Ye, D. Wang, *Phys. Rev. A* **103**, 023332 (2021).

53. T. Gullion, D. B. Baker, M. S. Conradi, *J. Magn. Reson.* **89**, 479 (1990).
54. J. Du *et al*., *Nature* **461**, 1265–1268 (2009).
55. The XY8 sequence effectively acts as a band-pass filter with, in our case, its pass-band centered at 10 kHz (*64*), which is higher than the dominant magnetic field noise spectrum range in our system.
56. S. de Léséleuc, D. Barredo, V. Lienhard, A. Browaeys, T. Lahaye, *Phys. Rev. Lett.* **119**, 053202 (2017).
57. A. de Paz *et al*., *Phys. Rev. Lett.* **111**, 185305 (2013).
58. P. N. Jepsen *et al*., *Nature* **588**, 403–407 (2020).
59. See fig. S2 in the supplementary materials.
60. C. A. Sackett *et al*., *Nature* **404**, 256–259 (2000).
61. L. Pezzè, A. Smerzi, M. K. Oberthaler, R. Schmied, P. Treutlein, *Rev. Mod. Phys.* **90**, 035005 (2018).
62. P. Yu, L. W. Cheuk, I. Kozyryev, J. M. Doyle, *New J. Phys.* **21**, 093049 (2019).
63. C. Hallas *et al*., *Phys. Rev. Lett.* **130**, 153202 (2023).
64. J. Choi *et al*., *Phys. Rev. X* **10**, 031002 (2020).
65. Y. Bao *et al*., Data for Dipolar spin-exchange and entanglement between molecules in an optical tweezer array. Zenodo (2023); https://doi.org/10.5281/zenodo.8404386.

ACKNOWLEDGMENTS

We thank M. D. Lukin and N. Y. Yao for carefully reading the manuscript. **Funding:** This material is based upon work supported by the US Department of Energy, Office of Science, National Quantum Information Science Research Centers, Quantum Systems Accelerator. Additional support is acknowledged from the Air Force Office of Scientific Research, the Asian Office of Aerospace Research and Development, the Army Research office, and the National Science Foundation (NSF). S.S.Y. acknowledges support from the NSF Graduate Research Fellowships Program. L.A. and S.S.Y. acknowledge support from the Harvard Quantum Initiative (HQI). E.C. acknowledges support from the National Research Foundation of Korea (2020R1A4A1018015, 2021M3H3A1085299, 2022M3E4A1077340, and 2022M3C1C8097622). **Author contributions:** Y.B., S.S.Y., L.A., E.C., W.K., K.-K.N., and J.M.D. contributed to the experimental effort. All authors discussed the results and contributed to the manuscript. **Competing interests:** The authors declare no competing interests. **Data and materials availability:** All data needed to evaluate the conclusions in this paper are present in the paper or in the supplementary materials. All data presented in this paper are deposited at Zenodo (*65*). **License information:** Copyright © 2023 the authors, some rights reserved; exclusive licensee American Association for the Advancement of Science. No claim to original US government works. https://www.science.org/about/science-licenses-journal-article-reuse

SUPPLEMENTARY MATERIALS

science.org/doi/10.1126/science.adf8999
Supplementary Text
Figs. S1 to S3
Reference (*66*)

Submitted 18 November 2022; accepted 12 October 2023
10.1126/science.adf8999

QUANTUM INFORMATION

On-demand entanglement of molecules in a reconfigurable optical tweezer array

Connor M. Holland[1]†, Yukai Lu[1,2]†, Lawrence W. Cheuk[1]*

Entanglement is crucial to many quantum applications, including quantum information processing, quantum simulation, and quantum-enhanced sensing. Because of their rich internal structure and interactions, molecules have been proposed as a promising platform for quantum science. Deterministic entanglement of individually controlled molecules has nevertheless been a long-standing experimental challenge. We demonstrate on-demand entanglement of individually prepared molecules. Using the electric dipolar interaction between pairs of molecules prepared by using a reconfigurable optical tweezer array, we deterministically created Bell pairs of molecules. Our results demonstrate the key building blocks needed for quantum applications and may advance quantum-enhanced fundamental physics tests that use trapped molecules.

Entanglement lies at the heart of quantum mechanics. It is central to the practical advantage provided by quantum devices (*1*–*3*) and relevant to understanding the behavior of many-body quantum systems (*4*). The ability to create entanglement controllably has been a long-standing experimental challenge. Molecules have been proposed as a promising platform for quantum simulation and quantum information processing because of their rich internal structure and long-lived interacting states (*5*–*8*). In the past two decades, much progress has been made in producing and controlling molecules at ultracold temperatures, both through coherent assembly of ultracold alkali atoms (*9*) and direct laser-cooling (*10*). Rapid advances have been made in recent years, including the creation of degenerate molecular gases (*11*, *12*), the creation of molecular magneto-optical traps (*10*, *13*–*15*), high-fidelity detection of single molecules (*16*–*18*), and laser-cooling of complex polyatomic molecules (*19*, *20*). In addition, coherent dipolar interactions have been observed in bialkali molecules trapped in optical lattices (*18*, *21*).

A major outstanding challenge to fully realizing the potential of molecules has been achieving deterministic entanglement with microscopic control. In this work, we realized on-demand entanglement between individual laser-cooled molecules trapped in a reconfigurable optical tweezer array (Fig. 1A). The approach of molecular tweezer arrays (*16*, *17*, *22*, *23*) combines the microscopic controllability offered by reconfigurable optical tweezer traps (*24*–*28*) with the ability to generate entanglement through the electric dipolar interaction between molecules. We specifically made use of effective spin-exchange interactions that arise between rotational states to entangle pairs of molecules into Bell states (Fig. 1B) (*29*), which are prototypical maximally entangled states of two particles. Our entanglement protocol implements an iSWAP gate (*8*) that, along with site-resolved single-qubit rotations achievable in our platform through the optical addressing of individual molecules, fulfills the requirement for universal quantum computation.

[1]Department of Physics, Princeton University, Princeton, NJ 08544, USA. [2]Department of Electrical and Computer Engineering, Princeton University, Princeton, NJ 08544, USA.
*Corresponding author. Email: lcheuk@princeton.edu
†These authors contributed equally to this work.

Preparing and initializing arrays of laser-cooled molecules

Our work starts with single laser-cooled calcium monofluoride (CaF) molecules trapped in a dynamically reconfigurable array of optical tweezer traps (*17*, *23*). Through a series of steps involving laser-cooling, optical trapping, and transport, single molecules are transferred from a magneto-optical trap into a one-dimensional (1D) array of 37 identical optical tweezer traps with a uniform spacing of 4.20(6) μm (numbers in parentheses are the standard deviation). Because our laser-cooling scheme relies on a closed optical cycle present only for the $X^2\Sigma(v = 0, N = 1)$ manifold in CaF (*30*)—where v and N denote the molecular vibrational and rotational state, respectively—the molecules loaded into the tweezers occupy a single rovibrational manifold.

To remove the randomness in tweezer occupation, we used a rearrangement approach pioneered in neutral atom experiments (*24*, *25*). We nondestructively detected the tweezer occupations using a variant of Λ-imaging (*31*). The empty tweezers were identified then switched off, and the remaining occupied tweezers were then rearranged into the desired 1D pattern. We characterized the rearrangement procedure by measuring the probability of successfully creating uniform arrays and found a single-particle rearrangement fidelity of 97.4(1)%. As shown in Fig. 2A, we were able to create uniform arrays up to a size of 16, with a probability >0.6. The rearrangement fidelity was limited by the nondestructive detection fidelity, with minimal loss [0.2(10)%] caused by movement in the tweezer traps.

After rearrangement, we initialized the internal state of the molecules, which were distributed among the 12 hyperfine states in the $X^2\Sigma(v = 0, N = 1)$ rovibrational manifold. To prepare molecules into a single hyperfine state, we optically pumped molecules into $|D\rangle = X^2\Sigma(v = 0, N = 1, J = 3/2, F = 2, m_F = 2)$, where J denotes the total angular momentum excluding nuclear spin, F denotes the total angular momentum, and m_F denotes its projection onto the quantization axis. Subsequent microwave sweeps along with an optical clean-out pulse transferred the molecules into the target final state $|\uparrow\rangle = X^2\Sigma(v = 0, N = 1, J = 1/2, F = 0, m_F = 0)$ (Fig. 2C). The overall fidelity of preparing molecules in $|\uparrow\rangle$ was 82.4(11)%. Our preparation sequence ensures that the dominant preparation error is in the form of unoccupied tweezers, with a small contribution coming from molecules prepared in the incorrect internal state $|+\rangle = X^2\Sigma(v = 0, N = 0, J = 1/2, F = 1, m_F = 1)$. The state initialization errors come from imperfect microwave transfer, polarization impurity of the optical pumping light, and loss caused by heating in the tweezer traps. After state preparation, we measured a molecular temperature of T = 151(10) μK.

Probing rotational coherence of single molecules

To produce entanglement through the dipolar interactions between molecules, we required long coherence times compared with the typical interaction timescales of ~10 ms at our tweezer separations. Achieving long coherence times for optically trapped molecules has been an ongoing experimental challenge, with steady advances being made. For molecules, different internal states can experience different trapping potentials that, in combination with motion caused by finite temperature, can lead to decoherence. For $^1\Sigma$ bialkali molecules, long coherence times of different nuclear spin states have been reported (*32*). Work using "magic" trapping conditions has also demonstrated extended coherence times between rotational states in both $^1\Sigma$ and $^2\Sigma$ molecules (*18*, *33*–*36*).

Because the effective spin-exchange interactions couple different rotational states, we wanted long rotational coherence times between the two interacting states $|\uparrow\rangle$ and $|\downarrow\rangle = X^2\Sigma(v = 0, N = 0, J = 1/2, F = 1, m_F = 0)$. Building on previous work in CaF (*36*), we identified a pseudo-magic trapping condition in which both spin states experience approximately identical trapping potentials. Our pseudo-magic condition takes into account vector and tensor shifts and is achieved by applying a magnetic field orthogonal to the tweezer light polarization at a reduced tweezer depth

compared with that used for initial loading and imaging.

To measure the resulting coherence time, we prepared pairs of tweezer traps in which one trap is empty and the other is occupied by a molecule initialized in $|\uparrow\rangle$. We next applied a Ramsey pulse sequence consisting of two $\pi/2$ microwave pulses (first pulse along $\hat{x}$, second pulse along $\hat{n} = \cos\theta\hat{x} + \sin\theta\hat{y}$) separated by a variable free evolution time (Fig. 3A). The remaining fraction of $|\uparrow\rangle$ molecules, $P_\uparrow$, oscillates as a function of θ, with the oscillation amplitude directly measuring the coherence. Fitting to an exponential decay curve yields a bare coherence time T_2^* of 2.5(3) ms. Adding a spin-echo improves the coherence time to T_2 = 29(2) ms. Following previous work that explored dipolar interactions of KRb molecules in an optical lattice (*21*, *37*), we implemented the XY8 dynamical decoupling sequence depicted in Fig. 3B and found that the $1/e$ coherence time was further extended to 215(30) ms (Fig. 3C). This is consistent with our understanding that the bare coherence times are primarily limited by slow (millisecond timescale) fluctuations of ambient magnetic fields.

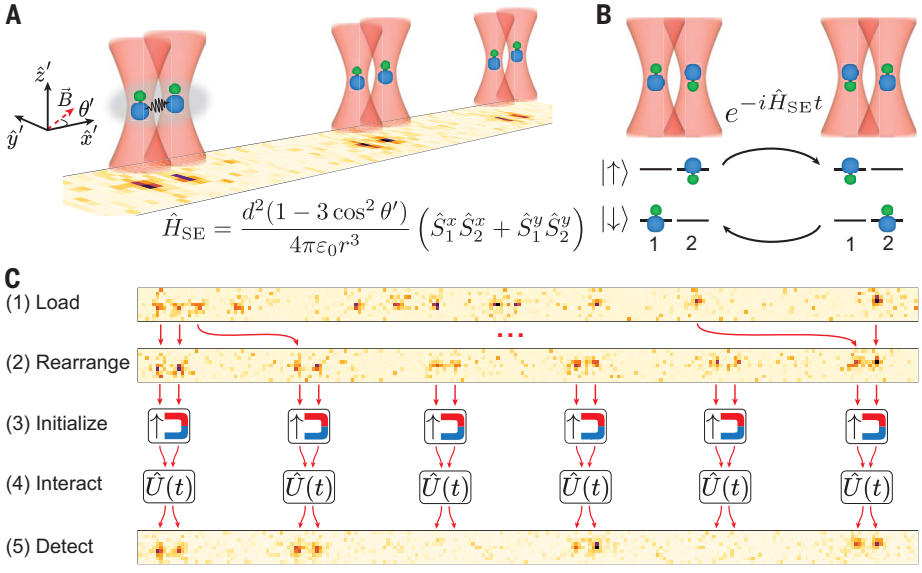

Fig. 1. Laser-cooled molecules in a reconfigurable optical tweezer array. (**A**) Single CaF molecules trapped in an optical tweezer array are prepared into closely separated tweezer pairs. Molecules in each pair held by separate tweezer traps interact through the long-range electric dipolar interaction $\hat{H}_{SE}$. (**B**) The electric dipolar interaction leads to dipolar spin-exchange of rotational excitations. (**C**) Molecules are loaded stochastically, detected nondestructively, and rearranged into the desired 1D configuration. The molecules are then initialized into a single internal state, and the pair separations are reduced to switch on interactions. After specific interaction times, the pairs are separated and detected state-selectively.

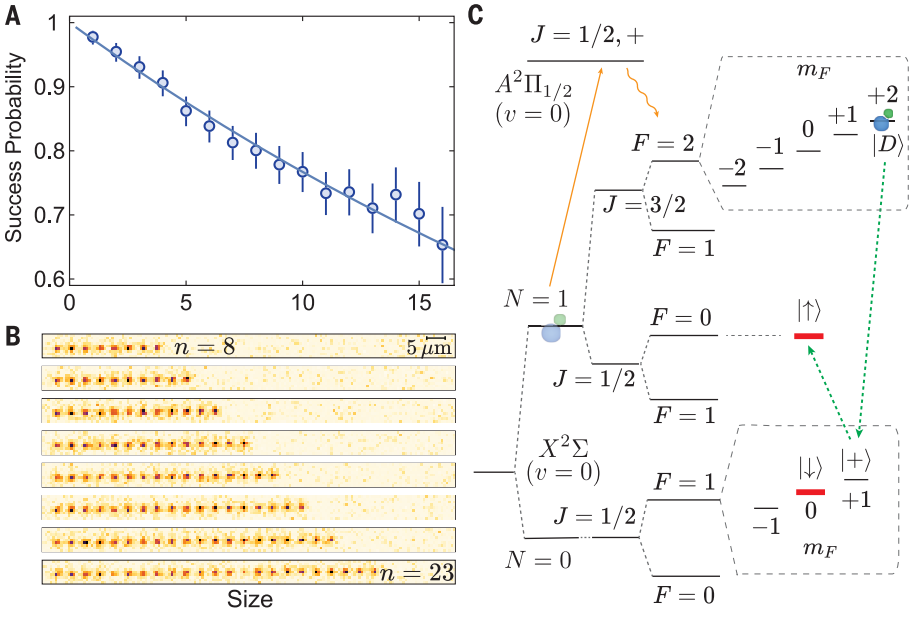

Fig. 2. Tweezer rearrangement and internal state initialization. (**A**) Probability of creating defect-free molecular arrays through rearrangement. A fit to p^n, where n is the array size, gives a single-particle rearrangement fidelity of p = 0.974(1). (**B**) Example images of defect-free arrays. (**C**) Optical pumping (orange arrow) prepares molecules in $|D\rangle$. Microwave sweeps (dashed green arrows) transfer $|D\rangle$ molecules to $|\uparrow\rangle$.

Observing coherent intermolecular interactions

Having achieved sufficiently long rotational coherence times, we next set out to observe coherent spin-exchange interactions. The long-range electric dipolar interaction between the molecules gives rise to resonant exchange of rotational excitations between $|\uparrow\rangle$ and $|\downarrow\rangle$. The resulting spin-exchange interaction is described by the Hamiltonian

$$H_{SE} = \frac{J}{2}\left(\hat{S}_1^+\hat{S}_2^- + \hat{S}_1^-\hat{S}_2^+\right) = J\left(\hat{S}_1^x\hat{S}_2^x + \hat{S}_1^y\hat{S}_2^y\right)$$

where $\hat{S}_i^+, \hat{S}_i^-, \hat{S}_i^x, \hat{S}_i^y$ are spin-1/2 operators for molecule i and

$$J = \frac{d^2}{4\pi\varepsilon_0}\frac{1}{r^3}\left(1 - 3\cos^2\theta'\right)$$

with $d = \langle\uparrow|\hat{\mathbf{d}}|\downarrow\rangle$ being the transition dipole moment, $r = |\vec{r}|$ being the intermolecular separation, θ' being the angle between $\vec{r}$ and the quantization axis, and ε_0 being the free space permittivity. Starting with two molecules in a product state, time evolution under $\hat{H}_{SE}$ can lead to entanglement. For example, two molecules initially prepared in the product state $|\uparrow\rangle \otimes |\downarrow\rangle$ become maximally entangled after interacting for a time $t = \pi\hbar/(2J)$, where $\hbar$ is Planck's constant h divided by 2π. In our system, the quantization axis is orthogonal to the intermolecular separation—that is, θ' = 90°.

To observe the effect of spin-exchange interactions, we first created pairs of $|\uparrow\rangle$ molecules at an initial separation of 4.20(6) μm, over which interactions were negligible. We next reduced the pair separation to 1.93(3) μm over 3 ms, at which the interaction strength J ($J = h \times 43$ Hz) becomes appreciable on the coherence timescale. Subsequently, we applied the Ramsey pulse sequence used above with θ = 0. To retain long coherence times, the XY8 decoupling pulses were kept on during the free

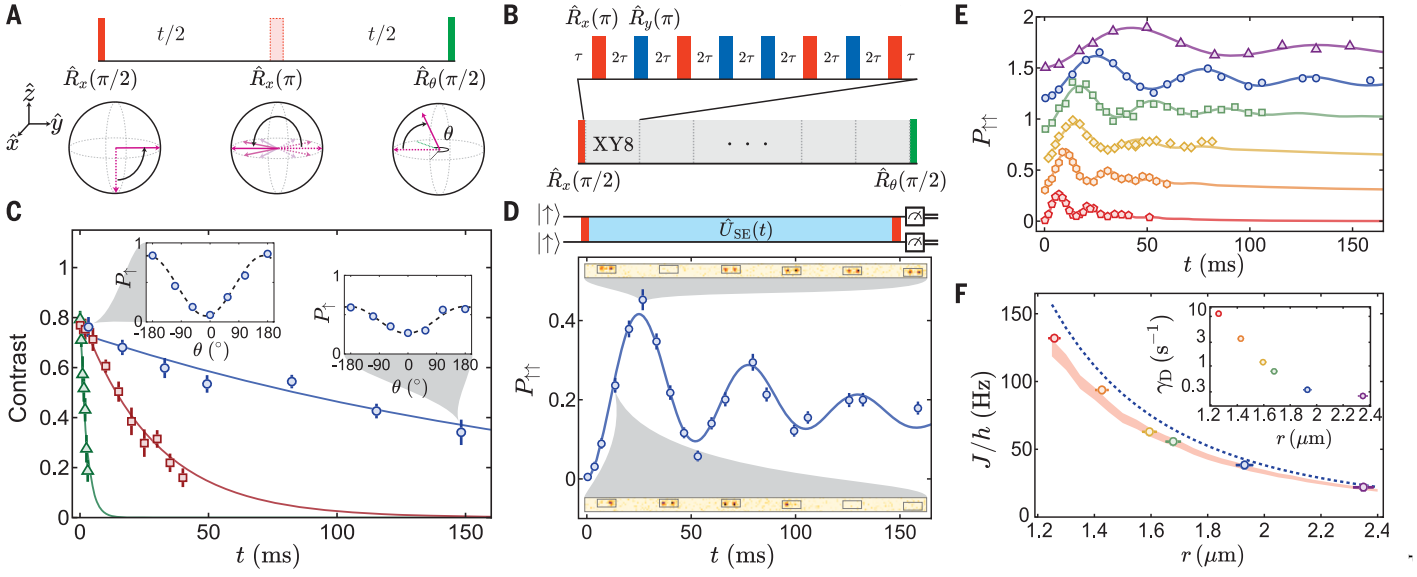

Fig. 3. Single-particle coherence and spin-exchange oscillations. (**A**) Ramsey pulse sequence used to measure rotational coherence. (Bottom) Bloch sphere diagrams show the action of the various pulses for a molecule initialized in $|\downarrow\rangle$. (**B**) The XY8 dynamical decoupling sequence. (**C**) Ramsey contrast of noninteracting molecules versus free evolution time t. Green triangles, red squares, and blue circles indicate the cases for which no spin-echo, one spin-echo, and the XY8 sequence is applied, respectively. Exponential fits give coherence times ($1/e$) of 2.5(3) ms, 29(2) ms, and 215(30) ms, respectively. (Insets) Ramsey fringes with corresponding sinusoidal fits indicated with the dashed lines. (**D**) Spin-exchange oscillations at a tweezer separation of 1.93(3) μm. Shown are the $|\uparrow\uparrow\rangle$ populations measured after the Ramsey pulse sequence, $P_{\uparrow\uparrow}$, as a function of interaction time t, for molecular pairs initialized in $|\uparrow\uparrow\rangle$. The solid curve is a fit to a phenomenological model. (Insets) Fluorescence images at the indicated times. (**E**) Spin-exchange oscillations at separations of 1.26(2) μm (red pentagons), 1.43(2) μm (orange hexagons), 1.60(2) μm (yellow diamonds), 1.68(2) μm (green squares), 1.93(3) μm (blue circles), and 2.35(3) μm (purple triangles). Curves are offset vertically by 0.3 for clarity. (**F**) The extracted spin-exchange strength J versus pair separation r. The light red band indicates the theoretical prediction taking into account the finite temperature of the molecules and the uncertainty in the electric dipole moment of CaF. The dashed blue curve indicates the prediction without taking into account finite temperature. (Inset) The single-particle loss rate γ_D versus pair separation r.

evolution time. Because the π-pulses in the XY8 sequence leave $\hat{H}_{SE}$ unchanged, spin-exchange interactions are preserved (*38*).

For a molecular pair initialized in $|\uparrow\uparrow\rangle$, the resulting state after the Ramsey sequence is given by

$$|\psi\rangle = ie^{-i\frac{Jt}{4\hbar}}\left[\sin\left(\frac{Jt}{4\hbar}\right)|\uparrow\uparrow\rangle + i\cos\left(\frac{Jt}{4\hbar}\right)|\downarrow\downarrow\rangle\right] \quad (1)$$

and $P_{\uparrow\uparrow}$ oscillates at an angular frequency of $J/(2\hbar)$. As shown in Fig. 3D, we observed oscillations of $P_{\uparrow\uparrow}$, directly revealing the presence of coherent spin-exchange interactions. By varying the pair separation between 1.26(2) and 2.35(3) μm, we verified that the interaction strength J, as extracted from the oscillation frequency, approximately scales as $1/r^3$, as expected for dipolar interactions (Fig. 3F). Experiments with bulk samples of bialkali molecules in optical lattices have observed coherent spin-exchange both through macroscopic measurements (*21*, *37*) and with single-molecule resolution (*18*), whereas in this work, we observed coherent interactions between individually prepared, laser-cooled molecules.

Examining the $P_{\uparrow\uparrow}$ oscillations in detail, we found that they damp more quickly when the molecules are closer. This could arise from increased molecular loss and reduced single-particle coherence times at close separations. Additionally, the thermal motion of molecules gives rise to disorder in the spin-exchange coupling constant J through variations in the intermolecular separations, leading to damping. At a fixed molecular temperature, this effect increases at closer separations. To determine which damping mechanism is dominant, we first measured single-particle loss rates and found that they increase at close separations (Fig. 3F, inset). We believe that the loss is caused by parametric heating specific to our scheme of generating tweezer traps using an acousto-optical deflector (AOD) and can be circumvented with other tweezer-generation techniques. Molecular loss, however, does not account for all of the observed damping, especially at close separations. Independently measured single-particle decoherence rates are also insufficient to explain the damping. This leaves finite molecular temperature as the dominant cause of damping at close distances. Simulations that used experimentally measured temperatures revealed damping rates comparable with the observations (supplementary text and fig. S2) (*39*).

Creating and verifying entanglement of molecules

Having established the presence of coherent spin-exchange interactions, we next used them to entangle molecules. Specifically, as proposed in (*8*), time evolution by $\hat{H}_{SE}$ for a specific time of $T = \pi\hbar/J$ implements an iSWAP gate, which is maximally entangling. By applying two additional π/2 pulses along the x axis before and after the iSWAP gate, one can convert a molecular pair prepared in $|\uparrow\uparrow\rangle$ into the Bell state $|\psi_B\rangle = \frac{1}{\sqrt{2}}(|\uparrow\uparrow\rangle + i|\downarrow\downarrow\rangle)$, which is maximally entangled. As a compromise between maximizing J and minimizing heating loss, we chose a pair separation of 1.93(3) μm for creating $|\psi_B\rangle$.

To demonstrate entanglement of molecules, we measured the Bell state creation fidelity $\mathcal{F} = \langle\psi_B|\rho|\psi_B\rangle$, where ρ is the experimentally obtained density matrix. As pointed out in (*40*), $\mathcal{F}$ acts as an entanglement witness, with $\mathcal{F} > 1/2$ indicating two-particle entanglement. To extract $\mathcal{F}$ experimentally, we made use of the relation (*41*)

$$\mathcal{F} = \frac{1}{2}\left(P_{\uparrow\uparrow} + P_{\downarrow\downarrow} + \mathcal{C}\right) \quad (2)$$

where $P_{\uparrow\uparrow}$ and $P_{\downarrow\downarrow}$ are the probabilities of measuring $|\uparrow\uparrow\rangle$ and $|\downarrow\downarrow\rangle$, respectively, and $\mathcal{C}$ is the amplitude of the coherence between $|\uparrow\uparrow\rangle$ and $|\downarrow\downarrow\rangle$.

To measure $P_{\uparrow\uparrow}$, we separated the two molecules after preparing $|\psi_B\rangle$ and subsequently

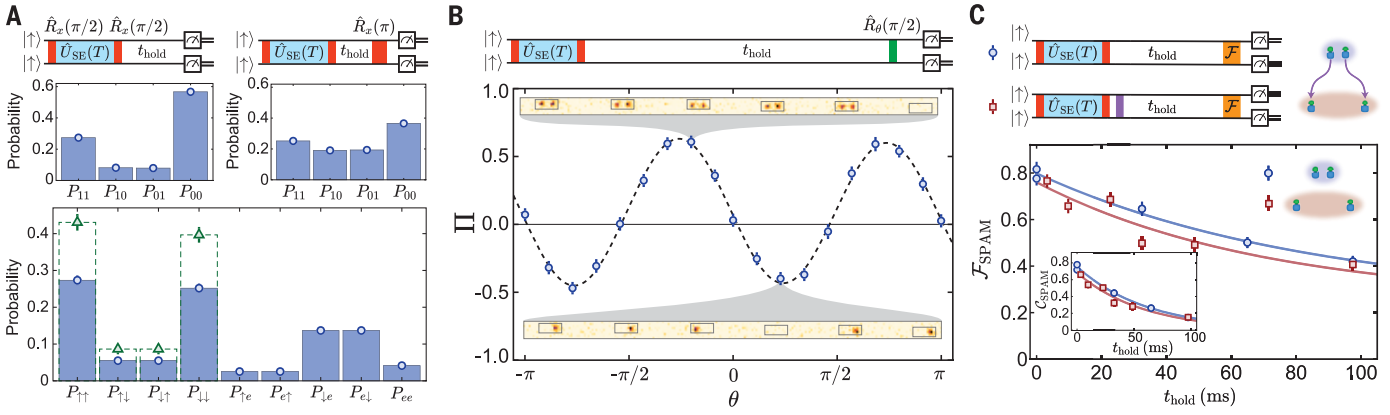

Fig. 4. Creating and probing Bell pairs. (**A**) (Top left) The two-tweezer detection probabilities P_{ij} for the Bell pairs. (Top right) Corresponding probabilities when an additional π pulse is applied before measurement. (Bottom) The full probabilities extracted from top left and top right. The SPAM-corrected populations for the $|\uparrow\rangle - |\downarrow\rangle$ subsystem are indicated with the green triangles. (**B**) Probing Bell state coherence through parity oscillations. The coherence $\mathcal{C}$ between $|\uparrow\uparrow\rangle$ and $|\downarrow\downarrow\rangle$ is obtained from the amplitude of the oscillations in Π as a function of θ. (Insets) Example images at the maxima and minima of Π. (**C**) SPAM-corrected Bell state fidelity $\mathcal{F}_{\mathrm{SPAM}}$ versus hold time t at the initial pair creation distance of 1.93(3) μm are indicated with blue circles. Red squares indicate the corresponding data for pairs separated to a larger distance of 4.20(6) μm after creation. (Inset) The contrast $\mathcal{C}_{\mathrm{SPAM}}$ versus hold time t for the two separations. The extracted 1/e lifetimes are ($\mathcal{F}_{\mathrm{SPAM}}$, $\mathcal{C}_{\mathrm{SPAM}}$) = [85(5) ms, 61(3) ms] at the Bell creation distance, and [70(16) ms, 57(8) ms] at the larger separation.

measured the probability that both tweezers in a pair appear bright. Because our imaging scheme detects only $|\uparrow\rangle$ molecules, to measure $P_{\downarrow\downarrow}$ we applied an additional π-pulse before detection (Fig. 4A) to convert molecules from $|\downarrow\rangle$ to $|\uparrow\rangle$. To obtain the coherence envelope $\mathcal{C}$, we measured parity oscillations as follows. We applied a π/2 pulse about a variable axis $\hat{n} = \cos\theta\hat{x} + \sin\theta\hat{y}$ after preparing $|\psi_B\rangle$. From the two-tweezer probabilities P_{ij}, we constructed the parity signal $\Pi = P_{11} + P_{00} - P_{10} - P_{01}$, where 1 and 0 denote a bright or dark tweezer site, respectively.

For a general density matrix that includes the possibility of empty tweezers ($|e\rangle$) caused by imperfect state preparation, Π can display modulation periodic in 2θ and θ. The 2θ modulation is directly related to the coherence between $|\uparrow\uparrow\rangle$ and $|\downarrow\downarrow\rangle$, whereas the θ modulation is related to single-molecule coherences, such as that between $|e\uparrow\rangle$ and $|e\downarrow\rangle$. The amplitude of the 2θ modulation directly gives $\mathcal{C}$. As shown in Fig. 4B, we found that Π displays modulation periodic in 2θ. The lack of oscillations periodic in θ is consistent with the pulse sequence used. Single molecules prepared in $|e\uparrow\rangle$ or $|\downarrow e\rangle$ effectively experienced a π-pulse, and no single particle coherence was created.

From the population and parity oscillation measurements, we obtained a raw Bell state fidelity of $\mathcal{F}_{\mathrm{RAW}} = 0.524(6)$. Correcting for detection errors, we obtained a Bell state fidelity $\mathcal{F} = 0.540(7)$. The raw and measurement-corrected fidelities were above 1/2, showing that entanglement was indeed present and created on demand.

Correcting additionally for state preparation errors, we obtained a state-preparation and measurement (SPAM)–corrected fidelity of $\mathcal{F}_{\mathrm{SPAM}} = 0.80(2)$. In the context of quantum information processing, the SPAM-corrected Bell state fidelity provides an indication of the quality of the iSWAP gate implemented through spin exchange. Nevertheless, full characterization of our iSWAP gate and a measurement of its fidelity will require full quantum process tomography. With relevance to quantum simulation, our measurements of spin-exchange interactions demonstrate the fundamental building block for simulating XY spin models. In particular, the phase of the 2θ oscillation in parity measures the relative phase between $|\uparrow\uparrow\rangle$ and $|\downarrow\downarrow\rangle$ in the Bell state, which is sensitive to the sign of J. The observed phase of the oscillation shows that $J > 0$, indicating antiferromagnetic spin-exchange interactions. In addition to quantum information processing and quantum simulation, the ability to create entanglement in our system also paves the way toward quantum-enhanced metrology with trapped molecules (*42*).

Having demonstrated deterministic creation of Bell pairs, we next probed their lifetime. We measured the Bell state fidelity $\mathcal{F}_{\mathrm{SPAM}}$ as a function of hold time and found a lifetime of 85(5) ms, which is largely consistent with but somewhat shorter than that expected from uncorrelated single-particle decoherence. We also examined whether the Bell pairs survive when separated to larger distances after their creation. Specifically, we separated the Bell pairs to a distance of 4.20(6) μm over 3 ms after their creation and measured $\mathcal{F}_{\mathrm{SPAM}}$ as a function of hold time. Within experimental uncertainty, we found a lifetime identical to the case without separation (Fig. 4C). This ability to preserve entanglement while separating molecules could allow one to bypass the limited range of dipolar interactions through movement of molecules and obtain arbitrary connectivity useful for quantum simulation and information processing. Similar abilities to preserve entanglement have recently been demonstrated in atomic tweezer arrays (*43*).

Last, we examined how Bell state fidelities can be improved. The measurement-corrected fidelities were affected substantially by state preparation infidelity, which is caused by a variety of technical imperfections such as incomplete microwave transfers. A detailed accounting of errors shows that state preparation fidelities exceeding 0.95 can be achieved (*39*). Separately, the SPAM-corrected Bell state fidelity, which reflects the quality of the iSWAP gate, is substantially affected by the finite molecular temperature. To reveal the importance of state preparation fidelity and molecular temperature, we implemented an alternate state preparation procedure (*39*) that both provides a higher state preparation fidelity [0.85(1)] and a lower molecular temperature [T = 107(5) μK]. The resulting fidelities without state preparation correction were improved to $\mathcal{F}_{\mathrm{RAW}} = 0.608(14)$ and $\mathcal{F} = 0.629(14)$, revealing the importance of state preparation (two-tweezer probabilities and parity oscillation data are provided in fig. S4) (*39*). In addition, $\mathcal{F}_{\mathrm{SPAM}}$ improves to 0.863(25) (*39*), suggesting that molecular temperature is a key factor in achieving high-fidelity entanglement.

Discussion and Outlook

The observed dependence of SPAM-corrected Bell state fidelities on temperature agrees well with numerical simulations, which indicate that lowering the molecular temperatures further by a factor of ~10 could allow fidelities to reach the 0.99 level (*39*). Such further cooling could be achieved with methods such as Raman sideband cooling for molecules

(*44*, *45*). Further improvements are also possible through optimized entanglement schemes. Recent theoretical work that used quantum optimal control has proposed a robust two-qubit entangling gate for CaF molecules in tweezer traps that provides entanglement fidelities exceeding 0.999, under the assumption that they are cooled near their motional ground state (*46*).

We have demonstrated on-demand entanglement of molecules in a reconfigurable optical tweezer array. Our work was enabled by several advances we have made in controlling laser-cooled molecules, including initialization of defect-free molecular arrays, achievement of long rotational coherence times in tightly focused tweezer traps, and observation of coherent dipolar interactions between individual laser-cooled molecules. The ability to entangle molecules on demand is a key building block toward simulating quantum spin models, processing quantum information, and performing quantum-enhanced measurements in the emerging platform of molecular tweezer arrays. Specifically for quantum simulation and information processing, the interactions between long-lived molecular states could offer long evolution times and deep circuit depths. With further advances in lowering molecular temperatures, molecular tweezer arrays could potentially provide performance similar to that of established platforms such as Rydberg atom arrays, trapped ions, and superconducting qubits. Our work on entangling molecules on demand, combined with the recent rapid progress in extending laser-cooling to molecular species of increasing complexity (*19*, *20*), opens research avenues such as quantum-enhanced precision measurement by using trapped molecules (*47*) and explorations of molecular collisions (*48*) and chemical reactions with entangled matter.

After the initial submission of this work, we became aware of related work reporting dipolar spin-exchange and entanglement between molecules in an optical tweezer array (*49*).

REFERENCES AND NOTES

1. M. A. Nielsen, I. L. Chuang, *Quantum Computation and Quantum Information* (Cambridge, Univ. Press, 2010).
2. N. Gisin, G. Ribordy, W. Tittel, H. Zbinden, *Rev. Mod. Phys.* **74**, 145–195 (2002).
3. J. Preskill, *Quantum* **2**, 79 (2018).
4. L. Amico, R. Fazio, A. Osterloh, V. Vedral, *Rev. Mod. Phys.* **80**, 517–576 (2008).
5. D. DeMille, *Phys. Rev. Lett.* **88**, 067901 (2002).
6. L. D. Carr, D. DeMille, R. V. Krems, J. Ye, *New J. Phys.* **11**, 055049 (2009).
7. J. A. Blackmore *et al*., *Quantum Sci. Technol.* **4**, 014010 (2018).
8. K.-K. Ni, T. Rosenband, D. D. Grimes, *Chem. Sci.* **9**, 6830–6838 (2018).
9. K.-K. Ni *et al*., *Science* **322**, 231–235 (2008).
10. J. F. Barry, D. J. McCarron, E. B. Norrgard, M. H. Steinecker, D. DeMille, *Nature* **512**, 286–289 (2014).
11. L. De Marco *et al*., *Science* **363**, 853–856 (2019).
12. A. Schindewolf *et al*., *Nature* **607**, 677–681 (2022).
13. S. Truppe *et al*., *Nat. Phys.* **13**, 1173–1176 (2017).
14. L. Anderegg *et al*., *Phys. Rev. Lett.* **119**, 103201 (2017).
15. A. L. Collopy *et al*., *Phys. Rev. Lett.* **121**, 213201 (2018).
16. L. R. Liu *et al*., *Science* **360**, 900–903 (2018).
17. L. Anderegg *et al*., *Science* **365**, 1156–1158 (2019).
18. L. Christakis *et al*., *Nature* **614**, 64–69 (2023).
19. D. Mitra *et al*., *Science* **369**, 1366–1369 (2020).
20. N. B. Vilas *et al*., *Nature* **606**, 70–74 (2022).
21. B. Yan *et al*., *Nature* **501**, 521–525 (2013).
22. J. T. Zhang *et al*., *Quantum Sci. Technol.* **7**, 035006 (2022).
23. C. M. Holland, Y. Lu, L. W. Cheuk, *Phys. Rev. Lett* **131**, 053202 (2023).
24. M. Endres *et al*., *Science* **354**, 1024–1027 (2016).
25. D. Barredo, S. de Léséleuc, V. Lienhard, T. Lahaye, A. Browaeys, *Science* **354**, 1021–1023 (2016).
26. A. Cooper *et al*., *Phys. Rev. X* **8**, 041055 (2018).
27. M. A. Norcia, A. W. Young, A. M. Kaufman, *Phys. Rev. X* **8**, 041054 (2018).
28. S. Saskin, J. T. Wilson, B. Grinkemeyer, J. D. Thompson, *Phys. Rev. Lett.* **122**, 143002 (2019).
29. J. S. Bell, *Physics Physique Fizika* **1**, 195–200 (1964).
30. B. K. Stuhl, B. C. Sawyer, D. Wang, J. Ye, *Phys. Rev. Lett.* **101**, 243002 (2008).
31. L. W. Cheuk *et al*., *Phys. Rev. Lett.* **121**, 083201 (2018).
32. J. W. Park, Z. Z. Yan, H. Loh, S. A. Will, M. W. Zwierlein, *Science* **357**, 372–375 (2017).
33. B. Neyenhuis *et al*., *Phys. Rev. Lett.* **109**, 230403 (2012).
34. F. Seeßelberg *et al*., *Phys. Rev. Lett.* **121**, 253401 (2018).
35. J. Lin, J. He, X. Ye, D. Wang, *Phys. Rev. A* **103**, 023332 (2021).
36. S. Burchesky *et al*., *Phys. Rev. Lett.* **127**, 123202 (2021).
37. J.-R. Li *et al*., *Nature* **614**, 70–74 (2023).
38. J. Choi *et al*., *Phys. Rev. X* **10**, 031002 (2020).
39. Experimental and simulation methods, additional supporting data, and supplementary text are available as supplementary materials.
40. C. A. Sackett *et al*., *Nature* **404**, 256–259 (2000).
41. Q. A. Turchette *et al*., *Phys. Rev. Lett.* **81**, 3631–3634 (1998).
42. L. Pezzè, A. Smerzi, M. K. Oberthaler, R. Schmied, P. Treutlein, *Rev. Mod. Phys.* **90**, 035005 (2018).
43. D. Bluvstein *et al*., *Nature* **604**, 451–456 (2022).
44. L. Caldwell, M. Tarbutt, *Phys. Rev. Res.* **2**, 013251 (2020).
45. Y. Lu, S. J. Li, C. M. Holland, L. W. Cheuk, Raman sideband cooling of molecules in an optical tweezer array. arXiv:2306.02455v1 [physics.atom-ph] (2023).
46. M. Hughes *et al*., *Phys. Rev. A* **101**, 062308 (2020).
47. B. L. Augenbraun *et al*., *New J. Phys.* **22**, 022003 (2020).
48. L. W. Cheuk *et al*., *Phys. Rev. Lett.* **125**, 043401 (2020).
49. Y. Bao *et al*., Dipolar spin-exchange and entanglement between molecules in an optical tweezer array. arXiv:2211.09780v1 [physics.atom-ph] (2023).
50. L. W. Cheuk, C. M. Holland, Y. Lu, On-demand entanglement of molecules in a reconfigurable optical tweezer array. Dryad (2023); https://doi.org/10.5061/dryad.j9kd51chh.
51. L. W. Cheuk, C. M. Holland, Y. Lu, On-demand entanglement of molecules in a reconfigurable optical tweezer array. Zenodo (2023); https://doi.org/10.5281/zenodo.8140983.

ACKNOWLEDGMENTS

We thank S. J. Li, W. Bakr's group, S. Gopalakrishnan, and J. Thompson for fruitful discussions. We also thank W. Bakr, J. Thompson, S. J. Li, and C. Chiu for careful readings of the manuscript. **Funding:** This work was supported by National Science Foundation grant 2207518, the Alfred P. Sloan Foundation, and Princeton University. **Author contributions:** Conceptualization: L.W.C. Methodology: C.M.H., Y.L., and L.W.C. Investigation: C.M.H., Y.L., and L.W.C. Visualization: C.M.H., Y.L., and L.W.C. Funding acquisition: L.W.C. Supervision: L.W.C. Writing – original draft: C.M.H., Y.L., and L.W.C. Writing – review and editing: C.M.H., Y.L., and L.W.C. **Competing interests:** The authors declare that they have no competing interests. **Data and materials availability:** Data and code are available at Dryad (*50*) and Zenodo (*51*). **License information:** Copyright © 2023 the authors, some rights reserved; exclusive licensee American Association for the Advancement of Science. No claim to original US government works. https://www.science.org/about/science-licenses-journal-article-reuse

SUPPLEMENTARY MATERIALS

science.org/doi/10.1126/science.adf4272
Materials and Methods
Supplementary Text
Figs. S1 to S5
Table S1
References (*52*–*56*)

Submitted 20 October 2022; resubmitted 30 November 2022
Accepted 28 September 2023
10.1126/science.adf4272

3D PRINTING

Self-enhancing sono-inks enable deep-penetration acoustic volumetric printing

Xiao Kuang[1]†, Qiangzhou Rong[2]†, Saud Belal[2]†, Tri Vu[2], Alice M. López López[1], Nanchao Wang[2], Mehmet Onur Arıcan[1], Carlos Ezio Garciamendez-Mijares[1], Maomao Chen[2], Junjie Yao[2]*, Yu Shrike Zhang[1]*

Volumetric printing, an emerging additive manufacturing technique, builds objects with enhanced printing speed and surface quality by forgoing the stepwise ink-renewal step. Existing volumetric printing techniques almost exclusively rely on light energy to trigger photopolymerization in transparent inks, limiting material choices and build sizes. We report a self-enhancing sonicated ink (or sono-ink) design and corresponding focused-ultrasound writing technique for deep-penetration acoustic volumetric printing (DAVP). We used experiments and acoustic modeling to study the frequency and scanning rate–dependent acoustic printing behaviors. DAVP achieves the key features of low acoustic streaming, rapid sonothermal polymerization, and large printing depth, enabling the printing of volumetric hydrogels and nanocomposites with various shapes regardless of their optical properties. DAVP also allows printing at centimeter depths through biological tissues, paving the way toward minimally invasive medicine.

Three-dimensional (3D) printing is attracting increasing attention with its ability to directly fabricate geometrically complex constructs for prototypes (*1*), high-performance materials (*2*, *3*), multimaterial parts (*4*, *5*), flexible electronics (*6*, *7*), medical devices (*8*), and engineered tissues (*9*, *10*). Various printing modalities, such as extrusion printing, inkjet printing, stereolithography, and powder-bed fusion, have been developed to print different materials, including thermoplastics, liquid photoinks, and solid polymer powders, among others (*11*, *12*). These printing methods use light or photothermal heating as energy sources to trigger selective material solidification in a layer-by-layer fashion. A build platform controlled by a linear translation stage is usually required to support the stepwise material solidification. Emerging printing techniques accompanied by new photocurable inks have been developed to improve printing speed (*13*, *14*), printing resolution (*15*–*17*), and printout functionality (*18*, *19*). Volumetric printing that creates 3D constructs without a build platform or an ink-renewal step can substantially improve printing speed and surface quality (*20*–*23*). The existing volumetric printing techniques use light to achieve selective photopolymerization in the volumes of optically transparent inks (*24*–*26*). However, the light attenuation by inks themselves, the presence of functional additives (e.g., photoabsorbers and fillers), or/and already-cured parts have imposed constraints on the material choices and the build sizes for light-based volumetric printing. Although infrared (IR) light can be used to improve light penetration to several millimeters (*26*–*28*), it remains technically challenging to deliver light deep into optically scattering media, such as biological tissues. Therefore, light-based volumetric printing has intrinsic limitations for application in deep-penetration digital manufacturing schemes and, further, in minimally invasive fabrication scenarios (*29*, *30*).

Compared with light, ultrasound waves (<10 MHz) can penetrate >100 times deeper into optically scattering materials and thus hold promise for depositing energy to trigger polymerization at depths (*31*). By means of an ultrasound bath or horn-based reactors, ultrasound waves can generate reactive oxygen species (ROS; i.e., hydroxyl and peroxide radicals) by cavitation of water, enabling vinyl monomer polymerization for hydrogel formation in several to tens of minutes (*32*, *33*). Ultrasound waves can also be focused into a small volume using a focused ultrasound (FUS) transducer. A FUS transducer can generate acoustic waves with positive and negative pressures alternating at megahertz frequency and propagating along the depth direction, and the high acoustic energy can be delivered into the focal zone with high precision. Previously, cavitation-based ultrasound printing was achieved by curing a polydimethylsiloxane resin (*34*). However, a build platform was required, and only relatively simple geometries could be printed, because the intense acoustic streaming by the high acoustic pressure disturbed the local ink at the focus region.

Here, we report phase-transition viscoelastic sonicated inks (hereafter, sono-inks) that simultaneously allow deep acoustic penetration, low acoustic streaming, and rapid sonothermal induced radical polymerization, collectively enabling deep-penetration acoustic volumetric printing (DAVP) (Fig. 1A). DAVP takes advantage of rapid material solidification by the sonothermal effect of the FUS focus in a viscoelastic sono-ink, which provides the building voxel to construct 3D objects without the need for a build platform. In DAVP, the FUS waves deliver deep-penetration acoustic energies with pressures up to several tens of megapascals to the local region at a distance of up to 64 mm (focal length) (Fig. 1B). The small oval-shaped FUS focal zone (full width at half maximum of the acoustic pressure field: 0.3 to 0.7 mm) is further narrowed by the nonlinear acoustic propagation effect at high acoustic pressure (*35*), collectively facilitating fast, high-resolution printing (Fig. 1C and fig. S1). Consequently, DAVP allows us to print geometrically complex materials precisely and volumetrically, even through nontransparent and optically scattering materials.

DAVP principle and self-enhancing sono-ink design

Traditionally, ultrasound-mediated cross-linking of the vinyl-based hydrogel precursors is slow, because of the low concentration of ROS generated by ultrasound-induced cavitation (see supplementary text in the supplementary materials). Besides, ROS can be rapidly quenched or diluted by robust acoustic streaming. Our simulation results showed that high-viscosity fluids could significantly reduce the acoustic streaming velocity (Fig. 1D and fig. S2). However, highly viscous ink feedstocks usually exhibit high acoustic attenuations and thus substantially reduce acoustic penetration (*36*). We hypothesized that a meticulously designed multicomponent viscoelastic sono-ink should suppress acoustic streaming while facilitating a fast sonothermal effect and thus trigger rapid and spatial radical polymerization of vinyl precursors for a deep-penetration fabrication scheme.

To formulate such a proof-of-concept sono-ink, we selected a vinyl oligomer of poly (ethylene glycol) diacrylate (PEGDA) as the base component, agar microparticles as the rheology modifier, poly(*N*-isopropyl acrylamide) (PNIPAm) as the self-enhancing acoustic absorber, and ammonium persulfate (APS) as the thermal initiator (fig. S3). Compared with PEGDA ink, PEGDA-based sono-ink (PEGDA/agar/PNIPAm at, for example, 20/10/3 wt/wt/wt % ratio) showed enhanced viscosities owing to the coil-to-globule phase transition of PNIPAm [transition temperature (T_t) = 34° to 36°C] (Fig. 1E and fig. S4). The viscosity of the sono-ink increased 92-fold, from 2.0 to 185.3 Pa·s, when heated from 25°C to 40°C at low shearing (0.05 Hz) (fig. S4C). Meanwhile, the sono-ink showed prominent shear

[1]Division of Engineering in Medicine, Department of Medicine, Brigham and Women's Hospital, Harvard Medical School, Cambridge, MA 02139, USA. [2]Department of Biomedical Engineering, Duke University, Durham, NC 27708, USA.
*Corresponding author. Email: junjie.yao@duke.edu (J.Y.); yszhang@bwh.harvard.edu (Y.S.Z.)
†These authors contributed equally to this work.

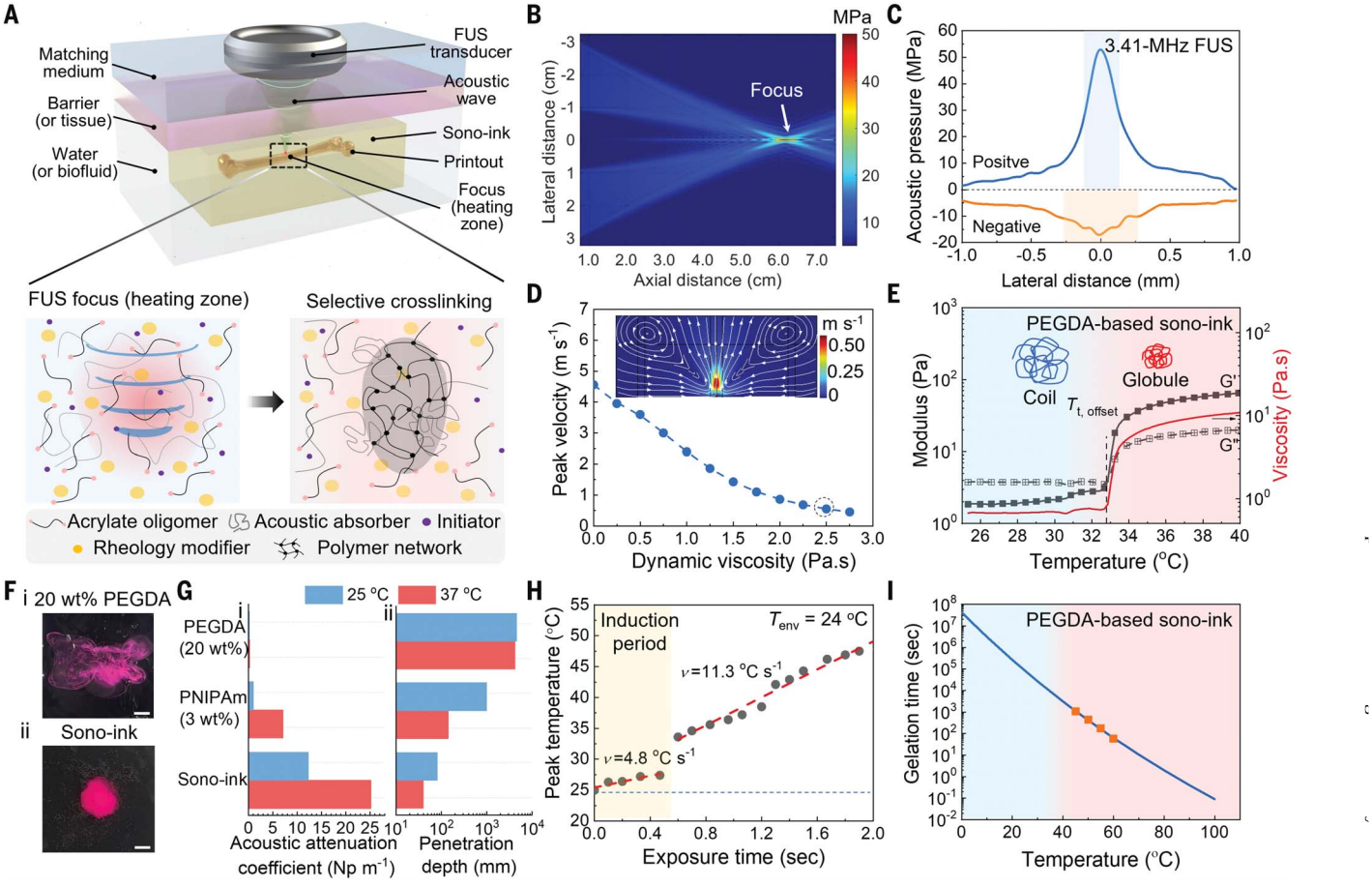

Fig. 1. Working principle of DAVP and design of self-enhancing sono-ink. (**A**) Scheme showing acoustic printing of constructs by selective curing of sono-ink using deep-penetration FUS. The sonothermal effect enhanced by the phase-transitioning acoustic absorber triggers the decomposition of the initiator for local polymerization of acrylate oligomers into polymer networks at the heating zone. (**B**) Simulated acoustic pressure field in water for the 3.41-MHz FUS transducer with an acoustic power of 50 W, using the nonlinear acoustic model. (**C**) Lateral pressure distribution of the 3.41-MHz FUS transducer with an output voltage (V_p) of 192 V. The shaded regions show the full width at half maximum of the positive and negative pressures (0.3 to 0.7 mm). (**D**) Simulated maximum velocity in the focal region versus the dynamic viscosity of the sono-ink. Inset acoustic streaming simulation shows the velocity field of fluids with a viscosity of 2.5 Pa·s. (**E**) Oscillation temperature sweep shows the enhanced moduli and viscosity of PEGDA-based sono-ink at a transition temperature (33° to 36°C) due to coil-to-globule transition of PNIPAm. (**F**) Acoustic streaming in different fluids at the focal region of 3.41-MHz FUS for 2-s exposure: 20 wt % PEGDA (i) and PEGDA/agar/PNIPAm sono-ink (ii). Scale bars: 5 mm. (**G**) Acoustic properties of the PEGDA/agar/PNIPAm sono-ink and its key components under 3.41-MHz FUS at 25° and 37°C: acoustic attenuation coefficient in linear scale (i) and penetration depth in log scale (ii). (**H**) Peak temperature in sono-ink at the heating zone near the FUS focus as a function of exposure time, at an environment temperature of 24°C. (**I**) Gelation time measured by rheology as a function of the curing temperature for PEGDA-based sono-ink supplemented with 1.0 w/w% APS. Orange squares represent the experiment data, and the solid blue line is the fitting curve by the Arrhenius law.

thinning, as reflected by an 87% reduction in viscosity under 100-Hz shearing at 25°C (fig. S4). This sono-ink design concept was generalizable to different formulations, including those using vinyl oligomers from natural polymers [e.g., gelatin methacryloyl (GelMA)] (fig. S4) or different phase-transition polymers with tunable transition temperatures ($T_{t,offset}$ = 20.9° to 38.5°C) (fig. S5 and table S1), as well as formulations adding various nanoparticles (table S2). Our sono-ink design resolved the long-standing dilemma between acoustic penetration depth and acoustic streaming. On the one hand, the shear thinning facilitated deep acoustic penetration under high-frequency acoustic waves. On the other hand, the viscosity enhancement by phase transition substantially reduced acoustic streaming. In contrast to the violent streaming in the PEGDA solution, the self-enhancing sono-ink exhibited negligible fluid flow at the FUS focus (Fig. 1F, fig. S6, and movie S1), as supported by the simulation (Fig. 1D).

To investigate the sono-ink's self-enhanced acoustic attenuation effect, we measured the acoustic attenuation coefficient (α) of the proof-of-concept sono-ink and key components at various temperatures (fig. S7). Because of the phase transition, the α of the PNIPAm (3 wt %) aqueous solution and PEGDA-based ink at the ultrasound frequency of 3.41 MHz increased with the temperature, for example, by 600 and 100%, respectively, from 25°C to 37°C (Fig. 1G). The α of the sono-ink (containing both PEGDA and PNIPAm) was 25.2 nepers per meter (Np m^{-1}) at a temperature of 37°C, which was 86-fold larger than that of 20 wt % PEGDA alone but still much lower than the α of soft biological tissues under the same conditions (table S3). Despite the self-enhanced acoustic attenuation, the acoustic waves could still achieve a large penetration depth ($D_p = 1/\alpha$) of 40 mm into the sono-ink at 37°C (Fig. 1G).

As a direct result of self-enhanced acoustic attenuation and viscosity, the phase-transition sono-ink exhibited a fast and self-enhanced heating effect. The PNIPAm solution and the sono-ink could be rapidly heated up to between

60° and 80°C at the heating zone after seconds of FUS exposure at mild input powers (<100 W) (fig. S8 and movie S2). PNIPAm played a critical role in achieving fast sonoheating, in contrast to the negligible heating of the 20 wt % PEGDA solution. To further investigate the self-enhanced heating effect, the heating-zone temperatures as a function of FUS exposure time were monitored by an IR thermal camera during FUS exposure at different environmental temperatures (T_{env}). At a T_{env} of 24°C—far below the $T_{t,\ offset}$ of PNIPAm—the peak temperature at the heating zone first showed a slow heating rate (4.8°C s^{-1}) and then, after the temperature leap at 36°C, a much-enhanced heating rate (11.3°C s^{-1}), as a result of the phase transition (Fig. 1H). The slow heating period, called the induction period, was reduced from 0.5 s to 0.1 s by raising the T_{env} to 33°C (close to $T_{t,\ offset}$) and entirely eliminated at T_{env} = 35°C (>$T_{t,\ offset}$) (fig. S9 and movie S3). In our printing technique, T_{env} was set slightly lower than $T_{t,\ offset}$ to allow for confined sonoheating at the FUS focus. It is worth noting that, as in thermal-based tissue ablation (*37*), our self-enhancing sono-ink enabled a prominent sonothermal effect under a high-duty cycle of 90%. We did not observe FUS-induced cavitation activities, as validated by active cavitation mapping (fig. S10 and movie S4). Therefore, it was concluded that FUS-induced cavitation is not responsible for the sono-ink solidification.

The self-enhanced sonothermal effect was leveraged to trigger the radical polymerization of vinyl oligomers for fast gelation. The gel-point conversion of the PEGDA-based sono-ink was ~0.3, as measured by Fourier transform infrared spectroscopy (fig. S11). In the presence of APS, the sono-inks proceeded with (sono)thermal-induced gelation, as illustrated by the rheological measurement (fig. S12). The temperature-sensitive gelation time (t_{gel}) followed the Arrhenius law, revealing a high activation energy (171 kJ mol^{-1}) (eq. S10). Consequently, long shelf life (t_{gel} = 167 days at 4°C) and on-demand fast curing (t_{gel} = 1.9 s at 80°C) were simultaneously achieved (Fig. 1I).

DAVP printing-resolution characterizations

We developed a 3D FUS printer, which was equipped with a FUS transducer at three ultrasound frequencies (2.05, 3.41, and 6.86 MHz), a 3D motorized translation stage, and a printing control system (fig. S13; see materials and methods in the supplementary materials for further details). We first studied the single-point printing resolution of DAVP. Upon FUS exposure in the sono-ink, a whitening region formed and quickly expanded beyond the FUS heating zone (fig. S14 and movie S5), as PNIPAm simultaneously acted as the self-enhancing acoustic absorber and the temperature indicator (*38*). IR thermal images of the sono-ink surface showed a clear temperature increase forming a heating zone (Fig. 2A). The heated surface area (diameter of up to 4 mm) was larger than the focal zone of the FUS transducer (0.45 mm at 3.41 MHz) because of the rapid thermal diffusion. Upon cooling, a piece of opaque solid formed at the center of the heating zone, and the uncured sono-ink returned to its original color. By comparing the curing size with the heating-zone temperature profile, we found that the curing temperature threshold was T_c = 67°C for the PEGDA-based sono-ink supplemented with 0.5 w/w% APS. Because of heat diffusion by the low-power cumulative FUS, the curing size increased with input power (or peak acoustic pressure) and exposure time (Fig. 2B and fig. S15). The nonlinear acoustic effect resulted in elevated acoustic intensity at the FUS focus by increasing the peak pressure and reducing the focal region (*39*, *40*), as shown by our nonlinear acoustic modeling (fig. S16). The simulation also captured the nonlinear acoustic propagation in the sono-ink, exhibiting weak reflection and scattering by different boundaries (such as plastics and tissues) in the far field (fig. S17), and negligible acoustic reflection and scattering at the interface formed by the sono-ink phase transition (fig. S18). Using the numerically modeled temperature map and the measured T_c, we investigated the increasing single-point curing size (0 to 4 mm in diameter) as a function of peak acoustic pressure (35 to 55 MPa) and exposure time (0 to 5 s) (Fig. 2C, fig. S19, and movie S6). T_c of the sono-inks could be readily reduced from 67°C to 62°C by increasing the APS concentration, because of the enhanced reaction rate (fig. S20 and eq. S8). Additionally, increasing the PEGDA concentration (40 wt %) increased the apparent T_c of the sono-ink, likely owing to additional heating by the exothermic effect of polymerization and reduced viscosity (fig. S21).

We further investigated the printing resolutions of DAVP by continuously scanning a line under different printing settings. An expanding heated region instantly formed at the front of the scanning FUS focus, as a result of the thermal diffusion within the ink, which was also confirmed by sonothermal modeling (Fig. 2D, fig. S22, table S4, and movie S7). The sono-ink was cross-linked only at the center of the heating zone, where the temperature increased above the curing threshold, forming anisotropic filaments. We also investigated the dependence of the curing size on several key parameters, including the scanning speed of the FUS focus, the FUS frequency and power, and thermal diffusion (figs. S23 to S25 and movie S8). Modeling results showed that the thin ink tank (6 mm) caused heat accumulation at the tank boundary, whereas a thicker tank (>10 mm) allowed for normal thermal diffusion around the focal region (fig. S26). Therefore, we used the 10-mm-thick ink tank to quantify the curing sizes (or printing resolutions) (Fig. 2E). First, increasing the scanning speed can improve the printing resolution. We observed overcuring in the longitudinal dimension (larger than design) at a slow scanning speed with all three ultrasound frequencies (2.05, 3.41, and 6.86 MHz), owing to excess heat accumulation. In comparison, undercuring (lower than design) was observed at high scanning speeds because of inadequate temperature increase at the two ends. The in-plane curing size was determined by the joint effect of the FUS scanning speed and thermal diffusion. For instance, the in-plane curing size at 3.41 MHz was improved from 7.6 mm to 1.6 mm by increasing the scanning speed from 0.4 mm s^{-1} to 0.8 mm s^{-1}. Similarly, the axial curing size was mostly determined by the FUS depth of focus and thermal diffusion. As an example, the 6.86-MHz FUS had a smaller depth of focus (1.69 mm) than the 2.05-MHz FUS (5.58 mm), but the sono-ink had a 10-fold acoustic absorption at 6.86 MHz and thus much higher heating efficiency. Eventually, the axial curing size ranged from 5.0 to 9.9 mm for the investigated printing parameters. The depth of focus here is defined as the size of the focal zone along the acoustic axis, in which the acoustic pressure drops to half of the peak value (table S5).

The printing resolution of DAVP can be flexibly adjusted by optimizing the FUS scanning speed, frequency, and power. Generally, the printing anisotropy (ratio of the axial and in-plane curing size) increased with the printing speed, mostly as a result of the decreased in-plane curing size (Fig. 2F). For example, when printing at 0.8 mm s^{-1} by the 6.86-MHz FUS, the cross section of printed filaments exhibited an oval shape with an axial size of 8.8 mm, which was 100% larger than the in-plane curing size (Fig. 2, G and H). The sonothermal curing mechanism also led to different microstructures within the FUS heating zone. The cured hydrogels displayed sub-micrometer pores in the PEGDA/PNIPAm matrix due to polymerization-induced phase separation, as shown by scanning electron microscopy (SEM) (Fig. 2I). SEM images suggested melting of agar microparticles owing to a high temperature of >85°C at the center of the heating zone (Fig. 2I, panel ii). However, the agar microparticles maintained a granular shape outside the center of the focal zone at various printing speeds and frequencies, similar to that achieved by bulk heating at 60° to 70°C (figs. S28 and S29). These results further excluded the presence of FUS-induced cavitation and confirmed the heat accumulation–based curing mechanism. Meanwhile, the enhanced surface quality of the printed filaments was confirmed by the uniform and smooth surface (fig. S29D).

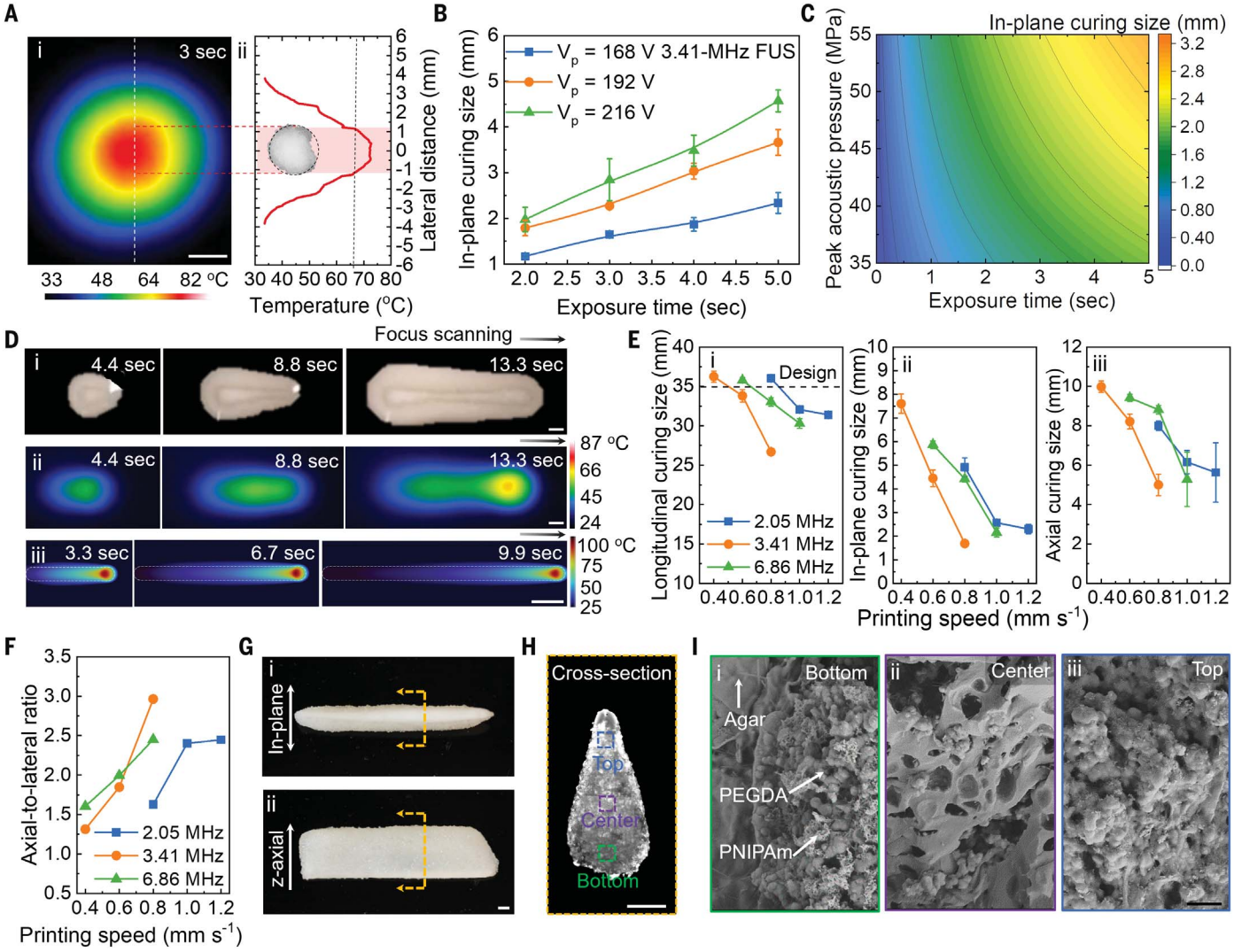

Fig. 2. Characterizations of DAVP printing resolution. (**A**) Typical surface temperature profile near the FUS focal region. The IR thermal image shows the in-plane temperature map (i) and temperature diagram at the cross section (ii). The inset shows the cured solid after 3-s FUS exposure (3.41 MHz) with the curing threshold temperature of 67°C. (**B**) In-plane curing size of printed solids versus FUS exposure time using PEGDA-based sono-ink (0.5 w/w% APS) at different V_p, as labeled. (**C**) Color-contour of modeled in-plane curing size at 3.41 MHz as a function of acoustic pressure and exposure time. (**D**) Snapshots of photographs (i) and IR thermal images (ii) near the FUS focal zone, as well as modeled temperature map on the focal plane (iii) at different time points during line printing using PEGDA-based sono-ink (1.0 w/w% APS) (FUS frequency: 3.41 MHz; printing speed: 1.5 mm s^{-1}). (**E**) Curing sizes for single-line DAVP printing using different printing speeds at various FUS frequencies as labeled: longitudinal size (i), in-plane size (ii), and *z*-axial size (iii). (**F**) Axial-to-lateral curing size ratio as a function of printing speed using various FUS frequencies, as labeled. (**G**) Photographs of printed filaments by single-line DAVP (6.86-MHz FUS at a speed of 0.8 mm s^{-1}): in-plane size (i) and axial size (ii). (**H**) Cross-sectional micrographs of printed filaments in (G) with three different marked regions. (**I**) SEM images of dried hydrogels in (H) at different regions: top (i), center (ii), and bottom (iii). Scale bars: 2 mm [(A), (D), (G), (H)] and 2 μm (I).

When performing multipath printing, the axial printing size (or printing thickness) increased, as a result of repeated FUS exposure along the acoustic axis at the scanned regions; however, the printing lengths were less sensitive to the number of printing paths (fig. S30). Additionally, the printing performance of DAVP was independent of the line-scanning direction of the 3D FUS printer. There were no significant differences in printing fidelity and mechanical properties (e.g., Young's moduli: 1.4 ± 0.1, 1.2 ± 0.3, and 1.3 ± 0.1 MPa) using different scanning directions (0°, 45°, and 90°, respectively) (fig. S31). Moreover, the printed sample at the 0° infill angle showed significantly higher stiffness than that by bulk heating (0.9 ± 0.1 MPa), likely because of the high temperature–induced fast matrix curing and agar welding.

DAVP of volumetric constructs and material generality

Deep penetration is the primary advantage of DAVP over conventional light-based 3D printing (Fig. 3A). For example, in a black-dyed sono-ink (0.5 w/w%), the penetration depths for the 2.05-, 3.41-, and 6.86-MHz ultrasound waves were 295.2, 86.8, and 28.2 mm at room temperature, respectively, which were, respectively, 600, 180, and 60 times as large as those for the 405-nm light (D_p = 0.48 mm) (Fig. 3B). As such, a large curing depth of 24 mm in the dyed sono-ink was achieved in 26 s at an axial scanning speed of 1 mm s^{-1} and 3.41-MHz FUS, whereas only a thin solid (2.4 mm) in the dye-stained photoink was obtained after photocuring for 165 s (fig. S32). The large penetration depth of DAVP, regardless of the optical properties of the ink, allowed us to volumetrically

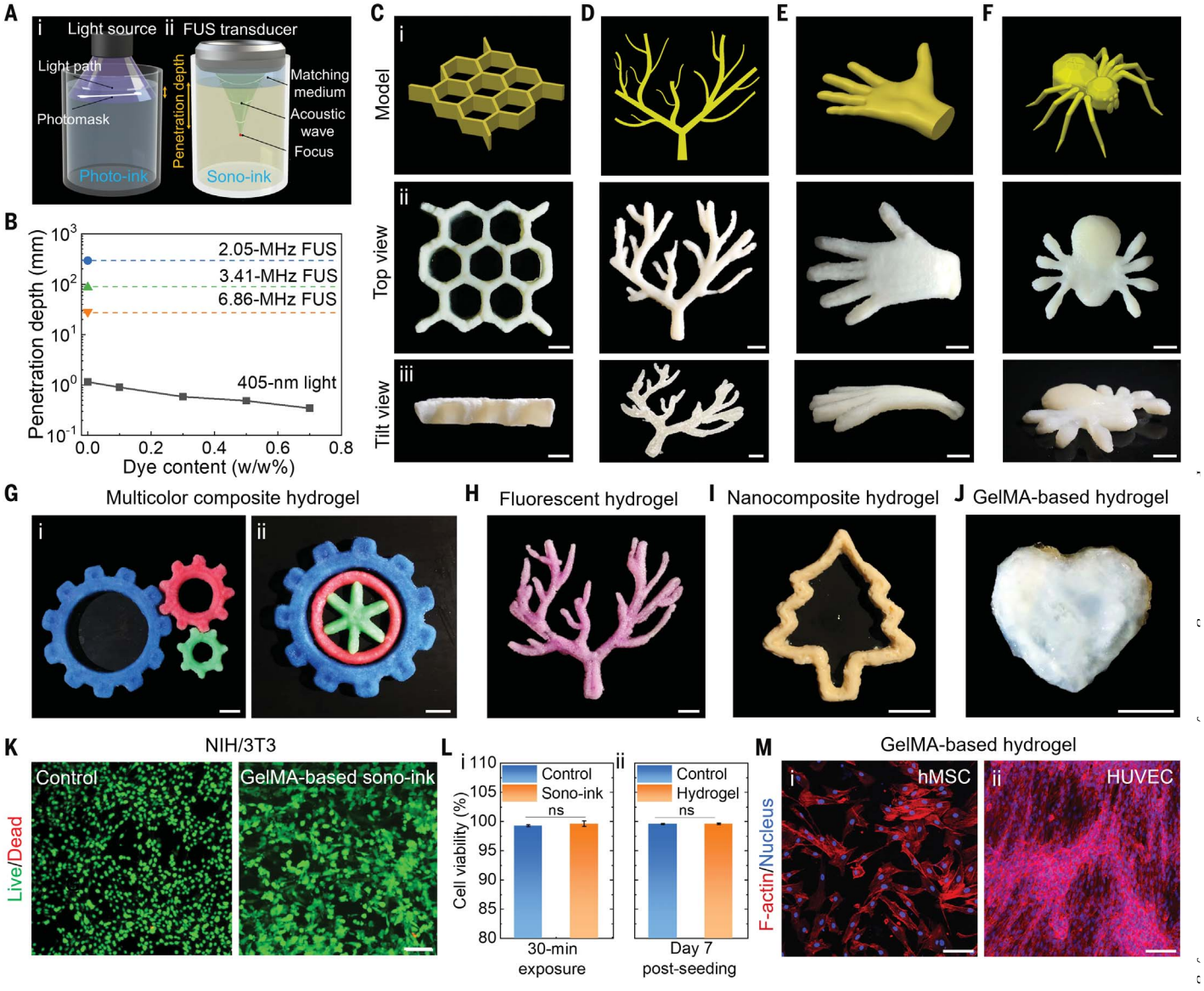

Fig. 3. DAVP performance and material generality. (**A**) Schematic illustrations for photocuring of photoinks (i) and FUS-curing of sono-inks (ii) with different penetration capabilities. (**B**) Penetration depth as a function of black-dye content for UV light (405 nm) and FUS at different frequencies, as labeled. (**C** to **F**) Design models (i), top-view (ii), and tilt-view photographs (iii) of printed constructs of various shapes using PEGDA-based sono-ink: honeycomb (C), vessel network (D), 3D hand (E), and spider (F). (**G** to **J**) Photographs of printed constructs using various sono-inks: multicolor three-part gear set (i) and a three-part wheel set (ii) by dye-stained PEGDA-based sono-inks consisting of different colors (G), vascular network model by a fluorescence-stained PEGDA-based sono-ink (0.1 w/w% rhodamine B) (H), tree-shaped model by a PEGDA-based nanocomposite sono-ink (10 wt % nanoclay) (I), and layered heart-shaped model by a GelMA-based protein sono-ink (J). (**K** to **M**) In vitro cytocompatibility of GelMA-based sono-inks and cured hydrogels: representative fluorescence micrographs of live (green)/dead (red) cells (NIH/3T3 fibroblasts) after 30-min exposure to DPBS (control) and GelMA-based sono-ink (K), quantitative cellular viability values of NIH/3T3 fibroblasts after 30-min exposure to GelMA-based sono-ink (i) and at day 7 after seeding on GelMA-based hydrogel (ii) (L), fluorescence micrographs showing F-actin staining of cells at day 7 after seeding on the GelMA/PNIPAm hydrogel using two cell types: human mesenchymal stem cells (hMSCs) (i) and human umbilical vein endothelial cells (HUVECs) (ii). F-actin, red; nucleus, blue. ns, no significant difference. Scale bars: 10 mm [(C) to (J)] and 100 μm [(K) and (M)].

print nontransparent 2D and 3D hydrogel constructs with different sizes and geometrical complexities, including letters and lattices with sharp corners and spirals and vessels with smooth surfaces and transitions (fig. S33, table S6, and movie S9). For example, a 10-layer honeycomb and a vascular network were printed at 3.41 MHz (Fig. 3, C and D, and table S6). A complex 3D hand model (67 mm by 53 mm by 10 mm) and a spider model (52 mm by 43 mm by 10 mm) were also printed at 6.86 MHz (Fig. 3, E and F; fig. S34; and table S6).

Using dye-stained PEGDA-based sono-inks, we printed opaque-colored hydrogel composites for prototypes, including a set of three gears of different sizes and an assembled wheel set of three colored parts (Fig. 3G and fig. S35). Altering the phase-transition polymers with higher T_t, such as poly(*N*-isopropylmethacrylamide) (PNIPMAm), could facilitate printing at body temperature (37°C) (fig. S35D). Additionally, fluorescence-stained sono-ink (0.1 wt % rhodamine B) was used to print a high-fidelity branched vascular network shape (81 mm by

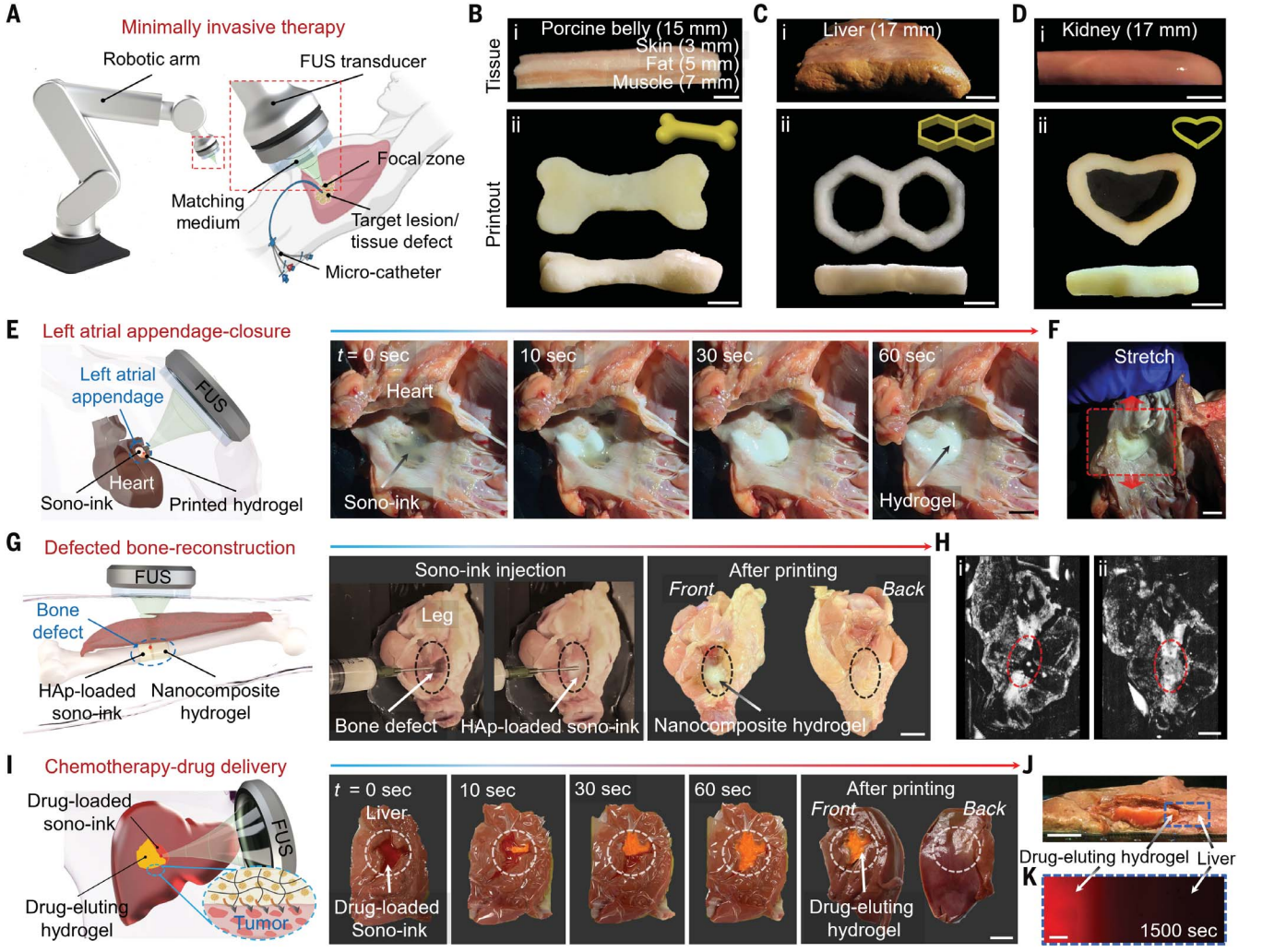

Fig. 4. DAVP for proof-of-concept through-tissue printing and minimally invasive therapy. (**A**) Scheme of minimally invasive therapy by through-tissue manufacturing of scaffolds on target lesions and tissues. (**B** to **D**) Tissue phantoms with marked thicknesses (i) and printed objects with associated digital models (ii) for through-tissue manufacturing: a bone-shaped model printed under porcine belly (B), a lattice printed under porcine liver (C), and a heart-shaped model printed under porcine kidney (D). Printing was performed with 2.05-MHz FUS at 0.6 mm s^{-1}. (**E** and **F**) DAVP for LAA closure for a 12-mm-thick goat heart: scheme and printing process at different time points (E), and stretching of closed LAA (F). (**G** and **H**) DAVP for defective bone reconstruction: scheme and photographs showing the procedures of manufacturing a nanocomposite filler material on a bone defect through 10-mm-thick skin and muscle (G), and ultrasound images of the bone defect (i) and the reconstructed bone (ii) (H). (**I** to **K**) DAVP for chemotherapy drug delivery for a 14-mm-thick porcine liver: scheme and photographs showing the procedure of printing drug-eluting hydrogels using a doxorubicin-loaded sono-ink on a liver lesion (I), cross-sectional photograph showing the printed hydrogel-liver interface (J), and fluorescence micrograph showing drug diffusion from the printed drug-eluting filler hydrogel to the liver at 1500-s contact (K). Scale bars: 10 mm [(B) to (J)] and 200 μm (K).

70 mm by 3 mm) (Fig. 3H). Further, a nanocomposite sono-ink consisting of 10 wt % nanoclay was exploited to print a four-layer tree shape (2 mm in thickness) (Fig. 3I). DAVP was also used to print protein-based biomaterials, as suggested by the tough-hydrogel heart model using the GelMA-based sono-ink (Fig. 3J and fig. S35, E and F). Both PEGDA- and GelMA-based sono-inks and their key components exhibited zero to low cytotoxicity using NIH/3T3 fibroblasts as a model cell line. High cell viability (>99%) similar to the control [using Dulbecco's phosphate-buffered saline (DPBS)] was observed after direct and indirect exposure to the sono-ink for up to 30 min (Fig. 3, K and L, and fig. S36). Moreover, similar to the control cultured in a petri dish, the GelMA-based hydrogel enabled high viability (>99%) and healthy attachment and proliferation of postseeded mammalian cells of different types (Fig. 3M and fig. S37), indicating its favorable bioactivity.

DAVP for through-tissue printing and constructive minimally invasive medicine

As a proof of concept, we applied DAVP for high-speed and high-resolution through-tissue manufacturing and minimally invasive medicine (Fig. 4A). First, we illustrated the ex vivo through-tissue printing using soft tissues of different types and dimensions (fig. S38 and table S7). For through-tissue printing, thick tissues (up to 17 mm thick) were placed on top of the sono-ink chamber in the FUS near field. We printed a bone-shaped construct at 2.05 MHz through an ex vivo porcine tissue phantom consisting of a skin layer (3 mm), a fat layer (5 mm), and a muscle layer (7 mm) (Fig. 4B). High-fidelity honeycombs were printed through a 15-mm-thick porcine tissue consisting of skin and muscle or a 17-mm-thick porcine liver tissue (Fig. 4C). Similarly, a hollow heart-shaped model was printed through a 17-mm-thick porcine kidney tissue (Fig. 4D and movie S10).

Nonvalvular atrial fibrillation is a prevalent cardiovascular disease related to the left atrial appendage (LAA) (*41*, *42*). Open-chest surgery or transcatheter procedures can seal off the LAA to reduce the risk of thromboembolism. However, surgical LAA closure is severely invasive, and the treatment is often incomplete (*41*). We demonstrated proof-of-concept DAVP-assisted LAA closure (Fig. 4E). We delivered the sono-ink through a catheter to the LAA of an ex vivo goat heart placed in the printing chamber. The sono-ink was then solidified using the 3D FUS printer at 3.41 MHz through a 12-mm-thick heart wall. Precise FUS focus scanning enabled selective curing of the sono-ink within the entire LAA volume while sparing surrounding heart tissues (fig. S39 and movie S11). After treatment, the cured hydrogels completely occluded the LAA and bonded well with the tissue wall, which could tolerate reasonable distortions that mimicked the heart beating (Fig. 4F).

We further explored the potential of the DAVP technique for tissue reconstruction and regeneration, such as treating large bone defects (*43*). As an illustration, the PEGDA/agar/PNIPMAm nanocomposite sono-ink consisting of 5 w/w% hydroxyapatite (HAp) nanoparticles was formulated to print a bone scaffold for a hypothetical bone loss treatment (Fig. 4G and movie S12). We used a chicken leg to create a fibula bone defect model (1 cm long). After injecting the nanocomposite sono-ink, we printed a beam-shaped HAp-laden composite material through the skin and muscle tissues (10 mm thick) to reshape the defective volume. The nanocomposite material could reconstruct the bone with seamless bonding to the native parts without influencing the surrounding tissues, as confirmed by ultrasound imaging (Fig. 4H).

We also demonstrated DAVP for therapeutic drug delivery by printing drug-eluting filler hydrogels on liver lesions (Fig. 4I). Doxorubicin, a clinical chemotherapy drug for treating a wide range of cancers, such as breast cancer and hepatocellular carcinoma, was used as a model drug (*44*). PEGDA/agar/PNIPMAm sono-ink consisting of 1 mg ml^{-1} of doxorubicin was formulated for printing chemotherapy drug-eluting hydrogels at the liver lesion sites at 37°C using FUS at various frequencies (fig. S40). DAVP enabled through-tissue printing and selective curing, as shown by the intimate hydrogel-tissue interfacial bonding (front side) and negligible burning of the intervening tissue (back side) (Fig. 4J and movie S13). The drug in the hydrogel gradually released and diffused into the liver tissue (effective diffusivity: 8.7×10^{8} cm^2 s^{-1}), forming an ~3-mm-thick effective therapeutic layer [5.8 μg ml^{-1} concentration (*44*)] within 7 days by modeling (Fig. 4K and fig. S41). We anticipated that this method could be used as postablative chemotherapy to improve cancer treatment.

We note that relatively high FUS energies were needed for through-tissue printing, mainly because of the acoustic attenuation by the intervening tissues. The acoustic energy loss might possibly result in overheating of the intervening tissues. To mitigate the risk of tissue overheating and to improve future in vivo printing efficiency, we developed a confocal-DAVP system in which the 3D FUS printer used two FUS transducers aligned in a cross-beam pattern, with their acoustic axes 90° apart and their foci overlapping (fig. S42). Taking advantage of the energy superposition of two acoustic foci, confocal-DAVP can achieve the curing temperature threshold in the combined foci, using roughly half of the output energy from each FUS transducer. Such a confocal configuration has two advantages: (i) the acoustic energy deposition in the local intervening position is reduced by ~50%, and thus the overheating risk is minimized; (ii) the printing resolution and speed can be improved, owing to better sonothermal confinement within the overlapped foci. Indeed, the axial printing resolution was improved to 0.7 mm, and the printing speed reached 8 mm s^{-1} (fig. S42). Accordingly, complex models, including a leaf-shaped structure (55 mm by 35 mm) and a vessel-like network (75 mm by 25 mm), were successfully printed using the confocal-DAVP, taking only 20 and 83 s, respectively (fig. S43, table S8, and movie S14).

Conclusions

Leveraging the deep-penetration capability of FUS waves, low acoustic streaming, and rapid sonopolymerization of the viscoelastic self-enhancing sono-inks, we have developed a DAVP technique that can volumetrically build constructs with high printing fidelity and resolution in the absence of a build platform. The use of a thermally responsive adaptive acoustic absorber resolves the conflict between acoustic streaming and deep penetration upon FUS exposure. The self-enhancing sono-ink and nonlinear acoustic propagation collectively enhanced the sonothermal heating at the FUS focus for fast and selective material solidification as the building voxel. The heat accumulation–based curing mechanism resulted in anisotropic printing resolution at a millimeter scale, which may be further improved by optimizing printing parameters of FUS frequency and scanning speed and by using the confocal dual-transducer configuration. The deep penetration of FUS waves allows the volumetric fabrication of opaque (nano)composites and printing through centimeter-thick tissues that are not attainable through state-of-the-art light-based printing techniques (table S9). The self-enhancing sono-ink design can be generalized for different systems, greatly expanding the materials library for acoustic printing techniques.

REFERENCES AND NOTES

1. J. R. Tumbleston *et al.*, *Science* **347**, 1349–1352 (2015).
2. S. Gantenbein *et al.*, *Nature* **561**, 226–230 (2018).
3. X. Zheng *et al.*, *Science* **344**, 1373–1377 (2014).
4. M. A. Skylar-Scott, J. Mueller, C. W. Visser, J. A. Lewis, *Nature* **575**, 330–335 (2019).
5. K. Liu, R. Sun, C. Daraio, *Science* **377**, 975–981 (2022).
6. H. Wei *et al.*, *Nat. Commun.* **12**, 2082 (2021).
7. H. Yuk *et al.*, *Nat. Commun.* **11**, 1604 (2020).
8. Y. Y. C. Choong *et al.*, *Nat. Rev. Mater.* **5**, 637–639 (2020).
9. L. Moroni *et al.*, *Nat. Rev. Mater.* **3**, 21–37 (2018).
10. A. Lee *et al.*, *Science* **365**, 482–487 (2019).
11. S. C. Ligon, R. Liska, J. Stampfl, M. Gurr, R. Mülhaupt, *Chem. Rev.* **117**, 10212–10290 (2017).
12. M. L. Bedell, A. M. Navara, Y. Du, S. Zhang, A. G. Mikos, *Chem. Rev.* **120**, 10744–10792 (2020).
13. D. A. Walker, J. L. Hedrick, C. A. Mirkin, *Science* **366**, 360–364 (2019).
14. M. P. de Beer *et al.*, *Sci. Adv.* **5**, eaau8723 (2019).
15. S.-F. Liu *et al.*, *Science* **377**, 1112–1116 (2022).
16. F. Han *et al.*, *Science* **378**, 1325–1331 (2022).
17. N. M. Larson *et al.*, *Nature* **613**, 682–688 (2023).
18. G. Villar, A. D. Graham, H. Bayley, *Science* **340**, 48–52 (2013).
19. X. Kuang *et al.*, *Sci. Adv.* **5**, eaav5790 (2019).
20. M. Shusteff *et al.*, *Sci. Adv.* **3**, eaao5496 (2017).
21. P. N. Bernal *et al.*, *Adv. Mater.* **31**, e1904209 (2019).
22. B. E. Kelly *et al.*, *Science* **363**, 1075–1079 (2019).
23. M. Xie *et al.*, *Nat. Commun.* **14**, 210 (2023).
24. M. Regehly *et al.*, *Nature* **588**, 620–624 (2020).
25. D. Loterie, P. Delrot, C. Moser, *Nat. Commun.* **11**, 852 (2020).
26. S. N. Sanders *et al.*, *Nature* **604**, 474–478 (2022).
27. J. Wong *et al.*, *Adv. Mater.* **35**, e2207673 (2023).
28. J. Zhu, Q. Zhang, T. Yang, Y. Liu, R. Liu, *Nat. Commun.* **11**, 3462 (2020).
29. M. Lee, R. Rizzo, F. Surman, M. Zenobi-Wong, *Chem. Rev.* **120**, 10950–11027 (2020).
30. Y. Chen *et al.*, *Sci. Adv.* **6**, eaba7406 (2020).
31. T. G. McKenzie, F. Karimi, M. Ashokkumar, G. G. Qiao, *Chemistry* **25**, 5372–5388 (2019).
32. B. Rokita, J. M. Rosiak, P. Ulanski, *Macromolecules* **42**, 3269–3274 (2009).
33. Z. Gao *et al.*, *ACS Macro Lett.* **8**, 1285–1290 (2019).
34. M. Habibi, S. Foroughi, V. Karamzadeh, M. Packirisamy, *Nat. Commun.* **13**, 1800 (2022).
35. R. T. Beyer, *Phys. Acoust.* **2**, 231–264 (1965).
36. L. Claes *et al.*, *Measurement* **184**, 109919 (2021).
37. P. V. Yuldashev *et al.*, *IEEE Trans. Ultrason. Ferroelectr. Freq. Control* **68**, 2837–2852 (2021).
38. A. Rahimzadeh, M. Rutsch, M. Kupnik, R. V. Klitzing, *Langmuir* **37**, 5854–5863 (2021).
39. A. Bhargava, V. C. Meesala, M. R. Hajj, S. Shahab, *Appl. Phys. Lett.* **117**, 064101 (2020).
40. S. Haddadi, M. T. Ahmadian, *Sci. Iran.* **25**, 2087–2097 (2018).
41. D. R. Holmes Jr., T. J. Simard, A. M. Killu, M. A. Alkhouli, *Mayo Clin. Proc.* **97**, 1525–1533 (2022).
42. H. Ueno, T. Imamura, S. Tanaka, N. Fukuda, K. Kinugawa, *J. Cardiol.* **81**, 420–428 (2023).
43. A. Stahl, Y. P. Yang, *Tissue Eng. Part B Rev.* **27**, 539–547 (2021).
44. L. Barraud *et al.*, *J. Hepatol.* **42**, 736–743 (2005).
45. X. Kuang *et al.*, Self-enhancing sono-inks enable deep-penetrating acoustic volumetric printing, Zenodo (2023); https://doi.org/10.5281/zenodo.8422050.

ACKNOWLEDGMENTS

This work was performed in part at the Center for Nanoscale Systems (CNS) at Harvard University, a member of the National Nanotechnology Infrastructure Network (NNIN), which is supported by the National Science Foundation under award number ECS0335765. We also thank D. A. Weitz from Harvard University for rheometer access, and P. Zhong from the Department of Mechanical Engineering and Materials Science at Duke University for assistance with acoustic cavitation mapping. **Funding:** This work is supported by the National Institutes of Health (R21EB025270, R01HL153857, R01HL165176, R01HL166522, and R01CA282451), the National Science Foundation (CBET-EBMS-1936105), and the Brigham Research Institute, all to Y.S.Z.; National Institutes of Health (NIH) [R21EB027981, R21EB027304, RF1NS115581 (BRAIN Initiative), R01NS111039, R01EB028143, R21EB027981, and R01EB031629], National Science Foundation

CAREER award 2144788, and Chan Zuckerberg Initiative Grant 2020-226178, all to J.Y. M.O.A. acknowledges funding support from the TÜBİTAK 2214-A Program (1059B141801395). **Author contributions:** X.K., J.Y., and Y.S.Z. conceived of the idea. X.K. designed the materials and methods. Q.R., S.B., X.K., M.C., T.V., and C.E.G.-M. designed the printer setup. X.K., A.M.L.L., and M.O.A. prepared the materials and conducted material characterizations. Q.R., S.B., T.V., N.W., and X.K. performed the printing and acoustic characterizations. Q.R. and X.K. developed the numerical models and conducted the simulations. X.K., Q.R., S.B., T.V., N.W., and C.E.G.-M. analyzed the results and processed visualizations. X.K., J.Y., and Y.S.Z. wrote the manuscript, with input from all authors. Y.S.Z. and J.Y. supervised the study. **Competing interests:** Y.S.Z. consults for Allevi by 3D Systems and sits on the scientific advisory board and holds options of Xellar, neither of which, however, participated in or biased this work. **Data and materials availability:** All data needed to evaluate the conclusions in the study are present in the paper and/or the supplementary materials. G-codes for printing and simulation codes for diffusion analysis are provided on Zenodo (*45*). **License information:** Copyright © 2023 the authors, some rights reserved; exclusive licensee American Association for the Advancement of Science. No claim to original US government works. https://www.science.org/about/science-licenses-journal-article-reuse

SUPPLEMENTARY MATERIALS

science.org/doi/10.1126/science.adi1563
Materials and Methods
Supplementary Text
Figs. S1 to S43
Tables S1 to S9
References (*46*–*81*)
MDAR Reproducibility Checklist
Movies S1 to S14

Submitted 6 April 2023; accepted 13 October 2023
10.1126/science.adi1563

CULTURAL COEVOLUTION

Culturally determined interspecies communication between humans and honeyguides

Claire N. Spottiswoode[1,2]*† and Brian M. Wood[3,4]*†

Species interactions that vary across environments can create geographical mosaics of genetic coevolution. However, traits mediating species interactions are sometimes culturally inherited. Here we show that traditions of interspecies communication between people and wild birds vary in a culturally determined geographical mosaic. Honey hunters in different parts of Africa use different calls to communicate with greater honeyguides (*Indicator indicator*) that lead them to bees' nests. We show experimentally that honeyguides in Tanzania and Mozambique discriminate among honey hunters' calls, responding more readily to local than to foreign calls. This was not explained by variation in sound transmission and instead suggests that honeyguides learn local human signals. We discuss the forces stabilizing and diversifying interspecies communication traditions, and the potential for cultural coevolution between species.

Species interactions such as mutualism, parasitism, and predation have generated much of life's diversity, playing out differently on different ecological stages in a geographical mosaic of genetic coevolution (*1*). However, interspecies interactions are often mediated by phenotypically plastic traits, including learned traits that vary geographically (*2*). Traits shaped by social learning can form stable cultural traditions in diverse animal species from humans to fruit flies to sperm whales, and these can vary markedly among populations (*3*). An intriguing, yet understudied, scenario may arise where two (or more) species reciprocally influence one another's fitness in an interaction mediated by learned traits in both species. Learned responses in one species could thus reinforce the learned traditions of the other, culminating in a process of interspecies cultural coevolution (*4*–*6*).

Humans have an unrivaled capacity for social learning (*7*). Our species' cultural adaptability has allowed us to invade new environments and dominate landscapes (*8*), and produces diverse behavioral responses in wild nonhuman species (*4*, *9*). In Africa, we should expect the longest periods of interaction between humans (or our ancestors) and other species. Here we investigated how human cultural traditions mediate an ancient, cooperative interaction between humans and a wild bird. Specifically, we asked whether geographically varying, learned traits facilitated mutualistic cooperation, and thus set the stage for cultural coevolution to occur.

We investigated interspecies communication between humans and greater honeyguides (*Indicator indicator*) (hereafter "honeyguides"), which lead people in Africa to wild bees' nests (*10*, *11*). Honeyguides naturally locate bees' nests and eat wax. Humans can subdue the bees and open their nests, thus exposing beeswax for the honeyguides and honey for themselves. Honeyguides across Africa give distinctive chattering calls to attract people and then indicate the direction to bees' nests by flying from tree to tree (*5*, *11*). Honeyguides thus exchange their knowledge of bees' nest locations for honey hunters' exceptional skills at subduing bees (typically using smoke), opening nests and exposing edible wax and bee brood. Humans possess technological, cognitive, and social capabilities that make us highly efficient honeyguide partners (*11*). Our hominin ancestors, like great apes today, would likely have eagerly sought honey (*12*, *13*). Their ability to acquire it would have been enhanced by stone tools (in use since 3.3 million years ago) and the mastery of fire (between 1.5 million and 350,000 years ago) (*13*–*16*). Recent changes now threaten the viability of the partnership, including apiculture, urbanization, increased availability of refined sugar, and exclusion of people from protected areas (*17*–*19*).

Where this partnership persists, marked cultural variability exists in the traits that mediate it, including how people attract honeyguides. Honey hunters often use specialized calls to advertise that they are looking for a honeyguide partner and to maintain cooperation while following a guiding bird. In one population, honeyguides have been shown to be more likely to cooperate with humans giving this signal (*5*). Honey hunters from the Yao cultural group in northern Mozambique typically give a loud trill followed by a grunt ("brrrr-hm") when seeking and following honeyguides (*5*), whereas honey hunters from the Hadza (also known as Hadzabe) cultural group in northern Tanzania use a melodic whistle (*16*) (examples in audio S1), and other cultures elsewhere in Africa use different, distinct calls in the same context (*11*, *20*–*22*). Members of the honey-hunting communities that inspired this study report that they learn these calls from their fathers or other elders, and that no-one diverges from these traditions because they will find less honey if they do (*5*).

Here we ask whether honeyguides are attracted to local rather than foreign honey-hunter signals, which would suggest that they learn the cultural traditions of mutualistic interactions with humans. Honeyguides' propensity to guide humans appears to be innate, as they attempt to guide within weeks of fledging parasitically from other species' nests, and to guide humans in regions where people rarely follow (*23*, *24*). However, it can either diminish or be reinforced on the basis of variable interactions with people (*23*). A priori, we expect that preferences for specific human signals would be learned by honeyguides, rather than arise though genetic local adaptation (*5*). In other contexts, songbirds learn and recognize local vocal dialects used by social group members (*25*, *26*). Greater honeyguide populations across Africa do not exhibit any obvious phenotypic or nuclear genetic divergence (*27*, *28*), consistent with high rates of gene flow. Alternatively, all honeyguides may be innately attracted to a range of honey-hunter signals, regardless of their prior exposure to them. We developed simple game-theoretic and optimal foraging models to explore why these interspecies communication traditions are consistent locally but vary between cultures.

Honeyguides have learned the signals of their local human partners

We conducted field experiments to ask whether honeyguides are more likely to initiate cooperation [i.e., approach a human and give distinctive guiding calls and behavior (*11*)] in response to signals of their local human culture, than to those of a foreign culture, or to arbitrary human sounds that serve merely as a cue of human presence. Following previously established methods (*5*, *29*), we carried out experimental transects simulating honey-hunting forays in Niassa Special Reserve in Mozambique (N = 77 transects of 15 min each) and in the Kidero Hills of northern Tanzania (N = 75 transects of 30 min each; longer transects were designed because we anticipated, and found, a lower density of bees and honeyguides in this drier environment). On each transect we played back one of three types of sounds (examples in audio S2): the Yao honey-hunting signal, the Hadza honey-hunting signal, or an arbitrary human sound (a honey hunter calling his name,

[1]Department of Zoology, University of Cambridge, Cambridge, UK. [2]FitzPatrick Institute of African Ornithology, Department of Biological Sciences, University of Cape Town, Cape Town, South Africa. [3]Department of Anthropology, University of California Los Angeles, Los Angeles, CA, USA. [4]Department of Human Behavior, Ecology, and Culture, Max Planck Institute for Evolutionary Anthropology, Leipzig, Germany.
*Corresponding author. Email: cns26@cam.ac.uk (C.N.S.); brianwood@anthro.ucla.edu (B.M.W.)
†These authors contributed equally to this work.

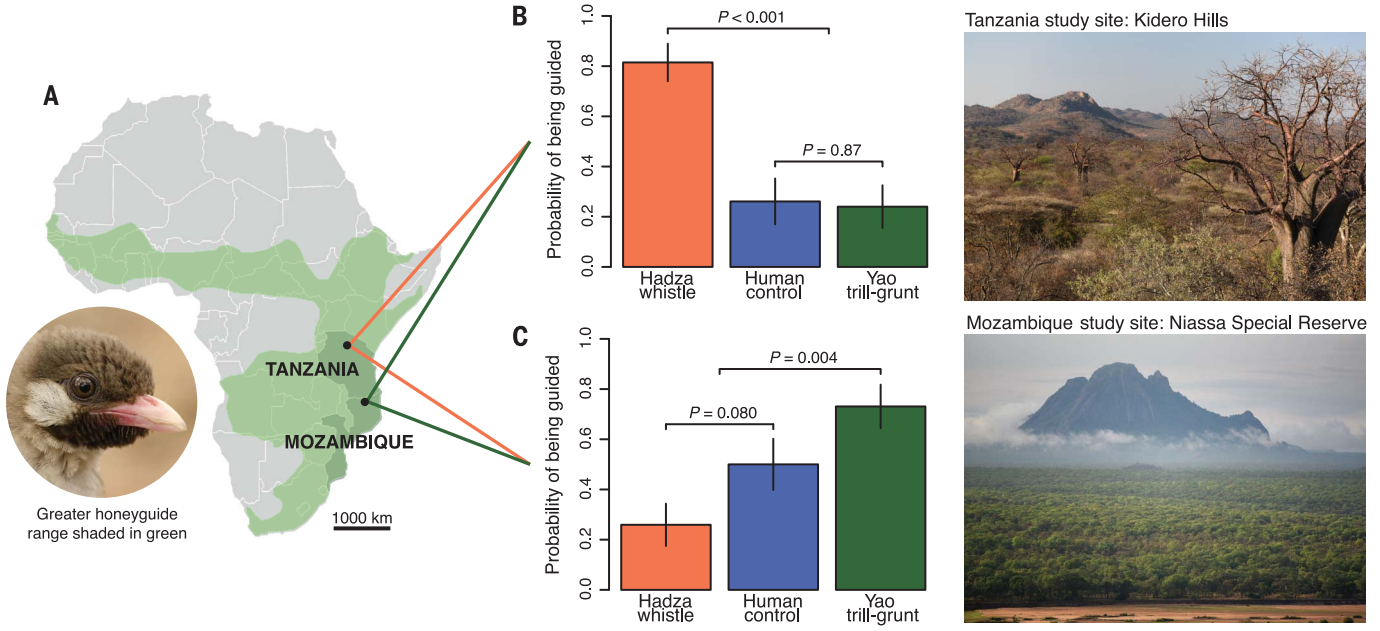

Fig. 1. Honeyguide cooperative behavior in response to experimental acoustic playbacks. We carried out the same experimental treatments at (**A**) Kidero Hills inhabited by Hadza people in Tanzania and Niassa Special Reserve inhabited by Yao people in Mozambique. Values are probabilities of honeyguides initiating cooperation with humans on (**B**) a 30-min search (Tanzania) or (**C**) a 15-min search (Mozambique), giving either Hadza (orange) or Yao (green) honey-hunting signals, or arbitrary human sounds (blue). *P*-values result from planned comparisons of response rates. Error bars span ±1 SE.

alternating across transects between Yao and Hadza voices, which were acoustically similar; fig. S1). We performed the same treatments, using the same set of playback exemplars, at both sites (Fig. 1A).

We found that in Tanzania, there was a 3.26 times higher probability of honeyguides initiating cooperation in response to local Hadza whistles (81.5% of transects) than to either foreign Yao trill-grunts (24%) or control sounds (26.1%) [Fig. 1B; logistic regression planned comparison (*30*) of local signal with foreign and control sounds, slope ± SE = 1.72 ± 0.40, $Z = 4.32$, $P < 0.0001$]. Honeyguides in Tanzania responded similarly to foreign Yao trill-grunts and to control sounds (slope ± SE = −0.06 ± 0.33, $Z = -0.17$, $P = 0.87$). In Mozambique, there was a 1.96 times higher probability of honeyguides initiating cooperation in response to local Yao trill-grunts (73.1% of transects) than to foreign Hadza whistles (25.9%) or control sounds (50% of transects) (Fig. 1C; logistic regression planned comparison of local signal to foreign and control sounds, slope ± SE = 1.02 ± 0.36, $Z = 2.85$, $P = 0.004$).

At each site, we also evaluated models with time of day and temperature variables, but they did not improve predictive accuracy (*29*). Acoustic treatment alone explained 36% and 20% of the variation in honeyguide response in Tanzania and Mozambique, respectively.

These results enable us to compare three hypotheses: that honeyguides have learned the culturally varying signals of their local human partners (learning); that honeyguides have innate preferences toward these sounds (sensory bias); or that certain sounds transmit better in different environments [sensory drive (*31*, *32*)]. Results are consistent with learning and sensory drive, but not sensory bias, because if Yao and Hadza honey-hunting signals were intrinsically attractive to honeyguides, honeyguides should respond most to both signal types at both sites.

To separate learning from sensory drive, we measured the acoustic attenuation of each playback exemplar in each environment, to test two predictions from the latter hypothesis: (i) Signals should attenuate faster in the foreign than local environment, and (ii) attenuation rates of exemplars should predict honeyguide responses. Results indicated that Hadza whistles attenuated the least, but all sounds attenuated similarly across environments (Fig. 2 and table S1). Therefore, honeyguides were not more likely to hear local signals given in their local habitat. Second, models that include the attenuation rates of exemplars (in the relevant environment) explained no additional variation in results (table S2). Thus, sensory drive is not a viable explanation. Our results are most consistent with the learning hypothesis, that honeyguides learn to prefer the signals used by their own local human partners.

Stability and diversity in interspecies signals

Why do stable traditions of interspecific communication arise, and why might they vary across cultures? Honeyguides respond adaptively to culturally varying human signals (Fig. 1), highlighting the benefits of mutual intelligibility. This should provide an incentive for signal stability across time. As honey hunters attest, once a local tradition of honeyguide–human communication is established, it would not pay a honey hunter to radically diverge from that tradition. Our data suggest that a honey hunter who changed their whistled signal to a trill-grunt in the Hadza region would find less than half as much honey (Fig. 3).

We used a game-theoretic model [(*29*), model 1] to confirm that these benefits of mutual intelligibility create a coordination game (*33*) in which the evolutionarily stable strategy is for the honey hunter to produce, and the honeyguide to respond to, the same local signals.

Next, we consider why signal forms might differ across cultures. The sounds that people use to signal to honeyguides vary greatly among cultures (*5*, *11*, *16*, *21*, *22*), including within 100 km of our study sites (*20*). We suggest that these differences may not always be arbitrary, because the ways that people interact with honeyguides are influenced by differing cultural histories and economic practices. The Hadza speak Hadzane, a language isolate reflecting their distinctive cultural heritage and genetic descent from hunter-gatherers who lived in the region before the arrival of herders and farmers over the last 4000 years (*34*–*36*). The main economic pursuits of Hadza men are collecting wild honey and hunting animals (*36*, *37*). While honey hunting, Hadza

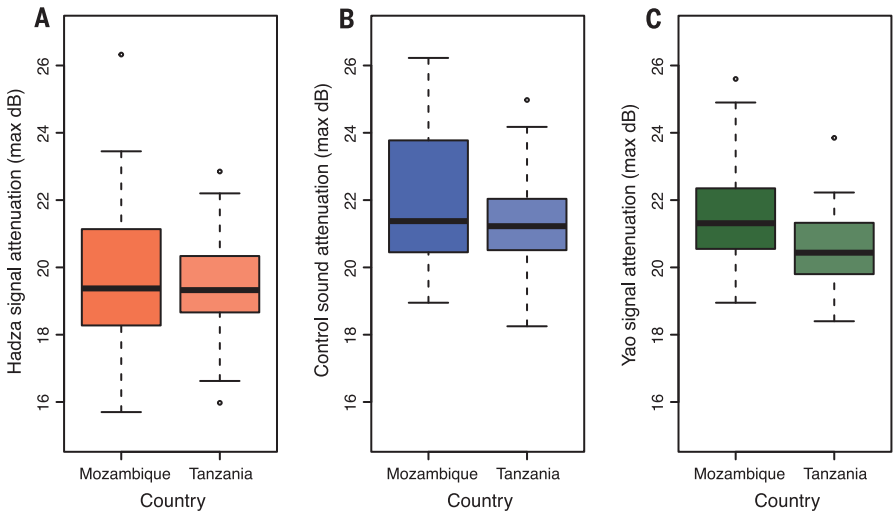

Fig. 2. Acoustic attenuation of honey-hunting signals used by different human cultures, and controls. (**A**) Whistles used by Hadza people in Tanzania, (**B**) arbitrary human sounds, and (**C**) trill-grunts used by Yao people in Mozambique all attenuate similarly from 3- to 30-m distance in their local environment compared to the foreign environment (maximum amplitudes of 77 sounds from different individuals played back in each environment; treatment × country interaction in linear model $P = 0.90$; table S1). Results were similar for mean amplitudes (table S1).

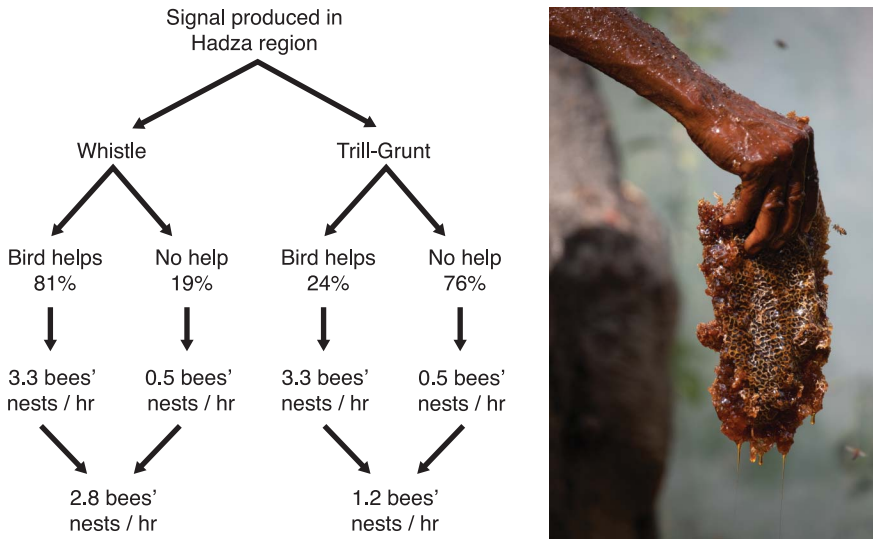

Fig. 3. The expected payoffs to whistling or trill-grunting in the Hadza region. Probabilities of guiding are taken from this study (Fig. 1). In a prior study, Hadza honey hunters found bees' nests at a rate of 3.3 per hour when helped by honeyguides, and 0.5 per hour without their help (*16*). A honey hunter in the Hadza region who committed to whistling to attract honeyguides for 30 min would be expected to find bees' nests at a rate of 2.8 per hour (0.81 × 3.3 + 0.19 × 0.5), whereas one who trill-grunted would realize a rate of 1.2 per hour (0.24 × 3.3 + 0.76 × 0.5). Bees' nests found with honeyguide assistance also yielded more honey than those found without honeyguides (*16*).

men also carry bows and arrows, and if prey are encountered, they quietly stalk them (*38*). Hadza hunters thus confront a trade-off between attracting honeyguides and not being detected by prey that fear human voices (*39*). In interviews carried out between 2015 and 2021, men stated that one reason they use whistles is to "sound like birds" (movies S1 and S2). Similarly, Hadza hunters also occasionally use whistles to communicate with other hunters. If whistles disguise human presence from game animals, Hadza hunters might plausibly be predisposed to whistling to attract honeyguides, rather than using vocal signals like those of the Yao, which are recognizably human, as confirmed by acoustic analysis (figs. S2 and S3). A nonmutually exclusive alternative is that whistles attenuate less (Fig. 2) and so better elicit cooperation where honeyguide densities are lower. These hypotheses parallel accounts of cultures worldwide that use whistled speech to (i) evade detection by game animals and prevent eavesdropping by outsiders, and (ii) communicate over long distances (*40*, *41*).

By contrast, the Yao speak an eastern Bantu language related to that of other agriculturalists in eastern Africa (*42*). In Niassa Special Reserve, farming and fishing are the main economic pursuits, supplemented by honey hunting, which a subset of adult men regularly undertake to generate cash and supplement household diets. Yao honey hunters here do not hunt mammals and are more concerned with avoiding dangerous animals (elephants, buffalo, lions). The conspicuousness of the signal they use could plausibly benefit them by scaring off these widely feared animals. Future research should test whether Yao trill-grunts broadcast human presence to mammals, and Hadza whistles disguise it. We did not design the current study to test these ideas, but note that at Niassa, there is a nonsignificant trend in which honeyguides responded to Hadza whistles less often than to control sounds of human presence (Fig. 1C). We investigated the competing demands of signaling to honeyguides and concealing cues from prey in an optimal foraging model [(*29*), model 2]. This suggests that the importance of mammal hunting could influence signal form in human–honeyguide communication.

Cultural coevolution of communication

Our field experiments and modeling suggest that honeyguides and humans influence one another through learned traits that culturally vary across different human populations (Fig. 1), while consistency within populations is maintained by the benefits of coordination (Fig. 3 and table S4). This leads to a learned communication system that makes honeyguides more likely to interact with a cooperative human, and humans more likely to elicit cooperative behavior from a honeyguide. Learned conventions thus maintain mutualistic coordination and discourage local people or birds from deviating from them. Thus, just as social conventions arising from coordination games lead to stability in word choice (*43*) and facilitate cooperation in humans (*33*), they likely also facilitate mutualistic interspecies cooperation.

These results are consistent with several predictions of a hypothesis of "cultural coevolution" between species (*4*). We find that cultural traditions in one species favor consistent learned responses in another species, which in turn reinforces the cultural traditions of the first.

There is evidence of cultural transmission of these traits through social learning in at least one species (humans) (*5*, *23*). Another criterion for cultural coevolution is that honeyguides also socially learn, a plausible hypothesis that is yet to be tested (*5*). In other bird species (*26*), preferences for conspecific local dialects are socially learned. Honeyguides have abundant opportunities for social learning because many honeyguides, including juveniles, are attracted to the sounds, sights, and smells of guiding events and honey harvests, and aggregate to scrounge from wax left behind (*44*, *45*). Social learning would benefit honeyguides as it is more efficient than individual learning in allowing a relatively large honeyguide population to learn the signals of a relatively small honey-hunter population. Honeyguide social learning could thus accelerate phenotypic adaptation to human cultural shifts in space or time (*4*), in turn favoring humans who shift to the new tradition. Such reciprocal reinforcement might operate in other examples of culturally-dependent interactions between humans and wildlife, both cooperative (*23*, *46*) and antagonistic (*47*), and between interacting nonhuman species. Cultural coevolution may form geographical mosaics that generate and maintain cultural biodiversity, just as geographical mosaics of genetic coevolution generate and maintain genetic biodiversity (*1*).

Culturally determined interspecies communication has implications for the evolution of cooperation. Once learned by honeyguides, culturally varying human signals facilitate honeyguides' ability to choose a good honey-hunter partner and thus increase the payoff from the mutualism for both species. This accords with our understanding that phenotypic plasticity can stabilize mutualisms, by facilitating choice of cooperative partners (*2*). Cultural traditions of consistent behavior are widespread in nonhuman animals (*3*) and could plausibly mediate other forms of interspecies cooperation. Reciprocal phenotypic plasticity through learning could thus facilitate mutualisms across generations and set the stage for stronger selection on adaptations linked to mutualisms (*2*).

Our experimental data show that a mosaic of interspecies communication traditions exist between people and birds, underpinned by learning in both species. The human–honeyguide partnership thus represents an ancient form of culturally dependent biodiversity (*19*, *23*). Any effort to help sustain these threatened interspecies partnerships should be based on an understanding of the forces shaping local traditions and generating geographical diversity (*19*, *48*).

REFERENCES AND NOTES

1. J. N. Thompson, *The Geographic Mosaic of Coevolution* (Univ. of Chicago Press, 2005).
2. A. A. Agrawal, *Science* **294**, 321–326 (2001).
3. A. Whiten, *Science* **372**, eabe6514 (2021).
4. J. M. Marzluff, T. Angell, *J. Ecol. Anthropol.* **9**, 69–75 (2005).
5. C. N. Spottiswoode, K. S. Begg, C. M. Begg, *Science* **353**, 387–389 (2016).
6. T. Dixit, *Evolution*, 10.1093/evolut/qpad082 (2023).
7. R. Boyd, P. J. Richerson, J. Henrich, *Proc. Natl. Acad. Sci. U.S.A.* **108** (suppl. 2), 10918–10925 (2011).
8. N. L. Boivin *et al.*, *Proc. Natl. Acad. Sci. U.S.A.* **113**, 6388–6396 (2016).
9. T. Gruber *et al.*, *Palgrave Commun.* **5**, 64 (2019).
10. A. Sparrman, *Philos. Trans. R. Soc. Lond.* **67**, 38–47 (1777).
11. H. A. Isack, H. U. Reyer, *Science* **243**, 1343–1346 (1989).
12. F. W. Marlowe *et al.*, *J. Hum. Evol.* **71**, 119–128 (2014).
13. R. Wrangham, *Casting the Net Wide: Papers in Honor of Glynn Isaac and His Approach to Human Origins Research*, J. Sept, D. Pilbeam, Eds. (Oxbow Books, 2012).
14. J. A. J. Gowlett, *Philos. Trans. R. Soc. Lond. B Biol. Sci.* **371**, 20150164 (2016).
15. S. Harmand *et al.*, *Nature* **521**, 310–315 (2015).
16. B. M. Wood, H. Pontzer, D. A. Raichlen, F. W. Marlowe, *Evol. Hum. Behav.* **35**, 540–546 (2014).
17. H. A. Isack, in *Int. Ornithol. Congr.*, N. J. Adams, R. H. Slotow, Eds. (BirdLife South Africa, Durban, South Africa, 1998), pp. 1351-1357.
18. M. Gruber, *Afr. Study Monogr.* **39**, 169–187 (2018).
19. J. E. M. van der Wal *et al.*, *Conserv. Lett.* **15**, e12886 (2022).
20. E. A. Laltaika, thesis, University of Cape Town (2021).
21. J. E. M. van der Wal, I. I. Gedi, C. N. Spottiswoode, *Front. Conserv. Sci.* **2**, 727479 (2022).
22. A. O. Kilawi, thesis, University of Cape Town (2023).
23. D. L. Cram *et al.*, *People Nat.* **4**, 841–855 (2022).
24. L. L. Short, J. F. M. Horne, *Toucans, Barbets and Honeyguides* (Oxford Univ. Press, 2001).
25. R. C. Anderson, S. Peters, S. Nowicki, *Behav. Ecol. Sociobiol.* **68**, 437–447 (2014).
26. J. Hyland Bruno, E. D. Jarvis, M. Liberman, O. Tchernichovski, *Annu. Rev. Linguist.* **7**, 449–472 (2021).
27. C. H. Fry, S. Keith, E. K. Urban, *The Birds of Africa* (Academic Press, 1988), vol. 3.
28. C. N. Spottiswoode, K. F. Stryjewski, S. Quader, J. F. R. Colebrook-Robjent, M. D. Sorenson, *Proc. Natl. Acad. Sci. U.S.A.* **108**, 17738–17742 (2011).
29. Materials and methods are available as supplementary materials.
30. G. D. Ruxton, G. Beauchamp, *Behav. Ecol.* **19**, 690–693 (2008).
31. J. A. Endler, *Philos. Trans. R. Soc. Lond. B Biol. Sci.* **340**, 215–225 (1993).
32. B. Hardt, L. Benedict, *Bioacoustics* **30**, 716–742 (2020).
33. E. A. Smith, *Genetic and Cultural Evolution of Cooperation*, P. Hammerstein, Ed. (MIT Press, 2003).
34. P. Skoglund *et al.*, *Cell* **171**, 59–71.e21 (2017).
35. A. Crowther, M. E. Prendergast, D. Q. Fuller, N. Boivin, *Quat. Int.* **489**, 101–120 (2018).
36. F. W. Marlowe, *The Hadza: Hunter-Gatherers of Tanzania* (Univ. of California Press, 2010).
37. B. M. Wood, F. W. Marlowe, *Hum. Nat.* **24**, 280–317 (2013).
38. B. M. Wood, F. W. Marlowe, *Hum. Nat.* **25**, 620–630 (2014).
39. L. Y. Zanette *et al.*, *Curr. Biol.* **33**, 4689–4696.e4 (2023).
40. J. Meyer, *Whistled Languages: A Worldwide Inquiry About Whistled Speech* (Springer, 2015).
41. R. G. Busnel, A. Classe, *Whistled Languages*, vol. 13 of *Communication and Cybernetics* (Springer-Verlag, Berlin, 1976).
42. T. E. Currie, A. Meade, M. Guillon, R. Mace, *Proc. Biol. Sci.* **280**, 20130695 (2013).
43. D. Hume, *A Treatise of Human Nature* (Courier Corporation, 2003).
44. D. J. Lloyd-Jones *et al.*, *Proc. Biol. Sci.* **289**, 20221443 (2022).
45. D. L. Cram *et al.*, *Proc. Biol. Sci.* **290**, 20232024 (2023).
46. M. Cantor, D. R. Farine, F. G. Daura-Jorge, *Proc. Natl. Acad. Sci. U.S.A.* **120**, e2207739120 (2023).
47. B. C. Klump *et al.*, *Curr. Biol.* **32**, R910–R911 (2022).
48. P. Brakes *et al.*, *Science* **363**, 1032–1034 (2019).

ACKNOWLEDGMENTS

We thank the Yao and Hadza honey-hunting communities for their inspiration and hospitality, and specifically Mo. Muamedi, Mu. Muamedi, F. Nampula, E. Waiti, and O. Yassene in Mozambique, and G. Felipo, M. Mdungai, G. Nyoha, M. Nyoha, B. Onawasi, and G. Sagiro in Tanzania, who assisted with field experiments. We thank M. Anyawire, C. Begg, K. Begg, A. Jorge, A. Mabulla, Administração Nacional das Áreas de Conservação, COSTECH, Mariri Environmental Centre, and Wildlife Conservation Society for support. We thank C. Blair, D. Cram, T. Dixit, L. Fogarty, A. Kandler, E. A. Laltaika, D. Lloyd-Jones, J. Lund, R. Magrath, J. Mitani, and J. van der Wal for comments or discussion, L. McEachern for video production, and the three anonymous reviewers for constructive feedback. **Funding:** European Research Council Consolidator Grant 725185 (C.N.S.); Biotechnology and Biological Sciences Research Council David Phillips Research Fellowship BB/J014109/1 (C.N.S.); National Geographic Society grant HJ-109R-17 (B.M.W.); Max Planck Institute for Evolutionary Anthropology (B.M.W.). **Author contributions:** Conceptualization: C.N.S., B.M.W. Methodology: C.N.S., B.M.W. Formal analysis: C.N.S., B.M.W. Investigation: C.N.S., B.M.W. Data curation: C.N.S., B.M.W. Writing – original draft: C.N.S., B.M.W. Funding acquisition: C.N.S., B.M.W. **Competing interests:** The authors declare that they have no competing interests. **Data and materials availability:** Code and data for reproducing all results are available through the Open Science Foundation with the following URL (https://osf.io/q24a6/) and DOI (10.17605/OSF.IO/Q24A6). **License information:** Copyright © 2023 the authors, some rights reserved; exclusive licensee American Association for the Advancement of Science. No claim to original US government works. https://www.sciencemag.org/about/science-licenses-journal-article-reuse

SUPPLEMENTARY MATERIALS

science.org/doi/10.1126/science.adh4129
Materials and Methods
Supplementary Text
Figs. S1 to S3
Tables S1 to S4
References (*49*–*54*)
MDAR Reproducibility Checklist
Audio S1 and S2
Movies S1 and S2

Submitted 2 March 2023; accepted 25 October 2023
10.1126/science.adh4129

CROP SCIENCE

Biofortification of iron content by regulating a NAC transcription factor in maize

Pengshuai Yan[1,2], Qingguo Du[1], Huan Chen[1], Zifeng Guo[1], Zhonghua Wang[1], Jihua Tang[2,3]*, Wen-Xue Li[1]*

Iron (Fe) deficiency remains widespread among people in developing countries. To help solve this problem, breeders have been attempting to develop maize cultivars with high yields and high Fe concentrations in the kernels. We conducted a genome-wide association study and identified a gene, *ZmNAC78* (*NAM/ATAF/CUC DOMAIN TRANSCRIPTION FACTOR 78*), that regulates Fe concentrations in maize kernels. We cultivated maize varieties with both high yield and high Fe concentrations in their kernels by using a molecular marker developed from a 42–base pair insertion or deletion (indel) in the promoter of *ZmNAC78*. *ZmNAC78* expression is enriched in the basal endosperm transfer layer of kernels, and the ZmNAC78 protein directly regulates messenger RNA abundance of Fe transporters. Our results thus provide an approach to develop maize varieties with Fe-enriched kernels.

Iron (Fe) is an essential microelement for human health. Fe deficiency occurs often in human diets and affects an estimated 2 billion people, especially infants, young children, and pregnant women (*1*, *2*). The risk of Fe deficiency is much greater in sub-Saharan Africa (*3*, *4*)—where maize is a staple food providing at least 30% of total calorie intake (*5*)—as compared with other regions. A diet high in maize, however, makes people prone to Fe deficiency, and Fe concentrations in maize endosperm are low (*6*). In Zimbabwe, for example, about 30% of pregnant and lactating women suffer from Fe deficiency, which weakens the immune system, stunts growth, and impairs cognitive development (*7*, *8*).

Although supplementation, dietary diversification, and commercial food fortification have been used to increase the micronutrient content of human diets, these measures have been unsatisfactory in developing countries because of low economic sustainability and low consumer acceptability (*9*, *10*). By contrast, biofortification through genetic modification of crops appears to be more promising (*11*). Genes related to Fe uptake and metabolism have been successfully genetically engineered to increase Fe content in edible parts of crops. For example, synergistic expression of *AtNAS1* (*NICTOTIANAMINE SYNTHASE 1*), *PvFERRITIN*, and *AfPHYTASE* increased Fe concentrations in rice endosperm (*12*); endosperm-targeted overexpression of *TaFERRITIN1-A* resulted in a 50 to 85% increase in the Fe content in wheat grain (*13*); and coexpression of a mutated *AtIRT1* (*IRON-REGULATED TRANSPORTER 1*) and *AtFERRITIN1* increased the Fe content in field-grown cassava (*14*).

Developing biofortified maize with high Fe concentrations in the kernels should be an effective way to alleviate Fe deficiency–induced anemia in sub-Saharan Africa, but the development of biofortified maize varieties has been limited. One challenge to biofortifying Fe in maize is that Fe concentrations in grain are negatively correlated with maize yield (*6*, *15*). In addition, the process of Fe loading into maize kernels is almost completely unknown. It is therefore valuable to identify genetic resources that could enhance Fe concentrations in maize kernels without reducing yield.

Results

Identification of ZmNAC78

We determined Fe concentrations in kernels of a maize natural-variation population growing in Sanya, Hainan Province, China. The population consisted of 273 maize inbred lines, including introgression lines, Chinese elite inbred lines [SPT (Sipingtou), LRC (Lvda Red Cob), PA (group A germplasm derived from modern US hybrids in China), PB (group B germplasm derived from modern US hybrids in China), Reid, Lancaster, and Iodent], and inbred lines from the US (table S1). The Fe concentrations in the kernels of this population ranged from 4.90 to 55.18 mg kg^{-1}, with a mean of 24.15 mg kg^{-1} (Fig. 1A and table S1). From this population, we randomly selected 20 inbred lines and planted them in Shunyi, Beijing, to investigate the repeatability of the Fe concentration phenotypes. Fe concentrations in maize kernels are substantially affected by soil conditions (*3*). Although soil properties differ considerably between Sanya (pH 4.9) and Shunyi (pH 8.2), the Fe concentrat[illegible] in maize kernels produced in Sanya were [illegible] related with those produced in Shunyi [Pearson's correlation coefficient (R) = 0.83; $P = 5 \times 10^{-6}$] (Fig. 1B).

Using 301,603 single-nucleotide polymorphisms (SNPs) with a minor allele frequency ≥0.05 and a missing rate <10.0% covering the whole maize genome, we conducted a genome-wide association study (GWAS) for Fe concentrations in maize kernels with the general linear model approach controlling population structure. On the basis of a linkage-disequilibrium region [coefficient of determination (R^2) ≥ 0.1] (*16*), a total of 11 SNPs were significantly associated with the Fe concentrations in maize kernels (Fig. 1C). All of the identified candidate genes associated with Fe concentrations in maize kernels are listed in table S2. In the population, Fe concentrations in kernels were significantly negatively correlated with 100-kernel weight (fig. S1A). To detect potential genes regulating kernel Fe concentrations in maize, we performed RNA sequencing (RNA-seq) on six inbred lines with different kernel Fe concentrations but similar 100-kernel weights to reduce bias from bioaccumulation by small kernels (fig. S1B). The RNA libraries yielded a total of >0.32 billion reads after adaptor trimming, and ~91.05% of the clean reads could be perfectly mapped to the maize B73 v4 reference genome (*17*). The abundance of each gene was determined in terms of reads per kilobase per million mapped reads (*18*). A total of 1531 genes differentially expressed between high- and low-Fe inbred lines on the basis of fold-change criteria >1.5 and $P < 0.05$ (*19*, *20*). Among the differentially expressed genes, 857 were up-regulated and 674 were down-regulated in high-Fe lines relative to low-Fe lines (fig. S1C).

We then investigated the mRNA abundances of the 11 candidate genes identified by GWAS in these RNA libraries. Because its expression level was low in all six inbred lines, *Zm00001d027400* was excluded from our analysis. Among the remaining 10 candidate genes, only *Zm00001d027395* [*ZmNAC78* (*NAM/ATAF/CUC DOMAIN TRANSCRIPTION FACTOR 78*)] had consistently higher expression in high-Fe lines compared with low-Fe lines (fig. S2A), and the expression levels of *ZmNAC78* were significantly positively correlated with Fe concentrations in the kernels of 30 randomly selected inbred lines (11 with high Fe concentrations, 4 with medium Fe concentrations, and 15 with low Fe concentrations) (fig. S2B). We therefore inferred that *ZmNAC78* might regulate Fe concentrations in maize kernels.

ZmNAC78 regulates Fe concentrations in maize kernels

We investigated the expression patterns of *ZmNAC78* in the Maize eFP Browser RNA-seq

[1]State Key Laboratory of Crop Gene Resources and Breeding, National Engineering Laboratory for Crop Molecular Breeding, Institute of Crop Sciences, Chinese Academy of Agricultural Sciences, Beijing 100081, China. [2]National Key Laboratory of Wheat and Maize Crop Science, College of Agronomy, Henan Agricultural University, Zhengzhou 450002, China. [3]Shennong Laboratory, Zhengzhou 450002, China.
*Corresponding author. Email: liwenxue@caas.cn (W-X.L.); tangjihua1@163.com (J.T.)

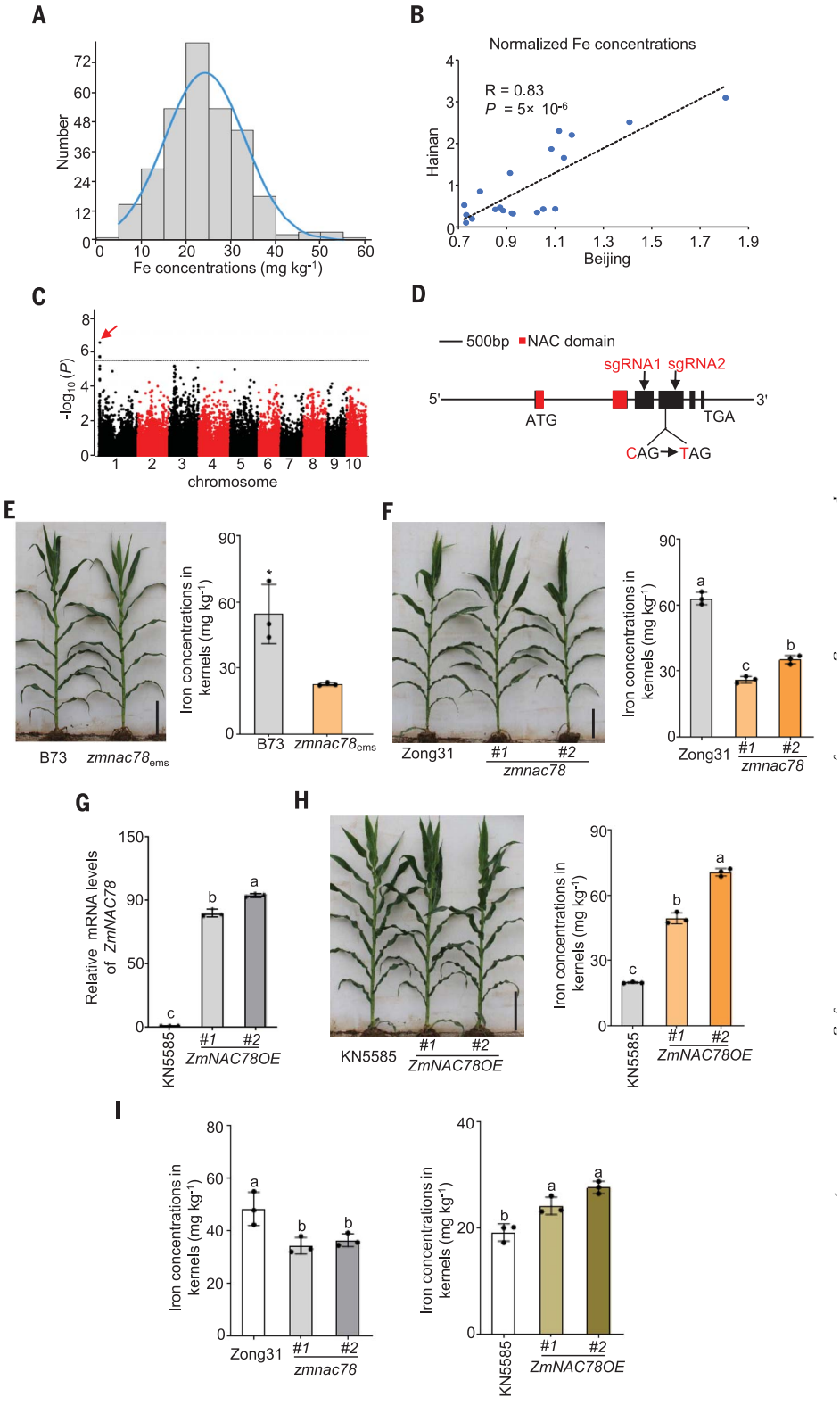

Fig. 1. *ZmNAC78* regulates Fe concentrations in maize kernels. (**A**) Fe concentrations in kernels are consistent with a normal distribution in a maize natural-variation population. (**B**) Pearson's correlation coefficient of Fe concentrations in kernels of randomly selected maize grown in Hainan Province versus randomly selected maize grown in Beijing. n = 20 inbred lines. (**C**) Manhattan plot for the GWAS. The dashed line represents the Bonferroni-adjusted significance threshold ($P = 3.3 \times 10^{-6}$). (**D**) Diagram illustrating the EMS-mutated site and synthetic guide RNAs (sgRNAs). The gene model is from MaizeGDB (*41*). (**E**) Effects of *ZmNAC78* EMS mutation on maize growth and Fe concentrations in kernels. (**F**) Effects of *ZmNAC78* loss of function on maize growth and Fe concentrations in kernels. (**G**) Detection of *ZmNAC78* mRNA abundance in *ZmNAC78OE* transgenic maize. (**H**) Effects of *ZmNAC78* overexpression on maize growth and Fe concentrations in kernels. (**I**) Fe concentrations in kernels of *ZmNAC78* loss-of-function mutants and *ZmNAC78OE* transgenic maize in Beijing. Scale bars in (E), (F), and (H), 30 cm. Error bars in (E) through (I) represent the standard deviation of three biological replicates. Asterisk in (E) indicates significant difference at $P < 0.05$ according to t tests. Means with the same letter in (F) through (I) are not significantly different at $P < 0.05$ according to one-way analysis of variance (ANOVA) followed by Tukey's multiple comparison test.

database (*21*) and found that *ZmNAC78* is preferentially expressed in the endosperm at 16 to 24 days after pollination (DAP) (fig. S3A), when nutrients rapidly accumulate in maize kernels. The expression patterns of *ZmNAC78* were verified by reverse transcription quantitative polymerase chain reaction (RT-qPCR) (fig. S3, B and C).

We obtained an ethyl methanesulfonate (EMS) mutant of *ZmNAC78* in the B73 background from the Maize EMS-induced Mutant Database (mutant ID: EMS4-16d24b) (*22*). EMS4-16d24b contains a C/T substitution in the fourth exon of *ZmNAC78*, which leads to a premature stop codon in the gene (Fig. 1D). We designated the mutant as $zmnac78_{ems}$. The mutation in $zmnac78_{ems}$ did not affect maize development (Fig. 1E). However, the Fe concentration in

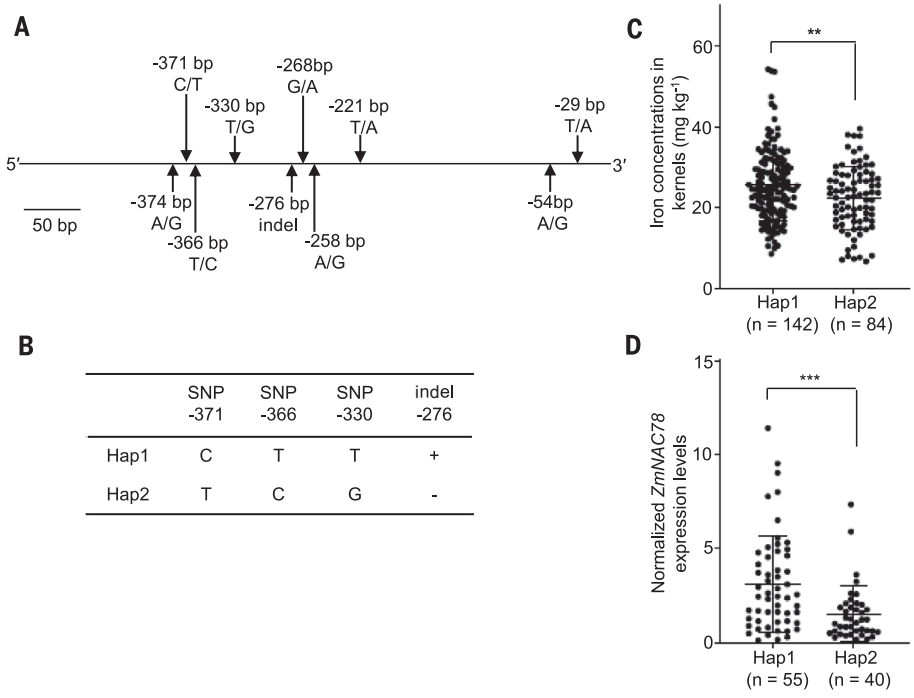

Fig. 2. Natural variation in the *ZmNAC78* core promoter is associated with Fe concentrations in maize kernels. (**A**) Diagram illustrating the differences in the core promoter between five high-Fe and five low-Fe inbred lines. (**B**) Identification of *ZmNAC78* haplotypes (Hap) on the basis of consistent variations in a maize natural-variation population. n = 226 inbred lines. (**C**) Fe concentrations in kernels in Hap1 and Hap2. (**D**) Expression levels of *ZmNAC78* in the kernels of Hap1 and Hap2. Asterisks in (C) and (D) indicate significant differences according to t tests. $^{**}P < 0.01$, $^{***}P < 0.001$.

the kernels of the $zmnac78_{ems}$ mutant was 22.69 mg kg^{-1}, which was 40% lower than that found in the kernels of the control line, B73 (Fig. 1E).

We generated *ZmNAC78* null mutants (*zmnac78*) in the Zong31 background with CRISPR-Cas9. Two guide RNAs were designed that targeted the sequence at nucleotides 677 to 695 and 1185 to 1203 after the ATG codon (Fig. 1D). The *zmnac78* mutants exhibited deletions of 35–base pair (bp) or 71-bp fragments in the coding sequence, which resulted in frameshifts (fig. S4). Consistent with observations in $zmnac78_{ems}$, the *zmnac78* mutant was similar to the control line Zong31 during vegetative development (Fig. 1F). Although the kernel length, kernel width, and 100-kernel weight were reduced in the *zmnac78* mutants (table S3), the Fe concentrations in kernels were still much lower in *zmnac78* mutants than in Zong31 (Fig. 1F). *ZmNAC78* is closely related to *ZmNAC57* in maize (fig. S5A), but the cDNA sequence and mRNA abundance of *ZmNAC57* were not altered in *zmnac78* mutants (fig. S5, B and C). This indicated that CRISPR-Cas9 did not produce off-target effects and that the reduction of Fe concentrations in kernels of the *zmnac78* mutants was due to *ZmNAC78* loss of function.

We constructed transgenic maize lines overexpressing *ZmNAC78* in the KN5585 background. We chose two transgenic lines (*OE#1* and *OE#2*) for further analysis (Fig. 1G). Overexpression of *ZmNAC78* did not affect the growth or 100-kernel weight of maize but significantly increased the Fe concentrations in kernels (Fig. 1H and table S3). The Fe concentrations in the kernels of *ZmNAC78*-overexpressing transgenic maize ranged from 49.4 to 70.5 mg kg^{-1}, which was 2.5 to 3.6 times the range in KN5585 (Fig. 1H).

All of the results presented to this point were from $zmnac78_{ems}$, *zmnac78* mutants, and *ZmNAC78OE* transgenic maize grown in Sanya, Hainan Province. The *zmnac78* mutants and *ZmNAC78* OE transgenic maize were also grown in Nankou (soil pH 7.5), Beijing. Compared with the Fe concentrations in the wild-type (WT) maize, those in kernels were reduced in *zmnac78* mutants and increased in *ZmNAC78OE* transgenic maize grown in Nankou, Beijing (Fig. 1I). These results demonstrated that *ZmNAC78* regulates Fe concentrations in maize kernels and that the regulation is independent of maize genotype and growing site.

Promoter natural variation affects ZmNAC78 mRNA abundance

In the natural-variation population, the expression levels of *ZmNAC78* were significantly positively associated with Fe concentrations in kernels (fig. S2B). We cloned the coding sequence (CDS) and the core promoter of *ZmNAC78* in five randomly selected high-Fe lines and five randomly selected low-Fe lines. The core promoter was defined as the ~500-bp region upstream of the transcription start site (TSS), which is where *cis*-regulatory elements accumulate (*23*). The CDS sequences of *ZmNAC78* were identical between high- and low-Fe lines (fig. S6). By contrast, the core promoter of *ZmNAC78* in high- and low-Fe lines differed at nine SNPs and one indel-276 (Fig. 2A and fig. S7).

We resequenced the core promoter of *ZmNAC78* from 226 maize inbred lines. SNP-330, SNP-366, SNP-371, and indel-276 showed consistent variations among the inbred lines. We grouped lines into two major haplotypes (Hap1 and Hap2) on the basis of these consistent variants (Fig. 2B). Fe concentrations in kernels were significantly higher in Hap1 than in Hap2 (Fig. 2C). We also determined the abundance of *ZmNAC78* mRNA in 55 randomly selected Hap1 inbred lines and 40 randomly selected Hap2 inbred lines. The abundance of *ZmNAC78* mRNA was much higher in Hap1 kernels than in Hap2 kernels (Fig. 2D), consistent with the high Fe concentrations in Hap1 kernels. These results suggested that natural variation in the core promoter region affects the expression levels of *ZmNAC78*.

Molecular marker–assisted selection of maize varieties with Fe-enriched kernels

To determine whether *ZmNAC78* underwent selection during maize breeding, we sequenced the core promoter of *ZmNAC78* from a previously reported maize population (*24*). The population included 60 public US inbred lines (Public-US), 83 USA elite commercial lines with expired Plant Variety Protection Act Certificates (Ex-PVP), 28 Chinese inbred lines released during 1960 to 1979 (CN1960&70s), 87 Chinese inbred lines released during 1980 to 1999 (CN1980&90s), and 20 Chinese inbred lines released after 2000 (CN2000&10s). We found that the frequency of the Hap1 allele increased over time, which was consistent with the inference that *ZmNAC78* was selected for during modern breeding in both the US and China (Fig. 3A). We further analyzed the frequency of the Hap1 allele in 168 Chinese elite inbred lines and found that the frequency of the Hap1 allele was high in SPT, Reid, and Lancaster (Fig. 3B). Reid × Lancaster is a very important heterotic combination in temperate regions (*25*). This suggested that the favorable Hap1 allele could be used for modern breeding.

To test this hypothesis, we conducted a hybrid cross between B73 (Hap1) and KN5585 (Hap2) to construct an $F_{2:3}$ population with 75 families. We randomly selected three Hap1 homozygous

families and three Hap2 homozygous families for analysis of Fe concentrations in kernels. Consistent with observations in our natural-variation population, the Hap1 families in the $F_{2:3}$ population had higher Fe concentrations and higher *ZmNAC78* mRNA abundances in kernels than were found in Hap2 families (fig. S8).

We therefore developed an indel marker to perform molecular marker–assisted selection of maize varieties with Fe-enriched kernels (fig. S9). The parents originated from Reid and/or Lancaster. Zhengdan958 was selected as the control because it has been grown in 13% of the maize planting area in China since 2004 (*26*). Five self-breeding varieties, including three from Hap1 (variety 1, 2, and 3) and two from Hap2 (variety 4 and 5), were planted alongside Zhengdan958 in Yuanyang, Henan Province (soil pH 8.5). Compared with Zhengdan958, variety 1 had both higher grain yield and higher Fe concentrations in kernels, and variety 2 had similar grain yield and higher Fe concentrations in kernels (Fig. 3, C and D). The self-breeding varieties and Zhengdan958 were also grown in Nanning, Guangxi Province (soil pH 6.4). In the subtropics (Nanning), grain yield and Fe concentrations were higher in variety 1 than in Zhengdan958 (Fig. 3, E and F). In both locations, the average Fe concentration was higher in Hap1 varieties than in Hap2 varieties (Fig. 3, C and E). These results suggested that *ZmNAC78* is a useful gene resource for achieving Fe biofortification in maize without reducing yield.

ZmNAC78 is enriched in the basal endosperm transfer layer

To clarify the molecular pathways by which *ZmNAC78* regulates Fe concentrations in maize kernels, we first determined the subcellular localization of ZmNAC78 protein. ZmNAC78-GFP and GFP-ZmNAC78 signals were detected only in the nucleus of maize leaf protoplasts (Fig. 4A). The localization was confirmed by colocalization with the nuclear marker gene, NFYA4 (NUCLEAR FACTOR Y, SUBUNIT A 4) (*27*).

ZmNAC78 contains a NAC domain, indicating that ZmNAC78 should have transcription-regulation activity. To test this hypothesis, pGBKT7-ZmNAC78 fusion plasmid was generated and cotransformed with the pGADT7 vector into the yeast strain Y2HGold. The yeast could survive on selective medium [synthetic defined (SD)/-Leu/-Trp/-His] along with an α-galactosidase activity (Fig. 4B). These results indicated that ZmNAC78 protein might have transcriptional-activation activity.

We then investigated the expression patterns of *ZmNAC78* by performing mRNA in situ hybridization using the 15-DAP B73 kernels. A clear signal was detected in the basal endosperm transfer layer (BETL) during the filling stage, and signals were also detected in

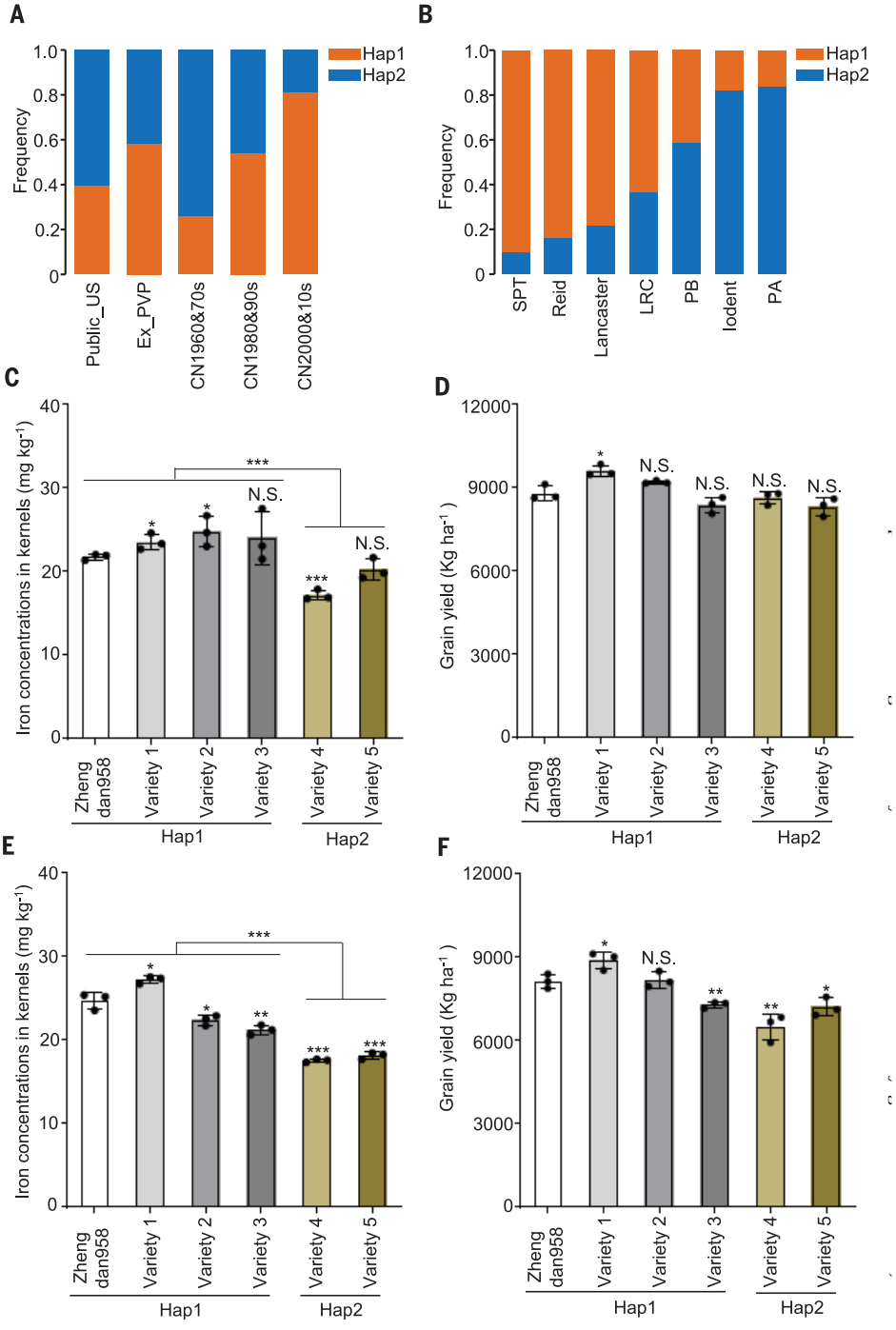

Fig. 3. Molecular marker–assisted breeding of maize with both increased Fe concentrations in the kernels and high yield. (**A**) Haplotype (Hap) frequency changes during breeding in the USA and China. (**B**) Hap frequency changes in Chinese elite inbred lines. The orange and blue colors in (A) and (B) represent Hap1 and Hap2, respectively. (**C**) Fe concentrations in kernels of Zhengdan958 and self-breeding varieties planted in Yuanyang, Henan Province. (**D**) Grain yields of Zhengdan958 and self-breeding varieties planted in Yuanyang, Henan Province. (**E**) Fe concentrations in kernels of Zhengdan958 and self-breeding varieties in Nanning, Guangxi Province. (**F**) Grain yields of Zhengdan958 and self-breeding varieties in Nanning, Guangxi Province. Error bars in (C) through (F) represent the standard deviation of three biological replicates. Asterisks in (C) through (F) indicate significant differences according to *t* tests. **P* < 0.05, ***P* < 0.01, ****P* < 0.001; N.S., not significant.

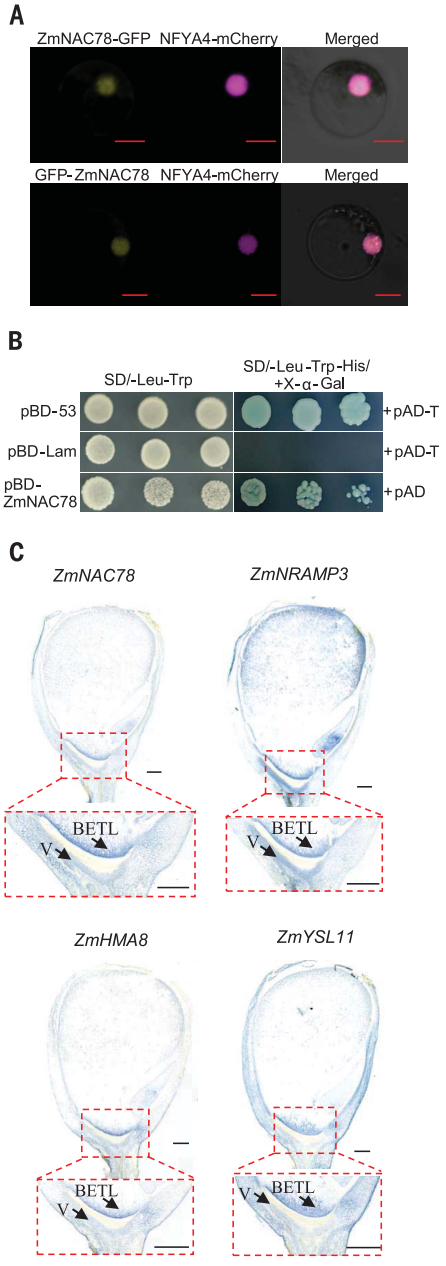

Fig. 4. Expression patterns of *ZmNAC78*. (**A**) Subcellular localization of ZmNAC78 protein. ZmNAC78-GFP (yellow) and GFP-ZmNAC78 (yellow) constructs were transiently coexpressed with the nuclear marker NFYA4-mCherry (magenta) in maize-leaf protoplasts. Scale bars, 10 μm. (**B**) Transcriptional-activation assay of ZmNAC78 protein in yeast. pBD-53 and pBD-Lam were used as a positive control and a negative control, respectively. (**C**) Expression patterns of *ZmNAC78*, *ZmNRAMP3*, *ZmHMA8*, and *ZmYSL11* in 15-DAP (days after pollination) B73 kernels as determined by in situ hybridization analysis. Scale bars in the whole kernels, 500 μm. Scale bars in the magnified views of the regions marked by the dashed red boxes, 100 μm. V, vascular; BETL, basal endosperm transfer layer.

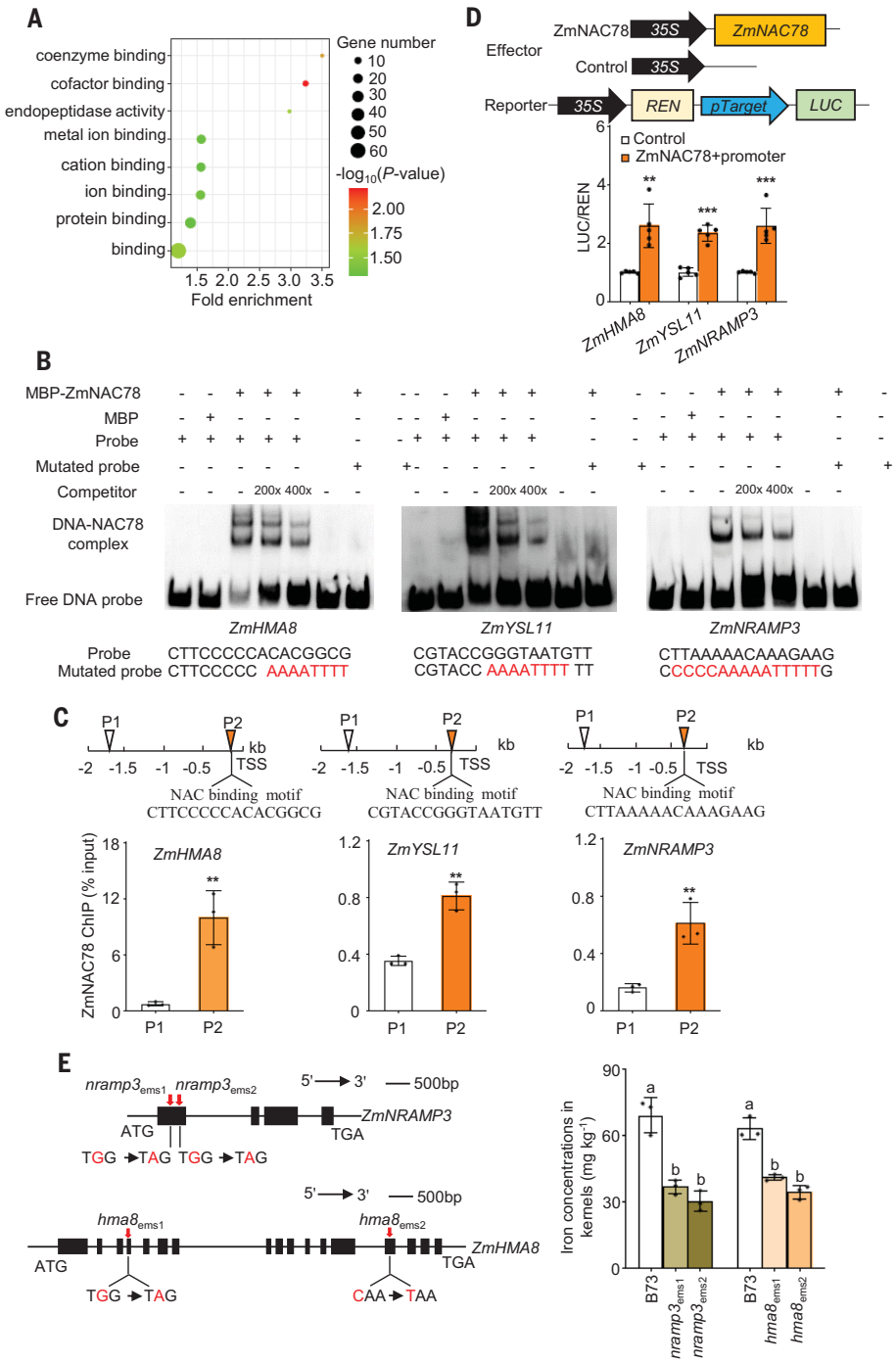

Fig. 5. ZmNAC78 regulates the expression of genes related to Fe uptake. (**A**) GO classifications of genes positively affected by *ZmNAC78* abundance. The point size represents the number of genes in the terms; the point color represents $-\log_{10}$ (*P* value). (**B**) EMSA with ZmNAC78 protein performed with the probes derived from the *ZmHMA8*, *ZmYSL11*, and *ZmNRAMP3* promoter. Competition for the labeled sequences was tested by adding an excess of unlabeled probes as indicated. Red represents the mutated sequence. The gene annotation is from MaizeGDB (*41*). (**C**) ChIP-qPCR assays verified the in vivo binding of ZmNAC78 to the *ZmHMA8*, *ZmYSL11*, and *ZmNRAMP3* promoter. (**D**) Transient-transactivation assay of ZmNAC78 protein with the *ZmHMA8*, *ZmYSL11*, and *ZmNRAMP3* promoter in maize mesophyll protoplasts. Relative REN (*Renilla* luciferase) activity was used as an internal control, and the relative LUC (Firefly luciferase)/REN ratios are shown. (**E**) Effects of *ZmNRAMP3* or *ZmHMA8* EMS mutation on Fe concentrations in maize kernels. Error bars represent the standard deviation of three biological replicates in (C) and (E) and of five biological replicates in (D). Asterisks in (C) and (D) indicate significant differences according to *t* tests. $^{**}P < 0.01$, $^{***}P < 0.001$. Means with the same letter in (E) are not significantly different at $P < 0.05$ according to one-way ANOVA followed by Tukey's multiple comparison test.

the vascular end of the pedicel, the pericarp, other endosperm cells, and the embryo (Fig. 4C and fig. S10).

ZmNAC78 regulates Fe uptake–related genes

To gain insight into the molecular events in the *ZmNAC78*-mediated signaling pathway, we compared the whole-transcriptome profiles of kernels of the *ZmNAC78OE* line, the *zmnac78* mutant, and their corresponding WT kernels at 15 DAP. The total of 12 RNA libraries yielded more than 0.25 billion reads after adaptor trimming, and ~89.70% of the clean reads could be mapped to the maize genome. We identified the genes directly affected by *ZmNAC78* on the basis of the following criteria: (i) fold-change > 1.5, (ii) P value < 0.05, and (iii) expression levels showing opposite trends between *ZmNAC78OE* maize and the *zmnac78* mutant. The expression levels of 99 genes were positively affected, and 1132 genes were negatively affected by *ZmNAC78* mRNA abundance (fig. S11 and table S4). Gene Ontology (GO) analysis showed that the 99 genes were related to metal ion binding (GO:0046872, P = 0.048), ion binding (GO:0043167, P = 0.044), and cation binding (GO:0043169, P = 0.049) (Fig. 5A).

We found that some genes or homologous genes have been previously reported to be essential for Fe distribution in maize kernels or the mobilization of vacuolar Fe stores in *Arabidopsis* seeds, such as genes that encode yellow stripe-like family (YSL) proteins (*28*) and natural resistance-associated macrophage protein (NRAMP) family proteins (*29*, *30*). In addition, proteins encoded by some of the genes have been reported to be involved in iron uptake, such as heavy-metal adenosine triphosphatases (HMAs) (*31*). We chose *ZmHMA8* (*Zm00001d027884*), *ZmYSL11* (*Zm00001d025888*), and *ZmNRAMP3* (*Zm00001d048129*) for further research. RT-qPCR data verified that these genes were up-regulated in *ZmNAC78OE* maize and down-regulated in the *zmnac78* mutant (fig. S12A). In agreement with the expression patterns of *ZmNAC78*, these three genes were preferentially expressed in the early stage of kernel development (fig. S12B). The promoter regions (2,000-bp region upstream of TSS) of *ZmHMA8*, *ZmYSL11*, and *ZmNRAMP3* contain one, one, and five NAC binding motifs, respectively (fig. S13). Electrophoretic mobility shift assay (EMSA) and chromatin immunoprecipitation (ChIP) analysis revealed that ZmNAC78 can directly bind to the promoters of *ZmHMA8*, *ZmYSL11*, and *ZmNRAMP3* (Fig. 5, B and C). Transient-expression assays in maize-leaf protoplasts further demonstrated that ZmNAC78 could activate the expression of the three genes (Fig. 5D).

We investigated the expression patterns of *ZmHMA8*, *ZmYSL11*, and *ZmNRAMP3* by performing mRNA in situ hybridization using 15-DAP B73 kernels. Although the expression patterns of *ZmHMA8*, *ZmYSL11*, and *ZmNRAMP3* varied in maize kernels, each of them could be detected in the BETL (Fig. 4C and fig. S10), which is at least partly consistent with the location of *ZmNAC78*. We then searched the EMS mutant collections and obtained two EMS mutants of *ZmNRAMP3* (mutant ID: EMS4-obfcc9 and EMS4-1cb309) and two EMS mutants of *ZmHMA8* (mutant ID: EMS4-1ce8be and EMS4-0c5a57). We could not obtain EMS mutants of *ZmYSL11*. The substitution in the exon of *ZmNRAMP3* and *ZmHMA8* leads to a premature stop codon in the two genes (Fig. 5E). Stop-gained *ZmNRAMP3* and *ZmHMA8* significantly reduced Fe concentrations in maize kernels (Fig. 5E). These results suggest that *ZmNRAMP3* and *ZmHMA8* are involved in loading of Fe into maize kernels.

Discussion

Micronutrient deficiency, also known as "hidden hunger," reduces nutritional security worldwide. The United Nations Sustainable Development Goal 2 is to end global hunger and reduce all kinds of malnutrition by 2030 (*4*). This goal could be partly achieved by the biofortification of staple food crops. Even though Fe-enriched rice, wheat, and cassava have been reported (*12*–*14*), Fe-enriched maize varieties have not been popular because of the negative correlation between Fe concentrations in kernels and grain yield (*6*, *15*). In this study, we eliminated the trade-off between kernel Fe concentration and grain yield by using molecular-assisted breeding to develop maize varieties with both high yield and high Fe concentrations in kernels.

There is some evidence that the NAC gene family may affect Fe homeostasis in plants. *OsNAP* is connected to Fe remobilization associated with senescence in rice (*32*). Additionally, Uauy *et al*. reported that *NAM-B1* accelerates senescence and increases Fe remobilization from leaves to developing grains in wheat (*33*). However, the adverse effects of senescence have limited the use of *NAM-B1* to increase Fe concentrations in grain. Our data suggest that the NAC family could directly regulate Fe uptake–related genes and enhance Fe concentrations in maize kernels. However, excessive Fe is toxic to plant cells, so it remains a possibility that higher *ZmNAC78* expression might suppress crop growth.

Transfer cells are located in the maize BETL, which is the only exchange surface between maternal and filial tissues in maize (*34*–*36*). By comparison, there is no morphologically distinct endosperm transfer region in rice, indicating that Fe loading may operate differently in rice as compared with maize (*37*, *38*). Although substantial progress has been made in elucidating the pathway of iron loading into rice grains (*39*, *40*), Fe biofortification in maize has not been well explored. Our results contribute to understanding the process of Fe loading into crop kernels.

REFERENCES AND NOTES

1. P. J. Aggett, in *Present Knowledge in Nutrition*, B. P. Marriott, D. F. Birt, V. A. Stallings, A. A. Yates, Eds. (Academic Press, ed. 11, 2020), pp. 375–392.
2. J. F. Briat, C. Dubos, F. Gaymard, *Trends Plant Sci.* **20**, 33–40 (2015).
3. D. Gashu *et al*., *Nature* **594**, 71–76 (2021).
4. T. Gödecke, A. J. Stein, M. Qaim, *Glob. Food Secur.* **17**, 21–29 (2018).
5. O. Ekpa, N. Palacios-Rojas, G. Kruseman, V. Fogliano, A. R. Linnemann, *Glob. Food Secur.* **17**, 48–56 (2018).
6. M. Bänziger, J. Long, *Food Nutr. Bull.* **21**, 397–400 (2000).
7. P. L. Sikosana, S. Bhebhe, S. Katuli, *Cent. Afr. J. Med.* **44**, 297–305 (1998).
8. R. E. Black *et al*., *Lancet* **371**, 243–260 (2008).
9. E. Pyo, B. L. Tsang, M. E. Parker, *Nutr. Rev.* **80**, 1062–1085 (2022).
10. R. D. Semba, S. Askari, S. Gibson, M. W. Bloem, K. Kraemer, *Adv. Nutr.* **13**, 80–100 (2022).
11. D. Kong, S. A. Khan, H. Wu, Y. Liu, H. Q. Ling, *J. Integr. Plant Biol.* **64**, 1157–1167 (2022).
12. J. Wirth *et al*., *Plant Biotechnol. J.* **7**, 631–644 (2009).
13. S. Borg *et al*., *J. Cereal Sci.* **56**, 204–213 (2012).
14. N. Narayanan *et al*., *Nat. Biotechnol.* **37**, 144–151 (2019).
15. J. K. Long, M. Bänziger, M. E. Smith, *Crop Sci.* **44**, 2019–2026 (2004).
16. S. Purcell *et al*., *Am. J. Hum. Genet.* **81**, 559–575 (2007).
17. Y. Jiao *et al*., *Nature* **546**, 524–527 (2017).
18. G. P. Wagner, K. Kin, V. J. Lynch, *Theory Biosci.* **131**, 281–285 (2012).
19. L. Wang, Z. Feng, X. Wang, X. Wang, X. Zhang, *Bioinformatics* **26**, 136–138 (2010).
20. F. Feng *et al*., *Plant Cell* **30**, 375–396 (2018).
21. G. M. Hoopes *et al*., *Plant J.* **97**, 1154–1167 (2019).
22. X. Lu *et al*., *Mol. Plant* **11**, 496–504 (2018).
23. C. Zou *et al*., *Proc. Natl. Acad. Sci. U.S.A.* **108**, 14992–14997 (2011).
24. B. Wang *et al*., *Nat. Genet.* **52**, 565–571 (2020).
25. Z. Chen *et al*., *Am. J. Plant Sci.* **10**, 298–308 (2019).
26. H. Liu *et al*., *Plant Biotechnol. J.* **18**, 185–194 (2020).
27. S. F. Zhou *et al*., *New Phytol.* **208**, 188–197 (2015).
28. J. Zang *et al*., *J. Exp. Bot.* **71**, 5896–5910 (2020).
29. E. L. Bastow *et al*., *Plant Physiol.* **177**, 1267–1276 (2018).
30. V. Lanquar *et al*., *EMBO J.* **24**, 4041–4051 (2005).
31. E. L. Zielazinski *et al*., *Metallomics* **5**, 1614–1623 (2013).
32. C. Liang *et al*., *Proc. Natl. Acad. Sci. U.S.A.* **111**, 10013–10018 (2014).
33. C. Uauy, A. Distelfeld, T. Fahima, A. Blechl, J. Dubcovsky, *Science* **314**, 1298–1301 (2006).
34. F. C. Felker, J. C. Shannon, *Plant Physiol.* **65**, 864–870 (1980).
35. R. D. Thompson, G. Hueros, H. Becker, M. Maitz, *Plant Sci.* **160**, 775–783 (2001).
36. R. W. Davis, J. D. Smith, B. G. Cobb, *Can. J. Bot.* **68**, 471–479 (1990).
37. K. J. Oparka, P. Gates, *Planta* **151**, 561–573 (1981).
38. S. Krishnan, P. Dayanandan, *J. Biosci.* **28**, 455–469 (2003).
39. J. Che, N. Yamaji, J. F. Ma, *New Phytol.* **230**, 1049–1062 (2021).
40. J. Che, K. Yokosho, N. Yamaji, J. F. Ma, *Plant Physiol.* **181**, 276–288 (2019).
41. J. L. Portwood 2nd *et al*., *Nucleic Acids Res.* **47**, D1146–D1154 (2019).
42. Y. Xue *et al*., *Nucleic Acids Res.* **51**, D18–D28 (2023).

ACKNOWLEDGMENTS

We thank Y. Li, B. Wang, C. Zhang, and C. Chu for their suggestions on the manuscript and H. Wang, L. Zhang, and X. Zhang for their technical assistance. **Funding:** This work was supported by the National Key Research and Development Program of China (2021YFF1000500), the Innovation Program of the Chinese Academy of Agricultural Sciences, the National Natural Science Foundation of China (grant 31861143004), and the Hainan Yazhou Bay Seed Lab (B23YQ1507). **Author contributions:** W.-X.L. and J.T. designed the research and supervised the project. P.Y. performed the experiments. Q.D. analyzed RNA-seq data. H.C., Z.G., and Z.W. performed the iron assay. W.-X.L. wrote the manuscript. **Competing interests:** The authors declare that they have no competing interests. **Data and materials availability:**

Raw sequence data generated during this study have been deposited in the BIG sub (*42*) with accession nos. CRA011946 and CRA011945 for RNA-seq. All other data needed to evaluate the conclusions in the paper are present in the paper or the supplementary materials. **License information:** Copyright © 2023 the authors, some rights reserved; exclusive licensee American Association for the Advancement of Science. No claim to original US government works. https://www.science.org/about/science-licenses-journal-article-reuse

SUPPLEMENTARY MATERIALS

science.org/doi/10.1126/science.adf3256
Materials and Methods
Figs. S1 to S13
Tables S1 to S7
References (*43*–*57*)
MDAR Reproducibility Checklist

Submitted 13 October 2022; resubmitted 23 August 2023
Accepted 6 November 2023
10.1126/science.adf3256

ORGANIC CHEMISTRY

Kinetic and thermodynamic control of C(sp^2)–H activation enables site-selective borylation

Jose B. Roque, Alex M. Shimozono, Tyler P. Pabst, Gabriele Hierlmeier, Paul O. Peterson, Paul J. Chirik*

Catalysts that distinguish between electronically distinct carbon-hydrogen (C–H) bonds without relying on steric effects or directing groups are challenging to design. In this work, cobalt precatalysts supported by *N*-alkyl-imidazole–substituted pyridine dicarbene (ACNC) pincer ligands are described that enable undirected, remote borylation of fluoroaromatics and expansion of scope to include electron-rich arenes, pyridines, and tri- and difluoromethoxylated arenes, thereby addressing one of the major limitations of first-row transition metal C–H functionalization catalysts. Mechanistic studies established a kinetic preference for C–H bond activation at the *meta*-position despite cobalt-aryl complexes resulting from *ortho* C–H activation being thermodynamically preferred. Switchable site selectivity in C–H borylation as a function of the boron reagent was thereby preliminarily demonstrated using a single precatalyst.

C–H functionalization has enhanced chemical synthesis by providing a direct method for the activation of otherwise inert bonds, providing a straightforward route to molecules with applications as pharmaceuticals, agrochemicals, and aromatics relevant to materials science. The development of site-selective reactions remains a grand challenge in metal-catalyzed C–H functionalization (*1*). A recent analysis of benzenoid-containing small-molecule active pharmaceutical ingredients (APIs) approved through 2019 revealed that the most common substitution patterns (1,2-; 1,4-; and 1,2,4-) are accessible by electrophilic aromatic substitution (S_EAr), whereas the least common (1,3-; 1,3,5-; and 1,2,3,5-) are absent because of the lack of methods for their synthesis (*2*). Thus, remote C–H functionalization methods for the selective formation of one constitutional isomer are transformative. Site-selective C(sp^2)–H borylation represents one of the most impactful C–H functionalization methods in organic synthesis because the C–B bond installed is readily and selectively transformed to a variety of other substituents using robust and well-established chemistry (*3*–*7*).

Progress in C(sp^2)–H borylation has centered on state-of-the-art iridium precatalysts, such as [Ir(COD)OMe]$_2$ (where COD is 1,5-cyclooctadiene), in combination with bipyridine ligands that operate principally with sterically driven site selectivity (*8*–*11*). To overcome the limitations of steric control, developments in regioselective iridium-catalyzed C–H borylation have relied on directing groups and intricate ligand engineering to exploit noncovalent interactions of specific functional groups with a recognition element on the ligand or an additive that orients the distal C–H bonds in proximity to the metal (*12*–*16*) (Fig. 1A). Although advances in ligand design have addressed the inherent sterically driven site selectivity, remote C(sp^2)–H borylation of medicinally relevant molecules, such as fluoroarenes, remains a substantial challenge owing to the weak coordinating ability of fluoro substituents and their similar size to hydrogen (*17*). As a result, a general method for remote C–H borylation of fluoroarenes has not been reported. Given the prevalence of fluorine in pharmaceuticals and the paucity of methods for nondirected, site-selective remote borylation, methods to synthesize or directly functionalize fluoroarenes are desirable (Fig. 1A). Inspired by accounts of cobalt catalysts supported by electron-rich pincer ligands offering complementary regioselectivity compared with iridium, the development of a cobalt-catalyzed remote C–H borylation was pursued (*18*–*21*).

The overall performance of first-row transition metal C–H borylation catalysts is limited by low activity, which in turn limits scope and overall synthetic utility (*20*, *21*). To overcome the limitations of previously reported cobalt catalysts, rigid but sterically accessible pincer ligands were targeted that are designed to limit destabilizing steric interactions during C–H activation and are supported by strong σ donors, resulting in a more electron-rich metal center (Fig. 1C). For example, computational studies on C–H activation with *ortho*-to-fluorine selective pyridine-bisphosphine-cobalt complex [4-Me-(^{iPr}PNP)Co(H)$_2$BPin] [**1-(H)$_2$BPin**] established a late transition state for C–H oxidative addition arising from distortion of the flexible pincer and steric interactions between the alkyl substituents on the phosphine (*22*, *23*). Although the rigid terpyridine-cobalt-alkyl complex 5,5″-Me$_2$-(^{Ar}TpyCo)(CH$_2$SiMe$_3$) (**2-CH$_2$SiMe$_3$**) enabled *meta*-to-fluorine selectivity by rate- and selectivity-determining C–H activation, the electron-deficient nature of the ligand inherently limits its performance because only a subset of electronic deficient fluorinated arenes provided modest yields, and catalyst deactivation was observed at elevated temperatures (*21*). As a result, *N*-alkyl-imidazole–substituted pyridine dicarbene (ACNC)–cobalt complexes were pursued because *N*-heterocyclic carbenes (NHCs) are strong electron donors, which offers the possibility of a sterically accessible catalyst that is also thermally robust (*24*). In this work, we describe the synthesis of sterically attenuated, NHC-based, and pincer-supported cobalt-alkyl and -aryl complexes and their activity for C(sp^2)–H activation resulting in the borylation of non-fluorinated arenes and heteroarenes and, ultimately, *meta*-selective C(sp^2)–H borylation of fluoroarenes and tri- and difluoromethoxylated arenes (Fig. 1B). The increased activity enabled switchable site selectivity in catalytic C–H functionalization because cobalt-aryl isomerization was competitive with C–B bond formation.

Synthesis of well-defined precatalyst

Our studies commenced with the synthesis of 3,5-Me$_2$-(^{iPr}ACNC)Co(Br)$_2$ (**3-Br$_2$**). Cobalt-alkyl complexes with this class of pincer bearing less sterically encumbering *N*-alkyl rather than sterically encumbering 2,6-diaryl substituents have been elusive owing to the propensity for competitive formation of bis(chelate) metal complexes (*25*, *26*). To circumvent this issue, an optimized procedure was developed whereby 3,5-Me$_2$-(^{iPr} ACNC)(HBr)$_2$ (**S1**) was added to a cold (−95°C) hexanes solution containing excess Co(HMDS)$_2$ (see supplementary materials for experimental details). This procedure, conducted on a gram scale, furnished a red solid in 93% yield identified as **3-Br$_2$** that was characterized by x-ray diffraction (Fig. 2A). Addition of 2.1 equivalents of MeLi to a suspension of **3-Br$_2$** in diethyl ether followed by filtration and subsequent analysis by proton nuclear magnetic resonance (^{1}H NMR) spectroscopy in benzene-d_6 established formation of a diamagnetic, C_{2v}-symmetric cobalt compound along with CH$_3$D formation. Single crystals obtained from this procedure established the identity of the product as the cobalt-aryl complex **3-C$_6$D$_5$** arising from C–D activation by a putative cobalt-methyl complex (Fig. 2A). Repeating this procedure in tetrahydrofuran (THF) enabled isolation of **3-Me**, and dissolution of the product in benzene-d_6 rapidly generated the cobalt-phenyl complex, establishing facile C–H activation reactivity. By contrast, the analogous cobalt-methyl complex bearing aryl substituents (**4-Me**) on the NHCs was unreactive toward activation of benzene-d_6 even upon heating to 80°C for 24 hours. To rationalize the differences in reactivity between **3-Me** and **4-Me**, the solid-state structures were analyzed and used to generate topographical steric maps using SambVca 2.1 (*27*)

Department of Chemistry, Princeton University, Princeton, NJ 08544, USA.
*Corresponding author. Email: pchirik@princeton.edu

(Fig. 2B). Comparison of the two plots shows significant shielding above and below the XZ plane defined by the CNC pincer plane by the wingtips of **4-Me**. Notably, **4-Me** has a significantly higher buried volume compared with **3-Me**. These results illustrate that multiple catalyst design principles must be satisfied. For example, despite being supported by strong donors, the steric disposition of the wingtip substituents on **4-Me** diminishes reactivity toward C–H activation.

Reaction development

Given the rapid activation of benzene, the C(sp^2)–H borylation activity of **3-Me** was evaluated (Fig. 3). Standard conditions for catalytic experiments used 1 equivalent of arene and 1 equivalent of B_2Pin_2 with 5 mol % of **3-Me** at room temperature in THF for 24 hours. A series of 3-substituted (**6a** to **6e**) fluoroarenes was evaluated, and the desired *meta*-fluoroarylboronates were obtained in high yield (>75%) and regioselectivity [>85:15 *meta*-to-*ortho* (m:o)]. The substrates evaluated contain directing groups commonly used in metal-catalyzed directed functionalization and led to lower yields when previously reported **2-CH_2SiMe_3** was used (e.g., **6b** to **6d**) (*28*). In previous studies, a substrate-controlled selectivity has been observed with fluorinated-aryl boronate esters (*29*). For example, when **6f** and **6g** were functionalized with precatalyst **1-$(H)_2$BPin**, the selectivity was inverted from 94:4 m:o to 20:80, respectively. Although mechanistically informative, changes in selectivity with minor modifications to the substrate limit predictability and ultimately hamper synthetic utility. Improved yields and catalyst-controlled high *meta*-selectivity were observed with **3-Me**, which highlights the superior performance of the NHC-based pincer cobalt precatalyst. A series of 2,6-difluoroaryls containing functional groups—including boronates, ethers, and esters (**6h** to **6m**)—was examined, and in all cases, high yields (>80%) and selectivities (>87:13 m:o) were obtained. The *para*-to-boron and *meta*-to-fluorine selectivity was observed independent of the substrate, which highlights the insensitivity of **3-Me** to substrate modifications and provides a more general and synthetically useful C–H borylation route to mixed diborylarenes. To probe the borylation selectivity of arenes with sterically accessible *ortho*- (to fluorine), *meta*-, and *para*-C–H bonds, a series of 2-substituted fluoroarenes was examined. The *meta*-arylboronate esters were the major products for all substrates studied (**6o** to **6s**).

Pyridines are an important class of substrate as the second most encountered heterocycle in US Food and Drug Administration (FDA)–approved pharmaceuticals, and they present electronically distinct C–H bonds [e.g., based on bond dissociation free energies (BDFEs) and pK_a values (where K_a is the acid dissociation constant)] (*30*). Borylation of 6-fluoro-2-picoline (**6t**) with **3-Me** furnished the (hetero)arylboronate product in 91% yield with 99:1 regioselectivity favoring the 4-position. The previously reported cobalt precatalyst **2-CH_2SiMe_3** suffered from low yields, whereas iridium/bipyridine catalysts provided poor selectivity (*31*–*33*). Borylation of a series of substituted pyridines (**6u** to **6aa**) with **3-Me** furnished the desired 4-functionalized products in good yields and selectivities greater than 87:13. The borylation of pyridines typically requires a directing group or the inclusion of sterically demanding aluminum-based Lewis acids to achieve synthetically useful selectivities (*34*).

Next, the overall performance of the designed pyridine dicarbene cobalt precatalyst was evaluated and compared with previously reported precatalysts. Standard conditions for catalytic experiments used 1 equivalent of both arene and B_2Pin_2 in the presence of 5 mol % of cobalt precatalyst in THF at ambient or elevated temperatures. Among the precatalysts evaluated, **3-Me** was the only one effective for the catalytic borylation of 1,3-dimethoxybenzene (**6ab**), reaching 50% conversion at 80°C. With relatively electron-rich substrates (**6ab** to **6ae**), solvent or excess quantities are often required for borylation activity with prior cobalt catalysts. Trifluoromethoxybenzene (**6af**) and a related derivative (**6ag**) were borylated at 23°C

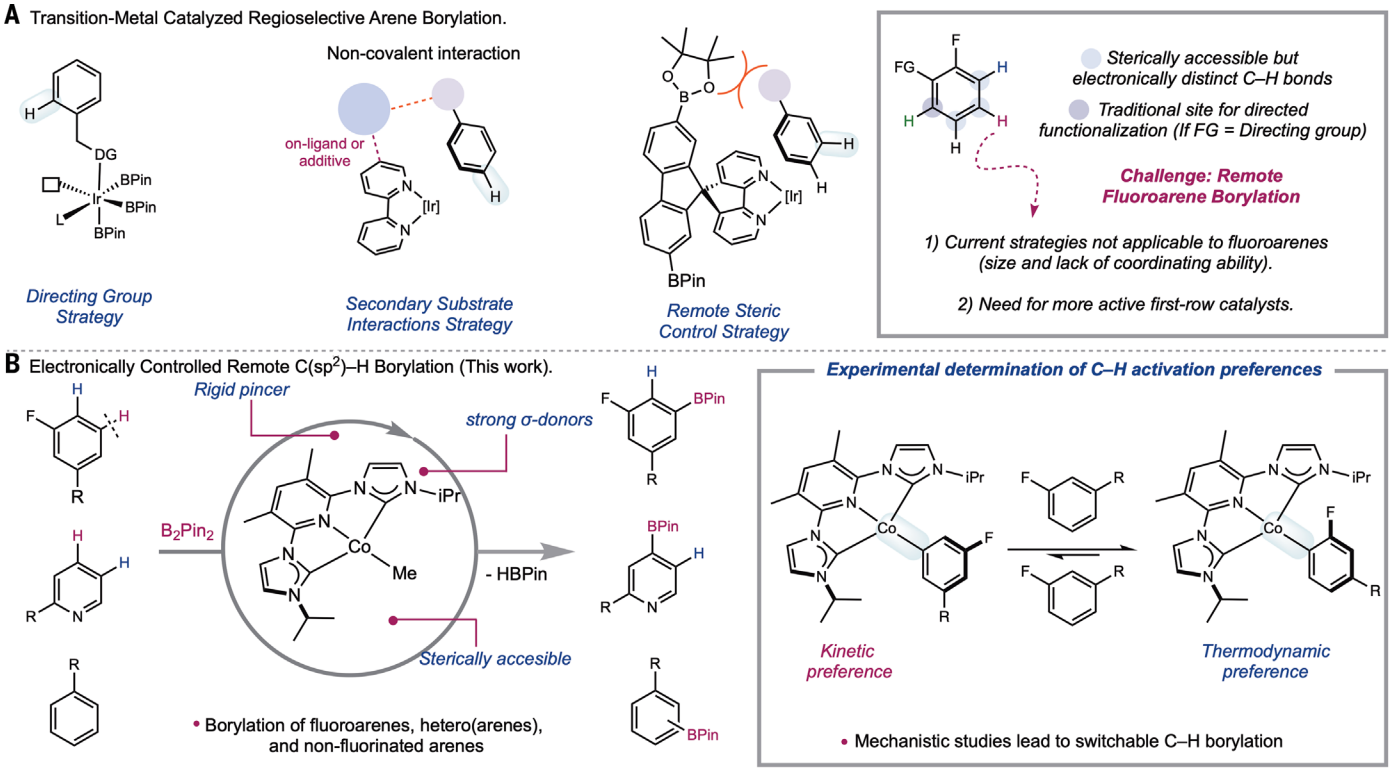
A Transition-Metal Catalyzed Regioselective Arene Borylation.
Non-covalent interaction
on-ligand or additive
Directing Group Strategy
Secondary Substrate Interactions Strategy
Remote Steric Control Strategy
Sterically accessible but electronically distinct C–H bonds
Traditional site for directed functionalization (If FG = Directing group)
Challenge: Remote Fluoroarene Borylation
1) Current strategies not applicable to fluoroarenes (size and lack of coordinating ability).
2) Need for more active first-row catalysts.
B Electronically Controlled Remote C(sp2)–H Borylation (This work).
Rigid pincer
strong σ-donors
B2Pin2
- HBPin
Sterically accesible
• Borylation of fluoroarenes, hetero(arenes), and non-fluorinated arenes
Experimental determination of C–H activation preferences
Kinetic preference
Thermodynamic preference
• Mechanistic studies lead to switchable C–H borylation

Fig. 1. Background and catalyst development. (**A**) Transition metal–catalyzed regioselective arene borylation. FG, functional group. (**B**) Electronically controlled remote C(sp^2)–H borylation (this work).

using **3-Me** to afford the *meta*-functionalized product with regioselectivity ratios of 91:9 and >99:1 m:o, respectively. Both **1-(H)$_2$Bpin** and **2-CH$_2$SiMe$_3$** failed to catalyze any detectable formation of the desired products even upon extended heating at 80°C. High *meta*-selectivity (84:16) was also observed with difluoromethoxy groups (**6ah**). Trifluoromethoxy (OCF_3) and difluoromethoxy (OCF_2H), typically introduced by radical addition, are highly desirable structural motifs in drug development processes because of their ability to fine-tune the physicochemical properties of drug candidates (*35*). These results highlight the importance of developing more active first-row metal catalysts because electronically controlled selectivity can be compatible with functional groups not amenable to directing group strategies.

The cobalt precatalyst with a phosphine-based pincer, **1-(H)$_2$Bpin**, promotes *para*-to-boronate ester selectivity; however, the scope is limited to electron-deficient fluorinated arylboronate esters (*29*). To generalize the electronically controlled selectivity, phenylboronic acid pinacol ester (**6ai**) and phenylboronic acid neopentylglycol ester (**6aj**) were examined and failed to give any of the desired product with any previously reported catalyst. Borylation with **3-Me** provided the desired products in 58% and 56% yields with 77:23 and 82:18 respective regioselectivity favoring functionalization at the *para*-to-boronate site. Among the precatalysts evaluated, **3-Me** was the only one effective for the catalytic borylation of methyl benzoate (**6ak**), providing the desired product in 64% yield with a regioselectivity of 77:23 favoring functionalization at the *para*-to-ester site. To evaluate the electronic influence of multiple substituents on an arene, substrates **6al**, **6am**, and **6an** were evaluated. One regioisomer was obtained when **6al** was evaluated, which highlights the reinforced *para*-to-ester and *meta*-to-fluorine selectivity. Borylation of **6am** led to one regioisomer, whereas **6an** led to preferential functionalization at the *para*-to-boronate site, overriding the *meta*-to-fluorine selectivity. 1,4 disubstituted fluoroarenes were also viable substrates. For example, borylation of 4-fluorotoluene and 4-fluorobenzotrifluoride led to preferential functionalization *ortho*-to-fluorine over sterically inaccessible C2 functionalization (figs. S133 and S134). The presence of Csp^2–X bonds in aromatics presents a chemoselectivity challenge because previously reported cobalt-catalyzed Csp^2–H borylation methods are incompatible with aryl halide substituents. For example, chlorobenzene (**6ao**) was an incompatible substrate with previously reported cobalt catalyst **1-(H)$_2$Bpin** and **2-CH$_2$SiMe** but was borylated in 61% yield and 86:14 regioselectivity favoring *meta*-to-chlorine product with **3-Me**, which highlights the specific kinetic preference for C–H over C–Cl borylation. To demonstrate the utility of the cobalt-catalyzed method for gram-scale synthesis, etoxazole (**5ap**), a chitin synthesis inhibitor, underwent borylation in 97% yield to afford **6ap**. In situ activation of **3-Br$_2$** with $KBHEt_3$ using standard Schleck technique could also be applied, resulting in the borylation of etoxazole (**5ap**) in 52% yield (fig. S9). Recent advancements in cross-coupling with Earth-abundant metals have been developed between alkyl and aryl halides with neopentylglycol(hetero)aryl boronic esters (*36*). To benefit from the distinctive site selectivity, a method was developed to synthesize neopentylglycolaryl boronic esters with **3-Me** and applied to the derivatization of etoxazole. Under the optimized conditions using bis(neopentyl glycolato)diboron, the desired product **7** was obtained in 91% isolated yield and characterized by x-ray diffraction. Performing the reaction with **2-CH$_2$SiMe** did not lead to the desired product, which highlights the limitations of previously reported cobalt catalysts for remote C–H borylation.

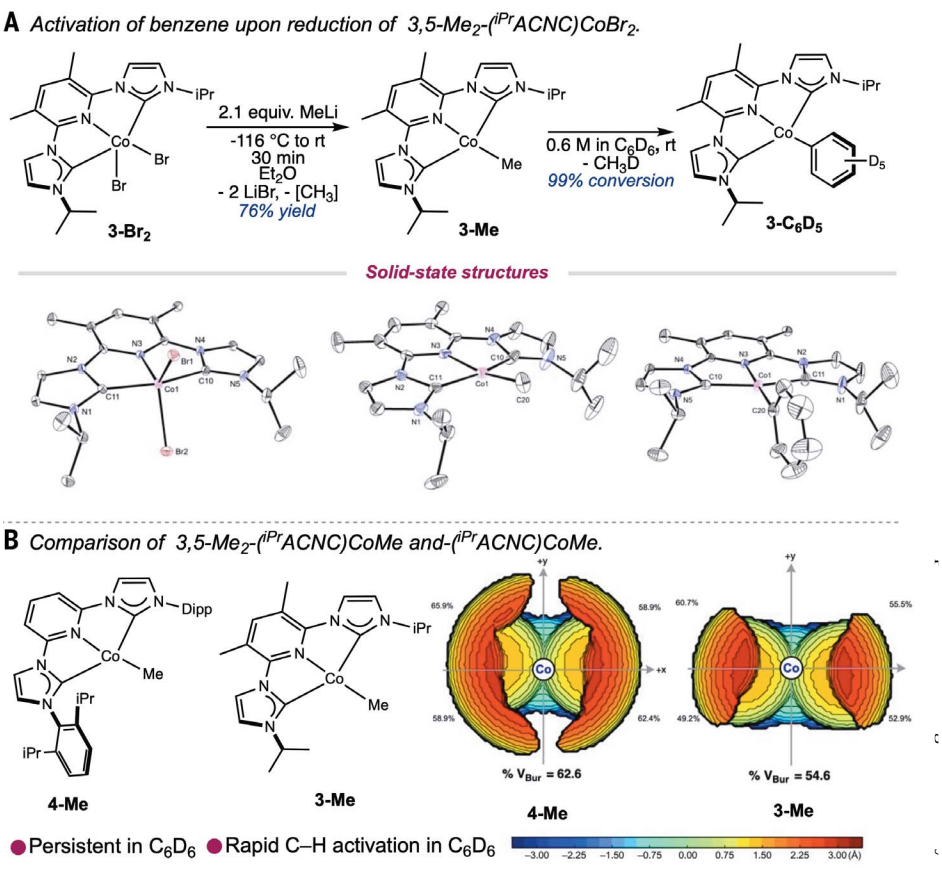

Fig. 2. Precatalyst synthesis and characterization. (**A**) Activation of benzene by **3-Me**. rt, room temperature. (**B**) Steric maps of [(^{iPr}CNC)Co] and [3,5-Me$_2$-(^{iPr}ACNC)Co] from the solid-state structures of the corresponding cobalt-methyl complexes generated in SambVca2.1. See supplementary materials for experimental details. %V_{Bur}, buried volume.

Mechanistic studies

To gain insight into the origin of selectivity for C–H borylation, the synthesis of cobalt(I)-fluoroaryl complexes relevant to catalysis were pursued. Treatment of a benzene-d_6 solution of **3-Me** with excess fluoroarene (**8**) at room temperature resulted in the formation of the corresponding cobalt(I)-aryl complex **3-Ar^F** arising from C–H activation at the *ortho*-to-fluorine site (Fig. 4A). No other signals corresponding to isomers of **3-Ar^F** were detected by ^{19}F NMR spectroscopy. Notably, the preferred C–H bond activated during catalysis is the *meta*-to-fluorine site leading to the *meta*-to-fluoroarylboronate product. To probe for intramolecular or pinacolborane (HBPin)–induced isomerization after the generation of the cobalt-aryl complex, the reaction of **3-Ar^F** with HBPin was examined. Treatment of **3-Ar^F** with excess HBPin resulted in the exclusive formation of the *ortho*-to-fluorine borylated product (Fig. 4A): No other isomers of the arylboronate were detected by ^{19}F NMR spectroscopy, which rules out isomerization before C–B bond formation. To rationalize the discrepancy between the stoichiometric experiments leading to the *ortho*-Co(I)–aryl complex and the major product observed in catalysis arising from C–B bond formation at the *meta*-site, the stoichiometric reaction of **3-Me** with a series of fluoroarenes was monitored by NMR spectroscopy. Treatment of

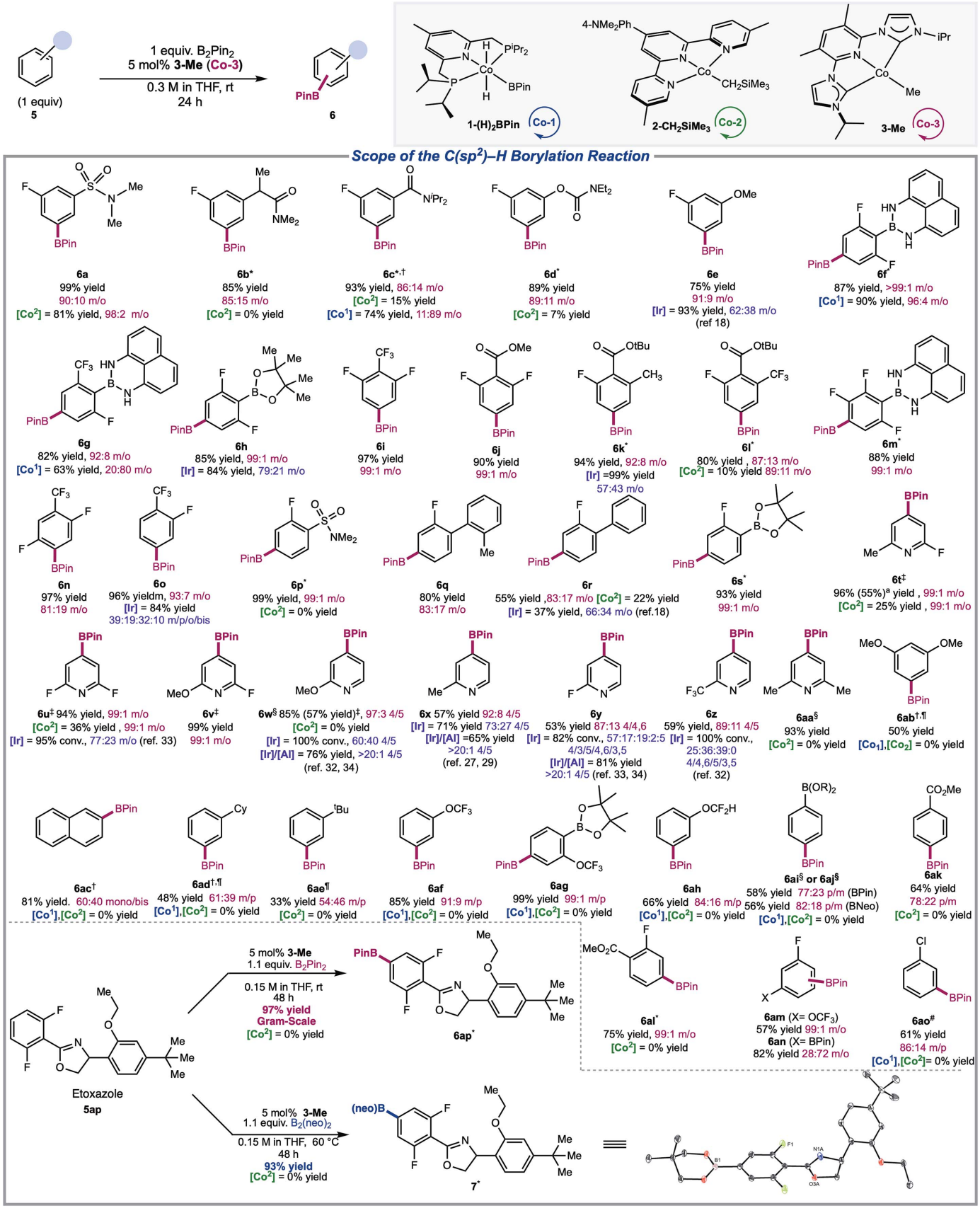

Fig. 3. C(sp^2)–H borylation of (hetero)arenes. Yields and selectivities were determined by ^{19}F NMR spectroscopy using a 4-fluorotoluene internal standard. *Isolated yield. †3 equivalents of B_2Pin_2. ‡0.3 mol % of **3-Me**. §50°C. ¶80°C. #3 equivalents of arene.

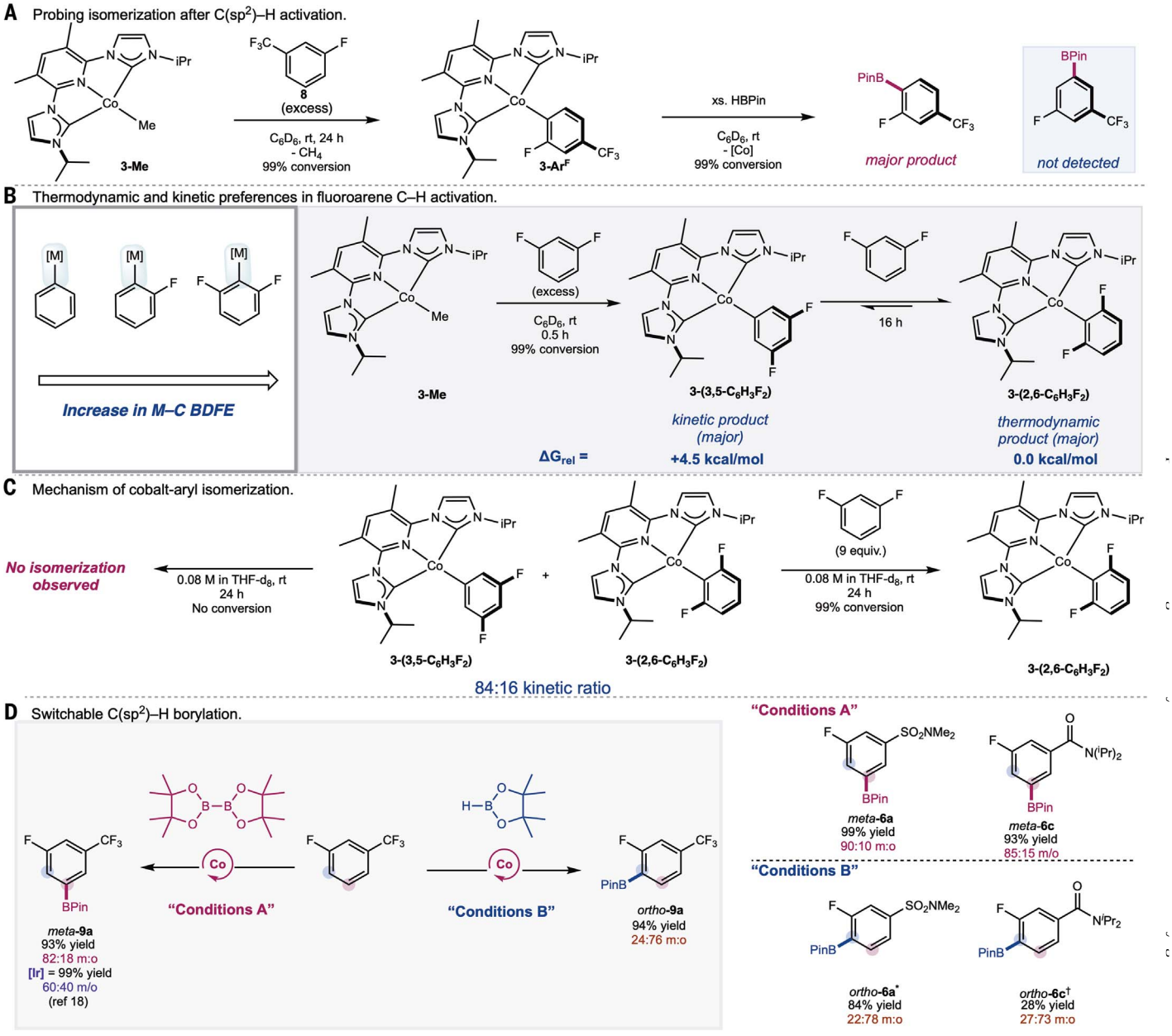

Fig. 4. Mechanistic considerations and kinetic versus thermodynamic selectivity. (**A**) Reaction of **3-Me** with **8** and probing isomerization of **3-Ar^F** upon treatment with HBPin. (**B**) Thermodynamic and kinetic preferences of C–H activation. (**C**) Switchable C–H borylation. See supplementary materials for experimental details. *4 equivalents of **5a**. †3 equivalents of **5c**.

3-Me with excess 1,3-difluorobenzene at room temperature furnished **3-(3,5-$C_6H_3F_2$)** (wherein the fluorine substituents are both *meta* to the cobalt-aryl bond) as the major product after 30 min. After 24 hours, **3-(3,5-$C_6H_3F_2$)** was converted to **3-(2,6-$C_6H_3F_2$)**, wherein both fluorine substituents occupy *ortho*-positions. With fluorobenzene, similarly distinct kinetic and thermodynamic preferences were observed as the *meta*-aryl isomer formed at early reaction times, then underwent isomerization to the *ortho*-variant as the reaction progressed (fig. S6). No detectable quantities of the *para*-isomer were observed by ^{19}F NMR spectroscopy throughout the course of the experiment (Fig. 4B). To probe the mechanism of cobalt-aryl isomerization, a kinetic ratio of **3-(3,5-$C_6H_3F_2$)** and **3-(2,6-$C_6H_3F_2$)** in 0.4 ml of THF-d_8 was transferred to a J-Young NMR tube, and the mixture was directly analyzed by ^{19}F NMR spectroscopy (Fig. 4C). After 24 hours, the ratio of **3-(3,5-$C_6H_3F_2$)** to **3-(2,6-$C_6H_3F_2$)** did not change. However, upon addition of excess 1,3 difluorobenzene, complete conversion to **3-(2,6-$C_6H_3F_2$)** was observed. These results demonstrate that excess fluoroarene is required for cobalt-aryl isomerization to occur. These observations support kinetically preferred C–H activation at the position *meta*-to-fluorine and thermodynamically favored formation of the *ortho*-isomer (*37*, *38*). The free energies of the fluoroaryl isomers were calculated with density functional theory (DFT) using the ωB97XD functional and the def2-TZVP basis set and corroborate the experimental observations that **3-(2,6-$C_6H_3F_2$)** is lowest in energy as a result of a thermodynamic *ortho*-to-fluorine effect (Fig. 4B). Experimental support for these trends with first-row metals has not previously been reported owing to the lack of reactivity of the metal-aryl complexes, which are typically synthesized by the addition

of an organometallic reagent to the metal halide precursors.

The observed aryl isomerization suggested that switchable site selectivity in catalytic C–H borylation should be possible. We postulated that if cobalt-aryl isomerization were faster than C–B bond formation, the selectivity would be inverted to favor the *ortho*-fluoroarylboronate product (Fig. 4C). Stirring a THF solution of **8** with HBPin with 5 mol % of **3-Me** at 50°C produced boronate ester **9a** in 94% yield and a 24:76 ratio favoring the *ortho*-isomer (*ortho*-**8a**). The switch in selectivity is attributed to a slower rate of C–B bond formation when using HBPin.

To assess the rate of C–B bond formation as a function of boron reagent, the catalytic borylation of **5a** with B_2Pin_2 and HBPin was monitored by ^{19}F NMR spectroscopy as a function of time (figs. S24 and S25). With HBPin, 19% conversion was observed after 19 hours. By contrast, with B_2Pin_2, 80% conversion was observed in 10 min. These results support a faster rate of C–B bond formation with B_2Pin_2. Repeating the experiment with DBPin resulted in no significant deuterium incorporation in **9a** (fig. S27). If DBPin were responsible for cobalt-aryl isomerization, hydrogen isotope exchange of the free arene should be observed, and the *ortho*-functionalized aryl boronate would contain significant deuterium incorporation at the *meta*-to-fluorine site. An inverse relationship was also observed between the selectivity for the *ortho*-fluoroaryl boronate ester and the equivalents of HBPin, which does not support an HBPin-induced cobalt-aryl isomerization mechanism (table S3). A series of additional mechanistic experiments (fig. S26) suggest that the isomerization to thermodynamically preferred cobalt-aryl takes place by intermolecular C–H activation of a second arene by *meta*-to-fluoroaryl cobalt intermediate. The preferred site of borylation was also switched when **5a** and **5c** were used as substrate (Fig. 4D). The different selectivities were obtained from a single catalyst by simply changing between two commercially available boron reagents. These observations contrast traditional approaches to switchable selectivity, where different ligands or transition metal complexes are required (*39*). Switchable C–H borylation was specific to **3-Me** because the selectivity did not alter significantly when **1-$(H)_2$Bpin** and **2-CH_2SiMe_3** were used as precatalyst (fig. S23). On the basis of insights from the stoichiometric experiments, the selectivity to favor formation of the *meta*-fluoroarylboronate was improved by increasing the equivalents of B_2Pin_2. For example, stirring a THF solution of **8** and **5c** with 2 equivalents of B_2Pin_2 with 5 mol % of **3-Me** for 24 hours improved the regioselectivity from 3:1 to 4.5:1 and from 3:1 to 5.6:1 in favor of *meta*-**9a** and *meta*-**6c**, respectively. Further studies are ongoing to expand the switchable C–H borylation scope and lower the equivalents of arene when using HBPin as the boron reagent (fig. S22).

Introduction of a sterically attenuated, electron-donating pincer has enabled the development of a cobalt precatalyst that exhibits high activity for C–H activation and C(sp^2)–H borylation. A combination of stoichiometric experiments and site selectivity from catalytic examples demonstrates a kinetic preference for functionalization of sites *meta* to fluorine that, in the presence of arene substrate, isomerize over time through C–H activation to *ortho*-aryl complexes. This feature enables switchable selectivity in catalytic C(sp^2)–H borylation, where tuning the relative rates of C–H activation and C–B bond formation modulates the preference for *ortho*- versus *meta*-functionalized products. These findings provide key catalyst design principles for site-selective C–H functionalization, exploiting kinetic and thermodynamic preferences of M–C versus C–H bond formation.

REFERENCES AND NOTES

1. L. Zhang, T. Ritter, *J. Am. Chem. Soc.* **144**, 2399–2414 (2022).
2. A. Nilova, L.-C. Campeau, E. C. Sherer, D. R. Stuart, *J. Med. Chem.* **63**, 13389–13396 (2020).
3. I. A. I. Mkhalid, J. H. Barnard, T. B. Marder, J. M. Murphy, J. F. Hartwig, *Chem. Rev.* **110**, 890–931 (2010).
4. M. M. M. Hassan, S. Guria, S. Dey, J. Das, B. Chattopadhyay, *Sci. Adv.* **9**, eadg3311 (2023).
5. Y. Kuroda, Y. Nakao, *Chem. Lett.* **48**, 1092–1100 (2019).
6. S. Rej, N. Chatani, *Angew. Chem. Int. Ed.* **61**, e202209539 (2022).
7. M. J. Ingleson, *ACS Catal.* **13**, 7691–7697 (2023).
8. J.-Y. Cho, M. K. Tse, D. Holmes, R. E. Maleczka Jr., M. R. Smith 3rd, *Science* **295**, 305–308 (2002).
9. T. Ishiyama *et al*., *J. Am. Chem. Soc.* **124**, 390–391 (2002).
10. G. A. Chotana, M. A. Rak, M. R. Smith3rd, *J. Am. Chem. Soc.* **127**, 10539–10544 (2005).
11. E. Caldeweyher *et al*., *J. Am. Chem. Soc.* **145**, 17367–17376 (2023).
12. U. Dutta, S. Maiti, T. Bhattacharya, D. Maiti, *Science* **372**, eabd5992 (2021).
13. L. Veth, H. A. Grab, P. Dydio, *Synthesis* **54**, 3482–3498 (2022).
14. B. Ramadoss, Y. Jin, S. Asako, L. Ilies, *Science* **375**, 658–663 (2022).
15. G. R. Genov, J. L. Douthwaite, A. S. K. Lahdenperä, D. C. Gibson, R. J. Phipps, *Science* **367**, 1246–1251 (2020).
16. M. T. Mihai, G. R. Genov, R. J. Phipps, *Chem. Soc. Rev.* **47**, 149–171 (2018).
17. N. A. Meanwell, *J. Med. Chem.* **61**, 5822–5880 (2018).
18. J. V. Obligacion, M. J. Bezdek, P. J. Chirik, *J. Am. Chem. Soc.* **139**, 2825–2832 (2017).
19. T. P. Pabst, J. V. Obligacion, É. Rochette, I. Pappas, P. J. Chirik, *J. Am. Chem. Soc.* **141**, 15378–15389 (2019).
20. H. Ren, Y.-P. Zhou, Y. Bai, C. Cui, M. Driess, *Chemistry* **23**, 5663–5667 (2017).
21. T. P. Pabst, P. J. Chirik, *J. Am. Chem. Soc.* **144**, 6465–6474 (2022).
22. H. Li, J. V. Obligacion, P. J. Chirik, M. B. Hall, *ACS Catal.* **8**, 10606–10618 (2018).
23. J. V. Obligacion, P. J. Chirik, *ACS Catal.* **7**, 4366–4371 (2017).
24. H. V. Huynh, *Chem. Rev.* **118**, 9457–9492 (2018).
25. A. A. Danopoulos, T. Simler, P. Braunstein, *Chem. Rev.* **119**, 3730–3961 (2019).
26. A. A. Danopoulos, J. A. Wright, W. B. Motherwell, S. Ellwood, *Organometallics* **23**, 4807–4810 (2004).
27. L. Falivene *et al*., *Nat. Chem.* **11**, 872–879 (2019).
28. M. E. Hoque, M. M. M. Hassan, B. Chattopadhyay, *J. Am. Chem. Soc.* **143**, 5022–5037 (2021).
29. T. P. Pabst, L. Quach, K. T. MacMillan, P. J. Chirik, *Chem* **7**, 237–254 (2021).
30. E. Vitaku, D. T. Smith, J. T. Njardarson, *J. Med. Chem.* **57**, 10257–10274 (2014).
31. J. S. Wright, P. J. H. Scott, P. G. Steel, *Angew. Chem. Int. Ed.* **60**, 2796–2821 (2021).
32. S. A. Sadler *et al*., *Org. Biomol. Chem.* **12**, 7318–7327 (2014).
33. M. Ding, J. A. Reuven, A. C. Hones, M. A. Fox, P. G. Steel, *Eur. J. Org. Chem.* **2022**, e202201005 (2022).
34. L. Yang, K. Semba, Y. Nakao, *Angew. Chem. Int. Ed.* **56**, 4853–4857 (2017).
35. J. W. Lee, K. N. Lee, M.-Y. Ngai, *Angew. Chem. Int. Ed.* **58**, 11171–11181 (2019).
36. L. R. Mills *et al*., *ACS Catal.* **12**, 1905–1918 (2022).
37. A. D. Selmeczy, W. D. Jones, M. G. Partridge, R. N. Perutz, *Organometallics* **13**, 522–532 (1994).
38. E. Clot, C. Mégret, O. Eisenstein, R. N. Perutz, *J. Am. Chem. Soc.* **131**, 7817–7827 (2009).
39. W. Liu *et al*., *J. Am. Chem. Soc.* **140**, 12247–12255 (2018).

ACKNOWLEDGMENTS

J.B.R. thanks Princeton University for a Presidential Postdoctoral Research Fellowship and J. Darmon (Princeton University) for insightful discussions. **Funding:** This study received support from National Institutes of Health grant 2R01GM121441. **Author contributions:** J.B.R. and P.J.C. conceived of the concept and designed experiments. J.B.R. conducted experiments and computational studies. A.M.S. conducted experiments during the revision of the manuscript. T.P.P. and G.H. performed x-ray crystallography. P.O.P. synthesized 3,5-Me_2-(^{iPr}ACNC) $(HBr)_2$. J.B.R. and P.J.C. wrote the manuscript with feedback from all authors. **Competing interests:** The authors declare that they have no competing interests. **Data and materials availability:** X-ray data are available in the Cambridge Crystallographic Data Center under CCDC numbers 2246986, 2246987, 2246988, and 2246989. All other data are available in the main text or the supplementary materials. **License information:** Copyright © 2023 the authors, some rights reserved; exclusive licensee American Association for the Advancement of Science. No claim to original US government works. https://www.science.org/about/science-licenses-journal-article-reuse

SUPPLEMENTARY MATERIALS

science.org/doi/10.1126/science.adj6527
Supplementary Text
Figs. S1 to S133
Tables S1 to S7
NMR Spectra
References (*40*–*66*)

Submitted 8 July 2023; accepted 10 October 2023
10.1126/science.adj6527

FOREST ECOLOGY

Drought sensitivity in mesic forests heightens their vulnerability to climate change

Robert Heilmayr[1,2]*, Joan Dudney[1,2], Frances C. Moore[3]

Climate change is shifting the structure and function of global forests, underscoring the critical need to predict which forests are most vulnerable to a hotter and drier future. We analyzed 6.6 million tree rings from 122 species to assess trees' sensitivity to water and energy availability. We found that trees growing in wetter portions of their range exhibit the greatest drought sensitivity. To test how these patterns of drought sensitivity influence vulnerability to climate change, we predicted tree growth through 2100. Our results suggest that drought adaptations in arid regions will partially buffer trees against climate change. By contrast, trees growing in the wetter, hotter portions of their climatic range may experience unexpectedly large adverse impacts under climate change.

Forests cover approximately 30% of Earth's land surface (*1*), absorb more carbon than all other terrestrial ecosystems (*2*, *3*), and provide trillions of dollars' worth of ecosystem services (*4*, *5*). Climate change, however, is causing pronounced changes in forests, including drought-induced diebacks and declines in productivity. Scientists warn that forests will continue to shift from carbon sinks to sources as climate change–related disturbances increase (*6*–*8*). To effectively manage and respond to these changes, there is a critical need for accurate predictions that detail which forests will be most vulnerable to drier and hotter conditions (*9*, *10*).

Precise estimates of forest vulnerability to drought depend on an understanding of how spatial variation in drought sensitivity interacts with anticipated changes in drought exposure (Fig. 1) (*11*–*13*). Will forests located near their dry-range edge be pushed beyond their physiological limits or can drought adaptation in drier regions insulate forests against hotter droughts? Answering this question rests on a clear understanding of trees' relative sensitivity to dry conditions across their range. However, past research exploring variation in drought sensitivity has yielded contradictory results, supporting either a "dry-range–sensitive" or a "drought-naïve" hypothesis.

The dry-range–sensitive hypothesis predicts that trees growing in drier portions of their range are the most drought sensitive. Trees growing in resource-poor conditions—for example, shallow soils, steep slopes, and aspects exposed to greater solar radiation—are often more climate and drought sensitive (*14*–*16*). Similarly, many studies have observed greater reductions in radial growth during drought at drier sites than at more-mesic sites (*15*, *17*–*22*). One explanation for these patterns is that increasing aridity in drier regions could exceed species' physiological limits, leading to marked declines in growth in response to drought (*10*, *23*).

By contrast, the drought-naïve hypothesis predicts that trees growing in wetter portions of their range are the most drought sensitive (*10*). Drought-naïve effects have been found in forests in the Pacific Northwest (*24*), pine forests in the Eastern Mediterranean (*25*), European beech trees (*Fagus sylvatica*) (*26*), and ponderosa pine (*Pinus ponderosa*) populations in North America (*27*). Higher drought sensitivity in wetter regions may reflect fewer drought adaptations as a result of lower drought exposure. Long-term drought exposure, which is often higher in arid regions, can shift phenotypic plasticity (*26*, *28*), tree density (*29*, *30*), and heritable traits that together confer greater drought resilience (*31*). Reconciling whether dry-range–sensitive or drought-naïve dynamics are more prevalent at a global scale can advance our ability to predict forest vulnerability to climate, which is fundamental to

[1]Environmental Studies Program, University of California, Santa Barbara, Santa Barbara, CA, USA. [2]Bren School of Environmental Science and Management, University of California, Santa Barbara, Santa Barbara, CA, USA. [3]Department of Environmental Science and Policy, University of California, Davis, Davis, CA, USA.
*Corresponding author. Email: rheilmayr@ucsb.edu

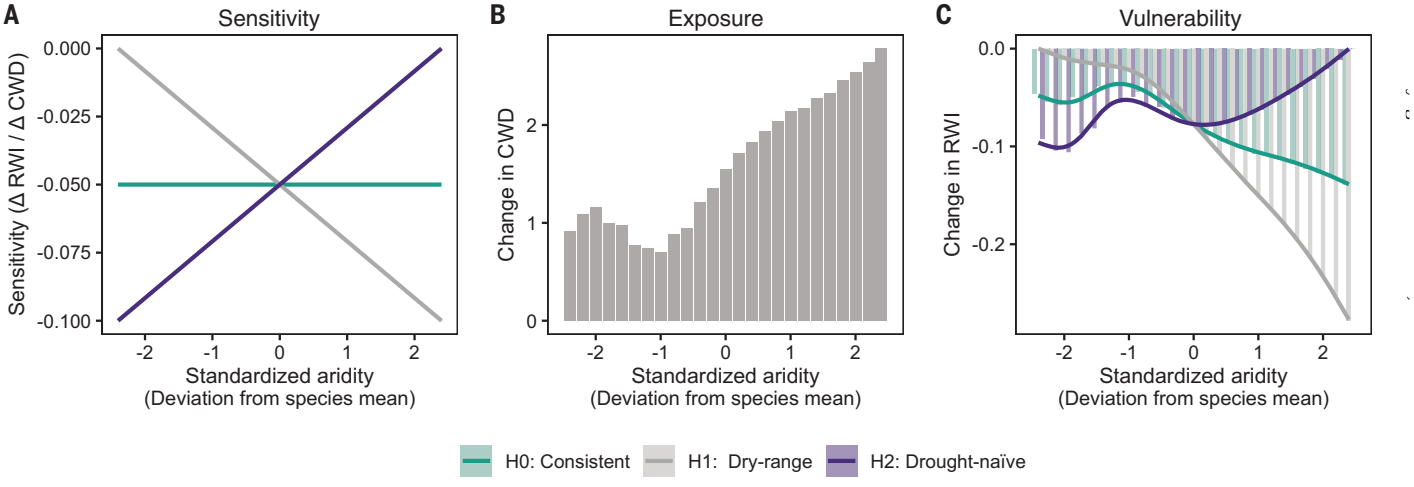

Fig. 1. Hypothesized vulnerability to climate change. (**A**) Three hypothesized patterns of heterogeneity in drought sensitivity across an aridity gradient: (H0) Trees show a consistent drought response across their species' climatic range (consistent sensitivity; green line); (H1) trees growing in more-arid portions of their range are more drought sensitive (dry-range sensitive; gray line); and (H2) trees growing in more-mesic portions of their range are more drought sensitive (drought-naïve; purple line). Sensitivity (*y* axis) is defined as a change in annual growth (measured using RWI) in response to interannual fluctuations in water availability (measured using CWD). Standardized aridity (*x* axis) is defined as the historic average CWD at a given location relative to the mean CWD experienced across a species' range. (**B**) Increases in CWD are widespread but anticipated to be highest in more-arid regions. Bar heights illustrate average increases in CWD CMIP5 models by 2100. (**C**) The interaction between sensitivity (A) and exposure (B) drives predicted changes in RWI, which we used as a measure of vulnerability. Colored lines and corresponding bars represent hypothesized patterns of vulnerability (change in RWI) when different patterns of sensitivity (A) interact with anticipated increases in drought exposure (B).

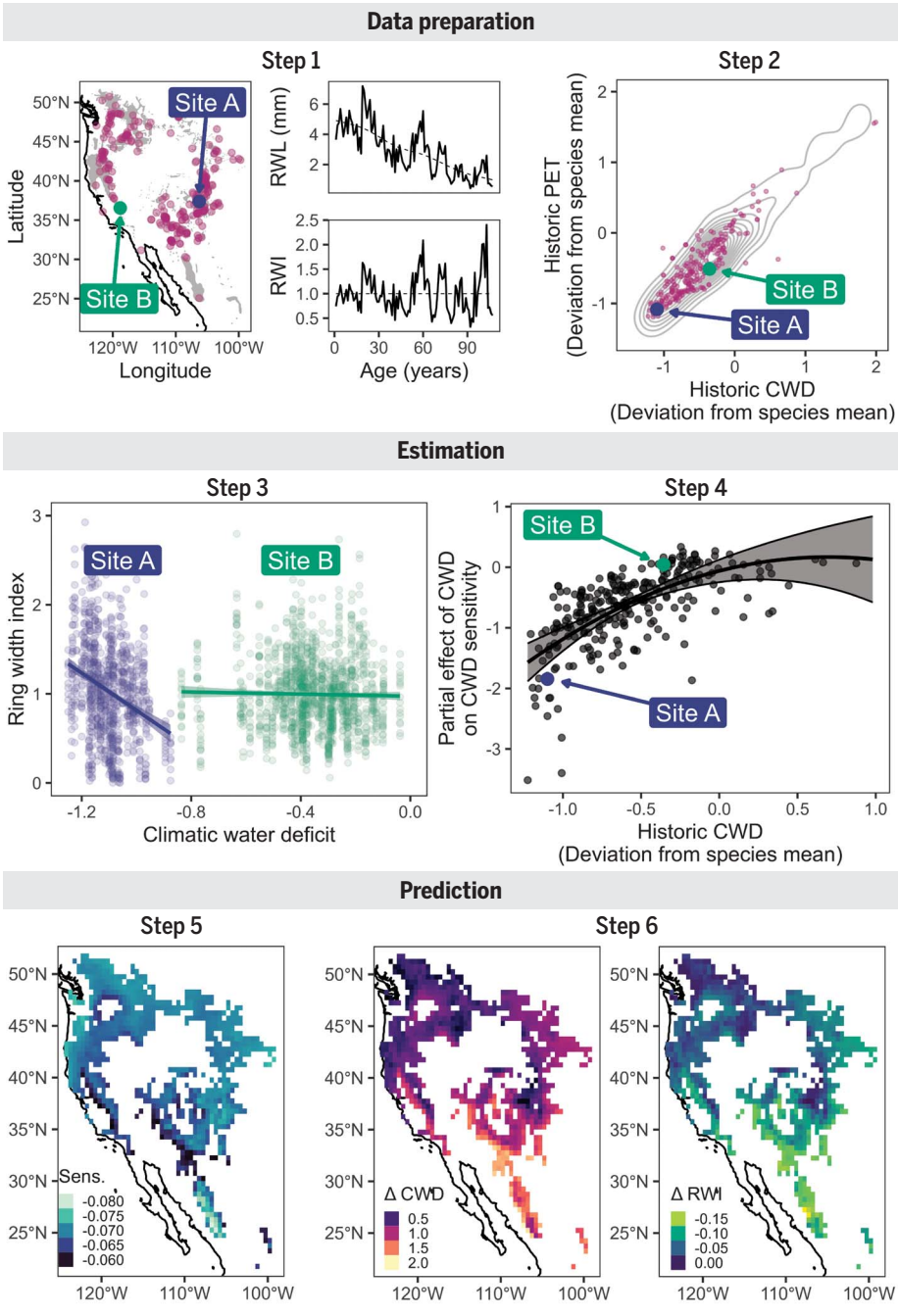

Fig. 2. Methodological approach, using data for *P. ponderosa* as an illustration. Step 1: We extracted tree-ring width measurements from ITRDB sites (pink dots, with two example sites highlighted in purple and green) and downloaded geographic species ranges for all species in the ITRDB (*P. ponderosa* distribution shown in gray). Then, we detrended raw ring width measurements into RWI. Step 2: We downloaded global climate data and calculated annual CWD and PET, which we standardized for each species using the historic climate experienced across the species' geographic range. The figure shows the distribution of mean PET and CWD between 1901 and 1980 across the ponderosa pine's full range (contours) and within ITRDB sites (dots). Step 3: We estimated sensitivity within each site. Step 4: We estimated heterogeneity in sensitivity across historic standardized CWD and PET using site-level sensitivity estimates. Although this figure illustrates this approach for the subset of PIPO sites, the primary model specification discussed in the rest of this paper conducts this analysis across all species. Step 5: We predicted sensitivity across the geographic range of all species. Step 6: We predicted change in RWI as a function of predicted sensitivities and CMIP5 predictions of changes in CWD and PET.

developing effective management strategies (*32*–*34*).

We address this long-standing debate by (i) identifying where trees exhibit the greatest sensitivity to changes in water and energy availability and (ii) predicting where forests will be most vulnerable to climate change. To quantify trees' sensitivity to weather fluctuations, we drew upon two large databases of annual tree-ring measurements: the International Tree Ring Data Bank (ITRDB) and the US Forest Service's Forest Inventory and Analysis (FIA) tree-ring dataset (*35*). The ITRDB data we analyzed includes 6.6 million annual observations of tree growth from 3775 sites spanning 122 species (listed in table S1). In addition to its geographic and taxonomic scope, an important benefit of the ITRDB is that the distribution of observed climatic conditions provides a fairly representative sample of macroscale climatic variation experienced across tree species' full geographic ranges (fig. S2). However, the ITRDB exhibits known biases toward trees growing in marginal conditions that exhibit relatively strong climate signals (*36*, *37*), which may overstate trees' sensitivity to weather (*15*). To ensure that our results were not an artifact of ITRDB biases, we replicated our analysis using FIA tree cores. Though FIA data are more geographically and taxonomically limited than those of the ITRDB, FIA tree cores are drawn from a systematic sampling design, thereby enabling a more representative understanding of ecological processes.

We analyzed these data using six steps (Fig. 2) (*38*). First, we detrended all tree-ring width measurements using standard dendrochronology approaches to generate annual observations of ring width index (RWI), a standardized measure of tree growth. Second, we characterized each tree species' climatic niche by extracting historic weather data across the entirety of each species' geographic range. We characterized weather and climate using potential evapotranspiration (PET) and climatic water deficit (CWD), two variables drawn from climatic water balance equations that emphasize the interacting roles that water and energy availability play in constraining tree species' ranges (*39*–*41*). Specifically, PET describes the atmospheric demand for water from vegetation, which is primarily a function of the amount of energy available to plants. By contrast, CWD quantifies shortages in water availability relative to this atmospheric demand. To enable comparisons across species, we standardized CWD and PET values using the distribution of historic CWD and PET experienced across the species' full range (fig. S1). Third, for each ITRDB site, we regressed annual, tree-level observations of RWI (step 1) on fluctuations in species-standardized weather (step 2) to estimate the sensitivity of individual sites to interannual

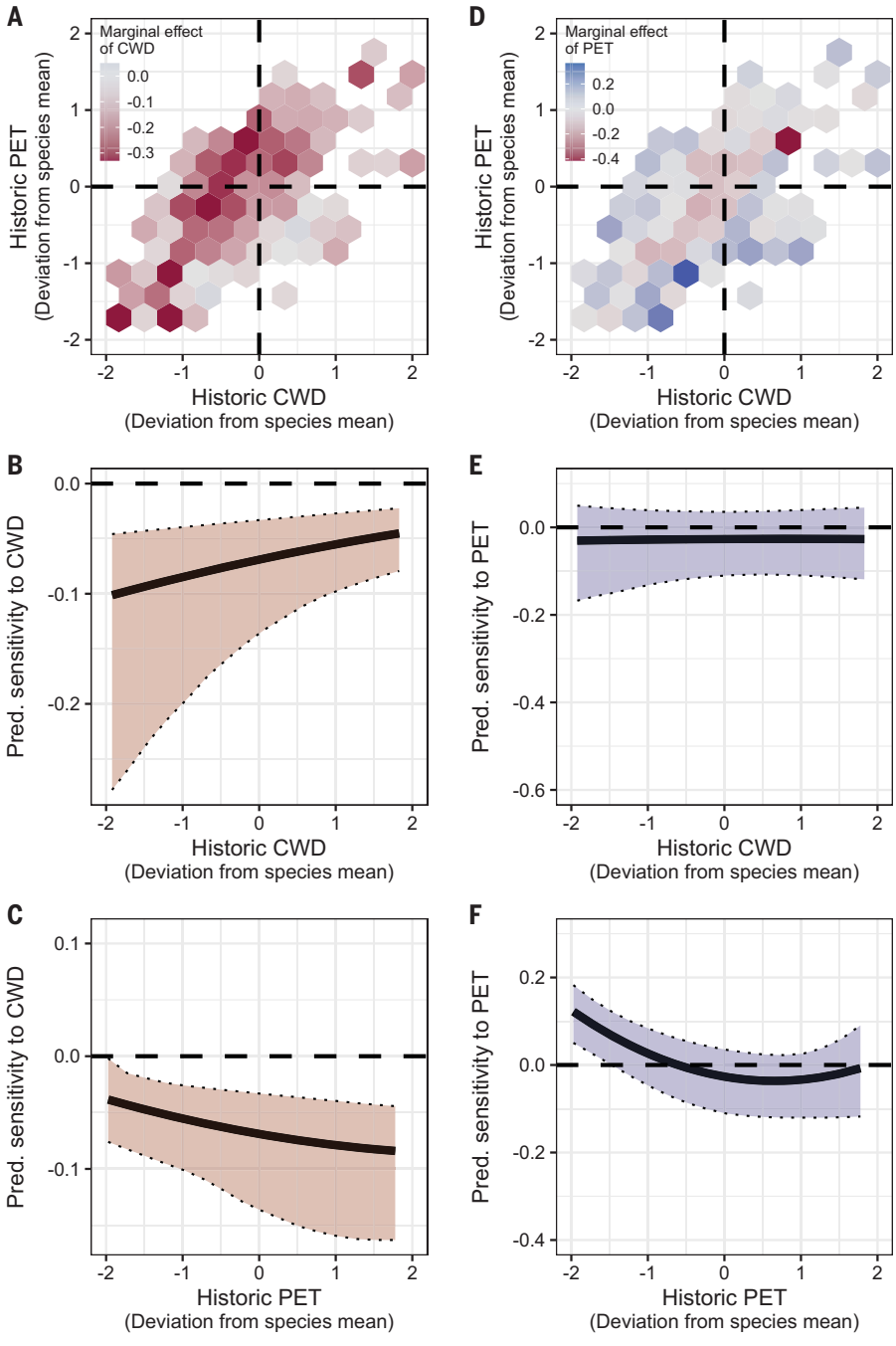

Fig. 3. Variation in sensitivity to CWD and PET across species' climatic niches. (**A** and **D**) Marginal effects of CWD (A) and PET (D) from site-specific, first-stage models, averaged within bins distributed across the standardized, historic CWD-PET climate space. First-stage coefficients represent the sensitivity of RWI to changes in CWD (high CWD sensitivity in dark red and low CWD sensitivity in gray). Sensitivity is measured as the change in RWI that would result from a 1-SD increase in CWD or PET. (**B**, **C**, **E**, and **F**) Second-stage models were used to summarize heterogeneity in sensitivity to CWD across a gradient of historic CWD (B) and PET (C) and heterogeneity in sensitivity to PET across historic CWD (E) and PET (F). Shading represents the 2.5 to 97.5% interquantile range from the block-bootstrapped second-stage model.

changes in CWD and PET. Fourth, we quantified how the sensitivities estimated in step 3 varied across sites along a gradient of historic, species-standardized climate. Fifth, using this estimate of heterogeneity in sensitivity along a climatic gradient, we predicted climatic sensitivities across each species' full geographic range. Finally, we estimated how climate change will shift tree growth across species' ranges by combining predicted sensitivities (step 5) with climate predictions from the Representative Concentration Pathway 6.0 scenario (RCP 6.0) of the Coupled Model Intercomparison Project Phase 5 (CMIP5). To ensure that our final results reflected the combined uncertainty of steps 3 to 6 of this analysis, we propagated uncertainty using a combination of Monte Carlo simulation and block bootstrapping.

Effects of CWD and PET on tree growth

Most ITRDB sites exhibited positive growth responses to increases in either water or energy availability (fig. S3), a pattern that is consistent with ecological theory and previous studies (*9*, *10*, *24*, *40*). Specifically, a site that experienced a 1 SD decline in CWD (relative to the distribution of CWD across the species' full range) experienced a 3.2% decline (95% confidence interval: −10.1 to −1.1) in RWI in the same year. The site-level, marginal effect of CWD was significantly negative ($p < 0.05$) for 54.6% of sites, whereas only 10.6% of sites exhibited a significantly positive relationship (fig. S3A). By contrast, the relationship between PET and growth varied greatly across sites, with significant positive relationships in 39.7% of sites and significant negative relationships in 25.3% of sites (fig. S3B). Site-level, distributed lag models provided further evidence that negative CWD shocks and positive PET shocks led to increases in growth, with the strongest effects occurring in the year of the shock rather than in lagged years (fig. S3, C and D).

Drier sites exhibit less sensitivity to drought

Consistent with the drought-naïve hypothesis, trees located in drier parts of their species' climatic range exhibited less sensitivity to drought than those in more mesic sites (Fig. 3). For example, our estimates of site-level sensitivity to CWD indicate that drier-than-average sites experienced a 12.8% decline (−22.3 to −6.0%) in annual growth in response to a 1-SD increase in CWD (Fig. 3A). By contrast, wetter-than-average sites experienced a larger 22.1% decline (−34.4 to −11.2%) in growth from a 1-SD increase in CWD. To summarize this variability in CWD sensitivity, we modeled sensitivity as a quadratic function of historic CWD and PET (Fig. 3, B and C). The regression results highlight that observed sensitivity declined with increasing CWD [slope at the species' mean, historic CWD = 0.015 (0.006 to 0.059)]. This slope indicates that a 1-SD increase in CWD leads to an approximately 1.5 percentage point greater decline in growth in sites located at their species' mean CWD than in a site that is 1 SD drier.

Trees also exhibited heterogeneity in their responses to annual increases in energy availability (Fig. 3, D to F). In the most energy-limited portions of species' ranges, trees often experienced large increases in growth in response

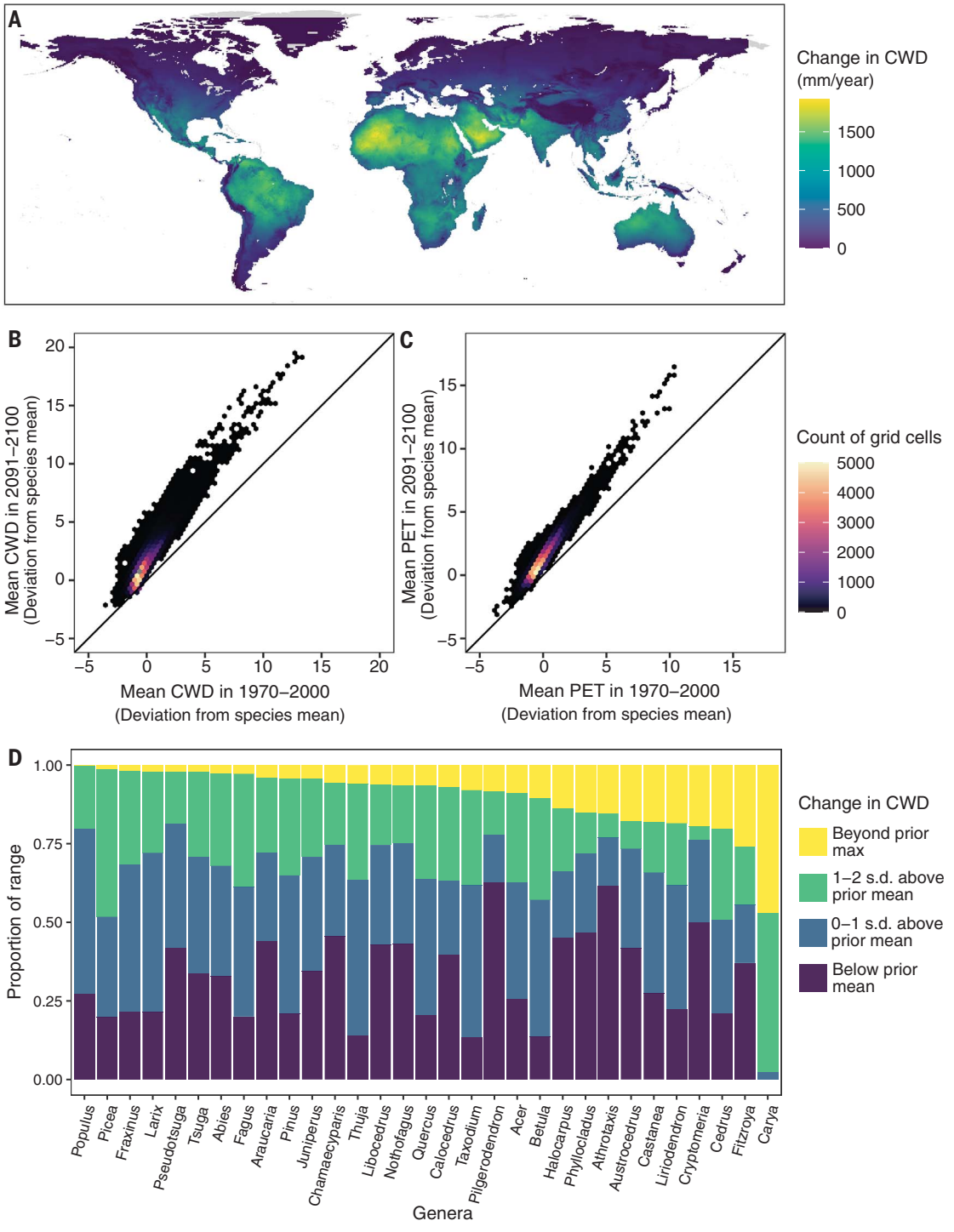

Fig. 4. Predicted changes in CWD and PET. (**A**) Spatial distribution of the mean predicted change in CWD through 2100. (**B** and **C**) Predicted increases in CWD (B) and PET (C) are largest in regions of high historic CWD and PET. (**D**) Predicted changes in CWD would push most species' historic ranges above their historic mean CWD. All plots compare changes between the historic (1970–2000) and end-of-century (2091–2100) predictions according to the average of CMIP5's 47 model runs for the RCP 6.0 scenario.

to increased PET. For example, in the coldest 10% of sites (<1.5 SD below the species' historic mean PET), growth increased 18.7% (8.7 to 25.1%) in response to a 1-SD increase in PET. However, this positive growth response to increased annual PET quickly declined across a gradient of historic PET (Fig. 3F). In sites with above-average historic PET, increased annual PET was associated with an insignificant decline in growth.

Our main conclusion—that tree sensitivity to CWD decreases across an aridity gradient—is robust to a variety of alternate models and datasets (*38*). For example, fig. S6 contrasts estimates of heterogeneity derived from systematically sampled, FIA tree-ring data against results derived from comparable ITRDB data. The similarity in results indicates that the drought-naïve effect we observed is unlikely to be the result of biases in ITRDB site selection.

In addition, we found that the drought-naïve effect persists under a wide variety of alternate approaches to data processing and analysis (fig. S5). Finally, although drought-sensitivity patterns vary across the 10 most common genera in the ITRDB, most exhibited a significant drought-naïve pattern of CWD sensitivity, whereas none of the genera exhibited a significantly higher sensitivity in the dry portions of their range (fig. S4). The results provide

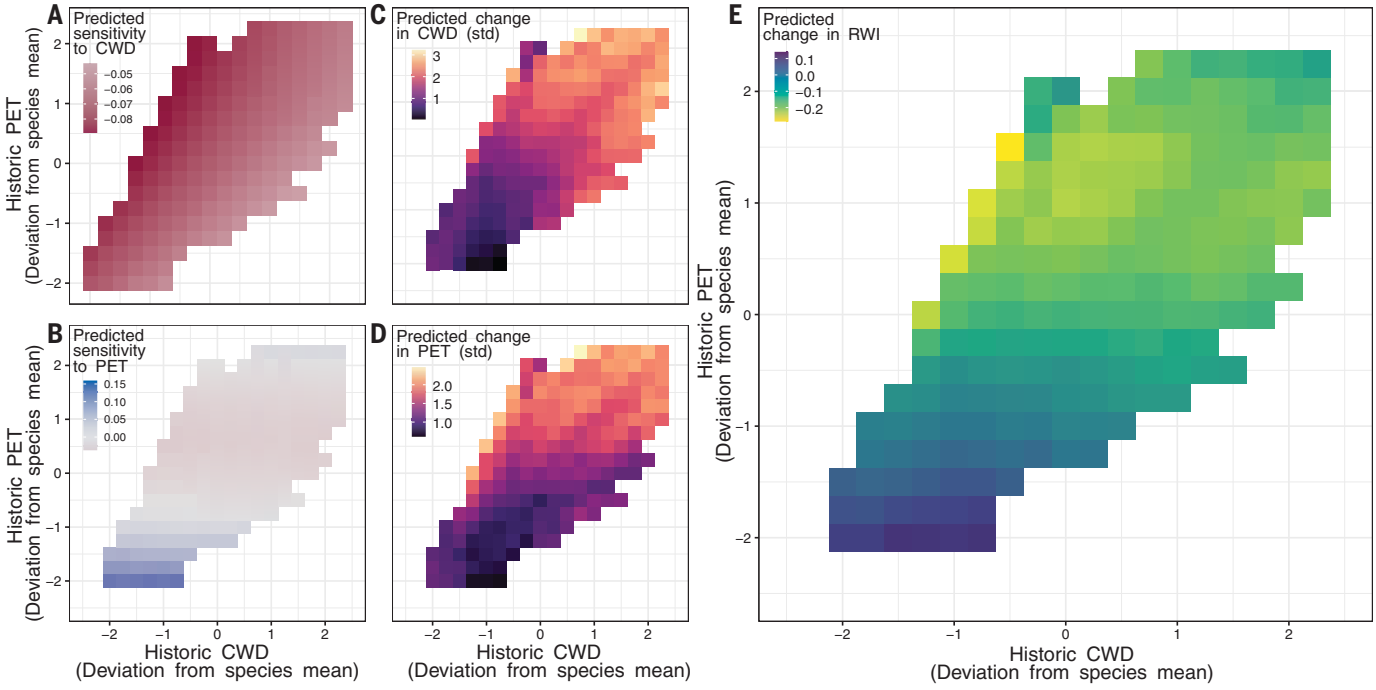

Fig. 5. Predicted changes in tree growth through 2100. (**A** and **B**) Predicted mean sensitivity of RWI to interannual changes in CWD (A) and PET (B) aggregated across the historic climatic ranges of all ITRDB species. Sensitivity is measured as the change in RWI that would result from a 1-SD increase in CWD or PET. (**C** and **D**) Forecasted changes in CWD (C) and PET (D) between CMIP5 RCP 6.0's historic (1970–2000) and end-of-century (2090–2100) periods, measured in standard deviations. (**E**) Resulting predictions of the impacts of climate change on tree growth (RWI) across species' historic climatic ranges.

further support for our conclusion that CWD sensitivity declines along a gradient of historic CWD.

Climatic changes across species ranges

Tree species will generally face much warmer and drier conditions by 2100 (Fig. 4). Specifically, CMIP5 model ensembles predict that the entirety of every species' range analyzed will experience increases in both mean PET and CWD (Fig. 4, B and C). On average, the mean PET across a species' range is anticipated to increase by 1.39 SD (0.45 to 3.05), whereas CWD is anticipated to increase by 1.41 SD (0.34 to 3.78). Supporting concerns about the emergence of "novel climates" (*42*, *43*), 11% of the average species' range will be drier than anywhere in that species' historic, climatic range (Fig. 4D). For some species (e.g., *Pinus pinea* and *Quercus faginea*), more than half of their current range is projected to be drier than the driest parts of their historic range.

Although the greatest increases in temperature are expected to occur in northern latitudes as a result of snow and ice albedo feedbacks (*44*), CMIP5 models predict higher rates of drying in warmer, lower latitudes (Fig. 4A). An important mechanism driving this pattern is the nonlinear effect of temperature on the water-holding capacity of the atmosphere (*45*, *46*). As a result of this nonlinear effect, PET is anticipated to increase more rapidly in hotter locations (Fig. 4C). Forecasted changes in annual precipitation across most ITRDB sites are not sufficient to offset warming-induced increases in atmospheric water demand, leading to pervasive increases in CWD. These increases in CWD are also anticipated to be most pronounced in dry and hot locations.

The largest growth declines are predicted to occur in wet and hot regions

Combining our estimates of sensitivity to CWD and PET with predicted changes in climate, we estimate that by 2100, tree growth will decline by 10.4% (−37.3 to +0.7%). More forests are predicted to experience declines in growth than increases in growth. Specifically, 51.2% of grid cells (representing the combination of a species and location) are predicted to experience a significant (>95% of Monte Carlo iterations) decline in growth. By contrast, only 0.6% of grid cells are predicted to experience a significant increase in growth. These results highlight that a hotter, drier planet will likely lead to major shifts in the health of global forests and their ability to sequester carbon.

Predictions of RWI changes through 2100 highlight that climate change may have a surprisingly pronounced and negative impact on trees growing in wetter, warmer portions of their range, whereas cooler parts of species' dry-range edges may be unexpectedly resilient to climate change. Figure 5 illustrates how spatial variation in sensitivity (Fig. 5, A and B) interacts with climate change exposure (Fig. 5, C and D) to yield heterogeneity in predicted RWI declines (Fig. 5E). The wetter but hotter-than-average portions of species' ranges are projected to experience a 17.2% decline in growth (−51.9 to −1.4%). By contrast, drier but cooler-than-average locations are predicted to experience a smaller 11.0% decline in growth (−33.9% to +0.3%). Grid cells predicted to experience increases in growth are primarily located in very energy-limited parts of species' historic ranges.

Capturing heterogeneity in sensitivity in ecological models is important to accurately predict the impacts of climate change. For example, a neutral model, in which predicted sensitivity to PET and CWD is constant across species' climatic ranges, would yield contrasting results to our model, which allows for spatial heterogeneity. Specifically, the neutral model would likely underestimate the negative impact of climate change in wetter regions but overestimate the negative impact in drier regions when compared with our model (fig. S7). These results highlight that the spatial heterogeneity in trees' climatic sensitivities will likely play a critical role in mediating the response of the world's forests to climate change.

Discussion

Trees growing in wet and warm portions of their range will likely experience the greatest declines in growth under climate change. This

pattern of vulnerability captures the interaction of heterogeneity in both exposure and sensitivity—historically wet forests are more sensitive to drier conditions, whereas hot forests will be exposed to the greatest increases in CWD. Though drought-induced declines in tree growth frequently occur in dry regions (*15*, *19*, *47*), our results support the hypothesis that the vulnerability of wetter forests to climate change is greatly underappreciated (*48*).

The drought-naïve pattern exhibited across ITRDB and FIA sites is likely the result of long-term adaptations to local climatic conditions. Drought adapted traits—for example, higher resistance to cavitation, lower leaf-area index, higher water-use efficiency, and wider hydraulic safety margins (*49*, *50*)—often emerge in regions that experience higher aridity and drought frequency (*51*–*53*). In theory, drought adaptations could occur at the scale of individuals (e.g., phenotypic plasticity) or local communities (e.g., tree density) or through evolutionary processes that occur across generations. Recent research, however, suggests that most climate adaptation develops over longer timescales than an individual tree's life span (*54*). This suggests that genetic adaptation is an important mechanism that protects trees from climate change, but it also highlights the risk that rapid warming may outpace the rate of adaptation.

Although sensitivity patterns for many genera are consistent with the drought-naïve effect (fig. S4), the sign, magnitude, and significance of this effect varies across taxa. Some of this variability is likely due to differences in tree traits (e.g., turgor loss point, xylem structure, leaf size) and mechanisms of acclimation (e.g., canopy thinning, trait plasticity, shifts in water allocation) (*23*, *48*). Interestingly, *Quercus* and *Taxodium*, the two genera that exhibited opposite (although insignificant) patterns of drought sensitivity, both have hotter species ranges than the other commonly sampled genera (fig. S4). This suggests that taxonomic differences in drought sensitivity may be partly explained by trade-offs between investments in heat and drought tolerance (*55*), as well as the physiological limits of climate adaptation. Future research that disentangles the primary mechanisms of drought and heat tolerance will improve estimates of species-level vulnerability to climate change.

The prevalence of drought-naïve effects is relevant for understanding climate change impacts across many scales of biological organization. Organisms and ecosystems with prior exposure to extreme weather (e.g., droughts and heat waves) are often less sensitive to extreme events than entities that lack past exposure. This pattern has been found across diverse systems, including soil microbial communities (*56*), insect species (*57*), bird populations (*58*), agricultural production (*59*), human mortality (*60*), and even biomes (*61*). Though the mechanisms that enable adaptation vary by system, relatively consistent patterns of sensitivity underscore the important role that adaptation could play in moderating the effects of climate extremes.

Because we quantified vulnerability using tree growth rather than mortality, our analysis provides incomplete insights into patterns of mortality under climate change. Declines in RWI have been shown to predict tree mortality (*62*, *63*), and the primary mechanisms of drought-induced mortality—hydraulic failure, carbon starvation, and defensive failure (*23*)—can be linked to changes in tree growth (*64*). Therefore, our predictions of growth declines in mesic regions suggest that increases in tree mortality may be surprisingly widespread. Nevertheless, declines in RWI can be an unreliable predictor of mortality (*64*, *65*). A tree's age, genotype, functional traits, and mechanisms of acclimation (*64*, *66*, *67*) are all important determinants of growth responses to drought, which can decouple the relationship between RWI and mortality. Importantly, our predictions of vulnerability might understate the risk of mortality at dry-range edges if there are thresholds in the relationship between tree growth and mortality (*68*). For example, trees likely require a minimum amount of growth to survive (*68*); therefore, the same percentage growth decline could be more harmful for slow-growing trees located at their dry-range edge than for trees growing in mesic areas (*10*). Future research that characterizes these nonlinear responses to drought could improve predictions of climate impacts (*42*, *43*).

Finally, our findings have important policy implications, both for conserving forests and managing terrestrial carbon sinks. Policy-makers who seek to protect forests from climate change may need to expand the focus of conservation interventions beyond species' dry-range edges. By contrast, drought adaptations in populations from drier regions could be useful for management interventions, including assisted migration into wetter regions. Additionally, although dynamic global vegetation models are increasingly sophisticated (*69*–*72*), very few, if any, account for the spatial variation in the climate sensitivity of carbon capture. Failing to account for drought-naïve effects can lead to overestimates of the resilience of carbon sinks in wetter regions. Improving forecasts of climate-change impacts on terrestrial carbon sinks by accounting for the variability in drought sensitivity will facilitate more-effective global policies aimed at reducing carbon emissions (*73*, *74*).

REFERENCES AND NOTES

1. Food and Agriculture Organization of the United Nations, Global Forest Resources Assessment 2005; https://www.fao.org/3/a0400e/a0400e00.htm [accessed 26 August 2020].
2. W. R. L. Anderegg *et al*., *Science* **368**, eaaz7005 (2020).
3. Y. Pan *et al*., *Science* **333**, 988–993 (2011).
4. R. Costanza *et al*., *Nature* **387**, 253–260 (1997).
5. R. Costanza *et al*., *Glob. Environ. Change* **26**, 152–158 (2014).
6. W. A. Kurz *et al*., *Nature* **452**, 987–990 (2008).
7. O. L. Phillips *et al*., *Science* **323**, 1344–1347 (2009).
8. K. Giles-Hansen, X. Wei, *Environ. Res. Lett.* **17**, 044049 (2022).
9. C. D. Allen *et al*., *For. Ecol. Manage.* **259**, 660–684 (2010).
10. W. R. L. Anderegg, L. D. L. Anderegg, K. L. Kerr, A. T. Trugman, *Glob. Change Biol.* **25**, 3793–3802 (2019).
11. M. Lindner *et al*., *For. Ecol. Manage.* **259**, 698–709 (2010).
12. I. Aubin *et al*., *Ecosphere* **9**, e02108 (2018).
13. T. J. Brodribb, J. Powers, H. Cochard, B. Choat, *Science* **368**, 261–266 (2020).
14. X. Zhang, P. Lv, C. Xu, X. Huang, T. Rademacher, *Agric. For. Meteorol.* **308–309**, 108611 (2021).
15. S. Klesse *et al*., *Nat. Commun.* **9**, 5336 (2018).
16. H. C. Fritts, D. G. Smith, J. W. Cardis, C. A. Budelsky, *Ecology* **46**, 393–401 (1965).
17. C. Desplanque, C. Rolland, F. H. Schweingruber, *Trees* **13**, 218–227 (1999).
18. F. Lebourgeois, C. B. K. Rathgeber, E. Ulrich, *J. Veg. Sci.* **21**, 364–376 (2010).
19. A. P. Williams *et al*., *Proc. Natl. Acad. Sci. U.S.A.* **107**, 21289–21294 (2010).
20. H. Liu *et al*., *Glob. Change Biol.* **19**, 2500–2510 (2013).
21. T. Kolář, P. Čermák, M. Trnka, T. Žid, M. Rybníček, *Agric. For. Meteorol.* **239**, 24–33 (2017).
22. L. D'Orangeville *et al*., *Glob. Change Biol.* **24**, 2339–2351 (2018).
23. N. G. McDowell *et al*., *Nat. Rev. Earth Environ.* **3**, 294–308 (2022).
24. D. Mildrexler, Z. Yang, W. B. Cohen, D. M. Bell, *Remote Sens. Environ.* **173**, 314–325 (2016).
25. D. Helman, I. M. Lensky, D. Yakir, Y. Osem, *Glob. Change Biol.* **23**, 2801–2817 (2017).
26. L. Cavin, A. S. Jump, *Glob. Change Biol.* **23**, 362–379 (2017).
27. I. M. McCullough, F. W. Davis, A. P. Williams, *For. Ecol. Manage.* **402**, 223–233 (2017).
28. B. Choat *et al*., *Nature* **491**, 752–755 (2012).
29. K. E. Gleason *et al*., *Ecosphere* **8**, e01849 (2017).
30. A. Aguirre, M. del Río, S. Condés, *For. Ecol. Manage.* **411**, 90–100 (2018).
31. R. López *et al*., *Ann. Bot.* **111**, 1167–1179 (2013).
32. T. M. Brooks *et al*., *Science* **313**, 58–61 (2006).
33. M. I. Williams, K. Dumroese, in *Forest Conservation in the Anthropocene: Science, Policy, and Practice*, V. A. Sample, R. P. Bixler, C. Miller, Eds. (Univ. Press of Colorado, 2016), pp. 113–123.
34. W. J. Wang, H. S. He, F. R. ThompsonIII, J. S. Fraser, W. D. Dijak, *Landsc. Ecol.* **32**, 1399–1413 (2017).
35. R. J. DeRose, J. D. Shaw, J. N. Long, *J. For.* **115**, 283–291 (2017).
36. F. Babst *et al*., *Quat. Sci. Rev.* **197**, 1–20 (2018).
37. S. Zhao, N. Pederson, L. D'Orangeville, *J. Biogeogr.* **46**, 355–368 (2019).
38. Materials and methods are available as supplementary materials.
39. N. L. Stephenson, *Am. Nat.* **135**, 649–670 (1990).
40. N. Stephenson, *J. Biogeogr.* **25**, 855–870 (1998).
41. D. D. Ackerly *et al*., *Front. Ecol. Environ.* **18**, 288–297 (2020).
42. J. W. Williams, S. T. Jackson, *Front. Ecol. Environ.* **5**, 475–482 (2007).
43. C. R. Mahony, A. J. Cannon, T. Wang, S. N. Aitken, *Glob. Change Biol.* **23**, 3934–3955 (2017).
44. Q. You *et al*., *Earth Sci. Rev.* **217**, 103625 (2021).
45. D. D. Breshears *et al*., *Front. Plant Sci.* **4**, 266 (2013).
46. A. Park Williams *et al*., *Nat. Clim. Change* **3**, 292–297 (2013).
47. J. Su *et al*., *For. Ecol. Manage.* **482**, 118841 (2021).
48. C. D. Allen, D. D. Breshears, N. G. McDowell, *Ecosphere* **6**, 1–55 (2015).
49. C. Pritzkow, V. Williamson, C. Szota, R. Trouvé, S. K. Arndt, *Tree Physiol.* **40**, 215–229 (2020).
50. J. M. R. Peters *et al*., *Glob. Change Biol.* **27**, 3620–3641 (2021).
51. Y. Osem, K. O'Hara, *Forestry* **89**, 338–349 (2016).
52. T. Chauvin, H. Cochard, V. Segura, P. Rozenberg, *For. Ecol. Manage.* **444**, 9–20 (2019).

53. R. López, F. J. Cano, N. K. Martin-StPaul, H. Cochard, B. Choat, *New Phytol.* **230**, 497–509 (2021).
54. J. Gantois, *Glob. Change Biol.* **28**, 6002–6020 (2022).
55. R. M. Marchin *et al*., *Glob. Change Biol.* **28**, 1133–1146 (2022).
56. R. Ochoa-Hueso *et al*., *Glob. Change Biol.* **24**, 2818–2827 (2018).
57. C. García-Robledo, E. K. Kuprewicz, C. L. Staines, T. L. Erwin, W. J. Kress, *Proc. Natl. Acad. Sci. U.S.A.* **113**, 680–685 (2016).
58. B. L. Bateman *et al*., *Landsc. Ecol.* **30**, 1095–1110 (2015).
59. E. E. Butler, P. Huybers, *Nat. Clim. Chang.* **3**, 68–72 (2013).
60. T. Carleton *et al*., *Q. J. Econ.* **137**, 2037–2105 (2022).
61. S. M. Vicente-Serrano *et al*., *Proc. Natl. Acad. Sci. U.S.A.* **110**, 52–57 (2013).
62. A. J. Das, J. J. Battles, N. L. Stephenson, P. J. van Mantgem, *Can. J. For. Res.* **37**, 580–597 (2007).
63. J. J. Camarero, A. Gazol, G. Sangüesa-Barreda, J. Oliva, S. M. Vicente-Serrano, *J. Ecol.* **103**, 44–57 (2015).
64. M. Cailleret *et al*., *Glob. Change Biol.* **23**, 1675–1690 (2017).
65. N. Bircher, M. Cailleret, H. Bugmann, *Ecol. Appl.* **25**, 1303–1318 (2015).
66. A. T. Trugman, *New Phytol.* **234**, 21–27 (2022).
67. N. L. Stephenson, A. J. Das, N. J. Ampersee, B. M. Bulaon, J. L. Yee, *J. Ecol.* **107**, 2383–2401 (2019).
68. J. Au *et al*., *Glob. Change Biol.* **29**, 5652–5665 (2023).
69. G. Krinner *et al*., *Global Biogeochem. Cycles* **19**, 2003GB002199 (2005).
70. B. Smith *et al*., *Biogeosciences* **11**, 2027–2054 (2014).
71. M. Fernández-Martínez *et al*., *Nat. Clim. Chang.* **9**, 73–79 (2019).
72. M. Forkel *et al*., *Sci. Rep.* **9**, 18757 (2019).
73. A. Favero, A. Daigneault, B. Sohngen, *Sci. Adv.* **6**, eaay6792 (2020).
74. L. Nascimento *et al*., *Clim. Policy* **22**, 158–174 (2022).
75. R. Heilmayr, Replication code and data for: Drought sensitivity in mesic forests heightens their vulnerability to climate change. Open Science Framework (2023); https://doi.org/10.17605/OSF.IO/RHJCF.
76. H. D. Grissino-Mayer, H. C. Fritts, *Holocene* **7**, 235–238 (1997).
77. Climatic Research Unit (University of East Anglia) and Met Office, CRU TS Version 4.04 (2020); https://crudata.uea.ac.uk/cru/data/hrg/cru_ts_4.04/ [accessed 9 March 2023].
78. World Climate Research Programme, Coupled Model Intercomparison Project Phase 5; https://esgf-node.llnl.gov/search/cmip5/.

ACKNOWLEDGMENTS

We thank R. Huezo for help parsing the ITRDB database and M. Leung for support in compiling our database of species range maps. We express our appreciation to the many contributors to the ITRDB. In addition, we thank S. Klesse and J. Shaw for providing access to the US Forest Service's National Forest Inventory and Analysis Program's Interior West tree-ring dataset. **Funding:** J.D. acknowledges support from the David H. Smith Conservation Research Fellowship. F.C.M. acknowledges support from the National Science Foundation (NSF award no. 1924378). **Author contributions:** R.H., J.D., and F.C.M. all contributed to the conceptualization, data curation, formal analysis, writing (original draft), and writing (review and editing) of this paper. **Competing interests:** The authors declare that they have no competing interests. **Data and materials availability:** All code used to clean data, conduct the analysis, and generate figures and results is available at this paper's Open Science Framework (OSF) repository (*75*). This repository also includes the preprocessed data necessary to reproduce all results, figures, and tables. Raw input data are available from the ITRDB (*76*), the Climate Research Unit (*77*), and the Coupled Model Intercomparison Project (*78*). **License information:** Copyright © 2023 the authors, some rights reserved; exclusive licensee American Association for the Advancement of Science. No claim to original US government works. https://www.science.org/about/science-licenses-journal-article-reuse

SUPPLEMENTARY MATERIALS

science.org/doi/10.1126/science.adi1071
Materials and Methods
Figs. S1 to S7
Table S1
References (*79*–*91*)
MDAR Reproducibility Checklist

Submitted 7 April 2023; accepted 26 October 2023
10.1126/science.adi1071

NUCLEOSYNTHESIS

Element abundance patterns in stars indicate fission of nuclei heavier than uranium

Ian U. Roederer[1]*†, Nicole Vassh[2], Erika M. Holmbeck[3], Matthew R. Mumpower[4,5], Rebecca Surman[6], John J. Cowan[7], Timothy C. Beers[6], Rana Ezzeddine[8], Anna Frebel[9,10], Terese T. Hansen[11], Vinicius M. Placco[12], Charli M. Sakari[13]

The heaviest chemical elements are naturally produced by the rapid neutron-capture process (*r*-process) during neutron star mergers or supernovae. The *r*-process production of elements heavier than uranium (transuranic nuclei) is poorly understood and inaccessible to experiments so must be extrapolated by using nucleosynthesis models. We examined element abundances in a sample of stars that are enhanced in *r*-process elements. The abundances of elements ruthenium, rhodium, palladium, and silver (atomic numbers Z = 44 to 47; mass numbers A = 99 to 110) correlate with those of heavier elements ($63 \leq Z \leq 78$, $A > 150$). There is no correlation for neighboring elements ($34 \leq Z \leq 42$ and $48 \leq Z \leq 62$). We interpret this as evidence that fission fragments of transuranic nuclei contribute to the abundances. Our results indicate that neutron-rich nuclei with mass numbers >260 are produced in *r*-process events.

The heaviest chemical elements are synthesized through the rapid neutron capture process (*r*-process). Sites where the *r*-process occurs include mergers of neutron stars, which have been observed (*1*–*3*). The nuclei produced by the *r*-process in these events depend on the composition of material ejected by the merger (*4*) and the properties of the progenitor neutron stars, including their equation of state (*5*). Freshly produced lanthanide elements (atomic numbers Z = 57 to 71) (*6*, *7*) and Sr (Z = 38) (*8*) have been observed in the ejecta of a neutron star merger event, but otherwise the detailed chemical composition has not been measured.

The detailed compositions of some ancient stars in the Milky Way have been determined from their spectra, which contain hundreds of absorption features of more t 40 *r*-process elements (*9*). The abund patterns of lanthanide elements in these stars are nearly identical, indicating a possible universality of *r*-process events and producing the same abundance ratios. The composition of each star is dominated by the ejecta of individual *r*-process events (*10*, *11*), such as neutron star mergers or rare types of supernova,

[1]Department of Astronomy, University of Michigan, Ann Arbor, MI 48109, USA. [2]TRIUMF (Tri-University Meson Facility), Vancouver, BC V6T 2A3, Canada. [3]Carnegie Observatories, Pasadena, CA 91101, USA. [4]Theoretical Division, Los Alamos National Laboratory, Los Alamos, NM 87545, USA. [5]Center for Theoretical Astrophysics, Los Alamos National Laboratory, Los Alamos, NM 87545, USA. [6]Department of Physics and Astronomy, University of Notre Dame, Notre Dame, IN 46556, USA. [7]Homer L. Dodge Department of Physics and Astronomy, University of Oklahoma, Norman, OK 73019, USA. [8]Department of Astronomy, University of Florida, Bryant Space Science Center, Gainesville, FL 32611, USA. [9]Department of Physics, Massachusetts Institute of Technology, Cambridge, MA 02139, USA. [10]Kavli Institute for Astrophysics and Space Research, Massachusetts Institute of Technology, Cambridge, MA 02139, USA. [11]Department of Astronomy, Stockholm University, AlbaNova University Center, SE-106 91 Stockholm, Sweden. [12]National Optical-Infrared Astronomy Research Laboratory, National Science Foundation, Tucson, AZ 85719, USA. [13]Department of Physics and Astronomy, San Francisco State University, San Francisco, CA 94132, USA.
*Corresponding author. Email: iuroederer@ncsu.edu
†Present address: Department of Physics, North Carolina State University, Raleigh, NC 27695, USA.

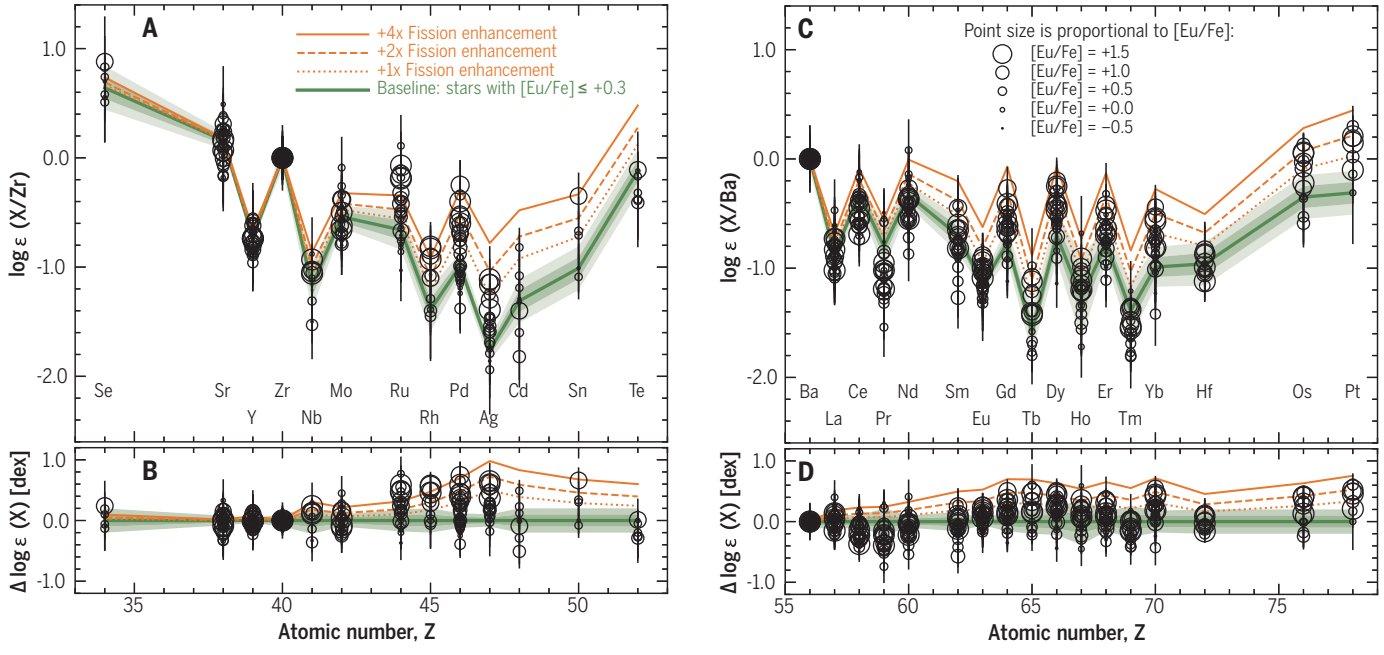

Fig. 1. Observed abundance patterns compared with fission model predictions. Shown are logarithmic abundances (open circles) measured for 30 *r*-process elements in the 42 stars of our sample, plotted as a function of atomic number. The symbol sizes are proportional to [Eu/Fe], and error bars indicate 1σ uncertainties. The green line is the empirical baseline pattern we defined as the mean abundance ratios for the subset of 13 stars with [Eu/Fe] ≤ +0.3. Light shading and dark green shading indicate ± 1 and ± 2 times the standard error in the baseline, respectively. The orange lines indicate models of fission fragments added to the baseline pattern; the dotted line has equal contributions from the baseline and the fission model, the dashed line has two parts fission fragments plus one part baseline pattern, and the solid line has four parts fission plus one part baseline. (**A**) Elements $34 < Z < 52$, normalized to Zr (solid circle). Elements are labeled at bottom. (**B**) Residuals between the data and the baseline pattern in (A). (**C** and **D**) Same as (A) and (B), respectively, but for elements $56 < Z < 78$, normalized to Ba (solid circle). Numerical values are provided in data S1.

which enriched the gas from which the stars formed (*12*).

Stellar sample and abundance measurements

We investigated the *r*-process using a sample of 42 stars in the Milky Way. We selected stars that were previously observed to have heavy elements known to be formed by the *r*-process, with no evidence of contamination from other processes [such as the slow neutron capture process (*s*-process)]. We adopted the element abundances of 31 heavy elements ($34 \leq Z \leq 90$) from data reported in 35 previous studies (*13*) then homogenized these abundances to a common scale using the atomic data reported in the original studies (*13*).

The ratio [Fe/H] is defined as $[\mathrm{Fe/H}] \equiv \log_{10}(N_{\mathrm{Fe}}) - \log_{10}(N_{\mathrm{Fe}})_{\odot}$, where N is the number density with subscript indicating the element, and $\odot$ indicates the value for the Sun. We use Fe as a measure of the overall enrichment by elements heavier than He (referred to as the metallicity). We use the ratio $[\mathrm{Eu/Fe}] \equiv \log_{10}(N_{\mathrm{Eu}}/N_{\mathrm{Fe}}) - \log_{10}(N_{\mathrm{Eu}}/N_{\mathrm{Fe}})_{\odot}$ as a measure of the enhancement of *r*-process elements relative to the metallicity. Our sample spans the ranges $-3.57 \leq [\mathrm{Fe/H}] \leq -0.99$ and $-0.52 \leq [\mathrm{Eu/Fe}] \leq +1.69$ (data S1).

Correlations between elements

The heavy-element abundance patterns in the selected stars are shown in Fig. 1 (individual elements are shown in figs. S3 and S4). We found that stars with higher [Eu/Fe] ratios have abundances of some elements (including Ru, Rh, Pd, Ag, Gd, Tb, Dy, and Yb) that are slightly enhanced relative to those in stars with lower [Eu/Fe] ratios. This excess is not an expected consequence of *r*-process universality.

We calculated an empirical baseline abundance pattern (tables S2 and S3) using the 13 stars (30% of the sample) with the lowest levels of *r*-process enhancement, $[\mathrm{Eu/Fe}] \leq +0.3$. The abundance excess—the difference between the individual abundance measurements in each star and the empirical baseline for that element—is shown for all stars in Fig. 1, B and D, and split into different groups of elements in Fig. 2. Three sets of elements behave similarly in our sample: Se, Sr, Y, Zr, Nb, and Mo ($34 \leq Z \leq 42$); Cd, Sn, and Te ($48 \leq Z \leq 52$); and Ba, La, Ce, Pr, Nd, and Sm ($56 \leq Z \leq 62$), shown in Fig. 2, A, C, and D, respectively. The abundance ratios of these elements exhibit no

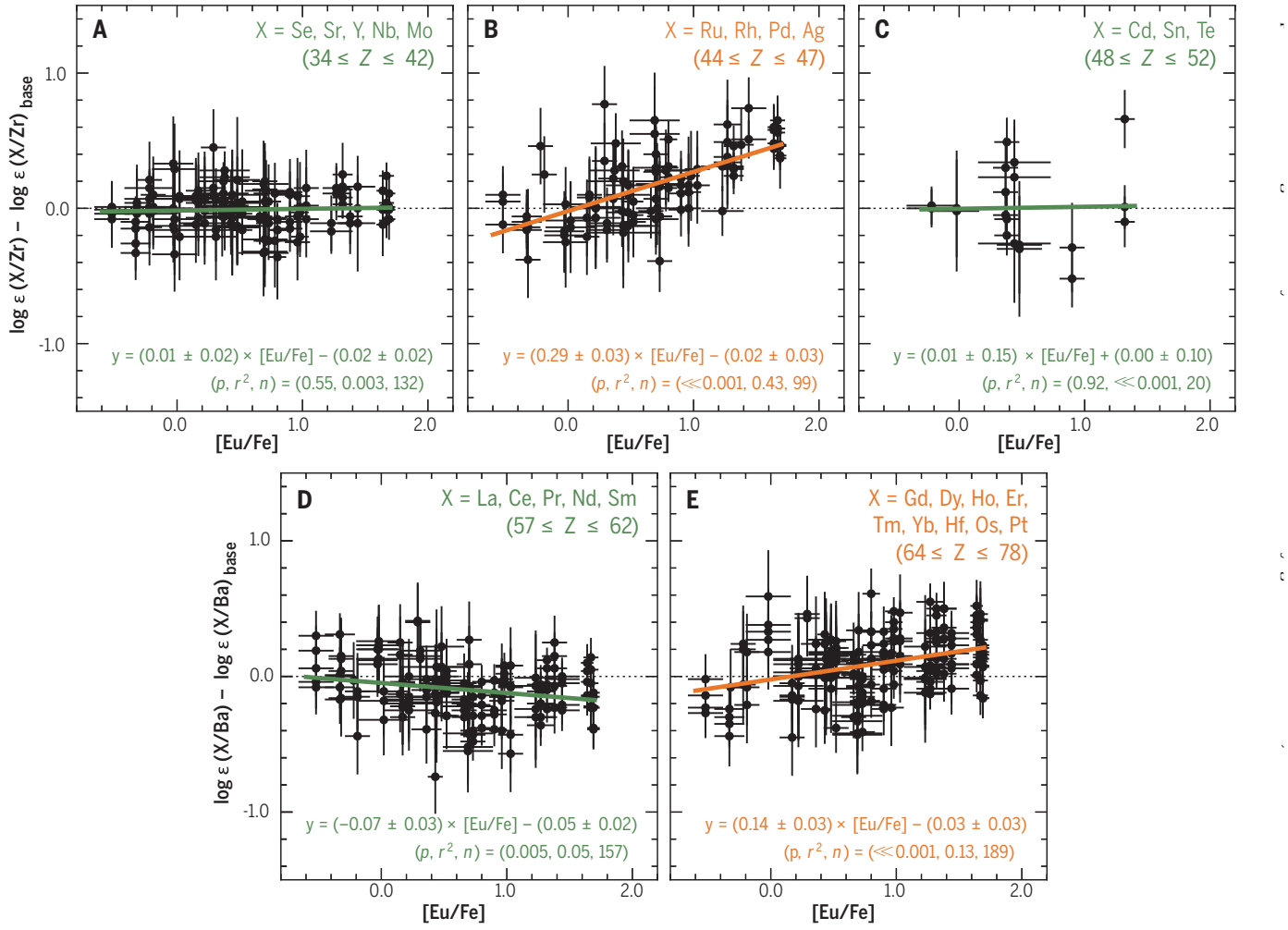
A
X = Se, Sr, Y, Nb, Mo
(34 ≤ Z ≤ 42)
y = (0.01 ± 0.02) × [Eu/Fe] – (0.02 ± 0.02)
(p, r², n) = (0.55, 0.003, 132)
B
X = Ru, Rh, Pd, Ag
(44 ≤ Z ≤ 47)
y = (0.29 ± 0.03) × [Eu/Fe] – (0.02 ± 0.03)
(p, r², n) = (≪0.001, 0.43, 99)
C
X = Cd, Sn, Te
(48 ≤ Z ≤ 52)
y = (0.01 ± 0.15) × [Eu/Fe] + (0.00 ± 0.10)
(p, r², n) = (0.92, ≪0.001, 20)
D
X = La, Ce, Pr, Nd, Sm
(57 ≤ Z ≤ 62)
y = (–0.07 ± 0.03) × [Eu/Fe] – (0.05 ± 0.02)
(p, r², n) = (0.005, 0.05, 157)
E
X = Gd, Dy, Ho, Er, Tm, Yb, Hf, Os, Pt
(64 ≤ Z ≤ 78)
y = (0.14 ± 0.03) × [Eu/Fe] – (0.03 ± 0.03)
(p, r², n) = (≪0.001, 0.13, 189)
log ε (X/Zr) – log ε (X/Zr)base
log ε (X/Ba) – log ε (X/Ba)base
[Eu/Fe]
1.0
0.0
-1.0
2.0

Fig. 2. Abundance ratios of groups of elements that do or do not correlate with [Eu/Fe]. (**A** to **E**) Different groups of elements, ordered by increasing atomic number *Z*. (A) $34 \leq Z \leq 42$. (B) $44 \leq Z \leq 47$. (C) $48 \leq Z \leq 52$. (D) $57 \leq Z \leq 62$. (E) $64 \leq Z \leq 78$. In (A) to (E), black data points are for one element abundance ratio in one star, with the error bars indicating 1σ uncertainties. Abundances have been normalized to Zr in (A) to (C) and Ba in (D) and (E), and the empirical baselines shown in Fig. 1 have been subtracted. Solid lines indicate ordinary least-squares linear fits to the data, and dotted lines indicate differences of zero. Green indicates flat trends (lines consistent with zero); we interpret these as indicating that those elements are produced together with Zr or Ba. Orange indicates correlations that are significantly (>4.6σ) different from zero; we interpret these as indicating those elements are produced together with Eu. Labels indicate the equation of each fitted line, the *P*-value of its Pearson correlation coefficient; the coefficient of determination, r^2; and the number of stars, *n* (*13*); these values are also listed in table S1. Separate plots for each element are shown in figs. S3 to S5.

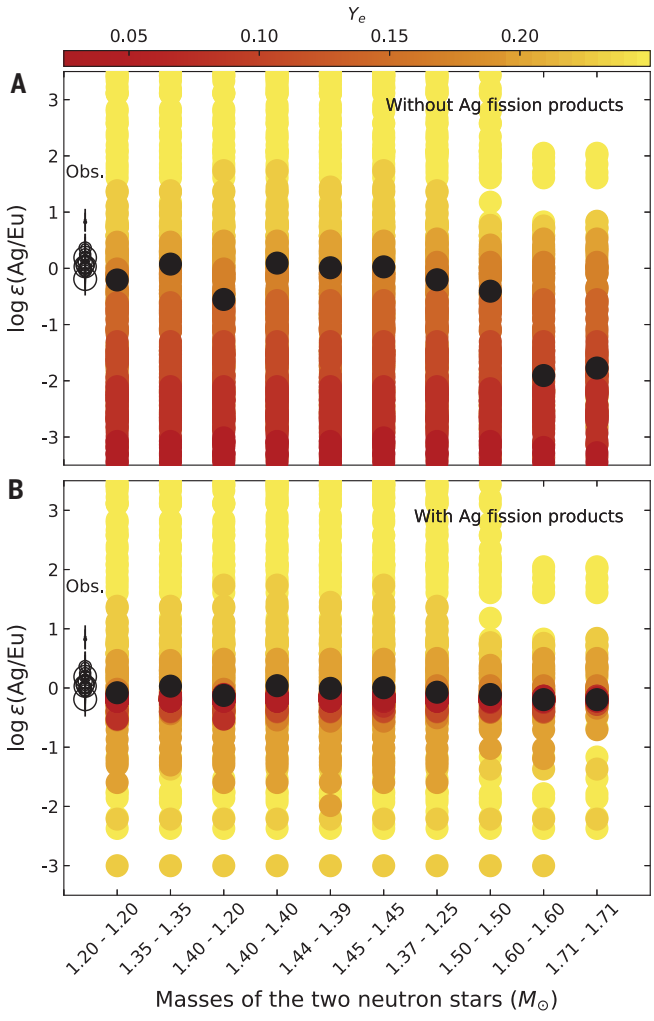

Fig. 3. Ag/Eu abundance ratios predicted with nucleosynthesis models. Predictions of log ε(Ag/Eu) from hydrodynamic simulations (*13*) of neutron star mergers are plotted as a function of the pair of progenitor masses. Overlapping colored dots indicate individual ejecta, and black dots indicate the mean mass-weighted abundance ratio (*13*). The color bar indicates the neutron richness (Y_e) of individual ejecta; lower Y_e ejecta are expected to experience more fission. Open circles indicate the observed ratios in our stellar sample, with sizes proportional to the [Eu/Fe] ratio in each star (as in Fig. 1). Results are shown for models (**A**) without including fission and (**B**) with fission included. When fission is included, we found that the predicted mass-weighted log ε(Ag/Eu) ratios are independent of the progenitor masses and are consistent with the observations.

correlation with [Eu/Fe] and therefore no excess (*13*).

Two other sets of elements exhibit significant (at least 4.6σ) positive correlations with [Eu/Fe] (*13*). These two sets include the elements Ru, Rh, Pd, and Ag ($44 \le Z \le 47$) and Gd, Tb, Dy, Ho, Er, Tm, Yb, Hf, Os, and Pt ($64 \le Z \le 78$), shown in Fig. 2, B and E, respectively. These correlations indicate an extension of *r*-process universality, so that many of the heavier *r*-process elements have abundances linked to those of a smaller number of lighter elements.

Interpretation as fission fragmentation

Two deviations from *r*-process universality have previously been identified (supplementary text). One consists of large differences [>1.5 decimal exponent (dex)] in the overall abundances of light *r*-process elements ($34 \le Z < 56$) relative to heavier ones ($Z \ge 56$) for some elements outside our range of interest ($44 \le Z \le 47$). The other deviation, known as the actinide boost, is characterized by small variations (<0.7 dex) in the abundances of the actinide elements Th ($Z = 90$) and U ($Z = 92$) relative to other heavy *r*-process elements. Neither of these deviations from *r*-process universality can explain the correlations in Fig. 2.

Our findings are also inconsistent with two-component models of *r*-process nucleosynthesis (*14*, *15*), in which one component (referred to as the weak, or limited, *r*-process) dominates the lighter *r*-process elements, and another (referred to as the main *r*-process) dominates the heavier *r*-process elements. Those two-component models segregate light- and heavy-element production so cannot produce abundance correlations between [Eu/Fe] and some, but not all, light *r*-process elements.

We propose that these element groups ($44 \le Z \le 47$ and $63 \le Z \le 78$) were instead produced as fission fragments of transuranic ($Z > 92$) elements that were synthesized in the *r*-process but have since decayed. Nucleosynthesis models have predicted that transuranic elements can be produced in *r*-process events if the ejecta contain very neutron-rich material (*16*–*18*). In this scenario, the synthesis of heavy elements terminates at some maximum mass, above which transuranic nuclei undergo fission and increase the abundances of *r*-process elements at lower masses (*19*).

Fission fragments would reduce any variations in the initial abundances of *r*-process seed nuclei. Natural variations in conditions at nucleosynthesis sites would produce variations in the abundances, but fission fragment deposition could overcome those variations (*20*), leading to fixed relative abundances between the fission products (such as Ag and Eu). Fixed abundance ratios have previously been proposed as a potential signature of fission, according to theoretical calculations and a smaller sample of stars (*21*). Shown in Fig. 3 are theoretical models of neutron star merger dynamical ejecta (*13*), which produce similar log ε(Ag/Eu) ratios [defined as $\log_{10}(N_{Ag}/N_{Eu})$] when fission is included. Models that do not include a fission component near $A = 110$ (Fig. 3A) are sensitive to differences in initial conditions, such as neutron star mass, so predict variable log ε(Ag/Eu) ratios in the ejecta. We refer specifically to fission products near $A = 110$, because all these models include some level of fission in their calculations.

After a neutron star merger event, an accretion disk can temporarily form around the remnant object. Material ejected from this disk is expected to contain few or no nuclei that undergo fission (*22*), so additional ejecta from the disk could produce even larger variations between events. The neutron richness and relative amounts of ejecta from different parts of a neutron star merger event are not well constrained, so there is an unknown contribution of *r*-process synthesis in the disk to elements beyond Sr ($Z = 38$), such as Ag and Pd. We used previous dynamical ejecta simulations (*23*) to investigate the predictions of models that include a fission component for the mass-weighted log ε(Ag/Eu) ratios. We found that they are approximately constant when fission is included (Fig. 3B), which is consistent with the observed stellar ratios. We expect similar results for models of other potential *r*-process sites. For example, the predicted neutron richness of the ejecta of supernovae produced by magnetized and rapidly rotating stars (magneto-rotational supernovae) depends on the strength of the magnetic field (*24*). If fission occurs in any *r*-process site, it acts to reduce the variation in abundance ratios.

We show in Fig. 1 the baseline abundance pattern calculated above, which we assume contains minimal contributions from fission. To illustrate different fission contributions, we also show in Fig. 1 abundance patterns with additional transuranic fission fragments enhanced by factors of 1, 2, and 4 times the baseline (*13*). These enhancement factors were chosen to span the range of abundance excesses we found for elements with $44 \le Z \le 47$ and $63 \le Z \le 78$ in the stars with the highest levels of

[Eu/Fe]. We found that fission fragmentation could explain the elements with the largest observed excesses, including Pd, Ag, Gd, and Yb (*13*). We estimate that up to half of stars known to have $-3.0 \leq$ [Fe/H] ≤ -1.5 could have contributions from fission fragments (*13*). Because the stars in our sample are old, this rate of fission-affected abundances is a property of the dominant *r*-process site in the early Universe.

We conclude that fission fragments of transuranic nuclei can explain the correlations we found between elements with $44 \leq Z \leq 47$ and $63 \leq Z \leq 78$. We investigated whether the observed behavior could be reproduced by other known nucleosynthesis processes—including the weak or main *s*-process, intermediate neutron-capture process, or weak *r*-process—but found that it cannot (supplementary text). Nor can it be explained by the actinide-boost phenomenon, which has previously been observed in some *r*-process–enhanced stars (supplementary text and fig. S6).

Many of the radioactive, neutron-rich nuclei produced during the *r*-process are inaccessible to laboratory experiments, so theoretical models are necessary to estimate their properties by extrapolating from more stable isotopes. Models predict that many of these nuclei have asymmetric fission fragment distributions, with a lighter peak and a heavier peak (*13*, *25*). We propose that the lighter fragments likely contribute to the Ru, Rh, Pd, and Ag abundances in our dataset. Neutron-rich nuclei with mass numbers $99 \leq A \leq 110$, produced directly through fission, are expected to experience β decay until they become the observed elements (*26*). If we assume that the heavier fragments contribute to the Eu and heavier elements ($A > 150$) in our sample, then nuclei with $A > 260$ (110 + 150) were produced in the *r*-process.

REFERENCES AND NOTES

1. B. P. Abbott, *Phys. Rev. Lett.* **119**, 161101 (2017).
2. P. S. Cowperthwaite *et al.*, *Astrophys. J. Lett.* **848**, L17 (2017).
3. N. R. Tanvir *et al.*, *Astrophys. J. Lett.* **848**, L27 (2017).
4. M. M. Kasliwal *et al.*, *Science* **358**, 1559–1565 (2017).
5. M. W. Coughlin *et al.*, *Mon. Not. R. Astron. Soc.* **480**, 3871–3878 (2018).
6. M. R. Drout *et al.*, *Science* **358**, 1570–1574 (2017).
7. D. Kasen, B. Metzger, J. Barnes, E. Quataert, E. Ramirez-Ruiz, *Nature* **551**, 80–84 (2017).
8. D. Watson *et al.*, *Nature* **574**, 497–500 (2019).
9. I. U. Roederer *et al.*, *Astrophys. J. Suppl. Ser.* **260**, 27 (2022).
10. A. P. Ji, A. Frebel, A. Chiti, J. D. Simon, *Nature* **531**, 610–613 (2016).
11. I. U. Roederer, K. Hattori, M. Valluri, *Astron. J.* **156**, 179 (2018).
12. J. J. Cowan *et al.*, *Rev. Mod. Phys.* **93**, 015002 (2021).
13. Materials and methods are available as supplementary materials.
14. F. Montes *et al.*, *Astrophys. J.* **671**, 1685–1695 (2007).
15. Y.-Z. Qian, G. J. Wasserburg, *Astrophys. J.* **687**, 272–286 (2008).
16. S. Wanajo *et al.*, *Astrophys. J. Lett.* **789**, L39 (2014).
17. M. Eichler *et al.*, *Astrophys. J.* **808**, 30 (2015).
18. S. Goriely, G. Martínez Pinedo, *Nucl. Phys. A.* **944**, 158–176 (2015).
19. I. V. Panov, I. Y. Korneev, F.-K. Thielemann, *Astron. Lett.* **34**, 189–197 (2008).
20. T. M. Sprouse *et al.*, *Phys. Rev. C* **101**, 055803 (2020).
21. N. Vassh, M. R. Mumpower, G. C. McLaughlin, T. M. Sprouse, R. Surman, *Astrophys. J.* **896**, 28 (2020).
22. J. M. Miller *et al.*, *Phys. Rev. D* **100**, 023008 (2019).
23. D. Radice *et al.*, *Astrophys. J.* **869**, 130 (2018).
24. M. Reichert, M. Obergaulinger, M. Eichler, M. Á. Aloy, A. Arcones, *Mon. Not. R. Astron. Soc.* **501**, 5733–5745 (2021).
25. J.-F. Lemaître, S. Goriely, A. Bauswein, H.-T. Janka, *Phys. Rev. C* **103**, 025806 (2021).
26. J. Beun, G. C. McLaughlin, R. Surman, W. R. Hix, *Phys. Rev. C Nucl. Phys.* **77**, 035804 (2008).
27. N. Vassh, r-process abundances in neutron star merger dynamical ejecta given different fission yields. Zenodo (2023); https://doi.org/10.5281/zenodo.7127232.

ACKNOWLEDGMENTS

We thank A. Aprahamian, E. Bell, B. Côté, Y. Hirai, G. Mathews, C. Sneden, and M. Wiescher for comments on early versions of the manuscript. **Funding:** We acknowledge support from the US National Science Foundation grants AST 1716251 (to A.F.); AST 1815403 (to I.U.R.); AST 1815767 (to I.U.R.); AST 2205847 (to I.U.R.); OISE-1927130 (IReNA; The International Research Network for Nuclear Astrophysics) (to T.C.B., A.F., and T.T.H.); PHY 14-30152 (JINA-CEE; Joint Institute for Nuclear Astrophysics–Chemical Evolution of the Elements) (to I.U.R., E.M.H., M.R.M., R.S., T.C.B., R.E., and A.F.); and PHY 2020275 (to R.S.). R.S. acknowledges support from the US Department of Energy grants DE-FG02-95-ER40934 and DE-SC0018232. We acknowledge additional support from NASA grants 80NSSC21K0627 (Astrophysics Data Analysis Program; to IUR); HST-GO-15657 (to I.U.R., T.C.B., A.F., and V.M.P.); HST-GO-15951 (to I.U.R., T.C.B., R.E., A.F., T.T.H., and C.M.S.); and HST-HF2-51481.001 (National Hubble Fellowship Program) (to E.M.H.). N.V. acknowledges support from the Natural Sciences and Engineering Research Council of Canada. M.R.M. acknowledges support from Los Alamos National Laboratory's Directed Research and Development program 20200384ER. T.T.H. acknowledges support from grant VR 2021-05556 from the Swedish Research Council. V.M.P. acknowledges support from NOIRLab, which is managed by the Association of Universities for Research in Astronomy under a cooperative agreement with the US National Science Foundation. **Author contributions:** Conceptualization: I.U.R. Formal Analysis: I.U.R. and T.C.B. Methodology: I.U.R., N.V., E.M.H., M.R.M., and R.S. Investigation: I.U.R. and N.V. Visualization: I.U.R., N.V., E.M.H., M.R.M., R.S., J.J.C., and T.C.B. Writing – original draft: I.U.R. and N.V. Writing – review and editing: I.U.R., N.V., E.M.H., M.R.M., R.S., J.J.C., T.C.B., R.E., A.F., T.T.H., V.M.P., and C.M.S. **Competing interests:** The authors declare that they have no competing interests. **Data and materials availability:** Our compilation of stellar abundance data for the 42 stars in our sample is available in data S1. The nucleosynthesis yields (*21*) we used as input for our fission calculations are archived at Zenodo (*27*). Our derived correlations are quantified in table S1, and the empirical *r*-process baseline abundances are listed in tables S2 and S3. **License information:** Copyright © 2023 the authors, some rights reserved; exclusive licensee American Association for the Advancement of Science. No claim to original US government works. https://www.science.org/about/science-licenses-journal-article-reuse

SUPPLEMENTARY MATERIALS

science.org/doi/10.1126/science.adf1341
Materials and Methods
Supplementary Text
Figs. S1 to S6
Tables S1 to S3
References (*28*–*130*)
Data S1

Submitted 30 September 2022; accepted 6 November 2023
10.1126/science.adf1341

FISHERIES

Large females connect Atlantic cod spawning sites

Esben Moland Olsen[1,2]*, Ørjan Karlsen[3], Jon Egil Skjæraasen[3]

The Earth's ecosystems are increasingly deprived of large animals. Global simulations suggest that this downsizing of nature has serious consequences for biosphere functioning. However, the historical loss of large animals means that it is now often impossible to secure empirical data revealing their true ecological importance. We tracked 465 mature Atlantic cod (*Gadus morhua*) during their winter spawning season and show that large females (up to 114 centimeters in length), which are still found in mid-Norway, were characterized by more complex movement networks compared with smaller females. Large males were sparse but displayed similar movement patterns. Our finding implies that management programs promoting large fish will have positive impacts on population resilience by facilitating the continued use of a diversity of spawning habitats and the connectivity between them.

Current ecosystems are often characterized by an absence of large animals. This downsizing of nature is part of the ongoing biodiversity crisis and involves the loss of larger species as well as the larger individuals within a species, both of which can be linked to historic and ongoing harvesting practices by humans (*1*). Such signatures of human activity can be traced back for millennia (*1*–*3*), which makes it difficult to infer the potential role of larger animals in intact ecosystems. Model simulations suggest that larger animals could have major influences on population dynamics, ecosystem functioning, and resilience to environmental change (*4*), and therefore they should be the focus of biodiversity restoration programs (*5*). For instance, large predators may impose strong top-down control and prevent destabilizing grazer outbreaks (*6*) and even promote genetic diversity at lower trophic levels (*7*). Large animals could also play a particularly important role in connecting ecosystems (*8*).

Here, we describe the role of large female Atlantic cod (*Gadus morhua*), which are comparable in body size to those typically reported in archaeological studies of cod bones dating back at least one millennium (*2*, *9*), in connecting coastal spawning sites. The Atlantic cod is a potentially dominant predator in North Atlantic coastal ecosystems, and individuals can grow to reach a body length well beyond 1 m (*2*, *10*). However, cod is also a prized catch in fisheries, and many populations have been seriously overfished, in some cases collapsed to a state where recovery is expected to be slow or even unlikely (*11*). Size-selective and intense fishing has also changed the life history of this fish and caused major truncations of historic age and size distributions (*9*, *12*). Larger female cod are highly fecund and may spawn >10 million eggs during a season (*13*, *14*). Larger females also typically produce higher-quality eggs and could therefore play an important role in population replenishment compared with the smaller conspecifics typically observed in today's populations (*14*–*17*). Females are thought to visit male territories for pairing and spawning (*18*, *19*), and multiyear homing to specific spawning grounds is known (*20*–*22*). One study also detected individual movements among spawning sites (*23*). However, the environmental and phenotypic predictors of such behavior remain unclear. The potential for reproduction to happen at multiple locations clearly exists because female cod are batch spawners. Typically, portions of eggs are matured and spawned approximately every 2 to 4 days throughout the spawning season (*15*), with the number of batches increasing with maternal body size (*16*).

We used acoustic telemetry (*24*) to map how individual female cod move during the spawning season within a network of coastal spawning sites in mid-Norway (Fig. 1). The spawning sites were identified as traditional fishing grounds where cod will aggregate during spawning and by scientific surveys on cod egg and juvenile distributions (*25*). At the onset of three consecutive spawning seasons (2017 to 2019), a total of 213 mature female cod were captured, tagged, and tracked within these spawning habitats (table S1) (*26*). The female cod ranged in body size from 42 to 114 cm and from 0.8 to 15.1 kg. A total of 24% (n = 50) of the tracked females were 80 cm or larger (*27*).

Effects of cod body size on connectivity

Whereas the smaller females were typically detected at a few neighboring sites only, the larger females were more mobile and were detected at more, and sometimes distant, sites (Fig. 1). These basic observations were confirmed by statistical analyses using a network approach in which the acoustic receivers deployed at fixed sites represent the nodes, and fish movements between receiver sites represent links (*26*–*28*). In our study, each fish was assigned a connectivity score representing the number of specific links detected during the spawning season (*29*). A residency index (RI), defined as the number of days that a particular cod was detected within the telemetry array during the spawning season (*30*), was included as a covariate in the statistical models. This was to account for the fact that some individuals are likely to be less strongly associated with the chosen study area or moving outside the listening range of the receivers for parts of the study duration. In our case, 21% of the females (n = 45) were detected for ≥75% of the days during the spawning season, whereas 49% (n = 104) were detected for <25% of the spawning season days. After an initial filtering (*26*), data on all females across observed sizes and residencies were included in the same statistical model selection (table S2 and fig. S2). The most parsimonious model for predicting a connectivity score included an effect of body size, whereas alternative models excluding the effect of body size received very little support and were thus not considered for inference (table S2). A positive effect of body size on movement among sites was very clear for resident individuals having a stronger overall association to the area covered by the telemetry array, and it was less clear for individuals only detected for minor parts of the spawning period (Fig. 2). The model predicted a connectivity score of 3.3 links [95% confidence interval (CI) = 2.6 to 4.2] for resident females (RI = 0.75) with a body size of 50 cm, compared with a predicted connectivity score of 8.2 links (95% CI = 5.9 to 11.3) for large (100 cm) resident females (table S3). A 100% increase in female cod body size was thus associated with a 148% increase in connectivity score. There was also a moderately negative correlation between female cod body size and residency (Pearson correlation coefficient = −0.20, P = 0.004), indicating that large females tended to move beyond the spawning sites included in our study area. Note that this correlation between the two predictor variables did not introduce a serious issue of collinearity when interpreting model predictions (variance inflation factor = 1.04).

In a second step, we analyzed the tracked movements of the 252 male cod included in the study (table S1 and fig. S2). These males ranged in body size from 42 to 110 cm, although only 5% (n = 12) were 80 cm or larger. A total of 30% (n = 75) of the males had an RI of ≥0.75, whereas 38% (n = 95) had an RI <0.25. As for females, the larger males tended to have more extensive movement networks compared with smaller males (Fig. 1). For small and resident males (length = 50 cm, RI = 0.75), the model predicted a connectivity score of 3.4 links (95% CI = 2.8 to 4.1; Fig. 2). By comparison, for large and resident males (length = 100 cm,

[1]Institute of Marine Research; Flødevigen, Arendal 4817, Norway. [2]Centre for Coastal Research, Department of Natural Sciences, University of Agder; Kristiansand 4604, Norway. [3]Institute of Marine Research; Bergen 5817, Norway.
*Corresponding author. Email: esbenmo@imr.no

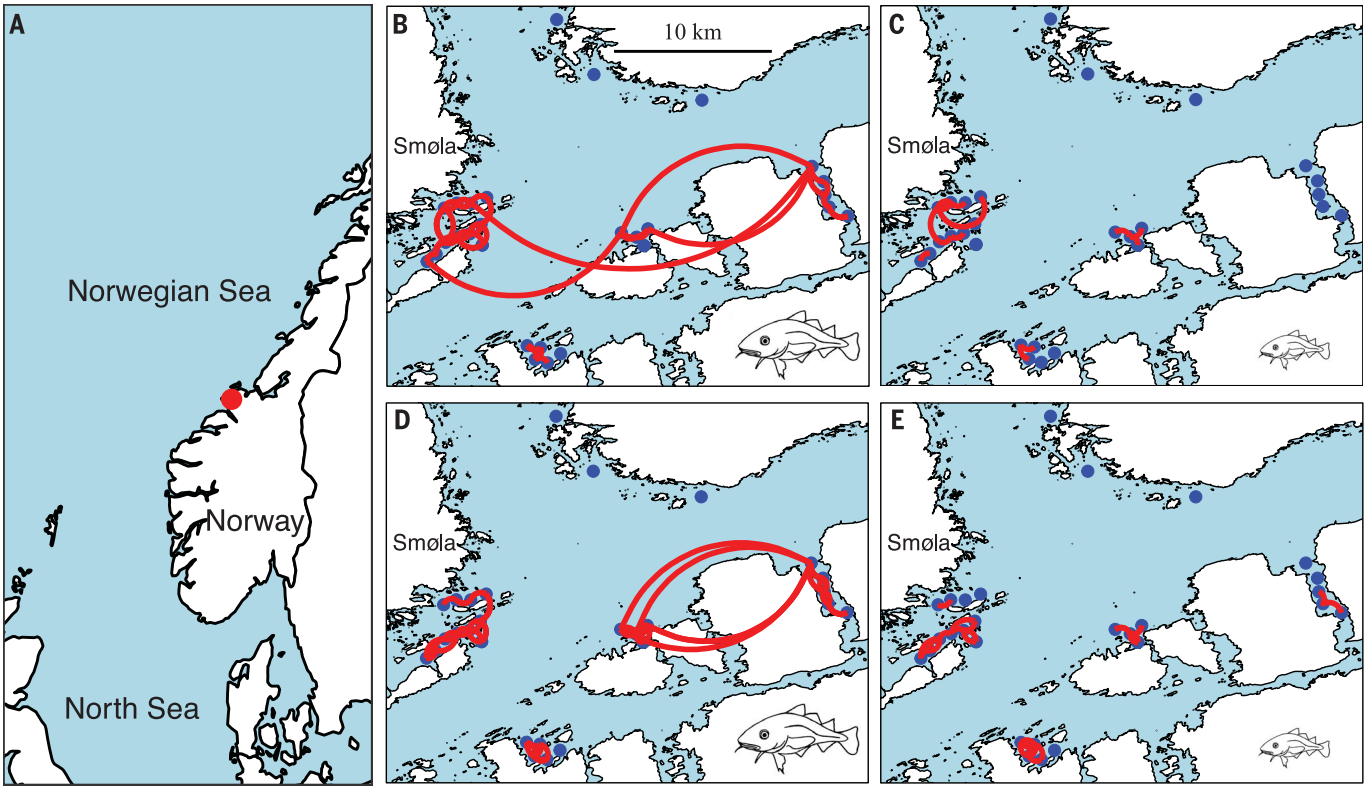

Fig. 1. Connectivity among Atlantic cod spawning sites. (**A**) Individual cod were tracked using acoustic telemetry in the Smøla region of northwestern Norway (red dot). (**B** to **E**) Red lines represent the combined movement networks (links) contributed by the 10 largest females [(B), 91 to 114 cm] versus the 10 smallest females [(C), 42 to 54 cm], the 10 largest males [(D), 79 to 110 cm], and the 10 smallest males [(E), 42 to 50 cm] present during at least 20% of the spawning season, inferred from detections stored by moored acoustic receivers (blue dots).

RI = 0.75), the predicted connectivity score was 7.1 links (95% CI = 5.5 to 9.3; Fig. 2 and table S3). In contrast to the females, there was no clear evidence that larger males were less resident than smaller males (Pearson correlation coefficient = −0.03, P = 0.61).

Cod tracked in this study were captured and released at five different locations within the study area (*26*). In a separate analysis, we examined the probability of cod moving among these more distant locations. In contrast to the finer-scale network analyses described above, each of the release locations refers to a larger area associated with multiple acoustic receivers (fig. S1). A total of 38% (n = 80) of the tagged female cod were detected at more than one release location during the spawning season. The probability of being detected at multiple release locations increased significantly with body length, estimated at 0.26 (SE = 0.06) for a 50-cm female compared with 0.56 (SE = 0.09) for a 100-cm female (table S4). A total of 27% (n = 68) of the tagged male cod were detected at multiple release locations. The probability of being detected at multiple release locations increased significantly with body length, estimated at 0.11 (SE = 0.03) for a 50-cm male compared with 0.83 (SE = 0.09) for a 100-cm male (table S4).

Connectivity and productivity of populations

Our study suggests that the contribution of large female fish to population productivity and stability may go beyond what is already recognized from their high-reproductive-energy output (*17*, *31*). From a population perspective, a network of spawning sites can indeed act to stabilize overall recruitment of broadcast spawning fish through a connectivity portfolio effect in which some sites are successful in some years, whereas other sites are successful in other years (*32*). Similarly, for Atlantic cod, the exact location where the pelagic eggs are spawned will influence in which habitats the juveniles eventually settle for growth and survival (*33*, *34*). There is evidence for spatial asynchrony in recruitment and juvenile growth of cod occurring on a scale of only a few tens of kilometers, including our study region (*25*, *35*), suggesting that what stands out as the most favorable spawning site varies temporally.

From the perspective of individual fitness and adaptive evolution, batch spawning by cod functions as part of a bet-hedging strategy that is advantageous in unpredictable environments such as the ocean (*31*). Recent modeling studies suggest that female cod can increase their fitness by spreading the risk across several reproductive events through a spawning season (*36*, *37*). Our study shows that this bet-hedging strategy likely involves spreading the risk in space as well as over time. Potential costs associated with such strategies might include reduced offspring quality in the batches spawned toward the end of the season (*16*). Furthermore, maximum body size can relate to life history traits such as growth, age and size at maturation, and longevity (*38*–*40*). Natural- and human-induced mortality and selection acting on these life history traits may therefore also influence the bet-hedging strategy and level of connectivity displayed by female cod. Linked to life histories, age and level of experience could also play a role in determining which spawning sites are visited and used by cod. There are many examples of social learning among fish (*41*), and it has been suggested that smaller cod may follow the lead of larger conspecifics on their migrations (*42*). Although age and size of cod are correlated, we do not know the exact age of the fish tracked in our study. The reason is that cod age is usually determined from seasonal growth zones in their otoliths (ear bones), and this technique requires that fish are euthanized.

Increased spatial bet hedging (i.e., spawning at multiple sites during a season) among larger females is, in our opinion, a parsimonious

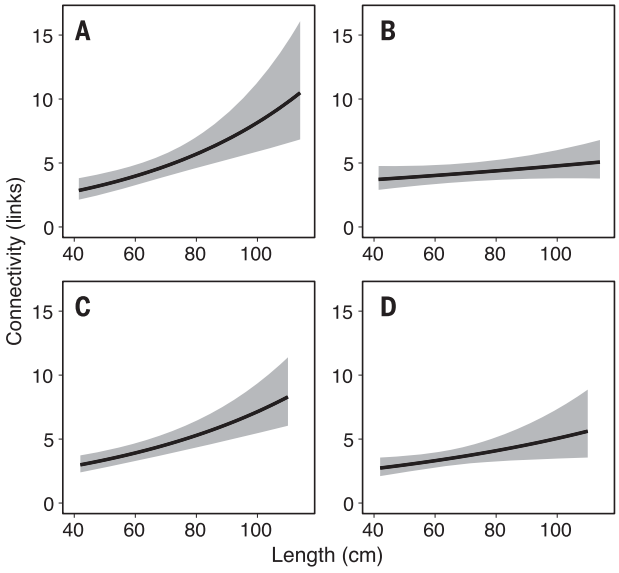

Fig. 2. Connectivity response to cod body size. Shown are Atlantic cod movement links as predicted for resident females [(**A**), RI = 0.75, detected 75% of spawning season], females with low residency [(**B**), RI = 0.25], resident males [(**C**), RI = 0.75], and males with low residency [(**D**), RI = 0.25] showing the mean prediction (black lines) and 95% CI (gray shading) within the range of observed body lengths. The structure of the underlying statistical models and associated parameter estimates are provided in tables S2 and S3.

interpretation of the observation that larger females tended to have a higher connectivity score. In addition, other mechanisms might also be playing out. Earlier studies on spawning cod in captivity have revealed a complex mating behavior in which male courtship displays and vocalizations precede pairing and spawning during characteristic "ventral mounts" (*18*, *43*). These behaviors potentially allow females to assess male quality and to exhibit nonrandom mate choice (*43*). Therefore, it is possible that larger females were more active in seeking out and assessing potential mates while not necessarily spawning during all visits to all locations. Their behavior would nevertheless add to the spatial complexity of the mating system.

The mating system of the cod has been described as a lek, in which at least some dominant males form clustered mating territories and engage in aggressive interactions toward other males, and male dominance is positively associated with body size (*18*, *43*). Our finding that male movements among sites was comparable to that of females suggests that the exact location of their territory is not fixed, but rather may shift during a spawning season, and that larger males are exploring more sites. Similarly, a study from the Gulf of Maine concluded that male cod probably do not remain faithful to a specific site when they form temporary individual territories (*19*).

Our study shows that downsizing of cod by fisheries, a widespread phenomenon, may contribute to substantially reduced connectivity and a fragmentation of spawning habitat use, which is likely to have a negative impact on the overall population productivity (*44*). At a larger spatial scale and population level, catch data from fisheries that were collected across one century suggest that depletion of old-growth age structure is associated with a long-term truncation of the spawning migration of Northeast Arctic cod (*45*) and a concurrent decline in recruitment success (*46*). Fisheries are predicted to disarm cod risk-spreading strategies by selecting against the largest individuals (*37*) and perhaps also by selecting directly against exploratory behaviors (*47*, *48*). Fishing may also effectively disrupt cod spawning aggregations (*49*). Furthermore, populations of Atlantic cod that are severely depleted by fisheries provide evidence for Allee effects in which the per capita population growth rate declines at low population densities, which will impair the ability of the population to recover should fishing pressure be reduced (*11*). Allee effects could be caused by mating systems becoming increasingly dysfunctional as population density decreases (*50*). In particular, cod spawning aggregations tend to be male dominated (*51*), so connectivity by large females may have an important influence on the operational sex ratio and therefore the functioning of the mating system at a given point in time.

We acknowledge that the importance of large individuals for population productivity, and thus the appropriate management and conservation measures, is still a matter of debate. For instance, Andersen *et al*. (*52*) pointed out that the largest female fish will usually be rare, so by accounting for typical fish demography, their expected impact on population replenishment will be limited. Similarly, a recent field study linking parents and offspring of a long-lived reef fish found that whereas reproductive success increased markedly with maternal body size, the numerous small mature females were responsible for a relatively large proportion of offspring replenishment even though the parents were sampled from protected sites within marine reserves (*53*). The latter study therefore advocated traditional minimum size limits as a useful management tool to complement the benefits offered by marine reserves. By contrast, another recent study concluded that for 32 of the world's largest fisheries, the typical assumption that egg production is simply proportional to spawner biomass will underestimate the contribution of larger individuals and, consequently, substantially overestimate the population reproductive potential (*54*). For northern cod found off Newfoundland and Labrador, the egg contribution from older females (≥10 years of age) has declined from an estimated 30 to 40% in the 1960s to a negligible level in more recent postcollapse years (*31*). To restore a safe operating space (*55*) for fisheries, strategies for maintaining the full potential of fish spawning habitat use, set by ecological and evolutionary constraints (*56*), should be integrated into management and conservation plans. To that end, a widely supported recommendation for rebuilding size and age structures is to implement slot-size limits in fisheries and fully protected marine reserves connected by seascape movement corridors (*44*, *54*, *57*, *58*).

Conclusions

The mobility expressed by large female cod during the spawning season shows that these fish can play an important role in facilitating connectivity among spawning habitats. Management actions directed toward rebuilding fish life histories could therefore be a meaningful way of improving overall population resilience. Even though the populations of cod in mid- and northern Norway are harvested and far from pristine (*59*), the continued existence of some very large individuals presents a valuable glimpse of what fully expressed and naturally adapted life histories may add in terms of movement behavior diversity. Unless the genetic basis for such life histories and behaviors has also been eroded by fisheries (*48*, *60*), our finding offers a positive perspective for conservation programs aimed at rebuilding more severely depleted populations and species.

REFERENCES AND NOTES

1. F. A. Smith, R. E. Elliott Smith, S. K. Lyons, J. L. Payne, *Science* **360**, 310–313 (2018).
2. J. B. C. Jackson *et al*., *Science* **293**, 629–637 (2001).
3. M. Sodeland *et al*., *Proc. Natl. Acad. Sci. U.S.A.* **119**, e2114904119 (2022).
4. B. J. Enquist, A. J. Abraham, M. B. J. Harfoot, Y. Malhi, C. E. Doughty, *Nat. Commun.* **11**, 699 (2020).
5. A. H. Schweiger, J.-C. Svenning, *People Nat.* **2**, 29–41 (2020).
6. R. L. Selden, S. D. Gaines, S. L. Hamilton, R. R. Warner, *Proc. Biol. Sci.* **284**, 20161936 (2017).
7. E. Foster *et al*., *Science* **374**, 333–336 (2021).
8. J. J. Williams, Y. P. Papastamatiou, J. E. Caselle, D. Bradley, D. M. P. Jacoby, *Proc. Biol. Sci.* **285**, 20172456 (2018).
9. J. H. Barrett, *J. Fish Biol.* **94**, 1033–1044 (2019).
10. K. T. Frank, B. Petrie, J. S. Choi, W. C. Leggett, *Science* **308**, 1621–1623 (2005).
11. J. A. Hutchings, *Proc. Biol. Sci.* **282**, 20150654 (2015).
12. E. M. Olsen *et al*., *Nature* **428**, 932–935 (2004).
13. E. Oosthuizen, N. Daan, *Neth. J. Sea Res.* **8**, 378–397 (1974).
14. G. Marteinsdottir, G. A. Begg, *Mar. Ecol. Prog. Ser.* **235**, 235–256 (2002).

15. O. S. Kjesbu, *J. Fish Biol.* **34**, 195–206 (1989).
16. N. E. Roney, R. A. Oomen, H. Knutsen, E. M. Olsen, J. A. Hutchings, *ICES J. Mar. Sci.* **75**, 1353–1361 (2018).
17. D. R. Barneche, D. R. Robertson, C. R. White, D. J. Marshall, *Science* **360**, 642–645 (2018).
18. V. M. Brawn, *Behaviour* **18**, 177–198 (1961).
19. M. J. Dean, W. S. Hoffman, D. R. Zemeckis, M. P. Armstrong, *ICES J. Mar. Sci.* **71**, 1474–1489 (2014).
20. D. Robichaud, G. A. Rose, *Can. J. Fish. Aquat. Sci.* **58**, 2325–2329 (2001).
21. J. E. Skjæraasen, J. J. Meager, Ø. Karlsen, J. A. Hutchings, A. Fernö, *ICES J. Mar. Sci.* **68**, 1472–1477 (2011).
22. D. R. Zemeckis, W. S. Hoffman, M. J. Dean, M. P. Armstrong, S. X. Cadrin, *ICES J. Mar. Sci.* **71**, 1356–1365 (2014).
23. D. R. Zemeckis *et al.*, *ICES J. Mar. Sci.* **74**, 1780–1796 (2017).
24. N. E. Hussey *et al.*, *Science* **348**, 1255642 (2015).
25. K. Dunlop *et al.*, *Estuar. Coast. Shelf Sci.* **279**, 108111 (2022).
26. Materials and methods are available as supplementary materials.
27. E. M. Olsen, Ø. Karlsen, J. E. Skjæraasen, Data for: Large females connect Atlantic cod spawning sites, Dryad (2023); https://doi.org/10.5061/dryad.tb2rbp074.
28. D. M. P. Jacoby, E. J. Brooks, D. P. Croft, D. W. Sims, *Methods Ecol. Evol.* **3**, 574–583 (2012).
29. P. Landi, H. O. Minoarivelo, Å. Brännström, U. Dieckmann, *Popul. Ecol.* **60**, 319–345 (2018).
30. M. Espinoza, E. J. Lédée, C. A. Simpfendorfer, A. J. Tobin, M. R. Heupel, *Ecol. Appl.* **25**, 2101–2118 (2015).
31. J. A. Hutchings, R. W. Rangeley, *Can. J. Zool.* **89**, 386–400 (2011).
32. H. B. Harrison, M. Bode, D. H. Williamson, M. L. Berumen, G. P. Jones, *Proc. Natl. Acad. Sci. U.S.A.* **117**, 25595–25600 (2020).
33. S. H. Espeland, J. Albretsen, E. M. Olsen, T. Bodvin, *ICES J. Mar. Sci.* **72**, 2578–2589 (2015).
34. M. B. O. Huserbråten, E. Moland, J. Albretsen, *Prog. Oceanogr.* **167**, 116–124 (2018).
35. L. A. Rogers, G. O. Storvik, H. Knutsen, E. M. Olsen, N. C. Stenseth, *J. Anim. Ecol.* **86**, 888–898 (2017).
36. S. Hočevar, J. A. Hutchings, A. Kuparinen, *Evol. Appl.* **14**, 1980–1992 (2021).
37. S. Hočevar, J. A. Hutchings, A. Kuparinen, *Proc. Biol. Sci.* **289**, 20221172 (2022).
38. A. Folkvord *et al.*, *Can. J. Fish. Aquat. Sci.* **71**, 1106–1112 (2014).
39. J. A. Hutchings, *A Primer of Life Histories: Ecology, Evolution, and Application* (Oxford Univ. Press, 2021).
40. A. Kuparinen, E. Yeung, J. A. Hutchings, *Acta Oecol.* **119**, 103917 (2023).
41. C. Brown, K. N. Laland, *Fish Fish.* **4**, 280–288 (2003).
42. G. A. Rose, *Nature* **366**, 458–461 (1993).
43. J. A. Hutchings, T. D. Bishop, C. R. McGregor-Shaw, *Can. J. Fish. Aquat. Sci.* **56**, 97–104 (1999).
44. S. A. Berkeley, M. A. Hixon, R. J. Larson, M. S. Love, *Fisheries (Bethesda, Md.)* **29**, 23–32 (2004).
45. A. F. Opdal, C. Jørgensen, *Glob. Chang. Biol.* **21**, 1521–1530 (2015).
46. J. Ohlberger, Ø. Langangen, L. C. Stige, *Ecol. Appl.* **32**, e2614 (2022).
47. E. M. Olsen, M. R. Heupel, C. A. Simpfendorfer, E. Moland, *Ecol. Evol.* **2**, 1549–1562 (2012).
48. S. Uusi-Heikkilä *et al.*, *Evol. Appl.* **8**, 597–620 (2015).
49. M. J. Dean, W. S. Hoffman, M. P. Armstrong, *N. Am. J. Fish. Manage.* **32**, 124–134 (2012).
50. S. Rowe, J. A. Hutchings, *Trends Ecol. Evol.* **18**, 567–572 (2003).
51. M. J. Morgan, E. A. Trippel, *ICES J. Mar. Sci.* **53**, 820–826 (1996).
52. K. H. Andersen, N. S. Jacobsen, P. D. van Denderen, *Can. J. Fish. Aquat. Sci.* **76**, 347–349 (2019).
53. C. P. Lavin, G. P. Jones, D. H. Williamson, H. B. Harrison, *Proc. Biol. Sci.* **288**, 20202714 (2021).
54. D. J. Marshall, M. Bode, M. Mangel, R. Arlinghaus, E. J. Dick, *Proc. Natl. Acad. Sci. U.S.A.* **118**, e2100695118 (2021).
55. J. Rockström *et al.*, *Nature* **461**, 472–475 (2009).
56. L. Ciannelli, K. Bailey, E. M. Olsen, *ICES J. Mar. Sci.* **72**, 285–296 (2015).
57. D. J. Marshall, S. Gaines, R. Warner, D. R. Barneche, M. Bode, *Front. Ecol. Environ.* **17**, 407–413 (2019).
58. K. Grorud-Colvert *et al.*, *Science* **373**, eabf0861 (2021).
59. K. M. Norderhaug, K. Nedreaas, M. Huserbråten, E. Moland, *Ambio* **50**, 163–173 (2021).
60. D. O. Conover, S. B. Munch, *Science* **297**, 94–96 (2002).

ACKNOWLEDGMENTS

We thank K. M. E. Schrøder, D. Lien, and E. Kanestrøm for invaluable help with sampling of fish and telemetry array maintenance; Ø. Langangen for advice on the statistical analyses; O. G. Sørøy at the MOWI seafood company for help with logistics during fish tagging operations; and two anonymous reviewers for insightful suggestions and comments on the original version of the manuscript. **Funding:** This work was supported by the Research Council of Norway (grant 294926 to E.M.O.) and the Norwegian Seafood Research Fund (grant 901230 to J.E.S.). **Author contributions:** Conceptualization: E.M.O., Ø.K., J.E.S.; Funding acquisition: E.M.O., Ø.K., J.E.S.; Investigation: E.M.O., Ø.K., J.E.S.; Methodology: E.M.O., Ø.K., J.E.S.; Project administration: J.E.S.; Visualization: E.M.O.; Writing – original draft: E.M.O., Ø.K., J.E.S.; Writing – review and editing: E.M.O., Ø.K., J.E.S. **Competing interests:** The authors declare no competing interests. **Data and materials availability:** All data and code used in the analyses are publicly available at Dryad (*27*). **License information:** Copyright © 2023 the authors, some rights reserved; exclusive licensee American Association for the Advancement of Science. No claim to original US government works. https://www.science.org/about/science-licenses-journal-article-reuse

SUPPLEMENTARY MATERIALS

science.org/doi/10.1126/science.adi1826
Materials and Methods
Figs. S1 to S3
Tables S1 to S4
References (*61–74*)
MDAR Reproducibility Checklist

Submitted 8 April 2023; accepted 31 October 2023
10.1126/science.adi1826

CELL BIOLOGY

Structural mechanism of outer kinetochore Dam1-Ndc80 complex assembly on microtubules

Kyle W. Muir*, Christopher Batters, Tom Dendooven, Jing Yang, Ziguo Zhang, Alister Burt, David Barford*

Kinetochores couple chromosomes to the mitotic spindle to segregate the genome during cell division. An error correction mechanism drives the turnover of kinetochore-microtubule attachments until biorientation is achieved. The structural basis for how kinetochore-mediated chromosome segregation is accomplished and regulated remains an outstanding question. In this work, we describe the cryo–electron microscopy structure of the budding yeast outer kinetochore Ndc80 and Dam1 ring complexes assembled onto microtubules. Complex assembly occurs through multiple interfaces, and a staple within Dam1 aids ring assembly. Perturbation of key interfaces suppresses yeast viability. Force-rupture assays indicated that this is a consequence of impaired kinetochore-microtubule attachment. The presence of error correction phosphorylation sites at Ndc80-Dam1 ring complex interfaces and the Dam1 staple explains how kinetochore-microtubule attachments are destabilized and reset.

Chromosome segregation is essential for the equal propagation of genetic information from parent to daughter cells, achieved through kinetochore-mediated coupling of sister chromatids to the mitotic spindle (*1*). Kinetochores are large macromolecular assemblies delineated into the inner centromere–binding and outer microtubule–binding complexes. The outer kinetochore couples the inner kinetochore CCAN (constitutive centromere associated network) to microtubules through three conserved complexes that comprise the Knl1-MIND-Ndc80 (KMN) network (*2*). MIND interconnects CCAN with both the Ndc80 and Knl1 complexes (Ndc80c and Knl1c). Knl1c functions in the spindle-assembly checkpoint (SAC) (*3*), whereas Ndc80c, a heterotetramer of Ndc80, Nuf2, Spc24, and Spc25, is the major microtubule-binding component of KMN.

Outer kinetochore attachment to microtubules is augmented by additional essential microtubule-dependent kinetochore components. Many fungi, including *Saccharomyces cerevisiae*, use the 10-subunit Dam1 complex (Dam1c), which self-assembles into a large ring around microtubules (*4*–*9*), whereas most metazoans contain the Ska complex (*2*). Although the Ndc80c and Dam1 or Ska complexes bind microtubules independently, full function and interaction strength requires both modules (*10*–*17*). A central unresolved question is how these complexes coordinately bind and track the dynamic microtubule plus end to ensure that kinetochores do not detach from the spindle (*10*, *12*, *15*, *16*, *18*, *19*). Because initial kinetochore-microtubule attachments are not necessarily bioriented, an error correction (EC) pathway, governed by antagonistic outer kinetochore phosphorylation by Aurora B kinase, ensures that erroneous attachments are weakened and reset (*20*–*24*). As kinetochores come under tension, a feature of biorientation, the outer kinetochore is dephosphorylated, attachments are stabilized, and the SAC is inactivated to trigger anaphase (*20*, *21*, *23*, *25*–*31*).

In yeast, centromere-localized Aurora B kinase phosphorylates Dam1c to suppress ring formation (*15*, *17*, *32*) and block its association with Ndc80c (*10*, *11*, *28*, *33*), which results in weakened end-on attachment (*34*, *35*). Phosphorylation of a second set of targets within the unstructured N terminus of Ndc80 ($Ndc80^{N\text{-}tail}$) also contributes to EC (*14*, *35*, *36*).

To obtain deeper mechanistic insight into Dam1c:Ndc80c (outer $kinetochore^{Dam1c:Ndc80c}$) assembly on microtubules and its regulation by EC, we reconstituted and determined the cryo–electron microscopy (cryo-EM) structure of the budding yeast outer $kinetochore^{Dam1c:Ndc80c}$–microtubule complex. We observe multiple contacts between Ndc80c and Dam1c. An N-terminal staple region of the Dam1 subunit ($Dam1^{Staple}$) binds the interprotomer interface of the Dam1c ring. The presence of embedded EC phosphorylation sites within the $Dam1^{Staple}$ and Ndc80c-Dam1c interfaces indicates why EC would drive both Dam1c ring disassembly and destabilize kinetochore-microtubule attachments.

Overall architecture of the yeast outer $kinetochore^{Dam1c:Ndc80c}$ bound to microtubules

Outer $kinetochore^{Dam1c:Ndc80c}$–microtubule complexes were assembled on cryo-EM grids by stepwise addition of taxol-stabilized microtubules, Ndc80c, and Dam1c (Fig. 1A and fig. S1A). Cryo–electron micrographs showed microtubules decorated with Dam1c rings ($Dam1c^{Ring}$) and Ndc80c fibrils (Fig. 1A). In the resul[illegible] consensus cryo-EM map, we observed a [illegible]dem organization of Ndc80c coiled-coil spokes emerging from the microtubule surface between diffuse Dam1c rings (Fig. 1A and fig. S2, A and B).

The intermediate resolution of the cryo-EM map and the incompatible symmetries between the 16 protomers of the $Dam1c^{Ring}$ and the 13 protofilament microtubule necessitated a divide and consolidate strategy for structure determination (materials and methods). This approach generated reconstructions of Ndc80c and a dimer of Dam1c protomers at resolutions of 3.5 Å and 3.15 Å, respectively (Fig. 1, B to D; fig. S2, B and C; fig. S3A; fig. S4; and table S1). Cryo-EM density was not visible for the Spc24:Spc25 subunits of Ndc80c. The coiled coils of Ndc80c emanate from the calponin homology (CH) domains of the Ndc80 and Nuf2 subunits ($Ndc80^{CH}$ and $Nuf2^{CH}$) at the surface of the microtubule to fold across the outer surface of the $Dam1c^{Ring}$. Here, we observed prominent density corresponding to the coiled-coil central region of the Ndc80:Nuf2 subunits (Fig. 1, C and D, and fig. S2C). To obtain a complete model of the complex, we generated a composite map that was composed of two copies of the $kinetochore^{Dam1c:Ndc80c}$ protomer unit by rigid-body fitting of the separate volumes into the consensus outer $kinetochore^{Dam1c:Ndc80c}$–microtubule cryo-EM map (Fig. 1D). We then folded the Ndc80:Nuf2 coils in the $Dam1c^{Protomer}$ component of the map until they were in proximity, with the coils emanating from the $Ndc80c^{CH}$ domains, and melded the models to generate a structural model of the yeast $kinetochore^{Dam1c:Ndc80c}$-microtubule complex (Fig. 1, D and E; table S3; and movie S1).

Structure and regulation of $Dam1c^{Ring}$ assembly by a Dam1 staple peptide

Two- and three-dimensional classification showed that the $Dam1c^{Ring}$ is tilted at variable angles relative to the microtubule (fig. S2, B and C, top left panel), similar to $Dam1c^{Ring}$ alone (*8*). Consistently, the tubulin surface beneath the ring is unoccupied except for diffuse density emerging from the α/β tubulin C-terminal tails (fig. S3B), which potentially represents the acidic E-hooks of α and β tubulin that enhance microtubule-Dam1c interactions (*5*, *8*). The $Dam1c^{Ring}$-microtubule interface potentially involves flexible participants, as supported by biochemical and cross-linking mass spectrometry data (*7*, *11*, *32*, *37*).

$Dam1c^{Ring}$ assembly follows a shoulder-to-shoulder configuration (*7*, *38*) (Fig. 1, C and E, and Fig. 2A). The interprotomer junctions are similar to the cryo-EM structure of a truncated *Chaetomium thermophilum* $Dam1c^{Ring}$ (*38*). In this structure, the map resolution is limited to 4.5 Å. By contrast, here we find that in all 10 subunits of *S. cerevisiae* Dam1c, most side chains within the globular core of the complex

MRC Laboratory of Molecular Biology, Cambridge CB2 0QH, UK.
*Corresponding author. Email: kmuir@mrc-lmb.cam.ac.uk (K.W.M.); dbarford@mrc-lmb.cam.ac.uk (D.B.)

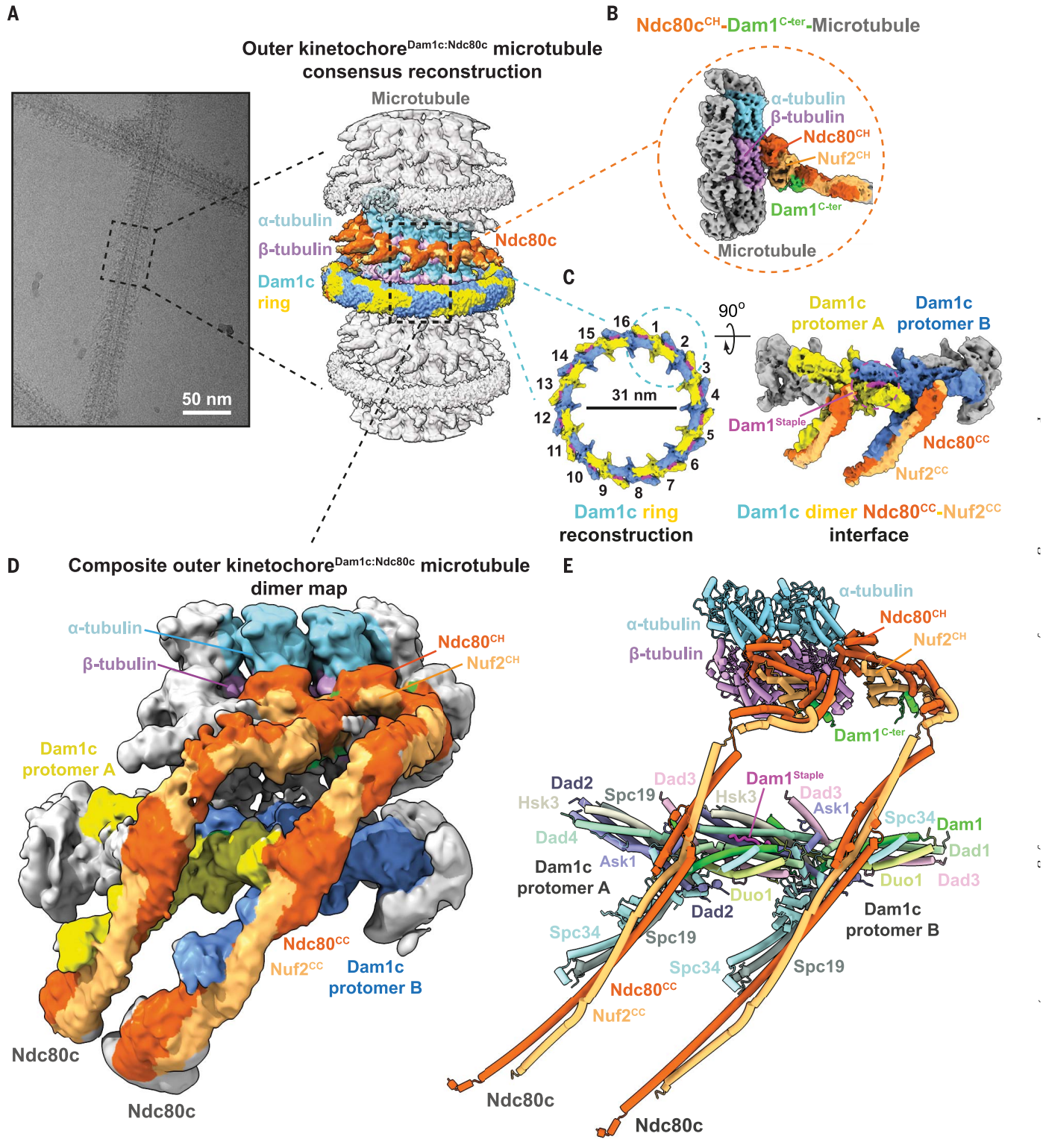

Fig. 1. Yeast outer kinetochore$^{Dam1c:Ndc80c}$ complexes assemble through multiple interfaces to tandemly decorate the microtubule. (**A**) Representative cryo-EM micrograph and corresponding consensus reconstruction of the outer kinetochore$^{Dam1c:Ndc80c}$-microtubule complex. (**B**) Cryo-EM density map of the Ndc80c^{CH}-Dam1$^{C\text{-}ter}$-microtubule reconstruction. (**C**) Cryo-EM reconstruction of the 16-subunit Dam1c^{Ring} and symmetry-expanded Dam1c dimer Ndc80^{CC}:Nuf2^{CC} interface. (**D** and **E**) Composite cryo-EM map (D) and corresponding atomic model (E) of a yeast outer kinetochore$^{Dam1c:Ndc80c}$–microtubule dimer (defined as two copies of α/β tubulin–Dam1c:Ndc80c). Dam1c^{Ring} augments outer kinetochore$^{Dam1c:Ndc80c}$ tracking of both polymerizing and depolymerizing microtubule tips (*11*, *15*, *16*). In the former, the structure suggests that Ndc80c is borne along as a passenger on the outer surface of the ring and need not necessarily bind the microtubule. In the latter, the complex is directly pushed by the ring.

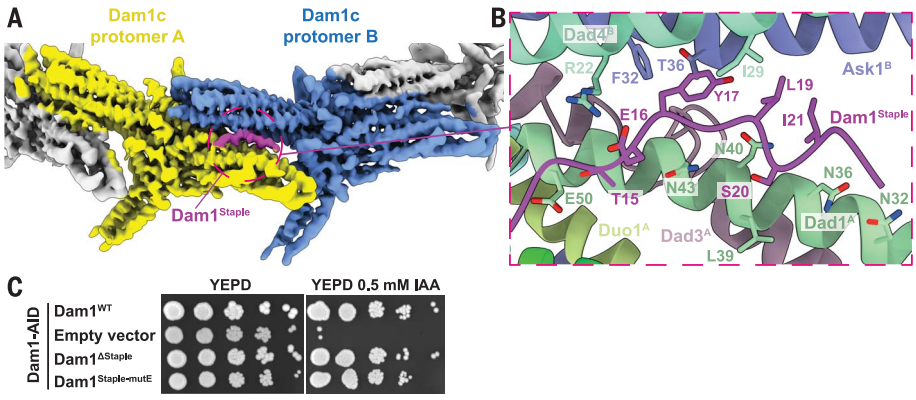

Fig. 2. Dam1 N terminus forms a staple to stabilize Dam1c^{Ring} assembly that is negatively regulated by Aurora B kinase. (**A**) Structure of the Dam1c protomer dimer interface shows a staple density (purple) between protomer A (yellow) and protomer B (blue). (**B**) Details of amino acid contacts at the Dam1c^{Protomer} dimer-Dam1^{Staple} interface. Ser^{20} is an Aurora B kinase phosphorylation site and is oriented toward the Dad1 subunit of protomer A. Dam1^{Staple} residues 13 to 23 are visible in cryo-EM density, whereas residues 1 to 12 and the connectivity to residue 55 of the remainder of Dam1 are not resolved. Mutation of Dad1 Glu^{50} to Asp impairs ring formation (*41*). (**C**) Dam1 auxin-depletion assays. Cells grown on YEPD agar and YEPD agar that contained 0.5 mM IAA are shown for each strain. Dam1$^{\Delta Staple}$, Dam1 mutant with residues 1 to 26 deleted; Dam1$^{Staple\text{-}mutE}$, Dam1 mutant with Y^{17}E, L^{19}E, and I^{21}E; IAA, indole-3-acetic acid; YEPD, yeast extract peptone dextrose. Single-letter abbreviations for the amino acid residues are as follows: A, Ala; C, Cys; D, Asp; E, Glu; F, Phe; G, Gly; H, His; I, Ile; K, Lys; L, Leu; M, Met; N, Asn; P, Pro; Q, Gln; R, Arg; S, Ser; T, Thr; V, Val; W, Trp; and Y, Tyr.

are resolved (fig. S3C). Additionally, we resolved a staple density located at the inter-Dam1c^{Protomer} interfaces that was truncated from *C. thermophilum* Dam1 (Fig. 2, A and B) (*38*). The Dam1^{Staple} comprises the N terminus (residues 1 to 26) of the Dam1 subunit. The staple bridges the Dam1 and Dad1 subunits of Dam1c^{ProtomerA} with the Ask1 and Dad4 subunits of Dam1c^{ProtomerB}. Contact with Dam1c^{ProtomerA} is through hydrogen bonding between Dam1^{Staple} residues Thr^{15} and Ser^{20} and Dad1^{A} (Fig. 2B). Binding to Dam1c^{ProtomerB} is mediated by a salt bridge between Arg^{22} of Dad4^{B} and Glu^{16} of Dam1^{Staple}, as well as packing of Dam1^{Staple} residues Tyr^{17}, Leu^{19}, and Ile^{21} against Ask1^{B} and Dad4^{B} (Fig. 2B). To test this interface in vivo, we performed rescue assays in an *S. cerevisiae* strain with an auxin-inducible degron (AID) tag inserted at the C terminus of the endogenous copy of Dam1 (table S2). We then integrated a series of Dam1 variants at the *LEU* locus. Cells grown on auxin with wild-type Dam1 as the ectopic copy rescued loss of endogenous Dam1, whereas cells that carried an empty vector failed to grow (Fig. 2C and fig. S1, B and C). Cells that carried either a Dam1$^{\Delta Staple}$ or Dam1$^{Staple\text{-}mutE}$ (Dam1 Tyr^{17}, Leu^{19}, and Ile^{21} to Glu) mutant were viable in the absence of wild-type Dam1 (Fig. 2C). In the cell, Dam1c^{Ring} assembly may be augmented by additional mechanisms that compensate for mutagenesis of the Dam1^{Staple} (*39*, *40*).

Ser^{20} of Dam1^{Staple}, a target of Aurora B kinase (*28*), is buried at the interprotomer interface close to Leu^{39}, Asn^{40}, and Asn^{43} of the Dad1 subunit of Dam1c^{ProtomerA} (Fig. 2B). Phosphorylation of Ser^{20} would cause steric hindrance and charge repulsion that would disrupt Dam1^{Staple} binding. Phosphorylation of Ser^{20} destabilizes Dam1c^{Ring} in vitro (*17*, *32*) and increases its diffusion on microtubules (*12*, *15*). Similarly, mutations at the Dam1^{Staple}-binding site (Fig. 2B) impair ring formation on microtubules (*41*). However, these mutations rescue loss of Aurora B kinase activity, presumably by driving increased kinetochore-microtubule attachment turnover (*41*, *42*). Consistent with the notion that Dam1^{Staple} regulates ring assembly, we found that the assembly of higher-order Dam1c is substantially impaired when the staple is deleted (fig. S1F and fig. S3, D and E).

Structure of the Ndc80c-microtubule interface

The Ndc80c microtubule-binding domain forms a club-like structure that is composed of its two CH domains (Fig. 1, B and E, and Fig. 3A). The underside of the club binds the α/β tubulin interface along the lateral axis of the protofilament, whereas the coiled-coil shaft of Ndc80:Nuf2 projects outward orthogonal to the CH domains. In contrast to human and *Caenorhabditis elegans*, in which Ndc80c binds to every lateral α/β tubulin interface (*43*, *44*), the yeast complex binds only at the α/β site, a mode of binding that is independent of Dam1c (fig. S5, A to C). No EM density is visible for the disordered Ndc80$^{N\text{-}tail}$, and therefore, we cannot account for how it contributes to kinetochore-microtubule attachments.

Binding of the Dam1 C terminus to Ndc80c is essential and is regulated by EC

We observed additional cryo-EM density at the base of the Ndc80:Nuf2 coiled coils that emerge from Ndc80c^{CH} (Fig. 1B and Fig. 3A). Although the additional density was not sufficiently well resolved to model de novo, cross-linking mass spectrometry and mutagenesis experiments suggest that this region of Ndc80c, called the helical hairpin (fig. S5A), interacts with Dam1c (*13*) through the Dam1 C terminus (*11*, *14*). We used AlphaFold2 to predict the structure of Ndc80:Nuf2 together with residues 201 to 343 of Dam1. The resulting prediction was a tripartite complex consistent with a subsequently solved crystal structure (*45*). Two short segments from the C terminus of Dam1 (Dam1$^{C\text{-}ter}$) dock onto the Ndc80c^{CH} domains. One of these (residues 251 to 272) nestles in an amphipathic pocket at the base of the Ndc80:Nuf2 coiled coils (Fig. 3B and fig. S5D), and another (residues 287 to 301) snakes around the back face of Ndc80c^{CH} (Fig. 3C and fig. S5E). Dam1 residues Ile^{258}, Leu^{259}, and Ile^{262} pack against Ndc80c^{CH} (Fig. 3B, upper panel). We introduced Dam1 mutants that bear triple alanine or glutamate substitution of these residues as ectopic copies into our Dam1-AID strain (Dam1$^{C\text{-}ter\text{-}mutA}$ and Dam1$^{C\text{-}ter\text{-}mutE}$, respectively) (fig. S1, B and C, and table S2). Upon depletion of endogenous Dam1, growth was severely impaired (Fig. 3D). Therefore, the integrity of the Dam1$^{C\text{-}ter}$-Ndc80c^{CH} interface is essential for proper kinetochore function and yeast cell viability.

During EC, residues at the Dam1$^{C\text{-}ter}$-Ndc80c^{CH} interface are phosphorylated by Aurora B kinase, specifically Dam1 Ser^{257}, Ser^{265}, and Ser^{292} (Fig. 3B, lower panel, and Fig. 3C, right panel) (*27*, *28*). Phosphorylation of these residues in vitro results in decreased strength and lifetime of outer kinetochore$^{Dam1c:Ndc80c}$ binding to microtubules (*10*, *11*), and phosphomimetics suppress impaired Aurora B kinase activity in vivo (*28*). Ser^{257} is oriented toward negatively charged residues on an α helix of Ndc80c (Fig. 3B, lower panel). Phosphorylation of Ser^{257} would be incompatible with binding of Dam1$^{C\text{-}ter}$ to Ndc80c^{CH}. Similarly, phosphorylated Ser^{265} and Ser^{292} would also be oriented toward negatively charged surfaces on Ndc80c (Fig. 3C, right panel). EC phosphorylation would thus weaken co-assembly of the outer kinetochore.

The central coiled-coil domain of Ndc80:Nuf2 folds across the outer rim of Dam1c

The Ndc80:Nuf2 central coiled coil docks near the Dam1c^{Protomer} interface against a pair of β strands from Spc34 that contain the EC target residue Thr^{199} (Fig. 3, E and F, and fig. S5F, left panel) and runs parallel with the C-terminal coiled coils of Spc34 and Spc19 (Fig. 3, E and G, and fig. S5F, right panel). Our structure is consistent with previous cross-linking mass spectrometry and insertion mutagenesis experiments, which indicate that the central segment of the Ndc80:Nuf2 coiled coils proximal to the conserved Ndc80 loop directly interacts with the

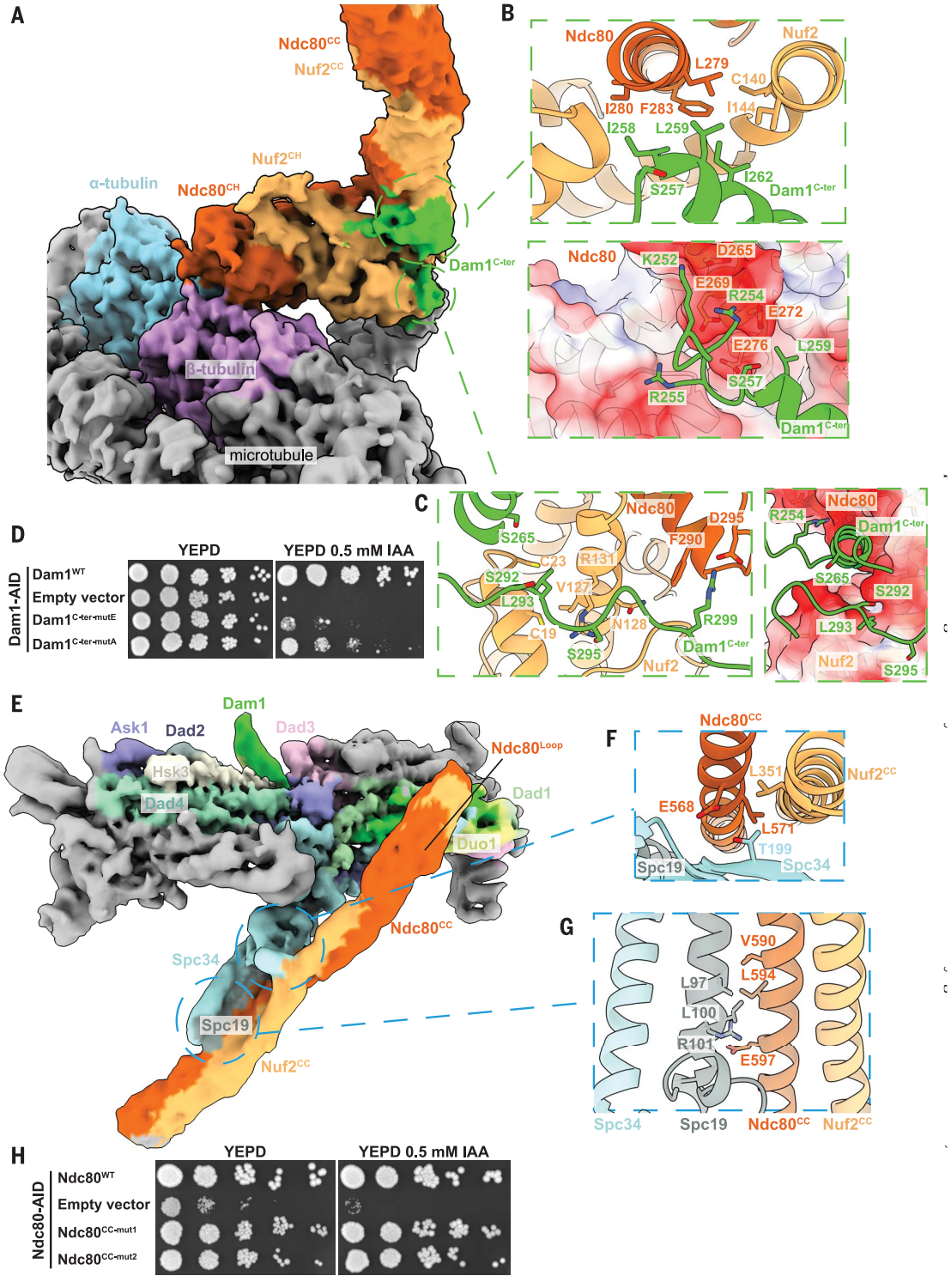

Fig. 3. The Dam1 and Ndc80 complexes associate through a microtubule-proximal interface and the outer surface of the Dam1c^{Ring}. (**A**) Cryo-EM reconstruction of the Ndc80c-Dam1c-microtubule interface. (**B** and **C**) Rigid-body placement of an AlphaFold2 prediction of the Ndc80c^{CH}-Dam1$^{C\text{-}ter}$ interface into cryo-EM density shows: (B) Dam1$^{C\text{-}ter}$ α helix packs against a hydrophobic interface generated by the Ndc80:Nuf2 coiled coil emerging from the Ndc80c^{CH} domain (upper panel), with surface charges on Ndc80c^{CH} and position of the Ser^{257} EC site on Dam1$^{C\text{-}ter}$ in the lower panel. (C) Dam1$^{C\text{-}ter}$ interface on the back side of the Ndc80c^{CH} (left panel) and positions of residues targeted by EC and surface charges (right panel). Ser^{265} and Ser^{292} are oriented toward negative charges that would drive dissociation of Dam1$^{C\text{-}ter}$ from Ndc80^{CH} during EC. (**D**) Dam1 rescue assays on auxin. Cells grown on YEPD agar and YEPD agar containing 0.5 mM IAA are shown for each strain. Dam1$^{C\text{-}ter\text{-}mutE}$, Dam1 mutant with I^{258}E, L^{259}E, and I^{262}E; Dam1$^{C\text{-}ter\text{-}mutA}$, Dam1 mutant with I^{258}A, L^{259}A, and I^{262}A. (**E**) Cryo-EM reconstruction of the Dam1c monomer–Ndc80:Nuf2 coiled-coil interface. The position of the Ndc80^{Loop} is highlighted in fig. S5D. (**F** and **G**) Rigid-body placement of an AlphaFold2 prediction of the Ndc80^{CC}:Nuf2^{CC} into cryo-EM density, together with our experimental model of Dam1c, shows the Ndc80^{CC}:Nuf2^{CC} binds Dam1c at two interfaces shown as insets: (F) Ndc80^{CC}:Nuf2^{CC} docks against a β-strand on Spc34, with the EC target site Thr^{199} oriented toward Ndc80c. (G) Spc19:Spc34 coiled coils pack against Ndc80^{CC}:Nuf2^{CC} by means of residues in Spc19 and Ndc80. (**H**) Ndc80 auxin-depletion assays. Cells grown on YEPD agar and YEPD agar that contained 0.5 mM IAA are shown for each strain. Ndc80$^{CC\text{-}mut1}$, Ndc80 coiled-coil mutant1 with E^{568}A, V^{590}A, L^{594}A, and E^{597}A; Ndc80$^{CC\text{-}mut2}$, Ndc80 coiled-coil mutant2 with E^{568}R, V^{590}W, L^{594}E, and E^{597}R.

Spc34:Spc19 C termini (*11*, *13*). After focused classification and flexible refinement, a distinct interruption in the coiled coil became apparent (Fig. 3E). This interruption corresponds to the Ndc80 loop (Ndc80^{Loop}), which enables us to infer the amino acid register of an AlphaFold2 prediction that comprises the remaining coiled coil (fig. S5G). We mapped sequence conservation onto the structure and observed that interfacial residues are well conserved, whereas outward-facing residues are not (fig. S5H).

To test the impact of mutating this interface in vivo, we generated a yeast strain in which the endogenous copy of Ndc80 bore a C-terminal AID tag (fig. S1, D and E, and table S2). Mutation of a series of four conserved interfacial residues on Ndc80 (Ndc80$^{CC\text{-}mut1}$ and Ndc80$^{CC\text{-}mut2}$)

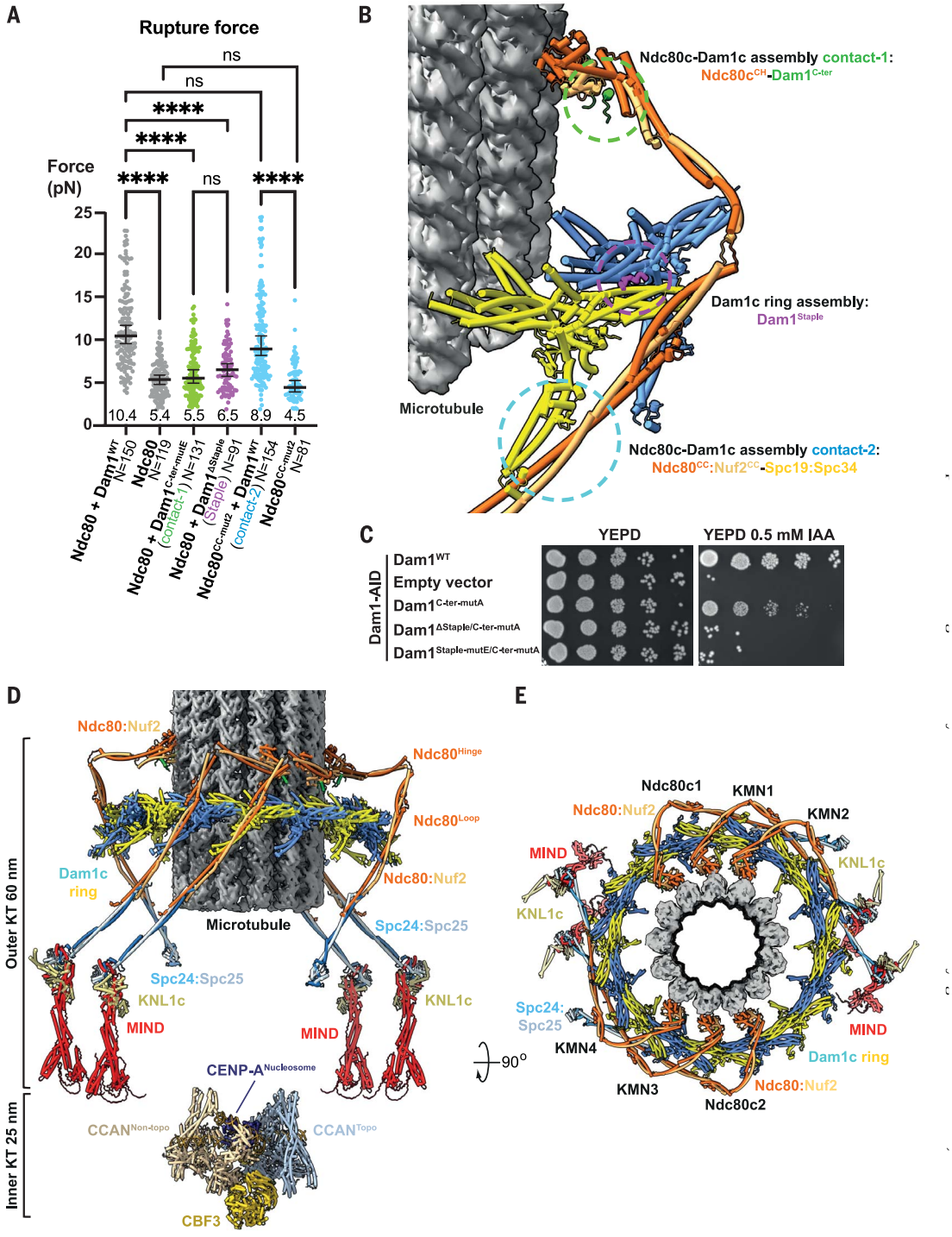

Fig. 4. Structural model for mitotic EC and chromosome segregation by the yeast kinetochore. (**A**) Force-rupture measurements of outer kinetochore–microtubule complexes. Each circle represents a single rupture event (the maximum trap force before rupturing). The total number of measurements for each condition are indicated with *N* values. The black bar represents the median rupture forces, with 95% confidence intervals (95% CIs). Numbers below the black bar indicate median values. A Kruskal-Wallis test to determine which medians are significantly different was performed. ****$P < 0.0001$; ns, not significant. Mutants of Dam1 and Ndc80 are defined in Fig. 2C and Fig. 3, D and H. WT, wild type. (**B**) Structure of an outer kinetochore$^{Dam1:Ndc80c}$ dimer bound to the microtubule. Outer kinetochore and Dam1c^{Ring} assembly contacts that are targeted by EC are highlighted. (**C**) Dam1 auxin-depletion assays. Cells grown on YEPD agar and YEPD agar that contained 0.5 mM IAA are shown for each strain. Dam1$^{C\text{-}ter\text{-}mutA}$, Dam1 mutant with I^{258}A, L^{259}A, and I^{262}A; Dam1$^{\Delta Staple/C\text{-}ter\text{-}mut\text{-}A}$, Dam1 mutant with residues 1 to 26 deleted, I^{258}A, L^{259}A, and I^{262}A; Dam1$^{Staple\text{-}mutE/C\text{-}ter\text{-}mut\text{-}A}$, Dam1 mutant with Y^{17}E, L^{19}E, I^{21}E, I^{258}A, L^{259}A, and I^{262}A. Simultaneous mutation of the Dam1 Staple (Dam1$^{\Delta Staple}$ and Dam1$^{Staple\text{-}mutE}$) and Dam1 C terminus (Dam1$^{C\text{-}ter\text{-}mutA}$) results in lethality. (**D**) Structural model of the complete yeast holo-kinetochore bound to a microtubule. Shown are the microtubule, Dam1c^{Ring}, four KMN network complexes, two Ndc80 complexes, and the CCAN inner kinetochore complex (composed of two CCAN promoters, CBF1, CBF3, and CENP-A nucleosome) (*49*). The flexible linkers connecting CCAN to the KMN network and Ndc80c are not shown. For clarity, shown are four of six possible KMN network complexes. The view is in plane with the microtubule helical axis. In this configuration, the end-to-end dimension of the kinetochore is ~85 nm, a value consistent with the relative location and separation of kinetochore components measured in metaphase yeast cells by using fluorescence localization microscopy (*52*, *62*). Shortening of the kinetochore as tension is reduced (*52*) could be facilitated through the flexible linkers connecting the inner kinetochore with MIND and Ndc80 complexes. KT, kinetochore. (**E**) Top view viewed from the microtubule minus end.

did not impair viability (Fig. 3H), which is consistent with in vitro observations that disruption of this interface by phosphorylation of Spc34 at Thr^{199} exerts a minor reduction in outer kinetochore–microtubule rupture forces (*10*). Indeed, our auxin-depletion experiments that disrupted the Dam1$^{C\text{-}ter}$-Ndc80c^{CH} interface (Fig. 3D) showed that the Ndc80c coiled coil–Spc34 interface is not sufficient for proper outer kinetochore function (*13*, *14*).

Disruption of outer kinetochore$^{Dam1c:Ndc80c}$ interfaces weakens microtubule attachments in vitro

The full load-bearing potential of the outer kinetochore and its ability to track dynamic

microtubule ends is dependent on co-assembly of Ndc80c and Dam1c (*10*–*17*, *33*). Disruption of coordinated binding to the microtubule is a central proposed mechanism for how EC regulates attachments (*10*–*13*, *15*, *16*, *33*–*35*, *46*).

In vitro optical trap experiments in which purified yeast kinetochores and reconstituted kinetochore-microtubule attachments are challenged have determined rupture forces of ~5 to 10 pN (*10*, *12*, *15*, *47*). To test the contribution that each of the interfaces in our structure makes to the ability of the outer kinetochore$^{Dam1c:Ndc80c}$ complex to withstand force, we purified a series of Dam1c and Ndc80c variants (fig. S1, F to I) and performed force-rupture assays (Fig. 4, A and B, and fig. S6) (*10*, *48*). We determined a median rupture force of 5.4 pN for Ndc80c alone that increased to 10.4 pN in the presence of Dam1c (Fig. 4A), which confirmed that the kinetochore$^{Dam1c:Ndc80c}$ complex withstands greater forces than does isolated Ndc80c (*10*, *12*, *15*). Mutation of the Dam1$^{C\text{-}ter}$ (Ndc80c^{CH} contact-1) and Dam1^{Staple} (ring assembly contact) substantially lowered the rupture forces to 5.5 pN and 6.5 pN, respectively. The Dam1$^{C\text{-}ter}$ mutant was not impaired in self-assembly (fig. S1I), consistent with (*5*); thus, it presumably acts by disrupting binding to Ndc80c^{CH}. By contrast, the Ndc80$^{CC\text{-}mut2}$ (Spc19:Spc34–Ndc80:Nuf2 coiled-coil contact-2) essentially had no effect on rupture strength when combined with Dam1c (Fig. 4, A and B). Hence, the mutation of outer kinetochore assembly through the Dam1$^{C\text{-}ter}$-Ndc80c^{CH} interface or disruption of Dam1c^{Ring} formation independently weakened microtubule binding. Our structural and biochemical results suggested that ablation of these functional elements of Dam1, targeted for inhibition by EC, would generate complexes that are unable to assemble rings, contact Ndc80c, or bear load (Fig. 4, A and B). To test whether concurrent disruption of these elements of Dam1c affected kinetochore function in vivo, we combined Dam1^{Staple} and Dam1$^{C\text{-}ter}$ mutants in our Dam1-AID strain (table S2). Mutagenesis of key Dam1$^{C\text{-}ter}$ residues to alanine (Dam1$^{C\text{-}ter\text{-}mutA}$) permitted weak growth that was completely abolished when the Dam1^{Staple} was deleted or mutated (Dam1$^{\Delta Staple}$ and Dam1$^{Staple\text{-}mutE}$, respectively) (Fig. 4C).

Consistent with EC driving attachment turnover by breaking outer kinetochore assembly, our force-rupture data correspond well to measurements of in vitro–reconstituted Dam1c phosphorylated at the respective interfaces by Aurora B (*10*, *12*, *15*), as well as for complexes that contained a phosphomimetic Dam1 Ser^{20}→Asp (S^{20}D) mutation (*12*, *34*). In addition, the severity of the force-rupture phenotypes correlated closely with the degree of viability defect caused by the corresponding mutants in cells. Mutagenesis of the interfaces identified in our structures likely caused reduced fitness in vivo because these cells form defective kinetochore-microtubule attachments that cannot support normal chromosome segregation.

Discussion

We consolidated previous structural findings and in vivo measurements of relative kinetochore subunit positions and stoichiometry with our outer kinetochore$^{Dam1c:Ndc80c}$ structure to generate a model for a yeast holo-kinetochore bound to a microtubule (Fig. 4, D and E). The inner kinetochore generates a total of eight Ndc80c linkages to the microtubule (*49*). These Ndc80c molecules are readily accommodated by the 16 binding sites of Dam1c^{Ring}, which is recruited through Ndc80c in a microtubule-dependent fashion (*50*). The flexible hinge between Ndc80c^{CH} and Ndc80^{Loop} (*51*) permits Ndc80 complexes to fold as hooks across the Dam1c^{Ring}, explaining how the coiled coils of Ndc80:Nuf2 dock in a parallel configuration across Spc19:Spc34 despite adherence of the Ndc80c^{CH} to the pseudohelical symmetry of the microtubule (*52*, *53*).

In budding yeast, several models for how EC detects attachment errors have gained prominence (*54*). Yeast EC is trifurcated among disruption of Dam1c^{Ring} assembly, disassembly of Dam1c-Ndc80c interfaces, and phosphorylation of Ndc80$^{N\text{-}tail}$ (*10*–*12*, *14*–*16*, *27*, *28*, *33*). Collectively, these inhibitory activities dismantle the Dam1c^{Ring} and dissolve kinetochore-microtubule attachments. We found that kinetochore$^{Dam1c:Ndc80c}$ assembly is mediated through multiple interfaces that are antagonized by EC, whereas Dam1c^{Ring} assembly is facilitated by a staple that contains an embedded EC target. In contrast to human Ndc80c, we did not observe inter-Ndc80c contacts, nor can we account for the flexible Ndc80$^{N\text{-}tail}$ (*43*, *55*). The Dam1, Ask1, and Spc34 subunits of Dam1c form a network of interactions between the Dam1c^{Ring} and Ndc80c that promote cooperative outer kinetochore assembly on the microtubule and are disrupted by EC (*10*, *11*, *13*, *14*). The region implicated in Ask1-Ndc80c binding is likely situated at the Ndc80c^{Hinge} and is too mobile to resolve in our cryo-EM maps (*11*). Our molecular models therefore account for two EC-sensitive contacts: the Dam1$^{C\text{-}ter}$-Ndc80c^{CH} and the Spc34–Ndc80:Nuf2^{CC} interfaces. At both, residues phosphorylated in EC would cause electrostatic and steric repulsion (Fig. 2B and Fig. 3, B and C), which explains how EC-mediated phosphorylation suppresses kinetochore$^{Dam1c:Ndc80c}$ assembly.

A fundamental paradox at the heart of EC is how initially weak, low-tension kinetochore attachments can escape rephosphorylation during attachment reset to form new connections to the microtubule. Ndc80c retains a degree of microtubule affinity even when Ndc80$^{N\text{-}tail}$ is either deleted (*14*, *56*) or incorporates EC phosphosites (*33*). However, it has remained unclear how Dam1c is reincorporated into the kinetochore if the Ndc80c-Dam1c interfaces are disrupted during EC. The major targets of phosphorylation that govern kinetochore$^{Dam1c:Ndc80c}$ assembly are within Dam1c (*10*, *11*, *27*, *28*). Achieving full attachment strength would thus require dephosphorylation and/or replacement of Dam1c. We propose that simple replacement of Dam1c by EC-mediated turnover would resolve the EC-reset paradox. After EC, kinetochores remain attached to the lateral face of the microtubule (*35*, *57*), and phosphorylated Dam1c diffuses away. However, Dam1c not associated with the kinetochore remains unphosphorylated (*29*) and is transported to the kinetochore by tracking microtubule plus ends. Unphosphorylated Dam1c then associates with Ndc80c to facilitate conversion from lateral to end-on attachment (*33*, *35*, *57*). This Ndc80c:Dam1c assembly could drive displacement of the outer kinetochore, which would render it resistant to the centromere-localized Aurora B kinase (*58*, *59*).

Two models posit how the mechanical energy of microtubule depolymerization is exploited by the kinetochore to segregate chromosomes: the conformational wave and biased diffusion. In the former, the curling protofilaments lever the kinetochore toward the spindle poles (*60*). In the biased diffusion model, an array of kinetochore attachments detaches and rebinds the tubulin lattice as it depolymerizes (*61*). Dam1c augments outer kinetochore tracking of both polymerizing and depolymerizing microtubule tips (*11*, *15*, *16*). Our findings support a model for kinetochore-mediated chromosome segregation wherein Dam1c^{Ring} acts as a topological sleeve that is pushed along by the curved protofilaments of the depolymerizing microtubule, driving Ndc80c translocation through steric occlusion. By generating multivalency through coordinating multiple Ndc80 complexes, Dam1c^{Ring} also enables biased diffusion. Association of outer kinetochore components through flexible peptidic interfaces mediates a tethering mechanism that prevents Ndc80c detaching from the microtubule when displaced by the advancing Dam1c^{Ring}, which thus pulls chromatids toward the spindle poles (*6*, *14*–*16*, *33*, *35*).

REFERENCES AND NOTES

1. A. D. McAinsh, A. L. Marston, *Annu. Rev. Genet.* **56**, 279–314 (2022).
2. J. J. van Hooff, E. Tromer, L. M. van Wijk, B. Snel, G. J. Kops, *EMBO Rep.* **18**, 1559–1571 (2017).
3. E. S. Fischer, *IUBMB Life* **75**, 289–310 (2023).
4. J. J. L. Miranda, P. De Wulf, P. K. Sorger, S. C. Harrison, *Nat. Struct. Mol. Biol.* **12**, 138–143 (2005).
5. S. Westermann *et al*., *Mol. Cell* **17**, 277–290 (2005).
6. S. Westermann *et al*., *Nature* **440**, 565–569 (2006).
7. H. W. Wang *et al*., *Nat. Struct. Mol. Biol.* **14**, 721–726 (2007).
8. V. H. Ramey *et al*., *Mol. Biol. Cell* **22**, 457–466 (2011).
9. C. T. Ng *et al*., *J. Cell Biol.* **218**, 455–473 (2019).
10. R. L. Flores *et al*., *J. Cell Biol.* **221**, e202107016 (2022).
11. J. O. Kim *et al*., *eLife* **6**, e21069 (2017).
12. N. T. Umbreit *et al*., *Nat. Commun.* **5**, 4951 (2014).
13. J. F. Tien *et al*., *Genetics* **195**, 159–170 (2013).
14. F. Lampert, C. Mieck, G. M. Alushin, E. Nogales, S. Westermann, *J. Cell Biol.* **200**, 21–30 (2013).
15. J. F. Tien *et al*., *J. Cell Biol.* **189**, 713–723 (2010).

16. F. Lampert, P. Hornung, S. Westermann, *J. Cell Biol.* **189**, 641–649 (2010).
17. D. R. Gestaut *et al*., *Nat. Cell Biol.* **10**, 407–414 (2008).
18. P. J. Huis in 't Veld, V. A. Volkov, I. D. Stender, A. Musacchio, M. Dogterom, *eLife* **8**, e49539 (2019).
19. L. A. Helgeson *et al*., *Proc. Natl. Acad. Sci. U.S.A.* **115**, 2740–2745 (2018).
20. S. Biggins *et al*., *Genes Dev.* **13**, 532–544 (1999).
21. T. U. Tanaka *et al*., *Cell* **108**, 317–329 (2002).
22. D. Cimini, B. Moree, J. C. Canman, E. D. Salmon, *J. Cell Sci.* **116**, 4213–4225 (2003).
23. S. Hauf *et al*., *J. Cell Biol.* **161**, 281–294 (2003).
24. S. Biggins, A. W. Murray, *Genes Dev.* **15**, 3118–3129 (2001).
25. K. F. DeLuca, S. M. Lens, J. G. DeLuca, *J. Cell Sci.* **124**, 622–634 (2011).
26. D. Cimini, X. Wan, C. B. Hirel, E. D. Salmon, *Curr. Biol.* **16**, 1711–1718 (2006).
27. C. Shang *et al*., *Mol. Biol. Cell* **14**, 3342–3355 (2003).
28. I. M. Cheeseman *et al*., *Cell* **111**, 163–172 (2002).
29. P. Keating, N. Rachidi, T. U. Tanaka, M. J. Stark, *J. Cell Sci.* **122**, 4375–4382 (2009).
30. H. Dewar, K. Tanaka, K. Nasmyth, T. U. Tanaka, *Nature* **428**, 93–97 (2004).
31. S. Mukherjee *et al*., *Dev. Cell* **49**, 63–76.e10 (2019).
32. A. Zelter *et al*., *Nat. Commun.* **6**, 8673 (2015).
33. H. Doodhi, T. Kasciukovic, L. Clayton, T. U. Tanaka, *J. Cell Biol.* **220**, e202011117 (2021).
34. K. K. Sarangapani, B. Akiyoshi, N. M. Duggan, S. Biggins, C. L. Asbury, *Proc. Natl. Acad. Sci. U.S.A.* **110**, 7282–7287 (2013).
35. M. Kalantzaki *et al*., *Nat. Cell Biol.* **17**, 421–433 (2015).
36. B. Akiyoshi, C. R. Nelson, J. A. Ranish, S. Biggins, *Genetics* **183**, 1591–1595 (2009).
37. T. Legal, J. Zou, A. Sochaj, J. Rappsilber, J. P. Welburn, *Open Biol.* **6**, 150237 (2016).
38. S. Jenni, S. C. Harrison, *Science* **360**, 552–558 (2018).
39. A. Gutierrez *et al*., *Curr. Biol.* **30**, 4491–4499.e5 (2020).
40. A. Dudziak *et al*., *EMBO J.* **40**, e108004 (2021).
41. M. A. B. Haase *et al*., *EMBO J.* **42**, e112600 (2023).
42. M. N. Clarke, T. Marsoner, M. A. Y. Adell, M. C. Ravichandran, C. S. Campbell, *EMBO J.* **42**, e111500 (2023).
43. G. M. Alushin *et al*., *Nature* **467**, 805–810 (2010).
44. E. M. Wilson-Kubalek, I. M. Cheeseman, R. A. Milligan, *Mol. Biol. Cell* **27**, 1197–1203 (2016).
45. J. A. Zahm, S. Jenni, S. C. Harrison, *Open Biol.* **13**, 220378 (2023).
46. K. K. Sarangapani, L. B. Koch, C. R. Nelson, C. L. Asbury, S. Biggins, *J. Cell Biol.* **220**, e202106130 (2021).
47. B. Akiyoshi *et al*., *Nature* **468**, 576–579 (2010).
48. C. L. Asbury, D. R. Gestaut, A. F. Powers, A. D. Franck, T. N. Davis, *Proc. Natl. Acad. Sci. U.S.A.* **103**, 9873–9878 (2006).
49. T. Dendooven *et al*., *Sci. Adv.* **9**, eadg7480 (2023).
50. Y. Li *et al*., *Genes Dev.* **16**, 183–197 (2002).
51. H. W. Wang *et al*., *J. Mol. Biol.* **383**, 894–903 (2008).
52. P. Aravamudhan, I. Felzer-Kim, K. Gurunathan, A. P. Joglekar, *Curr. Biol.* **24**, 1437–1446 (2014).
53. A. A. Kukreja, S. Kavuri, A. P. Joglekar, *Curr. Biol.* **30**, 4869–4881.e5 (2020).
54. A. J. Broad, J. G. DeLuca, *Essays Biochem.* **64**, 299–311 (2020).
55. G. M. Alushin *et al*., *Nat. Struct. Mol. Biol.* **19**, 1161–1167 (2012).
56. R. R. Wei, J. Al-Bassam, S. C. Harrison, *Nat. Struct. Mol. Biol.* **14**, 54–59 (2007).
57. K. Tanaka, E. Kitamura, Y. Kitamura, T. U. Tanaka, *J. Cell Biol.* **178**, 269–281 (2007).
58. L. J. García-Rodríguez, T. Kasciukovic, V. Denninger, T. U. Tanaka, *Curr. Biol.* **29**, 1536–1544.e4 (2019).
59. J. Fischböck-Halwachs *et al*., *eLife* **8**, e42879 (2019).
60. D. E. Koshland, T. J. Mitchison, M. W. Kirschner, *Nature* **331**, 499–504 (1988).
61. T. L. Hill, *Proc. Natl. Acad. Sci. U.S.A.* **82**, 4404–4408 (1985).
62. K. Cieslinski *et al*., *J. Cell Biol.* **222**, e202209094 (2023).

ACKNOWLEDGMENTS

We acknowledge Diamond Light Source for access and support of the cryo-EM facilities at the UK's national Electron Bio-imaging Centre (eBIC) (under proposal EM BI31336), funded by the Wellcome Trust, MRC, and BBRSC. We are grateful to the LMB EM facility for help with the EM data collection; to J. Grimmett, T. Darling, and I. Clayson for high-performance computing; and to J. Shi for help with insect cell expression, S. Chaaban for advice on microtubule cryo-EM, and V. J. Planelles Herrero for help with the optical tweezer study. We thank S. Yatskevich for discussions and N. Turner for comments on the manuscript. **Funding:** This study was supported by UKRI/Medical Research Council MC_UP_1201/6 (to D.B.) and Cancer Research UK C576/A14109 (to D.B.). **Author contributions:** Conceptualization: D.B. and K.W.M.; Methodology: K.W.M., C.B., T.D., J.Y., Z.Z., A.B., and D.B.; Investigation: K.W.M., C.B., T.D., J.Y., and Z.Z.; Visualization: K.W.M.; Funding acquisition: D.B.; Project administration: D.B. and K.W.M.; Writing – original draft: K.W.M.; Writing – review & editing: K.W.M., D.B., C.B., T.D., J.Y., Z.Z., and A.B. **Competing interests:** The authors declare that they have no competing interests. **Data and materials availability:** Atomic coordinates and cryo-EM density maps (also listed in table S1) have been deposited in the Protein Data Bank (www.rcsb.org) and the Electron Microscopy Data Bank (https://ebi.ac.uk/pdbe/emdb/): Ndc80c^{CH}–α/β tubulin–Dam1$^{C\text{-}ter}$ (PDB ID: 8QAU; map: EMD-18304), Dam1c protomer dimer–Ndc80^{CC}:Nuf2^{CC} (PDB ID: 8Q84; map: EMD-18246), Dam1c protomer monomer–Ndc80^{CC}:Nuf2^{CC} (PDB ID: 8Q85; map: EMD-18247), and Ndc80c-microtubule (map: EMD-18485). All other data are available in the main text or the supplementary materials. **License information:** Copyright © 2023 the authors, some rights reserved; exclusive licensee American Association for the Advancement of Science. No claim to original US government works. https://www.science.org/about/science-licenses-journal-article-reuse. This research was funded in whole by UKRI/Medical Research Council (MC_UP_1201/6) and Cancer Research UK (C576/A14109). The author will make the Author Accepted Manuscript (AAM) version available under a CC BY public copyright license.

SUPPLEMENTARY MATERIALS

science.org/doi/10.1126/science.adj8736
Materials and Methods
Figs. S1 to S6
Tables S1 to S3
References (*63*–*83*)
MDAR Reproducibility Checklist
Movie S1

Submitted 20 July 2023; accepted 25 October 2023
10.1126/science.adj8736

SEDIMENT LOADING

Watershed sediment cannot offset sea level rise in most US tidal wetlands

Scott H. Ensign[1]*, Joanne N. Halls[2], Erin K. Peck[3]

Watershed sediment can increase elevation of tidal wetlands struggling against rising seas, but where and how much watershed sediment helps is unknown. By combining contiguous US datasets on sediment loads and tidal wetland areas for 4972 rivers and their estuaries, we calculated that river sediment accretion will be insufficient to match sea level rise in 72% of cases because most watersheds are too small (median 21 square kilometers) to generate adequate sediment. Nearly half the tidal wetlands would require 10 times more river sediment to match sea level, a magnitude not generally achievable by dam removal in some regions. The realization that watershed sediment has little effect on most tidal wetland elevations shifts research priorities toward biological processes and coastal sediment dynamics that most influence elevation change.

Tidal wetlands are changing in location, extent, and type as sea level rises (*1*). Multidisciplinary efforts to predict these changes are working to inform management actions to help tidal wetlands offset sea level rise. One major focus is addressing how river-borne sediment contributes to tidal wetland elevation change under current (*2*) and future (*3*) climate and land use change, and how reservoir management (*4*) and dam removal (*5*) may augment coastal sediment loads. However, few near-coastal river gaging stations measure watershed sediment delivery directly to the coastal zone (*6*), and influential studies on the balance between river sediment flux and the tidal wetland area receiving that sediment have focused on very large rivers and their dams (*2*, *3*, *7*, *8*). This paucity of river sediment data and the bias of disciplinary discourse focusing on large rivers has, not unexpectedly, swayed studies on estuaries and tidal wetlands to frame hypotheses based on the patterns observed for large rivers and their tidal wetland deltas. Given that smaller rivers exponentially outnumber large rivers at the coast (*9*) and provide a large cumulative sediment load on active margins (*10*, *11*), a coast-wide accounting of all rivers' sediment fluxes and associated tidal wetland elevation change is needed to recenter expectations for the role rivers play in delivering sediment to tidal wetlands.

We addressed this need by assessing the extent to which contemporary river sediment load can offset the relative elevation loss of tidal wetlands occurring due to sea level rise across all rivers that drain to the contiguous US shoreline. We define this relationship as the accretion balance (i.e., the rate of vertical accretion on tidal wetlands due to river sediment minus a 2020 modeled rate of relative sea level rise: (*12*) for each cluster of tidal wetlands adjoining each estuary. Other wetland processes (organic matter production, compaction, subsidence, etc.) and non-riverine sediment sources were not included so that we could explore geographic patterns in the relationships between watershed size, river sediment delivery, and tidal wetland extent. Our intent was not to predict either an actual rate of tidal wetland sediment accretion or the future fate of a tidal wetland, but rather to describe the potential contribution of each river's sediment load to its adjoining tidal wetlands. Comparing our predictions for 93 tidal wetlands around the United States with previously repo… accretion rates led us to infer four categ… of tidal wetland condition with implications for research and management.

Regional differences in river sediment contribution to tidal wetland accretion

We developed a geospatial model (*13*, *14*) to predict the height that river-transported sediment could equate to if spread across tidal wetlands adjoining that river's estuary. The predicted annual sediment load for every river in the contiguous United States entering tidal waters with a watershed greater than 1 km^2 was derived from the US Geological Survey's SPAtially Referenced Regression On Watershed (SPARROW) attributes model; this load was converted to volume and distributed across tidal wetlands (as defined by the US Fish and Wildlife Service's National Wetland Inventory) adjoining that estuary. Estimated sediment load, tidal wetland area receiving this load, and bulk density of deposited river sediment affect uncertainty; we systematically increased the sediment load and underestimated tidal wetland area to intentionally overestimate the height of river sediment accretion (*13*). We did not adjust height downward to account for autocompaction or organic matter decay that would occur over time because our focus was merely a snapshot of annual change. Rivers and their estuaries were investigated at three spatial scales: (i) each tributary of an estuarine channel network, (ii) the aggregated estuarine network (as defined by the National Hydrography Dataset's

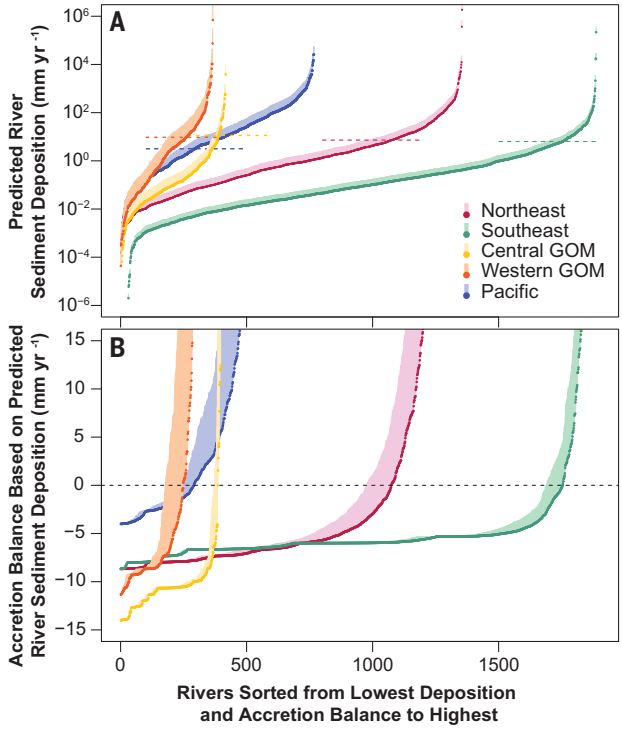

Fig. 1. Accretion and accretion balance of tidal wetlands adjoining 4972 rivers. (**A**) Accretion of river sediment on adjoining tidal wetlands (points) and SPARROW-derived sediment load regression uncertainty applied to each river's sediment load (lighter shaded bars extending upward from points). Dashed horizontal lines show the modeled 2020 rate of sea level rise for each region (*12*). (**B**) Values in (A) converted to accretion balance by subtracting the local rate of sea level rise. Both panels show the combination of terminal paths draining less than 21 km^2 and level paths draining more than 21 km^2 (*13*).

[1]Stroud Water Research Center, Avondale, PA 19311, USA. [2]Department of Earth and Ocean Sciences, University of North Carolina at Wilmington, Wilmington, NC 28403, USA. [3]University of Massachusetts Amherst, Amherst, MA 01003, USA.
*Corresponding author. Email: ensign@stroudcenter.org

level path and terminal path attributes, respectively), and (iii) a coast-wide scale spanning many terminal path estuaries.

The height of river sediment accretion ranged over 10 orders of magnitude, with rates in the Pacific and Western Gulf of Mexico generally higher than that of the Northeast, Southeast, and Central Gulf of Mexico (Fig. 1A); in these areas, accretion of river sediment lagged local sea level rise in at least 72, 90, and 89% of estuaries, respectively. By contrast, 48 and 69% of estuaries in the Western Gulf of Mexico and Pacific, respectively, could receive enough river sediment to offset sea level rise (Fig. 1B; all percentages reported throughout are based on the upper estimate of river sediment load represented by lighter shading in Fig. 1). These are likely overestimates of the potential accretion rate and subsequent accretion balance because we assumed all river-transported sediment was deposited on tidal wetlands (not subtidal areas) immediately adjoining the channel, and we modeled river sediment deposition along sub-estuaries without removing that sediment load from the supply available to the next sub-estuary downstream. Above and below ground organic matter production in tidal wetlands can generally add 3 mm yr^{-1} of elevation gain (*15*); adding this elevation to each of the results (Fig. 1B) only raised the percent of tidal wetlands capable of exhibiting positive accretion balance to 34, 14, 13, 52, and 91% in the Northeast, Southeast, Central Gulf of Mexico, Western Gulf of Mexico, and Pacific, respectively.

Small watersheds dominate the coast

Regional differences in river-transported sediment accretion and resulting accretion balance are a function of the distribution of watershed sizes, the effect of watershed size and sediment yield on sediment load, and wetland extent. Not unexpectedly (*9*), the distribution of watershed size is highly skewed toward very small watersheds (Fig. 2A identifies the 90th percentile; the median watershed sizes are 27, 7.5, 33, 12, and 25 km^2 in the Northeast, Southeast, Central Gulf of Mexico, Western Gulf of Mexico, and Pacific, respectively). These very small watersheds fringe the US coastline and their inclusion here sets the current study apart from previous continental-scale analyses of wetland condition that are limited to watersheds >50 km^2 (*16*), 100 km^2 (*17*), 10,000 km^2 (*18*), or 14,000 km^2 (*19*). The cause of regional differences in accretion balance (Fig. 1) becomes apparent when contrasting sediment loads with tidal wetland areas across regions (Fig. 2B). In all regions, the median sediment load of the smallest 90% of watersheds is several orders of magnitude less than the median of the largest 10% of watersheds. Thus, most US rivers are generally very small and their sediment loads too low to contribute a sediment volume to their tidal wetlands area that meaningfully affects elevation. If instead the tidal wetland area scaled in proportion with watershed size and corresponding sediment load, we would not have observed large deficits between wetland area and the sediment load required to offset sea level rise (dashed lines in Fig. 2B).

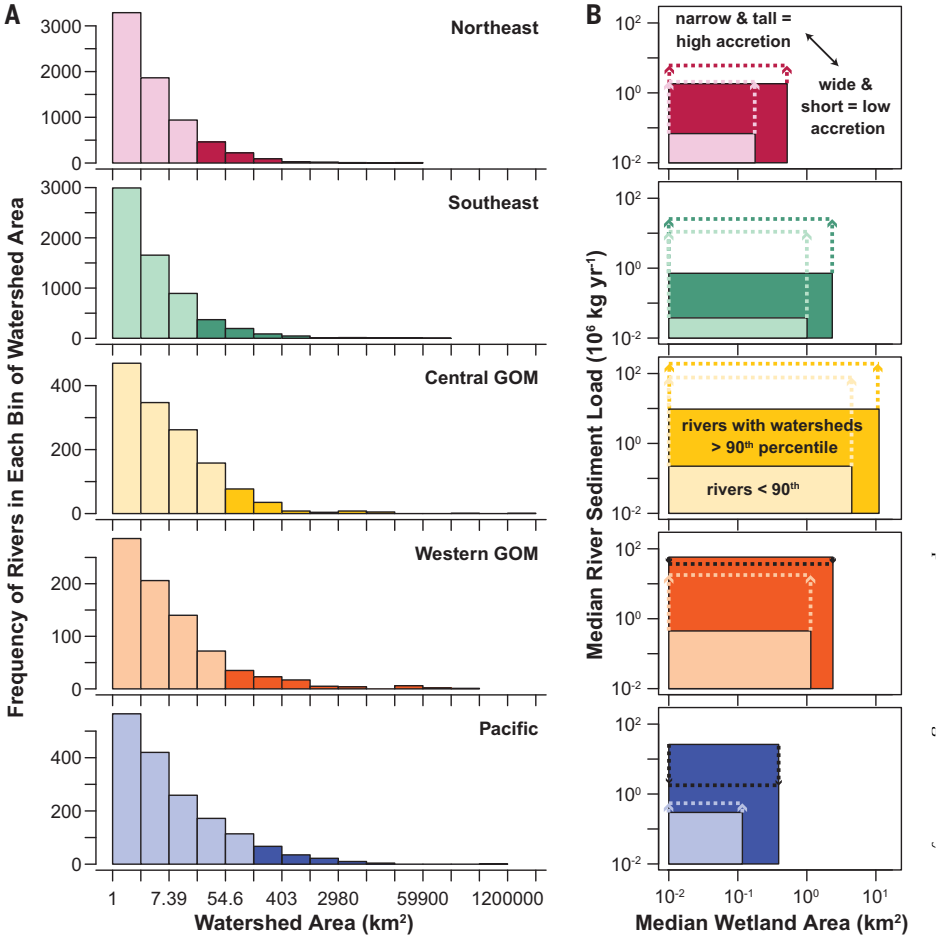

Fig. 2. The distribution of watershed size, sediment loads, and wetland area. (**A**) Histogram of watershed size at the coastline (according to the national hydrography dataset's level path attribute) with the largest 90th percentile noted by darker colors. (**B**) The median sediment load and tidal wetland area for rivers below and above the 90th percentile of watershed area; dashed lines indicate the river sediment load required to equal the regional rate of sea level rise on the median tidal wetland area shown. Narrow and tall bars indicate high accretion rates, with high sediment loads spread over a relatively small wetland area.

In addition to the fine-scale results presented in Figs. 1 and 2, we explored how coast-wide aggregate sediment loads could affect tidal wetlands (*13*). We assumed annual coast-wide mixing and homogenous distribution of river sediments, which may be realistic only for watersheds dominated by one or more large rivers. At this coarser scale of analysis we found that most areas on the East Coast had aggregate river sediment loads equating to accretion rates less than 3 mm yr^{-1} below local rates of sea level rise, whereas most coastal areas in the western Gulf of Mexico and Pacific coasts had aggregate river sediment loads capable of generating more than 3 mm yr^{-1} above sea level rise (Fig. 3).

The role of large river floods

Our analysis is based on average sediment loads from 1999 to 2014; therefore the influence of river floods of longer recurrence intervals are underrepresented in the results. Larger river floods may increase sediment delivery to estuaries, but watershed hydrology, geography, and estuarine morphology dictate the proportion that is trapped by coastal plain rivers before it reaches the estuary (*20*, *21*) versus how much is passed through to estuarine and offshore depocenters (*22*). This mixture of recently delivered river sediment and geologically older sediment derived from erosion of coastal landforms may be resuspended by tidal currents (especially where flood-dominant tidal asymmetry exists) (*23*, *24*), maintained within the turbidity maximum zone (*25*), and ultimately delivered to adjoining tidal wetlands.

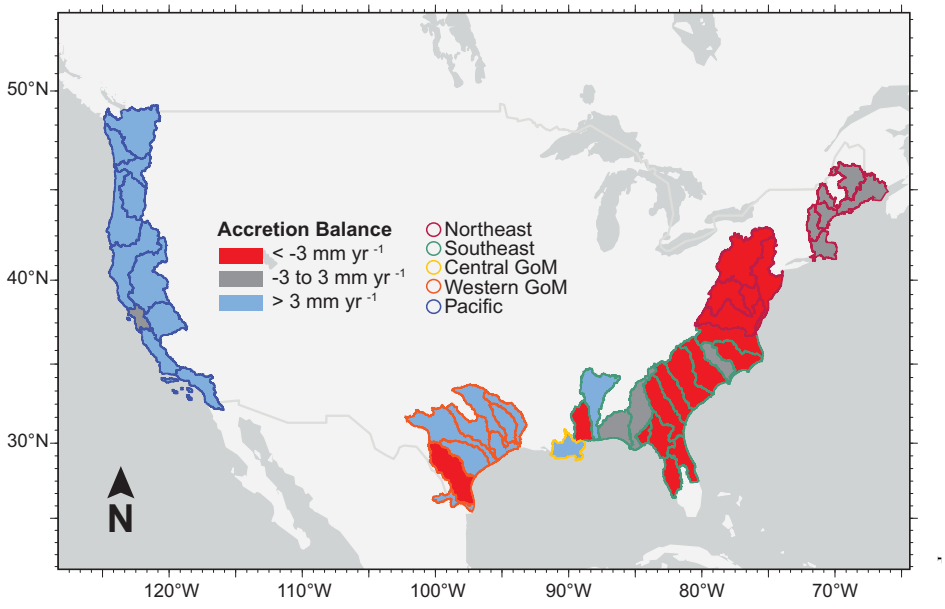

Fig. 3. Coast-wide accretion balance (accretion due to river sediment minus regional sea level rise) if all rivers' sediment subsidized regional tidal wetlands. If all river sediment within each Hydrologic Unit Code 4 boundary was dispersed evenly across all tidal wetland area, most areas in the Eastern United States and parts of the Gulf of Mexico would lag regional sea level rise by more than 3 mm yr^{-1} (3 mm yr^{-1} approximates how much wetland organic matter production could boost annual accretion). Some regions are omitted because appropriately scaled sediment load summary data were not available.

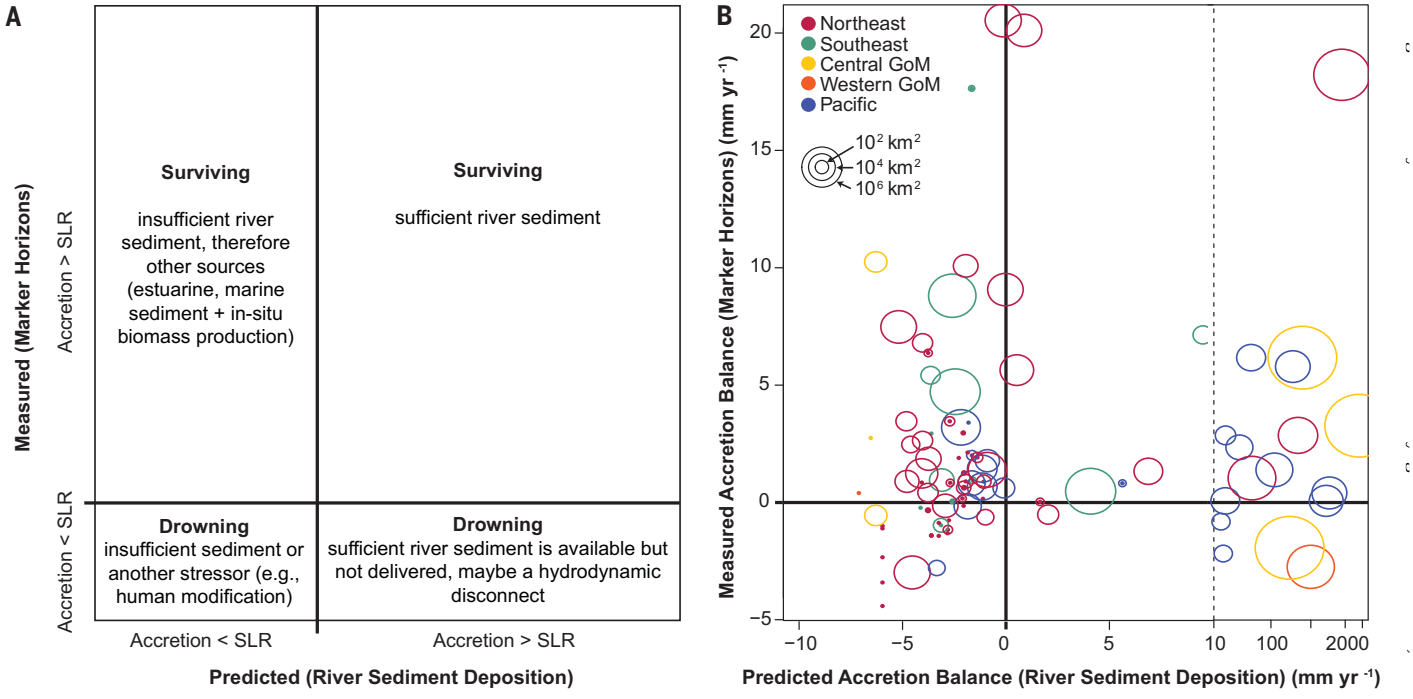

Fig. 4. Measured accretion balance of tidal wetlands versus predicted river-derived sediment accretion and sediment loads. (**A**) A conceptual parsing of potential relationships between river-derived sediment accretion and measured tidal wetland accretion with possible inferences. (**B**) Measured (from marker horizon measurements report in the literature) and predicted tidal wetland accretion balance. Circle size is proportional to watershed area; note break from linear to log-scale axis at 10 mm yr^{-1} on the horizontal axis.

Yet sediment delivery to estuaries from large watersheds (>10^3 km^2) and their coastal plain rivers during large floods may be lower than upstream measurements would suggest (*26*, *27*), in part because effects due to backwater slow and spread floodwater across broad coastal plains and enhance sediment deposition near the head of tide (*28*, *29*). Ultimately, the response of tidal wetlands to sea level rise over just the next decade will have considerable consequences on coastal habitats (*30*). Therefore, the exclusion of river floods with long recurrence intervals in our analysis may not necessarily affect our interpretation of the role of river sediment on tidal wetlands in the short term, particularly given the uncertainty in the magnitude of sediment actually delivered to estuaries during these events.

Inferring sediment dynamics from predicted versus observed accretion rates

We compared our predicted river sediment accretion balances with 93 marker horizon accretion measurements and their corresponding

accretion balances reported in the literature for tidal wetlands around the United States (in many cases averaged from multiple measurements at one site) (*13*). Given that our predictions account for river-supplied sediment—but not other factors affecting accretion balance—it was not expected that our predictions would correlate with observations. Instead, the intention with our comparison was to identify conditions indicative of sediment source and dynamics (Fig. 4A).

This analysis revealed that 22% of the measured-predicted pairs were both positive, indicating that river sediment delivered to these particular wetlands was capable of accounting for all of the measured accretion (upper right quadrant of Fig. 4B). In 23% of the pairs, both measured and modeled accretion balance were negative (lower left quadrant of Fig. 4B), suggesting that all sources of sediment were insufficient, and/or that compaction, diagenesis, or other processes are predominant. In 5% of the pairs, measured accretion balance was negative but modeled was positive, suggesting that river sediment supplies are sufficient but hydrodynamic processes prevent their delivery and accumulation on tidal wetlands and/or internal wetland processes such as compaction reduce wetland elevation. In 51% of the pairs, measured accretion balance was positive but modeled was negative (upper left quadrant of Fig. 4B), suggesting that another source of sediment besides modern river delivery of watershed sediment was required, such as near coastal sources (*31*) and marine sources (*32*), and/or that above and below ground autochthonous organic matter supply (*33*–*35*) is sufficient to offset sea level rise. River sediment load was not statistically related to tidal wetland sediment accretion (fig. S2; linear regression F statistic of 0.0079, 76 d.f., r^2 = −0.013, P = 0.929), as might be suspected from the high proportion of sites in the upper left quadrant of Fig. 4B. Unreasonably high predicted accretion balances are a result of our conservative modeling in which all river sediment is trapped on tidal wetlands, and in which tidal wetland area is often underrepresented in our model. We cannot be confident that these percentages represent the overall population of estuaries and tidal wetlands across the contiguous United States because the literature compiled (and those sites that are commonly studied) are not a random geographic selection of estuaries across all regions (*13*).

From the perspective of wetland research and habitat risk management, the inference that estuarine and marine sediment sources must help offset modern river sediment loads at these sites would warrant further focus on hydrodynamic factors affecting that sediment delivery and ecological factors affecting biomass production and decomposition (*33*–*35*). By contrast, habitat risk management for tidal wetlands that are drowning (Fig. 4B, lower right quadrant) could infer a physical or hydrodynamic impediment that prevents abundant river sediment from reaching tidal wetlands. This approach of parsing the influence of river sediment supply relative to measured accretion can help refine the research hypotheses addressed with other spatial (*36*) and conceptual (*37*) models of marsh dynamics.

The measurements of tidal wetland accretion and our predictions differ in their spatial scale: Measurements are specific to approximately one square meter whereas the modeled counterpart represents an entire grouping of tidal wetlands ranging in area from 0.1 to 100 km^2. This difference is most relevant to interpreting sites where spatial heterogeneity in sediment deposition may produce measurable positive accretion balance in some areas despite the overall negative condition for the mosaic of tidal wetlands (Fig. 4B, upper left quadrant). Given that most sites compared here share this condition and that wetland organic matter cannot drive all sites into positive accretion balance, we can infer that additional sediment sources and high spatial heterogeneity in tidal wetland accretion are common.

Discussion

River-borne sediment alone is insufficient to provide the needed elevation gain for tidal wetlands in most estuaries in the Northeast, Southeast, and parts of the Gulf of Mexico. Appreciation for this fact should reduce expectations for sediment connectivity between rivers and estuaries in the Eastern United States and instead focus attention on the hydrodynamic and ecological factors governing tidal wetland accretion. Although river sediment accretion is only one process of many contributing to tidal wetland elevation gain, our study reveals how minor a contribution this generally is. We attribute this pattern to the small size of most watersheds where they enter tidal waters, and the relatively small sediment loads produced as a result. Relative to the East Coast and eastern Gulf of Mexico, higher sediment yields, larger watershed sizes, and smaller areas of tidal wetlands in the western Gulf of Mexico and Pacific coasts generate greater potential for river-derived sediment accretion. These geographic patterns in the relationship between watershed size, river loads, and tidal wetland area have been previously recognized at local scales, but this is the first continent-wide examination of broader patterns in these relationships and their influence on estuaries and their tidal wetlands.

A frequent premise of coastal research (*22*, *38*) and a message in the popular science press (*39*) is that dams have reduced river sediment loads to the US coast and jeopardized tidal wetlands dependent on that river sediment. In reality, dam removal can enhance coastal sediment (*40*) and restore sediment conveyance across high gradient coastlines (*11*, *41*). Yet the effect of dams on a broader size range of rivers (most dams occur on small, not large rivers: (*42*) and resulting trends in coastal sediment delivery over time and space are not consistently negative (*43*–*46*). Our results show that at least 47% of rivers in the United States have river-derived accretion rates less than 0.5 mm yr^{-1}, and thus river sediment load would have to increase by at least one order of magnitude, not just single multiples, to appreciably affect tidal wetlands. For example, in the lower Hudson River valley sediment behind dams is roughly equal to 2 years of that region's sediment load (*5*). In the South Atlantic Bight, sediment interception by dams has decreased river loads by 55% (*47*), but care should be taken in translating these changes to the coast (*26*, *48*). At the broadest scale, North American rivers transport 19% less sediment to the coast than prior to human development (*49*). Therefore, dam removal—particularly on rivers crossing low gradient coastal plains on the Atlantic and Gulf of Mexico coastlines—may not ameliorate tidal wetlands threatened by sea level rise.

REFERENCES AND NOTES

1. N. Saintilan *et al*., *Science* **377**, 523–527 (2022).
2. E. N. Dethier, C. E. Renshaw, F. J. Magilligan, *Science* **376**, 1447–1452 (2022).
3. F. E. Dunn *et al*., *Environ. Res. Lett.* **14**, 084034 (2019).
4. G. P. Kemp, J. W. Day, J. D. Rogers, L. Giosan, N. Peyronnin, *Estuar. Coast. Shelf Sci.* **183**, 304–313 (2016).
5. D. K. Ralston, B. Yellen, J. D. Woodruff, *Estuaries Coasts* **44**, 1195–1215 (2021).
6. J. A. Warrick, J. D. Milliman, *Hydrol. Processes* **32**, 3561–3567 (2018).
7. J. P. M. Syvitski *et al*., *Nat. Geosci.* **2**, 681–686 (2009).
8. L. Giosan, J. Syvitski, S. Constantinescu, J. Day, *Nature* **516**, 31–33 (2014).
9. P. L. Guth, *Hydrol. Earth Syst. Sci.* **15**, 2091–2099 (2011).
10. J. D. Milliman, J. P. M. Syvitski, *J. Geol.* **100**, 525–544 (1992).
11. E. B. Watson, A. B. Gray, G. B. Pasternack, A. M. Woolfolk, *Cont. Shelf Res.* **182**, 1–11 (2019).
12. W. V. Sweet "Global and regional sea level rise scenarios for the United States: updated mean projections and extreme water level probabilities along U.S. Coastlines" (NOAA Technical Report NOS 01, 2022).
13. Materials and methods are available as supplementary materials.
14. J. N. Halls, S. H. Ensign, E. K. Peck, Sediment Pancakes: Riverine contributions to tidal wetland accretion in the contiguous United States (2023); https://tinyurl.com/SedimentPancake.
15. J. T. Morris *et al*., *Earths Futur.* **4**, 110–121 (2016).
16. J. H. Nienhuis *et al*., *Nature* **577**, 514–518 (2020).
17. J. P. M. Syvitski, C. J. Vörösmarty, A. J. Kettner, P. Green, *Science* **308**, 376–380 (2005).
18. D. E. Walling, D. Fang, *Global Planet. Change* **39**, 111–126 (2003).
19. S. Cohen, A. J. Kettner, J. P. M. Syvitski, B. M. Fekete, *Comput. Geosci.* **53**, 80–93 (2013).
20. J. D. Phillips, *Mar. Geol.* **98**, 121–134 (1991).
21. G. Noe, C. Hupp, *Ecosystems* **12**, 728–746 (2009).
22. A. B. Rodriguez, B. A. McKee, C. B. Miller, M. C. Bost, A. N. Atencio, *Nat. Commun.* **11**, 3249 (2020).
23. C. T. Friedrichs, D. G. Aubrey, *Estuar. Coast. Shelf Sci.* **27**, 521–545 (1988).
24. D. J. Nowacki, N. K. Ganju, *Geophys. Res. Lett.* **46**, 12250–12257 (2019).
25. H. Burchard, H. M. Schuttelaars, D. K. Ralston, *Annu. Rev. Mar. Sci.* **10**, 371–395 (2018).
26. D. E. Walling, *Geomorphology* **79**, 192–216 (2006).

27. M. C. Slattery, J. D. Phillips, *J. Environ. Manage.* **92**, 284–289 (2011).
28. S. L. Dykstra, B. Dzwonkowski, *Water Resour. Res.* **56**, e2019WR025743 (2020).
29. 1J. D. Phillips, *Earth Surf. Process. Landf.* **47**, 2044–2061 (2022).
30. L. Haaf *et al*., *Estuaries Coasts* **45**, 413–427 (2022).
31. R. J. Chant *et al*., *Estuaries Coasts* **44**, 608–626 (2021).
32. P. J. Mulholland, C. R. Olsen, *Estuar. Coast. Shelf Sci.* **34**, 95–107 (1992).
33. C. L. Stagg *et al*., *Ecosystems* **19**, 1445–1459 (2016).
34. R. E. Turner, E. M. Swenson, C. S. Milan, in *Concepts and Controversies in Tidal Marsh Ecology*, M. P. Weinstein, D. A. Kreeger, Eds. (Kluwer Academic Publishers, 2002), pp. 583–595.
35. S. C. Neubauer, *Estuar. Coast. Shelf Sci.* **78**, 78–88 (2008).
36. N. K. Ganju *et al*., *Nat. Commun.* **8**, 14156 (2017).
37. N. K. Ganju, N. J. Nidzieko, M. L. Kirwan, *J. Geophys. Res. Earth Surf.* **118**, 2045–2058 (2013).
38. M. Schuerch *et al*., *Nature* **561**, 231–234 (2018).
39. J. Robbins, Why the world's rivers are losing sediment and why it matters (Yale Environment 360, 2017); https://e360.yale.edu/features/why-the-worlds-rivers-are-losing-sediment-and-why-it-matters.
40. M. M. Foley *et al*., *Ecol. Monogr.* **87**, 552–577 (2017).
41. C. M. Willis, G. B. Griggs, *J. Geol.* **111**, 167–182 (2003).
42. J. R. Gardner, T. M. Pavelsky, M. W. Doyle, *Geophys. Res. Lett.* **46**, 2592–2601 (2019).
43. N. B. Weston, *Estuaries Coasts* **37**, 1–23 (2014).
44. G. P. Oelsner, E. G. Stets, *Sci. Total Environ.* **654**, 1225–1240 (2019).
45. J. C. Murphy, *Hydrol. Earth Syst. Sci.* **24**, 991–1010 (2020).
46. J. Gardner *et al*., *Environ. Res. Lett.* **18**, 064032 (2023).
47. K. McCarney-Castle, G. Voulgaris, A. J. Kettner, *J. Geol.* **118**, 399–416 (2010).
48. J. D. Phillips, M. C. Slattery, Z. A. Musselman, *Geomorphology* **62**, 17–34 (2004).
49. J. P. M. Syvitski, J. D. Milliman, *J. Geol.* **115**, 1–19 (2007).
50. S. Ensign, J. Halls, E. Peck, Regional deficiencies in river sediment supporting tidal wetlands in the US (HydroShare, 2023).
51. USGS, SPARROW Mappers (Water Resources Mission Area, 2020); https://www.usgs.gov/mission-areas/water-resources/science/sparrow-mappers.
52. USGS, NHDPlus High Resolution (National Hydrography, 2020); https://www.usgs.gov/national-hydrography/nhdplus-high-resolution.
53. NOAA, Sea Level Rise Data Download (NOAA, https://coast.noaa.gov/slrdata/).
54. NOAA, Data and Tools 2022 Sea Level Rise Technical Report, (NOAA, 2022); https://oceanservice.noaa.gov/hazards/sealevelrise/sealevelrise-data.html.
55. NOAA, Relative Sea Level Trends (NOAA Tides and Currents, 2023); https://tidesandcurrents.noaa.gov/sltrends/.

ACKNOWLEDGMENTS

We thank two preliminary reviewers and three anonymous reviewers for helpful feedback that improved the manuscript. **Funding:** This work was supported by the following: National Science Foundation Division of Earth Sciences grant 2049073 (S.H.E.). **Author contributions:** Conceptualization: S.H.E., J.N.H., E.K.P. Methodology: S.H.E., J.N.H., E.K.P. Visualization: S.H.E., J.N.H., E.K.P. Funding acquisition: S.H.E., Project administration: S.H.E. Writing – original draft: S.H.E. Writing – review and editing: S.H.E., J.N.H., E.K.P. **Competing interests:** Authors declare that they have no competing interests. **Data and materials availability:** All data produced and results described here are available in a HydroShare resource (*50*). River sediment loads were derived from the USGS SPARROW datasets (*51*). Hydrology and watershed size data were extracted from the NHDPlusHR datasets (*52*). Elevation and inundation data were extracted from NOAA's dataset (*53*). Current sea level rise estimates were extracted from the technical report data files (*54*) generated by Sweet *et al*. (*12*). Historic rates of sea level rise were extracted from NOAA's Tides & Currents website (*55*). **License information:** Copyright © 2023 the authors, some rights reserved; exclusive licensee American Association for the Advancement of Science. No claim to original US government works. https://www.sciencemag.org/about/science-licenses-journal-article-reuse

SUPPLEMENTARY MATERIALS

science.org/doi/10.1126/science.adj0513
Methods
Figs. S1 to S3
Tables S1 to S6
References (*56*–*79*)

Submitted 3 June 2023; accepted 16 October 2023
10.1126/science.adj0513

Post date 8 December 2

Erratum

Erratum for the Research Article "Ternary NiMo-Bi liquid alloy catalyst for efficient hydrogen production from methane pyrolysis" by L. Chen *et al.*

In the Research Article "Ternary NiMo-Bi liquid alloy catalyst for efficient hydrogen production from methane pyrolysis," fig. S8C has been revised to correct an error caused during data plotting. Some data points of conversion in fig. S8C (dashed line) were corrected. This revision does not affect the original interpretation of these data or the paper's conclusions.

10.1126/science.adm9972

WORKING LIFE

By **Theresa Mercer**

The support I needed

"I am so sorry," I tearfully said to my principal investigator (PI), explaining I would not be able to return from my maternity leave as originally planned. Before I became a parent, I had naïvely assumed a baby would fit right into my academic plans. But now, as the end of my leave loomed, I realized I couldn't simply carry on as I always had. For one, I had moved to the other side of the country to be with my husband, who held a tenured position. I had originally thought we would be able to establish a routine that was compatible with commuting, but now I saw that wasn't going to be realistic or sustainable. I also wanted some time to just be a mum. I didn't want to leave science forever, and I worried this decision might signal the end of my academic career—but I felt I had no other choice.

Thankfully, my PI had more foresight. He told me I didn't need to resign and that he could offer me a contract that would allow me to contribute to our project from afar. It proved to be an absolute career lifeline for me. I was able to maintain my academic affiliation, keep the papers bubbling away, attend meetings, read journal articles, and keep up to date with developments in my field—all around nap times and, later, nursery hours. Thanks to regular check-ins and invitations to meetings, I never felt like an outsider. Over the years, the PI and project manager hosted me for visits back to campus (often with baby in tow), offered me their desks for nappy changes, provided empathy as I went through a miscarriage, and continued my contract when I took my second maternity leave.

"Thanks to regular check-ins and invitations to meetings, I never felt like an outsider."

Five years after stepping back from academia, I felt ready to re-enter more fully. Because I had been able to keep my hand in during my time away, the prospect was much less daunting than it would have been otherwise. My confidence was reasonably intact, and my credentials and commitment to my field of work were clear to potential employers. I ended up landing a lecturer position that allowed me to slowly ease back in, focusing on teaching and scholarship with research taking a back seat. Going back to full-time work was certainly an adjustment, but ultimately just as reinvigorating and stimulating as I had hoped. And when, 4 years on, a senior lectureship position came up in the very group I had left a decade earlier, the timing was right. With both of my children in "big school," I was ready to really put my foot down on the career accelerator. I got the job, thanks in no small part to the experience I was able to accrue during my extended leave and my teaching-focused post.

Now, 6 months into my new role, I am happy to be right where it all began, with a supportive network and opportunities to get involved in so many interesting projects. I realize that while I was away I didn't stay as up to speed as many of my colleagues who continued full time in research, and I am navigating a very changed research landscape. Back in my day, we were still using paper maps to get to field sites! Thankfully, my manager fosters a safe space to explore and make mistakes. He also values and models work-life balance, including offering flexible work options and respecting family commitments and priorities. I couldn't ask for a better work environment, where the attitudes that made it possible for me to stay in science years ago are still part of the culture.

Over the years I have seen an increase in schemes designed to support those of us who return to academia after taking time away to start a family or care for relatives. These are certainly useful springboards. But what truly made the difference for me was support *during* that time away. I hope more institutions and PIs can come up with creative provisions for those in their workforce who don't want to give up their careers but want—or need—to take extended periods of leave. And to those who are taking such breaks, or considering it, know that returning is possible. Above all, on both sides: Please do not discount extended leavers. We have a lot to offer—if we are given the chance. ■

Theresa Mercer is a senior lecturer and program director at Cranfield University. Send your career story to SciCareerEditor@aaas.org.